

Scouring The Potential Of Novel Poylpyridine Vanadium(II,III) and Nickel(II) Complexes

Modelling, Synthesis And Characterization

Dissertation zur Erlangung des Grades
„Doktor der Naturwissenschaften“
im Promotionsfach Chemie

am Fachbereich Chemie, Pharmazie, Geographie
und Geowissenschaften
der Johannes Gutenberg-Universität Mainz

vorgelegt von
Matthias Dorn

geboren in Weilburg a. d. Lahn

Mainz, 2022

Die vorliegende Arbeit wurde im Zeitraum zwischen Oktober 2017 und August 2022 unter Anleitung von [REDACTED] am Department Chemie der Johannes Gutenberg-Universität Mainz angefertigt.

Mainz, Oktober 2022

Dekan*in: Prof. Dr. Tanja Schirmeister

1. Gutachter*in: [REDACTED]

2. Gutachter*in: [REDACTED]

Tag der mündlichen Prüfung: _____

Ich, Matthias Dorn, versichere, dass ich diese Promotionsarbeit selbstständig verfasst und keine anderen als die angegebenen schriftlichen und elektronischen Quellen genutzt habe. Alle Ausführungen, die anderen Schriften wörtlich oder sinngemäß entnommen wurden, habe ich kenntlich gemacht.

Datum: _____

Unterschrift: _____

Kurzzusammenfassung

3d-Übergangsmetallkomplexe mit den Elektronenkonfigurationen d^2 , d^3 , d^4 und d^8 verfügen über niederenergetische metallzentrierte angeregte Zustände, aus denen Phosphoreszenz möglich ist. Sie eignen sich hervorragend zur Entwicklung neuer künstlicher Phosphore. Im Prinzip ist Phosphoreszenz aus solchen Zuständen von tiefkalten Vanadium(III)-Verbindungen zwar bekannt, bislang konnte aber noch kein Vanadium(III)-Komplex hergestellt werden, der Phosphoreszenz bei Raumtemperatur zeigt. Im Falle von molekularen Vanadium(II)- und Nickel(II)-Verbindungen wurde bislang noch keine Phosphoreszenz beobachtet.

Im ersten Teil dieser Arbeit wird die Synthese und Charakterisierung eines bis-tridentaten homoleptischen Polypyridinvanadium(III)-Komplex $[V(\text{ddpd})_2]^{3+}$ beschrieben, der als erster Vanadium(III)-Komplex überhaupt auch bei Raumtemperatur phosphoresziert. Transiente Absorptionsspektroskopie, Lumineszenzspektroskopie und theoretische Berechnungen ergeben, dass die niedrige Phosphoreszenzquantenausbeute auf schnelle strahlungslose Relaxationsprozesse und ein langsames Intersystem crossing in die Singulettzustände zurückzuführen ist. Lebensdauermessungen am perdeuterierten Analogen des Komplexes lassen den Schluss zu, dass Energieübertrag auf C–H-Schwingungsobertöne für die Depopulation der emissiven Zustände eine untergeordnete Rolle spielt.

Zusätzlich wird mit $VCl_3(\text{ddpd})$ ein neuer heteroleptischer Komplex hergestellt und untersucht, der die starke Ligandenfeldaufspaltung des Polypyridinliganden mit der vergleichsweise hohen Spin-Bahn-Kopplungskonstante der Chloridoliganden vereint, um eine effektivere Bevölkering der emissiven Singulettzustände zu erreichen. Daneben sollte die reduzierte Symmetrie das Laporte-Verbot aufweichen und die Phosphoreszenz beschleunigen. Tatsächlich zeigt auch dieser Komplex die gewünschte Nahinfrarot-Phosphoreszenz bei Photoanregung im Festkörper und in Lösung. Ein prominenter strahlungsloser Prozess in diesem Komplex ist Energietransfer auf C–H-Schwingungsobertöne, der experimentell belegt werden konnte. Die Aufspaltung des Grundzustandes, die die strahlungslose Relaxation im Vergleich zu Komplexen mit nicht-entartetem Grundzustand weiter beschleunigt, wird theoretisch berechnet und experimentell bestätigt. Eine signifikante Steigerung der Phosphoreszenzquantenausbeute kann aber nicht erreicht werden. Photolyseexperimente in Kombination mit dichtefunktionaltheoretischen Berechnungen geben Aufschluss über die Reaktivität von $^3(\text{Ligand-zu-Metall})\text{-Charge-Transfer-Zuständen}$ des Komplexes und unterstreichen deren Bedeutung für das Design zukünftiger Vanadium- NIR-Phosphore.

Der zweite Teil befasst sich mit der Synthese und Charakterisierung zweier Isomere des neuen Polypyridinvanadium(II)-Komplexes $[V(\text{ddpd})_2]^{2+}$. In diesen Komplexen mischen $^2(\text{Metall-zu-Ligand})\text{-Charge-Transfer-Zustände}$ mit den niederenergetischen metallzentrierten Dublettzuständen, sodass Relaxation nur strahlungslos erfolgt. Die Isomere zeigen in ESR (Elektronenspinresonanz)-Experimenten eine langsame Spin-Gitter-Relaxation in Verbindung mit einer Phasenspeicherzeit, die die Eignung von Vanadium(II)-Komplexen zur Entwicklung molekularer Quantenbits nahelegt. Für das *mer*-Isomer kann außerdem eine langsame magnetische Relaxation festgestellt werden.

Die Herstellung eines Polypyridinnickel(II)-Komplexes $[\text{Ni}(\text{ddpd})_2]^{2+}$ und dessen Charakterisierung mittels optischer Spektroskopie und CAS-SCF-Rechnungen ist Gegenstand des dritten Teils der Arbeit. Die Untersuchungen ergeben im Gegensatz zu den Vanadiumkomplexen eine zu geringe Ligandenfeldaufspaltung, um die potentiell emissiven Singulettzustände und die Interkonfigurationszustände zu entflechten.

Abstract

3d transition metal complexes with the electron configurations d^2 , d^3 , d^4 and d^8 command low-energy metal centred states from which phosphorescence emission is conceivable. Therefore, they are an interesting subject in the development of novel artificial phosphors. Phosphorescence from vanadium(III) systems at cryogenic temperatures has been observed before in some cases, but to date, there are no vanadium(III) complexes capable of room temperature phosphorescence. In the case of molecular vanadium(II) and nickel(II) complexes, no phosphorescence has been observed to this date.

In the first part of this work, the synthesis and characterization of a homoleptic bis-tridentate polypyridine vanadium(III) complex $[V(\text{ddpd})_2]^{3+}$ are described, which is the first vanadium(III) complex to display room temperature phosphorescence. Transient absorption spectroscopy, luminescence spectroscopy and quantum-chemical calculations show that the low phosphorescence quantum yield is due to ultrafast non-radiative relaxation and slow intersystem crossing to the emissive singlet states. Luminescence lifetime measurements of the perdeuterated analogue evidence that energy transfer onto C–H vibrational overtones does not play a major role in the depopulation of the emissive states.

With $VCl_3(\text{ddpd})$, an additional novel heteroleptic complex is prepared and investigated, which combines the strong ligand field splitting with the high spin-orbit coupling constant of chlorido ligands to enhance intersystem crossing to the emissive singlet states. Its lower symmetry should also soften Laporte's rule to increase the radiative rate constant of the singlet states. Indeed, the complex displays the desired near-infrared (NIR) phosphorescence upon photoexcitation. A prominent non-radiative process in this complex is energy transfer to overtones of C–H vibrations, which could be verified experimentally. The ground state splitting, which may further accelerate non-radiative decay compared to complexes with a non-degenerate ground state, is calculated and experimentally confirmed. A significant improvement of the phosphorescence quantum yield cannot be achieved, however. Photolysis experiments together with density-functional theoretic calculations give insight into the reactivity of $^3(\text{ligand-to-metal})$ charge transfer states of the complex and underline their importance for the future design of vanadium NIR phosphors.

The second part takes issue with the synthesis and characterization two isomers of a novel polypyridine vanadium(II) complex $[V(\text{ddpd})_2]^{2+}$. In both complexes, $^2(\text{metal-to-ligand})$ charge transfer states mix with the low-energy metal centred doublet states. As a result, relaxation occurs exclusively non-radiatively. Both isomers display a slow spin-lattice relaxation and a high phase memory time in EPR (electron paramagnetic resonance) experiments, which suggests vanadium(II) complexes for the development of molecular qubits. In addition, slow magnetic relaxation in the *mer* isomer is asserted.

The synthesis of a polypyridine nickel(II) complex $[Ni(\text{ddpd})_2]^{2+}$ and its characterization by means of optical spectroscopy and CAS-SCF calculations is in the third part of this work. The investigation reveals a weak ligand field splitting that is insufficient to disentangle the

potentially emissive singlet states from metal-centred intraconfigurational states, contrary to the situation in the vanadium systems.

Table of Contents

Table of Contents.....	V
Abbreviations and Physical Quantities.....	VII
1. Introduction	1
1.1. <i>Excited State Decay Mechanisms.....</i>	3
1.1.1. Fluorescence and Phosphorescence	3
1.1.2. Energy Transfer	5
1.1.3. Dexter-type Electron Transfer	7
1.1.4. Intersystem Crossing Mechanisms.....	8
1.2. <i>Luminescence from 3d Transition Metal Complexes.....</i>	11
1.2.1. Spin-Flip Luminescence	12
1.2.2. Efficiency of Spin-Flip Luminescence.....	14
1.3. <i>New Spin-Flip Luminophores.....</i>	22
1.3.1. d ³ Vanadium(II)	22
1.3.2. d ² Vanadium(III)	23
1.3.3. d ⁸ -Nickel(II).....	25
1.4. <i>Application of Spin Flip Luminophores</i>	27
1.5. <i>Paramagnetic Ground States</i>	28
1.5.1. Single Molecule Magnets	28
1.5.2. Quantum bits	31
1.6. <i>Synthesis of Vanadium(II/III) and Nickel(II) Complexes.....</i>	34
2. Aim of this Work	39
3. Results and discussion	41
3.1. <i>A Vanadium(III) Complex with Blue and NIR-II Spin-Flip Luminescence in Solution.....</i>	43
3.2. <i>Ultrafast and long-time excited state kinetics of an NIR-emissive vanadium(III) complex I: Synthesis, spectroscopy and static quantum chemistry.....</i>	53
3.3. <i>Towards Luminescent Vanadium Complexes with Slow Magnetic Relaxation and Quantum Coherence</i>	65
3.4. <i>Structure and Electronic Properties of an Expanded Terpyridine Complex of Nickel(II) [Ni(ddpd)₂](BF₄)₂.....</i>	79
4. Summary and Outlook.....	87
5. References.....	91
6. Appendix	99
6.1. <i>Supporting Information to Chapter 3.1. („A Vanadium(III) Complex with Blue and NIR-II Spin-Flip Luminescence in Solution“)</i>	99
6.2. <i>Supporting Information to Chapter 3.2. (“Ultrafast and long-time excited state kinetics of an NIR-emissive vanadium(III) complex I: Synthesis, spectroscopy and static quantum chemistry“).....</i>	133

Table of Contents

6.3. Supporting Information to Chapter 3.3. (“Towards luminescent vanadium(II) complexes with slow magnetic relaxation”)	155
6.4 Supporting Information to Chapter 3.4 („Structure and Electronic Properties of an Expanded Terpyridine Complex of Nickel(II) [Ni(ddpd) ₂](BF ₄) ₂ ”)	219
7. Acknowledgements	224
8. Curriculum Vitae	225

Abbreviations and Physical Quantities

(Ph)OLED	(Phosphorescent) organic light-emitting diode
\hat{H}	Hamiltonian
$ M(Q_0) $	Transition dipole moment
S_M	Huang-Rhys factor
H_{ab}^2	Electronic coupling matrix element
N_A	Avogadro constant
k_B	Boltzmann constant
k_F	Fluorescence rate constant
k_{IC}	Internal conversion rate constant
k_{ISC}	Intersystem-crossing rate constant
k_P	Phosphorescence rate constant
k_{VR}	Rate constant of vibrational relaxation
k_{nr}	Rate constant of non-radiative decay
λ_s	Solvent reorganization energy
ϵ_0	Permittivity of the vacuum
Abs.	Absorption
B, C	Racah parameters
D, E	Zero-field splitting parameters
bISC	Back intersystem crossing
bpmp	2,6-bis(2-pyridylmethyl)pyridine
bpy	2,2'-bipyridine
CT	Charge transfer
ddpd	<i>N,N'</i> -dimethyl- <i>N,N'</i> -dipyridin-2-ylpyridine-2,6-diamine
dpc⁻	3,6-di-tert-butyl-1,8-di(pyridine-2-yl)-carbazolato
dqp	2,6-di(quinolin-8-yl)pyridine
DSSC	Dye-sensitized solar cell
E	Energy
en	1,2-ethylene diamine

Abbreviations and Physical Quantities

(HF)EPR	(High Field) Electron paramagnetic resonance
ES	Excited state
FCWD	Franck-Condon weighed density
GS	Ground state
H₂tpda	2,6-bis(2-pyridylamino)pyridine
IC	Internal conversion
ILCT	Intra-ligand charge transfer
ISC	Intersystem crossing
LC	Ligand-centered
LEC	Light-emitting electrochemical cell
LF	Ligand field
LFS (Δ_0)	Ligand field splitting
LLCT	Ligand-to-ligand charge transfer
LMCT	Ligand-to-metal charge transfer
MC	Metal-centered
MLCT	Metal-to-ligand-charge-transfer
MO	Molecular Orbital
NIR	Near-infrared
PES	Potential energy surface
phen	1,10-phenanthroline
ppy	Anion of 2-phenylpyridine
sen	4,4',4''-ethylidenetrakis(3-azabutane-1-amine)
SF	Spin-flip
SOC(ME)	Spin-orbit coupling (matrix element)
SOI	Spectral overlap integral
TADF	Thermally activated delayed fluorescence
TMC	Transition metal complex
tpe	1,1,1-tris(pyrid-2-yl)ethane
tpm	tris(2-pyridyl)methane

tpy	2,6-bis(2-pyridyl)pyridine
TS	Tanabe-Sugano
VR	Vibrational relaxation
η	Refractive index
Φ	Quantum yield
τ	Lifetime
T	Temperature
k	Orientation factor
n	Refractive index
ζ	Spin-orbit coupling constant
ZFS	Zero-field splitting

1. Introduction

Artificial lighting is one of the most fundamental achievements of mankind. Since Edison's invention of the light bulb in 1879, artificial lighting has greatly depended on the availability of electricity. In 2017, three quarters of the electricity generated worldwide was produced through fossil fuel combustion, and this type of combustion accounted for roughly two-thirds of global greenhouse gas emissions¹ including gasses such as carbon dioxide and methane.² The detrimental consequences of climate change are felt around the globe.³⁻⁵ Hence, one of the most pressing issues of our time is the transition from a fossil fuel-powered economy to one drawing power from renewable energy sources. An environmental-friendly and sustainable solution to this problem is the utilization of sunlight.

As a result, more and more attention was given to the development of dye-sensitized solar cells (DSSCs), innovative photocatalysis protocols, (phosphorescent) organic light-emitting diodes (OLEDs and PhOLEDs) as energy-saving lighting sources and to photochemical reactions which convert solar energy into chemical energy. Transition metal complexes (TMCs) are an important piece in this puzzle. A few outstanding examples will be provided which illustrate the applicability of TMCs in the context of solar energy conversion, artificial lighting and display technology.

Ruthenium complexes, for example, have been successfully employed as sensitizers in DSSCs, as they absorb light across the visible spectrum, have good electrochemical stability and possess advantageous excited state lifetimes⁶. Several TMC-based dyes have achieved conversion efficiencies of up to 13 %^{7,8} in the past, including the famous N3 dye developed by O'Reagan and Grätzel in 1991⁹. PhOLEDs typically rely on ruthenium, iridium, platinum or osmium as emissive centres^{10,11}. While OLEDs statistically convert only one out of four excitons into a photon^{10,12}, the heavy elements in PhOLEDs enable conversion efficiencies up to 100 % as both singlet and triplet excitons can be harvested. An interesting alternative to PhOLEDs and OLEDs are light-emitting electrochemical cells (LECs) given the easier manufacturing process¹³. But similarly, the most efficient TMC dyes applied in LECs are iridium(III) complexes¹⁴. The share of these precious metals in earth's crust is only very minor with abundancies of 10^{-6} to 10^{-7} mass percent¹⁵. Considering both the increasing demand for optoelectronics and the relatively small stocks of precious metals worldwide, it is evident that the demand cannot be met if we rely solely on precious metals.

First row transition metal elements are promising candidates for the development of novel artificial phosphors. Compared to their heavier homologues, they are highly abundant and more affordable. Iron complexes have garnered a lot of interest as potential charge-transfer (CT) luminophores and accordingly, a tremendous amount of work has been dedicated to the topic.¹⁶⁻²⁹ Yet only very few of the many complexes prepared exhibit the desired luminescence with quantum yields of up to 2 %.³⁰⁻³³

Introduction

In contrast, first row transition metal ions with the electron configurations d^2 , d^3 , d^4 and d^8 , offer low-energy metal-centred excited states which can be phosphorescent. Chromium(III) takes a special position among them. Its ability to emit near-infrared (NIR) radiation from these so-called spin-flip states has been utilized with the development of the first ruby laser in 1960 by Theodore H. Maiman.³⁴ The historical research efforts made in the past have generated a profound understanding of the photophysics and photochemistry of chromium(III) complexes,^{17,35–37} meaning that broader application of molecular chromium(III) systems in photocatalysis, optical signal transduction, bioimaging or sensing can be realized.

Vanadium(II) and vanadium(III) complexes are also theoretically capable of this type of emission. However, only a small number of publications take issue with the photophysical traits of $V^{II/III}$ complexes^{38–43} and these few luminescent systems studied are mostly solids.^{44–51} Most likely, the sensitivity of vanadium ions in low oxidation states towards hydrolysis and subsequent oxidation, as well as the propensity of vanadium(III) to disproportionate have contributed to this. Octahedral nickel(II) complexes are generally not as sensitive towards oxidation and, like vanadium(III) complexes, feature a triplet ground state and low-energy singlet excited states. Hence, NIR emission from nickel(II) complexes is also conceivable, but has yet to be realized as a sufficiently strong ligand field to enforce the necessary ordering of electronic states has not been achieved so far. Exploring the potential of vanadium(II/III) and nickel(II) complexes for spin-flip (SF) luminescence is therefore a challenging but promising objective.

This thesis will therefore look to explore various vanadium systems in low oxidation states, namely +II and +III, with regard to their photophysical properties and more specifically their luminescence. A secondary goal is the study of an analogous nickel(II) complex and its photophysical properties. The following sections will provide the necessary theoretical background, beginning with a summary on luminescence and competing relaxation pathways (section 2). Section 3 opens with general considerations and an overview on the types of luminescence originating from transition metal complexes, highlights spin-flip (SF) emission and elaborates on the factors that govern it. In section 4, a short description of possible applications of SF emitters is given. Lastly, state-of-the-art research on potential alternatives to chromium(III) is presented in section 5.

1.1. Excited State Decay Mechanisms

Luminescence is one of many possible energy dissipation mechanisms of TMCs in excited states. To understand why certain TMCs are non-luminescent and to figure out how they can be modified to ‘turn on’ emission, one needs to understand the processes by which excited states are populated and de-populated. This section provides an overview on the (photo-) physical processes leading to emission and competing non-radiative decay channels.

1.1.1. Fluorescence and Phosphorescence

For luminescence to occur, a luminophore in its electronic ground state (GS) must first be converted into an electronically excited state (ES). This is typically achieved by irradiating ultraviolet or visible light which is absorbed by the luminophore, populating an ES. The most common photophysical processes that follow irradiation of a transition metal complex (TMC) are summarized in the Jablonski diagram below (Fig.1) for a d^2 TMC with a triplet ground state (3GS) as is the case in vanadium(III).⁵² Following initial population of the

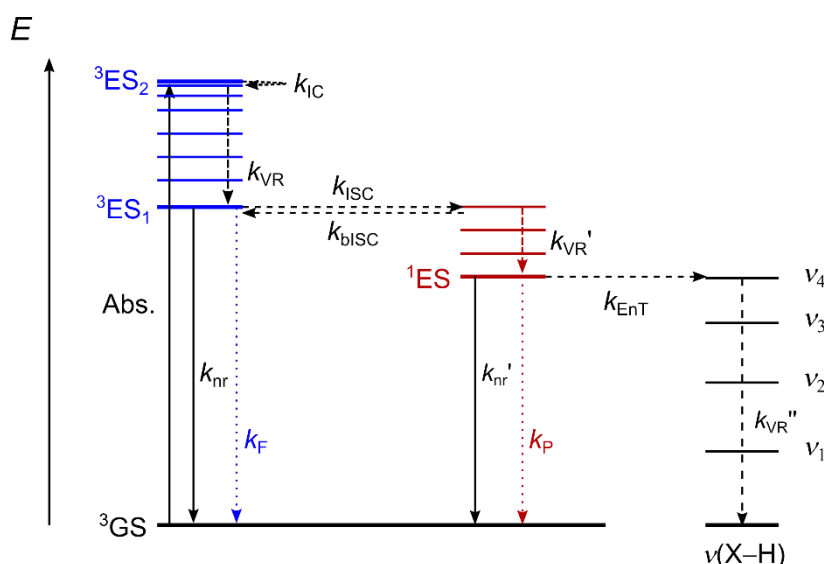


Figure 1: Simplified Jablonski diagram of a molecule with a triplet ground state (3GS) depicting primary physical processes following excitation. Abs.: Absorption. k_x : Rate constants of internal conversion (IC), vibrational relaxation (VR), (back-)intersystem crossing ((b)ISC), fluorescence (F), phosphorescence (P), non-radiative decay (nr), energy transfer (EnT). $\nu(X-H)$: C/O/N-H oscillator with vibrationally excited states ν_x .

Franck-Condon state (3ES_2), the first relaxation step typically is vibrational cooling (VR, k_{VR}) to reach the vibrational GS of the 3ES_2 . If lower ES of the same multiplicity are available (1ES_1), Kasha’s law predicts that internal conversion (IC, k_{IC}) and VR occur before the final fluorescence emission step (k_F) from the lowest ES of the same multiplicity 3ES_1 . Fluorescence is preferred over IC/VR if no vibrational levels of the 3GS are available for IC at this energy or if the coupling between 3ES_1 and 3GS is weak and, hence, the Franck Condon factors (*vide infra*) are too low. Alternatively, intersystem crossing (ISC, k_{ISC}) into a singlet excited state (1ES) can occur. From there, direct return to the 3GS through non-radiative decay k_{nr}' or phosphorescence k_P involving a spin-flip may occur, as well as back-

intersystem crossing (bISC) followed by either fluorescence or non-radiative decay (k_{nr}) which returns the molecule to its GS. Another possibility to dissipate excitation energy from the 1E state is energy transfer (EnT, k_{EnT}) to vibrational levels v_x of nearby C/N/O–H oscillators (X–H). Processes that involve a spin-flip are generally forbidden by quantum-mechanical selection rules, which demand spin conservation. However, this restriction can be softened by spin-orbit coupling. Several mechanisms are available, all of which are discussed in the following (see [section 1.1.4](#)).

Luminescence Lifetime and Quantum Yield

Two main characteristics of luminescent excited states are their lifetime τ and quantum yield Φ . An excited state's lifetime is defined in eq. 1 as the reciprocal of the sum over all radiative ($k_{r,tot}$) and non-radiative ($k_{nr,tot}$) deactivation rate constants (*tot.* - total), and represents the time between excitation and emission of a photon. The luminescence lifetimes of phosphorescent excited states ($\tau_p = 10^{-6}$ – 10^2 s) generally surpass those of fluorescent states by several orders of magnitude ($\tau_f = 10^{-10}$ – 10^{-7} s) due to a violation of the spin selection rule.⁵³

$$\tau = \frac{1}{k_F + k_P + k_{nr,tot}} = \frac{1}{k_{r,tot} + k_{nr,tot}} \quad (1)$$

The efficiency of luminescence is characterized by its quantum yield Φ which is defined as the ratio between the number of emitted (Γ) and absorbed ($\Gamma + k_{nr,tot}$) photons:

$$\phi = \frac{\Gamma}{\Gamma + k_{nr,tot}} \quad (2)$$

Eq. 2 can be adapted to obtain the quantum yield of phosphorescence Φ_p by eliminating fluorescence (k_F) from the total quantum yield:

$$\phi_P = \frac{\Gamma}{\Gamma + k_P + k_F + k_{nr,tot}} \quad (3)$$

The rate constants for both fluorescence k_F and phosphorescence k_P are given by the Einstein coefficients for spontaneous emission^{54,55}:

$$k_{F,P} = \frac{8\pi^2\eta^3\tilde{\nu}^3}{3\epsilon_0\hbar} |M(Q_0)|^2 \quad (4)$$

Herein, η is the solvent's refractive index, $\tilde{\nu}$ denominates the frequency of the radiative transition and ϵ_0 is the permittivity of the vacuum. $|M(Q_0)|$ specifies the transition dipole moment in the excited state geometry Q_0 . Hence, fluorescence as well as phosphorescence rates scale with the third power of the emission frequency and the second power of the transition dipole moment. Yet, strictly speaking, $k_{F,P} \propto \tilde{\nu}^3$ in eq. 4 only applies to atomic transitions or if one assumes a molecule with fixed nuclei.⁵⁵ In reality, nuclei are in motion which leads to broader emission bands, composed of a number of

vibrational transitions. This spectral broadening is accounted for by the Franck-Condon

factors $\int \left| \langle \psi_{GS_m}^* | \psi_{ES_0} \rangle \right|^2 dQ$ in eq. 5⁵⁴:

$$k_{F,P} = \frac{8\pi^2\eta^3}{3\epsilon_0\hbar} |M_{ES \rightarrow GS}(Q_0)|^2 \sum_{\tilde{\nu}} \tilde{\nu}^3 \int \left| \langle \psi_{GS_m}^* | \psi_{ES_n} \rangle \right|^2 dQ \quad (5).$$

Finally, for a ${}^1ES_1 \rightarrow {}^3GS$ transition (Fig. 1), k_P is linked to direct SOC through the transition dipole moment $M_{S \rightarrow T}(Q_0)$ within first-order perturbation theory:⁵⁴

$$M_{S \rightarrow T}(Q_0) = \sum_{j \in x,y,z} \left| \sum_m \frac{\langle {}^1ES | \hat{H}_{SOC} | {}^3ES_m \rangle}{(E({}^3ES_m) - E({}^1ES))} \cdot M_{{}^3ES_m,j}(Q_0) \right|^2 \quad (6)$$

The total transition dipole moment over all spatial directions $j \in x, y, z$ depends on the magnitude of spin-orbit coupling $\langle {}^1ES | \hat{H}_{SOC} | {}^3ES_m \rangle$ and the transition dipole moment $M_{{}^3ES_m,j}(Q_0)$ between triplet excited states ${}^3ES_{1,m}$ of different vibrational levels m and the 3GS .

1.1.2. Energy Transfer

Spontaneous non-radiative relaxation of excited states can diminish the luminescence efficiency of molecular luminophores. Two different mechanisms are available. Depending on the distortion of the molecule in the ES with respect to the GS, they are referred to as the weak and the strong coupling limit (Figure 2).^{54,56,57} In the weak coupling limit, the ES distortion is negligible and therefore, the potential well minima of GS and ES are (almost) vertically centred with only a minor shift along the distortional coordinate Q . These are also referred to as ‘nested states’. In contrast, the strong coupling limit implicates a large distortion in the ES and a large displacement which leads to a potential energy surface (PES) crossing.

Weak coupling limit

A transition in the weak coupling case starts with a horizontal (i.e. isoenergetic) tunneling step from the ES into the vibrationally hot ground state and is followed by vibrational relaxation within the GS.⁵⁶ The rate of non-radiative relaxation is given as:^{54,58}

$$k_{nr} = \frac{2\pi}{\hbar} \cdot \frac{H_{ab}^2}{\sqrt{4\pi\lambda_s k_B T}} \cdot \sum_{n_M} \left[\frac{S_M^{n_M}}{n_M!} \cdot \exp(-S_M) \cdot \exp\left(-\frac{(\Delta E - n_M \hbar \omega_M - \lambda_s)^2}{4\lambda_s k_B T}\right) \right] \quad (7)$$

Here, H_{ab} is the coupling matrix element and λ_s denotes the solvent reorganization energy. The dimensionless Huang-Rhys factor S_M provides a measure for the displacement of the ES potential well minimum with respect to the GS minimum along the distortional coordinate Q . n_M specifies the quantum number of the effective intraligand vibrational mode $\hbar \omega_M$ and ΔE indicates the energy difference between GS and ES in the vibrational ground state.

Due to the exponential dependency of the transition rate k_{nr} from ΔE , eq. 9 is often referred to as the 'energy gap law'⁵⁶- a smaller energy gap will yield larger k_{nr} in the weak coupling limit. Besides that, k_{nr} grows with the displacement of the ES potential well (larger S_M). In the summation over all vibrational quanta of the GS, the greatest contribution is made by those with the lowest quantum numbers n_M . Therefore, high-energy vibrations will enhance k_{nr} significantly stronger since they require lower overtones to match the ES energy. Stretching vibrations of C–H ($\omega_M \approx 3000 \text{ cm}^{-1}$), N–H ($\omega_M \approx 3400 \text{ cm}^{-1}$) and O–H oscillators ($\omega_M \approx 3700 \text{ cm}^{-1}$) for example will dissipate excitation ($\Delta E = 8000\text{-}14500 \text{ cm}^{-1}$) more efficiently than the lower energy vibrations of C=C bonds ($\omega_M \approx 1200\text{-}1600 \text{ cm}^{-1}$).^{56,59-61}

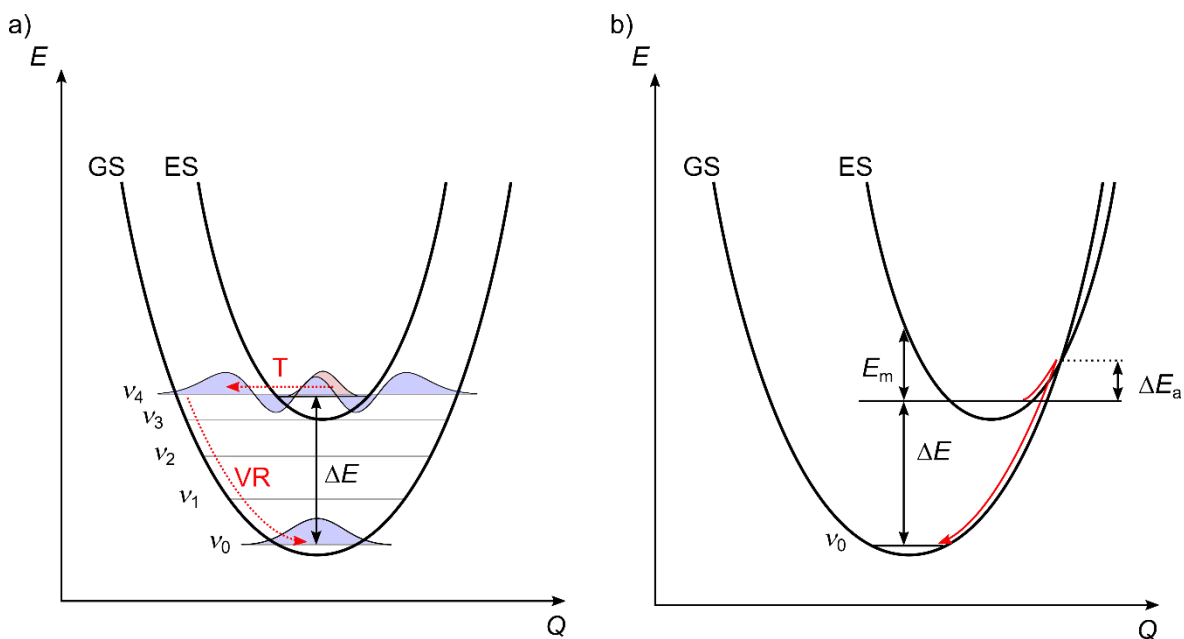


Figure 2: Potential energy wells of a ground state (GS) and an excited state (ES) for the (a) weak and (b) strong coupling limit. T: Tunneling step. VR: Vibrational relaxation. ν : Vibrational quanta. ΔE : Gap between $GS(\nu_0)$ and $ES(\nu_0)$. ΔE_a : Activation energy. E_m : Half Stokes shift.

Strictly speaking, this model holds if the oscillators are assumed to be harmonic, which is not the case in reality. A different approach to resolve this issue was taken in luminescence kinetic studies of lanthanide complexes, where an expression for k_{nr} is put forward that depends on the spectral overlap integral (SOI) of the luminescence band with those of the vibrational overtones that promote non-radiative decay:^{60,62}

$$k_{nr} = \frac{9000 \cdot \ln(10) \cdot k_r \cdot k^2}{128 \cdot \pi^2 \cdot N_A \cdot n^4 \cdot r_i^6} \cdot \int I_{norm}(\tilde{\nu}) \cdot \epsilon_{vib}(\tilde{\nu}) \cdot \tilde{\nu}^{-4} d\tilde{\nu} \quad (8)$$

Herein, k_r is the rate of radiative decay, N_A is Avogadro's number and n the refractive index of the medium. A dimensionless factor k^2 describes the relative orientation of the transition dipole moments of the emissive centre and the accepting oscillator, while the distance between oscillator i and emission centre is given by r_i . The final SOI is composed of two parameters, namely the normalized luminescence intensity I_{norm} and the decimal molar vibrational absorption coefficient ϵ_{vib} as functions of the respective wavenumber $\tilde{\nu}$. This description

is analogous to that of a Förster-type electron transfer process⁶³ and directly relates the efficiency of non-radiative decay to the spatial distance of emission centre and accepting vibrational mode ($k_{nr} \propto r_i^{-6}$). It has been successfully employed in the rationalization of energy transfer in NIR emitting lanthanide complexes and chromium(III) complexes before^{60,64} and provides a useful tool to estimate the impact of high energy oscillators on potential luminophores. Notably, energy can be transferred to oscillators of solvent molecules in this way as well, if they get close enough to the emissive centre.⁶⁴

Strong coupling limit

The transition rate k_{nr} for the strong coupling case is expressed as follows⁵⁶:

$$k_{nr} = \frac{k_B T}{\hbar} \frac{H_{ab}^2}{\sqrt{E_m (k_B T)^3}} \times \exp\left(\frac{-\Delta E_a}{k_B T}\right) \quad (9)$$

Herein, H_{ab} is, again, the coupling matrix element and E_m represents half the Stokes shift between excitation and emission energy.⁵⁶ ΔE_a denotes the energetic gap between the PES crossing point and the ES potential minimum. In contrast to the weak coupling limit, k_{nr} does not depend on ΔE . Instead, it features an Arrhenius-like behavior as a thermal activation barrier ΔE_a must be overcome to enable a transition. If the molecular distortion leads to a PES crossing in the potential energy minimum of the ES, the activation barrier vanishes and hence, non-radiative decay becomes very fast.

1.1.3. Dexter-type Electron Transfer

Phosphorescent excited states of TMCs, for example the doublet states of a chromium(III) complex,⁶⁵ can be quenched by triplet dioxygen ($^3\text{O}_2$) in a Dexter-type electron transfer to give singlet dioxygen ($^1\text{O}_2$) and the TMC in its ground state.⁶⁶ The general mechanism of a Dexter ET is shown below for a donor D and an acceptor A (Fig.3).

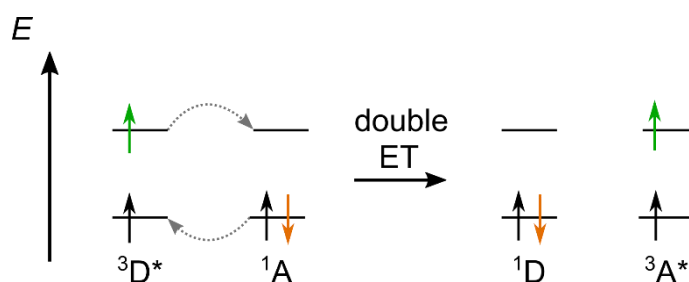


Figure 3: Concomitant electron Transfer (ET) from the LUMO of a donor molecule in an excited state (D^*) into that of an acceptor in the ground state (A) and from the HOMO of A into the HOMO of D^* , resulting in the formation of D and A^* .

Spin conservation is obeyed in the system as a whole since the spin state changes in donor and acceptor cancel each other out. The electron transfer rate k_{EnT} of a process following the Dexter mechanism is given as

$$k_{EnT} \propto (H_{DA})^2 \exp\left(\frac{-2r_{DA}}{L}\right) \cdot \text{SOI} \quad (10),$$

where H_{DA} represents the electronic coupling matrix element, r_{DA} the distance between Donor D and acceptor A and SOI refers to the normalized spectral overlap integral of the absorption spectrum of the acceptor with the emission spectrum of the donor. The transfer can be described as one electron moving from the higher lying occupied molecular orbital of the excited donor D^* to the LUMO of the acceptor. A second electron from the highest occupied molecular orbital (HOMO) of A is transferred into the lower half-filled orbital of D^* (Fig.3). As two electrons are exchanged, orbital overlap is required. The distance dependency is therefore more pronounced than in a Förster-type EnT which scales with r_{DA}^{-6} .

1.1.4. Intersystem Crossing Mechanisms

In contrast to fluorescence, efficient phosphorescence can only be achieved if ISC (k_{ISC} , Fig. 1) is fast while competing processes (IC, bISC, VR) are slow. It is therefore worthwhile to examine the different mechanisms of ISC more closely. Due to the change of multiplicity during an ISC ($\Delta S \neq 0$), this process classifies as spin-forbidden by quantum-mechanical selection rules, yet such transitions are common to TMCs.

Often, a TMC's large SOC constant ζ is used to rationalize the overcoming of the spin selection rule. To begin with, k_{ISC} depends on the SOC coupling matrix element (SOCME) for direct spin-orbit coupling \hat{H}_{SOC} based on Fermi's Golden rule within the Franck-Condon approximation.^{67,68}

$$k_{ISC}^{FC} = \frac{2\pi}{\hbar} \langle {}^3ES_{1,m} | \hat{H}_{SOC} | {}^1ES_{1,0} \rangle^2 \cdot FCWD \quad (11)$$

$\langle {}^3ES_{1,m} | \hat{H}_{SOC} | {}^1ES_{1,0} \rangle$ denotes the transition dipole moment in eq. 11. And further, \hat{H}_{SOC} can be expressed as

$$\hat{H}_{SOC} = \sum_i \hat{l}_i \hat{s}_i \zeta \quad (12).$$

With ζ scaling to fourth order with the nuclear charge Z_{eff}^4 , it is obvious that especially heavier TM ions such as ruthenium(II), iridium(III) or platinum(II) induce high k_{ISC} through strong direct SOC.⁶⁷ Besides, k_{ISC}^{FC} in eq. 11 depends on the density of vibrational states in the final electronic state weighed by their Franck-Condon-weighted density of states (FCWD). ISC is thus faster in molecules which not only have higher SOC constants, but also provide more densely packed vibrational states in the final state.

Direct SOC, however, is not always the primary mechanism of ISC. Comparison of the d^6 polypyridine complex $[Ru(bpy)_3]^{2+}$ **4**²⁺ with its lighter congener $[Fe(bpy)_3]^{2+}$ **5**²⁺ (bpy = 2,2'-bipyridine) (Fig.4a) gives a striking example of that: While $[Ru(bpy)_3]^{2+}$ displays room temperature phosphorescence at ca. 620 nm from a ³MLCT state with a quantum yield of $\Phi_{MeCN} \sim 9.5\%$ ⁶⁹ and a luminescence lifetime of $\tau = 1100$ ns in an acetonitrile solution⁷⁰, the analogous iron(II) complex is non-luminescent. In the ruthenium(II) complex **4**²⁺, the strong intrinsic ligand field splitting of the central 4d TM ion accounts for a high-energy ⁵T

state, which leaves the (emissive) $^3\text{MLCT}$ state as overall lowest-in-energy excited state (Fig. 4b).

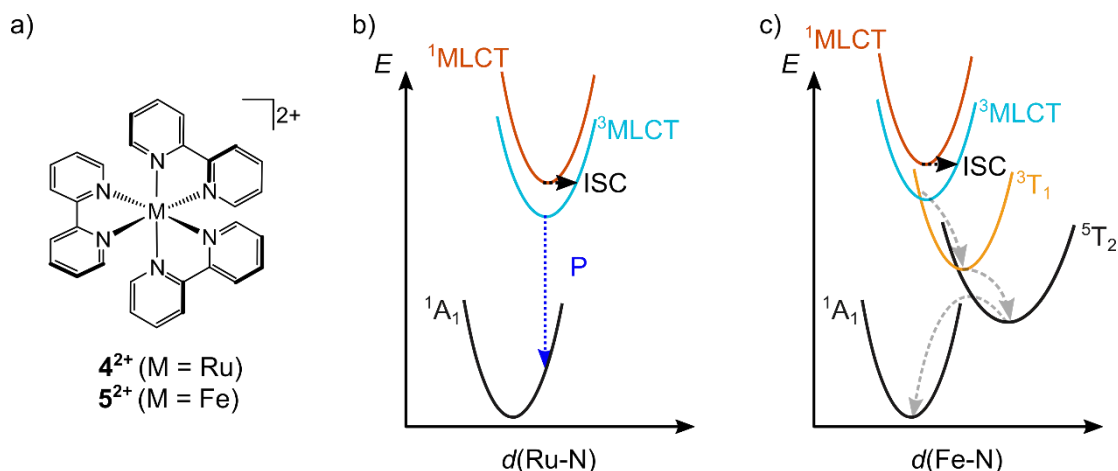


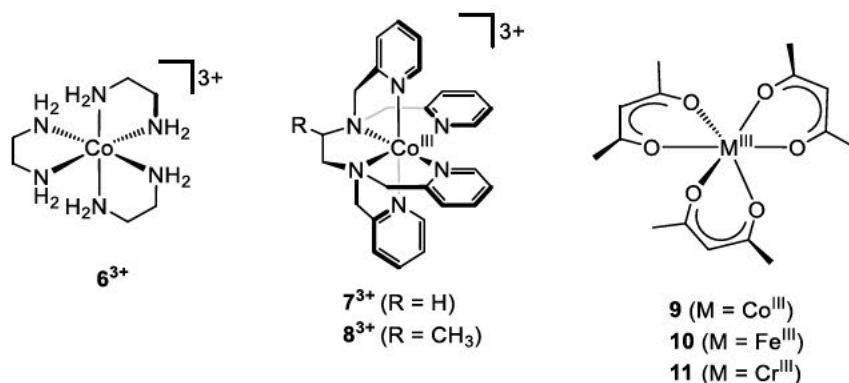
Figure 4: Tris(bipyridine) complexes 4^{2+} and 5^{2+} (a) and corresponding schematic potential well diagrams for 4^{2+} (b) and 5^{2+} (c). d : Distortional coordinate. Blue arrow: Phosphorescence (P). Black arrows: Intersystem crossing (ISC). Grey arrows: Non-radiative decay.

Ruthenium's high SOC constant ($\zeta(\text{Ru}^{2+}) = 1159 \text{ cm}^{-1}$)⁷¹ is considered the driving force of the efficient intersystem crossing (ISC) between the initially populated $^1\text{MLCT}$ ES and the $^3\text{MLCT}$ ES. The situation is different in $[\text{Fe}(\text{bpy})_3]^{2+}$ which features a broad $^1\text{MLCT}$ absorption band centred around 523 nm: A low ligand field splitting (LFS) places the ^5T state lowest in energy (Fig. 4b and c). Upon excitation into the $^1\text{MLCT}$, complex 5^{2+} undergoes rapid ISC into a $^3\text{MLCT}$ state with a time constant of $\tau_{\text{ISC}} < 20 \text{ fs}$ ⁷². It evolves into the ^5T MC state with unity quantum yield in less than 50 fs⁷³. Recovery of the ^1A GS is achieved within 0.67 ns.^{74–76} Considering the much lower SOC constant of iron(II) ($\zeta(\text{Fe}^{2+}) = 436 \text{ cm}^{-1}$)⁷¹, it is clear that mechanisms other than direct SOC must account for the unusually fast spin-forbidden $^1\text{MLCT} \rightarrow ^3\text{MLCT}$ ISC transition.

Similarly, cobalt(III) complexes with d^6 electron configuration such as $[\text{Co}(\text{en})_3]^{3+}$ **6**³⁺ (en = ethylenedi-1,2-amine), $[\text{Co}(\text{tpen})_3]^{3+}$ **7**³⁺ (tpen = tetrakis(2-pyridylmethyl)ethylenediamine) and $[\text{Co}(\text{tpnn})_3]^{3+}$ **8**³⁺ (tpnn = tetrakis(2-pyridylmethyl)-1,2-propylenediamine) as well as $\text{Co}^{\text{III}}(\text{acac})_3$ **9** (acac = trisacetylacetonate) undergo very fast non-radiative relaxation to the GS upon irradiation into the $^1\text{LMCT}$ band (Scheme 1).^{77,78} The complexes **6–8** show biphasic relaxation kinetics with a smaller time constant below $\tau_1 < 10 \text{ ps}$ ascribed to rapid ISC. A second, longer-lived component between $\tau_2 \sim 44 \text{ ps}$ in **7** and $\tau_2 \sim 0.5 \text{ ns}$ in **6**³⁺ is assigned to the decay of a ^5T ES to the ^1A GS. In the case of **9**, conversion of an initially excited $^1\text{LMCT}$ states into the ^3T states is completed in less than 150 fs and GS recovery is achieved in about 5 ps. However, there is no evidence for the involvement of a HS ^5T state.⁷⁸

The weak-field d^5 HS complex $\text{Fe}(\text{acac})_3$ **10** exemplifies that efficient non-radiative decay via MC states is not restricted to $3d^6$ complexes. Both $^4\text{MLCT}$ and $^4\text{LMCT}$ states are accessible upon irradiation and in both cases, the molecule undergoes non-radiative relaxation to the ^6A GS in about 60 ps.⁷⁹ The minor red-shift of two transient $\nu(\text{CO})$ and $\nu(\text{C}=\text{C})$ bands suggest the formation of a LF excited state that is only slightly distorted with

respect to the GS. Vibrational cooling of this ligand field ES is observed with a time constant of $\tau_{VC} = 3\text{-}9$ ps before GS recovery.



Scheme 1: Chromium(III), iron(III) and cobalt(III) complexes exhibiting ultrafast ISC dynamics.

With ISC time constants on the time scale of molecular vibrations, the generally accepted order of relaxation process rate constants ($k_{VR} > k_{IC} > k_{ISC}$) loses validity and ISC occurs outside of the Born-Oppenheimer regime.^{72,74,78,80–83} Hence, the full spin-orbit interaction is the result of spin-vibrational, spin-vibronic and direct spin-orbit coupling.

Indeed, there are some well-studied 3d TMCs in which ISC coupled to molecular vibrations has been identified: In 5^{2+} , for example, non-totally-symmetric modes of the bipyridine ligands were suggested to mediate the $^1MLCT \rightarrow ^5T$ transition⁷³. Moreover, in $Cr(acac)_3$ **11**, the initially excited 4T ligand field state evolves into a 2E state through a spin-vibronic mechanism with a rate constant of $k_{ISC} > 10^{13} \text{ s}^{-1}$ which competes with vibrational relaxation in the 4T state.^{82,83} Wavepacket simulations are in favor of these findings, as almost 40% of the 4T state's population is found to cross over into the doublet states within 250 fs.⁸⁴ The efficient ISC processes is attributed to a PES crossing of 4T and 2T states close to the Franck-Condon region which accounts for the efficient ISC. Ultrafast transient absorption experiments revealed vibrational coherence which is retained during the ISC.⁸³ The vibrational coordinate along which ISC supposedly occurs is a combination of Cr-O bond stretching and a scissor-like torsion of the ligand backbone, according to DFT calculations. VR in the 2E state follows with a time constant of $\tau_{VR} \approx 1$ ps. Finally, GS recovery is achieved within 1 ns, while 70–85 % of the GS population are recovered within only 15 ps according to transient IR spectroscopic experiments.⁸⁵ Another report on time-resolved IR spectroscopy of **11** in tetrachloroethylene suggests that thermally activated bISC to the quartet manifold is the path to GS recovery.⁸⁶ In comparison, the respective ISC time constant in the structurally related complex $Cr(tBu-acac)_3$ **12** ($tBu-acacH = 2,2,6,6$ -tetramethyl-3,5-heptanedione) with a bulkier ligand was found to be more than one order of magnitude higher than in **11** with 12 ps.⁸³ Apparently, the vibrational mode mediating ISC in **11** is not available in **12**, which slows down ISC considerably. The comparison of k_{ISC} of **11** and **12** in particular demonstrates the potential to tweak ISC rates by means of structural design.

These examples demonstrate that ultrafast intersystem crossing does not rely on a high SOC constant alone. Through spin-vibrational and spin-vibronic coupling, ISC in first row TMCs can compete with non-radiative relaxation processes and hence, could enable phosphorescence.

1.2. Luminescence from 3d Transition Metal Complexes

The creation of molecular TMC emitters requires precise knowledge of their electronic structure as their photophysical properties are largely determined by the energetic order and nature of their excited states. Thus, this section outlines important aspects of the electronic landscape of TMCs, both charge-transfer and spin-flip emitters will be introduced and evaluated

At the basis of the ES landscape of TMCs are their molecular orbitals (MO), created through interaction of the metal d orbitals with ligand orbitals of matching symmetry and energy (Fig. 5a).

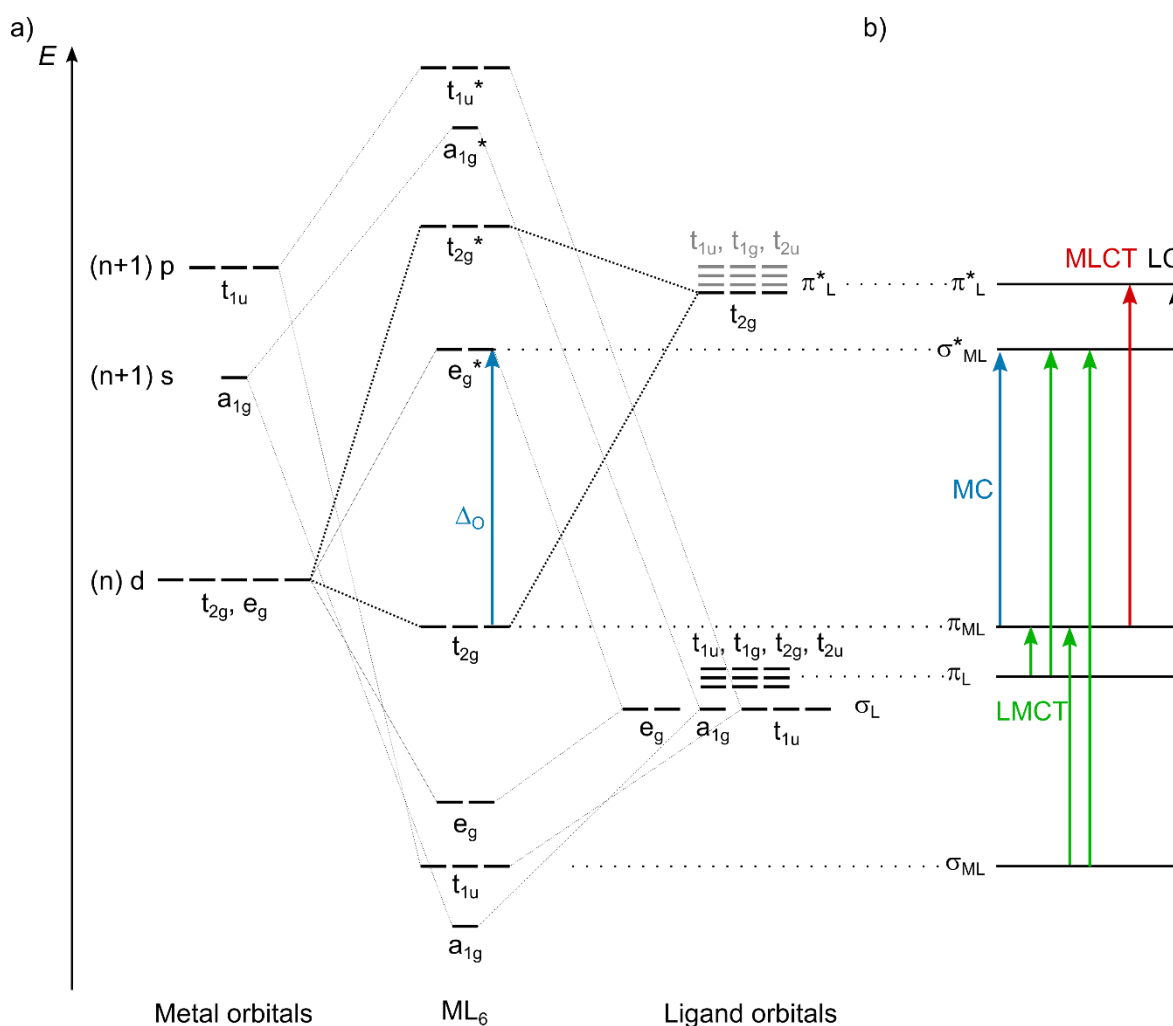


Figure 5: Molecular orbital diagram for an octahedral complex ML_6 with π -accepting ligands (a) and corresponding transitions between MO subsets (b).^{87,88}

The situation is illustrated schematically below for an ideal octahedral complex (point group O_h) in a MO diagram comprising metal orbitals and ligand group orbitals for π -accepting (blue) ligands. The five degenerate d orbitals are split into e_g^* and t_{2g} subsets. These frontier orbitals of ligand and metal centre are of particular interest as electronic transitions typically involve one or more orbitals of this subset. Between them, metal-centred (MC) transitions (ligand-field), ligand-centred transitions (LC) as well as different types of charge-transfer (CT) transitions are available, namely ligand-to-metal CT (LMCT), metal-to-ligand (MLCT) and ligand-centred (LC) transitions (Fig.5b). Ligand field states can be further divided into interconfigurational transitions between t_{2g} and e_g^* orbital subsets and intraconfigurational transitions which occur within the t_{2g} or e_g^* subset by virtue of a spin-flip (SF). The energetic splitting of t_{2g} (or t_{2g}^*) and e_g^* orbitals (Fig.5a) is referred to as ligand field splitting Δ_o and mirrors the energy of the lowest interconfigurational transition. The most common types of emission that can be defined from these considerations are charge transfer and spin-flip emission. While CT emission requires low-energy CT states relative to deactivating MC states and therefore is not tied to any specific d electron configuration of the metal centre, SF emission is possible only from TMCs with intraconfigurational MC states (spin-flip states) as the lowest ES. Phosphorescence from interconfigurational MC states³⁷ is also conceivable, but has been observed only in a few complexes of manganese(II)⁸⁹⁻⁹¹ and one hexacarbene cobalt(III) complex²¹ because of the large distortion of these states and will not be discussed in further detail.

1.2.1. Spin-Flip Luminescence

Whether a given TM is suited for SF emission can be determined from the Tanabe-Sugano diagram for the respective d electron configuration.^{92,93} These diagrams illustrate the splitting of the atomic terms of a metal centre in an octahedral ligand field into the respective ligand field terms. The LF term energies are plotted versus Δ_o and depend on Δ_o as well as the Racah parameters B and C .^{92,93} Both parameters describe the interelectronic repulsion in TM complexes, where C only affects states of a multiplicity lower than the maximum multiplicity. The relative term energies change with the C/B ratio and hence are different for every complex. As an example, the TS diagram for an ion featuring low-energy interconfigurational states like d^6 iron(II) may be compared to a d^3 system with low-energy spin-flip states such as chromium(III) or vanadium(II) (Fig. 6).^{92,93}

The quintet and triplet ES of iron(II) involve transitions between t_{2g} and e_g^* subshell. These states are characterized by a significant distortion with elongated M-L bonds induced by the occupation of σ -antibonding e_g^* orbitals. Hence, the ES geometries of 5MC and 3MC states deviate from that of the ground state (strong coupling limit, Fig. 2) which can even lead to potential surface crossings and typically enables ultrafast energy dissipation upon exciting MLCT states.

In the doublet states of octahedral d^3 chromium(III) complexes, however, electron redistribution occurs exclusively within the t_{2g} orbital set. Consequently, these states are virtually undistorted with respect to the ground state (weak coupling limit) and their energy

is largely unaffected by changes in Δ_o . At large values of Δ_o , the 2E and 2T_1 states become the lowest energy ES. Their energy is given as

$$E({}^2T_1) \approx 9B + 3C - 24 \left(\frac{B^2}{\Delta_o} \right) \quad (13)$$

$$E({}^2E) \approx 9B + 3C - 50 \left(\frac{B^2}{\Delta_o} \right) \quad (14)$$

according to ligand field theory.^{94,95} As these states are nested with the GS, the luminescence bands are typically very narrow with FWHM values in the range of only a few up to a few hundred inverse centimeters, depending on the number of emitting states, symmetry, temperature and medium.^{47,65,96}

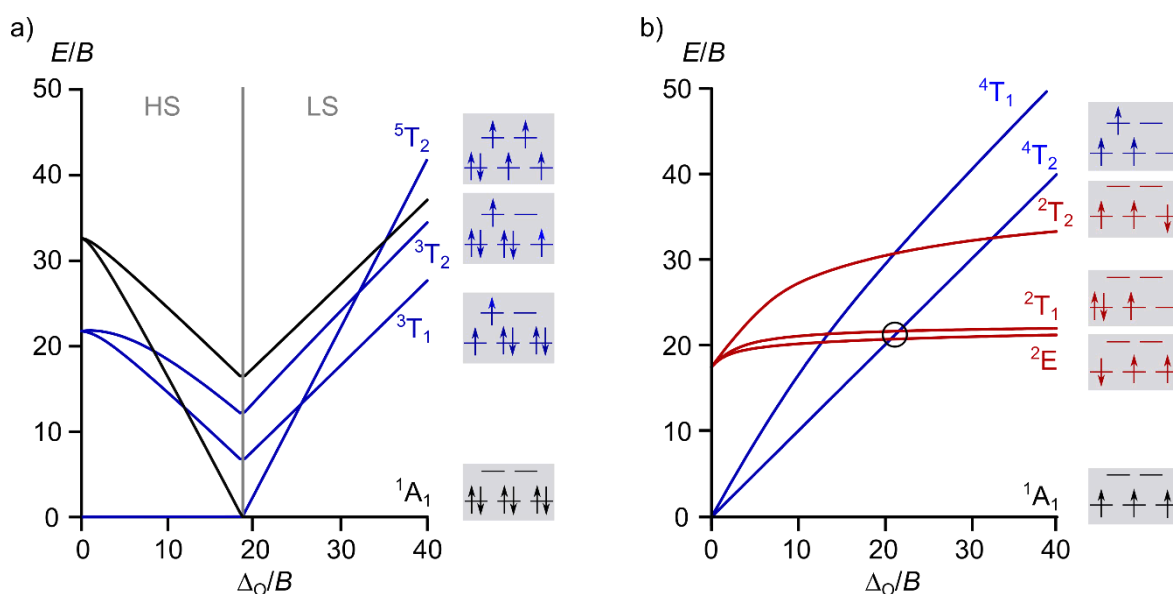


Figure 6: Simplified Tanabe-Sugano diagrams of a d^6 and a d^3 ion at a ratio of $C/B = 4.0$. HS: High-spin. LS: Low-spin. Blue: Interconfigurational states. Red: Intraconfigurational states.⁹⁷

For this reason, efficient population transfer via vibronic coupling is unavailable and non-radiative decay slows down. Spin-flip states can therefore possess long ES lifetimes and display phosphorescence, despite the fact that the emission is spin- and Laporte-forbidden in an ideal octahedral coordination environment. The first crossing point of intra- and interconfigurational states in the TS diagram constitutes the minimum ligand field splitting Δ_o/B that is necessary to enable spin-flip luminescence (Fig. 6b). If the energetic splitting of inter- and intraconfigurational states is not sufficiently large (in this case, the splitting of 4T_2 and ${}^2E/{}^2T_1$ states), bISC can occur. This may lead to either photodissociation⁹⁸ via 4T_2 state Jahn-Teller distortion⁹⁹ or fluorescence.^{100–102} With these considerations in mind, TS diagrams provide a good starting point in the interpretation of spectroscopic results. Yet, they come with some limitations which must be taken into account: Firstly, they refer to ideally octahedral complexes. In reality, however, deviations from an ideal geometry result in level splittings. Secondly, the excited state energies are always given for the GS geometry and do not reflect the energy of the vibrational ground state of the respective relaxed excited state. Furthermore, SOC and the resulting mixing of states with different

multiplicity is disregarded. And lastly, both lower GS symmetry and SOC can lift the degeneracy of LF terms and split them which is not considered in the TS diagrams.

SF emission relies heavily on the value of Δ_0 , as pointed out previously. However, first row TM ions offer significantly smaller LF splittings in comparison with their heavier analogues. This is due to the absence of radial nodes in the 3d orbitals' radial probability density functions which leads to a stronger d orbital contraction through the higher effective nuclear charge Z_{eff} than in 4d and 5d TMCs.¹⁰³ The consequence is that the 3d orbitals' radial expanse is almost identical with that of the 3s and 3p orbitals, enabling strong Pauli repulsion between metal core electrons and ligand valence electrons.¹⁰³ An effective metal-ligand orbital overlap is prevented as a result. A central aspect in the design of spin-flip (and charge transfer) emitters from third row TM ions therefore is to increase Δ_0 sufficiently to achieve the necessary ES ordering.

In summary, SF MC emission is theoretically possible from octahedrally coordinated TM ions with d^2 , d^3 , d^4 or d^8 electron configurations at a sufficiently large ligand field splitting Δ_0 .

1.2.2. Efficiency of Spin-Flip Luminescence

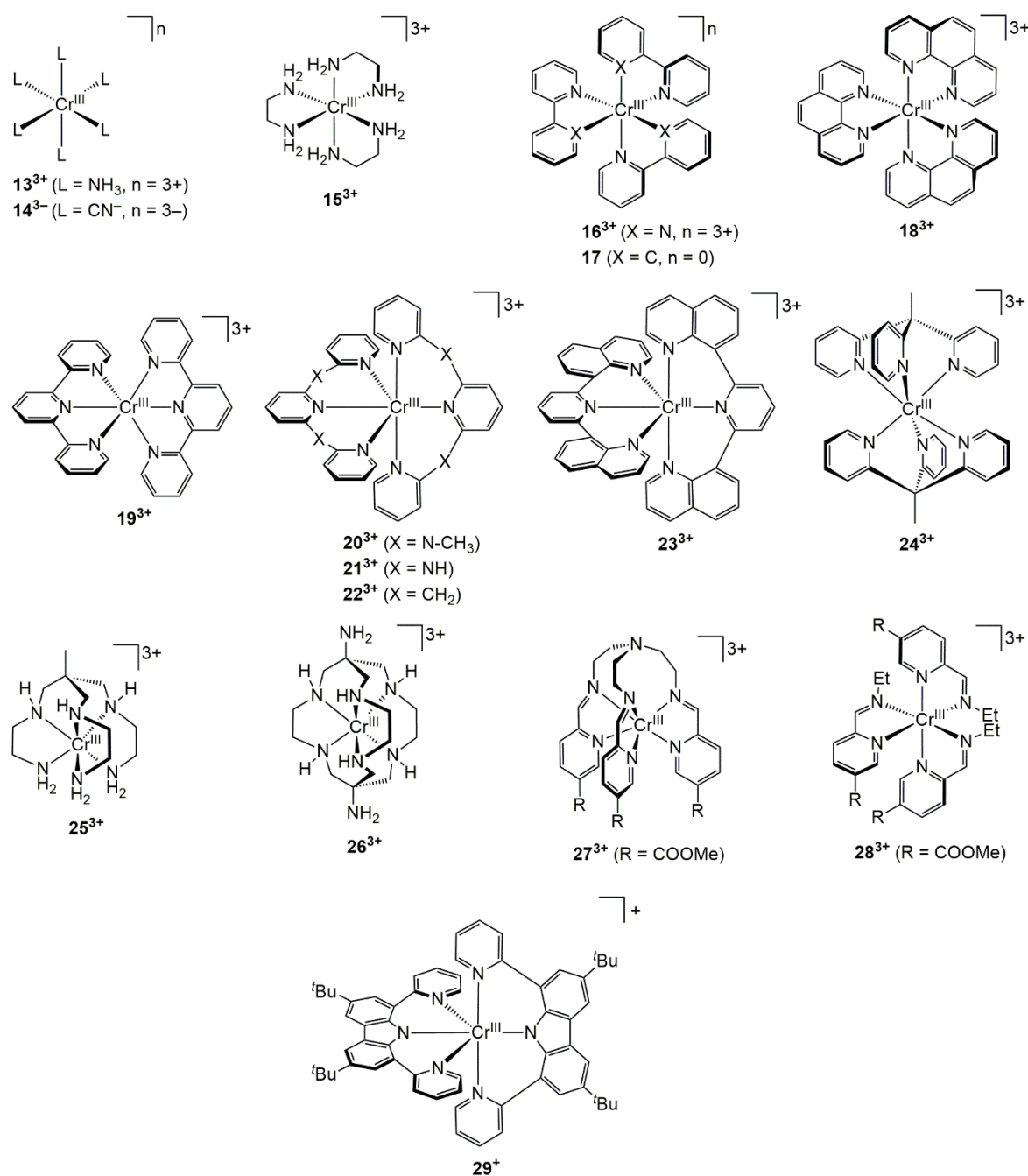
The occurrence of SF luminescence and its efficiency depend greatly on ligand design, as discussed in [section 1.2](#). Chromium(III) complexes set an instructive example in this regard. They have gained a lot of attention in the recent past as they often show SF luminescence, and numerous publications document their photophysical properties.^{17,35,37,97,104–107} This section shows the various ways in which ligand design can influence SF luminescence using chromium(III) SF emitters.

Enhancing the Ligand Field Splitting

As mentioned above, the key prerequisite to enable SF luminescence is to lift the energy of LF excited states above those of low-energy SF states (for a d^3 ion, that is $E(^4T_2) > E(^2E, ^2T_1)$). By employing strongly σ -donating ligands, the energy of metal-ligand anti-bonding e_g^* orbitals increases and hence, detrimental MC states are destabilized to achieve the desired ES order.

This can be accomplished with common strong field ligands already as in $[\text{Cr}(\text{NH}_3)_6]^{3+}$ **13**³⁺ or $[\text{Cr}(\text{CN})_6]^{3-}$ **14**³⁻, where SF phosphorescence can be observed (Scheme 2, Table 1).^{102,108,109} But monodentate ligands are generally more prone to substitution and quite flexible, which can then open additional relaxation pathways. Chelating ligands offer more rigid ligand scaffolds and do not disengage from the metal centre as easily due to the chelate effect. Fusing pairs of amine ligands in **13**³⁺ with ethylene bridges yields $[\text{Cr}(\text{en})_3]^{3+}$ **15**³⁺, which exhibits one order of magnitude higher SF quantum yields than **13**³⁺.¹⁰⁸ Yet, bISC occurs in complex **15**³⁺ from the doublet states into the 4T_2 state, indicating that the energy gap between those states is not sufficiently large.⁹⁸ Higher Δ_0 values can be achieved with polypyridine ligands such as bpy or phen (1,10-phenanthroline). In the respective tris-bidentate chromium(III) complexes $[\text{Cr}(\text{bpy})_3]^{3+}$ **16**³⁺ and $[\text{Cr}(\text{phen})_3]^{3+}$ **18**³⁺,

the energy gaps between the 4T_2 and the lowest doublet states assume values of 9600 cm^{-1} and 7600 cm^{-1} .^{110,111} Hence it is unlikely that thermally activated bISC contributes significantly to non-radiative decay. Even less flexible ligand scaffolds are obtained with the tridentate ligands such as tpy (2,6-bis(2-pyridyl)pyridine) in $[\text{Cr}(\text{tpy})_2]^{3+}$ **19**³. Its phosphorescence quantum yield and lifetime are, however, significantly lower than those of the aforementioned tris-bidentate complexes.^{112–114} This is due to the bite angles deviating from the ideal values ($\angle_{\text{proximal}}(\text{N}_{\text{prox}}-\text{Cr}-\text{N}_{\text{prox}}) = 90^\circ$ and $\angle_{\text{distal}}(\text{N}_{\text{distal}}-\text{Cr}-\text{N}_{\text{distal}}) = 180^\circ$) by *ca.* 12° and 24° , respectively, which yields a low Δ_o and enables bISC (Scheme 2).



Scheme 2: Pseudo -octahedral chromium(III) spin-flip emitters.

Introduction

To solve the issue of low bite angles in tridentate tpy-type ligands, they can be expanded to form six-membered ring chelate ligands. In doing so, a family of complexes termed “molecular rubies” was born – a name referencing their exceptional SF luminescence quantum yields and lifetimes in reminiscence of the original ruby ($\text{Al}_2\text{O}_3:\text{Cr}^{3+}$).^{34,65} The inserted motifs comprise methylene,⁹⁶ amine¹¹⁵ and methylamine⁶⁵ bridges yielding the complexes **20**³⁺-**22**³⁺ (Scheme 2). Each ligand coordinates in a meridional fashion to the chromium(III) centre with only minor deviations from optimum bite angle values (largest deviations $\alpha_{\text{proximal}} = 5^\circ$ and $\alpha_{\text{distal}} = 9^\circ$).^{65,96,115}

Table 1 Luminescence properties of selected mononuclear chromium(III) complexes. Emission wavelengths λ_{em} , luminescence lifetimes at room temperature τ_{RT} and at low temperature τ_{LT} as well as doublet state quantum yield values at room temperature. Data are given for aqueous solutions if not stated otherwise.

Number	Complex	$\lambda_{\text{em}} / \text{nm}$	$\tau_{\text{RT}} (\tau_{\text{RT,deox}}) [\tau_{\text{LT}}] / \mu\text{s}$	$\Phi (\Phi_{\text{deox}}) / \%$
13 ³⁺ 108,109	$[\text{Cr}(\text{NH}_3)_6]^{3+}$	667	2.2 [70]	5.5×10^{-4}
14 ³⁻ 102,108	$[\text{Cr}(\text{CN})_6]^{3-}$	≈ 820	0.14	$< 5 \times 10^{-6}$
15 ³⁺ 108,116	$[\text{Cr}(\text{en})_3]^{3+}$	670	1.85 [120]	6.2×10^{-3}
16 ³⁺ 108,117	$[\text{Cr}(\text{bpy})_3]^{3+}$	727	52 (74)	0.089
17 ¹¹⁸	$[\text{Cr}(\text{ppy})_3]$	910 ^a	9.5 ^a	0.03 ^a
18 ³⁺ 111,113,117	$[\text{Cr}(\text{phen})_3]^{3+}$	689/726	74 (224 ^b)	0.15
19 ³⁺ 112,119	$[\text{Cr}(\text{tpy})_2]^{3+}$	770	$< 0.14^c$ ($< 2^b$)	($< 0.00^b$)
20 ³⁺ 64	$[\text{Cr}(\text{ddpd})_2]^{3+}$	738/775	177 (899)	2.1 (11)
21 ³⁺ 115	$[\text{Cr}(\text{H}_2\text{tpda})_2]^{3+}$	738/782	150 (670)	1.5 (6.3)
22 ³⁺ 96	$[\text{Cr}(\text{bpmp})_2]^{3+}$	709 ^d	880 ^d (1550) ^d	9.8 ^d (15.8) ^d
23 ³⁺ 120	$[\text{Cr}(\text{dqp})_2]^{3+}$	727/747	83 (1270)	1.0 (5.2)
24 ³⁺ 121	$[\text{Cr}(\text{tpe})_2]^{3+}$	748	78 ^e (2800 ^e)	2.2 ^e (5.4 ^e)
25 ³⁺ 122	$[\text{Cr}(\text{sen})]^{3+}$	675 ^f	0.0001 ^g	-
26 ³⁺ 123	$[\text{Cr}(\text{sarN}_6)]^{3+}$	685	< 0.01	2
27 ³⁺ 124	-	700/740	(19) ^h	(6.1×10^{-4}) ^h
28 ³⁺ 124	-	No luminescence	-	-
29 ³⁺ 125	$[\text{Cr}^{\text{III}}(\text{dpc})_2]^+$	1067 ⁱ	2.0 ^{ij}	-

^a CH_2Cl_2 at 293 K. ^bDeaerated MeCN at 293 K. ^cMeCN under N_2 atmosphere. ^d0.1 M $\text{HClO}_4/\text{H}_2\text{O}$. ^e $\text{H}_2\text{O}/\text{HClO}_4$, BF_4^- salt. ^f $\text{H}_2\text{O}/\text{DMSO}$ glass. ^gExtrapolated from variable temperature lifetime measurements in glassy media. ^hDeaerated MeCN. ⁱMeCN at 77 K. ^jAmplitude averaged lifetime of biexponential fit with $\tau_1 = 1.4 \mu\text{s}$ (88 %) and $\tau_2 = 6.3 \mu\text{s}$ (12 %)

The first “molecular ruby” was $[\text{Cr}(\text{ddpd})_2]^{3+}$ **20**³⁺ (ddpd = *N,N'*-dimethyl-*N,N'*-dipyridin-2-ylpyridine-2,6-diamine). Improved Cr–N orbital overlap raises the ligand field splitting of this complex to 22990 cm^{-1} from 18750 cm^{-1} in its predecessor $[\text{Cr}(\text{tpy})_2]^{3+}$ **19**³⁺.^{65,119} A large ${}^4\text{T}_2/{}^2\text{E}$ energy gap of *ca.* 10090 cm^{-1} prevents thermally activated bISC to quartet states in **20**³⁺. The favorable ES order leads to dual spin-flip emission from the ${}^2\text{T}_1/{}^2\text{E}$ levels at 775 and 739 nm and a doublet ES lifetime of $\tau = 177\ \mu\text{s}$. Since these emissive doublet states are apart by only $\approx 630\text{ cm}^{-1}$, their population distribution follows Boltzmann law and, hence, the emission intensity ratio of both bands varies with temperature.¹²⁶ At room temperature in aqueous solution, a photoluminescence quantum yield of $\Phi = 2.1\%$ was determined (Table 1).⁶⁵ In oxygen-free media, the doublet states’ lifetime and quantum yield increase to $\tau = 899\ \mu\text{s}$ and $\Phi = 11\%$.⁶⁵ Because dissociative quartet states are only transiently populated, complex **20**³⁺ is highly photostable in the range of pH = 7–14.⁶⁵ Substitution of the N-methyl bridges with amine or methylene moieties yields the molecular rubies $[\text{Cr}(\text{H}_2\text{tpda})_2]^{3+}$ **21**³⁺ (H₂tpda = 2,6-bis(2-pyridylamino)pyridine) and $[\text{Cr}(\text{bpmp})_2]^{3+}$ **22**³⁺ (bpmp = 2,6-bis(2-pyridylmethyl)pyridine), respectively. Complex **21**³⁺ exhibits slightly lower quantum yield with $\Phi = 1.5\%$ in aqueous solution¹¹⁵ than **20**³⁺ which is still several orders of magnitude above the values reported for previously mentioned chromium(III) systems.^{108,111,119} Complex **22**³⁺ is strongly emissive in acidic aqueous solutions with a QY of $\Phi = 9.8\%$ and a doublet lifetime of $\tau = 880\ \mu\text{s}$.⁹⁶ Notably, the methylene bridges easily deprotonate once the ligand coordinates to a chromium(III) centre and as a result, the luminescence is quenched partially.⁹⁶ In acidic deoxygenated aqueous solutions, the doublet lifetime increases to $\tau = 1500\ \mu\text{s}$ and the QY amounts to $\Phi = 15.8\%$.⁹⁶ The success of six-membered ring chelates also pertains to the structurally related complexes $[\text{Cr}(\text{dqp})_2]^{3+}$ **23**³⁺ (dqp = 2,6-di(quinolin-8-yl)pyridine)¹²⁰ and $[\text{Cr}(\text{tpe})_2]^{3+}$ **24**³⁺ (tpe = 1,1,1-tris(pyrid-2-yl)ethane).¹²¹ In **24**³⁺, the tripodal tpe ligand coordinates facially to the metal ion and creates a centre of inversion.¹²¹ Just like the meridionally coordinating ligands of **20**³⁺–**23**³⁺, tpe imparts a strong LFS of 23200 cm^{-1} by maintaining trans-N–Cr–N angles close to 180° .¹²¹ Since the complex is centrosymmetric, however, Laporte’s rule rigorously applies.¹²¹ The results are doublet ES lifetimes significantly higher than those found for other molecular rubies (Table 1).¹²¹ In summary, the introduction of tridentate chelating ligands which form six-membered rings with the chromium(III) centre leads to favorable ES ordering in their respective complexes and enables quite efficient spin-flip emission. Yet, there are other important parameters which must be regarded.

Suppressing Non-Radiative Decay

Apart from bISC induced by insufficient values of Δ_0 , non-radiative decay can pose a severe problem in the design of efficient luminophores. Geometric distortions in the excited doublet states account for one of these pathways. By mixing the d orbitals, distortions in the excited state can lead to PES intersections with the ground state which opens a thermally activated non-radiative path back to the ground state (strong coupling limit, Fig. 2). Chromium(III) SF emitters of D_3 and D_{3h} symmetry like $[\text{Cr}(\text{bpy})_3]^{3+}$ **16**³⁺, $\text{Cr}(\text{pphy})_3$ **17** or $[\text{Cr}(\text{phen})_3]^{3+}$ **18**³⁺ are affected by trigonal distortions which provide this type of

relaxation pathway and rationalize their low QY values compared to the more rigid $[\text{Cr}(\text{ddpd})_2]^{3+}$ **20**³⁺ (Table 1).^{118,122,124,127} In the same vein, fusing the three en ligands of $[\text{Cr}(\text{en})_3]^{3+}$ **15**³⁺ with a capping moiety as done in $[\text{Cr}(\text{sen})]^{3+}$ **25**³⁺ (sen = 4,4',4''-ethylidenetris(3-azabutane-1-amine)) reduces the doublet ES lifetime by roughly four orders of magnitude (Table 1).^{108,116,122} Here, the ligand capping enables a trigonal distortion mode which is unavailable in $[\text{Cr}(\text{en})_3]^{3+}$ **15**³⁺.¹²² Similar, but more pronounced is the difference of ligand capping in complexes **27**³⁺ and **28**³⁺: While **28**³⁺ with a hexadentate tris-iminopyridine ligand capped by a tren (tris-(2-aminoethyl)amine) linker is non-luminescent, the non-capped variant **27**³⁺ shows phosphorescence from its doublet states at 740 and 700 nm with a lifetime in the range of $\tau = 17\text{--}19 \mu\text{s}$.¹²⁴ PES intersections are likely to contribute to non-radiative decay in $[\text{Cr}(\text{tpe})_2]^{3+}$ **24**³⁺ as well, even though the effect is not felt as strongly in this case.¹²¹

CT states can interfere with luminescence as well. Their admixture to SF states facilitates non-radiative return to the ground state through PES crossings as they are typically more distorted than SF states. Low-energy CT states go along with low redox potentials of the metal centre. Such is the case in vanadium(II), for example, which features low-energy MLCT states (see [section 1.3](#)).^{40–43,128} In molecular rubies with strong σ and weak π donation, however, CT states do not contribute to non-radiative decay because they are separated from the emissive doublet states by an appreciable energetic gap. This relation changes if anionic ligands with stronger π donor character are employed as in $[\text{Cr}(\text{dpc})_2]^+$ **29**⁺, where admixture of a ²LMCT state to the emissive ²MC state accounts for a more pronounced excited state distortion, a broader emission band and more efficient non-radiative decay.¹²⁵

With emission energies in the range of $9370\text{--}14900 \text{ cm}^{-1}$,^{108,125} SF emission can be further diminished by electronic-to-vibronic energy transfer to nearby C–H, O–H or N–H oscillators (chapter 2.2.1.). Such multiphonon relaxation has been reported to partially quench the SF luminescence of $[\text{Cr}(\text{NH}_3)_6]^{3+}$ **13**³⁺ and $[\text{Cr}(\text{en})_3]^{3+}$ **15**³, where ligand deuteration extends the doublet lifetimes at 77 K from 70 μs to 5230 μs and from 120 μs to 3030 μs , respectively.¹²² A similar observation was made for $[\text{Cr}(\text{H}_2\text{tpda})_2]^{3+}$ **21**³⁺, where deuteration of the amine bridging groups increases the QY from 8.8 % to 12 % and the luminescence lifetime from 770 μs to 1100 μs in acetonitrile solution.¹¹⁵ In undeuterated water, however, deuteron/proton exchange at the amine bridges is fast and only the combined effect of deuterating both solvent and ligand could be monitored.¹¹⁵ Selective deuteration of the ligand in $[\text{Cr}(\text{ddpd})_2]^{3+}$ **20**³⁺ provides a bit more detailed insight as C–H/D bonds are less acidic and hence, exchange with the solvent is unlikely. Varying deuteration patterns were tested.⁶⁴ In absence of ³O₂, which itself acts as luminescence quencher (see below), QY and lifetime values as high as $\Phi = 30 \%$ and $\tau = 2100 \mu\text{s}$ were achieved.⁶⁴ Exchanging protons in α -position of the terminal pyridine rings yielded the most significant improvement, underlining that the efficiency of the energy transfer process is a function of distance between donating and receiving end.⁶⁴ This pertains to the α -protons of $[\text{Cr}(\text{bpmp})_2]^{3+}$ **22**³⁺ as well with H/D exchange raising the phosphorescence QY from 20 to 25 % and the luminescence lifetime from 1.8 ms to 2.5 ms in D₂O/DClO₄.⁹⁶

Dexter-type energy transfer to triplet oxygen constitutes an additional hindrance to SF emission.⁶⁶ Quantum yields and luminescence lifetimes of $[\text{Cr}(\text{ddpd})_2]^{3+}$ **20**³⁺, for example, are roughly five times higher if measured in deoxygenated aqueous solution (Table 1).⁶⁵ Shielding the emissive centre from molecular dioxygen $^3\text{O}_2$ is difficult due to its small size, but could be achieved by employing sterically more demanding ligands which lower the accessibility of the metal centre or by embedding the centres in matrices.¹²⁹

Adjusting Emission Wavelength

Yet, there should be “windows” for weakly quenched SF emission where the SOI between luminescence band and the vibrational bands $\nu^{\text{C-H}}$ of C–H overtones n is low, because the energies of $\nu_n^{\text{C-H}}$ are rather constant for aromatic ligands. It is necessary to tune the emission energy to match such windows to prevent strong luminescence quenching (Fig. 7).

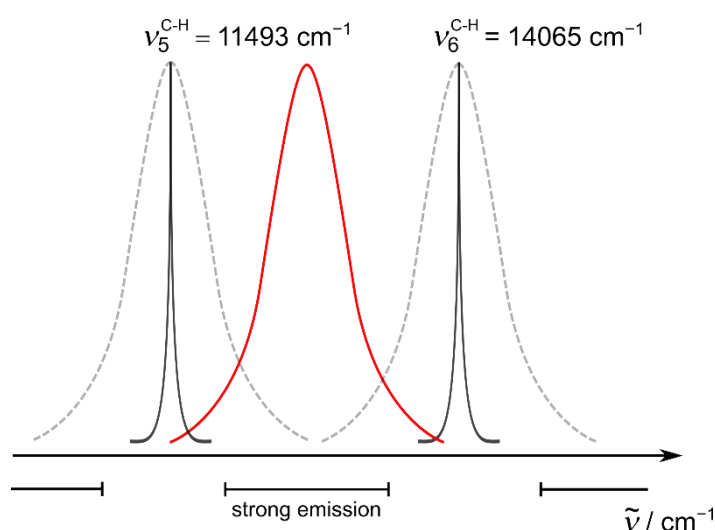


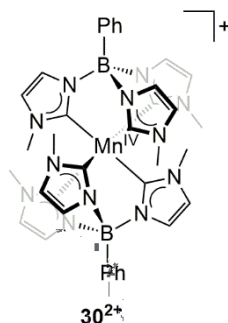
Figure 7: Windows for strong emission (red curve, bars below x axis) between fourth and fifth aromatic C-H overtones $\nu_{5,6}^{\text{C-H}}$ (black)⁶⁴ quenching the spin-flip luminescence (dotted grey curves).

According to LF theory, the energy of the SF states solely depends on interelectronic repulsion of the d electrons defined through the Racah parameters B and C .⁹⁴ Consequently, promising approaches to vary the energy of SF phosphorescence are 1) to alter the charge of the TM ion and 2) to change the covalency of the metal-ligand bond. Reducing the charge at the metal centre as well as enhancing the nephelauxetic effect both lower B and C and, hence, reduce the emission energy.

An upper boundary for the chromium(III) doublet emission can be estimated from the B value of the free Cr^{3+} ion in the gas phase (918 cm^{-1}). Assuming a C/B ratio of 4.0 and a LFS of $\Delta_0/B = 40$, the energy of the ^2E state would amount to ca. $21 B$ and occur at ca. 519 nm .⁹⁷ Chromium(III) complexes with neutral amine and polypyridine ligands listed in Table 1 display emission in the range of $667 - 782 \text{ nm}$. Replacing the amine ligands in **13**³⁺ with six mono-anionic cyanide ligands shifts the doublet state emission wavelength to 820 nm in $[\text{Cr}(\text{CN})_6]^{3-}$ **14**³⁻, which underscores the strong nephelauxetic effect of cyanide.¹⁰⁸ Similarly, substituting bpy in **16**³⁺ with the cyclometalating ppy ligand (ppy = 2-phenylpyridine) lowers the energy of the doublet states in *fac*- $[\text{Cr}(\text{ppy})_3]$ **17**, which displays phosphorescence

emission at 910 nm (Table 1).¹¹⁸ This represents a bathochromic shift of ca. 2370 cm^{-1} compared to $[\text{Cr}(\text{bpy}_3)]^{3+}$ **16**³⁺.¹⁰² Strongly σ/π -donating carbanionic donors combined with π -accepting pyridine moieties account for the higher degree of metal-ligand-covalency in this complex.¹¹⁸ The experimental findings are in line with complete active space self-consistent field (CAS-SCF) calculations which model the energy of the metal-centred excited states.¹¹⁸ The overall lowest emission energy of chromium(III) SF emitters reported so far is achieved by $[\text{Cr}(\text{dpc})_2]^+$ **29**⁺ ($\text{dpc}^- = 3,6$ -di-*tert*-butyl-1,8-di(pyridine-2-yl)-carbazolato) with an emission wavelength of 1067 nm.¹²⁵ A π -donating anionic amide framed by two π -accepting pyridine moieties accounts for a multidirectional π -electron density shift, which yields even more covalent bonds than in **17** and a low Racah B parameter of 470 cm^{-1} .¹²⁵ Yet, no luminescence was detected at room temperature. At 77 K, SF emission occurs from **29**⁺. Luminescence decay under the same conditions was modelled with a biexponential fit and yielded values of 1.4 μs (88 %) and 6.3 μs (12 %) (Table 1). Apparently, a more distorted ²LMCT provided by the electron-rich carbazolato moiety is admixed to the emissive state which accelerates non-radiative decay.¹²⁵

With regard to lowering or increasing the charge of the transition metal in order to achieve lower or higher emission energies, other $3d^3$ elements such as manganese(IV) and vanadium(II) come to mind. To date, however, no vanadium(II) complex and only a single molecular manganese(IV) complex, the pseudo-octahedral $[\text{Mn}\{\text{PhB}(\text{Melm})_3\}_2]^{2+}$ **30**²⁺ ($[\text{PhB}(\text{Melm})_3]^- = (\text{phenyl tris}(3\text{-methylimidazol-2-yl})\text{borate, Scheme 3})$, has been reported to exhibit SF emission.¹³⁰ Δ_0 could not be determined experimentally in this case because the d-d absorption bands are masked by a broad CT band ($\epsilon \approx 8000 \text{ M}^{-1}\text{cm}^{-1}$) peaking at 500 nm. A NIR spin-flip emission band was indeed observed at 814 nm in fluid solution at 298 K and ascribed to a ²E \rightarrow ⁴A₂ spin-flip transition, which fits the luminescence lifetime of 1.5 μs at 85 K.¹³⁰ Only $[\text{Cr}(\text{CN})_6]^{3-}$ **14**³⁻, $[\text{Cr}(\text{ppy})_3]$ **17** and $[\text{Cr}(\text{dpc})_2]^+$ **29**⁺ achieve similar or lower emission energies (Table 1).^{102,118,125} It is notable that despite the higher charge of the Mn^{IV} ion compared to Cr^{III}, the NIR emission of complex **30**²⁺ is of lower energy than those of most chromium(III) complexes, which indicates that Mn–C covalency has a stronger impact than the nuclear charge of the Mn^{IV} ion.



Scheme 3: Pseudo-octahedral phosphorescent manganese(IV) complex.

As has been shown in this section, there is not one all-determining criterion that makes or breaks spin-flip emitters. Rather than that, a number of interdependent factors shape the

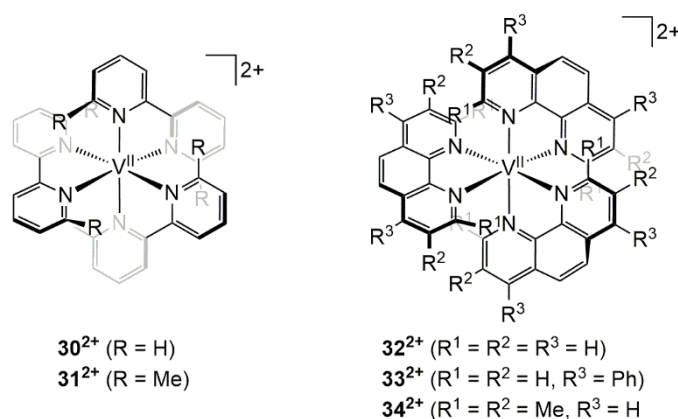
emission energy, luminescence lifetimes and quantum yields of these complexes, and often, it is challenging to properly balance all factors.

1.3. New Spin-Flip Luminophores

The factors governing SF luminescence that have been described in [section 1.2](#) will be important for understanding less commonly applied transition metal ions in SF luminophores. The following sections will present the state of the art research on several intriguing examples, namely vanadium(II), vanadium(III) and nickel(II). The unique features of each named ion will be discussed.

1.3.1. d^3 Vanadium(II)

The excited state landscape and, hence, the emission properties of vanadium(II) complexes should parallel those of chromium(III) complexes as they are isoelectronic. However, two differences can be derived from simple considerations: 1) Based on the Racah B parameters of the free ions (V^{2+} : 766 cm^{-1} , Cr^{3+} : 918 cm^{-1}), lower emission energies are expected for vanadium(II) complexes.⁹⁴ 2) The lower charge of the V^{2+} ion should entail a lower intrinsic ligand field splitting, which needs to be accounted for to avoid bISC to the $^4T_{2g}$ state.¹⁵ Literature on molecular vanadium(II) complexes is scarce, as only a small set of tris-bidentate polypyridine complexes **30**²⁺-**34**²⁺ has been examined (Scheme 4). In fact, none of them is luminescent.^{40-43,128}



Scheme 4: Polypyridine vanadium(II) complexes.

All complexes feature intense absorption up to 800 nm which originates from spin-allowed 4MLCT transitions.^{41,43,128} The lifetimes of the associated 4MLCT states are in the range of 0.5 - 2.0 ns as determined in flash-photolysis experiments in solution at 293 K, which excludes the population of a nested doublet state.⁴¹ At first, these findings were rationalized with the non-radiative decay of said 4MLCT states.⁴¹ Later, this assignment was brought into question as a 4MLCT should yield stimulated fluorescence, which could not be detected either in sub-picosecond TA experiments on solutions of **30**²⁺ and **32**²⁺, even at 100 K.⁴³ Instead, two low-energy doublet states of mixed 2MC and 2MLCT character were proposed based on electrochemical, TA and quantum chemical studies.⁴³ ISC into the $^2MC/{}^2MLCT$ manifold occurs within 200 fs, where the lower state is populated via IC within 3 ps. GS recovery is achieved after 430 ns and 1.6 ns, respectively. A higher degree of ES distortion inferred by the 2MLCT character is suggested to accelerate non-

radiative decay. This is in stark contrast to the virtually undistorted doublet states in many chromium(III) complexes.⁶⁵ Clearly, low-energy CT states are an obstacle in vanadium(II) complexes that is mostly absent in chromium(III) complexes (see section 1.2.). These findings are corroborated by another study that compares $[\text{V}(\text{bpy})_3]^{3+}$ **30**²⁺ and $[\text{V}(\text{phen})_3]^{3+}$ **32**²⁺ to their chromium(III) analogues. Quantum-chemical calculations predict the lowest doublet state of $[\text{V}(\text{bpy})_3]^{3+}$ **30**³⁺ to have a considerable ligand contribution.¹²⁸ Comparison of the crystal structures of **30**²⁺ and **32**²⁺ with their chromium(III) analogues corroborate this finding, as they reveal a more pronounced trigonal distortion of the vanadium complexes, which can be traced back to mixing of metal-d and ligand- π orbitals.¹²⁸ The orbital mixing is again rationalized with the lower charge of the V^{2+} ion compared to Cr^{3+} that accounts for expanded d orbitals and more covalent V-N bonds. This circumstance is also reflected in the more strongly contracted M-L bonds of **30**²⁺ and **32**²⁺ as compared to the respective chromium(III) complexes.¹²⁸

1.3.2. d^2 Vanadium(III)

Early studies demonstrate the SF emission of V^{3+} ions in elpasolite host lattices, such as $\text{CsNaYCl}_6:\text{V}^{3+}$.⁴⁶ Sharp phosphorescence emission bands above 1000 nm at temperatures as low as 7 K were observed. Above 100 K, thermally activated bISC leads to a broad fluorescence band originating from the ${}^3\text{T}_2$ state which dominates the emission spectrum.⁴⁶ This also applies to the ruby-analogue $\text{Al}_2\text{O}_3:\text{V}^{3+}$, which displays phosphorescence at 1026 nm below 80 K. The luminescence intensity is described to be three to four orders of magnitude lower than in ruby.¹³¹ However, its drastic bathochromic shift compared to ruby's emission at 694 nm indicates a lower B parameter in the V^{3+} -doped lattices.^{34,131} Similar to $[\text{CrF}_6]^{3-}$ and $[\text{Cr}(\text{NCS})_6]^{3+}$, the LFS is too small in these solids.^{100,102} SF phosphorescence of d^2 TM ions originates from the ${}^1\text{T}_2/{}^1\text{E}$ states at Δ_0 values above ca. $17B$, where the singlet terms surpass the lowest LF excited state ${}^3\text{T}_2$, according to the TS diagram (Fig. 8).^{92,93}

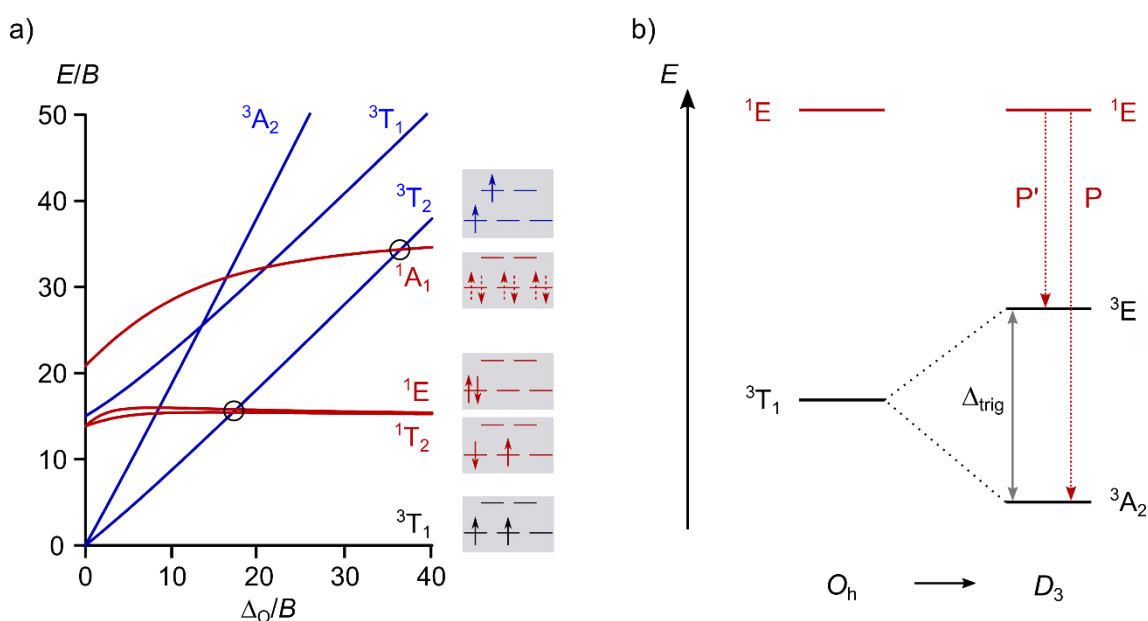
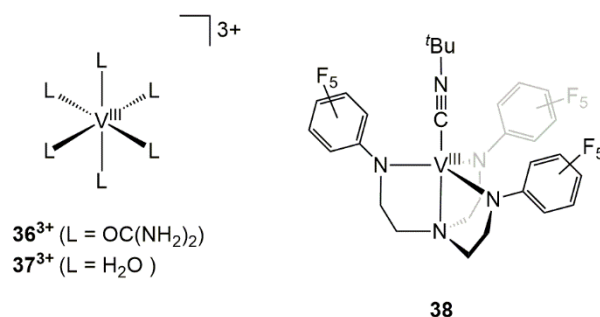


Figure 8: a) Simplified Tanabe-Sugano diagram of a d^2 ion in an octahedral ligand field at a ratio of $C/B = 4.0$. Blue: Interconfigurational states. Red: Intraconfigurational states. Microstates

Introduction

assignment based on CAS-SCF calculations on $[\text{VH}_6]^{3-}$ with dotted lines indicating strong mixing. b) Splitting of the ${}^3\text{T}_1(\text{O}_h)$ state in a D_3 -symmetric environment.⁹⁷ Δ_{trig} : Magnitude of trigonal splitting. P/P': Phosphorescence.

The degeneracy of the ${}^3\text{T}_1$ GS can be lifted through trigonal Jahn-teller distortion as in the $[\text{V}(\text{urea})_6]^{3+}$ **36**³⁺ (Scheme 5). A structured SF emission band with maxima at 992, 1009, 1011 and 1187 nm is observable in a glassy matrix at 77 K which can be traced back to a trigonal GS splitting Δ_{trig} of 1400 cm^{-1} (Fig. 8b).⁵² Results from Raman spectroscopy on **36**³⁺ corroborate this finding.⁵² An even larger value was determined for the hexa-aqua vanadium(III) cation $[\text{V}(\text{H}_2\text{O})_6]^{3+}$ **37**³⁺ embedded in a guanidinium sulphate matrix, where the JT-induced splitting amounts to 2720 cm^{-1} .¹³² Hence, the total SF luminescence intensity is distributed among several transitions from the ${}^1\text{E}/{}^1\text{T}_2$ levels to the ${}^3\text{A}_2$ and ${}^3\text{E}$ terms that arise from the JT distortion (Fig. 8b). Accordingly, the emission is dispersed over a wider spectral range in vanadium(III) complexes compared to chromium(III) SF emitters, which feature a totally symmetric ${}^4\text{A}_2$ GS.



Scheme 5: Luminescent hexa- and penta-coordinate vanadium(III) complexes.

Changing the symmetry to C_{3v} in the penta-coordinate complex $\text{V}((\text{C}_6\text{F}_5)_3\text{tren})(\text{CN}^t\text{Bu})$ **38** ($(\text{C}_6\text{F}_5)_3\text{tren} = 2,2',2''\text{-tris}[(\text{pentafluorophenyl})\text{amino}]triethylamine$) yields a totally symmetric ${}^3\text{A}$ ground state and hence, no trigonal distortion (Scheme 5).⁴⁴ Two weak absorption bands ($\varepsilon = 500\text{--}600\text{ M}^{-1}\text{ cm}^{-1}$) centred at 700 nm and 640 nm were assigned to spin-allowed, metal-centered transitions since their extinction coefficients are too low for CT transitions. Upon irradiation at 640 nm, a single luminescence band was observed in a 2-MeTHF glass at 77 K peaking at 1240 nm. It is undetectable at room temperature as non-radiative decay outcompetes the slower radiative process. One of these channels appears to be vibronic coupling to the axial isocyanide ligand.⁴⁴ FWHM values of 3 cm^{-1} and 400 cm^{-1} were measured for this NIR band in the solid state at 4 K and 298 K, respectively. This is an argument for spin-flip emission from the lowest singlet state which is a ${}^1\text{E}$ state in a C_{3v} symmetric complex.⁴⁴ The respective lifetimes amount to $11\text{ }\mu\text{s}$ at 4 K and $3\text{ }\mu\text{s}$ at 298 K and substantiate the occurrence of an intraconfigurational transition. The emission was found to be independent of the excitation wavelength and hence, excitation of different states results in the same decay pathway to the emissive ${}^1\text{E}$ state. Nanosecond TA experiments at 90 K lend further support to the population of a long-lived singlet state as ground-state bleach and two excited-state absorption bands decay on a microsecond scale.

A three-state-model is proposed based on TA measurements, which envisages ISC from the initially excited 3E state into the singlet manifold with a time constant of 4.2 ps. Then vibrational cooling ensues within 26 ps, followed by luminescence with a lifetime of 9 μ s from the 1E state, which is in agreement with the values obtained from emission spectroscopy.⁴⁴

1.3.3. d^8 -Nickel(II)

Nickel(II) displays a triplet GS similar to d^2 ions, but no Jahn-Teller-induced ground state splitting is expected here since the ground state is totally symmetric. Contrary to spin-flip states of d^2 ions, the spin flip here occurs in the e_g^* orbitals. The lowest singlet state 1E is composed of a state with a doubly occupied e_g^* orbital according to CAS-SCF calculations on the model complex $[\text{Ni}^{\text{II}}\text{H}_6]^{4-}$, which might account for a Jahn-Teller distortion in the excited state (Fig. 9).⁹⁷

In an octahedral ligand field, the 3F term of the free ion splits into a 3A_1 ground state and two triplet excited states, a lower 3T_2 and a higher energy 3T_1 (Fig. 9).^{92,93} At LFS values of $17 \Delta_0/B$ and $31 \Delta_0/B$, the lower 3T_2 crosses with the SF states 1T_2 and 1A_1 . Interestingly, the spin-forbidden transition to the 1E state has been observed in the absorption spectra of many nickel(II) complexes, such as $[\text{Ni}(\text{NH}_3)_6]^{2+}$ **39**³⁺, $[\text{Ni}(\text{bpy})_3]^{2+}$ **40**³⁺, $[\text{Ni}(\text{tpy})_3]^{2+}$ **41**²⁺, $[\text{Ni}(\text{phen})_3]^{2+}$ **41**³⁺ and $[\text{Ni}(\text{tpm})_2]^{2+}$ **42**³⁺ (tpm = tris(2-pyridyl)methane) (Scheme 6).¹³³⁻¹³⁶

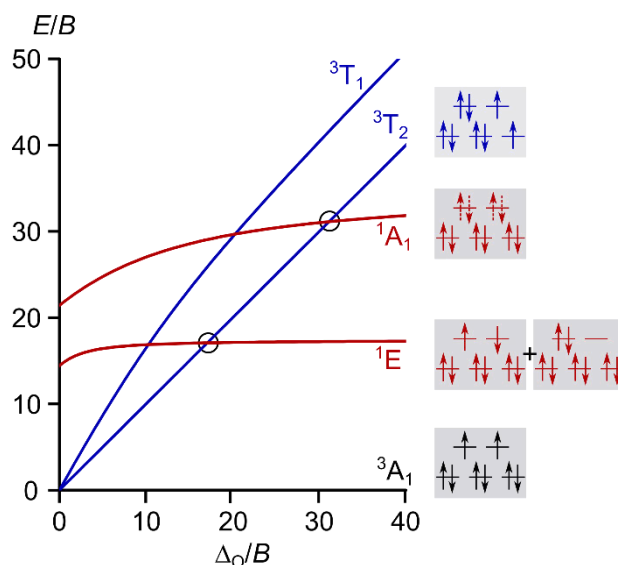
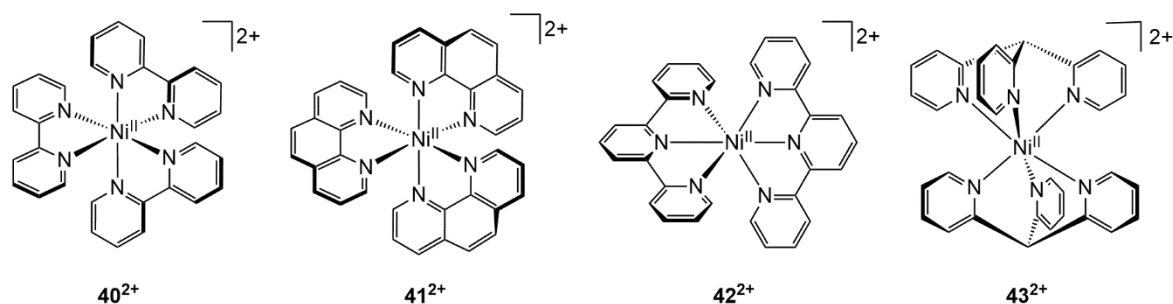


Figure 9: Simplified Tanabe-Sugano diagram of a d^8 ion in an octahedral ligand field at a ratio of $C/B = 4.0$. Blue: Interconfigurational states. Red: Intraconfigurational states. Microstates assignment based on CAS-SCF calculations on $[\text{NiH}_6]^{4-}$ with dotted lines indicating strong mixing.⁹⁷



Scheme 6: Pseudo-octahedral polypyridine nickel(II) complexes.

A widely accepted model invokes an intensity borrowing mechanism from the ${}^3A_1 \rightarrow {}^3T_1/{}^3T_2$ transitions.¹³⁷ Therein, the intensity I of the spin-forbidden band is given as

$$I = K \cdot \frac{\gamma^2}{\Delta E^2} \quad (15)$$

where K is a constant factor and γ denotes the coupling constant between singlet and triplet state. The energy difference of both states is expressed as ΔE .¹³⁷ In O_h symmetry, K equals $\sqrt{6}\lambda$ with λ being the spin-orbit coupling constant of the free ion.¹³⁸ A description of I according to eq 15, however, is valid only if the 1E state is the lowest excited state.¹³⁹

Depending on the magnitude of Δ_o , the ${}^3A_1 \rightarrow {}^1E$ transition is found at the high-energy or low-energy side of the ${}^3A_1 \rightarrow {}^3T_2$ band in complexes **40**²⁺-**43**²⁺. Hence, the respective values of Δ_o must be around $17 B$, and have to be increased significantly to prevent bISC to the triplet metal-centred states. It is highly unlikely for the 1E states to exhibit luminescence under such circumstances, in particular because the 3T_2 state will rapidly decrease in energy upon distortion. Yet **41**²⁺ and **43**²⁺ have been reported to show singlet state emission just recently.¹³⁴ The finding has been called into question as the weak luminescence bands of **41**²⁺ and **43**²⁺ detected at 80 K and 150 K are superimposable,¹³⁴ which seems odd considering the complexes' different symmetries. The dissimilar luminescence band shapes of analogue chromium(III) complexes $[\text{Cr}(\text{phen})_3]^{3+}$ **18**³⁺¹¹¹ and $[\text{Cr}(\text{tpe})_2]^{3+}$ **24**³⁺¹²¹ may be compared as a frame of reference.

Reaching the necessary high ligand field splitting here is not as straightforward as for other ions though, because nickel(II) complexes tend to adopt a square-planar coordination geometry with a singlet ground state in strong-field environments.¹⁵ Naturally, no spin-flip luminescence was found in any complex of the heavier homologues palladium(II) and platinum(II), which impart a larger LFS by themselves due to the primogenic effect.¹⁵ They require much more elaborate ligands to enforce an octahedral coordination geometry than chromium or iron, for instance.^{140–143}

1.4. Application of Spin Flip Luminophores

Near-infrared luminescence is of great interest for numerous applications such as optical signal transduction, sensing, lasing or bio imaging, for instance, ^{144–146} where lanthanides and precious elements are frequently employed.^{147–149} Novel NIR emitters based on first row TM ions could emerge as more affordable substitutes in the future, some interesting examples have been reported.

Direct excitation of the emissive MC states of lanthanides is not easily achieved since the respective $4f \rightarrow 4f$ transitions are Laporte-forbidden.¹⁵⁰ To enhance emission from a lanthanide ion, chromium(III) complexes can be incorporated together with lanthanide ions in polynuclear complexes. Their long-lived doublet excited states can serve as sensitizer for the desired lanthanide emission through $\text{Cr}^{3+} \rightarrow \text{Ln}^{3+}$ energy transfer. Bi- and tri-nuclear complexes $[\text{Cr}^{\text{III}}\text{Ln}^{\text{III}}(\text{L})_3]^{6+}$ ($\text{Ln} = \text{Nd}, \text{Yb}$) and $[\text{Cr}^{\text{III}}\text{Ln}^{\text{III}}\text{Cr}^{\text{III}}(\text{L})_3]^{9+}$ ($\text{Ln} = \text{Nd}, \text{Er}, \text{Yb}$) with helicate ligands L exhibit millisecond NIR luminescence from Ln^{3+} centres between 1000 and 1670 nm upon direct excitation of the chromium(III) ${}^2\text{E}$ states at 750 nm.^{151,152}

Besides sensitization of lanthanide NIR luminescence, chromium(III) SF luminophores are also suitable for other applications. The particularly efficient double emission of molecular ruby $\mathbf{20}^{3+}$ with sharp bands at 738 nm and 775 nm, for example, enables its use as ratiometric optical thermometer due to the small energy gap of 630 cm^{-1} between the two emissive states ${}^2\text{E}$ and ${}^2\text{T}_1$.^{126,153} The luminescence intensity distribution exhibits a Boltzmann-type behavior and varies with temperature.¹²⁶ Furthermore, the same complex has been proposed as pressure sensor in the solid state as well as in aqueous or methanolic solution.¹⁵⁴ Its ${}^2\text{E}$ emission band is red-shifted at $-14.1 \text{ cm}^{-1} \text{ kbar}^{-1}$ in solid and $-15 \text{ cm}^{-1} \text{ kbar}^{-1}$ in frozen solution when pressurized in a diamond anvil cell. Complex $\mathbf{20}^{3+}$ surpasses the shift of the ruby R lines (ca. $-0.7 \text{ cm}^{-1} \text{ kbar}^{-1}$)¹⁵⁵ by a factor of 20 in terms of sensitivity.¹⁵⁴ Due to its extraordinarily long doublet state lifetime, it can also act as photosensitizer for singlet oxygen. Dexter-type energy transfer from $\mathbf{20}^{3+}$ to ${}^3\text{O}_2$ generated ${}^1\text{O}_2$ with a 61 % quantum yield. Hence, $\mathbf{20}^{3+}$ was employed as photosensitizer in the oxidative functionalization of C–H bonds¹⁵⁶ and as oxygen sensor in solution.¹⁵³ Doublet-triplet energy transfer from molecular ruby $\mathbf{22}^{3+}$ to 9,10-diphenylanthracene occurs in a similar manner based on a high doublet excited state lifetime of 890 μs .¹⁵⁷ Green-to-blue triplet-triplet annihilation upconversion with a quantum yield of 12 % ensues, while sterically less hindered anthracenes undergo a [4+4] cycloaddition reaction instead.¹⁵⁷

A remarkable trait is the occurrence of circularly polarized luminescence (CPL) from chiral enantio-enriched complexes with tridentate 6-ring chelate ligands like ddpd or dqd.^{120,158} This special type of luminescence could be useful for three-dimensional displays or optical information storage or encryption, for instance.^{159–161} Due to their flexibility, the ligands are wrapped around the metal centre in a double helix fashion, resulting in the formation of (*P,P*) and (*M,M*) enantiomers. They can be separated by HPLC with chiral stationary phases to yield either left-handed or right-handed polarized emission. A measure for the

ratio of left-handed over right-handed polarized light intensity (I_L and I_R) is given by the dissymmetry factor g_{lum} in eq. 16.¹⁶²

$$g_{lum} = 2 \cdot \frac{(I_L - I_R)}{(I_L + I_R)} \approx 4 \frac{|m_{ba}|}{|\mu_{ab}|} \cdot \cos \tau_{ab} \quad (16)$$

The second part of eq. 16 describes g_{lum} as the ratio of magnetic and electronic transition dipole moments μ_{ab} and m_{ab} for a given transition $a \rightarrow b$ the angle τ_{ab} between both vectors. Spin-forbidden transitions imply high μ_{ab} and low m_{ab} , which applies to the radiative transition between 2E and 4A_2 in chromium(III) complexes and rationalizes the high dissymmetry factors found for $\mathbf{20}^{3+}$ ($g_{lum} = 0.09$)¹⁵⁸ and $\mathbf{23}^{3+}$ ($g_{lum} = 0.2$).¹²⁰

1.5. Paramagnetic Ground States

Besides luminescence, the unpaired d electrons of TM centres entail paramagnetism.^{163–165} Due to interelectronic repulsion between these electrons, paramagnetic ground states are subject to an additional splitting that is independent of any external magnetic field and, hence, is termed zero-field splitting (ZFS). Employing paramagnetic TMCs as single molecule magnets (SMMs)^{163,166–168} or single ion magnets (SIMs)^{169–171} heavily relies on ZFS, as does their potential use as quantum bits (qubits). This section will briefly outline the working principles of SMMs and qubits and comment on the suitability of vanadium(II/III) complexes in this context.

1.5.1. Single Molecule Magnets

SMMs permit data storage on a molecular level and thereby surpass the limitations of magnetic nanoparticles.¹⁶⁸ Information can be encoded in these molecules through a switch of the spin state. Accordingly, the function of a TMC acting as SMM rests on the existence of magnetically bistable ground states. A well-known example is the Mn_{12} -acetate, which owes its high GS spin of $S = 10$ to the magnetic exchange interaction of eight Mn^{IV} and four Mn^{III} centres.¹⁶³ However, the twenty-one GS spin sublevels are subject to ZFS which partly lifts their degeneracy in the absence of an external magnetic field (Fig. 10b). ZFS yields ten spin doublets called Kramer's doublets with $|M_s| = \pm 10$ to $|M_s| = \pm 1$ and a spin singlet, $M_s = 0$.

In a zero-field environment, both spin states of the lowest Kramer's doublet ($|M_s| = \pm 10$) are evenly populated and separated by an energy barrier U that can be overcome if the thermal energy of the system is sufficiently high (Fig. 10a). To magnetize the sample, an external magnetic field B_0 will be applied which stabilizes the $M_s = -10$ state while simultaneously destabilizing the $M_s = +10$ state. Accordingly, the barrier for a population transfer towards the $M_s = -10$ state decreases and the complex is magnetized (Fig. 10b).

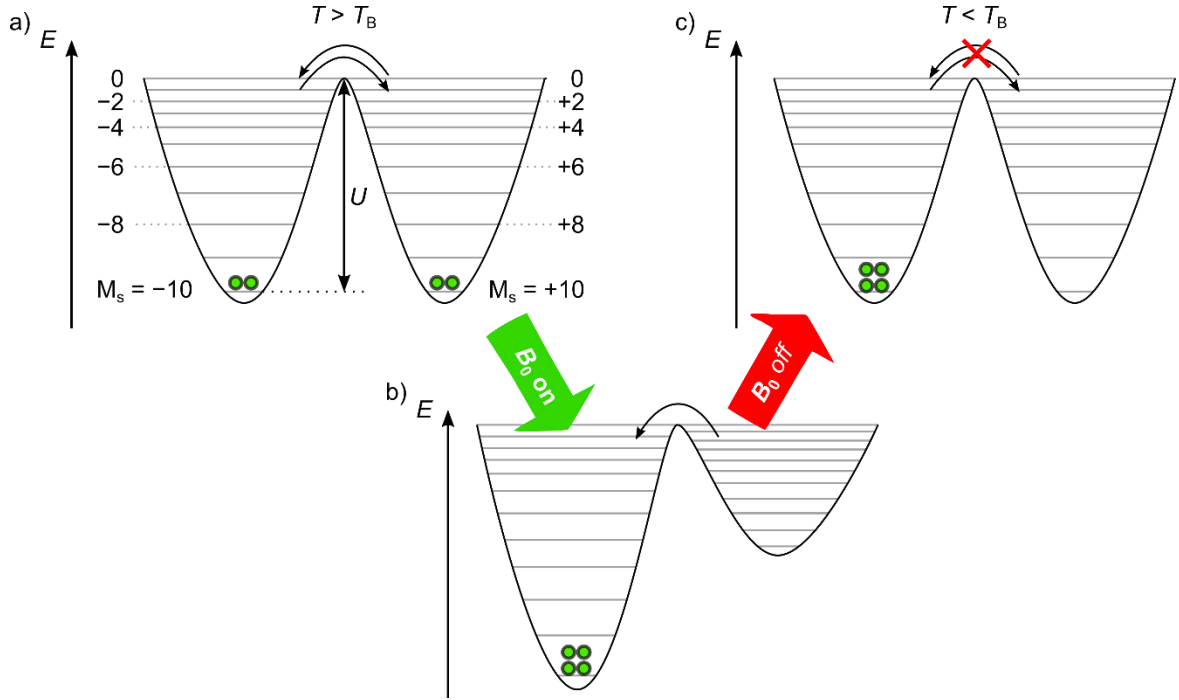


Figure 10: a) Potential wells of $|M_s| = \pm 10$ states a) in thermal equilibrium at $T > T_B$ without external magnetic field B_0 , b) with B_0 enabled and c) “frozen” in the $M_s = -10$ states at $T < T_B$ without B_0 (adapted from ref. ¹⁶⁸).

Switching off the external field will restore the degeneracy of both levels. If the temperature of the system is kept below the blocking temperature T_B , no thermal equilibration can occur and the sample’s magnetization will persist even in a zero-field environment (Fig. 10c). In that way, the spin states can be manipulated purposefully to store information. The barrier height U directly impacts the conditions of magnetic relaxation and therefore, knowledge of U is critical to assess a TMCs suitability as SMM or single ion magnet (SIM).

Here, the dependence of U on the axial ZFS parameter D as given by eq. 17a,b¹⁶⁸ is advantageous because sign and magnitude of D can be obtained through EPR measurements which enables the determination of the barrier’s height.

$$U = S^2 \cdot |D|; S = \text{integer} \quad (17a) \quad U = (S^2 - \frac{1}{4}) \cdot |D| \quad S = \text{non - integer} \quad (17b)$$

TMCs with a single paramagnetic centre hold advantages over those which comprise several TM ions as a higher number of paramagnetic centres reduces the magnetic anisotropy (i.e. the ZFS parameter D) and concomitantly the barrier height U ¹⁷² as D decreases with the total spin squared:¹⁷³

$$D \propto \frac{1}{S^2} \quad (18)$$

Zero-field splitting is purely anisotropic and the corresponding ZFS Hamiltonian \hat{H}_{ZFS} is characterized by the zero-field parameters D and E :¹⁶⁸

$$\hat{H}_{ZFS} = D\hat{S}_z^2 + E(\hat{S}_x^2 - \hat{S}_y^2) \quad (19)$$

The axial and transversal splitting parameters D and E express the directional components of the zero-field splitting, D_x , D_y and D_z , and they are defined as follows:¹⁷⁴

$$E = \frac{1}{2}(D_x - D_y) \quad (20)$$

$$D = \frac{3}{2}D_z \quad (21)$$

If the D parameter is positive, the states with smallest $|m_s|$ value are lowest in energy. If D is negative, the lowest-lying states are those with the highest $|m_s|$.¹⁶⁸ In the case of an octahedrally coordinated d^3 transition metal ion such as vanadium(II), the spin multiplet of the ${}^4A_{2g}$ ground state encompasses four degenerate spin states (Fig. 11a) split by ZFS (Fig. 11b).

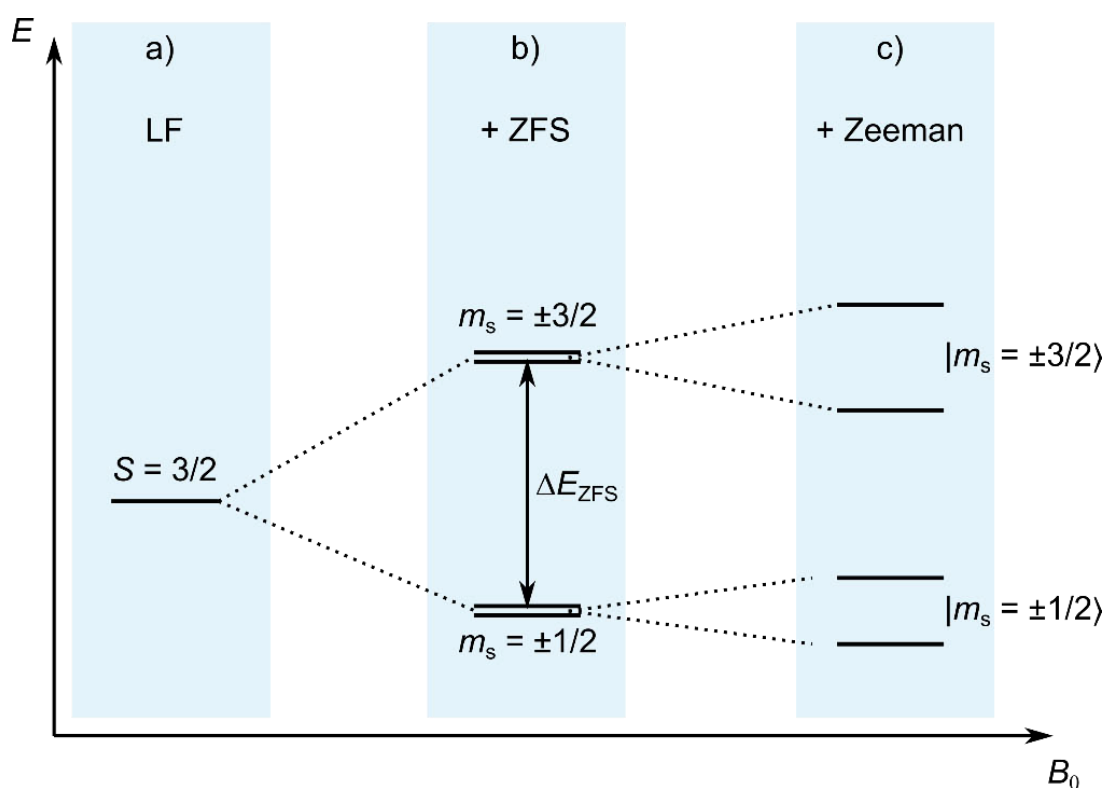


Figure 11: a) Splitting of the degenerate ${}^4A_{2g}$ ground state of a d^3 TMC through b) zero-field splitting and c) Zeeman interaction in an external magnetic field B_0 (c).

Application of an external magnetic field splits the two Kramer's doublets into four separate states due to the Zeeman effect (Fig. 11c). If the ZFS is significantly larger than the Zeeman splitting, states of the individual Kramer's doublets will not mix due to the large energy gap. Hence, vanadium(II) TMCs possess an electronic structure that could allow their use as SIMs in principle. The magnetic properties of the vanadium(II) complexes under study will therefore be explored.

1.5.2. Quantum bits

Quantum bits (qubits) are the fundamental information processing units of a quantum computer, which has been proposed in the 1980's by R. Feynman.¹⁷⁵ The superior performance of quantum computers in solving certain mathematical problems as in factoring large integer numbers,¹⁷⁶ for instance, has spurred research in the field of quantum computing within the last two decades and likewise, the interest in developing suitable qubits has grown.¹⁷⁷ One of the many forms qubits can come in are luminescent TMCs, and the NIR SF emission capability of vanadium(II/III) ions in the right coordination environment (see [section 1.3](#)) is promising in this regard. This section provides a concise picture of a qubit's mode of operation and points out the viability of vanadium(II/III) complexes as quantum information processing units.

In principle, any quantum-mechanical two-state system can be employed as qubit to process information with. More precisely, the spin state of a nucleus¹⁷⁸ or electron¹⁷⁹ or even the polarization state of a photon¹⁸⁰ can be exploited for this purpose. While a single qubit such as a quantum spin with $S = \frac{1}{2}$ could be emulated by a classical oscillator with randomly timed single-bit readout, a qubit is set apart from its classical counterpart by its ability to be in a superposition state which is essential to the power of quantum computing. In addition, the quantum entanglement of several qubits enables quantum teleportation as a means of information transfer.^{181,182} The prerequisites for a quantum-mechanical system acting as qubit can be envisioned by the example of a negatively charged nitrogen vacancy (NV⁻) centre in a diamond lattice with two electron spins ($S = 1$) acting as qubit:¹⁸³

- The qubit can be deliberately prepared in a spin-polarized state – it can be 'initialized'.
- The spin-polarized state can be read out, for example by photon emission.

Spin-polarization in NV⁻ centres can be achieved starting with off-resonant microsecond laser pulses at 532 nm to populate the spin-sublevels of the excited ³E state (Fig. X).¹⁸⁴ While the ³E spin ground state decays by emitting a photon of 637 nm wavelength, ISC to the intermediate ¹A₁ state is not observed. From the $m_s = \pm 1$ sublevels of the ³E state, however, a substantial amount of population is transferred to the ¹A₁ state due to a potential surface intersection. From there, relaxation to the different spin-substates of the ³A₂ GS ensues either directly or via the ¹E state. Hence, optical pumping for many cycles will ultimately empty the $m_s = \pm 1$ levels of the electronic GS and populate only the $m_s = 0$ states, yielding spin polarisation. When an external magnetic field is applied, the $m_s = \pm 1$ states are split due to Zeeman interaction and can be further manipulated with specific microwave pulse sequences to prepare the qubit in a superposition state which can then be employed for information processing.^{183–185} Spin-selective readout is possible due to the dependency of fluorescence intensity on the spin state.^{186,187} Notably, optical readout of a molecular qubit has recently been achieved with a dinuclear europium(III) complex.¹⁸⁸ A major obstacle are the coherence times of these superposition states which are reduced by coupling to molecular vibrations and magnetic moments.¹⁸⁹

The penta-coordinate vanadium(III) complex $V((C_6F_5)_3tren)(CN^tBu)$ **38** exemplifies the potential of vanadium(III) TMCs with respect to optically addressable qubit.⁴⁴ Just like the aforementioned NV^- centres in the diamond lattice, complex **38** exhibits a zero-field split 3A GS and a luminescent 1E excited state nested with the ground state which enables optical initialization and yields narrow SF emission bands with FWHM values of 3 cm^{-1} in solid state luminescence measurements at 4 K (Fig. 12). Yet, the individual spin sublevels of the GS of **38** cannot be resolved in zero-field photoluminescence measurements as was done for NV^- centres.

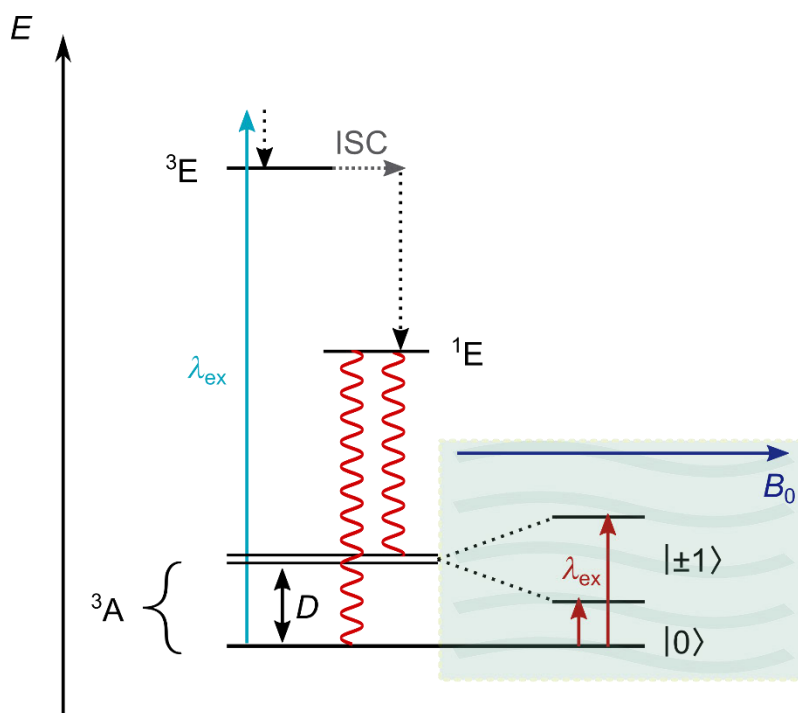


Figure 12: Jablonski diagram for a d^2 TMC with zero-field split 3A ground state. Vertical solid arrows: Optical excitation (red & light blue). Dotted arrows: Vibrational cooling (black) and ISC (grey). Wavy red lines: Photoluminescence. Box: Zeeman-split 3A spin states in an external magnetic field B_0 .

Applying an external magnetic field of up to 9 T enables their detection in variable field photoluminescence experiments. The ZFS in **38** is fourfold larger with $D = 3.6\text{ cm}^{-1}$ compared to the NV^- centre¹⁸³. This should entail a higher thermal spin polarization in **38** while maintaining EPR addressability.^[44] Pulsed EPR measurements at 240 GHz powered by a free electron laser enable experimental determination of the coherence times. The $M_s = -1$ transition at 6.44 GHz yields the highest phase memory times of 427 ns at 5 K, decreasing to 137 ns at 10 K. Hahn echo experiments reveal lower phase memory times of 339 ns and 178 ns for the $M_s = +1$ and $M_s = +2$ transitions at 3.75 GHz and 10.5 GHz. To improve molecular vanadium(III) qubits, achieving even higher D values is suggested which could enable photodetection of the spin sublevels of the 3A GS at lower or zero external field.⁴⁴

While vanadium(III) complexes with a GS spin triplet are promising candidates for optically addressable qubits, vanadium(II) complexes with a 4A_2 GS might be eligible as qubits even due to the higher number of spin sublevels.¹⁷⁷ But so far, all reported molecular vanadium(II) complexes have been shown to be non-luminescent due to unfavourable CT

state admixtures to their metal-centred SF sites,^{38,40–43} which poses a major hindrance for quantum information processing applications (section [1.3.2](#)).

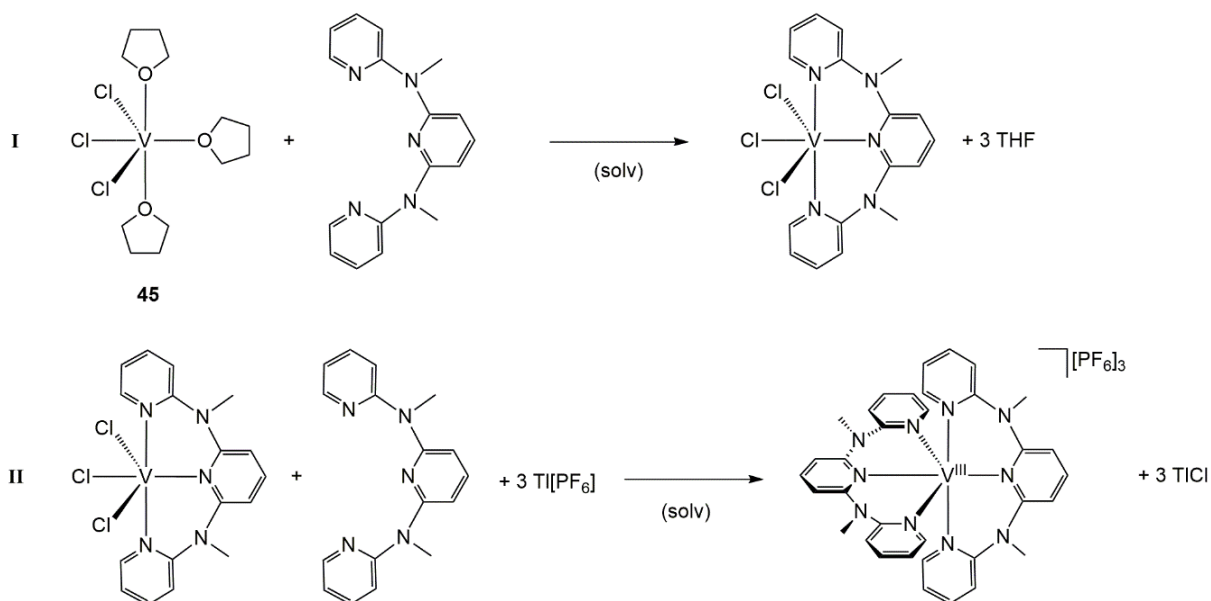
1.6. Synthesis of Vanadium(II/III) and Nickel(II) Complexes

This chapter will provide insight into the chemistry of vanadium, elaborate on the intricacies of preparing vanadium complexes in low oxidation states and provide a guideline to polypyridine vanadium(II/III) complexes.

After an initial claim to vanadium's discovery by M. A. del Rio in 1801 had been retracted, it was identified and named in 1830 by N. G. Sefström. The element is widely distributed in nature with an abundance of 0.013 % in earth's lithosphere¹⁵ and can be found in numerous ores, such as vanadinite $Pb_5(VO_4)_3Cl$, in the sulfide ore patronite $V^{IV}(S_2)_2$ or in carnotite $K_2(UO_2)_2(VO_4)_2 \cdot 3 H_2O$.¹⁵ It is recovered from these ores largely in the form of the divanadium pentoxide V_2O_5 , from which elemental vanadium can be prepared by reduction with calcium at 950°C or with aluminum. High purity vanadium can be obtained by the crystal bar process developed by van Arkel and de Boer.¹⁵ Metallic vanadium is a potent reductant ($E^0 = -2.11 V$)¹⁹⁰ - when exposed to air it is quickly covered with a passivating oxide layer. Similarly, vanadium(II) and vanadium(III) compounds are susceptible towards oxidation in the solid state and in solution to yield the particularly stable vanadyl ion $[V^{IV}O]^{2+}$.^{15,191} The vanadium di- and trihalides VX_3 ($X = Cl, Br, I$), for example, dissolve in water to give the hexa(aqua) cations $[V^{II/III}(H_2O)_6]^{2+/3+}$, which are readily oxidized to give blue solutions of $[VO(H_2O)_5]^{2+}$.¹⁹¹ Numerous reports document its preference for the oxidation state +IV in the presence of water and oxygen,^{15,191-194} hence the $[V^{IV}O]^{2+}$ motif is pervasive in vanadium coordination chemistry and has been studied extensively.¹⁹⁴⁻¹⁹⁹ Prolonged exposure to oxygen leads to the formation of oxovanadium(V) species such as V_2O_5 . While vanadyl complexes can be applied as catalysts in oxidation reactions,²⁰⁰⁻²⁰⁴ its d^1 electron configuration precludes luminescence from metal-centred states.

It is possible though to obtain non-oxo-vanadium complexes in the oxidation states +5, +4, +3, +2, 0 and -1 if water and oxygen are excluded.^{193,205-208} This requirement makes vanadium complex synthesis a lot more time-consuming and cumbersome than the preparation of, for example, analog nickel(II) or chromium(III) complexes, which can be handled under ambient conditions typically. It also accounts for the discrepancy between the amount of reports on the photophysics of chromium(III) complexes and that dedicated to vanadium(II/III) complexes: Only a handful of polypyridine vanadium complexes in the lower oxidation states +2 and +3 have been reported so far (see [section 1.3](#)).³⁸⁻⁴¹

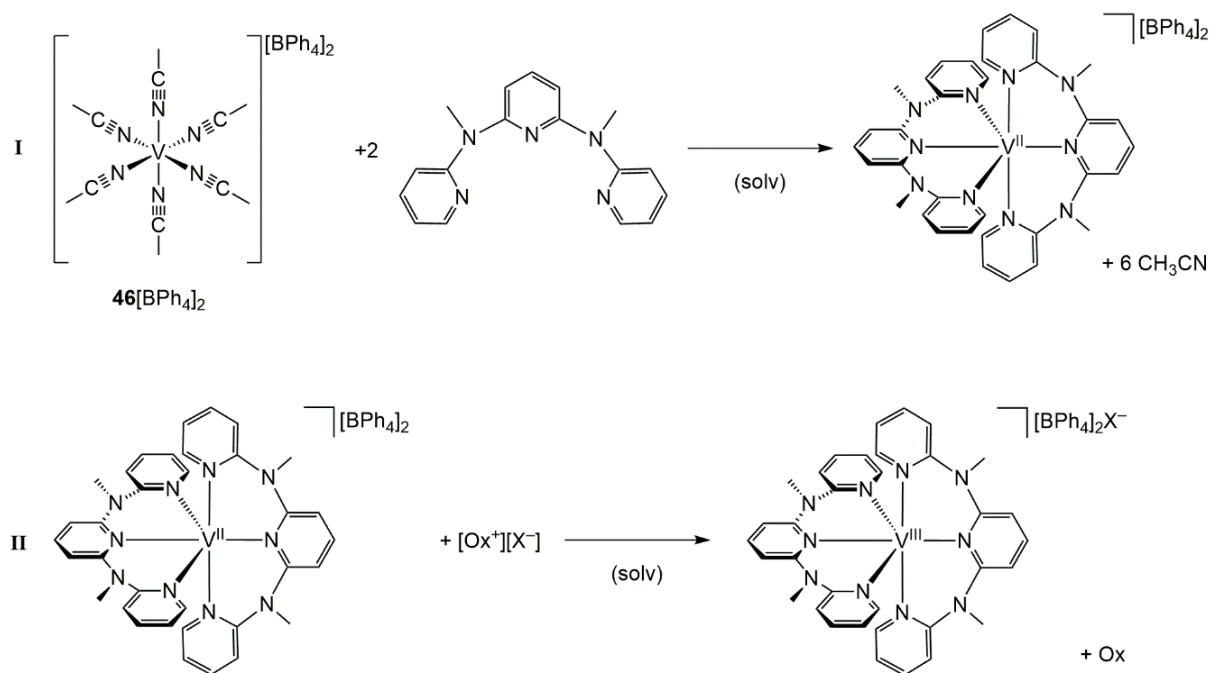
The successful preparation of polypyridine complexes requires suitable precursor complexes. As complexes with the polypyridine ligand ddpd are envisaged, the precursor complexes should be well soluble in organic solvents such as tetrahydrofuran, acetonitrile or dichloromethane. Solvent adducts of the trichlorides VCl_3L_3 ($L = CH_3CN$ (**44**), THF(**45**)) of vanadium(III) are well established and provide a good starting point for complex syntheses.^{209,210} By replacing the weakly coordinating solvent molecules with ddpd, a heteroleptic vanadium(III) complex $VCl_3(ddpd)$ should be formed first (Scheme 7) in analogy to $VCl_3(tpy)$ prepared earlier.²¹¹



Scheme 7: Two-step synthesis of the homoleptic $\text{mer-}[\text{V}(\text{ddpd})_2]^{3+}$ complex via the heteroleptic trichlorido vanadium(III) complex $\text{VCl}_3(\text{ddpd})$.

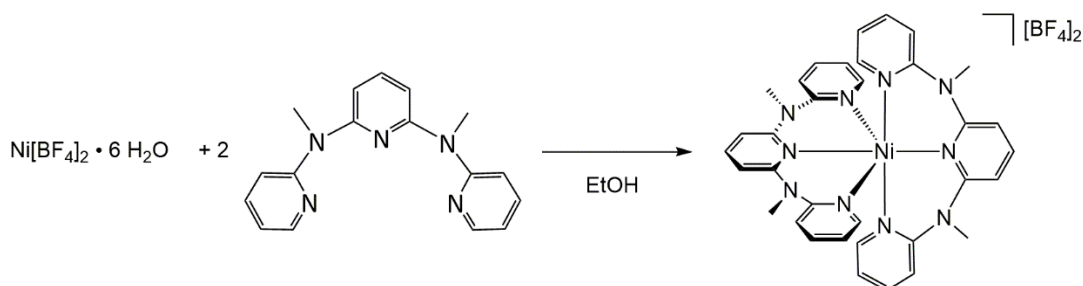
Subsequent abstraction of the halide ligands with thallium(I) or silver(I) salts in the presence of free ligand could yield a homoleptic ddpd complex.²¹¹ Both routes, however, come with a drawback: Silver(I) reagents could oxidize the vanadium(III) centre and thallium(I) salts are highly toxic. In a third step, to obtain vanadium(II) complexes, the metal centre needs to be reduced to V^{II} . Reduction of the ddpd ligand has been reported to occur well below -1.8 V in other first row TMCs and should not interfere.^{25,65,212} A suitable reductant can be determined by cyclic voltammetry.

Reacting three equivalents of sodium tetraphenylborate with $\text{VCl}_3(\text{CH}_3\text{CN})_3$ in acetonitrile at ambient temperature yields the hexa(acetonitrile) vanadium(II) complex $[\text{V}(\text{CH}_3\text{CN})_6][\text{BPh}_4]_2$ **46** $[\text{BPh}_4]_2$, which provides a convenient alternative to the halide abstraction reactions outlined above.²¹³ After coordinating two equivalents of ddpd and exchanging the tetraphenylborate with redox-stable hexafluorophosphate, for example, selective oxidation of the vanadium(II) centre should be easily achieved (Scheme 8). The $\text{V}^{\text{II/III}}$ redox couple of the less electron-rich complex $[\text{V}(\text{phen})_3]^{3+}$ is located at ca. $E_{1/2} = 0.01 \text{ V}$ (in CH_2Cl_2 vs Fc/Fc^+) while the ddpd ligand is oxidized well above $E_{1/2} > 0.75 \text{ V}$ (in MeCN , vs Fc/Fc^+) in comparable systems.^{41,65,214,215} Yet, the reaction mechanism leading to the formation of the precursor complex **46** $[\text{BPh}_4]_2$ has not yet been elucidated. The authors claim that acetonitrile not only serves as solvent, but also acts as reductant, reducing vanadium(III) to give vanadium(II).²¹³ This appears rather unlikely for two reasons: First, the redox potential of acetonitrile is too high to justify such a reaction. It finds broad use as solvent in electrochemistry experiments due to its wide potential window between ca. $+3 \text{ V}$ and -3 V .²¹⁶ In fact, substrate oxidation up to $E_{1/2} = +3.9 \text{ V}$ vs Fc/Fc^+ has been monitored in it.²¹⁷ Second, the solvent adduct **44** can be prepared by reacting VCl_3 in boiling acetonitrile without any signs of reduction.²¹⁰ Another serviceable precursor complex to obtain homoleptic polypyridine vanadium(II) complexes from can be hexa(acetonitrile) vanadium(II) triflate $[\text{V}(\text{CH}_3\text{CN})_6][\text{OTf}]_2$ **47** $[\text{OTf}]_2$, which is prepared from anhydrous trifluoromethanesulfonic acid and vanadium powder.



Scheme 8: Synthesis of the homoleptic mer -[V(ddpd)₂]^{2+/3+} complexes starting with a vanadium(II) precursor complex.

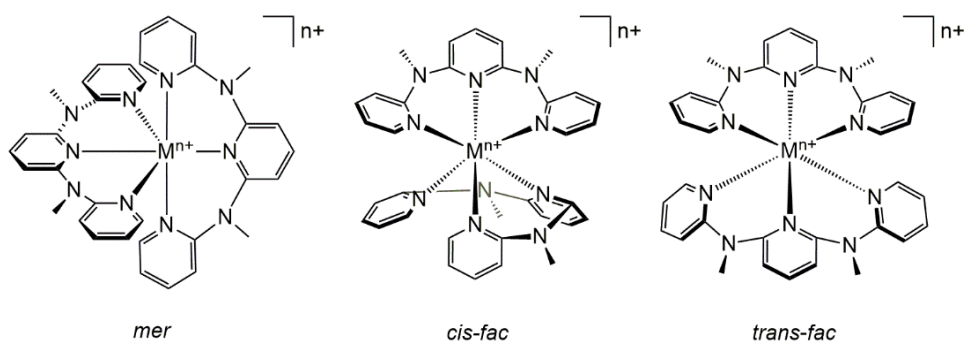
Synthesis protocols of polypyridine nickel(II) complexes do not require as much preparation and are carried out under ambient conditions generally. The preparation of the homoleptic nickel(II) complex utilizing the ddpd ligand has been done before starting from Ni^{II}[BF₄]₂²¹⁸ and is therefore expected to afford [Ni(ddpd)₂][BF₄]₂ without side reactions (Scheme 9).



Scheme 9: Synthesis of the homoleptic mer -[Ni(ddpd)₂][BF₄]₂ complex.

1.6.1. Isomers of ddpd Complexes

The high flexibility of the six-membered ring chelating ligand ddpd is a benefit that certainly fostered the preparation of a number of homoleptic and heteroleptic complexes with transition metal ions across the first transition metal row.^{25,65,212,214,215,219–221} In most cases, a pincer-type mode of coordination is the thermodynamically favored form, yielding the mer isomers (Scheme 10). In the case of [Co(ddpd)₂]²⁺ **48**²⁺, however, the cis - fac isomer could be kinetically trapped by rapid precipitation from a solution containing the ligand and Co[BF₄]₂ · 6 H₂O.²¹⁹ $Trans$ - fac isomers have not been observed with ddpd among 3d TMCs yet, although the flexibility of the six-membered ring chelating ligands enable the formation of a $trans$ - fac isomer in the ruthenium(II) dqp complex. Therefore, a $trans$ - fac isomer could potentially occur in novel ddpd complexes.²²²



Scheme 10: Diastereomeric forms of homoleptic $[M(\text{ddpd})_2]^{n+}$ complexes.

If $[V(\text{ddpd})_2]^{n+}$ existed in different diastereomeric forms, then all of them would very likely feature different photophysical properties and hence, every form would need to be isolated. Therefore, it will be investigated if there is a way to prepare the different diastereomeric forms selectively. Kinetically favored isomers can be obtained by rapid crystallization,²¹⁹ while column chromatography is suitable for isolating thermodynamically favored isomers. Lastly, fractional crystallization can be applied to obtain both from mixtures.²²³



2. Aim of this Work

Vanadium(II) and vanadium(III) ions in different solid host lattices and - in some rare cases - in complex molecules, display low-energy SF emission. However, the successful preparation of vanadium-based room-temperature NIR emissive complexes has yet to be achieved.

The main objective of this work is the design of molecular d^2 -vanadium(III) and d^3 -vanadium(II) transition metal complexes that exhibit long-lived NIR emission from spin-flip states upon photoexcitation at room temperature, in analogy to the molecular rubies.

To achieve this goal, exceptional strong-field ligands will have to be employed to ensure the appropriate excited state ordering, i.e., to ensure that the $^1E/{}^1T_2$ states are lower in energy than the lowest ligand field state 3T_2 by a few thousand wavenumbers in the case of d^2 vanadium(III) complexes. In this context, it is obvious to test the ddpd ligand first as it has proven highly effective with chromium(III) due to its distinct σ -donor properties and advantageous L-M-L bite angles. It also makes for a rigid ligand scaffold in a homoleptic complex that does not allow for any particularly detrimental distortions to promote non-radiative decay. Considering the lower Racah parameter B of vanadium(III) compared to chromium(III), lower emission energies are to be expected. It is therefore likely that energy transfer to C-H oscillators of the ligand or those located on solvent molecules will quench the emission to some extent. To probe the impact of multiphonon relaxation, the preparation of the respective deuterated complexes is planned. In d^3 -vanadium(II) polypyridine complexes, the more covalent metal-ligand bonds entail mixing of charge-transfer and metal-centred excited states as well as stronger distortions. So far, however, only electron-poor polypyridine ligands have been applied. Electron-rich ligands might offer different CT excited state energies and less mixing between SF and CT states. Preparing and characterizing polypyridine vanadium complexes with electron-rich ligands can inform further design choices and is therefore of fundamental interest.

A secondary objective is the exploration of homoleptic polypyridine nickel(II) complexes for spin-flip emission based on similar considerations.

To obtain information on the nature and energy of charge-transfer excited states, time-dependent DFT calculations will be carried out. Quantum-chemical CAS-SCF calculations will be performed on all target molecules to determine their validity in the prediction of spin-flip state energies of polypyridine nickel(II) as well as vanadium(II) and vanadium(III) complexes.



3. Results and discussion

All results of this doctorate have been summarized in scientific articles which were published in/submitted to peer-reviewed journals. Each article is reprinted in this section in accordance with the reprint policy of the respective journal.

All experiments, measurements and calculations mentioned in the following paragraphs have been performed by M. Dorn if not stated otherwise.

Synthesis, characterization and quantum-chemical calculations on the novel vanadium(III) complex $[V(\text{ddpd})_2]^{3+}$ are presented in section 3.1 “A Vanadium(III) Complex with Blue and NIR-II Spin-Flip Luminescence in Solution”. The title complex constitutes the first example of a vanadium(III) complex displaying room-temperature spin-flip luminescence in the range of 950 nm – 1150 nm in fluid solution. In addition, high-energy fluorescence was observed. These measurements were a joint effort of M. Dorn, J. Kalmbach from the group of Prof. M. Seitz (Universität Tübingen) and P. Boden from the group of Prof. M. Gerhards (Technische Universität Kaiserslautern). To evaluate the impact of energy transfer onto C–H acceptors, a perdeuterated variant of the ddpd ligand was provided by Jens Kalmbach and coordinated by M. Dorn. However, both NIR luminescence intensity and lifetime are insensitive toward ligand deuteration, which indicates that other deactivation pathways are dominant. Transient absorption spectroscopy and transient FTIR spectroscopy were employed in collaboration with A. Kruse from the group of Prof. S. Lochbrunner (Universität Rostock) and P. Boden, respectively. Both methods confirm the existence of a long-lived excited state component which matches with the observation of NIR phosphorescence. The experimental findings are corroborated by CAS-SCF calculations which yield metal-centred excited state energies that closely match the results from luminescence spectroscopy. Further insight into the early dynamics starting from a $^3\text{LMCT}$ state was obtained by non-adiabatic surface hopping including arbitrary couplings (SHARC) dynamics simulations, carried out by S. Gómez from the group of Prof. L. González.

Section 3.2, “Ultrafast and long-time excited state kinetics of an NIR-emissive vanadium(III) complex I: Synthesis, spectroscopy and static quantum chemistry” describes the preparation and characterization of a heteroleptic vanadium(III) complex, $V\text{Cl}_3(\text{ddpd})$. This pseudo-octahedral complex molecule displays singlet-triplet NIR luminescence between 1102 and 1256 nm at room temperature and in frozen solution, as measured by J. Kalmbach (Universität Tübingen) and P. Boden (Technische Universität Kaiserslautern). The luminescence band splitting is partly due to the split $^3\text{T}_1$ ground state and agrees well with both Raman spectroscopic measurements carried out by C. Dab (Université de Montreal, Prof. C. Reber) and CAS-SCF calculations. With a perdeuterated ddpd ligand provided by J. Kalmbach, the luminescence intensity increases and the phosphorescence lifetime at room temperature is extended from 0.5 μs to 3.3 μs . Step-scan-FTIR measurements carried out by P. Boden (Technische Universität Kaiserslautern) yield similar lifetimes. Femtosecond transient absorption spectroscopy performed by A. Kruse (Universität Rostock) reveals a broad excited state absorption band between 470 and 700 nm. This state evolves into a longer living one

within 1.5 ps. The long-lived state's lifetime surpasses the 1.4 ns time frame of the pump-probe experiment and is assigned to a spin-flip state.

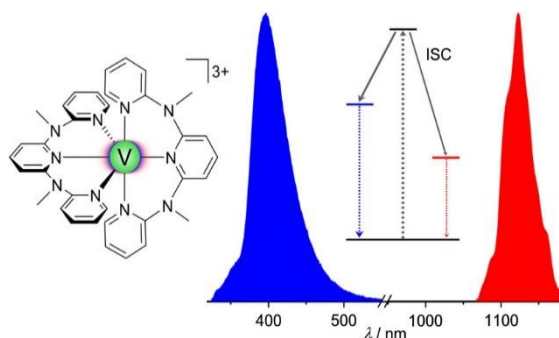
Section 3.3, "Towards Luminescent Vanadium Complexes With Slow Magnetic Relaxation And Quantum Coherence", covers the synthesis and characterization of two diastereomeric polypyridine vanadium(II) complexes. *Cis-fac*- and *mer*-[V(ddpd)₂][BPh₄]₂ can be selectively synthesized through temperature control. Once formed, the isomers do not interconvert spontaneously and no photoisomerization occurs under UV irradiation at 300 nm excitation wavelength. CAS-SCF-calculations locate the lowest spin-flip states ²E/²T₁ in both diastereomers more than 5000 cm⁻¹ below the lowest ligand-field excited state ⁴T₂ at the ground state geometry. While oxidation of the complexes turns on spin-flip luminescence at 77 K in a butyronitrile glass from the vanadium(III) centres, no luminescence occurs in the title complexes even at 77 K in the solid state. ²LMCT states are available which mix with ²MC states and provide a pathway for efficient non-radiative decay. Magnetic circular dichroism (MCD) spectroscopy performed by [REDACTED] reveals three components of the ⁴A_{2g}→⁴T_{2g} transition for both isomers which are well reproduced by CASSCF calculations. ZFS parameters *D* extracted from the MCD measurements for the *cis-fac* isomer (*D* = 0.38 cm⁻¹) fit the value obtained from magnetic susceptibility measurements (*D* = 0.40 cm⁻¹) performed by [REDACTED]. Signals observed in HF-EPR spectra of both isomers recorded by [REDACTED] are assigned to the transition within the lower Kramer's doublet (*m_s* = ±1/2) at *D* values of *D* = 0.47 cm⁻¹ and *D* = 0.20 cm⁻¹ for *cis-fac* and *mer* isomer, respectively. Furthermore, the *mer* isomer displays an out-of-phase signal in AC susceptometry measurements due to slow magnetic relaxation at 15 K and an external field of 4000 Oe. In the *cis-fac* isomer, the magnetic interaction is larger due to smaller V^{II}-V^{II} distances compared to the *mer* isomer (*cis-fac*: 8.079 Å; *mer*: 11.881 Å), hence the relaxation is too fast to be detected. A spin-lattice relaxation time of *t*₁ = 308 μs and a phase memory time of *t*_m = 1.1 μs at 5 K are found for the *mer* isomer in pulsed Q-band EPR measurements carried out by [REDACTED].

In section 3.4, "Structure and Electronic Properties of an Expanded Terpyridine Complex of Nickel(II) [Ni(ddpd)₂](BF₄)₂", the synthesis and characterization of a new nickel(II) complex are reported. The strongly σ-donating polypyridine ligand ddpd (ddpd = *N,N'*-dimethyl-*N,N'*-dipyridin-2-ylpyridine-2,6-diamine) enforces a nearly octahedral coordination geometry. This circumstance is reflected in an only slightly lifted degeneracy of the triplet and singlet excited states according to CAS-SCF calculations carried out by [REDACTED] from the group of [REDACTED]. The absorption spectrum of the title complex shows a shoulder on the high-energy flank of the spin-allowed ligand field transition ³A→³T₂, which originates from the spin-forbidden ³T₂→¹E transition. Since the energy gap between the ³T₂ and ¹E state is only minor ($\Delta E \approx 1400$ cm⁻¹ at the ground state geometry), excited state energy is dissipated non-radiatively and no luminescence is observed.

3.1. A Vanadium(III) Complex with Blue and NIR-II Spin-Flip Luminescence in Solution

Matthias Dorn, Jens Kalmbach, Pit Boden, Ayla Kruse, Sandra Gómez, Christoph Förster, Felix Kuczelinis, Luca M. Carrella, Laura A. Büldt, Nicholas H. Bings, Eva Rentschler, Stefan Lochbrunner, Leticia González, Markus Gerhards, Michael Seitz and Katja Heinze

J. Am. Chem. Soc. **2020**, 142, 7947–7955



This article reports on the synthesis and characterisation of the homoleptic vanadium(III) complex [V(ddpd)₂]³⁺ (ddpd = *N,N'*-dimethyl-*N,N'*-dipyridin-2-ylpyridine-2,6-diamine). It displays NIR spin-flip luminescence from ¹MC states and a broad fluorescence band in the UV region in fluid solution at room temperature.

Author Contributions

Synthesis and characterization of the deuterated and non-deuterated title compound, DFT and CAS-SCF calculations were carried out by Matthias Dorn. The deuterated [D₁₇]-ddpd ligand was prepared by Jens Kalmbach (group of Prof. Dr. M. Seitz). Static and time-resolved NIR luminescence measurements were performed by Jens Kalmbach. Pit Boden (group of Prof. Dr. M. Gerhards) carried out step-scan IR measurements. Ayla Kruse (group of Prof. Dr. S. Lochbrunner) accounted for transient absorption measurements. Sandra Gómez (group of Prof. Dr. L. González) performed non-adiabatic spin-flip dynamic calculations. Felix Kuczelinis (group of Prof. Dr. N. Bings) performed trace determination of chromium. Dr. Luca M. Carrella (group of Prof. Dr. E. Rentschler) performed magnetic susceptibility measurements. Dr. Christoph Förster solved the crystal structure of the title compound. The manuscript was written by Prof. Dr. Katja Heinze (90%) and Matthias Dorn (10%).

Supporting Information

can be found at pp. 99.

The full supporting information can be obtained [here](#).

"Reprinted with permission from Matthias Dorn, Jens Kalmbach, Pit Boden, Ayla Kruse, Chahinez Dab, Christian Reber, Gereon Niedner-Schatteburg, Stefan Lochbrunner, Markus Gerhards, Michael Seitz and Katja Heinze. Copyright 2020 American Chemical Society"

A Vanadium(III) Complex with Blue and NIR-II Spin-Flip Luminescence in Solution

Matthias Dorn, Jens Kalmbach, Pit Boden, Ayla Pöpcke, Sandra Gómez, Christoph Förster, Felix Kuczelinis, Luca M. Carrella, Laura A. Büldt, Nicolas H. Bings, Eva Rentschler, Stefan Lochbrunner, Leticia González, Markus Gerhards,* Michael Seitz,* and Katja Heinze*

Cite This: *J. Am. Chem. Soc.* 2020, 142, 7947–7955

Read Online

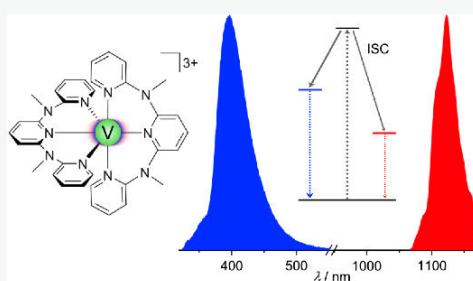
ACCESS |

Metrics & More

Article Recommendations

Supporting Information

ABSTRACT: Luminescence from Earth-abundant metal ions in solution at room temperature is a very challenging objective due to the intrinsically weak ligand field splitting of first-row transition metal ions, which leads to efficient nonradiative deactivation via metal-centered states. Only a handful of $3d^n$ metal complexes ($n \neq 10$) show sizable luminescence at room temperature. Luminescence in the near-infrared spectral region is even more difficult to achieve as further nonradiative pathways come into play. No Earth-abundant first-row transition metal complexes have displayed emission >1000 nm at room temperature in solution up to now. Here, we report the vanadium(III) complex $mer\text{-}[V(\text{ddpd})_2][\text{PF}_6]_3$, yielding phosphorescence around 1100 nm in valeronitrile glass at 77 K as well as at room temperature in acetonitrile with $1.8 \times 10^{-4}\%$ quantum yield (ddpd = *N,N'*-dimethyl-*N,N'*-dipyridine-2-ylpyridine-2,6-diamine). In addition, $mer\text{-}[V(\text{ddpd})_2][\text{PF}_6]_3$ shows very strong blue fluorescence with 2% quantum yield in acetonitrile at room temperature. Our comprehensive study demonstrates that vanadium(III) complexes with d^2 electron configuration constitute a new class of blue and NIR-II luminophores, which complement the classical established complexes of expensive precious metals and rare-earth elements.



INTRODUCTION

Luminescent complexes of Earth-abundant metal ions started to emerge only in the past few years.^{1–4} Typically, the abundant first-row transition metal ions are prone to subpicosecond nonradiative relaxation via low-energy metal-centered (MC) states, which precluded any useful emission until recently.^{4–6} The majority of the very few reported room-temperature luminescent complexes possess rather long-lived charge transfer (CT) states thanks to a high energy or the absence of the detrimental MC states. A d^6 -chromium(0) complex with isocyanide ligands shows $^3\text{MLCT}$ (metal-to-ligand CT) emission at 630 nm ($\tau = 2.2$ ns, $\Phi = 0.001\%$).⁷ d^6 -Cobalt(III) complexes with tridentate strong field ligands display blue emission from $^3\text{LMCT}$ (ligand-to-metal) states (440/412 nm, $\tau = 5.1/3.2 + 8.7$ ns, $\Phi = 0.7/0.4\%$).⁸ Fluorescence from $^2\text{LMCT}$ states is induced in d^5 -iron(III) complexes using carbene ligands (655 nm, $\tau = 1.96$ ns, $\Phi = 2.1\%$).^{9,10} Copper(I) complexes can exhibit quantum yields up to 100%; for example, two-coordinate d^{10} -copper(I) complexes of cyclic (alkyl)(amino)carbene and amide ligands emit from ligand-to-ligand charge transfer (LLCT) states between 492–580 nm ($\tau = 280\text{--}2500$ ns, $\Phi = 11\text{--}100\%$).¹¹ Clearly, the visible spectral region started to be covered by 3d CT emitters; room-temperature near-infrared (NIR-I, 780–1000 nm; NIR-II, 1000–1700 nm) emission in solution has not yet been reported with CT complexes of Earth-abundant metal ions. On

the other hand, strong NIR luminescence has been achieved by exploiting the spin-flip emission of d^3 -chromium(III) complexes using tridentate strong field ligands, leading to the so-called molecular rubies $[\text{Cr}(\text{L})_2]^{3+}$ ($\text{L} = \text{ddpd}$, tpe; ddpd = *N,N'*-dimethyl-*N,N'*-dipyridine-2-ylpyridine-2,6-diamine; tpe = 1,1,1-tris(pyrid-2-yl)ethane; 782–724 nm, $\tau = 670\text{--}4500$ μs , $\Phi = 5.2\text{--}30\%$, CH_3CN).^{12–17} However, emission above 900 nm or even above 1000 nm (NIR-II) at room temperature remains elusive with 3d metal complexes in solution.

In principle, near-infrared (NIR) luminescence enables exciting applications in telecommunications, laser, and LED/OLED or LEC technologies (OLED, organic light-emitting diode; LEC, light-emitting electrochemical cell) as well as in bioanalysis and bioimaging.^{18–22} NIR-II luminescence can be particularly beneficial for in vivo imaging with respect to tissue penetration as well as reduced autofluorescence of the background and scattering losses.^{18,19} Current materials are based on rare-earth elements, precious metals, and organic dyes often in conjunction with precious metals.^{23–28} The rare-

Received: February 22, 2020

Published: April 10, 2020



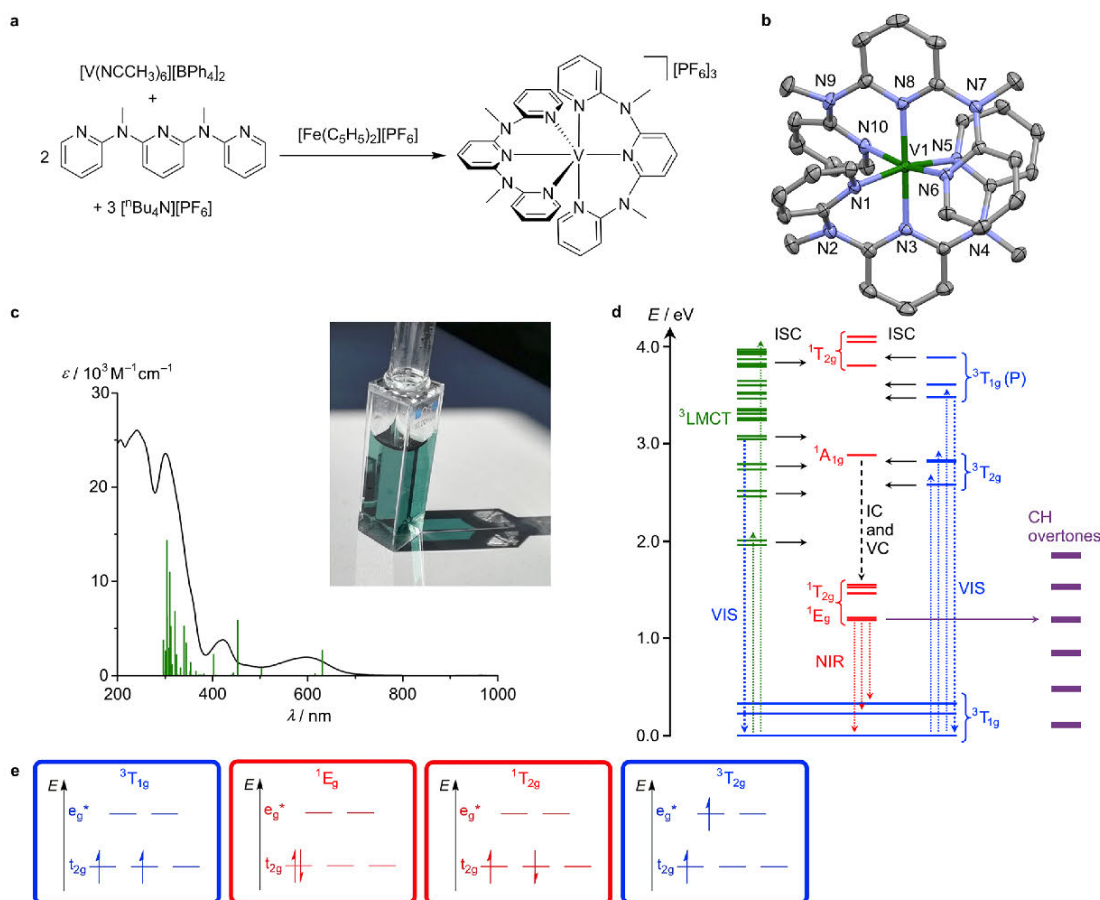


Figure 1. Synthesis, molecular structure, absorption spectrum of $[V(\text{ddpd})_2][\text{PF}_6]_3$, and Jablonski diagram of $[V(\text{ddpd})_2]^{3+}$. (a) Preparation of $[V(\text{ddpd})_2][\text{PF}_6]_3$. (b) Molecular structure of the cation of $[V(\text{ddpd})_2][\text{PF}_6]_3 \cdot 3\text{CH}_3\text{CN}$. Thermal ellipsoids are shown at 50% probability. Hydrogen atoms, counterions, and CH_3CN molecules are omitted for clarity. (c) Absorption spectrum and photograph of $[V(\text{ddpd})_2][\text{PF}_6]_3$ in CH_3CN . The vertical green bars correspond to spin-allowed transitions calculated by TD-DFT-UKS calculations (unshifted). (d) Jablonski diagram constructed from TD-DFT-UKS ($^3\text{LMCT}$ states in green) and CASSCF-NEVPT2 calculations (^3MC states in blue; ^1MC states in red); notation of MC states according to O_h symmetry; ISC, intersystem crossing; IC, internal conversion; VC, vibrational cooling; NIR, NIR emission; VIS, emission in the visible spectral region; CH overtones, multiphonon relaxation (experimental overtone energies from ref 13). (e) Representative microstates of the most relevant metal-centered triplet and singlet states.

earth ions typically display comparably sharp emission bands, and yet they are split by electron–electron repulsion, spin–orbit coupling, and the crystal field.²⁹ Organic emitters often show broad emission bands, which typically merely tail into the NIR spectral region; hence, some emission still occurs in the visible spectral region.

A fundamental problem of low-energy emission derives from the energy-gap law especially for distorted excited states. The rate constant for nonradiative decay that reduces the luminescence quantum yield Φ increases with decreasing energy difference between the emitting and the ground states.^{30,31} Nested, that is, weakly distorted, states (such as f – f and d – d spin-flip transitions) are hence better suited for NIR emission. Furthermore, high-energy oscillators, for example, OH from water or CH from coordinating ligands, can increase nonradiative decay via energy transfer to suitable OH/CH vibrational overtones.^{32,33} Lanthanide compounds, for example, Nd, Sm, Dy, or Yb, very often embedded in nanoparticles that lack detrimental CH oscillators, achieve

NIR-II luminescence due to their favorable excited-state levels originating from f – f transitions and the absence of high-energy oscillators.^{18,19,29} The quantum yields for molecular NIR emissive lanthanide complexes are rather small, although deuterated cage and fluorinated porphyrin complexes of Yb^{3+} showing emission around 1000 nm recently achieved exceptionally high quantum yields.^{34–36} However, rare-earth elements and precious metals are difficult and expensive to mine and purify, so that a huge interest arose in replacing these elements with Earth-abundant metals in luminescence applications.^{1–4}

Analogous to the d^3 electron configuration of the abundant metal chromium(III),^{2,12–17} an excited-state ordering with low-energy spin-flip states ($^1E_g/{}^1T_{2g}$) emerges from a d^2 electron configuration in an octahedral ligand field ($^3T_{1g}$ ground state), provided that a strong ligand field is imposed to increase the energy gap between the interconfigurational triplet state ($^3T_{2g}$) and the intraconfigurational singlet states ($^1E_g/{}^1T_{2g} < {}^3T_{2g}$ at $\Delta_o > 17.3 B$ in the standard Tanabe–

Sugano diagram; see Figure S1; Δ_o and B are the ligand field parameters). We hypothesized that this situation can be realized by octahedral vanadium(III) complexes in a strong ligand field. The energy of potentially emissive singlet states of vanadium(III) has been determined by absorption spectroscopy on classical vanadium(III) compounds with O-donor ligands, such as $V^{3+}:Al_2O_3$, $[V(H_2O)_6]^{3+}$, $[V(urea)_6]^{3+}$, and $[V(ox)_3]^{3-}$,^{37–41} and by 2p3d resonant inelastic X-ray scattering on $V(acac)_3$, as $\sim 10\,000\text{ cm}^{-1}$ ($\sim 1000\text{ nm}$) (urea = $OC(NH_2)_2$, ox = $[C_2O_4]^{2-}$, acac = $[CH_3(CO)CH(CO)CH_3]^-$).⁴² This energy excellently matches the targeted window for luminescence applications in the NIR-II region. However, the known vanadium(III) compounds display after excitation and intersystem crossing (ISC) only very weak phosphorescence at low temperature, if phosphorescence is observed at all.^{37–41} For example, the phosphorescence intensity of $V^{3+}:Al_2O_3$ is 3–4 orders of magnitude smaller than that of the R lines of ruby ($Cr^{3+}:Al_2O_3$), and the vanadium(III) spin-flip emission has been only detected in the solid state at low temperatures so far.^{37,38} Instead, (delayed) fluorescence from vanadium centered ${}^3T_{2g}$ states occurs in compounds with ligand field strengths close to $17.3 B$.^{43,44} Consequently, back-ISC from ${}^1E_g/{}^1T_{2g}$ to ${}^3T_{2g}$ states must be suppressed. This can in principle be achieved by further increasing the ligand field strength, thus shifting the ${}^3T_{2g}$ states to higher energy relative to the singlet states. On the other hand, to promote ISC from the triplets to the singlet manifold besides large spin–orbit coupling, a high density of singlet states in the energy region of the ${}^3T_{2g}$ states is beneficial.⁴⁵ According to ligand field theory, an additional singlet term (${}^1A_{1g}$) crosses the ${}^3T_{2g}$ term at very high ligand field strengths ($\Delta_o > 36.6 B$ in the standard Tanabe–Sugano diagram; Figure S1). Consequently, an even larger ligand field splitting than $\Delta_o \gg 17.3 B$, $\Delta_o \approx 36.6 B$, could be advantageous to promote ISC to the singlet states via the high-energy ${}^1A_{1g}$ state in vanadium(III) complexes. In this study, such a large ligand field splitting will be targeted.

The strong-field ligand ddpd already enabled spectacular room-temperature quantum yields above 10% and microsecond-lifetimes in solution in the prototypical molecular ruby $[Cr(ddpd)_2]^{3+}$.¹² Ligand and solvent deuteration even boosted the quantum yield to 30% and the lifetime to 2300 μs .¹³ However, an analogous coordination chemistry of vanadium(III) and oligopyridine ligands is underdeveloped.^{46,47} *cis-fac*- $[V(ddpd)_2][PF_6]_3 \times 3CH_3CN$ is the first reported stable homoleptic polypyridine vanadium(III) complex.⁴⁶ Yet, the bond lengths in *cis-fac*- $[M(ddpd)_2]^{3+}$ isomers are typically longer than those in *mer*-isomers due to the ligand deformation, which reduces the actual ligand field strength.⁴⁶

Here, we demonstrate that the strong field ligand ddpd promotes ISC in a novel close-to-octahedral vanadium(III) complex *mer*- $[V(ddpd)_2][PF_6]_3$. Consequently, the complex shows NIR-II phosphorescence at low as well as at room temperature in solution. In addition, a strong blue fluorescence is observed. To deeper elucidate the key challenges for luminescent vanadium(III) complexes, we recorded fs-transient absorption spectra and ns-step-scan FTIR spectra for *mer*- $[V(ddpd)_2][PF_6]_3$. To judge the influence of multiphonon relaxation via CH overtones, we prepared and studied the deuterated analogue $[V([D_{17}]\text{-ddpd})_2][PF_6]_3$. Static quantum chemical and nonadiabatic molecular dynamics simulations provide a comprehensive insight into the electronic

excited-state properties and ultrafast dynamics of *mer*- $[V(\text{ddpd})_2]^{3+}$.

RESULTS

Synthesis, X-ray Structure, and Characterization of $[V^{III}(\text{ddpd})_2]^{3+}$. The dark green complex *mer*- $[V^{III}(\text{ddpd})_2][PF_6]_3$ was efficiently synthesized from $[V(CH_3CN)_6][BPh_4]_2$ and ddpd⁴⁶ followed by oxidation with ferrocenium hexafluorophosphate (Figure 1a). Full characterization is collected in Figures S2–S5. The starting vanadium material $VCl_3(CH_3CN)_3$ was checked for chromium trace impurities by ICP-MS yielding $(4.01 \pm 0.31)\ \mu g\ g^{-1}\ Cr$, assuring that emission from conceivable luminescent chromium(III) species will not interfere. The deuterated complex $[V([D_{17}]\text{-ddpd})_2][PF_6]_3$ was prepared from $[D_{17}]\text{-ddpd}$ in an analogous manner with a total degree of deuteration of 93.6%D in the ligand and in the complex according to ESI⁺ mass spectrometry (Figures S6–S9). Importantly, the α -protons, closest to the vanadium center, are almost quantitatively substituted by deuterium (99% by 1H NMR spectroscopy).

The vanadium(III) oxidation state in *mer*- $[V(\text{ddpd})_2][PF_6]_3$ was confirmed by elemental analysis, mass spectrometry, magnetometry, cyclic voltammetry, and single-crystal X-ray diffraction analysis (Figures 1b, S4, S5 and Table S1). The magnetic moment of $[V(\text{ddpd})_2][PF_6]_3$ between 300 and 50 K amounts to $\chi T \approx 1.0\text{ cm}^3\text{ K mol}^{-1}$ as expected for an $S = 1$ ground state. Below 50 K, the magnetic moment decreases due to zero-field splitting. The low-temperature part was modeled with $g = 1.946$ and a zero-field splitting of $D_{\text{exp}} = +2.87(11)\text{ cm}^{-1}$ (Figure S4).^{47,48} The vanadium(III) complex is reversibly reduced at -0.275 V vs ferrocene (Figure S5). In the solid state, the central ion in $[V(\text{ddpd})_2]^{3+}$ is coordinated by six pyridine donors. The $[VN_6]$ coordination geometry is nearly octahedral as shown by the octahedral shape parameter being quite close to zero ($S(\text{OC-6}) = 0.63$; Tables S1 and S2). The $[VN_6]$ symmetry is, however, less perfect than in $[Cr^{III}(\text{ddpd})_2]^{3+}$ complexes ($S(\text{OC-6}) = 0.29\text{--}0.43$),⁴⁶ as a consequence of the Jahn–Teller active partially filled t_{2g} shell. As compared to the metrics of the *cis-fac*- $[V(\text{ddpd})_2]^{3+}$ isomer, the V–N bond lengths to the four terminal pyridines in *mer*- $[V(\text{ddpd})_2]^{3+}$ decreased by $0.025\text{--}0.053(9)\text{ \AA}$, while V–N distances to the central pyridines increased only slightly by $0.008/0.022(8)\text{ \AA}$.⁴⁶ The overall smaller $[VN_6]$ coordination cage of *mer*- $[V(\text{ddpd})_2]^{3+}$ and its close-to-octahedral symmetry impose the desired large ligand field splitting Δ_o .

The electronic absorption spectrum of *mer*- $[V(\text{ddpd})_2][PF_6]_3$ in CH_3CN reveals a broad absorption band around 597 nm (Gaussian deconvolution: 616, 570 nm), a shoulder at $\sim 475\text{ nm}$, an asymmetric band at 422 nm (Gaussian deconvolution: 429, 412 nm), and very intense bands at 301 nm (Figures 1c and S10). All bands are quite intense ($\epsilon \gg 1000\text{ M}^{-1}\text{ cm}^{-1}$) as compared to typical metal-centered transitions, suggesting significant CT character. These intense CT bands conceal the weaker Laporte-forbidden $d\text{--}d$ transitions, preventing their observation and hence experimental determination of Δ_o . To assign the absorption bands and to obtain the excited-state level ordering including the MC states, quantum chemical calculations were performed (Tables S1–S4).

Static Quantum Chemical Calculations. The overall geometry of $[V(\text{ddpd})_2]^{3+}$ is well reproduced by unrestricted Kohn–Sham Density Functional Theory (DFT–UKS) calculations (CPCM(acetonitrile)–RJLCOSX–UB3LYP–D3BJ–

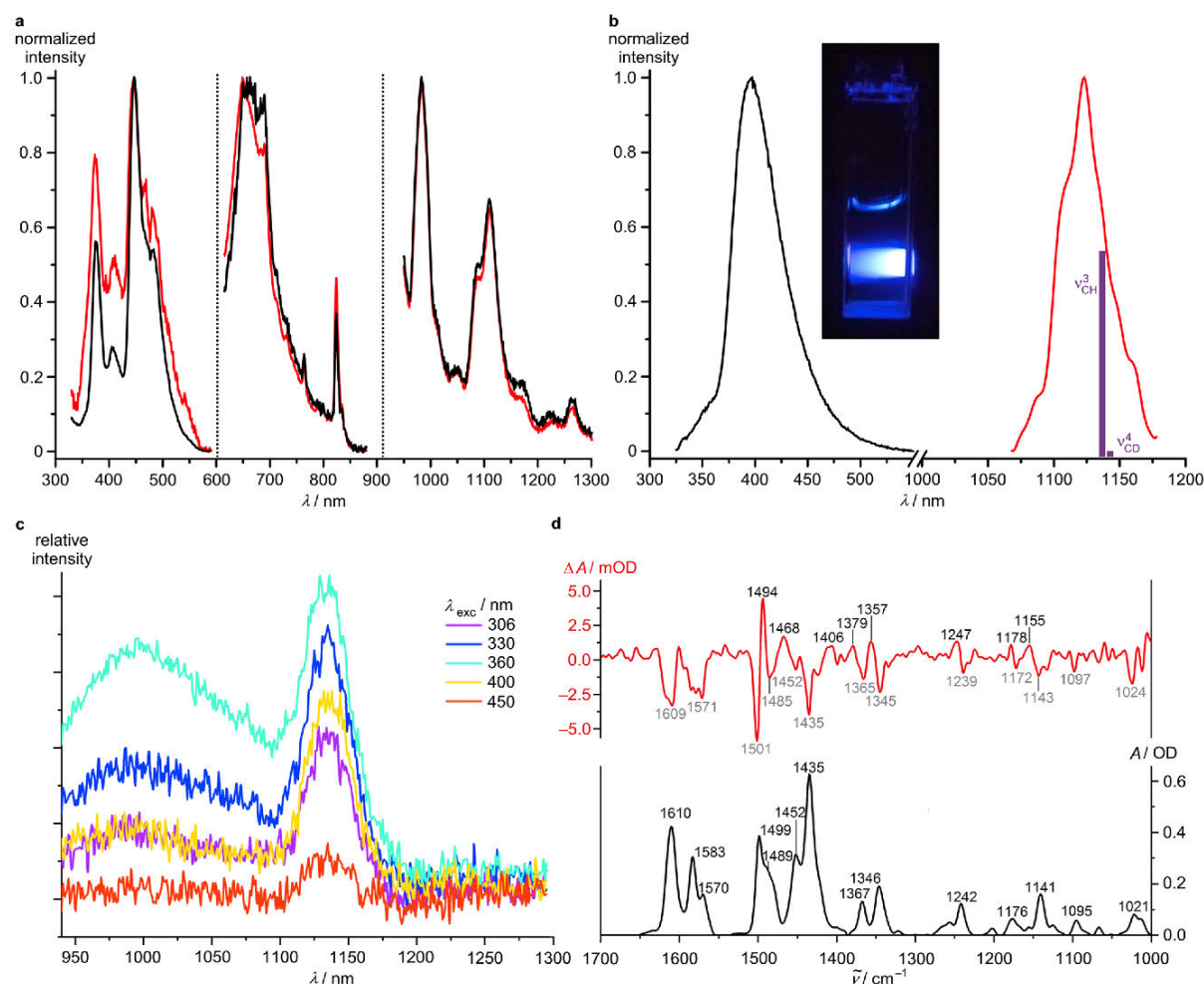


Figure 2. (a) Normalized luminescence spectra of $[V(\text{ddpd})_2][\text{PF}_6]_3$ (black) and $[V([\text{D}_{17}]\text{-ddpd})_2][\text{PF}_6]_3$ (red) ($\lambda_{\text{exc}} = 306$ nm, $^n\text{BuCN}$, 77 K). Intensities in the different spectral regions are not to scale due to different detectors and gratings used. GG455 and RG850 long pass filters were employed for the low-energy spectra, respectively. (b) Normalized luminescence spectra of $[V(\text{ddpd})_2][\text{PF}_6]_3$ ($\lambda_{\text{exc}} = 306$ nm, CD_3CN , 298 K). Intensities in the different spectral regions are not to scale due to different detectors and gratings used. The integral ratio of the two bands amounts to $I(\text{VIS}):I(\text{NIR}) = 2.1:1.8 \times 10^{-4}$. Purple vertical bars indicate relevant CH and CD overtones. Their length approximately illustrates the $\nu^3_{\text{CH}}:\nu^4_{\text{CD}}$ intensity ratio.¹³ The photograph illustrates the blue fluorescence of $[V(\text{ddpd})_2][\text{PF}_6]_3$ ($\lambda_{\text{exc}} = 350$ nm, CH_3CN , 298 K). (c) Luminescence spectra of $[V(\text{ddpd})_2][\text{PF}_6]_3$ ($\lambda_{\text{exc}} = 306\text{--}450$ nm, butyronitrile glass, 20 K). (d) Ground-state FTIR (black) and step-scan FTIR spectra (red) of $[V(\text{ddpd})_2][\text{PF}_6]_3$ at 20 K ($\lambda_{\text{exc}} = 355$ nm, KBr pellet, 0–300 ns).

ZORA/def2-TZVPP) with a maximum deviation in V–N bond lengths of 0.028 Å and N–V–N bond angles of 1.3° (Table S1; octahedral shape parameter $S(\text{OC-6}) = 0.68$). Mulliken spin population analysis yields 2.07 at the vanadium center, similar to that calculated for $[V(\text{bpy})_3]^{3+}$ (2.11),⁴⁷ accounting for the two unpaired electrons.

To assign the intense CT bands, time-dependent DFT-UKS calculations at the same level of theory were employed (Tables S3 and S4; Figure 1c). The absorption band at 597 nm corresponds to $^3\text{LMCT}$ transitions from the bridging nitrogen atoms to vanadium (calcd 631/616 nm; Figure 1c,d). The shoulder and bands between 500 and 390 nm originate from $^3\text{LMCT}$ transitions as well (calcd 503, 453, 444 nm; Figure 1c,d). The $^3\text{T}_{1g} \rightarrow ^3\text{T}_{2g}$ ligand field transition (in octahedral symmetry) is split due to the lower symmetry (calcd 441 and 413 nm) and superimposed onto the stronger $^3\text{LMCT}$ bands

in this spectral region (Figure 1c). As compared to vanadium(III) complexes with oxygen donor ligands, for example, $V(\text{acac})_3$,^{37–41,48} the ligand field splitting of $[V(\text{ddpd})_2]^{3+}$ ($\Delta_o \approx 23\,440$ cm^{-1}) is larger by more than 2500 cm^{-1} , confirming our conceptual approach of using ddpd as a strong ligand to prevent back-ISC.⁴⁶

Expectedly, the $^3\text{T}_{1g}$ ground state splits as well, and yet the TD-DFT-UKS calculated energy gaps are unreasonably large (Table S3). To better describe the MC triplet and singlet states (Figure 1e) and the ground-state splitting, complete-active-space self-consistent field (CASSCF) calculations including spin–orbit coupling (SOC for estimation of the zero-field splitting D) in conjunction with fully internally contracted N-electron valence perturbation theory to second-order (FIC-NEVPT2) CASSCF(6,12)-FIC-NEVPT2 on optimized $[V(\text{ddpd})_2]^{3+}$ were performed (Tables S5, S6 and Figure S11).^{39,48} Figure 1d depicts the calculated order of

these MC triplet and singlet states derived from CASSCF-NEVPT2 and the $^3\text{LMCT}$ states derived from TD-DFT-UKS calculations. The $^3\text{T}_{1g}$ ground state splits with $\Delta E = 1873$ and 2687 cm^{-1} , while the lowest excited triplet state $^3\text{T}_{2g}$ splits into $20\,844$, $22\,706$, and $22\,803\text{ cm}^{-1}$. The zero-field splitting was calculated as $D_{\text{calcd}} = +6.8\text{ cm}^{-1}$, larger than the experimental value $D_{\text{exp}} = +2.87(11)\text{ cm}^{-1}$, yet similar to the experimental and calculated data of $\text{V}(\text{acac})_3$ ($D_{\text{exp}} = +6.9\text{ cm}^{-1}$; $D_{\text{calcd}} = +9.6\text{ cm}^{-1}$).⁴⁸

A series of five singlet states originating from the $^1\text{T}_{2g}$ and $^1\text{E}_g$ terms is located between the triplet ground and excited states. This excited-state ordering confirms the large ligand field splitting with $\Delta_o > 17.3 B$. The two lowest singlet states centered at 9612 and 9736 cm^{-1} (Figure S11) are only weakly split by $\Delta E = 124\text{ cm}^{-1}$. A sixth (isolated) singlet state ($^1\text{A}_{1g}$) is predicted at $23\,283\text{ cm}^{-1}$, slightly above the highest level of the $^3\text{T}_{2g}$ states by 480 cm^{-1} . This calculation suggests that Δ_o is slightly smaller than $36.6 B$ (in a standard Tanabe–Sugano diagram with $C/B = 4.42$, Figure S1). The combined TD-DFT-UKS and CASSCF-NEVPT2 calculations indicate that several states ($^3\text{LMCT}$, $^3\text{T}_{2g}$ and $^1\text{A}_{1g}$) lie in the 3.1 – 2.6 eV (400 – 480 nm) region.

Steady-State and Time-Resolved Spectroscopy.

Steady-state emission spectra with excitation at 306 nm (4.05 eV) at 77 K in a valeronitrile glass matrix show rich spectral features between 370 and 1150 nm (Figure 2a). Obviously, several states are emissive upon high-energy excitation. The NIR-II emission is also observed in butyronitrile glass at 10 K with excitation wavelengths between 306 and 450 nm . The highest intensity occurs at an excitation wavelength of 360 nm , where the luminescence is twice as strong as that at 306 nm excitation, while the luminescence almost vanishes when exciting with 450 nm (Figure 2c). Tuning the excitation wavelength populates different electronically excited triplet states, which might exhibit different ISC efficiencies as sketched in Figure 1d and consequently lead to different phosphorescence intensities. In the solid state (KBr pellet; Figure S14a,b), the NIR-II emission is not observed, probably resulting from self-quenching. The emission in solution is sensitive to the presence of oxygen. A biexponential lifetime of several hundred nanoseconds is associated with the sharp NIR emission bands at 1100 nm (790 ns (93%), 8800 ns (7%), Table S7 and Figure S12). The long lifetime is in a similar range as compared to the excited singlet state lifetime reported for V^{3+} doped in $\text{NaMgAl}(\text{ox})_3$ at 11 K ($\tau < 500\text{ ns}$).⁴¹ All emission bands show vibrational progression, while the ground-state splitting might also account for the observed pattern.

On the basis of the quantum chemical calculations (Figure 1d), the emission energies, and the lifetimes (Figures S12, S13 and Table S7), we assign the high-energy emission bands (374 , 447 , and 660 nm) and the NIR-I/NIR-II emission bands (982 and $1088/1109\text{ nm}$) to fluorescence and phosphorescence, respectively. The NIR-I and NIR-II phosphorescence originates from the two almost degenerate lowest excited singlet states (with $^1\text{E}_g$ and $^1\text{T}_{2g}$ parentage) decaying radiatively to the split ground-state levels (Figure 1d). From these NIR-I/NIR-II phosphorescence bands, the experimental ground-state splitting is estimated as 1080 cm^{-1} (averaged $1088/1109\text{ nm}$), which is somewhat smaller than that obtained by the CASSCF-NEVPT2 calculations (1873 cm^{-1} ; Figure 1d). As a reference, a splitting of 880 cm^{-1} was calculated for $\text{V}(\text{acac})_3$ by SOC-CASSCF($12,10$)-NEVPT2,⁴⁸ while a value of 1400 cm^{-1} was

experimentally determined for $[\text{V}(\text{urea})_6][\text{ClO}_4]_3$.⁴⁰ Excitation of $^3\text{LMCT}$ states at lower energy (600 nm) does not lead to the NIR-II luminescence, demonstrating that these $^3\text{LMCT}$ states do not efficiently evolve to the emissive singlet states (Figure 1d).

In diluted deaerated CD_3CN solution, dual emission at 396 and $1109/1123\text{ nm}$ occurs even at 298 K upon excitation at 306 nm (Figure 2b). The high-energy blue emission is even observable by the naked eye at room temperature in solution and in a KBr pellet (Figures 2b and S14c). The quantum yield of the high energy fluorescence is very high with $\Phi = 2.1\%$ and surpasses the quantum yield of the blue emission of the recently reported blue emissive cobalt(III) complexes ($\Phi = 0.7/0.4\%$).⁸ The emission decay at 396 nm is biexponential with τ_{396} of 3.2 (56%) and 8.2 (44%) ns and 1.7 (51%) and 6.3 (49%) ns at 298 and 77 K , respectively. We assign this fluorescence to $^3\text{T}_{1g}(\text{P}) \rightarrow ^3\text{T}_{1g}$ or to $^3\text{LMCT}$ transitions (Figure 1d). Indeed, two $^3\text{LMCT}$ states are calculated around 3 eV by TD-DFT calculations and $^3\text{T}_{2g}(\text{P})$ states around 3.46 eV by CASSCF-NEVPT2 calculations, which could account for the biexponential decay as sketched in Figure 1d with blue vertical arrows (Tables S3 and S6).

Beyond the intense blue emission of $[\text{V}(\text{ddpd})_2][\text{PF}_6]_3$, the observed room-temperature NIR-II phosphorescence of $[\text{V}(\text{ddpd})_2][\text{PF}_6]_3$ in solution is unique. The NIR quantum yield of $\Phi = 1.8 \times 10^{-4}\%$ is not very high, but the rather sharp emission band (fwhm ca. 325 cm^{-1}) is clearly observable. To the best of our knowledge, no other complexes with Earth-abundant metal ions display NIR-II luminescence in frozen and in fluid solution (Figure 2a–c). The ground-state splitting of the $^3\text{T}_{1g}$ levels (Figure 1d) rather than vibrational progression likely accounts for the asymmetric band shape. This differs from NIR emission bands of chromium(III) complexes, which possess an orbitally nondegenerate ground state ($^4\text{A}_2$) and consequently deliver sharp phosphorescence bands.^{12–17}

To obtain information on the long-lived excited singlet states, the complex (in a KBr pellet) was excited with 355 nm at 20 K and probed by step-scan FT-IR spectroscopy. The measured FTIR ground-state spectrum is in excellent agreement with the DFT-UKS calculated spectrum of $[\text{V}(\text{ddpd})_2]^{3+}$ (Figure S15). The recorded step-scan difference spectrum collected between 0 and 300 ns after the pulse shows the ground-state bleach (negative bands) and excited-state absorption (positive bands) (Figure 2d). The latter vibrational bands correspond to the lowest energy long-lived singlet state. A monoexponential lifetime of about 290 ns was determined by performing a global exponential fit for the most prominent positive and negative peaks in the step-scan difference spectrum (Figure S16). The observation of step-scan FTIR spectra further confirms the presence of long-lived excited states.

The lifetime of this emissive excited state depends on the efficiency of nonradiative decay processes. Especially, NIR luminescence is prone to multiphonon relaxation via CH overtones, which could be diminished by deuteration.^{13,32,33} Indeed, the second aromatic CH overtone ($\nu^3_{\text{CH}} = 8972\text{ cm}^{-1}$) as estimated from CH overtone IR spectroscopy of $6,6'$ -dimethyl-2,2'-bipyridine¹³ has a significant spectral overlap with the NIR-II emission bands of $[\text{V}(\text{ddpd})_2][\text{PF}_6]_3$ (Figure 2b). For the deuterated derivative, the third CD overtone at $\nu^4_{\text{CD}} = 8755\text{ cm}^{-1}$ is the most relevant one (Figure 2b).¹³ Because of the lower energy and lower extinction coefficient of

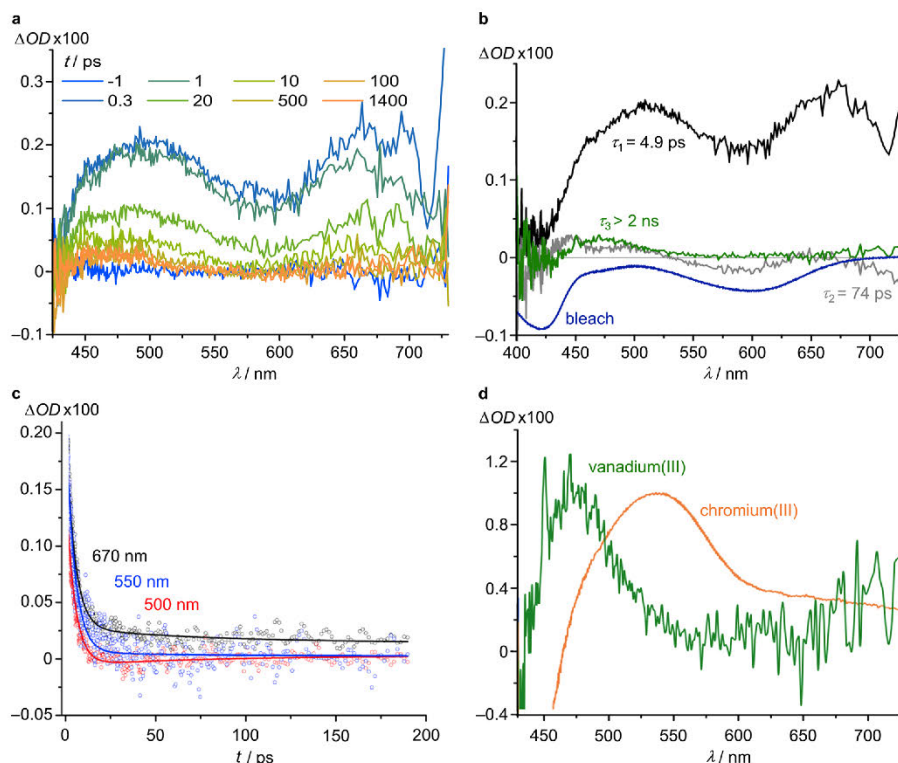


Figure 3. Femtosecond-transient absorption spectroscopy of $[\text{V}(\text{ddpd})_2][\text{PF}_6]_3$. (a) Transient absorption spectra of $[\text{V}(\text{ddpd})_2][\text{PF}_6]_3$ in CH_3CN excited with 400 nm laser pulses. (b) Bleach (blue) and decay associated amplitude spectra labeled with the corresponding time constants: $\tau_1 = 4.9$ ps ($\sim 70\%$, black), $\tau_2 = 74$ ps ($\sim 20\%$, gray), and long-living component with a time constant $\tau_3 > 2$ ns ($\sim 10\%$, green). (c) Transient signals as a function of the pump-probe delay time observed at 670 nm (black), 550 nm (blue), and 500 nm (red). The fits to the experimental data correspond to triexponential decays with $\tau_{1,2} = 4.9, 74$ ps and a time constant $\tau_3 > 2$ ns. (d) Scaled amplitude spectra of the long-lived components of $[\text{V}(\text{ddpd})_2][\text{PF}_6]_3$ (green) and $[\text{Cr}(\text{ddpd})_2][\text{BF}_4]_3$ (orange) (chromium(III) data from ref 49).

the third CD overtone ν^4_{CD} , the spectral overlap with the vanadium NIR-II emission band should be smaller. Consequently, the nonradiative rate constant for the deuterated complex should be smaller than that for the protio derivative. As long as this multiphonon pathway dominates the decay of the singlet states, the NIR quantum yield and lifetime of $[\text{V}([\text{D}_{17}]\text{-ddpd})_2]^{3+}$ should be larger than those of $[\text{V}(\text{ddpd})_2]^{3+}$. However, within experimental uncertainty, we cannot observe significant differences between the NIR emission intensities and lifetimes of $[\text{V}([\text{D}_{17}]\text{-ddpd})_2]^{3+}$ and $[\text{V}(\text{ddpd})_2]^{3+}$ at 298 and 77 K (Figures S12, S13, S17, S18 and Table S7). This suggests that other nonradiative pathways dominate the decay of the lowest energy singlet states in $[\text{V}(\text{ddpd})_2]^{3+}$. Presumably, the split ground-state levels favor ISC to the ground state (Figure 1d).

The dual emission of $[\text{V}(\text{ddpd})_2][\text{PF}_6]_3$ in the blue and NIR-II spectral region demonstrates the huge energy difference of ca. 2 eV between these two luminescent states. The observed intense fluorescence of $[\text{V}(\text{ddpd})_2]^{3+}$ suggests that the ISC rates from the triplets to the singlets are not particularly large. This slow ISC then opens other pathways (fluorescence, nonradiative decay from the triplets) before the singlet states are populated to higher extents.

The initial dynamics was then probed by fs-transient absorption (TA) spectroscopy. TA spectra of $[\text{V}(\text{ddpd})_2][\text{PF}_6]_3$ in CH_3CN recorded after excitation with femtosecond laser pulses at 620 nm (~ 2 eV) show excited-state absorptions

(ESA) at around 500 and 670 nm (Figure S19). With a time constant of 6.3 ps, the ground state is essentially recovered. Hence, the $^3\text{LMCT}$ states do not significantly evolve to the emissive singlets as was already demonstrated by the steady-state luminescence data. This is consistent with the assumption that efficient ISC requires a high density of final states in the energy region of interest.⁴⁵ Around 2 eV, such singlet states are unavailable for $[\text{V}^{\text{III}}(\text{ddpd})_2]^{3+}$ (Figure 1d). However, a singlet state is present at higher energy ($^1\text{A}_{1g}$, 2.89 eV from the CASSCF-NEVPT2 calculation; Figure 1d).

TA spectra recorded after excitation at 400 nm (3.1 eV; $^3\text{LMCT}$ and $^3\text{T}_{2g}$ states) exhibit a dominant ultrafast decay to the ground state with a time constant of 4.9 ps and a second weaker time constant of 74 ps (Figures 3 and S20). On the nanosecond time scale, a small component persists showing an excited-state absorption around 460 nm (Figure 3c and d). We assign this component to the long-lived singlet state(s), similar to the analogous amplitude spectrum of $[\text{Cr}(\text{ddpd})_2]^{3+}$, representing its emissive doublet states, at longer times scales (Figure 3d).⁴⁹ These results agree with the observation that a small fraction of the triplet population evolves to the singlet states via ISC. Obviously, the low-energy $^3\text{LMCT}$ states are less competent to feed the spin-flip singlet states than the $^3\text{T}_{2g}$ and higher energy $^3\text{LMCT}$ states. Conceptually, the energy tuning of $^3\text{LMCT}$ and $^3\text{T}_{2g}$ states as well as identification of suitable antenna systems should enable an even more efficient

population of the emissive singlet states of vanadium(III) complexes.

Molecular Dynamics Calculations. To gain deeper insight into the complex spin-flip dynamics of $[V(\text{ddpd})_2]^{3+}$ after excitation, dynamics simulations starting from the $^3\text{LMCT}$ manifold in acetonitrile were performed. Specifically, nonadiabatic surface hopping including arbitrary couplings (SHARC) dynamics simulations with a linear vibronic coupling (LVC) model were employed.⁵⁰ Initially, 100 fs was propagated from the four lowest $^3\text{LMCT}$ states located at 3.5–3.7 eV (354–333 nm) (Table S3 and Figures S21, S22), where we found one $^3\text{LMCT}$ state with a significant amount of trapped population. Subsequently and starting from this state (2^3LMCT) located at 3.59 eV (345 nm), we propagated during 50 000 fs and observed IC to the ^3MC states ($^3\text{T}_{2g}$ and $^3\text{T}_{1g}$ ground states) and ISC to a singlet state 2^1MC (Figures 1d and 4).

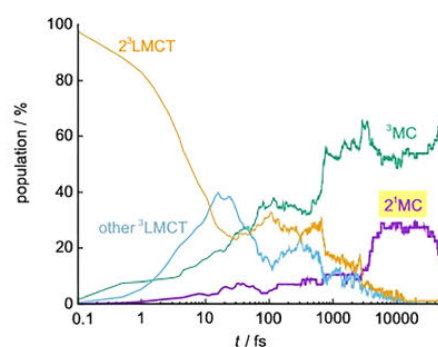


Figure 4. Time-evolution of the population of the excited states during 50 000 fs (in logarithmic scale) after starting the dynamics on the 2^3LMCT state (the longest lived triplet state after 100 fs, Figure S22). The label “other $^3\text{LMCT}$ ” stands for the population in any other state except for the 2^3LMCT . The label “ ^3MC ” corresponds to the sum of populations in every triplet MC state, indicating the total amount of internal conversion. Population in any other singlet state except for 2^1MC is negligible and not plotted.

The singlet $^1\text{LMCT}$ manifold acts as a mere spectator during the dynamics. The most populated metal-centered singlet state 2^1MC was then optimized within the LVC method. The optimized geometry (Table S8) lies 1.10 eV (1127 nm) above the $^3\text{T}_{1g}$ ground state, in very good agreement with the experimental emission energy, thus validating the dynamical approach. The dynamics calculations confirm that the 2^3LMCT state at high energy (3.59 eV) undergoes ISC to a singlet state of MC character, while no lower energy $^1\text{LMCT}$ states around 2 eV are involved in the excited-state evolution toward the emissive ^1MC state, as was already suggested by the steady-state and time-resolved experimental data.

CONCLUSION

Our study extends the very series of luminescent metal complexes with Earth-abundant 3d metal ions (Cr, Fe, Co, Cu) to the early 3d transition metal vanadium. The vanadium(III) complex $\text{mer}-[V(\text{ddpd})_2]^{3+}$ with a tuned large ligand field splitting exhibits a deep-blue emission at room temperature in solution and a long-lived phosphorescence above 1000 nm. This expands the spectral region previously accessible with 3d metal complexes (vis and NIR-I) to the

NIR-II region for the first time. Conceptual design principles for NIR-II luminescent vanadium(III) complexes evolved, highlighting the distinct roles of ligand-to-metal charge transfer states, intersystem crossing, and multiphonon relaxation. This first success in designing blue and NIR-II emissive complexes of the Earth-abundant metal vanadium raises the prospect of employing luminescent vanadium complexes in the future. Especially, dual emissive complexes could find applications as optical probes with a built-in internal reference for chemical or physical perturbations. Work in this direction is currently in progress.

ASSOCIATED CONTENT

Supporting Information

The Supporting Information is available free of charge at <https://pubs.acs.org/doi/10.1021/jacs.0c02122>.

Data of quantum chemical calculations, synthetic procedures, and analytical and spectroscopic data of $[V(\text{ddpd})_2][\text{PF}_6]_3$ (PDF)

X-ray crystallographic data for $\text{mer}-[V(\text{ddpd})_2][\text{PF}_6]_3 \cdot 3\text{CH}_3\text{CN}$ (CIF)

AUTHOR INFORMATION

Corresponding Authors

Markus Gerhards – Department of Chemistry and Research Center Optimas, TU Kaiserslautern, Kaiserslautern 67663, Germany; orcid.org/0000-0002-8748-2940; Email: gerhards@chemie.uni-kl.de

Michael Seitz – Institute of Inorganic Chemistry, University of Tübingen, Tübingen 72076, Germany; orcid.org/0000-0002-9313-2779; Email: michael.seitz@uni-tuebingen.de

Katja Heinze – Department of Chemistry, Johannes Gutenberg University of Mainz, Mainz 55128, Germany; orcid.org/0000-0003-1483-4156; Email: katja.heinze@uni-mainz.de

Authors

Matthias Dorn – Department of Chemistry, Johannes Gutenberg University of Mainz, Mainz 55128, Germany

Jens Kalmbach – Institute of Inorganic Chemistry, University of Tübingen, Tübingen 72076, Germany

Pit Boden – Department of Chemistry and Research Center Optimas, TU Kaiserslautern, Kaiserslautern 67663, Germany

Ayla Pöpcke – Institute for Physics and Department of Life, Light and Matter, University of Rostock, Rostock 18051, Germany

Sandra Gómez – Institute of Theoretical Chemistry, Faculty of Chemistry, University of Vienna, Vienna 1090, Austria

Christoph Förster – Department of Chemistry, Johannes Gutenberg University of Mainz, Mainz 55128, Germany

Felix Kuczelinis – Department of Chemistry, Johannes Gutenberg University of Mainz, Mainz 55128, Germany

Luca M. Carrella – Department of Chemistry, Johannes Gutenberg University of Mainz, Mainz 55128, Germany

Laura A. Büldt – Institute of Inorganic Chemistry, University of Tübingen, Tübingen 72076, Germany

Nicolas H. Bings – Department of Chemistry, Johannes Gutenberg University of Mainz, Mainz 55128, Germany

Eva Rentschler – Department of Chemistry, Johannes Gutenberg University of Mainz, Mainz 55128, Germany; orcid.org/0000-0003-1431-3641

Stefan Lochbrunner – Institute for Physics and Department of Life, Light and Matter, University of Rostock, Rostock 18051, Germany

Leticia González – Institute of Theoretical Chemistry, Faculty of Chemistry, University of Vienna, Vienna 1090, Austria;

orcid.org/0000-0001-5112-794X

Complete contact information is available at:
<https://pubs.acs.org/10.1021/jacs.0c02122>

Notes

The authors declare no competing financial interest.

ACKNOWLEDGMENTS

Financial support from the Deutsche Forschungsgemeinschaft [DFG, Priority Program SPP 2102 “Light-controlled reactivity of metal complexes” (GE 961/10-1, HE 2778/15-1, LO 714/11-1, SE 1448/8-1, GO 1059/8-1)] is gratefully acknowledged. Parts of this research were conducted using the supercomputer Mogon and advisory services offered by Johannes Gutenberg University Mainz (<https://hpc.uni-mainz.de>), which is a member of the AHRP and the Gauss Alliance e.V. as well as at the Vienna Scientific Cluster (VSC3).

REFERENCES

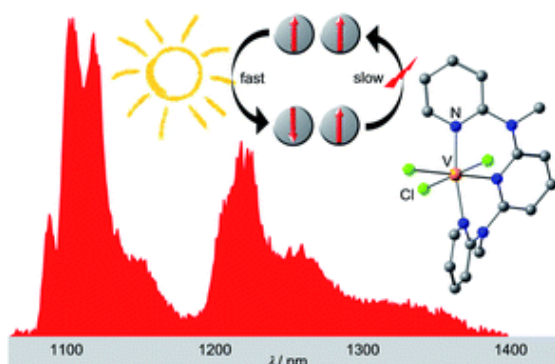
- (1) (a) Wenger, O. S. Photoactive Complexes with Earth-Abundant Metals. *J. Am. Chem. Soc.* **2018**, *140*, 13522–13533. (b) Förster, C.; Heinze, K. Photophysics and photochemistry with Earth-abundant metals - fundamentals and concepts. *Chem. Soc. Rev.* **2020**, *49*, 1057–1070.
- (2) Otto, S.; Dorn, M.; Förster, C.; Bauer, M.; Seitz, M.; Heinze, K. Understanding and Exploiting Long-lived Near-infrared Emission of a Molecular Ruby. *Coord. Chem. Rev.* **2018**, *359*, 102–111.
- (3) Bizzarria, C.; Spuling, E.; Knoll, D. M.; Volz, D.; Bräse, S. Sustainable metal complexes for organic light-emitting diodes (OLEDs). *Coord. Chem. Rev.* **2018**, *373*, 49–82.
- (4) McCusker, J. K. Electronic structure in the transition metal block and its implications for light harvesting. *Science* **2019**, *363*, 484–488.
- (5) Wagenknecht, P. S.; Ford, P. C. Metal centered ligand field excited states: Their roles in the design and performance of transition metal based photochemical molecular devices. *Coord. Chem. Rev.* **2011**, *255*, 591–616.
- (6) Zhang, W.; Alonso-Mori, R.; Bergmann, U.; Bressler, C.; Chollet, M.; Galler, A.; Gawelda, W.; Hadt, R. G.; Hartsock, R. W.; Kroll, T.; Kjær, K. S.; Kubiček, K.; Lemke, H. T.; Liang, H. W.; Meyer, D. A.; Nielsen, M. M.; Purser, C.; Robinson, J. S.; Solomon, E. I.; Sun, Z.; Sokaras, D.; van Driel, T. B.; Vankó, G.; Weng, T. C.; Zhu, D.; Gaffney, K. J. Tracking excited-state charge and spin dynamics in iron coordination complexes. *Nature* **2014**, *15*, 345–348.
- (7) Büldt, L. A.; Guo, X.; Vogel, R.; Prescimone, A.; Wenger, O. S. A Tris(dioscyanide)chromium(0) Complex Is a Luminescent Analog of Fe(2,2'-Bipyridine)₃²⁺. *J. Am. Chem. Soc.* **2017**, *139*, 985–992.
- (8) Pal, A. K.; Li, C.; Hanan, G. S.; Zysman-Colman, E. Blue Emissive Cobalt(III) Complexes and Their Use in the Photocatalytic Trifluoromethylation of Polycyclic Aromatic Hydrocarbons. *Angew. Chem., Int. Ed.* **2018**, *57*, 8027–8031.
- (9) Chábera, P.; Liu, Y.; Prakash, O.; Thyraug, E.; El Nahhas, A.; Honarfar, A.; Essén, S.; Fredin, L. A.; Harlang, T. C. B.; Kjær, K. S.; Handrup, K.; Ericson, F.; Tatsuno, H.; Morgan, K.; Schnadt, J.; Haggström, L.; Ericsson, T.; Sobkowiak, A.; Lidin, S.; Huang, P.; Styring, S.; Uhlig, J.; Bendix, J.; Lomoth, R.; Sundström, V.; Persson, P.; Wärnmark, K. A low-spin Fe(III) complex with 100-ps ligand-to-metal charge transfer photoluminescence. *Nature* **2017**, *543*, 695–699.
- (10) Kjær, K. S.; Kaul, N.; Prakash, O.; Chábera, P.; Rosemann, N. W.; Honarfar, A.; Gordivska, O.; Fredin, L. A.; Bergquist, K.-E.; Haggström, L.; Ericsson, T.; Lindh, L.; Yartsev, A.; Styring, S.; Huang, P.; Uhlig, J.; Bendix, J.; Strand, D.; Sundström, V.; Persson, P.; Lomoth, R.; Wärnmark, K. Luminescence and reactivity of a charge-transfer excited iron complex with nanosecond lifetime. *Science* **2019**, *363*, 249–253.
- (11) Hamze, R.; Peltier, J. L.; Sylvinson, D.; Jung, M.; Cardenas, J.; Haiges, R.; Soleilhavoup, M.; Jassar, R.; Djurovich, P. I.; Bertrand, G.; Thompson, M. E. Eliminating nonradiative decay in Cu(I) emitters: > 99% quantum efficiency and microsecond lifetime. *Science* **2019**, *36*, 601–606.
- (12) Otto, S.; Grabolle, M.; Förster, C.; Kreitner, C.; Resch-Genger, U.; Heinze, K. [Cr(ddpd)₂]³⁺: A molecular, water-soluble, highly NIR-emissive ruby analogue. *Angew. Chem., Int. Ed.* **2015**, *54*, 11572–11576.
- (13) Wang, C.; Otto, S.; Dorn, M.; Kreidt, E.; Lebon, J.; Sršan, L.; Di Martino-Fumo, P.; Gerhards, M.; Resch-Genger, U.; Seitz, M.; Heinze, K. Deuterated Molecular Ruby with Record Luminescence Quantum Yield. *Angew. Chem., Int. Ed.* **2018**, *57*, 1112–1116.
- (14) Otto, S.; Förster, C.; Wang, C.; Resch-Genger, U.; Heinze, K. A strongly luminescent chromium(III) complex acid. *Chem. - Eur. J.* **2018**, *24*, 12555–12563.
- (15) Otto, S.; Harris, J.; Heinze, K.; Reber, C. Molecular ruby under pressure. *Angew. Chem., Int. Ed.* **2018**, *57*, 11069–11073.
- (16) Treiling, S.; Wang, C.; Förster, C.; Reichenauer, F.; Kalmbach, J.; Boden, P.; Harris, J. P.; Carrella, L. M.; Rentschler, E.; Resch-Genger, U.; Reber, C.; Seitz, M.; Gerhards, M.; Heinze, K. Luminescence and Light-driven Energy and Electron Transfer from an Exceptionally Long-lived Excited State of a Non-innocent Chromium(III) Complex. *Angew. Chem., Int. Ed.* **2019**, *58*, 18075–18085.
- (17) (a) Jiménez, J. R.; Doistau, B.; Cruz, C. M.; Besnard, C.; Cuerva, J. M.; Campaña, A. G.; Piguet, C. Chiral Molecular Ruby [Cr(dqp)₂]³⁺ with Long-Lived Circularly Polarized Luminescence. *J. Am. Chem. Soc.* **2019**, *141*, 13244–13252. (b) Dec, C.; Zinna, F.; Kitzmann, W. R.; Pescitelli, G.; Heinze, K.; Di Bari, L.; Seitz, M. Strong Circularly Polarized Luminescence of an Octahedral Chromium(III) Complex. *Chem. Commun.* **2019**, *55*, 13078–13081.
- (18) (a) Bünzli, J.-C. G.; Eliseeva, S. V. Lanthanide NIR luminescence for telecommunications, bioanalyses and solar energy conversion. *J. Rare Earths* **2010**, *28*, 824–842. (b) Bünzli, J.-C. G. Lanthanide light for biology and medical diagnosis. *J. Lumin.* **2016**, *170*, 866–878.
- (19) Ibrahim-Ouali, M.; Dumur, F. Recent Advances on Metal-Based Near-Infrared and Infrared Emitting OLEDs. *Molecules* **2019**, *24*, 1412.
- (20) Ye, H. Q.; Li, Z.; Peng, Y.; Wang, C. C.; Li, T. Y.; Zheng, Y. X.; Sapelkin, A.; Adamopoulos, G.; Hernández, I.; Wyatt, P. B.; Gillin, W. P. Organo-erbium systems for optical amplification at telecommunications wavelengths. *Nat. Mater.* **2014**, *13*, 382–386.
- (21) Carlos, L. D.; Ferreira, R. A. S.; Bermudez, V. d. Z.; Ribeiro, S. J. L. Lanthanide-Containing Light-Emitting Organic-Inorganic Hybrids: A Bet on the Future. *Adv. Mater.* **2009**, *21*, 509–534.
- (22) Foucault-Collet, A.; Gogick, K. A.; White, K. A.; Villette, S.; Pallier, A.; Collet, G.; Kieda, C.; Li, T.; Geib, S. J.; Rosi, N. L.; Pctoud, S. Lanthanide near infrared imaging in living cells with Yb³⁺ nano metal organic frameworks. *Proc. Natl. Acad. Sci. U. S. A.* **2013**, *110*, 17199–17204.
- (23) Yang, Q.; Hu, Z.; Zhu, S.; Ma, R.; Ma, H.; Ma, Z.; Wan, H.; Zhu, T.; Jiang, Z.; Liu, W.; Jiao, L.; Sun, H.; Liang, Y.; Dai, H. Donor Engineering for NIR-II Molecular Fluorophores with Enhanced Fluorescent Performance. *J. Am. Chem. Soc.* **2018**, *140*, 1715–1724.
- (24) Cai, Y.; Wei, Z.; Song, C.; Tang, C.; Han, W.; Dong, X. Optical nano-agents in the second near-infrared window for biomedical applications. *Chem. Soc. Rev.* **2019**, *48*, 22–37.
- (25) Zhang, M.; Zheng, W.; Liu, Y.; Huang, P.; Gong, Z.; Wei, J.; Gao, Y.; Zhou, S.; Li, X.; Chen, X. A New Class of Blue-LED-Excitable NIR-II Luminescent Nanoprobes Based on Lanthanide-Doped CaS Nanoparticles. *Angew. Chem., Int. Ed.* **2019**, *58*, 9556–9560.

- (26) Zhu, S.; Yung, B. C.; Chandra, S.; Niu, G.; Antaris, A. L.; Chen, X. Near Infrared-II (NIR-II) Bioimaging via Off-Peak NIR-I Fluorescence Emission. *Theranostics* **2018**, *8*, 4141–4151.
- (27) Wang, P.; Fan, Y.; Lu, L.; Liu, L.; Fan, L.; Zhao, M.; Xie, Y.; Xu, C.; Zhang, F. NIR II nanoprobe in-vivo assembly to improve image-guided surgery for metastatic ovarian cancer. *Nat. Commun.* **2018**, *9*, 2898.
- (28) Schulze, M.; Steffen, A.; Würthner, F. Near IR Phosphorescent Ruthenium(II) and Iridium(III) Perylene Bisimide Metal Complexes. *Angew. Chem., Int. Ed.* **2015**, *54*, 1570–1573.
- (29) Bünzli, J.-C. G.; Eliseeva, S. V. Basics of Lanthanide Photophysics. In *Lanthanide Luminescence: Photophysical, Analytical and Biological Aspects*; Hänninen, P., Härmä, H., Eds.; Springer-Verlag: Berlin Heidelberg, 2010.
- (30) Englman, R.; Jortner, J. The energy gap law for radiationless transitions in large molecules. *Mol. Phys.* **1970**, *18*, 145–164.
- (31) Casper, J. V.; Kober, E. M.; Sullivan, B. P.; Meyer, T. J. Application of the Energy Gap Law to the Decay of Charge-Transfer Excited States. *J. Am. Chem. Soc.* **1982**, *104*, 630–632.
- (32) Sveshnikova, E. B.; Ermolaev, V. L. Inductive-Resonant Theory of Nonradiative Transitions in Lanthanide and Transition Metal Ions. *Opt. Spectrosc.* **2011**, *111*, 34–50.
- (33) Kreidt, E.; Kruck, C.; Seitz, M. Non-radiative Deactivation of Lanthanoid Luminescence by Multiphonon Relaxation in Molecular Complexes. *Handbook on the Physics and Chemistry of Rare Earths*; Elsevier: Amsterdam, 2018; Vol. 53, pp 35–79.
- (34) Doffek, C.; Seitz, M. The Radiative Lifetime in Near-IR-Luminescent Ytterbium Cryptates: The Key to Extremely High Quantum Yields. *Angew. Chem., Int. Ed.* **2015**, *54*, 9719–9721.
- (35) Hu, J.-Y.; Ning, Y.; Meng, Y.-S.; Zhang, J.; Wu, Z.-Y.; Gao, S.; Zhang, J.-L. Highly near-IR emissive ytterbium(III) complexes with unprecedented quantum yields. *Chem. Sci.* **2017**, *8*, 2702–2709.
- (36) Zhang, J.-X.; Chan, W.-L.; Xie, C.; Zhou, Y.; Chau, H.-F.; Maity, P.; Harrison, G. T.; Amassian, A.; Mohammed, O. F.; Tanner, P. A.; Wong, W.-K.; Wong, K.-L. Impressive near-infrared brightness and singlet oxygen generation from strategic lanthanide-porphyrin double-decker complexes in aqueous solution. *Light: Sci. Appl.* **2019**, *8*, 46.
- (37) Kittilstved, K. R.; Hauser, A. Electronic structure and photophysics of pseudo-octahedral vanadium(III) oxo complexes. *Coord. Chem. Rev.* **2010**, *254*, 2663–2676.
- (38) Reber, C.; Güdel, H. U. Near Infrared Luminescence Spectroscopy of $\text{Al}_2\text{O}_3:\text{V}^{3+}$ and $\text{YF}_3:\text{V}^{3+}$. *Chem. Phys. Lett.* **1989**, *154*, 425–431.
- (39) Landry-Hum, J.; Bussière, G.; Daniel, C.; Reber, C. Triplet Electronic States in d^2 and d^3 Complexes Probed by Absorption Spectroscopy: A CASSCF/CASPT2 Analysis of $[\text{V}(\text{H}_2\text{O})_6]^{3+}$ and $[\text{Ni}(\text{H}_2\text{O})_6]^{2+}$. *Inorg. Chem.* **2001**, *40*, 2595–2601.
- (40) Beaulac, R.; Tregenna-Piggott, P. L. W.; Barra, A.-L.; Högni, Weihe; Luneau, D.; Reber, C. The Electronic Ground State of $[\text{V}(\text{urea})_6]^{3+}$ Probed by NIR Luminescence, Electronic Raman, and High-Field EPR Spectroscopies. *Inorg. Chem.* **2006**, *45*, 3399–3407.
- (41) Kittilstved, K. R.; Hauser, A. Electronic structure of V^{3+} in $\text{NaMgAl}(\text{ox})_3 \cdot 9\text{H}_2\text{O}$ probed by Fourier Transform spectroscopy. *J. Lumin.* **2009**, *129*, 1493–1496.
- (42) Van Kuiken, B. E.; Hahn, A. W.; Maganas, D.; DeBeer, S. Measuring Spin-Allowed and Spin-Forbidden d-d Excitations in Vanadium Complexes with 2p3d Resonant Inelastic X-ray Scattering. *Inorg. Chem.* **2016**, *55*, 11497–11501.
- (43) Reber, C.; Güdel, H. U.; Meyer, G.; Schleid, T.; Daul, C. A. Optical Spectroscopic and Structural Properties of V^{3+} -Doped Fluoride, Chloride, and Bromide Elpasolite Lattices. *Inorg. Chem.* **1989**, *28*, 3249–3258.
- (44) Wenger, O. S.; Güdel, H. U. Luminescence spectroscopy of V^{3+} -doped $\text{Cs}_2\text{NaYCl}_6$ under high pressure. *Chem. Phys. Lett.* **2002**, *354*, 75–81.
- (45) Penfold, T. J.; Gindensperger, E.; Daniel, C.; Marian, C. M. Spin-Vibronic Mechanism for Intersystem Crossing. *Chem. Rev.* **2018**, *118*, 6975–7025.
- (46) Förster, C.; Dorn, M.; Reuter, T.; Otto, S.; Davarci, G.; Reich, T.; Carrella, L.; Rentschler, E.; Heinze, K. Dpd as Expanded Terpyridine: Dramatic Effects of Symmetry and Electronic Properties in First Row Transition Metal Complexes. *Inorganics* **2018**, *6*, 86.
- (47) Bowman, A. C.; Sproules, S.; Wieghardt, K. Electronic Structures of the $[\text{V}(\text{bpy})_3]^{z+}$ ($z = 3+, 2+, 0, 1-$) Electron Transfer Series. *Inorg. Chem.* **2012**, *51*, 3707–3717.
- (48) Van Stappen, C.; Maganas, D.; DeBeer, S.; Bill, E.; Neese, F. Investigations of the Magnetic and Spectroscopic Properties of V(III) and V(IV) Complexes. *Inorg. Chem.* **2018**, *57*, 6421–6438.
- (49) Otto, S.; Nauth, A. M.; Ermilov, E.; Scholz, N.; Friedrich, A.; Resch-Genger, U.; Lochbrunner, S.; Opatz, T.; Heinze, K. Photo Chromium: Sensitizer for Visible Light-Induced Oxidative C-H Bond Functionalization - Electron or Energy Transfer? *ChemPhotoChem* **2017**, *1*, 344–349.
- (50) Plasser, F.; Gómez, S.; Menger, M. F. S. J.; Mai, S.; González, L. Highly efficient surface hopping dynamics using a linear vibronic coupling model. *Phys. Chem. Chem. Phys.* **2019**, *21*, 57–69.

3.2. Ultrafast and long-time excited state kinetics of an NIR-emissive vanadium(III) complex I: Synthesis, spectroscopy and static quantum chemistry

Matthias Dorn, Jens Kalmbach, Pit Boden, Ayla Kruse, Chahinez Dab, Christian Reber, Gereon Niedner-Schatteburg, Stefan Lochbrunner, Markus Gerhards, Michael Seitz and Katja Heinze

Chem. Sci. **2021**, 142, 7947–7955



The heteroleptic pseudo-octahedral d^2 -vanadium(III) complex $VCl_3(\text{ddpd})$ ($\text{ddpd} = N,N'$ -dimethyl- N,N' -dipyridine-2-yl-pyridine-2,6-diamine) with a 3T_2 ground state displays NIR spin-flip luminescence at room temperature from the $^1E/{}^1T_1$ excited states. Ligand deuteration reduces non-radiative decay via energy transfer to C-H oscillators.

Author Contributions

Synthesis and characterization of the title compound as well as photostability measurements, DFT and CAS-SCF calculations were carried out by Matthias Dorn. Static and time-resolved NIR luminescence measurements were performed by Jens Kalmbach (group of Prof. Dr. M. Seitz) and Pit Boden (group of Prof. Dr. M. Gerhards). Vibrational overtone analysis was carried out by Jens Kalmbach. Pit Boden accounted for step-scan IR measurements. Raman spectra were recorded by Chahinez Dab (group of Prof. C. Reber). Ayla Kruse (group of Prof. Dr. S. Lochbrunner) accounted for transient absorption measurements. Dr. Christoph Förster solved the crystal structure of the title compound. The manuscript was written by Prof. Dr. Katja Heinze (90%) and Matthias Dorn (10%)

Supporting Information

can be found at pp. 133.

The full supporting information can be obtained [here](#).

“Reproduced from Ref. ²²⁴ with permission from the Royal Society of Chemistry.”

Cite this: *Chem. Sci.*, 2021, 12, 10780

All publication charges for this article have been paid for by the Royal Society of Chemistry

Ultrafast and long-time excited state kinetics of an NIR-emissive vanadium(III) complex I: synthesis, spectroscopy and static quantum chemistry†‡

Matthias Dorn,^a Jens Kalmbach,^b Pit Boden,^c Ayla Kruse,^d Chahinez Dab,^e Christian Reber,^e Gereon Niedner-Schatteburg,^c Stefan Lochbrunner,^d Markus Gerhards,^c Michael Seitz^{*b} and Katja Heinze^{*a}

In spite of intense, recent research efforts, luminescent transition metal complexes with Earth-abundant metals are still very rare owing to the small ligand field splitting of 3d transition metal complexes and the resulting non-emissive low-energy metal-centered states. Low-energy excited states decay efficiently non-radiatively, so that near-infrared emissive transition metal complexes with 3d transition metals are even more challenging. We report that the heteroleptic pseudo-octahedral d²-vanadium(III) complex VCl₅(ddpd) (ddpd = *N,N'*-dimethyl-*N,N'*-dipyridine-2-yl-pyridine-2,6-diamine) shows near-infrared singlet → triplet spin-flip phosphorescence maxima at 1102, 1219 and 1256 nm with a lifetime of 0.5 μs at room temperature. Band splitting, ligand deuteration, excitation energy and temperature effects on the excited state dynamics will be discussed on slow and fast timescales using Raman, static and time-resolved photoluminescence, step-scan FTIR and fs-UV pump-vis probe spectroscopy as well as photolysis experiments in combination with static quantum chemical calculations. These results inform future design strategies for molecular materials of Earth-abundant metal ions exhibiting spin-flip luminescence and photoinduced metal–ligand bond homolysis.

Received 16th April 2021
Accepted 7th July 2021

DOI: 10.1039/d1sc02137k

rsc.li/chemical-science

Introduction

The control of photophysical properties of transition metal complexes by chemical means, especially for applications in lighting, imaging, sensing, photonics, dye sensitised solar cells, phototherapy or photocatalysis, is a very active research field.^{1–8} However, most applications rely on noble metal complexes with d⁶ or d⁸ electron configurations such as ruthenium(II), iridium(III) or platinum(II).⁹ The success of these precious metals in photophysics and photochemistry can be ascribed, among other beneficial features, to their intrinsically large

ligand field splitting¹⁰ and their large spin–orbit coupling (SOC) constants $\zeta \gg 1000 \text{ cm}^{-1}$.¹¹ Finally, these properties enable the efficient population of the photoactive and luminescent long-lived triplet metal-to-ligand charge transfer (³MLCT) states as lowest excited states after intersystem crossing (ISC).¹²

Aiming at a sustainable future photochemistry less dependent on rare and precious metals, Earth-abundant metals are currently heavily explored and novel concepts have been put forward^{13–18} including some second row metals,^{19–22} but in particular the first row transition metals.^{13–18} The 3d transition metals possess a weaker ligand field splitting¹⁰ and smaller SOC¹¹ posing severe challenges to the design of the excited state landscape,¹⁴ yet several recent breakthroughs have been reported, e.g. on copper(I),^{23,24} nickel(0,II),^{25,26} cobalt(III),²⁷ iron(II,III),^{28–31} chromium(0/III)^{32–35} and vanadium(III).³⁶ Beyond the conventionally exploited MLCT excited states,¹² LMCT states of the low-spin d⁵ electron configuration of iron(III)¹⁸ and spin-flip states of the d³ electron configuration of chromium(III)¹³ are emerging as novel paradigmatic excited states useful for photoapplications.

The currently most successful spin-flip emitters are based on the so-called molecular ruby motif, e.g. in [Cr(ddpd)₂]³⁺, with tridentate pyridine-type ligands forming six-membered chelate rings (ddpd = *N,N'*-dimethyl-*N,N'*-dipyridine-2-yl-pyridine-2,6-diamine).^{33,34,37} Applications already emerged in the areas of sensing,^{38–40} photocatalysis,³⁷ photodynamic therapy,⁴¹ photon

^aDepartment of Chemistry, Johannes Gutenberg University of Mainz, Duesbergweg 10-14, 55128 Mainz, Germany. E-mail: katja.heinze@uni-mainz.de

^bInstitute of Inorganic Chemistry, University of Tübingen, Auf der Morgenstelle 18, 72076 Tübingen, Germany

^cDepartment of Chemistry and Research Center Optimas, Technical University Kaiserslautern, Erwin-Schrödinger-Straße, 67663 Kaiserslautern, Germany

^dInstitute for Physics and Department of Life Light and Matter, University of Rostock, 18051 Rostock, Germany

^eDépartement de chimie, Université de Montréal, Montréal, Québec, H3C 3J7, Canada

† During manuscript finalisation, Prof. Markus Gerhards unexpectedly passed away on Dec. 28th 2020.

‡ Electronic supplementary information (ESI) available: Details the quantum chemical calculations, luminescence spectra, Raman spectra, luminescence decay, vibrational overtone analysis, step-scan FTIR spectra, IR spectral decay, photostability, cyclic voltammogram. See DOI: 10.1039/d1sc02137k



upconversion⁴² and the generation of circularly polarised emission.^{43–45}

Very recently, vanadium started to spark interest as potential novel near-infrared (NIR) luminophore⁴⁶ motivated by its high natural abundance and complementary properties to the chromium(III) spin-flip luminophores and sensitisers.^{36,47} Rappé and Damrauer demonstrated, that the d³-vanadium(II) electron configuration in the well-known [V(bpy)₃]²⁺ and [V(phen)₃]²⁺ complexes⁴⁸ (Chart 1, bpy = 2,2'-bipyridine, phen = 1,10-phenanthroline) leads to the population of non-luminescent excited doublet states with mixed ²MC/²MLCT character within 2.5–3 ps after excitation.⁴⁷ The lifetimes of the mixed excited states of [V(bpy)₃]²⁺ and [V(phen)₃]²⁺ are 0.43 ns and 1.6 ns, respectively.^{47,49} Yet, emission from these vanadium(II) complexes has not been observed at wavelengths shorter than 1600 nm even at low temperature.⁴⁷

Analogous to the intra- and interconfigurational electronic transitions derived from the d³ electron configuration (⁴T₂ and ²E/²T₁), the d² electron configuration with a ³T₁ ground state in octahedral symmetry provides low-energy spin-flip singlet states (¹E/¹T₂) and triplet states (³T₂) with respective intra- and interconfigurational transitions.⁵⁰ This electron configuration is realised, for example, in octahedral vanadium(III) complexes and solid state materials with vanadium(III) in octahedral sites.^{51–53} The electronic structure of basic d²-vanadium(III) complexes, e.g. [V(H₂O)₆]³⁺ and [V(urea)₆]³⁺, including the ground state splitting of the orbitally degenerate ³T₁ ground state and the zero-field splitting, has been obtained from Raman, luminescence, and high-frequency high-field electron paramagnetic resonance spectroscopies.^{51–53} A particularly interesting application of d²-luminescent materials is upconversion based on sequential ground state and excited state absorption,⁵⁴ as has been shown for example with d²-titanium(II) solid state materials such as MgCl₂:Ti.⁵⁴

Upconversion with molecular complexes has been demonstrated utilizing d³-chromium(III) complexes.^{42,55} The five-coordinate d²-vanadium(III) complex V((C₆F₅)₃tren)(CN^tBu) emits at 1240 nm in the solid state and frozen solution and was suggested as optically addressable molecular quantum bit candidate ((C₆F₅)₃tren = 2,2',2''-tris[[pentafluorophenyl]amino]triethylamine).⁵⁶ Consequently, the advancement of emissive molecular materials exploiting the d² electronic configuration would be very valuable for diverse photonic applications such as NIR emission, upconversion and quantum technology.

The d²-vanadium(III) polypyridine complex [V(ddpd)₂]³⁺ emits in the NIR (1100 nm), observed for the first time even at room temperature in solution (Chart 1).³⁶ Its phosphorescent singlet state with a lifetime of 0.79 μs/8.8 μs (93%/7%; 77 K in butyronitrile glass) is populated within picoseconds after excitation. Yet, the efficiency of the population transfer to the singlet states by ISC is rather small as confirmed by non-adiabatic molecular dynamics calculations.³⁶ Unexpectedly, and in contrast to the analogous chromium(III) spin-flip emitters, the decay of the phosphorescent spin-flip states of [V(ddpd)₂]³⁺ is insensitive to ligand deuteration, in spite of the significant spectral overlap of the NIR emission with the second aromatic C–H overtone ν_{CH}³ of the ligand. This suggests that other non-radiative decay pathways are more relevant than the multiphonon relaxation involving high-energy C–H oscillators⁵⁷ in this particular case.³⁶

A profound understanding of the decisive excited states and the excited state dynamics of these polypyridine vanadium(III) chromophores on ultrafast (population of emissive states) and slow timescales (depopulation of emissive states) is lacking. To better understand the novel class of d²-spin-flip luminophores based on vanadium(III) with respect to the population and decay of the emissive spin-flip states, we selected the chlorido vanadium(III) complex VCl₃(ddpd) (Chart 1)⁵⁸ for a detailed study of the photodynamics at ultrashort (sub-picosecond) to microsecond timescales (Chart 1).

Spin-orbit effects are weak in vanadium(III) complexes based on the lower intensity of the singlet transitions compared to the triplet bands by more than three orders of magnitude.⁵⁹ Our choice of molecular system is guided by two considerations: (i) the slow ISC rate defined by the small SOC constant of vanadium(III) (ζ ≈ 210/206/220 cm⁻¹)^{11,60,61} can increase due to the influence of the coordinated chlorido ligands with their higher SOC constant (ζ ≈ 547 cm⁻¹)⁶¹ as compared to nitrogen (ζ ≈ 76 cm⁻¹).⁶¹ (ii) The symmetry reduction by using different ligand types can relax Laporte's rule⁶² and increase the radiative rate from metal-centred spin-flip states.³⁵

We report here that the heteroleptic VCl₃(ddpd)⁵⁸ complex is NIR-emissive at room temperature (Chart 1). We undertook a detailed photophysical study using Raman spectroscopy, variable temperature and variable pressure steady-state photoluminescence spectroscopy, fs-transient absorption spectroscopy, time-resolved photoluminescence and variable temperature step-scan FTIR spectroscopy to cover the ground state splitting, as well as the ultrafast and slow time regimes of the excited state kinetics. To elucidate whether non-radiative relaxation of the luminescent singlet states *via* aromatic

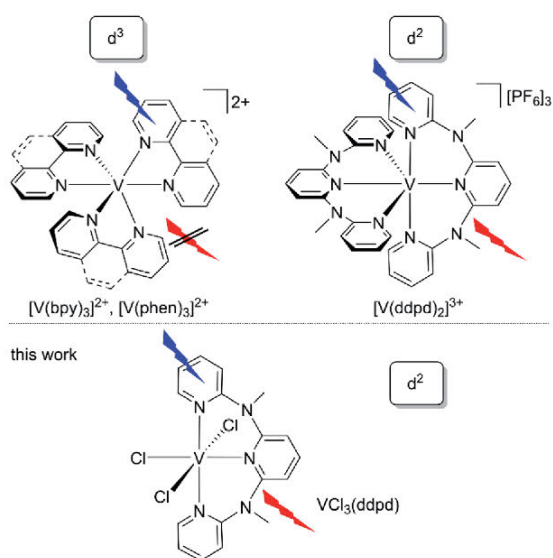


Chart 1 Structures of vanadium(II) and luminescent vanadium(III) polypyridine complexes.



3T states is substantial reflecting the low symmetry of the complex. The five lowest excited singlet states of $^1E/{}^1T_2$ parentage are calculated at 10 086/10 161/10 949/11 068/11 309 cm^{-1} . These spread over 1200 cm^{-1} (Fig. 1b). As the energy of the lowest singlet state is significantly lower than the lowest excited triplet state by *ca.* 4900 cm^{-1} , NIR phosphorescence from the singlet state to the split ground state is conceivable (Fig. 1b). Extended calculations using an even larger active space will be presented in the accompanying paper.⁶³

Excitation of solid $\text{VCl}_3(\text{ddpd}[\text{D}_0])$ with 350 nm (ILCT) at 298 K results in the appearance of two NIR emission bands (Fig. 2a). At 77 K, the emission bands increase in intensity and develop a characteristic fine structure (Fig. 2a). Discernible peaks occur at 1102, 1219 and 1256 nm (9074, 8203, 7962 cm^{-1}). Considering the calculated ground state splitting, we assign these clearly visible band maxima to radiative transitions from the lowest excited singlet state(s) to the split ground state (Fig. 1b). The resulting experimental ground state splitting of *ca.* 800 and 1100 cm^{-1} excellently agrees with the CASSCF-NEVPT2 calculated splitting (755 and 1076 cm^{-1}). The experimental ground state splitting refers to the geometry minimum of the singlet state, while the CASSCF-NEVPT2 calculated splitting refers to the ground state geometry. As spin-flip states are rather nested, the geometry differences should be marginal. Raman spectra of $[\text{V}(\text{H}_2\text{O})_6]^{3+}$ and $[\text{V}(\text{urea})_6]^{3+}$ show broad electronic Raman transitions around 1900–2900 cm^{-1} and 1400 cm^{-1} , respectively,^{51,52} due to the trigonal ground-state splitting. For $\text{VCl}_3(\text{ddpd}[\text{D}_0])$, we observe two broad electronic Raman transitions around 500 and 900 cm^{-1} in its Raman spectrum in accordance with its lower symmetry (Fig. 2b). These energies fit well to the splitting assigned by luminescence spectroscopy (Fig. 2a) and obtained from the CASSCF-NEVPT2 calculations.

The finer details of the NIR luminescence band structure can be tentatively assigned to population of the close-lying singlet states with the difference between the two lowest singlet states calculated as 75 cm^{-1} and to enabling vibrations around 120 cm^{-1} . Indeed, Cl–V–Cl deformation vibrations (125, 136, 159 cm^{-1} ; unscaled) appear in this energy region according to the DFT calculations (ESI, Fig. S4†).

Upon pressurizing solid $\text{VCl}_3(\text{ddpd}[\text{D}_0])$ to 7 kbar, two very weak NIR emission bands at approximately 9100 and 9280 cm^{-1} (lowest energy detectable with the employed detector) shift to higher energy by $\approx 10 \text{ cm}^{-1} \text{ kbar}^{-1}$. (Fig. S5, ESI†). This hypsochromic shift of the emission bands differs from the bathochromic behaviour encountered by the d^3 complex $[\text{Cr}(\text{ddpd})_2]^{3+}$ at increasing pressure.³⁹ This unusual pressure-sensitivity is probably a combined effect of energy changes of the emissive singlet states and of the ground state splitting under increasing pressure. The broad, electronic Raman bands assigned to transitions within the split $^3T_{1g}$ ground state experience variations in intensity and broaden strongly with increasing pressure (Fig. S6, ESI†). At pressures higher than 30 kbar the broadening, most likely due to effects of non-hydrostatic pressure, dominates and the bands can no longer be observed. These observations illustrate that luminescence

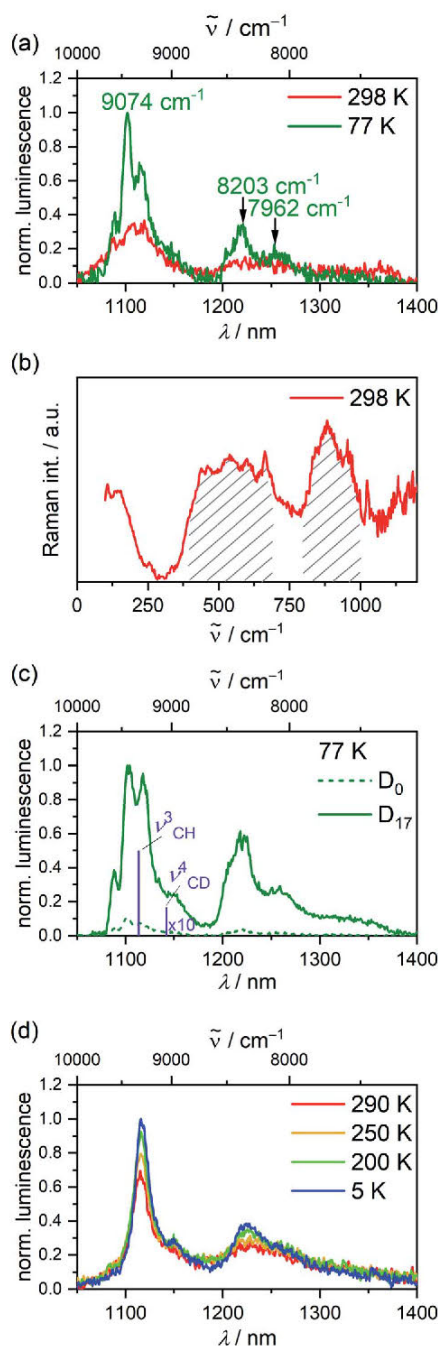


Fig. 2 (a) Luminescence spectra of $\text{VCl}_3(\text{ddpd}[\text{D}_0])$ at 298 K (red) and 77 K (green) ($\lambda_{\text{exc}} = 350 \text{ nm}$), (b) solid state Raman spectrum of neat $\text{VCl}_3(\text{ddpd}[\text{D}_0])$ at 298 K ($\lambda_{\text{exc}} = 785 \text{ nm}$). Electronic Raman transitions between the 3T_1 ground state components are highlighted. (c) Luminescence spectra of neat $\text{VCl}_3(\text{ddpd}[\text{D}_0])$ (green dotted line) and $\text{VCl}_3(\text{ddpd}[\text{D}_{17}])$ (green solid line) at 77 K ($\lambda_{\text{exc}} = 350 \text{ nm}$). Purple bars indicate the positions of the ν_{CH}^3 and ν_{CD}^4 overtones. (d) Luminescence spectra of $\text{VCl}_3(\text{ddpd}[\text{D}_{17}])$ as KBr pellet at 5–290 K ($\lambda_{\text{exc}} = 350 \text{ nm}$).

shifts different from those for spin-flip transitions with nondegenerate ground states are expected for vanadium(III) complexes.



The NIR luminescence of $\text{VCl}_3(\text{ddpd}-[\text{D}_{17}])$ at 298 K in the solid state under inert conditions ($\lambda_{\text{exc}} = 350 \text{ nm}$) decays monoexponentially with $\tau_{298}^{\text{H}} = 0.5 \mu\text{s}$ (ESI, Fig. S7 \ddagger). This long lifetime confirms the assignment as phosphorescence. With the fully deuterated ligand $\text{ddpd}-[\text{D}_{17}]^{36}$ installed in $\text{VCl}_3(\text{ddpd}-[\text{D}_{17}])$, the NIR luminescence intensity strongly increases compared to that of the non-deuterated complex (Fig. 2c). Concomitantly, the luminescence lifetime at 298 K increases to $\tau_{298}^{\text{D}} = 3.3 \mu\text{s}$ ($\lambda_{\text{obs}} = 1106 \text{ nm}$) and $3.4 \mu\text{s}$ ($\lambda_{\text{obs}} = 1222 \text{ nm}$) (Fig. S8 and S9, ESI \ddagger). The deuteration effect confirms that multiphonon relaxation (Fig. 1b) is substantial in $\text{VCl}_3(\text{ddpd}-[\text{D}_0])$. The estimated spectral overlap integral (SOI) of the second C-H_{ar} overtone ν_{CH}^3 (ref. 34) of the ligand at 8972 cm^{-1} is significant, while the relevant third CD_{ar} overtone ν_{CD}^4 (ref. 34) at 8755 cm^{-1} has a much lower SOI due to its lower extinction coefficient (ESI, Fig. S10–S12 \ddagger). Based on the vibrational overtone and SOI calculation, the rate constant for this overtone-mediated non-radiative decay mechanism should diminish by a factor of 36 (ESI, Fig. S10–S16 \ddagger). This qualitatively matches the observed intensity enhancement upon deuteration. The observation of an isotope effect confirms that multiphonon relaxation is a major non-radiative decay path of the singlet states in this complex dominating other non-radiative decays. This finding contrasts the observations for the homoleptic complex $[\text{V}(\text{ddpd})_2][\text{PF}_6]_3$ and its deuterated isotopologue where other decay pathways appear to dominate the non-radiative decay of the NIR-emissive states.³⁶

Cooling solid $\text{VCl}_3(\text{ddpd}-[\text{D}_n])$ both as neat powder and as KBr pellet increases the luminescence intensity (Fig. 2a, d; and S17–S19, ESI \ddagger). For example, cooling $\text{VCl}_3(\text{ddpd}-[\text{D}_{17}])$ from 290 to 200 K yields a 1.5-fold increased integrated NIR intensity, while further cooling to 5 K only has a minor effect (Fig. 2d; and S17–S19, ESI \ddagger). This suggests the presence of a thermally activated non-radiative pathway accessible at temperatures above 200 K.

To probe the structure, the vibrational signature and possible distortions of the long-lived excited singlet states at high and low temperature, step-scan FTIR spectra of $\text{VCl}_3(\text{ddpd}-[\text{D}_0])$ and $\text{VCl}_3(\text{ddpd}-[\text{D}_{17}])$ were recorded in KBr pellets (Fig. 3; and S20–S23, ESI \ddagger). The ground state FTIR spectra of $\text{VCl}_3(\text{ddpd}-[\text{D}_0])$ and $\text{VCl}_3(\text{ddpd}-[\text{D}_{17}])$ in KBr pellets at 290 K are well reproduced by DFT calculated frequencies scaled by 0.98 (Fig. 3a and S21, ESI \ddagger). The characteristic ν_{CC} , ν_{CN} and δ_{CH} modes of the terminal and central pyridine rings around 1599 , 1495 and 1442 cm^{-1} shift to lower energy by approximately $35\text{--}75 \text{ cm}^{-1}$ upon deuteration of the ligand in $\text{VCl}_3(\text{ddpd}-[\text{D}_{17}])$.

Step-scan FTIR spectra recorded for $\text{VCl}_3(\text{ddpd}-[\text{D}_0])$ and $\text{VCl}_3(\text{ddpd}-[\text{D}_{17}])$ in a KBr pellet with $\lambda_{\text{exc}} = 355 \text{ nm}$ collected over 0–500 ns at 290 and 20 K are depicted in Fig. 3a, S20, S21 and S23 (ESI \ddagger). The long-lived excited singlet states give rise to positive and negative bands corresponding to the population of the excited singlet states and ground state bleach, respectively. The excited state spectra of $\text{VCl}_3(\text{ddpd}-[\text{D}_0])$ and $\text{VCl}_3(\text{ddpd}-[\text{D}_{17}])$ at 290 and 20 K are derived from the respective step-scan and the ground state spectra (Fig. 3b; and S22, ESI \ddagger). Temperature has only a minor influence on the excited state spectra of $\text{VCl}_3(\text{ddpd}-[\text{D}_0])$

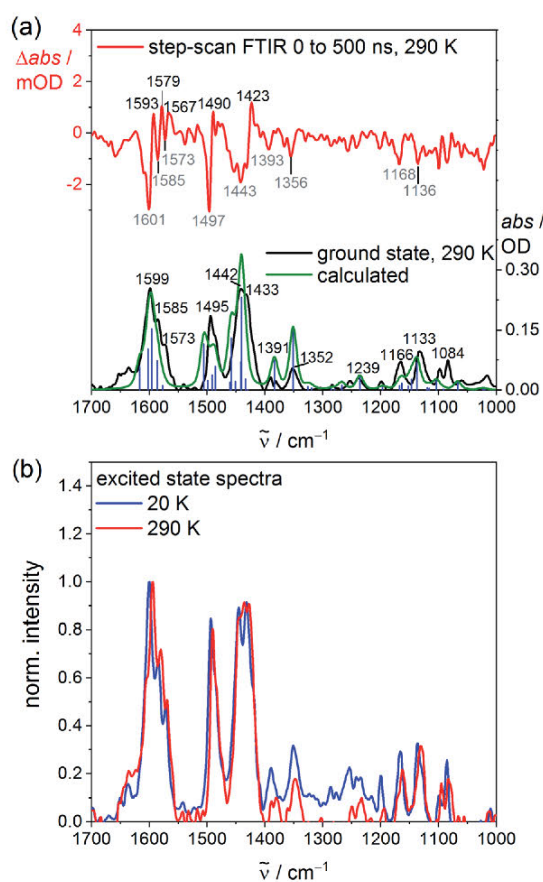


Fig. 3 (a) Experimental (black), DFT-calculated ground state (green) and step-scan FTIR spectra (top, $\lambda_{\text{exc}} = 355 \text{ nm}$; 0–500 ns) of $\text{VCl}_3(\text{ddpd}-[\text{D}_0])$ in a KBr pellet at 290 K (red) and (b) excited state FTIR spectra of $\text{VCl}_3(\text{ddpd}-[\text{D}_0])$ in a KBr pellet obtained from step-scan FTIR spectra ($\lambda_{\text{exc}} = 355 \text{ nm}$; 0–500 ns) (small contributions of 3% of the respective ground state spectrum added to the step-scan spectrum) at 20 K (blue) and 290 K (red).

(Fig. 3b), but modifies the relative excited state IR intensities of the deuterated derivative $\text{VCl}_3(\text{ddpd}-[\text{D}_0])$ (Fig. S22, ESI \ddagger).

The evolution of prominent IR bands after excitation of $\text{VCl}_3(\text{ddpd}-[\text{D}_0])$ over time was fitted in a global analysis giving a monoexponential decay with $\tau_{290\text{K}}^{\text{H}} = 0.6 \mu\text{s}$ at 290 K (Fig. S24, ESI \ddagger) excellently fitting to the decay observed by photoluminescence spectroscopy at 298 K. Cooling to 20 K approximately doubles the excited state lifetime to $\tau_{20\text{K}}^{\text{H}} = 1.3 \mu\text{s}$ (Fig. S25, ESI \ddagger). This confirms that thermally activated non-radiative pathways are operative at room temperature in addition to the multiphonon relaxation *via* C–H oscillators,⁵⁷ which takes place at all temperatures. Surprisingly, the step-scan data of the deuterated complex $\text{VCl}_3(\text{ddpd}-[\text{D}_{17}])$ deliver excited state lifetimes of $\tau_{290\text{K}}^{\text{D}} = 0.6 \mu\text{s}$ and $\tau_{20\text{K}}^{\text{D}} = 1.2 \mu\text{s}$ at 290 and 20 K, respectively (Fig. S26 and S27, ESI \ddagger), similar to $\text{VCl}_3(\text{ddpd}-[\text{D}_0])$. This differs from the higher room temperature lifetime of $\text{VCl}_3(\text{ddpd}-[\text{D}_{17}])$ $\tau_{298}^{\text{D}} = 3.3/3.4 \mu\text{s}$ obtained by time-correlated single photon counting (Fig. S8 and S9, ESI \ddagger ; see above). Possibly, the step-scan FTIR experiment mainly detects one of



the emissive singlet states but fails to probe the second emissive singlet state. According to the CASSCF-NEVPT2 calculations, the two lowest singlet states derive from terms with essentially 1E and 1T_2 character, respectively, with a very small energy difference of only 75 cm^{-1} (Table S6, ESI †). As the orbital population of the 1T_2 -derived term matches that of the lowest term of the split 3T_2 ground state (Fig. S3, ESI †), this excited state possesses the same equilibrium nuclear configuration as the ground state (nested state). Consequently, step-scan FTIR spectroscopy would not be able to detect this excited state. Clearly, a model of the excited state decay of the two lowest energy singlet excited states to the split ground state requires at least five electronic states. For a kinetic model of the non-radiative decay *via* high- and low-frequency modes⁵⁷ these comparably close-lying electronic states (Fig. 1b) would have to be combined with the different anharmonic vibrational C–H/C–D modes as well as the pyridine ring vibrational ladders. The latter modes are also affected by deuteration according to the ground state FTIR spectra of $\text{VCl}_3(\text{ddpd}-[D_0])$ and $\text{VCl}_3(\text{ddpd}-[D_{17}])$ (Fig. 3a and S21, ESI †).

As $\text{VCl}_3(\text{ddpd})$ is only poorly soluble in typical solvents, a detailed reliable study of its weak NIR luminescence in solution is unfortunately impeded, especially when exciting at the very weak 3MC band. Furthermore, we noted a follow-up reaction upon irradiating $\text{VCl}_3(\text{ddpd}-[D_0])$ at $350 \pm 5\text{ nm}$ (ILCT) in acetonitrile solution. The absorption spectrum changes and an emission band at *ca.* 400 nm grows in over time (Fig. S28 and S29, ESI †). The photostability is much higher under irradiation at $400 \pm 5\text{ nm}$ including consideration for absorption and light intensity of the light source. (Fig. S30–S32, ESI †). This suggests that the low energy 3T_2 , ${}^1T_2/{}^1E$ and $\text{ddpd} \rightarrow \text{V}^3\text{LMCT}$ states are not responsible for the photoreactivity (Fig. 1b). At the higher excitation energy and with the assumption that LMCT states are likely involved (Fig. 1), we speculate that V–Cl homolysis could occur in solution. The well-known fact, that M–Cl bonds of reducible metal ions are prone to photoinduced homolysis has regained considerable interest in organic photoredox catalysis in particular for copper^{69–71} and nickel.^{72–75} VCl_3 itself is photo-reduced to vanadium(II) in alcoholic solutions *via* excitation into LMCT states (chloride-to-vanadium or alkoxide-to-vanadium charge transfer).⁷⁶ A ${}^3\text{LMCT}$ state with chloride-to-vanadium character was found by TDDFT at 324 nm (state 14 shifted hypsochromically by 3400 cm^{-1} , Tables S3, S4, and Fig. S2, ESI †). This ${}^3\text{LMCT}$ state could qualify as excited state with V–Cl dissociative character. To probe the conceivable $\text{V}^{\text{III/II}}$ reduction process, a cyclic voltammogram of $\text{VCl}_3(\text{ddpd}-[D_0])$ was recorded in CH_3CN . The cathodic scan reveals an irreversible reduction wave at $E_p = -1.11\text{ V}$ versus ferrocene/ferrocenium with an oxidative follow-up wave at $E_p = -0.25\text{ V}$ and a reductive wave at -0.83 V (Fig. S33, ESI †). This behaviour can be associated with chloride loss upon electron capture, similar to the reported preparation of $\text{VCl}_2(\text{py})_4$ from VCl_3 , pyridine and zinc dust as reductant.⁷⁷ Consequently, we consider V–Cl bond homolysis as a viable reaction path under UV light photolysis in fluid solution. In contrast to this photoreactivity of the chlorido complex, the homoleptic complex $[\text{V}(\text{ddpd})_2][\text{PF}_6]_3$ appears comparably photostable in solution,

which can be ascribed to the absence of suitable dissociative LMCT states.³⁶

Finally we explored the reaction path from the Franck-Condon excited triplet state to the long-lived singlet states by ultrafast transient absorption spectroscopy in CH_3CN . To diminish the dissociative processes assigned to high-energy ${}^3\text{LMCT}$ states with Cl \rightarrow V character, 400 nm pulses were employed populating essentially ${}^3\text{LMCT}$ states with NMe(ddpd) \rightarrow V character (Tables S3, S4 and Fig. S2, ESI †). After excitation, a broad excited state absorption (ESA) from 470–700 nm appears in addition to an ESA around 410 nm (Fig. 4a). The ground state bleach fits to the dip in the transient absorption spectrum around 463 nm (Fig. 1a and 4b).

The broad ESA evolves with $\tau_1 = 1.5\text{ ps}$ to a long-lived state with a maximum at 543 nm (Fig. 4b). This state persists much longer than the time window of 1.4 ns of the pump-probe experiment, which is given by the length of the motorized delay stage in the setup. Since electronic relaxation between electronically excited states of the same spin multiplicity is typically rather fast, one of the lowest excited states of the different spin multiplicities should be responsible for the long-

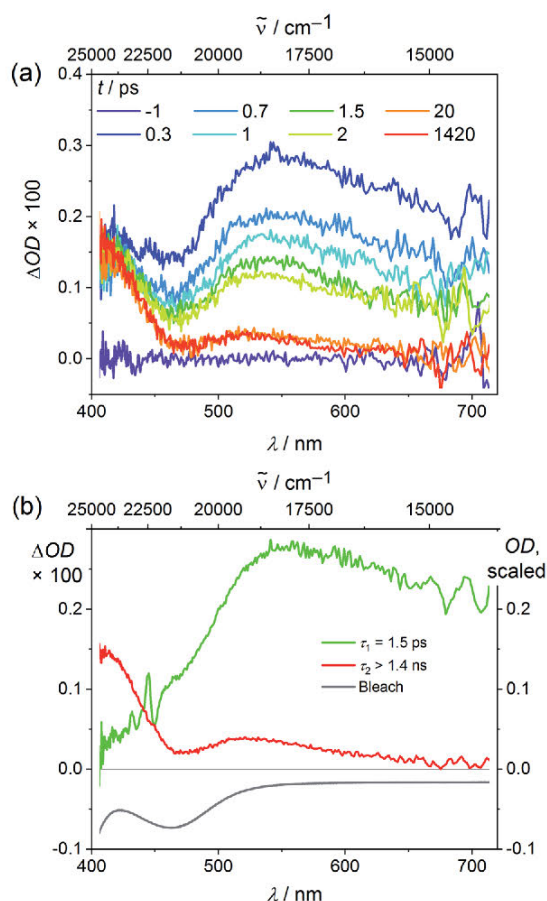


Fig. 4 (a) Transient absorption spectra of $\text{VCl}_3(\text{ddpd}-[D_0])$ in CH_3CN excited with fs laser pulses at 400 nm (298 K) and (b) decay associated amplitude spectra (red, green) with indicated lifetimes and the ground state bleach (grey).



lived state, *i.e.* the 3T_2 state or the $^1E/{}^1T_2$ states (Fig. 1). Significant population in a long living electronically excited triplet state should result in fluorescence, since the radiative transition to the ground state would be spin allowed and Laporte's rule is relaxed in the complex. However, no luminescence is observed at wavelengths below 1050 nm as would be expected for triplet states (Fig. 1). This excludes that a significant excited state population is trapped in any triplet state. A partitioning of excited state population in triplet and singlet states, as it was observed in $[V(\text{ddpd})_2]^{3+}$ (ref. 36) does not occur with $VCl_3(\text{ddpd})$. The persistent TA component is therefore assigned to the long-lived $^1E/{}^1T_2$ states. Clearly, ISC to the singlet manifold and vibrational cooling proceed to completion within a few ps. The rate constant for ISC k_{ISC} is at least $1/\tau_1 = 6.7 \times 10^{11} \text{ s}^{-1}$. Trajectory surface hopping simulations within a linear vibronic coupling model will derive a detailed kinetic model of the initial dynamics and the efficiency of the ISC processes ($\tau_{\text{ISC, simulation}} = 1.7 \pm 0.3 \text{ ps}$) in the accompanying paper.⁶³

Experimental

Synthesis. $VCl_3(\text{ddpd}-D_0)$ was prepared according to ref. 58. The deuterated complex $VCl_3(\text{ddpd}-[D_{17}])$ was prepared analogously using the deuterated ligand $\text{ddpd}-[D_{17}]$ prepared according to ref. 36.

Electrochemical experiments were carried out on a BioLogic SP-200 voltammetric analyser using platinum wires as counter and working electrodes and a 0.01 M $\text{Ag}/\text{Ag}[\text{NO}_3]$ electrode as reference electrode. Cyclic voltammetry and square wave measurements were carried out at scan rates of 50–200 mV s^{-1} using 0.1 M $[\text{Bu}_4\text{N}][\text{PF}_6]$ in CH_3CN as supporting electrolyte. Potentials are referenced against the ferrocene/ferrocenium couple.

Photolysis experiments were carried out in CH_3CN using an Asahi Spectra Max-303 Xenon Light Source (300 W, Fig. S32, ESI †), together with $350 \pm 5 \text{ nm}$ and $400 \pm 5 \text{ nm}$ filters, respectively.

UV/Vis photoluminescence spectra during photolysis experiments were collected on a Varian Cary Eclipse spectrometer.

UV/Vis/NIR spectra were recorded on a Varian Cary 5000 spectrometer using 1.0 cm cells.

Raman and luminescence spectra under pressure at wavelengths up to 1050 nm were measured with a Renishaw InVia microscope (488 and 785 nm laser wavelengths) and a HPDO diamond anvil cell.

Temperature-dependent steady-state NIR luminescence experiments down to 5 K were conducted on a Horiba Jobin Yvon Fluorolog 3-22 τ spectrometer equipped with a 450 W xenon lamp and a DSS - IGA020L NIR detector (850 nm $< \lambda_{\text{em}} < 1550 \text{ nm}$). Spectral selection was realized with double and single grating monochromators in the excitation and emission paths, respectively (excitation: 1200 grooves per mm; near-IR emission 600 grooves per mm). A combination of two long-pass filters (FELH0500 Thorlabs, transmission $\geq 92\%$ above 500 nm and FELH0850 Thorlabs, transmission $\geq 98\%$ above 1000 nm) was used in the emission channel to avoid higher order excitation light. For the preparation of KBr pellets,

the compounds (*ca.* 1.0 mg for $VCl_3(\text{ddpd}-[D_0])$ and 0.5 mg for $VCl_3(\text{ddpd}-[D_{17}])$) were mixed with dry KBr (*ca.* 200 mg, stored in a compartment dryer at 80 °C, purchased from Merck) and ground to a homogenous mixture. This mixture was filled into an evacuable pellet die with a diameter of 13 mm and sintered at a pressure of 0.75 GPa. Measurements on neat powders were conducted by homogenous spreading of the neat sample between two CaF_2 windows (13 mm diameter, 1 mm thick). Experiments at temperatures between 5 K and 290 K were performed using a closed-cycle helium cryostat (ColdEdge, 101J cryocooler). The cryocooler was equipped with a pellet holder (copper) and CaF_2 windows.

Steady-state NIR luminescence experiments on neat samples down to 77 K were conducted on a Horiba Fluorolog-3 spectrofluorimeter equipped with a 450 W xenon lamp for steady-state measurements. Emitted light was detected either by a Hamamatsu R2658P PMT detector (200 nm $< \lambda_{\text{em}} < 1010 \text{ nm}$) or by a Hamamatsu H10330-75 PMT detector (950 nm $< \lambda_{\text{em}} < 1700 \text{ nm}$). Spectral selection in the excitation path was accomplished by a DFX monochromator (double gratings: 1200 grooves per mm, 330 nm blaze) and in the emission paths in the visible/NIR spectral region ($\lambda_{\text{em}} < 1010 \text{ nm}$) by a spectrograph iHR550 (single gratings: either 1200 grooves per mm, 500 nm blaze or 950 grooves per mm, 900 nm blaze) and in the NIR spectral region ($\lambda_{\text{em}} > 950 \text{ nm}$) by a spectrograph iHR320 (single grating: 600 grooves per mm, 1000 nm blaze).

Near-IR luminescence lifetimes of the phosphorescent transitions were determined at 298 K (solid samples in standard NMR tubes under argon) with a PTI Quantmaster QM4 spectrofluorimeter equipped with a 75 W continuous xenon short arc lamp as excitation source (Hamamatsu L4633: pulse width *ca.* 1.5 μs FWHM). Emission was monitored using a PTI P1.7R detector module (Hamamatsu PMT R5509-72 with a Hamamatsu C9525 power supply operated at 1500 V and a Hamamatsu liquid N_2 cooling unit C9940 set to $-80 \text{ }^\circ\text{C}$). For the measurements above 1000 nm, a long-pass filter RG-850 (Schott, 3.0 mm thickness, transmission $>98\%$ above 970 nm) was used in the emission channel in order to avoid higher order excitation light. Spectral selection was achieved by single grating monochromators (excitation: 1200 grooves per mm, 300 nm blaze; Vis emission: 1200 grooves per mm, 500 nm blaze; near-IR emission: 600 grooves per mm, 1200 nm blaze) and an additional UG11 bandpass filter (Schott, 3.0 mm thickness) in the excitation channel. Lifetime data analysis (deconvolution, statistical parameters, *etc.*) was performed using the software package FeliX32 from PTI. Lifetimes were determined by deconvolution of the decay profiles with the instrument response function, which was determined using an empty NMR tube as scatterer. Estimated uncertainties for the lifetimes of the near-IR emission determined with this setup are 20%.

Time-resolved FTIR experiments were performed with the FTIR spectrometer Bruker Vertex 80v, operated in the step-scan mode. A liquid-nitrogen-cooled mercury cadmium telluride (MCT) detector (Kolmar Tech., Model KV100-1-B-7/190) with a rise time of 25 ns, connected to a fast preamplifier and a 14 bit transient recorder board (Spectrum Germany, M314142, 400 MS



s^{-1}), was used for signal detection and processing. The laser setup used for the measurements includes a Q-switched Nd:YAG laser (Innolas SpitLight Evo I) generating pulses with a pulse duration of about 6 ns at a repetition rate of 100 Hz. The third harmonic (355 nm) of the Nd:YAG laser was used directly for sample excitation. The UV pump beam was attenuated to about 1.8 mJ per shot at a diameter of 9 mm. The beam was directed onto the sample and adjusted to have a maximal overlap with the IR beam of the spectrometer. The sample chamber was equipped with anti-reflection-coated germanium filters to prevent the entrance of laser radiation into the detector and interferometer compartments. The KBr pellets were prepared as described in the section on luminescence spectroscopy, however, with a smaller amount of sample of *ca.* 0.2 mg and *ca.* 200 mg KBr. The strongest peak in the ground state spectrum showed an absorption of about 0.4 OD with the mentioned concentration. *T*-dependent measurements were performed using a closed-cycle helium cryostat (ARS Model DE-202A) reaching a temperature of about 20 K at the sample. The cryocooler was equipped with a pellet holder and CaF₂ windows. The temporal resolution of the 14 bit transient recorder board was chosen to 5 ns for VCl₃(ddpd-[D₀]) and 10 ns for VCl₃(ddpd-[D₁₇]). The time where the laser pulse reached the sample was set as zero point in all spectra. The time delay between the start of the experiment and the laser pulse was controlled with a Stanford Research Systems DG535 delay generator. The spectral region was limited by undersampling to 1975 to 0 cm⁻¹ for VCl₃(ddpd-[D₀]) and 988–1975 cm⁻¹ for VCl₃(ddpd-[D₁₇]) with a spectral resolution of 4 cm⁻¹ resulting in 1110 and 555 interferogram points, respectively. An IR broadband filter (850–1750 cm⁻¹) and CaF₂ windows (no IR transmission <1000 cm⁻¹) prevented problems when performing a Fourier transformation (*i.e.* no IR intensity outside the measured region should be observed). FTIR ground state spectra were recorded systematically to check if there is no sample degradation. Estimated uncertainties for the excited state lifetimes are on the order of 10%.

Transient absorption spectra of VCl₃(ddpd-[D₀]) were recorded applying a pump-probe setup with an excitation wavelength of 400 nm. The setup is pumped by a Ti:sapphire laser system (Spectra-Physics, Spitfire Pro) which provides ultrashort laser pulses centred at 800 nm with a repetition rate of 1 kHz. By frequency doubling its output with a BBO-crystal pump pulses with a centre wavelength of 400 nm and a pulse duration of 200 fs were obtained. For probing, a white light continuum generated with a CaF₂ crystal was used. Both beams, with polarizations arranged in magic angle, were focused onto the sample leading to pump and probe spots with diameters of 170 μm and 80 μm, respectively. Transient absorption spectra were recorded by dispersing the probe beam after the sample with a prism and detecting its spectral intensity distribution with a CCD array. The metal complex was dissolved in acetonitrile under argon atmosphere and the obtained sample was filled into a 1 mm fused silica cuvette. The concentration was 1.5×10^{-3} M resulting in an optical density of 0.18 at 400 nm. Significantly higher concentrations

were not accessible because of the moderate solubility of the compound in acetonitrile.

Quantum chemical calculations. The characterization of the absorption spectrum was done employing two types of quantum chemical calculations: (i) density functional theory in its unrestricted form and (ii) multiconfigurational theory with an active space tailored to predict the MC states. The first method is labelled as “Unrestricted Kohn–Sham” orbitals DFT (UKS), the second as “SOC-CASSCF(6,12)-FIC-NEVPT2”. These two methods are complementary to each other, as the first gives energies of the CT states, while the second one provides the energies of the MC states and the ground state splitting.⁷⁸

Unrestricted Kohn–Sham orbitals DFT (UKS): All calculations were performed using the quantum computing suite ORCA 4.0.1.12.⁷⁹ Geometry optimization (Tables S1 and S2†) was performed using unrestricted Kohn–Sham orbitals DFT (UKS) and the B3LYP functional^{80–82} in combination with Ahlrichs’ split-valence triple- ζ basis set def2-TZVPP for all atoms.^{83,84} Tight convergence criteria were chosen for DFT-UKS calculations (keywords tightscf and tightopt). All DFT-UKS calculations make use of the resolution of identity RIJ (Split-RI-J) approach for the Coulomb term in combination with the chain-of-spheres approximation for the exchange term (COSX).^{85,86} The zero order relativistic approximation was used to describe relativistic effects in all calculations (keyword ZORA).⁸⁷ Grimme’s empirical dispersion correction D3(BJ) was employed (keyword D3BJ).^{88,89} To account for solvent effects, a conductor-like screening model (keyword CPCM) modelling acetonitrile was used in all calculations.^{90,91} TDDFT-UKS calculations were performed at the same level of theory using unrestricted Kohn–Sham orbitals (UKS). Fifty vertical spin-allowed transitions were calculated (Tables S3 and S4†).

Harmonic frequency calculations for the IR assignments were performed using Turbomole 7.4 (ref. 92 and 93) on the optimized geometry (RIJCOSX-UB3LYP-D3BJ/def2-TZVP). The vibrational frequencies were scaled by a factor of 0.98, which is typical for the chosen method and basis set, to minimize the differences between the experimental and calculated frequencies. A Gaussian convolution with a full-width at half-maximum of 15 cm⁻¹ was applied to the calculated vibrational transitions.

SOC-CASSCF(6,12)-FIC-NEVPT2: calculations of ground- and excited-state properties with respect to metal-centered (MC) states were performed using the complete-active-space self-consistent field method in conjunction with the fully internally contracted N-electron valence perturbation theory to second order based on a fully internally contracted (FIC) wave function (FIC-NEVPT2)^{94,95} in order to recover missing dynamic electron correlation. In order to accurately model the ligand field, active spaces were chosen to encompass the dominating bonding/antibonding orbitals formed between vanadium and the ligand. An active space of (6,12) along with 10 triplet roots and 9 singlet roots was selected (Tables S5 and S6†). In addition to the minimal active space of (2,5) comprising the 3d orbitals, two occupied V–N σ bonding orbitals and a second d shell⁹⁶ were included in these calculations.



Conclusions

The pseudo-octahedral vanadium(III) complex $\text{VCl}_3(\text{ddpd})$ with the strong-field ligand ddpd shows spin-flip phosphorescence at room temperature at 1102, 1219 and 1256 nm after excitation into charge-transfer bands. Several factors are relevant for this emission from a 3d transition metal complex to occur:

(i) The ligand field splitting in $\text{VCl}_3(\text{ddpd})$ is large enough to place the emissive singlet states $^1\text{E}^1\text{T}_2$ below the distorted metal-centred triplet excited states $^3\text{T}_2$.

(ii) Lower temperature disables thermally activated non-radiative pathways increasing the photoluminescence, yet even at room temperature a weak emission is still observed.

(iii) Deuteration of the ddpd ligand reduces non-radiative energy transfer to C–H overtones increasing the photoluminescence.

(iv) The radiative rate might be higher in non-centrosymmetric pseudo-octahedral vanadium complexes, although this effect of Laporte's parity rule was not experimentally confirmed in this particular case.

(v) The ISC rate constant from the triplet to the singlet manifold is high ($k_{\text{ISC}} > 6.7 \times 10^{11} \text{ s}^{-1}$) as confirmed by the molecular dynamics simulations in the accompanying paper.⁶³ This high rate could be an effect of the heavier chloride atoms (heavy atom effect), efficient vibronic coupling and/or enhanced SOC due to large differences in orbital type between the two states ($^3\text{LMCT} \rightarrow ^1\text{MC}$),⁹⁷ although other ultrafast pathways might still compete with ISC.

Challenges with the emission from excited states of $\text{d}^2\text{-VCl}_3(\text{ddpd})$ arise from the large ground state splitting which spreads the emission bands over *ca.* 2400 cm^{-1} . This range is larger by almost two orders of magnitude than the corresponding spin-flip emission of $\text{d}^3\text{-metal}$ complexes with orbitally non-degenerate ground states, a very significant difference for transitions involving essentially nested states. The considerable ground state splitting further reduces the already small energy gap between the emissive state and the ground state enabling a higher non-radiative decay according to the energy gap law. A second aspect of $\text{VCl}_3(\text{ddpd})$ as phosphorescent emitter concerns the excited state reactivity of LMCT states with chloride \rightarrow vanadium charge-transfer character in solution. As these states can lead to V–Cl homolysis in solution reducing the photoluminescence and finally decomposing the complex, solution photostability is a particularly important aspect for future applications of vanadium(III) complexes in solution.

This study emphasises that design strategies toward efficient $\text{d}^2\text{-NIR}$ emitters require a particular attention to the ISC efficiency from the triplets to the singlet states and potential dissociative unimolecular reactions at ultrafast timescales as well as on the radiative and non-radiative relaxation of the singlets at longer times. Details of the ultrafast excited state dynamics of $\text{VCl}_3(\text{ddpd})$ up to 10 ps are discussed in the accompanying paper.⁶³

Data availability

Experimental and computational data are available as ESI.

Author contributions

MD prepared the complex, performed all ground state characterization and photolysis experiments and the quantum chemical calculations, JK and MS measured and analysed the luminescence and lifetime data of the neat complex, measured and analysed the NIR absorption data and performed the SOI calculations, CD and CR measured and analysed the Raman spectra and the spectra under pressure, PB, GNS and MG measured and analysed the step-scan FT-IR spectra and the temperature dependent luminescence spectra of the complex in KBr pellets, AK and SL measured and analysed the transient absorption spectra, MS and KH devised the concept. KH supervised the project and wrote the manuscript.

Conflicts of interest

There are no conflicts to declare.

Acknowledgements

Financial support from the Deutsche Forschungsgemeinschaft [DFG, Priority Program SPP 2102 "Light-controlled reactivity of metal complexes" GE 961/10-1, HE 2778/15-1, LO 714/11-1, SE 1448/8-1] is gratefully acknowledged. Parts of this research were conducted using the supercomputer Mogon and advisory services offered by Johannes Gutenberg University Mainz (<http://www.hpc.uni-mainz.de>), which is a member of the AHRP and the Gauss Alliance e.V. and the supercomputer Elwetritsch and advisory services offered by the TU Kaiserslautern (<https://elwe.rhrk.uni-kl.de>) which is a member of the AHRP. CR and CD thank the Natural Sciences and Engineering Research Council (Canada) for research grants and the Fonds du recherche du Québec – Nature et technologies for a postdoctoral fellowship (CD).

Notes and references

- R. D. Costa, E. Ort, H. J. Bolink, F. Monti, G. Accorsi and N. Armaroli, *Angew. Chem., Int. Ed.*, 2012, **51**, 8178.
- K. K.-W. Lo, *Acc. Chem. Res.*, 2015, **48**, 2985.
- M. Schäferling, *Angew. Chem., Int. Ed.*, 2012, **51**, 3532.
- F. Heinemann, J. Karges and G. Gasser, *Acc. Chem. Res.*, 2017, **50**, 2727.
- A. Hagfeldt, G. Boschloo, L. C. Sun, L. Kloo and H. Pettersson, *Chem. Rev.*, 2010, **110**, 6595.
- C. K. Prier, D. A. Rankic and D. W. C. MacMillan, *Chem. Rev.*, 2013, **113**, 5322.
- J. M. R. Narayanam and C. R. J. Stephenson, *Chem. Soc. Rev.*, 2011, **40**, 102.
- T. P. Yoon, M. A. Ischay and J. Du, *Nat. Chem.*, 2010, **2**, 527.
- V. Balzani, G. Bergamini, S. Campagna and F. Puntoriero, *Photochemistry and Photophysics of Coordination Compounds: Overview and General Concepts. in Photochemistry and Photophysics of Coordination Compounds I, Topics in Current Chemistry*, ed. V. Balzani and S. Campagna, Springer, Berlin, 2007, pp. 1–36.



- 10 J. K. McCusker, *Science*, 2019, **363**, 484.
- 11 S. Koseki, N. Matsunaga, T. Asada, M. W. Schmidt and M. S. Gordon, *J. Phys. Chem. A*, 2019, **123**, 2325.
- 12 V. W. Yam, A. K. Chan and E. Y. Hong, *Nat. Rev. Chem.*, 2020, **4**, 528.
- 13 O. S. Wenger, *J. Am. Chem. Soc.*, 2018, **140**, 13522.
- 14 C. Förster and K. Heinze, *Chem. Soc. Rev.*, 2020, **49**, 1057.
- 15 S. Otto, M. Dorn, C. Förster, M. Bauer, M. Seitz and K. Heinze, *Coord. Chem. Rev.*, 2018, **359**, 102.
- 16 O. S. Wenger, *Chem.-Eur. J.*, 2019, **25**, 6043.
- 17 C. Bizzarri, E. Spuling, D. M. Knoll, D. Volz and S. Bräse, *Coord. Chem. Rev.*, 2018, **373**, 49.
- 18 P. Chábera, L. Lindh, N. W. Rosemann, O. Prakash, J. Uhlig, A. Yartsev, K. Wärnmark, V. Sundström and P. Persson, *Coord. Chem. Rev.*, 2020, **426**, 213517.
- 19 P. Herr, F. Glaser, L. A. Büldt, C. B. Larsen and O. S. Wenger, *J. Am. Chem. Soc.*, 2019, **141**, 14394.
- 20 L. A. Büldt, X. Guo, A. Prescimone and O. S. Wenger, *Angew. Chem., Int. Ed.*, 2016, **55**, 11247.
- 21 Y. Zhang, T. S. Lee, J. M. Favale, D. C. Leary, J. L. Petersen, G. D. Scholes, F. N. Castellano and C. Milsmann, *Nat. Chem.*, 2020, **12**, 345.
- 22 Y. Zhang, T. S. Lee, J. L. Petersen and C. Milsmann, *J. Am. Chem. Soc.*, 2018, **140**, 5934.
- 23 R. Hamze, J. L. Peltier, D. Sylvinson, M. Jung, J. Cardenas, R. Haiges, M. Soleilhavoup, R. Jazzar, P. I. Djurovich, G. Bertrand and M. E. Thompson, *Science*, 2019, **36**, 601.
- 24 M. Gernert, L. Balles-Wolf, F. Kerner, U. Mueller, A. Schmiedel, M. Holzapfel, C. M. Marian, J. Pflaum, C. Lambert and A. Steffen, *J. Am. Chem. Soc.*, 2020, **142**, 8897.
- 25 L. A. Büldt, C. B. Larsen and O. S. Wenger, *Chem.-Eur. J.*, 2017, **23**, 8577.
- 26 Y.-S. Wong, M.-C. Tang, M. Ng and V. W.-W. Yam, *J. Am. Chem. Soc.*, 2020, **142**, 7638.
- 27 A. K. Pal, C. Li, G. S. Hanan and E. Zysman-Colman, *Angew. Chem., Int. Ed.*, 2018, **57**, 8027.
- 28 P. Chábera, Y. Liu, O. Prakash, E. Thyraug, A. El Nahhas, A. Honarfar, S. Essén, L. A. Fredin, T. C. B. Harlang, K. S. Kjær, K. Handrup, F. Ericson, H. Tatsuno, K. Morgan, J. Schnadt, L. Häggström, T. Ericsson, A. Sobkowiak, S. Lidin, P. Huang, S. Styring, J. Uhlig, J. Bendix, R. Lomoth, V. Sundström, P. Persson and K. Wärnmark, *Nature*, 2017, **543**, 695.
- 29 K. S. Kjær, N. Kaul, O. Prakash, P. Chábera, N. W. Rosemann, A. Honarfar, O. Gordivska, L. A. Fredin, K.-E. Bergquist, L. Häggström, T. Ericsson, L. Lindh, A. Yartsev, S. Styring, P. Huang, J. Uhlig, J. Bendix, D. Strand, V. Sundström, P. Persson, R. Lomoth and K. Wärnmark, *Science*, 2019, **363**, 249.
- 30 T. Jiang, Y. Bai, P. Zhang, Q. Han, D. B. Mitzi and M. J. Therien, *Proc. Natl. Acad. Sci. U. S. A.*, 2020, **117**, 20430.
- 31 J. Steube, A. Pöpcke, O. S. Bokareva, T. Reuter, S. Demeshko, R. Schoch, S. Hohloch, F. Meyer, K. Heinze, O. Kühn, S. Lochbrunner, M. Bauer, submitted (preprint at DOI: 10.21203/rs.3.rs-64316/v1).
- 32 L. A. Büldt, X. Guo, R. Vogel, A. Prescimone and O. S. Wenger, *J. Am. Chem. Soc.*, 2017, **139**, 985.
- 33 S. Otto, M. Grabolle, C. Förster, C. Kreitner, U. Resch-Genger and K. Heinze, *Angew. Chem., Int. Ed.*, 2015, **54**, 11572.
- 34 C. Wang, S. Otto, M. Dorn, E. Kreidt, J. Lebon, L. Sršan, P. Di Martino-Fumo, M. Gerhards, U. Resch-Genger, M. Seitz and K. Heinze, *Angew. Chem., Int. Ed.*, 2018, **57**, 1112.
- 35 S. Treiling, C. Wang, C. Förster, F. Reichenauer, J. Kalmbach, P. Boden, J. P. Harris, L. Carrella, E. Rentschler, U. Resch-Genger, C. Reber, M. Seitz, M. Gerhards and K. Heinze, *Angew. Chem., Int. Ed.*, 2019, **58**, 18075.
- 36 M. Dorn, J. Kalmbach, P. Boden, A. Pöpcke, S. Gómez, C. Förster, F. Kuczelinis, L. M. Carrella, L. Büldt, N. Bings, E. Rentschler, S. Lochbrunner, L. González, M. Gerhards, M. Seitz and K. Heinze, *J. Am. Chem. Soc.*, 2020, **142**, 7947.
- 37 S. Otto, A. M. Nauth, E. Ermilov, N. Scholz, A. Friedrich, U. Resch-Genger, S. Lochbrunner, T. Opatz and K. Heinze, *ChemPhotoChem*, 2017, **1**, 344.
- 38 S. Otto, N. Scholz, T. Behnke, U. Resch-Genger and K. Heinze, *Chem.-Eur. J.*, 2017, **23**, 12131.
- 39 S. Otto, J. Harris, K. Heinze and C. Reber, *Angew. Chem. Int. Ed.*, 2018, **57**, 11069.
- 40 C. Wang, S. Otto, M. Dorn, K. Heinze and U. Resch-Genger, *Anal. Chem.*, 2019, **91**, 2337.
- 41 U. Basu, S. Otto, K. Heinze and G. Gasser, *Eur. J. Inorg. Chem.*, 2019, **37**.
- 42 J. Kalmbach, C. Wang, Y. You, C. Förster, H. Schubert, K. Heinze, U. Resch-Genger and M. Seitz, *Angew. Chem. Int. Ed.*, 2020, **59**, 1884.
- 43 J.-R. Jiménez, B. Doistau, C. M. Cruz, C. Besnard, J. M. Cuerva, A. G. Campaña and C. Piguet, *J. Am. Chem. Soc.*, 2019, **141**, 13244.
- 44 C. Dee, F. Zinna, W. R. Kitzmann, G. Pescitelli, K. Heinze, L. Di Bari and M. Seitz, *Chem. Commun.*, 2019, **55**, 13078.
- 45 J.-R. Jiménez, M. Poncet, S. Míguez-Lago, S. Grass, J. Lacour, C. Besnard, J. M. Cuerva, A. G. Campaña and C. Piguet, *Angew. Chem., Int. Ed.*, 2021, **60**, 10095.
- 46 H. Xiang, J. Cheng, X. Ma and X. Zhou, *Chem. Soc. Rev.*, 2013, **42**, 6128.
- 47 R. D. Dill, R. I. Portillo, S. G. Shepard, M. P. Shores, A. K. Rappé and N. H. Damrauer, *Inorg. Chem.*, 2020, **59**, 14706.
- 48 A. C. Bowman, S. Sproules and K. Wieghardt, *Inorg. Chem.*, 2012, **51**, 3707.
- 49 A. W. Maverick, S. S. Shah, C. Kirmaier and D. Holten, *Inorg. Chem.*, 1987, **26**, 774.
- 50 Y. Tanabe and S. Sugano, *J. Phys. Soc. Jpn.*, 1954, **9**, 766.
- 51 P. L. W. Tregenna-Piggott, D. Spichiger, G. Carver and B. Frey, *Inorg. Chem.*, 2004, **43**, 8049.
- 52 R. Beaulac, P. L. W. Tregenna-Piggott, A.-L. Barra, H. Weihe, D. Luneau and C. Reber, *Inorg. Chem.*, 2006, **45**, 3399.
- 53 K. R. Kittilstved and A. Hauser, *Coord. Chem. Rev.*, 2010, **254**, 2663.
- 54 D. R. Gamelin and H. U. Güdel, *Acc. Chem. Res.*, 2000, **33**, 235.
- 55 L. Aboshyan-Sorgho, C. Besnard, P. Pattison, K. R. Kittilstved, A. Aebischer, J.-C. G. Bünzli, A. Hauser and C. Piguet, *Angew. Chem., Int. Ed.*, 2011, **50**, 4108.



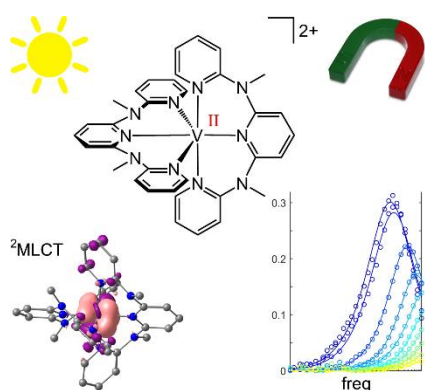
- 56 M. S. Fataftah, S. L. Bayliss, D. W. Laurenza, X. Wang, B. T. Phelan, C. B. Wilson, P. J. Mintun, B. D. Kovos, M. R. Wasielewski, S. Han, M. S. Sherwin, D. D. Awschalom and D. E. Freedman, *J. Am. Chem. Soc.*, 2020, **142**, 20400–20408.
- 57 E. Kreidt, C. Kruck and M. Seitz, *Handbook on the Physics and Chemistry of Rare Earths*, Elsevier, Amsterdam, 2018, vol. 53, pp. 35–79.
- 58 C. Förster, M. Dorn, T. Reuter, S. Otto, G. Davarci, T. Reich, L. Carrella, E. Rentschler and K. Heinze, *Inorganics*, 2018, **6**, 86.
- 59 G. Bussière, R. Beaulac, B. Cardinal-David and C. Reber, *Coord. Chem. Rev.*, 2001, **219**, 509.
- 60 J. Bendix, M. Brorson and C. E. Schaffer, *Inorg. Chem.*, 1993, **32**, 2838.
- 61 M. Blume and R. E. Watson, *Proc. R. Soc. London, Ser. A*, 1963, **271**, 565.
- 62 O. Laporte and W. F. Meggers, *J. Opt. Soc. Am.*, 1925, **11**, 459.
- 63 J. P. Zobel, T. Knoll and L. González, *Chem. Sci.*, 2021, DOI: 10.1039/D1SC02149D.
- 64 L. E. Manzer, J. Deaton, P. Sharp and R. R. Schrock, *Inorg. Synth.*, 1982, **21**, 135.
- 65 A. Breivogel, C. Förster and K. Heinze, *Inorg. Chem.*, 2010, **49**, 7052.
- 66 F. Plasser, *J. Chem. Phys.*, 2020, **152**, 084108.
- 67 S. Mai, F. Plasser, J. Dorn, M. Fumanal, C. Daniel and L. González, *Coord. Chem. Rev.*, 2018, **361**, 74.
- 68 C. Van Stappen, D. Maganas, S. DeBeer, E. Bill and F. Neese, *Inorg. Chem.*, 2018, **57**, 6421.
- 69 J. K. Kochi, *J. Am. Chem. Soc.*, 1962, **84**, 2121.
- 70 A. Hossain, S. Engl, E. Lutsker and O. Reiser, *ACS Catal.*, 2019, **9**, 1103.
- 71 R. Fayad, S. Engl, E. O. Danilov, C. E. Hauke, O. Reiser and F. N. Castellano, *J. Phys. Chem. Lett.*, 2020, **11**, 5345.
- 72 S. J. Hwang, D. C. Powers, A. G. Maher, B. L. Anderson, R. G. Hadt, S.-L. Zheng, Y.-S. Chen and D. G. Nocera, *J. Am. Chem. Soc.*, 2015, **137**, 6472.
- 73 S. J. Hwang, B. L. Anderson, D. C. Powers, A. G. Maher, R. G. Hadt and D. G. Nocera, *Organometallics*, 2015, **34**, 4766.
- 74 O. S. Wenger, *Chem.–Eur. J.*, 2021, **27**, 2270.
- 75 S. K. Kariofillis and A. G. Doyle, *Acc. Chem. Res.*, 2021, **54**, 988.
- 76 Y. Doi and M. Tsutsui, *J. Am. Chem. Soc.*, 1978, **100**, 3243.
- 77 J. J. H. Edema, W. Stauthamer, F. Van Bolhuis, S. Gambarotta, W. J. J. Smeets and A. L. Spek, *Inorg. Chem.*, 1990, **29**, 1302.
- 78 D. Reinen, M. Atanasov, P. Köhler and D. Babel, *Coord. Chem. Rev.*, 2010, **254**, 2703.
- 79 F. Neese, *Wiley Interdiscip. Rev.: Comput. Mol. Sci.*, 2018, **8**, e1327.
- 80 A. D. Becke, *J. Chem. Phys.*, 1993, **98**, 5648.
- 81 C. Lee, W. Yang and R. G. Parr, *Phys. Rev. B: Condens. Matter Mater. Phys.*, 1988, **37**, 785.
- 82 B. Miehlich, A. Savin, H. Stoll and H. Preuss, *Chem. Phys. Lett.*, 1989, **157**, 200.
- 83 F. Weigend and R. Ahlrichs, *Phys. Chem. Chem. Phys.*, 2005, **7**, 3297.
- 84 F. Weigend, *Phys. Chem. Chem. Phys.*, 2006, **8**, 1057.
- 85 F. Neese, F. Wennmohs, A. Hansen and U. Becker, *Chem. Phys.*, 2009, **356**, 98.
- 86 R. Izsák and F. Neese, *J. Chem. Phys.*, 2011, **135**, 144105–1–144105–11.
- 87 D. A. Pantazis, X.-Y. Chen, C. R. Landis and F. Neese, *J. Chem. Theory Comput.*, 2008, **4**, 908.
- 88 S. Grimme, S. Ehrlich and L. Goerigk, *J. Comput. Chem.*, 2011, **32**, 1456.
- 89 S. Grimme, J. Antony, S. Ehrlich and H. Krieg, *J. Chem. Phys.*, 2010, **132**, 154104.
- 90 S. Miértus, E. Scrocco and J. Tomasi, *Chem. Phys.*, 1981, **55**, 117.
- 91 V. Barone and M. Cossi, *J. Phys. Chem. A*, 1998, **102**, 1995.
- 92 F. Furche, R. Ahlrichs, C. Hättig, W. Klopper, M. Sierka and F. Weigend, *Wiley Interdiscip. Rev.: Comput. Mol. Sci.*, 2014, **4**, 91.
- 93 TURBOMOLE V7.4 2019, a development of University of Karlsruhe and Forschungszentrum Karlsruhe GmbH, 1989–2007, TURBOMOLE GmbH, since 2007; available from <http://www.turbomole.com>.
- 94 C. Angeli, R. Cimiraglia, S. Evangelisti, T. Leininger and J.-P. Malrieu, *J. Chem. Phys.*, 2001, **114**, 10252.
- 95 C. Angeli and R. Cimiraglia, *Theor. Chem. Acc.*, 2002, **107**, 313.
- 96 K. Pierloot, *Int. J. Quantum Chem.*, 2011, **111**, 3291.
- 97 T. Penfold, E. Gindensperger, C. Daniel and C. M. Marian, *Chem. Rev.*, 2018, **118**, 6975.



3.3. Towards Luminescent Vanadium Complexes with Slow Magnetic Relaxation and Quantum Coherence

Matthias Dorn, David Hunger, Christoph Förster, Robert Naumann, Joris van Slageren and Katja Heinze

Chem. Eur. J. **2022**, e202202898 (accepted)



In contrast to polypyridine vanadium(III) complexes, two isomers of the title complex [V(ddpd)₂]²⁺ (ddpd = *N,N'*-dimethyl-*N,N'*-dipyridine-2-yl-pyridine-2,6-diamine) are found to be non-luminescent due to metal-to-ligand admixture to potentially emissive spin-flip states. Both complexes exhibit a small zero-field splitting of ca. 0.2 cm⁻¹ in EPR experiments. AC susceptometry reveals an out-of-phase signal below 15 K at an external field of 4000 Oe. Shorter V^{II}-V^{II} distances in the *cis-fac* isomer lead to faster magnetic relaxation.

Author Contributions

Matthias Dorn prepared and characterized the title compound via absorption spectroscopy, IR spectroscopy and cyclic voltammetry and performed quantum chemical calculations. Matthias Dorn and Robert Naumann performed emission spectroscopy measurements. David Hunger (group of Prof. Dr. J. v. Slageren) performed EPR measurements, magnetic measurements and related quantum-chemical calculations. Dr. Christoph Förster solved the crystal structure of the title compound. The manuscript was written by Prof. Dr. Katja Heinze (45%), Prof. Dr. Joris van Slageren (45%) and Matthias Dorn (10%).

Supporting information

can be found at pp. 155.

The full supporting information can be obtained [here](#).

“Reprinted with the permission of Dorn, M.; Hunger, D.; Förster, C.; Naumann, R.; van Slageren, J.; Heinze, K.; Chem. Eur. J. 2022, e202202898. Copyright © 2015 WILEY-VCH Verlag GmbH & Co. KGaA, Weinheim”

Towards Luminescent Vanadium(II) Complexes with Slow Magnetic Relaxation and Quantum Coherence

Matthias Dorn,^{[a]‡} David Hunger,^{[b]‡} Christoph Förster,^[a] Robert Naumann,^[a] Joris van Slageren,^{*[b]} and Katja Heinze^{*[a]}

[a] M. Dorn, Dr. C. Förster, Dr. R. Naumann, Prof. Dr. K. Heinze
Department of Chemistry, Johannes Gutenberg University, Duesbergweg 10-14, 55128 Mainz, Germany
E-mail: katja.heinze@uni-mainz.de. www.ak-heinze.chemie.uni-mainz.de

[b] D. Hunger, Prof. Dr. J. van Slageren
Institute of Physical Chemistry and Center for Integrated Quantum Science and Technology, University of Stuttgart, Pfaffenwaldring 55,
70569 Stuttgart, Germany. E-mail: slageren@ipc.uni-stuttgart.de. www.ipc.uni-stuttgart.de/slageren

‡These authors contributed equally.

Supporting information for this article is given via a link at the end of the document.

Abstract: Molecular entities with doublet or triplet ground states find increasing interest as potential molecular quantum bits (qubits). Complexes with higher multiplicity might even function as qudits and serve to encode further quantum bits. Vanadium(II) ions in octahedral ligand fields with quartet ground states and small zero-field splittings qualify as qubits with optical read out thanks to potentially luminescent spin-flip states. We identified two V^{2+} complexes $[V(\text{ddpd})_2]^{2+}$ with the strong field ligand N,N -dimethyl- N,N -dipyridine-2-yl-pyridine-2,6-diamine (ddpd) in two isomeric forms (*cis-fac* and *mer*) as suitable candidates. The energy gaps between the two lowest Kramers doublets amount to 0.2 and 0.5 cm^{-1} allowing pulsed EPR experiments at conventional Q-band frequencies (35 GHz). Both isomers possess spin-lattice relaxation times T_1 of around 300 μs and a phase memory time T_M of around 1 μs at 5 K. Furthermore, the *mer* isomer displays slow magnetic relaxation in an applied field of 400 mT. While the vanadium(III) complexes $[V(\text{ddpd})_2]^{3+}$ are emissive in the near-IR-II region, the $[V(\text{ddpd})_2]^{2+}$ complexes are non-luminescent due metal-to-ligand charge transfer admixture to the spin-flip states.

Introduction

Molecular quantum bits (qubits) based on $S = 1/2$ systems such as copper(II)^[1] or vanadium(IV)^[2-4] possess long coherence times, while qubits based on non-spin- $1/2$ ions, e.g. europium(III), vanadium(III) in trigonal bipyramidal ligand fields, chromium(IV) in tetrahedral ligand fields or nickel(II) in pseudo octahedral ligand fields,^[5] are rare. The advantage of high-spin ions over two-level ($S = 1/2$) ions is that the several qubits can be encoded into one complex, or the enlarged Hilbert space provided by the additional levels of such so-called qudits can be used, e.g., for quantum error correction.^[6] A second advantage of high-spin complexes, is that their spin quantum state may be addressed optically, through optically detected magnetic resonance techniques, as widely employed for $S = 1$ nitrogen-vacancy defects in diamond.^[7] In fact, optical readout of molecular qubits has been recently achieved.^[8] A thoroughly studied ion with $S = 3/2$ is chromium(III). Chromium(III) complexes (quartet ground state, $S = 3/2$) with suitable ligand fields have been developed into highly versatile materials for photonic and photocatalytic applications, including sensing,^[9-11] upconversion,^[12,13] circularly polarized luminescence^[14,15] and photo(redox) catalysis.^[16-19] The magnetic ground state $S = 3/2$ of the highly luminescent molecular ruby $[\text{Cr}(\text{ddpd})_2]^{3+}$ with the spin-flip^[20] emission band peaking at 778 nm^[21] shows a long coherence time of 8.4(1) μs (ddpd = N,N -dimethyl- N,N -dipyridine-2-yl-pyridine-2,6-diamine).^[22] Yet, optical read-out^[8,23] or manipulation was unsuccessful, warranting the further search for optically addressable molecular qubits.^[22]

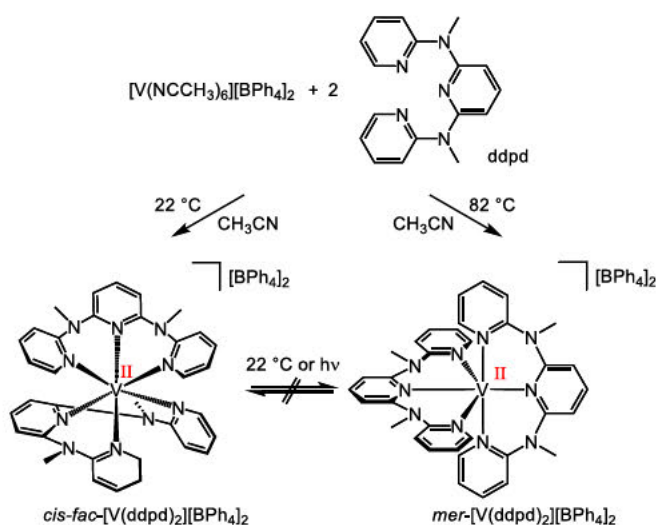
Isoelectronic vanadium(II) ions in an octahedral environment such as $\text{MgO}:V^{2+}$ display their spin-flip emission band (${}^2E_g \rightarrow {}^4A_{2g}$; O_h notation) at around 869 nm.^[24,25] However, all reported molecular vanadium(II) complexes are non-luminescent.^[26-33] Damrauer, Shores and Rappé thoroughly investigated the excited states of the classical 2,2'-bipyridine and phenanthroline vanadium(II)

complexes $[V(\text{bpy})_3]^{2+}$ and $[V(\text{phen})_3]^{2+}$ [26-31] and concluded that the lowest excited states are distorted mixed ${}^2\text{MLCT}/{}^2\text{MC}$ states rather than pure metal-centered (MC) spin-flip (${}^2\text{E}_g$ derived) states, nested with the ground state (MLCT = metal-to-ligand charge transfer).^[32] Addition of electron withdrawing substituents to the N-donor ligands increases the ${}^2\text{MC} - {}^2\text{MLCT}$ mixing, so that this mixed doublet state can even become the ground state instead of the ${}^4\text{A}_2$ state.^[33] Consequently, to prevent strong mixing and to gain access to a pure spin-flip excited state as in $\text{MgO}:\text{V}^{2+}$ without ${}^2\text{MLCT}$ admixture, the electron accepting properties of the ligands should be diminished. Concomitantly, the ligands must exert a large ligand field splitting in order to place the ${}^2\text{E}_g/{}^2\text{T}_{1g}$ levels as lowest excited states below the ${}^4\text{T}_{2g}$ ligand field excited states (O_h notation). Ideally, the ligand field should be so strong that the next higher doublet levels ${}^2\text{T}_{2g}$ become degenerate with the ${}^4\text{T}_{2g}$ levels which would accelerate the intersystem crossing process to the doublet manifold.^[20,34] Such an energy scheme is accomplished in the molecular ruby $[\text{Cr}(\text{ddpd})_2]^{3+}$ with the strong field ligand ddpd.^[20] The ddpd ligand was even capable to induce detectable spin-flip luminescence in liquid solution in d^2 vanadium(III) complexes.^[35] Building on this concept, this study aims to investigate the generality of this strategy, by investigating the excited state ordering and the magnetic properties of d^3 - $[\text{V}(\text{ddpd})_2]^{2+}$ complexes isoelectronic to the molecular ruby d^3 - $[\text{Cr}(\text{ddpd})_2]^{3+}$ and featuring a strong field polypyridine ligand with electron-donating substituents, i.e. less pronounced \square accepting properties than e.g. typical 2,2'-bipyridine or 2,2':6',2''-terpyridine ligands. As the flexible ddpd ligand allows for meridional and cis-facial diastereomers,^[36-38] we will also address the influence of the stereochemistry on electronically excited states and ground state magnetic behavior of vanadium(II) complexes in this study.

Results and Discussion

The *cis-fac*- and *mer*-vanadium(II) complex isomers *cis-fac*- $[\text{V}(\text{ddpd})_2]^{2+}$ and *mer*- $[\text{V}(\text{ddpd})_2]^{2+}$ were obtained from $[\text{V}(\text{NCCH}_3)_6][\text{BPh}_4]_2$ and ddpd as the kinetic and thermodynamic products at room temperature and in boiling CH_3CN , respectively (Supporting Information). Both salts were characterized by IR spectroscopy, mass spectrometry and elemental analyses (Supporting Information, Figures S1–S4). Although these analytical data do not allow assigning the stereochemistry, we note slight differences in the IR fingerprint region that allow distinguishing the isomers (Supporting Information, Figure S2).

Once formed, they do not interconvert at room temperature, as expected for substitutionally kinetically inert complexes with d^3 electron configurations.^[39] The respective diastereomeric d^2 vanadium(III) complexes *cis-fac*- $[\text{V}(\text{ddpd})_2]^{3+}$ and *mer*- $[\text{V}(\text{ddpd})_2]^{3+}$ had been isolated before.^[35,38]



Scheme 1. Temperature-controlled synthesis of *cis-fac*- $[\text{V}(\text{ddpd})_2][\text{BPh}_4]_2$ and *mer*- $[\text{V}(\text{ddpd})_2][\text{BPh}_4]_2$.

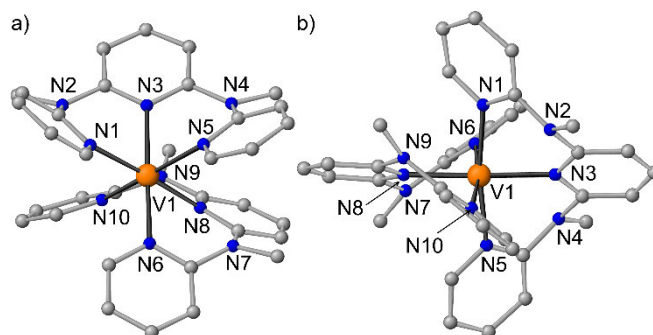


Figure 1. Molecular structures of the cations of a) *cis-fac*-[V(ddpd)₂][PF₆]₂ and b) *mer*-[V(ddpd)₂][BPh₄]₂ determined by XRD. Counter ions and hydrogen atoms are omitted for clarity.

Single crystals of *cis-fac*-[V(ddpd)₂]²⁺ and *mer*-[V(ddpd)₂]²⁺ suitable for X-ray diffraction (XRD) analyses were obtained from CH₃CN solutions of the [PF₆]⁻ and [BPh₄]⁻ salts, respectively (Figure 1, Supporting Information, Tables S1–S2). The experimentally obtained metrics of the dications agree well with those obtained from Density Functional Theory (DFT) calculations including solvent modelling, relativistic effects and dispersion correction (CPCM-(acetonitrile)-RIJCOSX-UB3LYP-D3BJ-ZORA/def2-TZVPP; Supporting Information, Tables S1–S4).

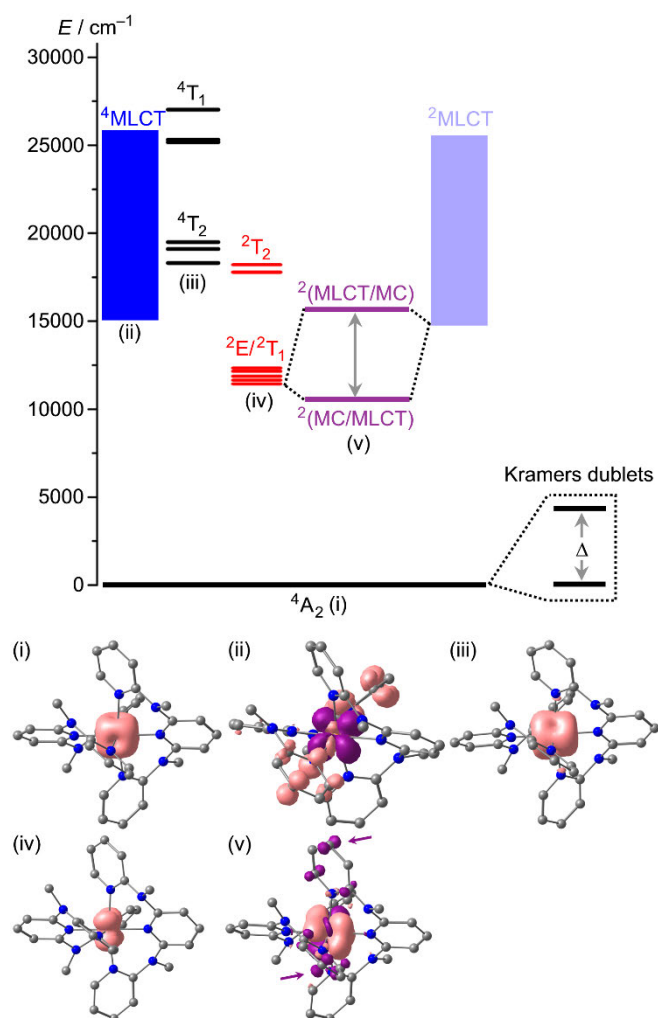


Figure 2. Proposed energy level diagram of *mer*-[V(ddpd)₂]²⁺ with the pure metal-centred states (black and red) obtained from the CASSCF-NEVPT2 calculation (TZVPP basis), the ⁴MLCT states (large number of states indicated by blue squares) estimated from the experimental absorption spectrum and the time-dependent (TD)-DFT

calculation and the ${}^2\text{MLCT}$ states (pale blue) set to the ${}^4\text{MLCT}$ energies. The mixing between ${}^2\text{E}_g$ and ${}^2\text{MLCT}$ states (purple) is set to an arbitrary value. (i) Spin density of the ${}^4\text{A}_2$ ground state from the CASSCF-NEVPT2 calculation. (ii) Difference electron density of the lowest ${}^4\text{MLCT}$ state obtained from the TD-DFT calculation (isosurface value of 0.003 a.u.; purple = electron depletion; orange = electron density gain). (iii) Spin density of the lowest ${}^4\text{T}_{2g}$ derived state from the CASSCF-NEVPT2 calculation. (iv) Spin density of the lowest ${}^2\text{E}_g$ derived state from the CASSCF-NEVPT2 calculation. (v) Spin density of the optimized lowest doublet state (${}^2\text{MC}/{}^2\text{LMCT}$) from a DFT geometry optimization calculation with the ligand contributions highlighted by arrows.

Calculations of ground and excited state properties with respect to the pure ligand field excited states for both complex cations $\text{cis-fac-[V(ddpd)}_2\text{]}^{2+}$ and $\text{mer-[V(ddpd)}_2\text{]}^{2+}$ were performed at the ground state geometry using the complete-active-space self-consistent field method including spin-orbit coupling (SOC-CASSCF)^[40,41] for calculation of the zero-field splitting D and E in conjunction with strongly contracted N-electron valence perturbation theory to second order (SC-NEVPT2)^[42,43] in order to recover missing dynamic electron correlation (Supporting Information, Tables S5–S6, Figures S5–S6).

As is evident from the calculations, the pure ${}^2\text{E}_g/{}^2\text{T}_{1g}$ -derived spin-flip states lie well below the ${}^4\text{T}_{2g}$ and ${}^4\text{T}_{1g}$ levels (Figure 2a for $\text{mer-[V(ddpd)}_2\text{]}^{2+}$; Supporting Information, Figure S7 for $\text{cis-fac-[V(ddpd)}_2\text{]}^{2+}$). In fact, the ${}^4\text{T}_{2g}$ levels are nearly degenerate with the next higher set of doublet levels (${}^2\text{T}_{2g}$, Figure 2a). According to the calculations, spin-flip luminescence would be expected around 851 and 872 nm from the lowest diabatic doublet level (${}^2\text{E}_g$) of $\text{cis-fac-[V(ddpd)}_2\text{]}^{2+}$ and $\text{mer-[V(ddpd)}_2\text{]}^{2+}$, respectively (Supporting Information, Figures S5–S6. This is in the expected range when compared to the MgO:V^{2+} emission (869 nm)^[24,25] and the ${}^2\text{G}$ free ion term of vanadium(II) (1.49 eV, 828 nm).^[44] However, neither complex displays emission after irradiation with 400 or 450 nm at room temperature and at 77 K in solution or in the solid state. The photoluminescence quantum yield must therefore be below 10⁻⁴%.

Prolonged irradiation with 300 nm light, where the complexes absorb more strongly (Figure 3; strongly allowed LC and LLCT transitions), leads to a fluorescence band at 395 nm that increases with irradiation time (Supporting Information, Figure S8). Excitation spectra suggest that this band arises from traces of the fluorescent (protonated) ligand ddpd (Supporting Information, Figure S9),^[38] which is obviously photoliberated from the complexes under these conditions. Photoisomerization of the complexes ($\text{cis-fac} \rightarrow \text{mer}$ or $\text{mer} \rightarrow \text{cis-fac}$) is not observed as seen from the unchanged shape of the absorption bands of the irradiated cis-fac or mer complex isomers (Supporting Information, Figure S10).

The absorption spectra of the orange-red complexes in acetonitrile hint at possible reasons for the lacking spin-flip emission (Figure 3). Intense absorption bands from approximately 400 – 650 nm ($\lambda_{\text{max}}(\text{cis-fac-[V(ddpd)}_2\text{]}^{2+}) = 486$ nm; $\lambda_{\text{max}}(\text{mer-[V(ddpd)}_2\text{]}^{2+}) = 490$ nm) arise from low-energy ${}^4\text{MLCT}$ transitions according to TD-DFT calculations ($\text{cis-fac-[V(ddpd)}_2\text{]}^{2+}$: 387 – 620 nm; $\text{mer-[V(ddpd)}_2\text{]}^{2+}$: 362 – 622 nm; Tables S7–S10, Figures S11–S12). In reasonable agreement, electrochemical data (Supporting Information, Figures S13) estimate the HOMO–LUMO gap as 2.0 eV (610 nm) and 2.1 eV (591 nm), respectively. With the oxidation assigned to the vanadium(II/III) couple and the reduction to a ligand-centered redox process,^[38] this fits to the MLCT assignment of the absorption spectral data. Chemical oxidation of $\text{cis-fac-[V(ddpd)}_2\text{]}^{2+}$ and $\text{mer-[V(ddpd)}_2\text{]}^{2+}$ with $\text{Ag[BF}_4\text{]}$ yields the corresponding vanadium(III) complexes.^[38,35] Re-reduction with cobaltocene fully or partially recovers the vanadium(II) absorption spectra of the cis-fac and mer isomers, respectively (Supporting Information, Figures S14–S15).

$\text{mer-[V(ddpd)}_2\text{]}^{3+}$ formed by oxidation of $\text{mer-[V(ddpd)}_2\text{]}^{2+}$ with $\text{Ag[BF}_4\text{]}$ shows spin-flip luminescence (${}^1\text{E}'/{}^1\text{T}_2 \rightarrow {}^3\text{T}_1$) around 1100 nm in butyronitrile at 78 K as reported previously (Supporting Information, Figure S16).^[35] Under these conditions, $\text{cis-fac-[V(ddpd)}_2\text{]}^{3+}$ prepared from oxidation of $\text{cis-fac-[V(ddpd)}_2\text{]}^{2+}$ with $\text{Ag[BF}_4\text{]}$ is NIR-II luminescent as well (Supporting Information, Figure S16). $\text{cis-fac-[V(ddpd)}_2\text{]}^{3+}$ displays a structured emission band between 1150 and 1250 nm from ${}^1\text{E}_g/{}^1\text{T}_{2g}$ states to the split ${}^3\text{T}_{1g}$ ground state (O_h notation). Shape and energy of this emission band differs from the emission band of $\text{mer-[V(ddpd)}_2\text{]}^{3+}$, while the shape rather resembles the emission pattern of $\text{Cs}_2\text{NaYCl}_6\text{:V}^{3+}$ and $\text{VCl}_3(\text{ddpd})$.^[45,46]

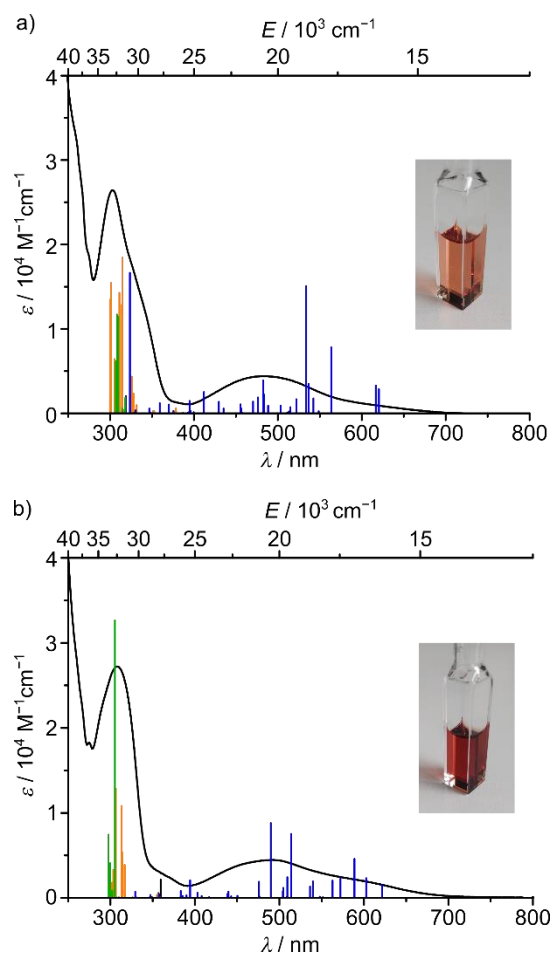


Figure 3. UV/Vis absorption spectra of a) *cis-fac*-[V(ddpd)₂][BPh₄]₂ and b) *mer*-[V(ddpd)₂][BPh₄]₂ in CH₃CN and TD-DFT transitions calculated for the respective dications with the colour code indicating the character of the transition according to charge transfer analyses (blue: ⁴MLCT; orange: ⁴LC; dark green ⁴LLCT; black: ⁴MC; MLCT = metal-to-ligand charge transfer; LC = ligand-centred; LLCT = ligand-to-ligand charge transfer; MC = metal-centred). The insets show photographs of CH₃CN solutions of the respective complexes.

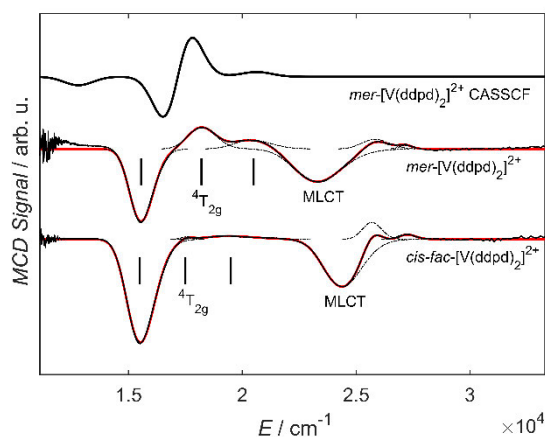


Figure 4. MCD spectra of 1 mM solutions (butyronitrile/propionitrile 1:1) of *cis-fac*-[V(ddpd)₂][BPh₄]₂ at 5 K/7 T (bottom) and of *mer*-[V(ddpd)₂][BPh₄]₂ at 5 K/5 T (middle), as well as the corresponding spectrum for *mer*-[V(ddpd)₂]²⁺ obtained from CASSCF (SVP basis) calculations (top). Measurements are shown as black solid lines, spectral components as black dashed lines and their sum as red solid lines.

Magnetic circular dichroism (MCD) spectroscopy was employed to extract more fine structure of the broad absorption band of the vanadium(II) complexes (Supporting Information, Figures S17–S18). The MCD spectra were deconvoluted as sums of Gaussian peaks giving six components (*cis-fac*-[V(ddpd)₂]²⁺: 27250, 25710, 24380, 19420, 17570, 15520 cm⁻¹; *mer*-[V(ddpd)₂]²⁺: 27170, 25840, 23280, 20420, 18210, 15550 cm⁻¹). The three components at lower energies (15520, 17570, 19420 cm⁻¹ and 15550, 18210, 20420 cm⁻¹ for the *cis-fac* and the *mer* isomer, respectively) are assigned to the three components of the ⁴T_{2g} (O_h notation) excited state. The prominent signals at 24380 (*cis-fac* isomer) and at 23280 cm⁻¹ (*mer* isomer) are assigned to ⁴MLCT transitions. The MCD spectrum pertaining to the ⁴T_{2g} derived states is well reproduced with a CASSCF-NEVPT2 calculation with an active space of CAS(7,7) and with a def2-SVP basis set. A red shift of the calculated transitions is observed, when the basis set size is increased to def2-TZVP (Supporting Information, Figure S18). With the three components of the ⁴T_{2g} (O_h) state identified, it is possible to use ligand field theory to link the observed transitions to the ground state zero-field splitting (ZFS) parameters, which can later be useful for the evaluation of further experiments. For this, the components of the Λ tensor have to be calculated. The Λ tensor describes the residual orbital angular momentum of the ground state due to coupling of excited states and it is linked to the ZFS parameters via $D = -\frac{1}{2}\lambda^2(2\Lambda_{zz} - \Lambda_{xx} - \Lambda_{yy})$ and $E = -\frac{1}{2}\lambda^2(\Lambda_{xx} - \Lambda_{yy})$, with the spin orbit coupling (SOC) constant λ .^[47] For the higher symmetric *mer*-[V(ddpd)₂]²⁺ the derivation is analogue to *mer*-[Cr(ddpd)₂]³⁺, since both possess D₂ symmetry. This has been carried out before.^[22] With the ⁴T_{2g} energies obtained from MCD for *mer*-[V(ddpd)₂]²⁺ and a SOC constant of 168 cm⁻¹,^[48] ZFS parameters of $D = 1.39$ cm⁻¹ and $E = 0.34$ cm⁻¹ are found. *cis-fac*-[V(ddpd)₂]²⁺ features with C₂ a lower symmetry than *mer*-[V(ddpd)₂]²⁺, hence the derivation of the Λ tensor has to be carried out in this point group (see Supporting Information). The ZFS parameters obtained for *cis-fac*-[V(ddpd)₂]²⁺ this way are $D = 0.38$ cm⁻¹ and $E = 0.10$ cm⁻¹.

The strongly allowed low-energy component at ca. 644 nm (Figure 3) is assigned to the transition to the lowest energy ⁴MLCT state at the ground state geometry (Figure 2a for *mer*-[V(ddpd)₂]²⁺; Supporting Information, Figure S7a for *cis-fac*-[V(ddpd)₂]²⁺). The lowest (diabatic) ²MLCT states might be at similar energies to the corresponding ⁴MLCT states. These energies are relatively close to the calculated energies of the diabatic spin-flip states (Figure 2a). Consequently, mixing of the diabatic spin-flip and ²MLCT states is possible (Figures 2a, 2e).^[32] Although the absorption maxima of *cis-fac*-[V(ddpd)₂]²⁺ and *mer*-[V(ddpd)₂]²⁺ are shifted to the blue as compared to [V(bpy)₃]²⁺ and [V(phen)₃]²⁺ ($\lambda_{\text{max}} = 650$ nm) due to the electron-rich ddpd ligand,^[26-32] this seems not yet sufficient to fully prevent mixing of ²E_g/²T_{1g} and ²MLCT states. Indeed, DFT calculations of the geometry optimized lowest doublet states of *cis-fac*-[V(ddpd)₂]²⁺ and *mer*-[V(ddpd)₂]²⁺ confirm an admixture of charge transfer character in this optimized lowest doublet excited state (Figure 2f for *mer*-[V(ddpd)₂]²⁺; Supporting Information, Figure S7f for *cis-fac*-[V(ddpd)₂]²⁺; Tables S11–S12): The Mulliken spin density at vanadium exceeds one (*cis-fac*-[V(ddpd)₂]²⁺: 1.25 *mer*-[V(ddpd)₂]²⁺: 1.11), the spin distribution differs from that of the hypothetical pure ²E_g spin-flip state obtained from the CASSCF-NEVPT2 calculations (Fig. 2e) and ρ spin density is found at the terminal pyridine rings of the ddpd ligands. In addition, the V–N bonds contract in the doublet states as expected for an MLCT admixture (*cis-fac*-[V(ddpd)₂]²⁺: $\rho_{\text{av}} = 0.016$ Å; *mer*-[V(ddpd)₂]²⁺: $\rho_{\text{av}} = 0.019$ Å), while a pure spin-flip state should be nested. Although the MLCT character of the lowest energy doublet states of [V(ddpd)₂]²⁺ appears much less distinct than in [V(bpy)₃]²⁺ and [V(phen)₃]²⁺^[32] due to the higher energies of the ρ^* orbitals of the pyridines of ddpd and thus the higher energies of the diabatic ²MLCT states, the geometric distortion in the true adiabatic doublet state seems to be sufficient to facilitate non-radiative decay. Clearly, the ρ -accepting nature of the ligands needs to be further decreased to enable spin-flip luminescence in vanadium(II) complexes.

The potential suitability of a complex as molecular qubit is determined by its electronic structure as well as its spin dynamics. Concerning the former, the microstates of an $S = 3/2$ ion are split into two Kramers doublets in the absence of a magnetic field, which correspond to $m_S = \pm 3/2$ and $\pm 1/2$ respectively in the absence of rhombic zero-field splitting ($E = 0$ in eq. 1). To be able to use the inter-Kramers-doublet transitions for quantum operations, the energy gap should not be larger than the microwave frequency of the spectrometer employed, putting an upper limit on the value of D . The sign of D is less important. Secondly, in case the intradoublet transition of the $m_S = \pm 3/2$ doublet is to be used, this transition is

formally EPR-forbidden. The presence of a small rhombic ZFS partially allows this transition and this may therefore be favorable.

As a starting point for the investigation of the electronic structure of the complexes, we carried out magnetic susceptibility measurements. Both vanadium(II) complexes possess nearly temperature-independent χT values of $1.857 \text{ cm}^3 \text{ K mol}^{-1}$ and $1.863 \text{ cm}^3 \text{ K mol}^{-1}$ for *cis-fac* and *mer*-[V(ddpd)₂]²⁺, respectively. Both values are consistent with three unpaired electrons with a *g* value slightly smaller than 2 (for *g* = 2, this is $1.875 \text{ cm}^3 \text{ K mol}^{-1}$) (Figure 2b; Supporting Information, Figures S19–S22). From 8 K downwards, χT decreases slightly which we attribute to a small ZFS, where a fit yielded a *D* value (eq. 1) of $D = 0.4 \text{ cm}^{-1}$ for *cis-fac*-[V(ddpd)₂]²⁺. For *mer*-[V(ddpd)₂]²⁺ such a decrease is not observed, indicating an even smaller ZFS than in the *cis-fac* case. To obtain deeper insight into the ZFS spin Hamiltonian parameters *D* and *E* (eq. 1), high-field electron paramagnetic resonance (HFEP) spectroscopy at frequencies of up to 375 GHz was carried out for both isomers (Figure 5 for *mer*-[V(ddpd)₂]²⁺; Supporting Information, Figure S23 for *cis-fac*-[V(ddpd)₂]²⁺).

$$H = \mu_B \hat{\mathbf{S}} \cdot \mathbf{g} \cdot \mathbf{B} + D \hat{S}_z^2 + E (\hat{S}_x^2 - \hat{S}_y^2) \quad (1)$$

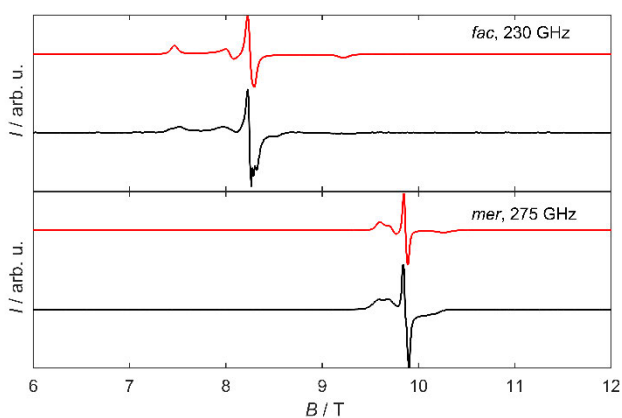


Figure 5. Measured HFEP spectra of *cis-fac*-[V(ddpd)₂][BPh₄]₂ and *mer*-[V(ddpd)₂][BPh₄]₂ at 5 K at the frequencies as indicated (black) together with simulations based on the spin Hamiltonian parameters given in the text (red).

The HFEP spectra consist of three resonance lines, where the central one is assigned to the $m_s = -1/2$ to $m_s = +1/2$ transition (high-field limit notation). The spectra were simulated using the spin Hamiltonian from eq. 1 with $D = +0.47(2) \text{ cm}^{-1}$, $E = 0.09(1) \text{ cm}^{-1}$ ($E/D = 0.19$), $g_1 = 1.99(1)$, $g_2 = 1.99(1)$ and $g_3 = 2.00(1)$ for *cis-fac*-[V(ddpd)₂]²⁺ and $D = +0.20(5) \text{ cm}^{-1}$, $E = 0.02(1) \text{ cm}^{-1}$ ($E/D = 0.08$), $g_1 = 1.986(1)$, $g_2 = 1.993(2)$ and $g_3 = 1.996(2)$ for *mer*-[V(ddpd)₂]²⁺, respectively. The *D* value of the meridional isomer is nearly identical to that found for *mer*-[Cr(ddpd)₂]³⁺.^[22] The zero-field energy gap Δ between the two Kramers doublets given by $\Delta = \sqrt{D^2 + 3E^2}$ is $\Delta = 0.50 \text{ cm}^{-1}$ and 0.20 cm^{-1} for the *cis-fac* and *mer* isomers, respectively (Figure 2a), for *mer*-[V(ddpd)₂]²⁺, this is roughly half of that of *mer*-[Cr(ddpd)₂]³⁺ ($\Delta = 0.41 \text{ cm}^{-1}$).^[22]

In order to determine the sign of *D*, temperature dependent HFEP spectra were carried out in the range from 5 K to 20 K. For both isomers, the temperature dependent HFEP spectra can be well simulated with the parameters obtained from the frequency dependence, in particular with a positive sign of the *D* value. In contrast to this, simulations with a negative sign of *D* show a completely different temperature behavior from the one found experimentally (Supporting Information, Figures S24 and S26). Since ⁵¹V (natural abundance 99.15 %) possesses a nuclear spin of $I = 7/2$, hyperfine splitting of the resonance lines can be expected in the spectra. No such splitting was observed in the HFEP spectra,^[49] which we attribute to the line width exceeding the hyperfine splitting strength. To probe possible hyperfine interactions, EPR experiments were carried out at X-band frequency (9.45 GHz) in frozen solution (butyronitrile/propionitrile 1:1) at 7 K. In the case of *mer*-[V(ddpd)₂]²⁺, hyperfine shoulders

are found on a broad resonance line centered at 340 mT (Supporting Information, Figure S27). These shoulders are separated by 7 mT, which is equivalent to a hyperfine splitting A of $6.5 \times 10^{-3} \text{ cm}^{-1}$. For *cis-fac*-[V(ddpd)₂]²⁺, no such shoulders are observed, but signals are broadened due to hyperfine interactions (Supporting Information, Figure S27). Both spectra can be well simulated with $A = 6.5(6) \times 10^{-3} \text{ cm}^{-1}$, assuming $g_{\text{iso}} = 1.94(1)$ and ZFS parameters of $D = 0.30(2) \text{ cm}^{-1}$ and $E/D = 0.3$ in the *cis-fac* case and $g_{\text{iso}} = 1.989(5)$, $D = 0.12(2) \text{ cm}^{-1}$ and $E/D = 0.08$ in the *mer* case, which is in good agreement with the values found by HFEPR spectroscopy. For these simulations, the Hamiltonian in eqn. (1) was expanded by the conventional hyperfine interaction term $\hat{S}\mathbf{A}\hat{I}$.

While CASSCF(12,7) (TZVPP basis) calculations predict small negative values for D irrespective of the NEVPT2 correction, a CASSCF(7,7) (SVP basis) calculation on *mer*-[V(ddpd)₂]²⁺ delivers a small positive D value in agreement with the experimentally determined data (see Supporting Information for details). Hence, the sign of the D values of vanadium(II) complexes appears difficult to predict on this level of theory, while the signs of the ZFS parameters of the isoelectronic chromium(III) complex [Cr(ddpd)₂]³⁺ lacking low-energy charge transfer states were correctly predicted by CASSCF calculations.^[22]

To assess their suitability as molecular qubits, we investigated the spin dynamics of the complexes by means of pulsed Q-band EPR spectroscopy and AC susceptometry. In this regard, the electron coherence time is of particular interest, since it is a benchmark criterion for molecular quantum bit (qubit) candidates. While the majority of vanadium-based qubits feature the metal ion in its more stable oxidation state V^{IV}, with a spin $S = 1/2$ ground state, the [V(ddpd)₂]²⁺ complexes presented here possess a ground state of $S = 3/2$. Such high spin qubits provide further states that can be used as additional qubits. The nuclear spin of ⁵¹V of $I = 7/2$ leads to additional hyperfine states rendering an even higher number of encoded qubits in one molecule conceivable.

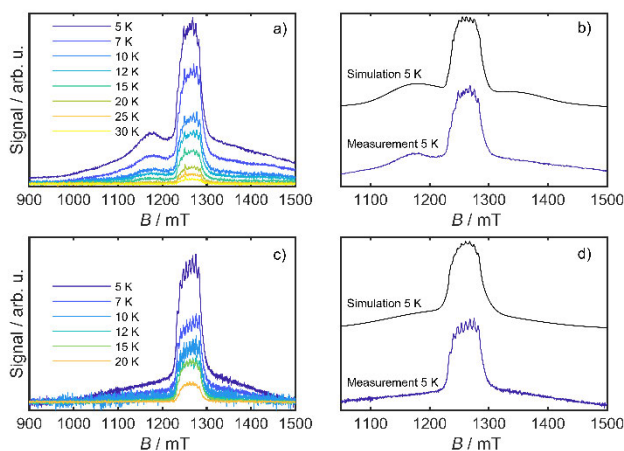


Figure 6. a) Temperature dependent electron spin echo detected (ESE) spectrum of *cis-fac*-[V(ddpd)₂][BPh₄]₂ at 35 GHz (3 mM in propionitrile/butyronitrile), b) Corresponding simulation at 5 K, based on the parameters given in the text. c) ESE spectrum of *mer*-[V(ddpd)₂][BPh₄]₂ (3 mM in propionitrile/butyronitrile) at the temperatures indicated. d) Corresponding simulation at 5 K based on the parameters given in the text.

Pulsed Q-band EPR spectra were recorded of both isomers in a 3 mM frozen solutions of butyronitrile/propionitrile 1:1 at 35 GHz in a temperature range from 5 K up to 30 K. Echo detected spectra of both species feature a prominent central signal at around $g = 2$, that displays distinct hyperfine peaks due to coupling of the $S = 3/2$ electron spin to the $I = 7/2$ V^{II} center. This signal is due to the transition in the $m_s = \pm 1/2$ ground state Kramers doublet. The central line is accompanied by broad signals, which is due to the zero field split transition from the lower lying $m_s = \pm 1/2$ manifold to the higher lying $m_s = \pm 3/2$ states. In the case of *cis-fac*-[V(ddpd)₂]²⁺ this broad signal is more distinct due to its higher D value. In both cases, the ZFS signals are broadened by a large D -strain. Simulations are in good agreement with the measured spectra, when smaller D values than those found by means of static

Results and Discussion

spectroscopy are assumed ($D = 0.11(3) \text{ cm}^{-1}$ and $A = 6.0 \times 10^{-3} \text{ cm}^{-1}$ for the *cis-fac* and $D = 0.10(3) \text{ cm}^{-1}$ and $A = 6.4 \times 10^{-3} \text{ cm}^{-1}$ for the *mer* isomer). The phase memory time T_m was determined by means of the Hahn-Echo sequence for both isomers in the same temperature range as the echo detected spectra. The echo decay curves show a modulation in all cases. These oscillations are due to a change of the nuclear spin while the electron spin echo experiment is recorded and are known as electron spin echo envelop modulation (ESEEM). The frequency of this ESEEM can be extracted when the subtraction of the experiment and the exponential decay, that is used to describe the decay of the echo intensity (eqn. 2), is Fourier transformed.

$$I(\tau) = I(0)\exp(-\tau/T_M)^k \quad (2)$$

From the Fourier transform, three main frequencies can be extracted for both isomers at 2.1, 5.3 and 10 MHz (Supporting Information, Figures S32 and S33). The frequency pattern is quite similar to that found previously for *mer*-[Cr(ddpd)₂]³⁺. In the Cr^{III} case, the ESEEM was attributed to double quantum transitions of the neighboring ¹⁴N nuclei.

To probe the coherence times of the various magnetic states that are spectroscopically accessible, Hahn echo decays were recorded for both isomers at the highest intensity of the spectrum, in both cases at around $g = 2$ (1266 mT and 1275 mT for the *cis-fac* and *mer* isomer, respectively), and in the flanks of the spectrum (1175 mT and 1100 mT, respectively). The decays were fitted by means of equation (2) and revealed phase memory times for both isomers of 1 μs at 5 K at the position of the central spectral signal at 1266 and 1275 mT, respectively. When the coherence times are measured in the flanks of the spectra (1172 mT and 1100 mT), a much faster relaxation of 0.79 μs and 0.41 μs (*cis-fac* and *mer* isomer, respectively) is observed (Supporting Information, Figures S29 and S31). This is due to the fact, that at that magnetic field, transitions involving the $m_S = \pm 3/2$ Kramers doublet are excited.

With increasing temperatures up to 12 K, the phase memory times remain essentially constant in both cases, but start to drop at higher temperatures down to 0.4 μs at 30 K for *cis-fac*-[V(ddpd)₂][BPh₄]₂ and down to 0.6 μs in the case of *mer*-[V(ddpd)₂][BPh₄]₂. While the phase memory times are almost equivalent for both isomers, the stretch factor k behaves completely different in both cases. The stretch factor provides unique information about the main relaxation process. While for $1 < k < 1.5$ the physical motion of the nuclei is predominant, it is for $2 < k < 2.5$, that nuclear spin diffusion is the dominating process.^[22] Up to 7 K, the stretch factors of the *cis-fac* and the *mer* isomer are almost the same at 1.80 ± 5 , hinting towards a mixed relaxation process. However, the temperature dependence of the stretch factors of both isomers is completely different. While for *cis-fac*-[V(ddpd)₂]²⁺ the stretch factor increases to 2.27 with increasing temperatures, it decreases in the case of *mer*-[V(ddpd)₂]²⁺ down to 1.12 at 20 K. A decrease of stretch factors with growing temperatures was found before in the case of *mer*-[Cr(ddpd)₂]³⁺, indicating a limitation of the coherence time by the physical motion of nuclei with increasing temperatures for the *mer* isomers of [M(ddpd)₂]ⁿ⁺ complexes. The increase of k with growing temperatures for *cis-fac*-[V(ddpd)₂]²⁺ hints towards nuclear spin diffusion limitation of coherence times. A possible explanation for this can be the more rigid ligand system of the *cis-fac* orientation of the two ddpd ligands, leading to a reduction in the physical motion of the surrounding nuclei quenching this relaxation pathway

The spin lattice relaxation time, which is the upper limit for the phase coherence time, was determined by means of the inversion-recovery sequence at the same temperatures as the phase coherence time. It was found to be at around 300 μs at 5 K for both isomers. Upon heating, it is decreasing to around 40 μs at 12 K. Interestingly with even higher temperature, the spin–lattice relaxation time stays largely constant up to 30 K.

To investigate the magnetization dynamics of both samples even further and also in a non diluted matrix, AC susceptometry was carried out on pressed pellets of both isomers. While *cis-fac*-[V(ddpd)₂][BPh₄]₂ does not show any slow relaxation of the magnetization in zero field or with an applied external field, *mer*-[V(ddpd)₂][BPh₄]₂ features an out-of-phase signal below 15 K and at an applied external magnetic field of 400 mT. The relaxation times found by means of AC susceptometry are slightly shorter than those found by pulsed EPR spectroscopy. This is due to the fact, that in the EPR measurements, frozen

solution samples are used, while for AC susceptometry, a pressed powder pellet is used, leading to different relaxation times.

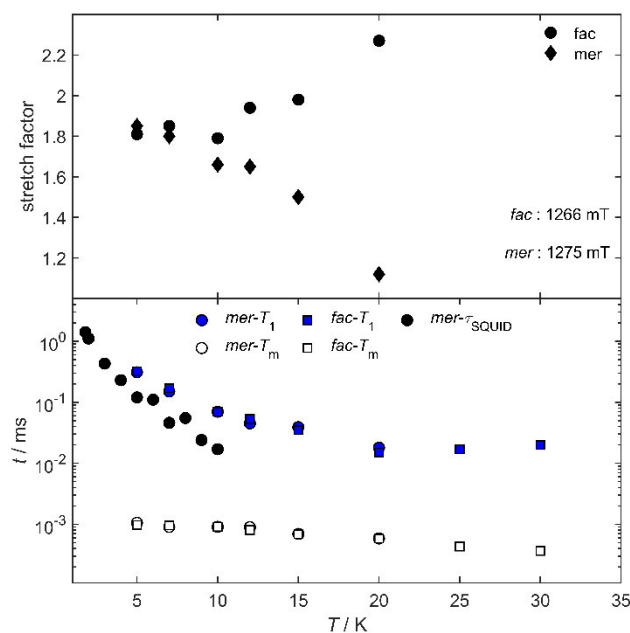


Figure 7. Bottom: T_1 (blue filled symbols) and T_M (non-colored symbols) of *cis-fac*-[V(ddpd)₂][BPh₄]₂ (squares) and *mer*-[V(ddpd)₂][BPh₄]₂ (circles), measured at 1266 mT and 1275 mT, respectively. As black circles relaxation times, obtained by AC susceptometry for *mer*-[V(ddpd)₂][BPh₄]₂. Top: Stretch factors of the corresponding fits of the echo-decay curves based on eqn. 2.

mer-[V(ddpd)₂]²⁺ appears to be the first vanadium(II) complex showing slow magnetization.^[50,51] With the d³ electron configuration in an octahedral field, the electronic situation of vanadium(II) is analogous to that of a high-spin d⁷ cobalt(II) ion in a tetrahedral field which has been shown to enable large ZFS and relaxation energy barriers.^[52]

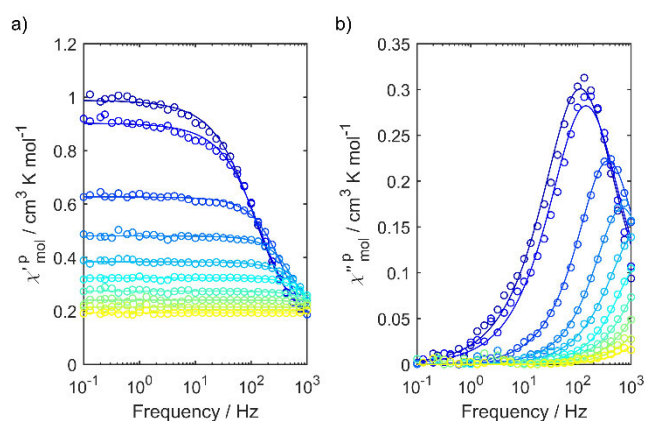


Figure 8. In-phase (a) and out-of-phase (b) component of the AC susceptibility of *mer*-[V(ddpd)₂][BPh₄]₂ from 1.8 K to 10 K at an applied external magnetic field of 400 mT. Measured values are shown as open circles, while simultaneous fits of the in-phase and out-of-phase component to the standard modified Debye function are shown as solid lines.

Conclusions

Two novel vanadium(II) complexes with the electron-rich tridentate polypyridine ligand *N,N*-dimethyl-*N,N*-dipyridine-2-yl-pyridine-2,6-diamine (ddpd) differing only in the ligand coordination mode (*cis*-facial

vs. meridional) were isolated as the kinetic and thermodynamic products, respectively. These isomers *cis-fac*-[V(ddpd)₂][BPh₄]₂ and *mer*-[V(ddpd)₂][BPh₄]₂ are stable with respect to isomerization at room temperature and under light irradiation in solution, while prolonged irradiation with UV-B light leads to ligand dissociation. No ruby-like spin-flip luminescence is detected for either complex. However, one-electron oxidation delivers the corresponding NIR-II luminescent vanadium(III) complexes. The lacking spin-flip luminescence of the vanadium(II) complexes arises from mixing of the spin-flip states with low-energy ²MLCT states leading to distortion and efficient non-radiative decay of the excited states. Clearly, even the electron-rich ddpd ligand possesses π* orbitals with too low energy providing the low-energy MLCT states. Future ligand design aims to eliminate the low-energy MLCT states, while providing a strong enough ligand field for vanadium(II).

Zero-field splitting splits the ⁴A_{2g} ground states of the d³ vanadium(II) ion into two Kramers doublets with energy gaps of ca. 0.5 and 0.2 cm⁻¹ for the *cis-fac* and *mer* isomer, respectively, enabling pulsed EPR measurements. While *cis-fac*-[V(ddpd)₂][BPh₄]₂ does not show slow magnetic relaxation at an applied field below 15 K, *mer*-[V(ddpd)₂][BPh₄]₂ features an out-of-phase signal. This isomer possesses a spin-lattice relaxation time *T*₁ = 308 μs and a phase memory time *T*_M = 1.1 μs at 5 K according to pulsed EPR measurements, recommending vanadium(II) complexes as potential molecular quantum bits.

Consequently, the present study lays the foundations for developing vanadium(II) complexes with tuned spin-flip excited states lacking MLCT admixture and tuned magnetic relaxation as candidates for optically addressable molecular qubits.

Experimental Section

Details of the syntheses, spectroscopic, computational and simulation data are collected in the supporting information. Deposition Number(s) <url href="https://www.ccdc.cam.ac.uk/services/structures?id=doi:10.1002/chem.202202898"> 2177572 (for *mer*-[V(ddpd)₂][BPh₄]₂), 2177573 (for *cis-fac*-[V(ddpd)₂][PF₆]₂)</url> contain(s) the supplementary crystallographic data for this paper. These data are provided free of charge by the joint Cambridge Crystallographic Data Centre and Fachinformationszentrum Karlsruhe <url href="http://www.ccdc.cam.ac.uk/structures">Access Structures service</url>.

Acknowledgements

This work has been financially supported by the Deutsche Forschungsgemeinschaft (DFG) under grant INST 247/1018-1 (K. H.) and the Priority Program SPP 2102 "Light-controlled reactivity of metal complexes" HE2778/15-1, as well as by DFG grant SL104/10-1 and the Landesgraduiertenförderung of the State of Baden-Württemberg. Parts of this research were conducted using the supercomputer MOGON and advisory services offered by Johannes Gutenberg University Mainz (<http://www.hpc.uni-mainz.de>) and the supercomputer Elwetritsch and advisory services offered by the TU Kaiserslautern (<https://elwe.rhrk.uni-kl.de>), which are members of the AHRP and the Gauss Alliance e.V. We thank Dr. Dieter Schollmeyer for collecting the XRD data and Dimitri Zorn for assistance with some absorption spectroscopic experiments.

Conflict of Interest

The authors declare no conflict of interest.

Data Availability Statement

The data that support the findings of this study are available in the supplementary material of this article.

Keywords: electron paramagnetic resonance • excited state order • magnetic relaxation • spin-flip • vanadium

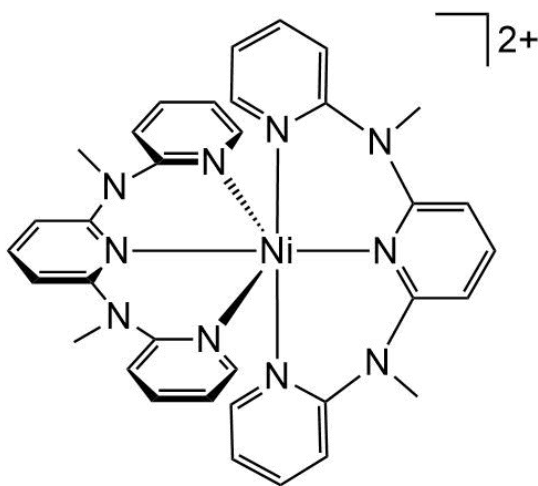
- [1] a) K. Bader, D. Dengler, S. Lenz, B. Endeward, S.-D. Jiang, P. Neugebauer, J. van Slageren, *Nat. Commun.* **2014**, *5*, 5304; b) S. Lenz, K. Bader, H. Bamberger, J. van Slageren. *Chem. Commun.* **2017**, *53*, 4477–4480.
- [2] M. Atzori, E. Morra, L. Tesi, A. Albino, M. Chiesa, L. Sorace, R. Sessoli, *J. Am. Chem. Soc.* **2016**, *138*, 11234–11244.
- [3] C.-J. Yu, M. J. Graham, J. M. Zadrozny, J. Niklas, M. D. Krzyaniak, M. R. Wasielewski, O. G. Poluektov, D. E. Freedman, *J. Am. Chem. Soc.* **2016**, *138*, 14678–14685.
- [4] J. M. Zadrozny, J. Niklas, O. G. Poluektov, D. E. Freedman, *ACS Cent. Sci.* **2015**, *1*, 488–492.
- [5] a) K. S. Kumar, D. Serrano, A. M. Nonat, B. Heinrich, L. Karmazin, L. J. Charbonnière, P. Goldner, M. Ruben, *Nat. Commun.* **2021**, *12*, 2152; b) D. Serrano, S. K. Kuppusamy, B. Heinrich, O. Fuhr, D. Hunger, M. Ruben, P. Goldner, *Nature* **2022**, *603*, 241–248. c) M. S. Fataftah, S. L. Bayliss, D. W. Laorenza, X. Wang, B. T. Phelan, C. B. Wilson, P. J. Mintun, B. D. Kovos, M. R. Wasielewski, S. Han, M. S. Sherwin, D. D. Awschalom, D. E. Freedman, *J. Am. Chem. Soc.* **2020**, *142*, 20400–20408; d) S. L. Bayliss, D. W. Laorenza, P. J. Mintun, B. D. Kovos, D. E. Freedman, D. D. Awschalom, *Science* **2020**, *370*, 1309–1312; e) M. K. Wojnar, D. W. Laorenza, R. D. Schaller, D. E. Freedman, *J. Am. Chem. Soc.* **2020**, *142*, 14826–14830.
- [6] H. Biard, E. Moreno-Pineda, M. Ruben, E. Bonet, W. Wernsdorfer, F. Balestro, *Nat. Commun.* **2021**, *12*, 4443.
- [7] R. Schirhagl, K. Chang, M. Loretz, C. L. Degen, *Ann. Rev. Phys. Chem.* **2014**, *65*, 83–105.
- [8] D. Serrano, S. K. Kuppusamy, B. Heinrich, O. Fuhr, D. Hunger, M. Ruben, P. Goldner. *Nature* **2022**, *603*, 241–246.
- [9] S. Otto, N. Scholz, T. Behnke, U. Resch-Genger, K. Heinze, *Chem. Eur. J.* **2017**, *23*, 12131–12135.
- [10] S. Otto, J. Harris, K. Heinze, C. Reber, *Angew. Chem.* **2018**, *130*, 11236–11240; *Angew. Chem. Int. Ed.* **2018**, *57*, 11069–11073.
- [11] C. Wang, S. Otto, M. Dorn, K. Heinze, U. Resch-Genger, *Anal. Chem.* **2019**, *91*, 2337–2344.
- [12] J. Kalmbach, C. Wang, Y. You, C. Förster, H. Schubert, K. Heinze, U. Resch-Genger, M. Seitz, *Angew. Chem.* **2020**, *132*, 18966–18970; *Angew. Chem. Int. Ed.* **2020**, *59*, 18804–18808.
- [13] C. Wang, F. Reichenauer, W. R. Kitzmann, C. Kerzig, K. Heinze, U. Resch-Genger, *Angew. Chem.* **2022**, *134*, e202202238; *Angew. Chem. Int. Ed.* **2022**, *61*, e202202238.
- [14] C. Dee, F. Zinna, W. R. Kitzmann, G. Pescitelli, K. Heinze, L. Di Bari, M. Seitz, *Chem. Commun.* **2019**, *55*, 13078–13081.
- [15] J.-R. Jiménez, B. Doistau, C. M. Cruz, C. Besnard, J. M. Cuerva, A. G. Campaña, C. Piguet, *J. Am. Chem. Soc.* **2019**, *141*, 13244–13252.
- [16] S. M. Stevenson, M. P. Shores, E. M. Ferreira, *Angew. Chem. Int. Ed.* **2015**, *54*, 6506–6510.
- [17] S. Otto, A. M. Nauth, E. Ermilov, N. Scholz, A. Friedrich, U. Resch-Genger, S. Lochbrunner, T. Opatz, K. Heinze, *ChemPhotoChem* **2017**, *1*, 344–349.
- [18] S. Sittel, R. Naumann, K. Heinze, *Front. Chem.* **2022**, *10*, 887439.
- [19] T. H. Bürgin, F. Glaser, O. S. Wenger, *J. Am. Chem. Soc.* **2022**, *144*, 14181–14194.
- [20] a) W. R. Kitzmann, J. Moll, K. Heinze, *Photochem. Photobiol. Sci.* **2022**, *21*, 1309–1331; b)
- [21] a) S. Otto, M. Grabolle, C. Förster, C. Kreitner, U. Resch-Genger, K. Heinze, *Angew. Chem.* **2015**, *127*, 11735–11739; *Angew. Chem. Int. Ed.* **2015**, *54*, 11572–11576; b) W. R. Kitzmann, C. Ramanan, R. Naumann, K. Heinze, *Dalton Trans.* **2022**, *51*, 6519–6525.
- [22] S. Lenz, H. Bamberger, P. P. Hallmen, Y. Thiebes, S. Otto, K. Heinze, J. van Slageren, *Phys. Chem. Chem. Phys.* **2019**, *21*, 6976–6983.
- [23] S. L. Bayliss, D. W. Laorenza, P. J. Mintun, B. D. Kovos, D. E. Freedman, D. D. Awschalom. *Science* **2020**, *370*, 1309–1312.
- [24] G. Vilianni, O. Pilla, M. Montagna, A. Boyrivent, *Phys. Rev. B* **1981**, *23*, 18–27.
- [25] M. D. Sturge, *Phys. Rev.* **1963**, *130*, 639–646.
- [26] E. König, S. Herzog, *S. J. Inorg. Nucl. Chem.* **1970**, *32*, 601–611.
- [27] I. Fujita, T. Yazaki, Y. Torii, H. Kobayashi, *Bull. Chem. Soc. Jpn.* **1972**, *45*, 2156–2161.
- [28] A. C. Bowman, S. Sproules, K. Wieghardt, *Inorg. Chem.* **2012**, *51*, 3707–3717.

- [29] S. S. Shah, A. W. Maverick, *Inorg. Chem.* **1986**, *25*, 1867–1871.
- [30] A. W. Maverick, S. S. Shah, C. Kirmaier, D. Holten, *Inorg. Chem.* **1987**, *26*, 774–776.
- [31] S. S. Shah, A. W. Maverick, *Inorg. Chem.* **1987**, *26*, 1559–1562.
- [32] a) R. D. Dill, R. I. Portillo, S. G. Shepard, M. P. Shores, A. K. Rappé, N. H. Damrauer, *Inorg. Chem.* **2020**, *59*, 14706–14715; b) J. P. Joyce, R. I. Portillo, C. M. Nite, J. M. Nite, M. P. Nguyen, A. K. Rappé, M. P. Shores, *Inorg. Chem.* **2021**, *60*, 12823–12834.
- [33] J. P. Joyce, R. I. Portillo, A. K. Rappé, M. P. Shores, *Inorg. Chem.* **2022**, *61*, 6376–6391.
- [34] T. J. Penfold, E. Gindensperger, C. Daniel, C. M. Marian, *Chem. Rev.* **2018**, *118*, 6975–7025.
- [35] M. Dorn, J. Kalmbach, P. Boden, A. Pöpcke, S. Gómez, C. Förster, F. Kuczelinis, L. M. Carrella, L. Büldt, N. Bings, E. Rentschler, S. Lochbrunner, L. González, M. Gerhards, M. Seitz, K. Heinze, *J. Am. Chem. Soc.* **2020**, *142*, 7947–7955.

3.4. Structure and Electronic Properties of an Expanded Terpyridine Complex of Nickel(II) $[\text{Ni}(\text{ddpd})_2](\text{BF}_4)_2$

Matthias Dorn, Katharina Mack, Luca M. Carrella, Eva Rentschler, Christoph Förster and Katja Heinze

Z. Anorg. Allg. Chem. **2018**, 644, 706–712



Herein, the electrochemical, magnetic and optical properties as well as the solid state structure of the new nickel(II) complex $[\text{Ni}(\text{ddpd})_2]^{2+}$ (ddpd = *N,N'*-dimethyl-*N,N'*-dipyridin-2-ylpyridine-2,6-diamine) are described. The lowest spin-flip state ^1E is energetically close to the first ligand-field excited state $^3\text{T}_2$ which precludes phosphorescence from the ^1E state. Due to an intensity borrowing mechanism, the spin-forbidden $^3\text{A} \rightarrow ^1\text{E}$ transition is observable in the absorption spectra of the title complex.

Author Contributions

Matthias Dorn prepared and characterized the title compound via absorption and emission spectroscopy, IR spectroscopy and cyclic voltammetry. Crystals suited for X-RAY diffractometry were grown by Katharina Mack. Dr. Luca M. Carrella (group of Prof. Dr. E. Rentschler) performed magnetic susceptibility measurements. Dr. Christoph Förster solved the crystal structure of the title compound and performed all quantum-chemical calculations. The manuscript was written by Dr. Christoph Förster (70%), Prof. Dr. Katja Heinze (20%) and Matthias Dorn (10%).

Supporting information

can be found at pp. 219.

The full supporting information can be obtained [here](#).

“Reprinted with the permission of Dorn, M.; Mack, K.; Carrella, L. M.; Rentschler, E.; Förster, C.; Heinze, K.; Z. Anorg. Allg. Chem. 2015, 641, 2083–2092. Copyright © 2015 WILEY-VCH Verlag GmbH & Co. KGaA, Weinheim”

Structure and Electronic Properties of an Expanded Terpyridine Complex of Nickel(II) $[\text{Ni}(\text{ddpd})_2](\text{BF}_4)_2$

Matthias Dorn,^[a] Katharina Mack,^[a] Luca M. Carrella,^[a] Eva Rentschler,^[a] Christoph Förster,^{*[a]} and Katja Heinze^{*[a]}

Dedicated to Prof. Peter Comba on the Occasion of his 65th Birthday

Abstract. The synthesis, structure in the solid state, electrochemical, magnetic and optical properties of a new nickel(II) complex $[\text{Ni}(\text{ddpd})_2]^{2+}$ bearing the tridentate *N,N'*-dimethyl-*N,N'*-dipyridin-2-

ylpyridine-2,6-diamine (ddpd) ligand are presented. The optical properties are discussed within the framework of ligand field theory.

Introduction

The electron donating expanded terpyridine type (tpy = 2,2';6',2''-terpyridine) ligand *N,N'*-dimethyl-*N,N'*-dipyridin-2-ylpyridine-2,6-diamine (ddpd) has been established for heteroleptic push-pull bis(tridentate) ruthenium(II) complexes in a ligand-metal-ligand N–M–N bite angle optimization approach (90°, 180°) to increase the M–L orbital overlap and hence to increase the ligand field strength.^[1,2] The strong ligand field induced by the six-membered chelate rings of ddpd led to advantageous photophysical properties in ruthenium(II),^[1–5] low-spin iron(II),^[6,7] and chromium(III)^[8–11] complexes.

The flexibility of the ddpd ligand allows for a dynamic Jahn-Teller distortion in $[\text{Cu}(\text{ddpd})_2]^{2+}$.^[12] The Jahn-Teller splitting is larger than that of $[\text{Cu}(\text{tpy})_2]^{2+}$.^[12] Compared to five-membered chelate rings, the larger flexibility of six-membered chelates enables an energetically less favored *cis*-facial coordination in $[\text{Co}(\text{ddpd})_2]^{2+}$ in addition to the thermodynamically preferred meridional isomer.^[13,14] The equilibration of octahedral $[\text{Zn}(\text{ddpd})_2]^{2+}$ complexes with trigonal-bipyramidal $\text{ZnCl}_2(\text{ddpd})$ and tetrahedral $[\text{ZnCl}_4]^{2-}$ in the presence of chloride ions demonstrates the coordination diversity of d¹⁰ ions in the absence of ligand field stabilization.^[15] A remaining gap in the series of 3dⁿ-metal(II) bis(ddpd) complexes with *n* = 6–10 is $[\text{Ni}(\text{ddpd})_2]^{2+}$ (**1**²⁺), a 3d⁸-metal polypyridine complex.

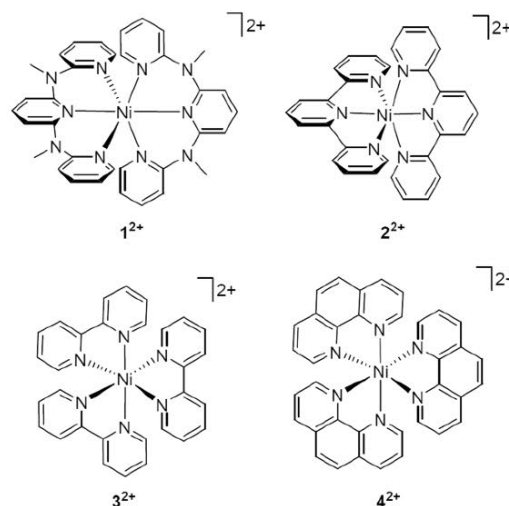
Closely related pseudo-octahedral nickel(II) complexes are $[\text{Ni}(\text{tpy})_2]^{2+}$ (**2**²⁺),^[16–19] $[\text{Ni}(\text{bipy})_3]^{2+}$ (**3**²⁺),^[18–25] and $[\text{Ni}(\text{phen})_3]^{2+}$ (**4**²⁺),^[19–22,25] (bipy = 2,2'-bipyridine; phen = 1,10-phenanthroline) (Scheme 1).

* C. Förster
E-Mail: cfoerster@uni-mainz.de

* K. Heinze
E-Mail: katja.heinze@uni-mainz.de

[a] Institute of Inorganic Chemistry and Analytical Chemistry
Johannes Gutenberg University of Mainz
Duesbergweg 10–14
55128 Mainz, Germany

Supporting information for this article is available on the WWW under <http://dx.doi.org/10.1002/zaac.201800101> or from the author.



Scheme 1. Polypyridine nickel(II) complex cations **1**²⁺–**4**²⁺.

$[\text{Ni}(\text{tpy})_2]^{2+}$ has been employed as an electrocatalyst for carbon dioxide reduction and recently even for photocatalytic CO_2 reduction in combination with quantum dot sensitizers.^[26–30] Under these conditions, a tpy ligand is believed to dissociate from the nickel ion.^[29,30]

The optical properties of polypyridine nickel(II) complexes are largely based on ligand field transitions in the UV/Vis/NIR region. These transition arise from a $(t_{2g})^6(e_g)^2$ electron configuration, corresponding to a ${}^3A_{2g}$ ground state (in idealized O_h symmetry). The tpy, bipy and phen ligands induce a comparably strong ligand field in **2**²⁺–**4**²⁺, corresponding to a ligand field strength Δ_o around 17 *B* in the Tanabe Sugano diagram with the Racah parameters *B* and *C* (Figure 1).^[31–33] In this region, the respective spin-allowed ${}^3A_{2g} \rightarrow {}^3T_{2g}$ and spin-forbidden/spin-flip ${}^3A_{2g} \rightarrow {}^1E_g$ transitions are very close in energy.^[17,21–23,25] This leads to an interconfigurational interaction, which is manifested in the high intensity of the spin-

forbidden 1E_g band. This observation has been discussed already by Jørgensen and Ballhausen.^{121,341} The intensity borrowing^[35] of the spin-forbidden 1E_g state from the spin-allowed $^3T_{2g}$ state can be described qualitatively by $I = \text{const} (\gamma^2 / \Delta E^2)^{211}$ with the coupling constant of the states $\gamma = 6^{1/2} \lambda^{1341}$ (λ = spin-orbit coupling constant) and $\Delta E = E(^3T_{2g}) - E(^1E_g)$, the energy difference of the $^3T_{2g}$ and 1E_g states. According to this relation, mixing of these states becomes very effective for small energy differences and strong spin-orbit coupling. The resulting UV/Vis/NIR spectra of octahedral nickel(II) complexes,^{135–371} have been further reproduced with a quantitative theoretical model developed by Neuhauser et al.^[38] to obtain the coupling constant γ from the mixing of these states.

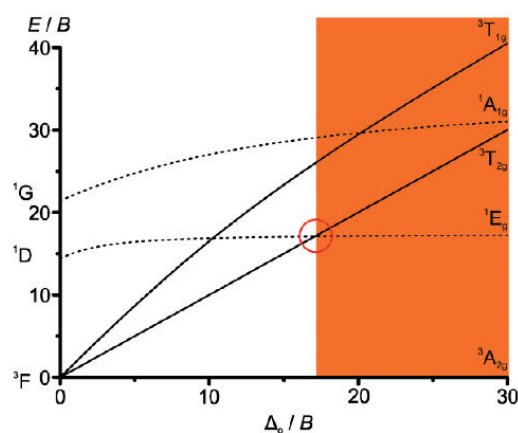


Figure 1. Partial Tanabe Sugano diagram ($B/C = 4.71$) with crossing point of the 1E_g and $^3T_{2g}$ states highlighted and marked region with $E(^1E_g) < E(^3T_{2g})$.

Far right from the $^1E_g/{}^3T_{2g}$ crossing point, namely at very high ligand field strength, a phosphorescent emission from the 1E_g state could be possible by blocking the back intersystem crossing to the $^3T_{2g}$ state, analogously to the molecular near-IR emitter of chromium(III) (Figure 1).¹¹¹ On the other hand, $^3T_{2g}$ fluorescence of nickel(II) doped into MgO and other host lattices has been observed, suggesting a ligand field splitting Δ_0 below the crossing point.^{139–421}

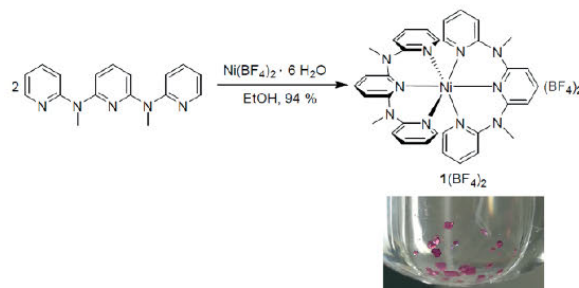
In this study, $[\text{Ni}(\text{ddpd})_2]^{2+}$ (1^{2+}) is described with respect to its ligand field properties, covering synthesis, single-crystal X-ray diffraction, paramagnetic ^1H NMR spectroscopy, magnetic susceptibility measurements, UV/Vis/NIR spectroscopy, cyclic voltammetry and density functional theory (DFT) as well as complete active space self-consistent field N-electron valence state perturbation theory (CASSCF-NEVPT2) calculations.

Results and Discussion

Synthesis, Geometric Structure, and Electrochemistry

The tridentate ligand ddpd cleanly reacts with $\text{Ni}(\text{BF}_4)_2 \cdot 6 \text{H}_2\text{O}$ in EtOH to form the homoleptic complex

$[\text{Ni}(\text{ddpd})_2](\text{BF}_4)_2$ as a pink crystalline solid in excellent yield (94%) (Scheme 2).



Scheme 2. Synthesis of $1(\text{BF}_4)_2$ and photograph of crystals of $1(\text{BF}_4)_2$.

Single crystals suitable for X-ray diffraction were obtained from diffusion of ethyl ether into a concentrated solution of $1(\text{BF}_4)_2$ in MeCN. $1(\text{BF}_4)_2$ crystallizes as $[\text{Ni}(\text{ddpd})_2](\text{BF}_4)_2 \cdot 2\text{MeCN}$ in the orthorhombic space group $Fddd$, isostructural to homoleptic *mer*- $[M(\text{ddpd})_2](\text{BF}_4)_2 \cdot 2\text{MeCN}$ ($M = \text{Fe}$,^[6] Co ,^[13] Zn ^[15]). The NiN_6 coordination arrangement corresponds to a slightly compressed octahedron with four longer Ni–N bonds to the peripheral pyridine rings [Ni1–N1: 2.0923(15) Å] and two slightly shorter bonds to the central pyridine rings [Ni1–N2: 2.058(2) Å] (Figure 2a).

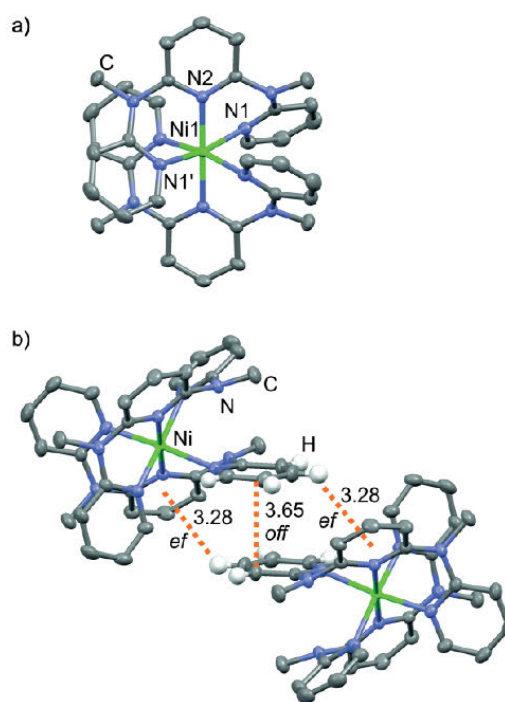


Figure 2. (a) Molecular structure of the cation of $[\text{Ni}(\text{ddpd})_2](\text{BF}_4)_2 \cdot 2\text{MeCN}$ with partial atom numbering (thermal ellipsoids set at 50% probability, hydrogen atoms are omitted for clarity). (b) π interactions between the cations (distances in Å, only relevant hydrogen atoms are shown).

For tpy complexes, e.g. $[\text{Ni}(\text{tpy})_2](\text{ClO}_4)_2 \cdot 0.5\text{H}_2\text{O}$ with Ni–N distances of 1.999(2) and 2.117(2) Å in average, respectively, the octahedral compression is much more pronounced.^[43] The N–Ni–N angles spanned by a single ddpd ligand amount to 84.64(4)° (N1–Ni1–N2) and 169.28(8)° (N1–Ni1–N1'), respectively. These angles are significantly larger than those of $[\text{Ni}(\text{tpy})_2](\text{ClO}_4)_2 \cdot 0.5\text{H}_2\text{O}$ [77.74(8)°, 155.40(8)°].^[43] On the other hand they deviate stronger from the ideal octahedral values of 90° and 180° than those of the low-spin $[\text{Fe}(\text{ddpd})_2]^{2+}$ complex.^[6] The packing of the cations in $[\text{Ni}(\text{ddpd})_2](\text{BF}_4)_2 \cdot 2\text{MeCN}$ can be described with intermolecular π interactions with one offset face-to-face (*off*) and two edge-to-face (*ef*) interactions between ligands of two neighboring complex cations (Figure 2b), typical for meridional complexes with aromatic *N*-donor ligands.^[44–46]

Density functional theory calculations (CPCM(acetonitrile)-RJCOSX-B3LYP-D3BJ-ZORA/dcf2-SVP) essentially reproduce the Ni–N distances (2.070–2.093 Å) and N–Ni–N bond angles (85.7–171.3°) of the structure determined in the solid state.

The quasireversible electrochemical oxidation of I^{2+} to nickel(III) in acetonitrile/ $n\text{Bu}_4\text{N}][\text{PF}_6]$ occurs at $E_{1/2} = 1.22$ V, followed by an irreversible oxidation at $E_p = 1.71$ V vs. ferrocene (Figure S1, Supporting Information). The latter process is ligand centered.^[15] Electrochemical reduction of I^{2+} is irreversible (–2.03 V). Further cathodic waves in the range from –1.5 to 0.5 V are associated to follow-up products.

Magnetic and Electronic Properties

The ^1H NMR spectrum of $\text{I}(\text{BF}_4)_2$ in CD_3CN shows the expected set of seven paramagnetically shifted resonances in the range $\delta = 2.81$ –106 ppm (Figure S2, Supporting Information). Since ^1H , ^1H COSY and NOESY experiments did not yield any correlations, merely the resonance at $\delta = 2.81$ ppm can be assigned to the protons of the methyl groups based on the integral of these resonances.

A $\chi_{\text{M}}T$ value of $1.11 \text{ cm}^3 \cdot \text{K} \cdot \text{mol}^{-1}$ is observed at room temperature. This is slightly higher than the expected value of $1.00 \text{ cm}^3 \cdot \text{K} \cdot \text{mol}^{-1}$ for an $S = 1$ ion. With a *g*-value of 2.12 for nickel(II) ion, a perfect match with the susceptibility data is obtained, in full agreement with reported *g*-values for Ni^{II} .^[47] The $\chi_{\text{M}}T$ value remains constant down to 8 K as expected for a simple paramagnet (Figure S3, Supporting Information). Further cooling leads to a drop of the $\chi_{\text{M}}T$ value to $0.86 \text{ cm}^3 \cdot \text{K} \cdot \text{mol}^{-1}$ at 2 K. This can be either due to zero field splitting (ZFS) or weak antiferromagnetic intermolecular interactions (Figure 2b). To estimate the ZFS parameter *D*, field dependent magnetization data were collected between 10 K and 2 K. No saturation of the magnetization even at low temperatures and high fields can be observed, indicating a strong ZFS. The field dependence of the magnetization reaches a value of $2.02 N\mu_{\text{B}}$ at 2 K and 7 T, which is slightly higher than the expected one of $2 N\mu_{\text{B}}$. Satisfactory simulations of the data were obtained either with $D = +2.98(11) \text{ cm}^{-1}$ and $g = 2.13(1)$ (Figure S4, Supporting Information) or with $D = -4.62(18) \text{ cm}^{-1}$ and $g = 2.15(1)$ (Figure S5, Supporting Infor-

mation). According to the crystallographic data (*vide supra*), a compressed octahedral coordination arrangement is present in $[\text{Ni}(\text{ddpd})_2]^{2+}$. This should result in a positive *D* value, which is also supported by CASSCF(12,7)-DLPNO-NEVPT2 calculations (def2-SVP, def2-JK, RI-JK, ZORA, CPCM(acetonitrile)) with $D_{\text{calcd}} = +3.56 \text{ cm}^{-1}$. On the other hand, the related bis(terpyridine)nickel(II) complex with strongly compressed octahedral environment features a negative ZFS with $D = -6.10 \text{ cm}^{-1}$.^[47] Rajaraman and co-workers have shown that the sign and magnitude of *D* for $[\text{Ni}(\text{iz})_6]^{2+}$ (*iz*, 1*H*-imidazole) strongly depends on the counterions, which induce structural deviations in $[\text{Ni}(\text{iz})_6]^{2+}$.^[48] These subtle effects are extremely difficult to reproduce computationally in some cases.^[48]

In the UV/Vis/NIR absorption spectrum of $\text{I}(\text{BF}_4)_2$ in MeCN the spin-allowed ligand field transitions appear at $\lambda = 521 \text{ nm}$ ($^3\text{A}_{2g} \rightarrow ^3\text{T}_{1g}$; 19200 cm^{-1}) and at $\lambda = 787 \text{ nm}$ ($^3\text{A}_{2g} \rightarrow ^3\text{T}_{2g}$; 12700 cm^{-1} ; Gaussian deconvolution) (Figure 3). The $^3\text{T}_{2g}$ band features a pronounced shoulder assigned to the spin-flip transition $^3\text{A}_{2g} \rightarrow ^1\text{E}_g$. Gaussian deconvolution results in a band at $\lambda = 885 \text{ nm}$ (11300 cm^{-1}) for this spin-flip (Figure 3b). The small discrepancy of the fit can be traced back to a symmetry lower than O_h (*vide supra*), slightly lifting the orbital degeneracy of the excited states (*vide infra*) and consequently requiring more than two bands.

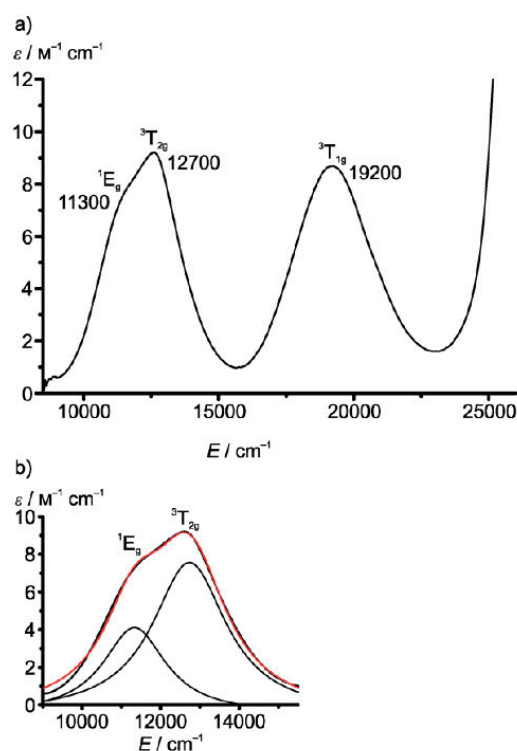


Figure 3. (a) UV/Vis/NIR spectrum of $\text{I}(\text{BF}_4)_2$ in acetonitrile with absorption band assignments. (b) Gaussian deconvolution of overlapping $^1\text{E}_g$ and $^3\text{T}_{2g}$ bands, fitted curve in red.

The relatively high intensity of the spin-forbidden $^1\text{E}_g$ absorption is due to an interconfigurational interaction with the

Table 1. Electronic data and ligand field parameters of polypyridine complexes of nickel(II) (E , Δ_o , B , C / cm^{-1}).

	1E_g	${}^3T_{2g}$	${}^3T_{1g}$	Δ_o	B ^{d)}	C ^{d)}	B/C
1^{2+} ^{a)}	11300	12700	19200	12700	734	2840	3.87
2^{2+} ^{b)} [17]	10600	12350	18500	12350	682	2680	3.94
3^{2+} ^{c)} [25]	11800	12700	19300	12700	754	3010	3.99
4^{2+} ^{c)} [25]	11500	12800	19200	12800	711	3020	4.25

a) In acetonitrile. b) In the solid state. c) In methanol. d) All Racah parameters given in this work were calculated from equations given in reference^[49].

energetically close lying ${}^3T_{2g}$ state enabled by spin-orbit coupling effects.^[35] The energy of the ${}^3T_{2g}$ term equals the ligand field strength Δ_o . The Racah parameters B and C can be determined from the energies of the ${}^3T_{1g}$ and 1E_g states (Table 1).^[31–33,49] The ligand field parameters Δ_o , B , C of 1^{2+} are very similar to those of the tris(bipyridine)nickel(II) complex 3^{2+} . In comparison with the related bis(tridentate) complex 2^{2+} , the tridentate ddpd ligand induces a stronger ligand field than the tpy ligand by 350 cm^{-1} . A further observation is that the B/C ratio is significantly smaller than the Tanabe-Sugano diagrams typically shown in textbooks ($B/C = 4.71$) (Figure 1).^[50,51]

CASSCF(12,7)-DLPNO-NEVPT2 calculations (def2-SVP, def2-JK, RI-JK, ZORA, CPCM(acetonitrile)) were performed with a geometry optimized structure of 1^{2+} (CPCM(acetonitrile)-RI-B3LYP-D3BJ-ZORA/def2-SVP) and an active space consisting of the ligand field orbitals t_{2g} , e_g in idealized O_h symmetry and the two Ni–N σ bonding counterparts to the e_g orbitals (Figure 4a).

The degeneracy of the calculated ${}^3T_{2g}$, ${}^3T_{1g}$, and the 2E_g states is lifted only slightly (Figure 4b). The averaged calculated excited triplet state energies, corresponding to the ${}^3T_{2g}$ ($E_{\text{calcd}} = 12120\text{ cm}^{-1}$) and ${}^3T_{1g}$ ($E_{\text{calcd}} = 19890\text{ cm}^{-1}$) states in O_h symmetry, fit very well to the experimental observations. On the other hand, the 1E_g state is calculated 2880 cm^{-1} above the ${}^3T_{2g}$ state in average, which is at odds with the experimental assignment. Probably, the inclusion of spin-orbit coupling, the increase of the active space or the usage of triple- ζ basis sets could improve the theoretical results. Yet, this is beyond the scope of the current study. In a CASSCF(8,13) study of $[\text{Ni}(\text{H}_2\text{O})_6]^{2+}$ by Reber and co-workers, only the energies of the triplet states were reported and hence a comparison concerning the accuracy of relative energies of singlet and triplet states in octahedral Ni^{II} complexes is impossible.^[52] A further improvement concerning the accuracy of calculated transition energies may be achieved by ligand field DFT calculations, which gave good results for hexaaqua complexes of 3d metal ions $V^{2+/3+}$ -Ni²⁺.^[53]

Conclusions

The geometry of the novel homoleptic nickel(II) complex $[\text{Ni}(\text{ddpd})_2]^{2+}$ is closer to octahedral symmetry than that of $[\text{Ni}(\text{tpy})_2]^{2+}$ both in terms of Ni–N bond lengths and in terms of N–Ni–N bond angles. This coordination arrangement exerts a stronger ligand field splitting by 350 cm^{-1} . However, the 1E_g spin-flip excited state is still close to the lowest energy ${}^3T_{2g}$ ligand field state. This allows for intensity borrowing of the

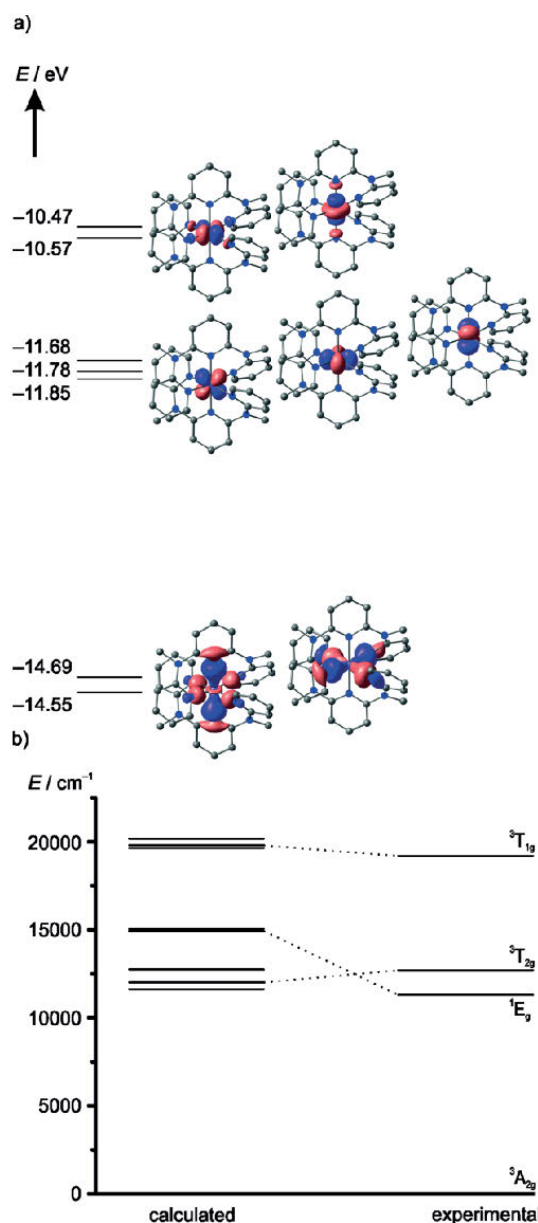


Figure 4. (a) Calculated energies of active orbitals of the CASSCF(12,7)-DLPNO-NEVPT2 calculation (def2-SVP, def2-JK, RI-JK, ZORA, CPCM(acetonitrile), isosurface value: 0.05). (b) Calculated and experimental energies of lowest singlet and triplet states.

spin-forbidden absorption but precludes luminescence from the spin-flip state. The smaller distortion of $[\text{Ni}(\text{ddpd})_2]^{2+}$ also furnishes a smaller absolute value of the zero field splitting parameter D than found for $[\text{Ni}(\text{tpy})_2]^{2+}$.

Experimental Section

General Procedures: Nickel(II) tetrafluoroborate hexahydrate was purchased from Acros Organics and used without further purification. N,N' -Dimethyl- N,N' -dipyridin-2-ylpyridine-2,6-diamine (ddpd) was prepared according to the literature.¹¹ UV/Vis/NIR spectra were recorded with a Varian Cary 5000 spectrometer in 1 cm cuvettes. IR spectra were recorded with a Bruker Alpha FT-IR spectrometer with ATR unit, containing a diamond crystal. NMR spectra were recorded with a Bruker Avance DRX 400 spectrometer at 400.31 MHz (^1H) at 25 °C. All resonances are reported in ppm vs. the solvent signal as internal standard: CD_3CN (^1H , $\delta = 1.94$ ppm).¹⁵⁴ ESI⁺ mass spectra were obtained with a Micromass QToF Ultima API mass spectrometer from acetonitrile solutions of the analyte. Elemental analysis was performed in the microanalytical laboratory of the chemical institutes of the University of Mainz. DC magnetic studies were performed with a Quantum Design MPMS-XL-7 SQUID magnetometer on powdered microcrystalline samples embedded in eicosane to avoid orientation of the crystallites under applied field. Experimental susceptibility data were corrected for the underlying diamagnetism using Pascal's constants. The temperature dependent magnetic contribution of the holder and of the embedding matrix eicosane were experimentally determined and subtracted from the measured susceptibility data. Variable temperature susceptibility data were collected in a temperature range of 2–300 K under an applied field of 1 Tesla, while magnetization data were collected between 2 and 10 K and magnetic fields up to 7 Tesla. The program phi was used for fitting of the data.¹⁵⁵ Electrochemical experiments were carried out with a BioLogic SP-50 voltammetric analyzer using a platinum working electrode, a platinum wire as counter electrode, and a 0.01 M Ag/AgNO_3 CH_3CN electrode as reference electrode. The measurements were carried out at a scan rate of 100 mV s^{-1} for cyclic voltammetry experiments using 0.1 M $[\text{nBu}_4\text{N}][\text{PF}_6]$ as supporting electrolyte and 0.002 M of the sample in dichloromethane. Potentials are given relative to the ferrocene / ferrocenium couple.

Crystal Structure Determination: Intensity data were collected with a Bruker AXS Smart1000 CCD diffractometer with an APEX II detector and an Oxford cooling system using $\text{Mo-K}\alpha$ radiation ($\lambda = 0.71073$ Å) at 193(2) K. The diffraction frames were integrated using the Bruker SMART software package¹⁵⁶ and most were corrected for absorption with MULABS¹⁵⁷ of the PLATON software package¹⁵⁸. The structure was solved by direct methods and refined by the full-matrix method based on F^2 using the SHELXL software package.^{159,60} All non-hydrogen atoms were refined anisotropically, whereas the positions of all hydrogen atoms were generated with appropriate geometric constraints and allowed to ride on their respective parent atoms with fixed isotropic thermal parameters.

Crystal Data: $\text{C}_{38}\text{H}_{40}\text{B}_2\text{F}_8\text{N}_{12}\text{Ni}$ (897.15); orthorhombic; $Fddd$; $a = 14.1388(4)$ Å, $b = 21.4518(6)$ Å, $c = 26.1391(8)$ Å, $V = 7928.1(4)$ Å³; $Z = 8$; density, calcd. = 1.503 $\text{g}\cdot\text{cm}^{-3}$, $\mu = 0.574$ mm⁻¹; $F(000) = 3696$; crystal size 0.520 × 0.400 × 0.310 mm; $\theta = 1.893$ – 28.183° ; $-18 \leq h \leq 18$, $-28 \leq k \leq 28$, $-34 \leq l \leq 34$; reflection collected = 67194; reflection unique = 2433 [$R(\text{int}) = 0.0463$]; completeness to $\theta = 25.242^\circ = 100.0\%$; semi empirical absorption correction from equivalents; max. and min. transmission 1.11511 and 0.86897; data 2433;

restraints 3, parameters 168; goodness-of-fit on $F^2 = 1.149$; final indices [$I > 2\sigma(I)$] $R_1 = 0.0388$, $wR_2 = 0.1067$; R indices (all data) $R_1 = 0.0417$, $wR_2 = 0.1082$; largest diff. peak and hole 0.448 and -0.425 e $\cdot\text{Å}^{-3}$.

Crystallographic data (excluding structure factors) for the structure in this paper have been deposited with the Cambridge Crystallographic Data Centre, CCDC, 12 Union Road, Cambridge CB21EZ, UK. Copies of the data can be obtained free of charge on quoting the depository number CCDC-1829268 (Fax: +44-1223-336-033; E-Mail: deposit@ccdc.cam.ac.uk, http://www.ccdc.cam.ac.uk).

DFT Calculations: DFT calculations were carried out using the ORCA program package (version 4.0.1).¹⁶¹ All calculations were performed using the B3LYP functional^[62–64] and employ the RIJCOSX approximation.^[65,66] Relativistic effects were calculated at the zeroth order regular approximation (ZORA) level.¹⁶⁷ The ZORA keyword automatically invokes relativistically adjusted basis sets. To account for solvent effects, a conductor-like screening model (CPCM) modeling acetonitrile was used in all calculations.^[68] Geometry optimizations were performed using Ahlrichs' split-valence double- ξ basis set def2-SVP which comprises polarization functions for all non-hydrogen atoms.^[69,70] Atom-pairwise dispersion correction was performed with the Becke-Johnson damping Scheme (D3BJ).^[71,72] The presence of energy minima was checked by numerical frequency calculations. Explicit counterions and/or solvent molecules were not taken into account.

CASSCF Calculations: In the CASSCF calculations, dynamic electron correlation was taken into account by internally contracted N-electron valence state perturbation theory (NEVPT2)^[73–75] in the domain based local pair natural orbital (DLPNO)^[76] approach. To obtain the ZFS parameter D , the DOSOC keyword has been included. D is calculated by using second-order perturbation theory. For CASSCF(12,7)-DLPNO-NEVPT2 calculations (def2-SVP,^[69,70] def2-JK,^[77] RI-JK,^[78,79] ZORA,¹⁶⁷ CPCM(acetonitrile)^[68]), the active space consisted of the ligand field orbitals t_{2g} , e_g in idealized O_h symmetry and of the two Ni–N σ bonding counterparts to the e_g orbitals, corresponding to 12 electrons correlated in 7 active orbitals.

Synthesis of $1(\text{BF}_4)_2$: $\text{Ni}(\text{BF}_4)_2 \cdot 6\text{H}_2\text{O}$ (42.2 mg, 0.123 mmol, 1.0 equiv.) was dissolved in ethanol (1.0 mL) whilst stirring to give a pale green solution. A solution of ddpd (82.5 mg, 0.270 mmol, 2.2 equiv.) in ethanol (1.4 mL) was added while stirring at ambient temperature. A pinkish solid precipitated immediately. Diethyl ether was added (15 mL) to complete the precipitation. The solid was filtered off and washed with diethyl ether (20 mL). The solvent was removed under reduced pressure to give a pinkish powder. Yield: 94.5 mg (0.116 mmol, 94%) $\text{C}_{34}\text{H}_{34}\text{B}_2\text{F}_8\text{NiN}_{10}$; calcd. C 50.11; H 4.21; N 17.19%; found: C 49.64; H 4.21; N 17.13%. IR (ATR): $\tilde{\nu} = 1583$ (m), 1571 (m), 1492 (m), 1476 (w), 1451 (m), 1428 (s), 1364 (w), 1335 (m), 1311 (vw), 1255 (vw), 1230 (w), 1175 (vw), 1152 (vw), 1133 (m), 1051 (vs. b), 1034 (vs. b), 944 (m), 863 (w), 810 (m), 777 (s), 752 (m), 740 (m), 709 (w), 641 (vw), 624 (vw), 579 (m), 512 (m), 449 (vw), 426 (w) cm^{-1} . MS (ESI⁺, MeCN): m/z (%) = 320.11 (96) $[\text{M} - (\text{BF}_4)_2]^{2+}$, 727.23 (100) $[\text{M} - \text{BF}_4]^+$. ^1H NMR (CD_3CN , 400.31 MHz): $\delta = 106$ (br, s), 65.0 (s, 2 H), 53.0 (s, 2 H), 41.4 (s, 2 H), 17.0 (s, 1 H), 10.70 (s, 2 H), 2.81 (s, 6 H, H^9) ppm. UV/Vis/NIR (MeCN): λ ($\epsilon / \text{M}^{-1}\cdot\text{cm}^{-1}$) = 521 (8.69), 787 (7.56), 885 (4.11) nm. CV (CH_3CN , $[\text{nBu}_4\text{N}][\text{PF}_6]$): $E_{1/2} / E_p = -2.03$ (irr.), +1.22 (qrev.), +1.71 (irr.) V vs. $\text{FcH} / \text{FcH}^+$.

Supporting Information (see footnote on the first page of this article): Spectral, analytical and computational data of $1(\text{BF}_4)_2$; Cyclic voltam-

mogram, ^1H NMR spectrum, T vs. T plot, M vs. B plots including simulations, ATR-IR spectrum, ESI^+ mass spectrum, DFT calculated coordinates.

Acknowledgements

Parts of this research were conducted using the supercomputer Mogon and advisory services offered by the Johannes Gutenberg University Mainz (www.hpc.uni-mainz.de), which is a member of the AHRP and the Gauss Alliance e.V. We thank *Regine Jung-Pothmann* for the collection of the diffraction data and *Dr. Mihail Mondeshki* for help with the paramagnetic NMR experiments.

Keywords: Spin-flip; Ligand field theory; N ligands; Tridentate ligands; Nickel

References

- [1] A. Breivogel, C. Förster, K. Heinze, *Inorg. Chem.* **2010**, *49*, 7052–7056.
- [2] A. Breivogel, C. Kreitner, K. Heinze, *Eur. J. Inorg. Chem.* **2014**, *2014*, 5468–5490.
- [3] A. Breivogel, M. Meister, C. Förster, F. Laquai, K. Heinze, *Chem. Eur. J.* **2013**, *19*, 13745–13760.
- [4] A. Breivogel, M. Park, D. Lee, S. Klassen, A. Kühnle, C. Lee, K. Char, K. Heinze, *Eur. J. Inorg. Chem.* **2014**, *2014*, 288–295.
- [5] A. Breivogel, S. Wooh, J. Dietrich, T. Y. Kim, Y. S. Kang, K. Char, K. Heinze, *Eur. J. Inorg. Chem.* **2014**, *2014*, 2720–2734.
- [6] A. K. C. Mengel, C. Förster, A. Breivogel, K. Mack, J. R. Ochsmann, F. Laquai, V. Ksenofontov, K. Heinze, *Chem. Eur. J.* **2015**, *21*, 704–714.
- [7] A. K. C. Mengel, C. Bissinger, M. Dorn, O. Back, C. Förster, K. Heinze, *Chem. Eur. J.* **2017**, *23*, 7920–7931.
- [8] S. Otto, M. Grabolle, C. Förster, C. Kreitner, U. Resch-Genger, K. Heinze, *Angew. Chem.* **2015**, *127*, 11735–11739; *Angew. Chem. Int. Ed.* **2015**, *54*, 11572–11576.
- [9] S. Otto, A. M. Nauth, E. Ermilov, N. Scholz, A. Friedrich, U. Resch-Genger, S. Lochbrunner, T. Opatz, K. Heinze, *ChemPhotoChem.* **2017**, *1*, 344–349.
- [10] C. Wang, S. Otto, M. Dorn, E. Kreidt, J. Lebon, L. Sršan, P. Di Martino-Fumo, M. Gerhards, U. Resch-Genger, M. Seitz, K. Heinze, *Angew. Chem.* **2018**, *130*, 1125–1130; *Angew. Chem. Int. Ed.* **2018**, *57*, 1112–1116.
- [11] S. Otto, M. Dorn, C. Förster, M. Bauer, M. Seitz, K. Heinze, *Coord. Chem. Rev.* **2018**, *359*, 102–111.
- [12] K. Mack, A. Wünsche von Leupoldt, C. Förster, M. Ezhevskaya, D. Hinderberger, K. W. Klinkhammer, K. Heinze, *Inorg. Chem.* **2012**, *51*, 7851–7858.
- [13] C. Förster, K. Mack, L. M. Carrella, V. Ksenofontov, E. Rentschler, K. Heinze, *Polyhedron* **2013**, *52*, 576–581.
- [14] C. Förster, T. E. Gorelik, U. Kolb, V. Ksenofontov, K. Heinze, *Eur. J. Inorg. Chem.* **2015**, *2015*, 920–924.
- [15] S. Otto, J. Moll, C. Förster, D. Geißler, C. Wang, U. Resch-Genger, K. Heinze, *Eur. J. Inorg. Chem.* **2017**, *2017*, 5033–5040.
- [16] J. S. Judge, W. A. Baker, *Inorg. Chim. Acta* **1967**, *1*, 245–248.
- [17] W. Henke, D. Reinen, *Z. Anorg. Allg. Chem.* **1977**, *436*, 187–200.
- [18] R. Prasad, D. B. Scaife, *J. Electroanal. Chem. Interfacial Electrochem.* **1977**, *84*, 373–386.
- [19] J. England, E. Bill, T. Weyhermüller, F. Neese, M. Atanasov, K. Wieghardt, *Inorg. Chem.* **2015**, *54*, 12002–12018.
- [20] F. Basolo, J. C. Hayes, H. M. Neumann, *J. Am. Chem. Soc.* **1954**, *76*, 3807–3809.
- [21] C. K. Jørgensen, L. H. Smith, G. Hanshoff, H. Prydz, *Acta Chem. Scand.* **1955**, *9*, 1362–1377.
- [22] M. A. Robinson, J. D. Curry, D. H. Busch, *Inorg. Chem.* **1963**, *2*, 1178–1181.
- [23] R. D. Hancock, G. J. McDougall, *J. Chem. Soc., Dalton Trans.* **1977**, 67–70.
- [24] R. A. Palmer, T. S. Piper, *Inorg. Chem.* **1966**, *5*, 864–878.
- [25] D. A. V. Griend, D. K. Bediako, M. J. DeVries, N. A. DeJong, L. P. Heeringa, *Inorg. Chem.* **2008**, *47*, 656–662.
- [26] C. Arana, S. Yan, M. Keshavarz, K. T. Potts, H. D. Abruña, *Inorg. Chem.* **1992**, *31*, 3680–3682.
- [27] C. Arana, M. Keshavarz, K. T. Potts, H. D. Abruña, *Inorg. Chim. Acta* **1994**, *225*, 285–295.
- [28] J. A. Ramos Sende, C. R. Arana, L. Hernandez, K. T. Potts, M. Keshavarz-K, H. D. Abruña, *Inorg. Chem.* **1995**, *34*, 3339–3348.
- [29] N. Elgrishi, M. B. Chambers, V. Artero, M. Fontecave, *Phys. Chem. Chem. Phys.* **2014**, *16*, 13635–13644.
- [30] M. F. Kuehnle, K. L. Orchard, K. E. Dalle, E. Reisner, *J. Am. Chem. Soc.* **2017**, *139*, 7217–7223.
- [31] Y. Tanabe, S. Sugano, *J. Phys. Soc. Jpn.* **1954**, *9*, 753–766.
- [32] Y. Tanabe, S. Sugano, *J. Phys. Soc. Jpn.* **1954**, *9*, 766–779.
- [33] G. Racah, *Phys. Rev.* **1942**, *62*, 438–462.
- [34] A. D. Liehr, C. J. Ballhausen, *Ann. Phys.* **1959**, *6*, 134–155.
- [35] E. González, A. Rodrigue-Witchel, C. Reber, *Coord. Chem. Rev.* **2007**, *251*, 351–363.
- [36] M.-C. Nolet, A. Michaud, C. Bain, D. Zargarian, C. Reber, *Photochem. Photobiol.* **2006**, *82*, 57–63.
- [37] G. Bussièrre, C. Reber, D. Neuhauser, D. A. Walter, J. I. Zink, *J. Phys. Chem. A* **2003**, *107*, 1258–1267.
- [38] D. Neuhauser, T. J. Park, J. I. Zink, *Phys. Rev. Lett.* **2000**, *85*, 5304–5307.
- [39] J. E. Ralph, M. G. Townsend, *J. Phys. C* **1970**, *3*, 8.
- [40] M. V. Iverson, W. A. Sibley, *J. Lumin.* **1979**, *20*, 311–324.
- [41] B. Wu, S. Zhou, J. Ruan, Y. Qiao, D. Chen, C. Zhu, J. Qiu, *Opt. Express* **2008**, *16*, 1879.
- [42] C. Lin, L. Li, S. Dai, C. Liu, Z. Zhao, C. Bocker, C. Rüssel, *J. Phys. Chem. C* **2016**, *120*, 4556–4563.
- [43] C. Anderer, C. Näthor, W. Bensch, *IUCrData* **2016**, *1*, 1373.
- [44] E. C. Constable, K. Harris, C. E. Housecroft, M. Neuburger, J. A. Zampese, *CrystEngComm* **2010**, *12*, 2949.
- [45] C. Janiak, *J. Chem. Soc., Dalton Trans.* **2000**, 3885–3896.
- [46] M. L. Scudder, H. A. Goodwin, I. G. Dance, *New J. Chem.* **1999**, *23*, 695–705.
- [47] O. Waldmann, J. Hassmann, P. Müller, D. Volkmer, U. S. Schubert, J.-M. Lehn, *Phys. Rev. B* **1998**, *58*, 3277–3285.
- [48] S. K. Singh, T. Gupta, P. Badkur, G. Rajaraman, *Chem. Eur. J.* **2014**, *20*, 10305–10313.
- [49] K. Knox, R. G. Shulman, S. Sugano, *Phys. Rev.* **1963**, *130*, 512–516.
- [50] L. H. Gade in *Koordinationschemie, 1st Ed.*, Wiley-VCH, Weinheim, Germany **2010**.
- [51] J. E. Huheey, E. A. Keiter, R. L. Keiter, *Anorganische Chemie, 5th ed.* (Ed.: R. Steudel), de Gruyter, Berlin, Germany **2014**.
- [52] J. Landry-Hum, G. Bussièrre, C. Daniel, C. Reber, *Inorg. Chem.* **2001**, *40*, 2595–2601.
- [53] F. Vlahović, M. Perić, M. Gruden-Pavlović, M. Zlatar, *J. Chem. Phys.* **2015**, *142*, 214111.
- [54] G. R. Fulmer, A. J. M. Miller, N. H. Sherden, H. E. Gottlieb, A. Nudelman, B. M. Stoltz, J. E. Bercaw, K. I. Goldberg, *Organometallics* **2010**, *29*, 2176–2179.
- [55] N. F. Chilton, R. P. Anderson, L. D. Turner, A. Soncini, K. S. Murray, *J. Comput. Chem.* **2013**, *34*, 1164–1175.
- [56] SMART Data Collection and SAINT-Plus Data Processing Software for the SMART Systems (various versions), Bruker Analytical X-ray Instruments, Inc., Madison, Wisconsin, USA, **2000**.
- [57] R. H. Blessing, *Acta Crystallogr., Sect. A* **1995**, *51*, 33–38.
- [58] A. L. Spek, *Acta Crystallogr., Sect. D* **2009**, *65*, 148–155.
- [59] G. M. Sheldrick, *Acta Crystallogr., Sect. A* **2015**, *71*, 3–8.
- [60] G. M. Sheldrick, *SHELXL-2014/7* University of Göttingen, Göttingen, Germany, **2014**.
- [61] F. Neese, *WIREs Comput. Mol. Sci.* **2012**, *2*, 73–78.
- [62] A. D. Becke, *J. Chem. Phys.* **1993**, *98*, 5648–5652.

- [63] C. Lee, W. Yang, R. G. Parr, *Phys. Rev. B* **1988**, *37*, 785–789.
- [64] B. Michlich, A. Savin, H. Stoll, H. Preuss, *Chem. Phys. Lett.* **1989**, *157*, 200–206.
- [65] F. Neese, F. Wennmohs, A. Hansen, U. Becker, *Chem. Phys.* **2009**, *356*, 98–109.
- [66] R. Izsák, F. Neese, *J. Chem. Phys.* **2011**, *135*, 144105.
- [67] D. A. Pantazis, X.-Y. Chen, C. R. Landis, F. Neese, *J. Chem. Theory Comput.* **2008**, *4*, 908–919.
- [68] V. Barone, M. Cossi, *J. Phys. Chem. A* **1998**, *102*, 1995–2001.
- [69] F. Weigend, R. Ahlrichs, *Phys. Chem. Chem. Phys.* **2005**, *7*, 3297–3305.
- [70] F. Weigend, *Phys. Chem. Chem. Phys.* **2006**, *8*, 1057–1065.
- [71] S. Grimme, J. Antony, S. Ehrlich, H. Krieg, *J. Chem. Phys.* **2010**, *132*, 154104.
- [72] S. Grimme, S. Ehrlich, L. Goerigk, *J. Comput. Chem.* **2011**, *32*, 1456–1465.
- [73] C. Angeli, R. Cimiraglia, J.-P. Malrieu, *Chem. Phys. Lett.* **2001**, *350*, 297–305.
- [74] C. Angeli, R. Cimiraglia, S. Evangelisti, T. Leininger, J.-P. Malrieu, *J. Chem. Phys.* **2001**, *114*, 10252–10264.
- [75] C. Angeli, R. Cimiraglia, J.-P. Malrieu, *J. Chem. Phys.* **2002**, *117*, 9138–9153.
- [76] Y. Guo, K. Sivalingam, E. F. Valeev, F. Neese, *J. Chem. Phys.* **2016**, *144*, 94111.
- [77] F. Weigend, *J. Comput. Chem.* **2008**, *29*, 167–175.
- [78] F. Weigend, M. Kattannek, R. Ahlrichs, *J. Chem. Phys.* **2009**, *130*, 164106.
- [79] S. Kossmann, F. Neese, *Chem. Phys. Lett.* **2009**, *481*, 240–243.

Received: March 16, 2018

Published online: June 25, 2018

4. Summary and Outlook

The photophysical properties of vanadium(II) and vanadium(III) complexes are of considerable interest as potential substitutes for the costlier precious metal NIR emitters such as ruthenium(II), europium(III) and terbium(III) and could well complement the existing chromium(III) spin-flip systems. The exploration of their optical properties and excited state dynamics and, ultimately, the synthesis of vanadium complexes capable of room-temperature NIR emission were the main objectives of this work. In doing so, the results of this thesis should aid future ligand design and enable the preparation of more efficient molecular vanadium phosphors.

In this work, the successful preparation of two vanadium(III) room-temperature NIR-emitters is reported. This marks a significant improvement over earlier vanadium spin-flip luminophores since room temperature phosphorescence had not been achieved prior to this doctorate. The complexes described herein benefit from the favorable bite angles and σ -donor capabilities of the ddpd ligand (ddpd = *N,N'*-dimethyl-*N,N'*-dipyridin-2-ylpyridine-2,6-diamine) which leads to a favorable excited state ordering. Both the heteroleptic $\text{VCl}_3(\text{ddpd})$ and the homoleptic *mer*- $[\text{V}(\text{ddpd})_2][\text{PF}_6]_3$ exhibit NIR luminescence from spin-flip states at 77 K. The NIR emission of $\text{VCl}_3(\text{ddpd})$ and $[\text{V}(\text{ddpd})_2]^{3+}$ persists even at room temperature and their luminescence properties and ground state splitting have been examined in detail.

In solid $\text{VCl}_3(\text{ddpd})$, three NIR luminescence bands located at 9074, 8203 and 7962 cm^{-1} are observable upon irradiation at 350 nm. A room-temperature lifetime of 0.5 μs was found which fits a spin-forbidden transition. The phosphorescence pattern mirrors the triplet ground state splitting, which is corroborated by Raman spectra of solid $\text{VCl}_3(\text{ddpd})$ and quantum-chemical CAS-SCF calculations. However, irradiation at 350 nm in acetonitrile solution also leads to photolysis as evidenced by changes in the absorption spectrum and the emergence of a fluorescence band at 400 nm. On the grounds of cyclic voltammetry, TD-DFT calculations and earlier reports on M-Cl bond homolysis, a homolytic cleavage of the V-Cl bond was proposed. Irradiation at 400 nm and below leaves the complex intact and enables TA spectroscopic characterization. Excitation into the broad CT band at 400 nm yields excited state absorption at 400-470 nm. A long-lived component of the ESA was assigned to the $^1\text{E}/^1\text{T}_2$ states. Thermally activated non-radiative decay is operational in $\text{VCl}_3(\text{ddpd})$ since both luminescence intensity and lifetime increase upon cooling. An extension of the NIR luminescence lifetime from 0.5 μs to 3.3 μs in the solid state was observed upon ligand deuteration and attributed to reduced energy transfer to C-H oscillators. The finding is supported by spectral overlap integral analysis between luminescence bands and C-H/D overtones. Excited state lifetimes determined by step-scan FTIR spectroscopy are similar for both deuterated and parent complex which is due to one of two energetically close emissive states being IR-silent.

$[\text{V}(\text{ddpd})_2][\text{PF}_6]_3$ features a high ligand field splitting of $\Delta_0 \approx 36.6$ and exhibits NIR phosphorescence from singlet states at 10183 cm^{-1} and 9191/9017 cm^{-1} , in agreement with CAS-SCF calculations. A biexponential luminescence lifetime of 790 ns (93%) and 8800 ns (7%)

and a luminescence quantum yield of $\Phi = 1.8 \times 10^{-4} \%$ were determined. Additionally, fluorescence at 26737, 22371 and 15151 cm^{-1} competes with the phosphorescence at 77 K. At ambient temperature, only the high energy fluorescence band is observable with a quantum yield of $\Phi = 2.1 \%$. It is assigned to $^3\text{LMCT}$ or ligand field transitions based on TD-DFT and CAS-SCF calculations. While TA measurements at 400 nm excitation wavelength likewise indicate that a small fraction of the initially excited molecules evolves into a long lived state, measurements at lower excitation wavelength show only ground state recovery within picoseconds. Multiphonon relaxation, however, does not play a significant role in this case as the phosphorescence lifetime and intensity of the perdeuterated complex $[\text{V}(\text{D}_{17}\text{-ddpd})_2][\text{PF}_6]_3$ remain virtually unchanged with respect to the parent complex. In summary, ISC from triplet states into the singlet manifold in this complex is generally slow compared to non-radiative decay pathways other than multiphonon relaxation, despite the complexes large ligand field splitting. At excitation energies of 400 nm and above, a small fraction of the excitation state population undergoes ISC into the singlet states and yields spin-flip phosphorescence.

cis-fac- and *mer*- $[\text{V}(\text{ddpd})_2][\text{BPh}_4]_2$ could be selectively synthesized. The isomers do not interconvert spontaneously and no photoisomerization occurs under UV irradiation at 300 nm excitation wavelength. However, they are not entirely photostable as fluorescence of the protonated ligand could be detected under these conditions which grows more intense with prolonged irradiation. According to CAS-SCF-calculations, the lowest spin-flip states $^2\text{E}/^2\text{T}_1$ in both diastereomers are located more than 5000 cm^{-1} below the lowest ligand-field excited state $^4\text{T}_2$. Yet, no luminescence occurs in the title complexes even at 77 K in the solid state as low-energy $^2\text{LMCT}$ states are available that mix with ^2MC states and provide an efficient non-radiative decay pathway. Oxidation of the complexes enables spin-flip luminescence at 77 K in a butyronitrile glass from the vanadium(III) centres of both *cis-fac*- and *mer*- $[\text{V}(\text{ddpd})_2][\text{BPh}_4]_2[\text{BF}_4]$. Both isomers possess a spin-lattice relaxation time of 300 μs and a phase memory time of 1 μs at 5 K, which suggests vanadium(II) complexes could be used for the development of molecular quantum bits. In addition, the *mer* isomer displays an out-of-phase signal below 15 K at an applied external field of 4000 Oe in AC susceptometry measurements.

Apart from d^2 and d^3 vanadium complexes, the d^8 -nickel(II) complex $[\text{Ni}(\text{ddpd})_2][\text{BF}_4]_2$ was investigated for SF emission. Its N–Ni–N angles spanned by a single ddpd ligand are significantly larger than those in the analog tpy complex and hence, the title complexes LF splitting is larger by 350 cm^{-1} . Spin-allowed ligand field transitions to the $^3\text{T}_1$ and $^3\text{T}_2$ are visible in the absorption spectrum of the complex at 521 nm and at 787 nm, respectively. A high-energy shoulder of the $^3\text{A}_2 \rightarrow ^3\text{T}_2$ is assigned to the spin-forbidden $^3\text{A}_2 \rightarrow ^1\text{E}$ transition. It is observable due to an interconfigurational interaction with the energetically close lying $^3\text{T}_2$ state enabled by SOC effects. As the energetic separation of the $^3\text{T}_2$ and ^1E state is small ($\Delta E \approx 1400 \text{ cm}^{-1}$), non-radiative decay dominates and no luminescence is observed.

In summary, the employment of the electron-rich strong field ligand resulted in the successful preparation of a series of vanadium(II) and vanadium(III) complexes as well as a nickel(II) complex. The vanadium(III) complexes feature NIR-luminescence which persists even at ambient temperature. Using a variety of spectroscopic methods and quantum-chemical

calculations, a reasoning could be given for the efficient non-radiative relaxation in the vanadium(II) and nickel(II) systems. The detrimental impact of low-energy LMCT charge transfer states in vanadium(II) complexes could be solved through implementation of ligands with higher energy π orbitals. Preliminary screening of potential complexes by means of DFT calculations can help streamline the process. Improving on the vanadium(III) complexes is, however, less straightforward as the means to selectively tune ISC rates are not as straightforward. In general, the higher ligand field splitting of carbene ligands might prove useful as more crossing points to the singlet manifold become available with a higher ligand field splitting. Following the same line of argument, carbenes could aid with the disentanglement of inter- and intraconfigurational metal-centred excited states in nickel(II) complexes in the future.

5. References

- [1] D. Gielen, F. Boshell, D. Saygin, M. D. Bazilian, N. Wagner, R. Gorini, *Energy Strategy Rev.* **2019**, *24*, 38–50.
- [2] M. A. K. Khalil, *Annu. Rev. Energy. Environ.* **1999**, *24*, 645–661.
- [3] R. Almar, R. Ranasinghe, E. W. J. Bergsma, H. Diaz, A. Melet, F. Papa, M. Vousdoukas, P. Athanasiou, O. Dada, L. P. Almeida, E. Kestenare, *Nat. Commun.* **2021**, *12*, 3775.
- [4] P. von der Gathen, R. Kivi, I. Wohltmann, R. J. Salawitch, M. Rex, *Nat. Commun.* **2021**, *12*, 3886.
- [5] Y. Pokhrel, F. Felfelani, Y. Satoh, J. Boulange, P. Burek, A. Gädeke, D. Gerten, S. N. Gosling, M. Grillakis, L. Gudmundsson, N. Hanasaki, H. Kim, A. Koutroulis, J. Liu, L. Papadimitriou, J. Schewe, H. Müller Schmied, T. Stacke, C.-E. Telteu, W. Thiery, T. Veldkamp, F. Zhao, Y. Wada, *Nat. Clim. Chang.* **2021**, *11*, 226–233.
- [6] A. Hagfeldt, G. Boschloo, L. Sun, L. Kloo, H. Pettersson, *Chem. Rev.* **2010**, *110*, 6595–6663.
- [7] M. Grätzel, *J. Photochem. Photobiol. C: Photochem. Rev.* **2003**, *4*, 145–153.
- [8] M. K. Nazeeruddin, F. de Angelis, S. Fantacci, A. Selloni, G. Viscardi, P. Liska, S. Ito, B. Takeru, M. Grätzel, *J. Am. Chem. Soc.* **2005**, *127*, 16835–16847.
- [9] B. O'Regan, M. Grätzel, *Nature* **1991**, *353*, 737–740.
- [10] C.-M. Che, C.-C. Kwok, C.-F. Kui, S.-L. Lai, K.-H. Low in *Comprehensive Inorganic Chemistry II* (Hrsg.: J. Reedijk), Elsevier, Amsterdam, **2013**.
- [11] P.-T. Chou, Y. Chi, *Chem. Eur. J.* **2007**, *13*, 380–395.
- [12] S. Shi, M. C. Jung, C. Coburn, A. Tadde, D. Sylvinson M R, P. I. Djurovich, S. R. Forrest, M. E. Thompson, *J. Am. Chem. Soc.* **2019**, *141*, 3576–3588.
- [13] K. Schlingman, Y. Chen, R. S. Carmichael, T. B. Carmichael, *Adv. Mater.* **2021**, *33*, e2006863.
- [14] R. D. Costa, E. Ortí, H. J. Bolink, F. Monti, G. Accorsi, N. Armaroli, *Angew. Chem. Int. Ed.* **2012**, *51*, 8178–8211.
- [15] A. F. Holleman, N. Wiberg, *Holleman Wiberg. Grundlagen und Hauptgruppenelemente*, 103. Aufl., De Gruyter, Berlin, Boston, **2017**.
- [16] O. S. Wenger, *Chem. Eur. J.* **2019**, *25*, 6043–6052.
- [17] C. Förster, K. Heinze, *Chem. Soc. Rev.* **2020**, *49*, 1057–1070.
- [18] J. K. McCusker, *Science* **2019**, *363*, 484–488.
- [19] M. C. Carey, S. L. Adelman, J. K. McCusker, *Chem. Sci.* **2019**, *10*, 134–144.
- [20] B. C. Paulus, S. L. Adelman, L. L. Jamula, J. K. McCusker, *Nature* **2020**, *582*, 214–218.
- [21] S. Kaufhold, N. W. Rosemann, P. Chábera, L. Lindh, I. Bolaño Losada, J. Uhlig, T. Pascher, D. Strand, K. Wärnmark, A. Yartsev, P. Persson, *J. Am. Chem. Soc.* **2021**, *143*, 1307–1312.
- [22] S. G. Shepard, S. M. Fatur, A. K. Rappé, N. H. Damrauer, *J. Am. Chem. Soc.* **2016**, *138*, 2949–2952.
- [23] S. M. Fatur, S. G. Shepard, R. F. Higgins, M. P. Shores, N. H. Damrauer, *J. Am. Chem. Soc.* **2017**, *139*, 4493–4505.
- [24] L. L. Jamula, A. M. Brown, D. Guo, J. K. McCusker, *Inorg. Chem.* **2014**, *53*, 15–17.
- [25] A. K. C. Mengel, C. Förster, A. Breivogel, K. Mack, J. R. Ochsmann, F. Laquai, V. Ksenofontov, K. Heinze, *Chem. Eur. J.* **2015**, *21*, 704–714.
- [26] A. Britz, W. Gawelda, T. A. Assefa, L. L. Jamula, J. T. Yarranton, A. Galler, D. Khakhulin, M. Diez, M. Harder, G. Doumy, A. M. March, É. Bajnóczi, Z. Németh, M. Pápai, E. Rozsályi, D. Sárosiné Szemes, H. Cho, S. Mukherjee, C. Liu, T. K. Kim, R. W. Schoenlein, S. H. Southworth, L. Young, E. Jakubikova, N. Huse, G. Vankó, C. Bressler, J. K. McCusker, *Inorg. Chem.* **2019**, *58*, 9341–9350.
- [27] P. Dierks, A. Pápcke, O. S. Bokareva, B. Altenburger, T. Reuter, K. Heinze, O. Kühn, S. Lochbrunner, M. Bauer, *Inorg. Chem.* **2020**, *59*, 14746–14761.

References

- [28] J. Steube, L. Burkhardt, A. Pöpcke, J. Moll, P. Zimmer, R. Schoch, C. Wölper, K. Heinze, S. Lochbrunner, M. Bauer, *Chem. Eur. J.* **2019**, *25*, 11826–11830.
- [29] I. M. Dixon, F. Alary, M. Boggio-Pasqua, J.-L. Heully, *Dalton Trans.* **2015**, *44*, 13498–13503.
- [30] P. Chábera, Y. Liu, O. Prakash, E. Thyrhaug, A. E. Nahhas, A. Honarfar, S. Essén, L. A. Fredin, T. C. B. Harlang, K. S. Kjær, K. Handrup, F. Ericson, H. Tatsuno, K. Morgan, J. Schnadt, L. Häggström, T. Ericsson, A. Sobkowiak, S. Lidin, P. Huang, S. Styring, J. Uhlig, J. Bendix, R. Lomoth, V. Sundström, P. Persson, K. Wärnmark, *Nature* **2017**, *543*, 695–699.
- [31] K. S. Kjær, N. Kaul, O. Prakash, P. Chábera, N. W. Rosemann, A. Honarfar, O. Gordivska, L. A. Fredin, K.-E. Bergquist, L. Häggström, T. Ericsson, L. Lindh, A. Yartsev, S. Styring, P. Huang, J. Uhlig, J. Bendix, D. Strand, V. Sundström, P. Persson, R. Lomoth, K. Wärnmark, *Science* **2019**, *363*, 249–253.
- [32] M. Bauer, J. Steube, A. Pöpcke, O. Bokareva, T. Reuter, S. Demeshko, R. Schoch, S. Hohloch, F. Meyer, K. Heinze, O. Kühn, S. Lochbrunner **2020**, (submitted).
- [33] W. Leis, M. A. Argüello Cordero, S. Lochbrunner, H. Schubert, A. Berkefeld, *J. Am. Chem. Soc.* **2022**, *144*, 1169–1173.
- [34] T. H. Maiman, *Nature* **1960**, *187*, 493–494.
- [35] L. S. Forster, *Chem. Rev.* **1990**, *90*, 331–353.
- [36] O. S. Wenger, *J. Am. Chem. Soc.* **2018**, *140*, 13522–13533.
- [37] Dorn, M., East, N. R., Förster, C., Kitzmann, W. R., Moll, J., Reichenauer, F., Reuter, T., Stein, L., Heinze, K. & J. Reedijk (Hrsg.) *Comprehensive inorganic chemistry III*, Elsevier, **2022**.
- [38] A. C. Bowman, S. Sproules, K. Wiegardt, *Inorg. Chem.* **2012**, 3707–3717.
- [39] A. C. Bowman, J. England, S. Sproules, T. Weyhermüller, K. Wiegardt, *Inorg. Chem.* **2013**, 2242–2256.
- [40] S. S. Shah, A. W. Maverick, *Inorg. Chem.* **1986**, *25*, 1867–1871.
- [41] A. W. Maverick, S. S. Shah, C. Kirmaier, D. Holten, *Inorg. Chem.* **1987**, *26*, 774–776.
- [42] I. Fujita, T. Yazaki, Y. Torii, H. Kobayashi, *Bull. Chem. Soc. Jpn* **1972**, *45*, 2156–2161.
- [43] R. D. Dill, R. I. Portillo, S. G. Shepard, M. P. Shores, A. K. Rappé, N. H. Damrauer, *Inorg. Chem.* **2020**, *59*, 14706–14715.
- [44] M. S. Fataftah, S. L. Bayliss, D. W. Laorenza, X. Wang, B. T. Phelan, C. B. Wilson, P. J. Mintun, B. D. Kovos, M. R. Wasielewski, S. Han, M. S. Sherwin, D. D. Awschalom, D. E. Freedman, *J. Am. Chem. Soc.* **2020**, *142*, 20400–20408.
- [45] R. Dingle, P. J. McCarthy, C. J. Ballhausen, *J. Chem. Phys.* **1969**, *50*, 1957–1962.
- [46] C. Reber, H. U. Güdel, *J. Lumin.* **1988**, *42*, 1–13.
- [47] C. Reber, H. U. Güdel, *Chem. Phys. Lett.* **1989**, *154*, 425–431.
- [48] O. S. Wenger, H. U. Güdel, *Chem. Phys. Lett.* **2002**, *354*, 75–81.
- [49] M. D. Sturge, *Phys. Rev.* **1963**, *130*, 639–646.
- [50] A. Hauser, H. U. Güdel, *J. Lumin.* **1982**, *27*, 249–256.
- [51] B. Gaelli, A. Hauser, H. U. Guedel, *Inorg. Chem.* **1985**, *24*, 2271–2275.
- [52] R. Beaulac, P. L. W. Tregenna-Piggott, A.-L. Barra, H. Weihe, D. Luneau, C. Reber, *Inorg. Chem.* **2006**, *45*, 3399–3407.
- [53] J. R. Lakowicz, *Principles of Fluorescence Spectroscopy*, Springer US, Boston, MA, **2006**.
- [54] G. S. Ming Tong, K. T. Chan, X. Chang, C.-M. Che, *Chem. Sci.* **2015**, *6*, 3026–3037.
- [55] S. J. Strickler, R. A. Berg, *J. Chem. Phys.* **1962**, *37*, 814–822.
- [56] R. Englman, J. Jortner, *Mol. Phys.* **1970**, *18*, 145–164.
- [57] T. J. Penfold, E. Gindensperger, C. Daniel, C. M. Marian, *Chem. Rev.* **2018**, *118*, 6975–7025.
- [58] B. S. Brunschwig, N. Sutin, *Comment. Inorg. Chem.* **1987**, *6*, 209–235.
- [59] M. Hesse, H. Meier, B. Zeeh (Hrsg.) *Spektroskopische Methoden in der organischen Chemie. 102 Tabellen*, Thieme, Stuttgart, **2005**.

-
- [60] C. Doffek, N. Alzakhem, C. Bischof, J. Wahsner, T. Güden-Silber, J. Lügger, C. Platas-Iglesias, M. Seitz, *J. Am. Chem. Soc.* **2012**, *134*, 16413–16423.
- [61] R. L. Swofford, M. E. Long, M. S. Burberry, A. C. Albrecht, *J. Chem. Phys.* **1977**, *66*, 664–668.
- [62] V. L. Ermolaev, E. B. Sveshnikova, *Russ. Chem. Rev.* **1994**, *63*, 905–922.
- [63] T. Förster, *Ann. Phys. (Berlin, Ger.)* **1948**, *437*, 55–75.
- [64] C. Wang, S. Otto, M. Dorn, E. Kreidt, J. Lebon, L. Sršan, P. Di Martino-Fumo, M. Gerhards, U. Resch-Genger, M. Seitz, K. Heinze, *Angew. Chem. Int. Ed.* **2018**, *57*, 1112–1116.
- [65] S. Otto, M. Grabolle, C. Förster, C. Kreitner, U. Resch-Genger, K. Heinze, *Angew. Chem. Int. Ed.* **2015**, *54*, 11572–11576.
- [66] D. L. Dexter, *J. Chem. Phys.* **1953**, *21*, 836–850.
- [67] C. M. Marian, *WIREs Comput. Mol. Sci.* **2012**, *2*, 187–203.
- [68] A. Steffen, B. Hupp in *Comprehensive Coordination Chemistry III*, pp. 5-7
- [69] K. Suzuki, A. Kobayashi, S. Kaneko, K. Takehira, T. Yoshihara, H. Ishida, Y. Shiina, S. Oishi, S. Tobita, *Phys. Chem. Chem. Phys.* **2009**, *11*, 9850–9860.
- [70] A. Juris, V. Balzani, F. Barigelletti, S. Campagna, P. Belser, A. von Zelewsky, *Coord. Chem. Rev.* **1988**, *84*, 85–277.
- [71] S. Koseki, N. Matsunaga, T. Asada, M. W. Schmidt, M. S. Gordon, *J. Phys. Chem. A* **2019**, *123*, 2325–2339.
- [72] W. Gawelda, A. Cannizzo, V.-T. Pham, F. van Mourik, C. Bressler, M. Chergui, *J. Am. Chem. Soc.* **2007**, *129*, 8199–8206.
- [73] G. Auböck, M. Chergui, *Nat. Chem.* **2015**, *7*, 629–633.
- [74] C. Bressler, C. Milne, V.-T. Pham, A. Elnahas, R. M. van der Veen, W. Gawelda, S. Johnson, P. Beaud, D. Grolimund, M. Kaiser, C. N. Borca, G. Ingold, R. Abela, M. Chergui, *Science* **2009**, *323*, 489–492.
- [75] C. Consani, M. Prémont-Schwarz, A. Elnahas, C. Bressler, F. van Mourik, A. Cannizzo, M. Chergui, *Angew. Chem. Int. Ed.* **2009**, *48*, 7184–7187.
- [76] A. Cannizzo, C. J. Milne, C. Consani, W. Gawelda, C. Bressler, F. van Mourik, M. Chergui, *Coord. Chem. Rev.* **2010**, *254*, 2677–2686.
- [77] J. K. McCusker, K. N. Walda, R. C. Dunn, J. D. Simon, D. Magde, D. N. Hendrickson, *J. Am. Chem. Soc.* **1993**, *115*, 298–307.
- [78] L. Ferrari, M. Satta, A. Palma, L. Di Mario, D. Catone, P. O’Keeffe, N. Zema, T. Prospero, S. Turchini, *Front. Chem.* **2019**, *7*, 348.
- [79] E. M. S. Maçôas, R. Kananavicius, P. Myllyperkiö, M. Pettersson, H. Kunttu, *J. Phys. Chem. A* **2007**, *111*, 2054–2061.
- [80] H. T. Lemke, K. S. Kjær, R. Hartsock, T. B. van Driel, M. Chollet, J. M. Glowacki, S. Song, D. Zhu, E. Pace, S. F. Matar, M. M. Nielsen, M. Benfatto, K. J. Gaffney, E. Collet, M. Cammarata, *Nat. Commun.* **2017**, *8*, 15342.
- [81] J. E. Monat, J. K. McCusker, *J. Am. Chem. Soc.* **2000**, *122*, 4092–4097.
- [82] E. A. Juban, J. K. McCusker, *J. Am. Chem. Soc.* **2005**, *127*, 6857–6865.
- [83] J. N. Schrauben, K. L. Dillman, W. F. Beck, J. K. McCusker, *Chem. Sci.* **2010**, *1*, 405–410.
- [84] H. Ando, S. Iuchi, H. Sato, *Chem. Phys. Lett.* **2012**, *535*, 177–181.
- [85] E. M. S. Maçôas, R. Kananavicius, P. Myllyperkiö, M. Pettersson, H. Kunttu, *J. Am. Chem. Soc.* **2007**, *129*, 8934–8935.
- [86] E. M. S. Maçôas, S. Mustalahti, P. Myllyperkiö, H. Kunttu, M. Pettersson, *J. Phys. Chem. A* **2015**, *119*, 2727–2734.
- [87] R. N. Perutz, O. Torres, A. Vlček in *Comprehensive Inorganic Chemistry II* (Hrsg.: J. Reedijk), Elsevier, Amsterdam, **2013**, 232.

References

- [88] F. Puntoriero, F. Nastasi, M. Galletta, S. Campagna in *Comprehensive Inorganic Chemistry II* (Hrsg.: J. Reedijk), Elsevier, Amsterdam, **2013**, 260–262.
- [89] J. Chen, Q. Zhang, F.-K. Zheng, Z.-F. Liu, S.-H. Wang, A.-Q. Wu, G.-C. Guo, *Dalton Trans.* **2015**, 44, 3289–3294.
- [90] Y. Suffren, N. O'Toole, A. Hauser, E. Jeanneau, A. Brioude, C. Desroches, *Dalton Trans.* **2015**, 44, 7991–8000.
- [91] A. S. Berezin, K. A. Vinogradova, V. A. Nadolinny, T. S. Sukhikh, V. P. Krivopalov, E. B. Nikolaenkova, M. B. Bushuev, *Dalton Trans.* **2018**, 47, 1657–1665.
- [92] Y. Tanabe, S. Sugano, *J. Phys. Soc. Jpn.* **1954**, 9, 766–779.
- [93] Y. Tanabe, S. Sugano, *J. Phys. Soc. Jpn.* **1954**, 9, 753–766.
- [94] A. B. P. Lever, *Inorganic electronic spectroscopy*, 1. Aufl., Elsevier, Amsterdam, **1968**.
- [95] I. Prigogine (Hrsg.) *Advances in Chemical Physics*, John Wiley & Sons, **1963**.
- [96] F. Reichenauer, C. Wang, C. Förster, P. Boden, N. Ugur, R. Báez-Cruz, J. Kalmbach, L. M. Carrella, E. Rentschler, C. Ramanan, G. Niedner-Schatteburg, M. Gerhards, M. Seitz, U. Resch-Genger, K. Heinze, *J. Am. Chem. Soc.* **2021**, 143, 11843–11855.
- [97] W. R. Kitzmann, J. Moll, K. Heinze, *Photochem. Photobiol. Sci.* **2022**, 21, 1309–1331.
- [98] R. Ballardini, G. Varani, H. F. Wasgestian, L. Moggi, V. Balzani, *J. Phys. Chem.* **1973**, 77, 2947–2951.
- [99] R. Knochenmuss, C. Reber, M. V. Rajasekharan, H. U. Güdel, *J. Chem. Phys.* **1986**, 85, 4280–4289.
- [100] E. Koglin, W. Krasser, *Z. Naturforsch. A* **1973**, 28, 1131–1135.
- [101] F. Castelli, L. S. Forster, *J. Am. Chem. Soc.* **1975**, 97, 6306–6309.
- [102] S.-N. Chen, G. B. Porter, *J. Am. Chem. Soc.* **1970**, 92, 2189–2190.
- [103] M. Kaupp, *J. Comput. Chem.* **2006**, 28, 320–325.
- [104] O. S. Wenger, *Chem. Eur. J.* **2021**, 27, 2270–2278.
- [105] A. D. Kirk, *Coord. Chem. Rev.* **1981**, 39, 225–263.
- [106] P. S. Wagenknecht, P. C. Ford, *Coord. Chem. Rev.* **2011**, 255, 591–616.
- [107] S. Otto, M. Dorn, C. Förster, M. Bauer, M. Seitz, K. Heinze, *Coord. Chem. Rev.* **2018**, 359, 102–111.
- [108] A. D. Kirk, G. B. Porter, *J. Phys. Chem.* **1980**, 84, 887–891.
- [109] K. K. Chatterjee, L. S. Forster, *Spectrochim. Acta* **1964**, 20, 1603–1609.
- [110] A. Hauser, M. Maeder, W. T. Robinson, R. Murugesan, J. Ferguson, *Inorg. Chem.* **1987**, 26, 1331–1338.
- [111] B. Doistau, G. Collet, E. A. Bolomey, V. Sadat-Noorbakhsh, C. Besnard, C. Piguet, *Inorg. Chem.* **2018**, 57, 14362–14373.
- [112] J. C. Barbour, A. J. I. Kim, E. deVries, S. E. Shaner, B. M. Lovaasen, *Inorg. Chem.* **2017**, 56, 8212–8222.
- [113] N. Serpone, M. A. Jamieson, M. S. Henry, M. Z. Hoffman, F. Bolletta, M. Maestri, *J. Am. Chem. Soc.* **1979**, 101, 2907–2916.
- [114] A. M. McDaniel, H.-W. Tseng, N. H. Damrauer, M. P. Shores, *Inorg. Chem.* **2010**, 49, 7981–7991.
- [115] S. Otto, C. Förster, C. Wang, U. Resch-Genger, K. Heinze, *Chem. Eur. J.* **2018**, 24, 12555–12563.
- [116] R. Fukuda, R. T. Walters, H. Macke, A. W. Adamson, *J. Phys. Chem.* **1979**, 83, 2097–2103.
- [117] K. D. Barker, K. A. Barnett, S. M. Connell, J. W. Glaeser, A. J. Wallace, J. Wildsmith, B. J. Herbert, J. F. Wheeler, N. A. P. Kane-Maguire, *Inorg. Chim. Acta* **2001**, 316, 41–49.
- [118] L. Stein, P. Boden, R. Naumann, C. Förster, G. Niedner-Schatteburg, K. Heinze, *Chem. Commun.* **2022**, 58, 3701–3704.
- [119] J.-R. Jiménez, B. Doistau, C. Besnard, C. Piguet, *Chem. Commun.* **2018**, 54, 13228–13231.

-
- [120] J.-R. Jiménez, B. Doistau, C. M. Cruz, C. Besnard, J. M. Cuerva, A. G. Campaña, C. Piguet, *J. Am. Chem. Soc.* **2019**, *141*, 13244–13252.
- [121] S. Treiling, C. Wang, C. Förster, F. Reichenauer, J. Kalmbach, P. Boden, J. P. Harris, L. M. Carrella, E. Rentschler, U. Resch-Genger, C. Reber, M. Seitz, M. Gerhards, K. Heinze, *Angew. Chem. Int. Ed.* **2019**, *58*, 18075–18085.
- [122] M. W. Perkovic, M. J. Heeg, J. F. Endicott, *Inorg. Chem.* **1991**, *30*, 3140–3147.
- [123] P. Comba, A. W. H. Mau, A. M. Sargeson, *J. Phys. Chem.* **1985**, *89*, 394–396.
- [124] A. M. McDaniel, H.-W. Tseng, E. A. Hill, N. H. Damrauer, A. K. Rappé, M. P. Shores, *Inorg. Chem.* **2013**, *52*, 1368–1378.
- [125] N. Sinha, J.-R. Jiménez, B. Pfund, A. Prescimone, C. Piguet, O. S. Wenger, *Angew. Chem. Int. Ed. Engl.* **2021**, *60*, 23722–23728.
- [126] S. Otto, N. Scholz, T. Behnke, U. Resch-Genger, K. Heinze, *Chem. Eur. J.* **2017**, *23*, 12131–12135.
- [127] H. Xiang, J. Cheng, X. Ma, X. Zhou, J. J. Chruma, *Chem. Soc. Rev.* **2013**, *42*, 6128–6185.
- [128] J. P. Joyce, R. I. Portillo, C. M. Nite, J. M. Nite, M. P. Nguyen, A. K. Rappé, M. P. Shores, *Inorg. Chem.* **2021**, *60*, 12823–12834.
- [129] C. Wang, W. R. Kitzmann, F. Weigert, C. Förster, X. Wang, K. Heinze, U. Resch-Genger, *ChemPhotoChem* **2022**, *6*.
- [130] J. P. Harris, C. Reber, H. E. Colmer, T. A. Jackson, A. P. Forshaw, J. M. Smith, R. A. Kinney, J. Telsler, *Can. J. Chem.* **2017**, *95*, 547–552.
- [131] Z. Goldschmidt, W. Low, M. Foguel, *Phys. Lett.* **1965**, *19*, 17–18.
- [132] D. Spichiger, G. Carver, C. Dobe, J. Bendix, P. L. Tregenna-Piggott, R. Meier, G. Zahn, *Chem. Phys. Lett.* **2001**, *337*, 391–397.
- [133] J. Reedijk, P. W. N. M. van Leeuwen, W. L. Groeneveld, *Recl. Trav. Chim. Pays-Bas* **1968**, *87*, 129–143.
- [134] M. K. Wojnar, D. W. Laorenza, R. D. Schaller, D. E. Freedman, *J. Am. Chem. Soc.* **2020**, *142*, 14826–14830.
- [135] M.-C. Nolet, A. Michaud, C. Bain, D. Zargarian, C. Reber, *Photochem. Photobiol.* **2006**, *82*, 57–63.
- [136] A. T. Baker, D. C. Craig, A. D. Rae, *Aust. J. Chem.* **1995**, *48*, 1373.
- [137] C. K. Jørgensen, L. H. Smith, G. Hanshoff, H. Prydz, *Acta Chem. Scand.* **1955**, *9*, 1362–1377.
- [138] A. D. Liehr, C. Ballhausen, *Ann. Phys.* **1959**, *6*, 134–155.
- [139] E. González, A. Rodrigue-Witchel, C. Reber, *Coord. Chem. Rev.* **2007**, *251*, 351–363.
- [140] N. Takeda, D. Shimizu, N. Tokitoh, *Inorg. Chem.* **2005**, *44*, 8561–8568.
- [141] F. Pointillart, C. Train, F. Villain, C. C. D. Moulin, P. Gredin, L.-M. Chamoreau, M. Gruselle, G. Aullon, S. Alvarez, M. Verdaguer, *J. Am. Chem. Soc.* **2007**, *129*, 1327–1334.
- [142] D. A. Safin, M. G. Babashkina, Y. Garcia, *Dalton Trans.* **2013**, *42*, 902–905.
- [143] N. Takeda, T. Isobe, N. Tokitoh, *Heteroatom Chem.* **2007**, *18*, 549–556.
- [144] J.-C. G. Bünzli, S. V. Eliseeva, *J. Rare Earths* **2010**, *28*, 824–842.
- [145] H. Q. Ye, Z. Li, Y. Peng, C. C. Wang, T. Y. Li, Y. X. Zheng, A. Sapelkin, G. Adamopoulos, I. Hernández, P. B. Wyatt, W. P. Gillin, *Nat. Mater* **2014**, *13*, 382–386.
- [146] J.-C. G. Bünzli, *J. Lumin.* **2016**, *170*, 866–878.
- [147] Y. Cai, Z. Wei, C. Song, C. Tang, W. Han, X. Dong, *Chem. Soc. Rev.* **2019**, *48*, 22–37.
- [148] M. Zhang, W. Zheng, Y. Liu, P. Huang, Z. Gong, J. Wei, Y. Gao, S. Zhou, X. Li, X. Chen, *Angew. Chem. Int. Ed. Engl.* **2019**, *58*, 9556–9560.
- [149] M. Schulze, A. Steffen, F. Würthner, *Angew. Chem. Int. Ed. Engl.* **2015**, *54*, 1570–1573.
- [150] R. Reisfeld, C. K. Jørgensen (Hrsg.) *Inorganic Chemistry Concepts, Vol. 1*, Springer Berlin Heidelberg, Heidelberg, **1977**.

References

- [151] S. Torelli, D. Imbert, M. Cantuel, G. Bernardinelli, S. Delahaye, A. Hauser, J.-C. G. Bünzli, C. Piguet, *Chem. Eur. J.* **2005**, *11*, 3228–3242.
- [152] L. Aboshyan-Sorgho, H. Nozary, A. Aebischer, J.-C. G. Bünzli, P.-Y. Morgantini, K. R. Kittilstved, A. Hauser, S. V. Eliseeva, S. Petoud, C. Piguet, *J. Am. Chem. Soc.* **2012**, *134*, 12675–12684.
- [153] C. Wang, S. Otto, M. Dorn, K. Heinze, U. Resch-Genger, *Anal. Chem.* **2019**, *91*, 2337–2344.
- [154] S. Otto, J. P. Harris, K. Heinze, C. Reber, *Angew. Chem. Int. Ed.* **2018**, *57*, 11069–11073.
- [155] R. A. Forman, G. J. Piermarini, J. D. Barnett, S. Block, *Science* **1972**, *176*, 284–285.
- [156] S. Otto, A. M. Nauth, E. Ermilov, N. Scholz, A. Friedrich, U. Resch-Genger, S. Lochbrunner, T. Opatz, K. Heinze, *ChemPhotoChem.* **2017**, *1*, 344–349.
- [157] C. Wang, F. Reichenauer, W. R. Kitzmann, C. Kerzig, K. Heinze, U. Resch-Genger, *Angew. Chem. Int. Ed. Engl.* **2022**.
- [158] C. Dee, F. Zinna, W. R. Kitzmann, G. Pescitelli, K. Heinze, L. Di Bari, M. Seitz, *Chem. Commun.* **2019**, *55*, 13078–13081.
- [159] L. Xu, Y. Feng, D. Yu, Z. Zheng, X. Chen, W. Hong, *Adv. Mater. Technol.* **2020**, 2000373.
- [160] Y. Deng, M. Wang, Y. Zhuang, S. Liu, W. Huang, Q. Zhao, *Light: Sci. Appl.* **2021**, *10*, 76.
- [161] C. D. Stanciu, F. Hansteen, A. V. Kimel, A. Kirilyuk, A. Tsukamoto, A. Itoh, T. Rasing, *Phys. Rev. Lett.* **2007**, *99*, 47601.
- [162] E. Kreidt, L. Arrico, F. Zinna, L. Di Bari, M. Seitz, *Chemistry* **2018**, *24*, 13556–13564.
- [163] R. Sessoli, D. Gatteschi, A. Caneschi, M. A. Novak, *Nature* **1993**, *365*, 141–143.
- [164] J. Blahut, L. Benda, J. Kotek, G. Pintacuda, P. Hermann, *Inorg. Chem.* **2020**, *59*, 10071–10082.
- [165] I. V. Kurganskii, E. S. Bazhina, A. A. Korlyukov, K. A. Babeshkin, N. N. Efimov, M. A. Kiskin, S. L. Veber, A. A. Sidorov, I. L. Eremenko, M. V. Fedin, *Molecules (Basel, Switzerland)* **2019**, *24*.
- [166] A. V. Funes, L. Carrella, E. Rentschler, P. Alborés, *Dalton Trans.* **2014**, *43*, 2361–2364.
- [167] A. W. Cook, J. D. Bocarsly, R. A. Lewis, A. J. Touchton, S. Morochnik, T. W. Hayton, *Chem. Sci.* **2020**, *11*, 4753–4757.
- [168] A. Zabala-Lekuona, J. M. Seco, E. Colacio, *Coord. Chem. Rev.* **2021**, *441*, 213984.
- [169] J. Vallejo, A. Pascual-Álvarez, J. Cano, I. Castro, M. Julve, F. Lloret, J. Krzystek, G. de Munno, D. Armentano, W. Wernsdorfer, R. Ruiz-García, E. Pardo, *Angew. Chem. Int. Ed.* **2013**, *52*, 14075–14079.
- [170] D. E. Freedman, W. H. Harman, T. D. Harris, G. J. Long, C. J. Chang, J. R. Long, *J. Am. Chem. Soc.* **2010**, *132*, 1224–1225.
- [171] B. Yao, M. K. Singh, Y.-F. Deng, Y.-N. Wang, K. R. Dunbar, Y.-Z. Zhang, *Inorg. Chem.* **2020**, *59*, 8505–8513.
- [172] M. Murugesu, M. Habrych, W. Wernsdorfer, K. A. Abboud, G. Christou, *J. Am. Chem. Soc.* **2004**, *126*, 4766–4767.
- [173] F. Neese, D. A. Pantazis, *Faraday discussions* **2011**, *148*, 229-38; discussion 299-314.
- [174] J. A. Clayton, K. Keller, M. Qi, J. Wegner, V. Koch, H. Hintz, A. Godt, S. Han, G. Jeschke, M. S. Sherwin, M. Yulikov, *Phys. Chem. Chem. Phys.* **2018**, *20*, 10470–10492.
- [175] R. P. Feynman, *Int J Theor Phys* **1982**, *21*, 467–488.
- [176] Peter W. Shor, *Algorithms for Quantum Computing: Discrete Log and Factoring*, **1994**.
- [177] T. D. Ladd, F. Jelezko, R. Laflamme, Y. Nakamura, C. Monroe, J. L. O'Brien, *Nature* **2010**, *464*, 45–53.
- [178] L. M. Vandersypen, M. Steffen, G. Breyta, C. S. Yannoni, M. H. Sherwood, I. L. Chuang, *Nature* **2001**, *414*, 883–887.
- [179] C.-J. Yu, M. J. Graham, J. M. Zadrozny, J. Niklas, M. D. Krzyaniak, M. R. Wasielewski, O. G. Poluektov, D. E. Freedman, *J. Am. Chem. Soc.* **2016**, *138*, 14678–14685.
- [180] G. J. Milburn, *Phys. Scr.* **2009**, *T137*, 14003.

-
- [181] J. N. Nelson, J. Zhang, J. Zhou, B. K. Rugg, M. D. Krzyaniak, M. R. Wasielewski, *J. Chem. Phys.* **2020**, *152*, 14503.
- [182] B. K. Rugg, M. D. Krzyaniak, B. T. Phelan, M. A. Ratner, R. M. Young, M. R. Wasielewski, *Nat. Chem.* **2019**, *11*, 981–986.
- [183] R. Hanson, O. Gywat, D. D. Awschalom, *Phys. Rev. B* **2006**, *74*.
- [184] A. Batalov, C. Zierl, T. Gaebel, P. Neumann, I.-Y. Chan, G. Balasubramanian, P. R. Hemmer, F. Jelezko, J. Wrachtrup, *Phys. Rev. Lett.* **2008**, *100*, 77401.
- [185] B. Diler, S. J. Whiteley, C. P. Anderson, G. Wolfowicz, M. E. Wesson, E. S. Bielejec, F. Joseph Heremans, D. D. Awschalom, *npj Quantum Inf* **2020**, *6*.
- [186] D. M. Irber, F. Poggiali, F. Kong, M. Kieschnick, T. Lühmann, D. Kwiatkowski, J. Meijer, J. Du, F. Shi, F. Reinhard, *Nat Commun* **2021**, *12*, 532.
- [187] A. Gruber, A. Dräbenstedt, C. Tietz, L. Fleury, J. Wrachtrup, C. von Borczyskowski, *Science* **1997**, *276*, 2012–2014.
- [188] K. S. Kumar, D. Serrano, A. M. Nonat, B. Heinrich, L. Karmazin, L. J. Charbonnière, P. Goldner, M. Ruben, *Nat Commun* **2021**, *12*, 2152.
- [189] J. R. Morgan, E. P. Chock, W. D. Hopewell, M. A. El-Sayed, R. Orbach, *J. Phys. Chem.* **1981**, *85*, 747–751.
- [190] C. E. Housecroft, A. G. Sharpe, *Inorganic chemistry*, 2. Aufl., Prentice Hall, Harlow, **2006**.
- [191] A. Piccini, N. Brizzi, *Z. Anorg. Chem.* **1899**, *19*, 394–404.
- [192] R. G. Cavell, H. C. Clark, *J. Chem. Soc.* **1962**, 2692.
- [193] S. Herzog, *Z. Anorg. Allg. Chem.* **1958**, *294*, 155–180.
- [194] J. Selbin, *Chem. Rev.* **1965**, *65*, 153–175.
- [195] M. R. Maurya, S. Khurana, W. Zhang, D. Rehder, *Eur. J. Inorg. Chem.* **2002**, *2002*, 1749–1760.
- [196] M. R. Maurya, *Coord. Chem. Rev.* **2019**, *383*, 43–81.
- [197] M. Sutradhar, A. J. Pombeiro, *Coord. Chem. Rev.* **2014**, *265*, 89–124.
- [198] M. Maurya, *Coord. Chem. Rev.* **2003**, *237*, 163–181.
- [199] P. Galloni, V. Conte, B. Floris, *Coord. Chem. Rev.* **2015**, *301-302*, 240–299.
- [200] T. A. Alsalim, J. S. Hadi, E. A. Al-Nasir, H. S. Abbo, S. J. J. Titinchi, *Catal Lett* **2010**, *136*, 228–233.
- [201] G. Grivani, G. Bruno, H. A. Rudbari, A. D. Khalaji, P. Pourteimouri, *Inorg. Chem. Commun.* **2012**, *18*, 15–20.
- [202] R. R. Langeslay, D. M. Kaphan, C. L. Marshall, P. C. Stair, A. P. Sattelberger, M. Delferro, *Chem. Rev.* **2019**, *119*, 2128–2191.
- [203] T. F. Silva, T. C. M. Leod, L. M. Martins, M. F. C. Da Guedes Silva, M. A. Schiavon, A. J. Pombeiro, *J Mol Catal A Chem* **2013**, *367*, 52–60.
- [204] S. Singhal, S. L. Jain, B. Sain, *Chem. Commun.* **2009**, 2371–2372.
- [205] T. A. Kabanos, A. M. Z. Slawin, D. J. Williams, J. D. Woollins, *J. Chem. Soc., Chem. Commun.* **1990**, 193–194.
- [206] T. A. Kabanos, J. D. Woollins, *J. Chem. Soc., Dalton Trans.* **1991**, 1347.
- [207] C. J. Hawkins, T. A. Kabanos, *Inorg. Chem.* **1989**, *28*, 1084–1087.
- [208] R. Ercoli, F. Calderazzo, A. Alberola, *J. Am. Chem. Soc.* **1960**, *82*, 2966–2967.
- [209] E. Kurras, *Naturwissenschaften* **1959**, *46*, 171.
- [210] M. W. Duckworth, G. W. A. Fowles, R. A. Hoodless, *J. Chem. Soc.* **1963**, 5665.
- [211] J. C. Dobson, H. Taube, *Inorg. Chem.* **1989**, *28*, 1310–1315.
- [212] S. Otto, J. Moll, C. Förster, D. Geißler, C. Wang, U. Resch-Genger, K. Heinze, *Eur. J. Inorg. Chem.* **2017**, *2017*, 5033–5040.
- [213] S. J. Anderson, F. J. Wells, G. Wilkinson, B. Hussain, M. B. Hursthouse, *Polyhedron* **1988**, *7*, 2615–2626.

References

- [214] A. K. C. Mengel, C. Bissinger, M. Dorn, O. Back, C. Förster, K. Heinze, *Chem. Eur. J.* **2017**, *23*, 7920–7931.
- [215] C. Förster, M. Dorn, T. Reuter, S. Otto, G. Davarci, T. Reich, L. Carrella, E. Rentschler, K. Heinze, *Inorganics* **2018**, *6*, 86.
- [216] N. Elgrishi, K. J. Rountree, B. D. McCarthy, E. S. Rountree, T. T. Eisenhart, J. L. Dempsey, *J. Chem. Educ.* **2018**, *95*, 197–206.
- [217] J. Cassidy, S. B. Khoo, S. Pons, M. Fleischmann, *J. Phys. Chem.* **1985**, *89*, 3933–3935.
- [218] Katharina Mack, *Neue Übergangsmetall-Komplexe des N,N'-dimethyl-N,N'-dipyridin-2-ylpyridin-2,6-diamins. Strukturelle, magnetische und optische Eigenschaften*. Diploma Thesis, Mainz, **2012**.
- [219] C. Förster, T. E. Gorelik, U. Kolb, V. Ksenofontov, K. Heinze, *Eur. J. Inorg. Chem.* **2015**, *2015*, 920–924.
- [220] A. K. C. Mengel, W. Cho, A. Breivogel, K. Char, Y. Soo Kang, K. Heinze, *Eur. J. Inorg. Chem.* **2015**, *2015*, 3299–3306.
- [221] K. Mack, A. Wünsche von Leupoldt, C. Förster, M. Ezhevskaya, D. Hinderberger, K. W. Klinkhammer, K. Heinze, *Inorg. Chem.* **2012**, *51*, 7851–7858.
- [222] M. Jäger, R. J. Kumar, H. Görls, J. Bergquist, O. Johansson, *Inorg. Chem.* **2009**, *48*, 3228–3238.
- [223] F. R. Keene, G. H. Searle, *Inorg. Chem.* **1972**, *11*, 148–156.
- [224] M. Dorn, J. Kalmbach, P. Boden, A. Kruse, C. Dab, C. Reber, G. Niedner-Schatteburg, S. Lochbrunner, M. Gerhards, M. Seitz, K. Heinze, *Chem. Sci.* **2021**, *12*, 10780–10790.

6. Appendix

6.1. Supporting Information to Chapter 3.1. („A Vanadium(III) Complex with Blue and NIR-II Spin-Flip Luminescence in Solution“)

A vanadium(III) complex with blue and NIR-II spin-flip luminescence in solution

Matthias Dorn¹, Jens Kalmbach², Pit Boden³, Ayla Pöpcke⁴, Sandra Gómez⁵, Christoph Förster¹, Felix Kuczelinis¹, Luca M. Carrella¹, Laura A. Büldt², Nicolas H. Bings¹, Eva Rentschler¹, Stefan Lochbrunner⁴, Leticia González⁵, Markus Gerhards*³, Michael Seitz*² and Katja Heinze*¹

¹Department of Chemistry, Johannes Gutenberg University of Mainz, Duesbergweg 10-14, 55128 Mainz, Germany.

²Institute of Inorganic Chemistry, University of Tübingen, Auf der Morgenstelle 18, 72076 Tübingen, Germany.

³Department of Chemistry and Research Center Optimas, TU Kaiserslautern, Erwin-Schrödinger-Straße, 67663 Kaiserslautern, Germany.

⁴Institute for Physics and Department of Life, Light and Matter, University of Rostock, 18051 Rostock, Germany.

⁵Institute of Theoretical Chemistry, Faculty of Chemistry, University of Vienna, Währinger Straße 17, 1090 Vienna, Austria.

Supporting Information

Appendix

General Procedures. Diethyl ether and petroleum ether (40/60) were distilled over sodium, acetonitrile over calcium hydride and butyronitrile over Na_2CO_3 . VCl_3 (anhydrous, 95 %; ABCR), 10% Pd/C (dry, unreduced; Acros Organics), CD_3I (>99.5 %D, stabilized with copper, Sigma-Aldrich) and 2,6-diaminopyridine (Sigma-Aldrich) were used as received. For NMR spectroscopy and synthesis, deuterated solvents with a deuteration level of at least 99.8 % were used. Column chromatography was performed using silica gel 60 (Merck, 0.04–0.063 mm). Analytical thin layer chromatography (TLC) was done on silica gel 60 F254 plates (Merck, coated on aluminum sheets). The ligand ddpd^1 and $[\text{V}(\text{NCCH}_3)_6][\text{BPh}_4]_2$ ² were prepared according to reported procedures. NMR spectroscopic and mass spectrometric data match the literature values. A glovebox (UniLab/MBraun, Ar 4.8, $\text{O}_2 < 100$ ppm, $\text{H}_2\text{O} < 1$ ppm) was used for storage and weighing of sensitive compounds.

NMR spectra were recorded on a Bruker Avance DRX 400 or AVII+400 NMR spectrometer at 400.31 MHz (^1H). All resonances are reported in ppm versus the solvent signal as internal standard.³

IR spectra were recorded with a Bruker Alpha FTIR spectrometer with an ATR unit containing a diamond crystal.

ESI⁺ mass spectra were recorded on a Micromass Q-TOF-Ultima spectrometer by the central analytical facility of the Department of Chemistry (University of Mainz) or on a Bruker Daltonics Esquire 3000 plus mass spectrometer by the central analytical facility of the Department of Chemistry (University of Tübingen).

DC magnetic studies were performed with a Quantum Design MPMS-XL-7 SQUID magnetometer on powdered microcrystalline samples. Experimental susceptibility data were corrected for the underlying diamagnetism using Pascal's constants. The temperature dependent magnetic contribution of the holder and of the embedding eicosane matrix was experimentally determined and subtracted from the measured susceptibility data. Variable temperature susceptibility data were collected in a temperature range of 2 – 300 K under an applied field of 0.1 Tesla.

Electrochemical experiments were carried out on a BioLogic SP-200 voltammetric analyzer using platinum wires as counter and working electrodes and a 0.01 M Ag/Ag[NO_3] electrode as reference electrode. Cyclic voltammetry and square wave measurements were carried out at scan rates of 50–200 mV s^{-1} using 0.1 M [$^n\text{Bu}_4\text{N}$][PF_6] in CH_3CN as supporting electrolyte. Potentials are referenced against the ferrocene/ferrocenium couple. UV/Vis/NIR spectra were recorded on a Varian Cary 5000 spectrometer using 1.0 cm cells.

Luminescence experiments. For luminescence experiments, CD_3CN (99.8 %D, NMR grade) or spectrophotometric grade toluene as well as H_2O were used. Prior to use, all solvents were deoxygenated by three freeze-pump-thaw cycles and eventually sealed under dry, dioxygen-free argon atmosphere. Luminescence measurements at room temperature and at 77 K were performed on the following instruments:

a) The first instrument was a Horiba Fluorolog-3 spectrofluorimeter equipped with a 450 W Xenon lamp for steady-state measurements. Emitted light was detected either by a Hamamatsu R2658P PMT detector ($200 \text{ nm} < \lambda_{\text{em}} < 1010 \text{ nm}$) or by a Hamamatsu H10330-75 PMT detector ($950 \text{ nm} < \lambda_{\text{em}} < 1700 \text{ nm}$). Spectral selection in the excitation path was accomplished by a DFX monochromator (double gratings: 1200 grooves/mm, 330 nm blaze) and in the emission paths in the visible/NIR spectral region ($\lambda_{\text{em}} < 1010 \text{ nm}$) by a spectrograph iHR550 (single gratings: either 1200 grooves/mm, 500 nm blaze or 950 grooves/mm, 900 nm blaze) and in the NIR spectral region ($\lambda_{\text{em}} > 950 \text{ nm}$) by a spectrograph iHR320 (single grating: 600 grooves/mm, 1000 nm blaze). Luminescence lifetimes of the visible emission around 390 nm was determined at 298 K in standard fluorescence cuvettes (1 cm path length, quartz suprasil) with a pulsed LED (DeltaDiode-310, $\lambda_{\text{exc}} = 306 \text{ nm} \pm 10 \text{ nm}$, pulse width ca. 1.0 ns, $P_{\text{avg}} = 5 \mu\text{W}$). Lifetime data analysis (deconvolution, statistical parameters, etc.) was performed using the software package DAS from Horiba. Lifetimes were

determined by deconvolution of the decay profiles with the instrument response function, which was determined using a dilute aqueous dispersion of colloidal silica (Ludox® AM-30).

b) The second instrument was a PTI Quantamaster QM4 spectrofluorimeter equipped with a 75 W continuous xenon short arc lamp as excitation source. Emission was monitored using a PTI P1.7R detector module (Hamamatsu PMT R5509-72 with a Hamamatsu C9525 power supply operated at 1500 V and a Hamamatsu liquid N₂ cooling unit C9940 set to -80°C). For the measurements between 600 nm and 900 nm, a long-pass filter GG-455 (Schott, 3.0 mm thickness, transmission 98 – 95 % in the spectral region mentioned) was used in the emission channel in order to avoid higher order excitation light. The same approach was taken for NIR measurements above 1000 nm with a long-pass filter RG-850 (Schott, 3.0 mm thickness, transmission > 98 % above 970 nm). Spectral selection was achieved by single grating monochromators (excitation: 1200 grooves/mm, 300 nm blaze; vis emission: 1200 grooves/mm, 500 nm blaze; near-IR emission: 600 grooves/mm, 1200 nm blaze). Near-IR luminescence lifetimes of the phosphorescent transition $^1E_g/{}^1T_{2g} \rightarrow {}^3T_{1g}$ were determined at 77 K (liquid N₂ cuvette, sample dissolved in deoxygenated ⁿBuCN in standard NMR tubes under argon) with a xenon flash lamp as excitation source (Hamamatsu L4633: pulse width ca. 1.5 μs FWHM). Lifetime data analysis (deconvolution, statistical parameters, etc.) was performed using the software package FeliX32 from PTI. Lifetimes were determined by deconvolution of the decay profiles with the instrument response function, which was determined using an empty NMR tube as scatterer.

Partial quantum yields in the visible and the NIR spectral regions were determined using the following equation:

$$\Phi_x = \Phi_r * (\text{Grad}_x / \text{Grad}_r) * (\eta_x^2 / \eta_r^2)$$

where η is the refractive index and Grad is the linearly fitted slope from the plot of the integrated luminescence intensity (corrected for instrument response) versus the absorbance at the excitation wavelength. The subscripts 'x' and 'r' refer to the sample and reference, respectively. The vanadium samples were prepared in deoxygenated CD₃CN ($\eta_x = 1.341$) at 298 K under argon (vide supra). For the emission around 390 nm, quinine sulfate in 0.1 M aqueous H₂SO₄ ($\eta_r = 1.33$) was used after excitation at $\lambda_{\text{exc}} = 308$ nm as a reference material with a fluorescence quantum yield of $\Phi_r = 54.6$ %.⁴ For the NIR emission band ($^1E_g/{}^1T_{2g} \rightarrow {}^3T_{1g}$), Yb(tta)₃(phen) in toluene ($\eta_r = 1.496$) was used after excitation at $\lambda_{\text{exc}} = 308$ nm with a quantum yield of $\Phi_r = 1.1$ %.⁵ For the measurement of the ytterbium standard emission, the signal had to be attenuated by a neutral density filter (Newport, neutral density filter FSQ-ND10, transmission around 1000 nm ca. 11.0±0.2 %) in the emission. The attenuation factor was taken into account mathematically during the integration of the emission bands for the quantum yield calculations.

c) Steady state luminescence measurements in frozen butyronitrile solution down to 20 K were recorded on a Horiba Jobin Yvon Fluorolog 3-22 τ spectrometer equipped with a 450 W xenon lamp and a DSS – IGA020L NIR detector (900 nm < λ_{em} < 1500 nm). Spectral selection was realized with double and single grating monochromators in the excitation and emission paths, respectively (excitation: 1200 grooves/mm; near-IR emission 600 grooves/mm). A long-pass filter RG-850 (Edmund Optics, transmission > 98 % above 970 nm) was used in the emission channel to avoid higher order excitation light. The butyronitrile solution was cooled down to 20 K with a closed cycle helium cryostat (ARS Model DE-202A). The cryo cooler was equipped with a cuvette holder and CaF₂ windows. Measurements were performed in fluorescence cuvettes (1 cm path length, quartz suprasil).

d) Steady state luminescence measurements by using KBr pellets were performed on a Horiba Jobin Yvon FluoroMax-2 using the described cryostat. A 150 W xenon lamp was used for sample excitation and detection was realized with a R928 photomultiplier detector. Spectral selection was achieved with single grating monochromators in the excitation and emission paths, respectively (excitation: 1200 grooves/mm, 330 nm blaze; emission: 1200 grooves/mm, 500 nm blaze). Long-pass filters with cut-off wavelengths of 420 nm or

S3

600 nm were used depending on the measurement. KBr pellets of $[V(\text{ddpd})_2][\text{PF}_6]_3$ (ca. 0.5 mg) were prepared by mixing with dry KBr (ca. 200 mg), grinding to a homogeneous mixture and pressing into a pellet.

Time-resolved FTIR experiments were performed with an FTIR spectrometer Bruker Vertex 80v, operated in the step-scan mode. KBr pellets of $[V(\text{ddpd})_2][\text{PF}_6]_3$ (ca. 0.5 mg) were prepared by mixing with dry KBr (ca. 200 mg, stored at 80 °C) and grinding to a homogeneous mixture. This mixture was filled in an evacuable pellet die with a diameter of 13 mm and sintered at a pressure of 0.75 GPa. The strongest peak in the ground state spectrum showed an absorption of about 0.6 OD with the mentioned concentration. Measurements with cryogenically cooled KBr pellets (20 K and 290 K at the sample) were performed with a closed cycle helium cryostat (ARS Model DE-202A). The cryo cooler was equipped with a homebuilt pellet holder and CaF_2 windows. A liquid-nitrogen-cooled mercury cadmium telluride (MCT) detector (Kolmar Tech., Model KV100-1-B-7/190) with a rise time of 25 ns, connected to a fast preamplifier and a 14-bit transient recorder board (Spectrum Germany, M3I4142, 400 MS s^{-1}), was used for signal detection and processing. The laser setup includes a Q-switched Nd:YAG laser (Innolas SpitLight Evo I) generating pulses with a band-width of 6 – 9 ns at a repetition rate of 100 Hz. The third harmonic (355 nm) of the Nd:YAG laser was used for sample excitation. The UV pump beam was attenuated to about 2.0 mJ per shot at a diameter of 9 mm. The beam was directed onto the sample and adjusted to have a maximal overlap with the IR beam of the spectrometer. The sample chamber was equipped with anti-reflection-coated germanium filters to prevent the entrance of laser radiation into the detector and interferometer compartments. The time delay between the start of the experiment and the UV laser pulse was controlled with a Stanford Research Systems DG535 delay generator. A total of 10400 coadditions were recorded at each interferogram point. The spectral region was limited by undersampling to 988 – 1975 cm^{-1} with a spectral resolution of 4 cm^{-1} resulting in 555 interferogram points. An IR broad band filter (850 – 1750 cm^{-1}) and the CaF_2 windows (no IR transmission < 1000 cm^{-1}) of the cryostat prevented problems when performing a Fourier transformation (*i.e.* no IR intensity outside the measured region should be observed). FTIR ground state spectra were recorded systematically to check for sample degradation. A more detailed description of the step-scan setup is given here.⁶

Transient absorption spectra were recorded applying a pump-probe setup with a time resolution of 100 fs. A noncollinear optical parametric amplifier (NOPA) tuned to a center wavelength of 620 nm was used for excitation and a white light continuum, generated with a CaF_2 crystal, for probing. Both the white light generation and the NOPA were pumped by a regenerative Ti:sapphire laser system operating at 775 nm with a repetition rate of 1 kHz. The polarizations of the pump and probe pulses were set to magic angle with respect to each other to avoid effects due to orientational relaxation. Pump and probe beam were focused onto the sample resulting in overlapping spots with diameters of approximately 270 μm and 110 μm , respectively. The sample was dissolved in acetonitrile and filled into a 1 mm fused silica cuvette. The optical density was set at 600 nm to 0.3 – 0.5 to obtain transient spectra with a good signal to noise ratio. This corresponds to concentrations of 1.8 – 2.5 $\times 10^{-3}$ M for the complex. The solutions were perfused with argon for approximately two minutes. For the measurements with an excitation wavelength of 400 nm a second pump-probe setup was used based on a Ti:Sapphire laser system (Spectra-Physics, Spitfire Pro) with a center wavelength of 800 nm and a repetition rate of 1 kHz. By frequency doubling applying a BBO crystal pump pulses at 400 nm with a pulse duration of 200 fs were obtained. The white light continuum for the probe was again generated with a CaF_2 crystal. Both beams with polarizations arranged in magic angle were focused onto the sample leading to spots with diameters of 170 μm for the pump and 80 μm for the probe. The sample was dissolved in CH_3CN and filled into a 1 mm fused silica cuvette. The optical density was set to 0.7 at 400 nm which corresponds to an optical density of 0.4 at 600 nm and to a concentration of 2.5 $\times 10^{-3}$ M. The same sample was used as in the aforementioned measurement with an excitation at 620 nm.

Elemental analyses were conducted by the microanalytical laboratory of the department of chemistry of the University of Mainz.

Trace determination of chromium in the presence of vanadium. Mass spectrometrical analysis of the starting materials for traces of Cr were performed by the Laboratory for Inorganic Trace Analysis and Plasma Spectrometry, University of Mainz. The chromium concentrations in $\text{VCl}_3(\text{THF})_3$, and $\text{VCl}_3(\text{CH}_3\text{CN})_3$ were determined by microwave assisted acid digestion and subsequent SN-ICP-MS (solution nebulization-inductively coupled plasma-mass spectrometry) measurement. Initially, the approximate chromium concentrations were determined via digestion and subsequent ICP-MS measurement of ~ 10 mg of the respective compound using a three point external calibration with concentrations between 0.5 ng ml^{-1} and 50 ng ml^{-1} . Based on these results, the procedure to achieve valid quantitative results was as follows: An amount of (40–130) mg per sample was weighted and digested in 6 mL nitric acid (70 % p.a. grade, Fisher Chemical, Fisher Scientific GmbH, Germany) and 2 ml hydrogen peroxide solution (30 % p.a. grade, ROTIPURAN®, Carl Roth, Germany) using an Ethos 2000plus microwave assisted digestion system (Milestone Inc, Shelton, CT, USA). The first step of the heating program was a temperature ramp to 140°C within 7.5 min followed by a second ramp to 200°C within 5 min. This temperature was held for 10 min and afterwards increased to 220°C within 5 min before holding this temperature for 20 mins. Prior to digestion, $100 \mu\text{l}$ of a $10 \mu\text{g ml}^{-1}$ Y-solution were added to compensate for analyte loss during the digestion and subsequent sample preparation steps. The obtained solutions were diluted to 25 ml with ultrapure water (Millipore, Milli-Q System, USA) from which five aliquots of 1 ml were diluted to 10 ml each. For quantification via standard addition, Cr and Y were added at concentrations between 0 and 5 ng ml^{-1} , and 0 and 8 ng ml^{-1} , respectively. Sc was added at a concentration of 4 ng ml^{-1} as internal standard. For ICP-MS measurements, a sample introduction system consisting of a concentric MicroMist™ nebulizer (Agilent Technologies, Santa Clara, CA, USA) and a double pass spray chamber (Agilent Technologies, Santa Clara, CA, USA) were coupled to a quadrupole ICP-MS instrument 7800 (Agilent Technologies, Santa Clara, CA, USA). The signal intensities of $^{45}\text{Sc}^+$, $^{52}\text{Cr}^+$, $^{53}\text{Cr}^+$ and $^{89}\text{Y}^+$ were measured for data evaluation. The optimum instrumental parameters of the developed ICP-MS method are as follows: plasma power: 1550 W, plasma gas flow rate: 15 l min^{-1} , auxiliary gas flow rate: 0.9 l min^{-1} , nebulizer gas flow rate: $0.99\text{--}1.05 \text{ l min}^{-1}$, sampler and skimmer cone: Ni, He gas flow rate (cell gas): 2 ml min^{-1} , data acquisition: 0.3 s integration time, 30 sweeps per replicate, 6 replicates.

$\text{VCl}_3(\text{NCMe})_3$: $(4.01 \pm 0.31) \mu\text{g/g}$ (U ; $k=2$); $\text{VCl}_3(\text{THF})_3$: $(3.45 \pm 0.10) \mu\text{g/g}$ (U ; $k=2$).

Crystal structure determination. Intensity data were collected with a STOE IPDS-2T diffractometer and an Oxford cooling system and corrected for absorption and other effects using Mo K_α radiation ($\lambda = 0.71073 \text{ \AA}$). The diffraction frames were integrated using the STOE X-Area software package⁷, and most were corrected for absorption with MULABS⁸ of the PLATON package.⁹ The structure was solved by direct methods and refined by the full-matrix method based on F^2 using the SHELXTL software package.^{10,11} All non-hydrogen atoms were refined anisotropically, while the positions of all hydrogen atoms were generated with appropriate geometric constraints and allowed to ride on their respective parent carbon atoms with fixed isotropic thermal parameters. CCDC 1958562 ($[\text{V}(\text{ddpd})_2][\text{PF}_6]_3 \times 3\text{CH}_3\text{CN}$) contains the supplementary crystallographic data for this paper. These data are provided free of charge by The Cambridge Crystallographic Data Centre.

Crystallographic Data of *mer*- $[\text{V}(\text{ddpd})_2][\text{PF}_6]_3 \times 3\text{CH}_3\text{CN}$. $\text{C}_{40}\text{H}_{43}\text{F}_{18}\text{N}_{13}\text{P}_3\text{V}$ (1191.72); triclinic; $P\bar{1}$; $a = 11.483(2) \text{ \AA}$, $b = 11.901(2) \text{ \AA}$, $c = 18.093(4) \text{ \AA}$, $\alpha = 90.88(3)^\circ$, $\beta = 96.38(3)^\circ$, $\gamma = 91.60(3)^\circ$; $V = 2456.0(9) \text{ \AA}^3$; $Z = 2$; density, calcd. = 1.612 g cm^{-3} , $T = 193(2) \text{ K}$, $\mu = 0.415 \text{ mm}^{-1}$; $F(000) = 1208$; crystal size $0.620 \times 0.520 \times 0.460 \text{ mm}$; $\theta = 2.437$ to 28.426 deg. ; $-15 \leq h \leq 15$, $-15 \leq k \leq 14$, $-24 \leq l \leq 24$; rfln collected = 25922; rfln unique = 12253 [$R(\text{int}) = 0.0416$]; completeness to $\theta = 25.242 \text{ deg.} = 99.8 \%$; semi empirical absorption correction from equivalents; max. and min. transmission 1.11737 and 0.90264; data 12253; restraints 84, parameters 747; goodness-of-fit on $F^2 = 1.028$; final indices [$I > 2\sigma(I)$] $R_1 = 0.0409$, $wR_2 = 0.1060$; R indices (all data) $R_1 = 0.0548$, $wR_2 = 0.11126$; largest diff. peak and hole 0.391 and $-0.489 \text{ e \AA}^{-3}$.

Computational Details.

The characterization of the absorption spectrum was done employing two types of quantum chemical calculations: i) density functional theory in its unrestricted form, as for open shell species unrestricted orbitals are expected to deliver best geometries and energy values in comparison to restricted orbitals, and ii) multiconfigurational theory with an active space tailored to predict accurately the MC states. The first method is labelled below as “Unrestricted Kohn-Sham orbitals DFT (UKS), the second as “SOC-CASSCF(6,12)-FIC-NEVPT2”. These two methods are complementary to each other, as the first gives the best energetics for the LMCT states, while the second provides accurately the position of the MC states. The simulation of the excited state molecular dynamics states related to the spin-flip was done using surface hopping, below labeled as “non-adiabatic spin-flip dynamics calculations”. As explained in more detailed here, the electronic structure theory calculations underlying the molecular dynamics were done with the same computational protocol as the DFT calculations, but using restricted orbitals, in order to obtain pure spin states.

Static unrestricted Kohn-Sham orbitals DFT (UKS): All calculations were performed using the quantum computing suite ORCA 4.0.1.¹² Geometry optimization (Tables S1 – S2) was performed using unrestricted Kohn-Sham orbitals DFT (UKS) and the B3LYP functional¹³ in combination with Ahlrichs’ split-valence triple- ζ basis set def2-TZVPP for all atoms.^{14,15} Tight convergence criteria were chosen for DFT-UKS calculations (keywords `tightscf` and `tightopt`). All DFT-UKS calculations make use of the resolution of identity (Split-RI-J) approach for the Coulomb term in combination with the chain-of-spheres approximation for the exchange term (COSX).^{16,17} The zero order relativistic approximation was used to describe relativistic effects in all calculations (keyword ZORA).^{18,19} Grimme’s empirical dispersion correction D3(BJ) was employed (keyword D3BJ).^{20,21} To account for solvent effects, a conductor-like screening model (keyword CPCM) modeling acetonitrile was used in all calculations.²² Explicit counterions and/or solvent molecules were neglected. TD-DFT-UKS calculations were performed at the same level of theory using unrestricted Kohn-Sham orbitals (UKS). Fifty vertical spin-allowed transitions were calculated (Tables S3 – S4).

SOC-CASSCF(6,12)-FIC-NEVPT2: Calculations of ground- and excited-state properties with respect to metal-centered (MC) states were performed using the complete-active-space self-consistent field method (including spin-orbit coupling (SOC-CASSCF)^{23,24} for calculation of the zero-field splitting D) in conjunction with the fully internally contracted N-electron valence perturbation theory to second order (FIC-NEVPT2)^{25,26} in order to recover missing dynamic electron correlation. SOC was treated through the mean-field (SOMF) approximation^{27,28}, and the effective Hamiltonian approach²⁹⁻³¹ was used to compute the spin-Hamiltonian parameters. In order to accurately model the ligandfield, active spaces were chosen to encompass the dominate bonding/antibonding orbitals formed between vanadium and the ligand. An active space of (6,12) along with 10 triplet roots and 12 singlet roots was selected (Tables S5 – S6). In addition to the minimal active space of (2,5), two occupied V-N σ bonding orbitals and a second d shell³² were included in these calculations (Table S5).

Non-adiabatic spin-flip dynamic calculations were accomplished using the SHARC (Surface Hopping including ARbitrary Couplings)³³⁻³⁶ molecular dynamics program suite with the pySHARC driver. The electronic Hamiltonian was approximated using a linear vibronic coupling (LVC) method³⁷ based on TDDFT vertical excitations calculated using the methodological details described above with one essential difference. The open-shell (UKS) ground state electronic wave function used as a reference for the previous TDDFT calculations delivers electronic states that cannot be labelled according to their spin multiplicity (i.e., they are not eigenfunctions of the spin operator). As we need explicit couplings between pure singlet and pure triplet states, a RKS approach, where the two unpaired electrons are forced to be paired in one restricted orbital, is used to do single point calculations on the UKS optimized geometry and obtain pure triplet states as a linear response of a pure singlet state. The obtained RKS energies are also listed in Table S3. Since there is only one reference closed-shell orbital instead of two – as one would have in an open-shell triplet state – some electronic states are missing in the RKS approach with respect to the UKS calculation. In the RKS

approach, the assignment of the state characters has been done dividing the molecule into three fragments (metal center and two ddpd ligands) and calculating charge transfer (CT) numbers, as implemented in the TheoDore software package.³⁸ The quantitative wave function analysis is presented in Fig. S21 and the largest contribution is used to state the main state character in Table S3.

A total of 48 coupled diabatic electronic states (12x3 triplets and 12 singlets, listed in Table S8) were included in the SHARC-LVC calculations. For the 100 fs simulations (Fig. S22), 4 sets of 54, 69, 60, 59 trajectories were excited 100 % to the lowest 1^3LMCT , 2^3LMCT , 3^3LMCT and 4^3LMCT states, respectively. In the 50 ps simulation (Figure 4), 294 trajectories were included, starting from the 2^3LMCT state, which was identified as the longest-lived state during the previous 100 fs. The nuclear motion was propagated with a 0.5 fs step, and the electronic wave function was integrated with a 0.02 fs step, using the local diabatization scheme.³⁹ During a hop, the full momentum vector was rescaled to conserve total energy. The energy-based decoherence correction⁴⁰ with the standard parameter of 0.1 a.u. was used. 1000 initial geometries were sampled from a harmonic Wigner distribution of the UKS ground state; from the 231 available normal modes, one imaginary mode (-30 cm^{-1}) and the highest 33 (from 3047 to 3279 cm^{-1}) were excluded due to anharmonicities. These modes correspond to the large amplitude torsions of the methyl groups, which cannot be described by a linear model potential. For each of the remaining 196 normal modes, 4415 intrastate and 18827 interstate vibronic couplings were calculated using a numerical differentiation scheme and the computation of wave function overlaps between the states at the reference geometry and the displaced geometries. We note that the optimized geometry of the singlet reference state and that of the triplet ground state are very similar (RMSD = 0.584), justifying the use of the UKS frequencies as seed for the initial conditions.

Using the LVC framework, the optimization of the longest-lived singlet state (2^1MC) leads to the structure given in Table S9. This state lays 1.1 eV above the triplet ground state and it is assigned as the NIR emissive state.

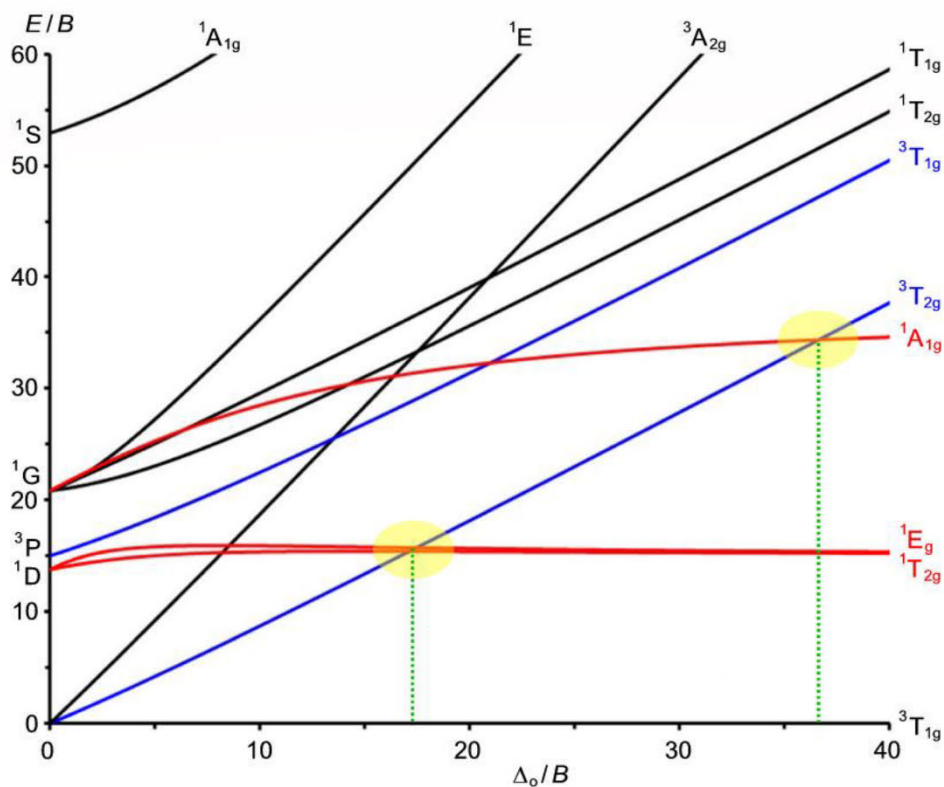


Figure S1. Tanabe Sugano diagram for octahedral transition metal complexes with d^2 electron configuration ($C/B = 4.42$). Relevant excited triplet states in blue, relevant singlet states in red, important crossing points highlighted in yellow.⁴²

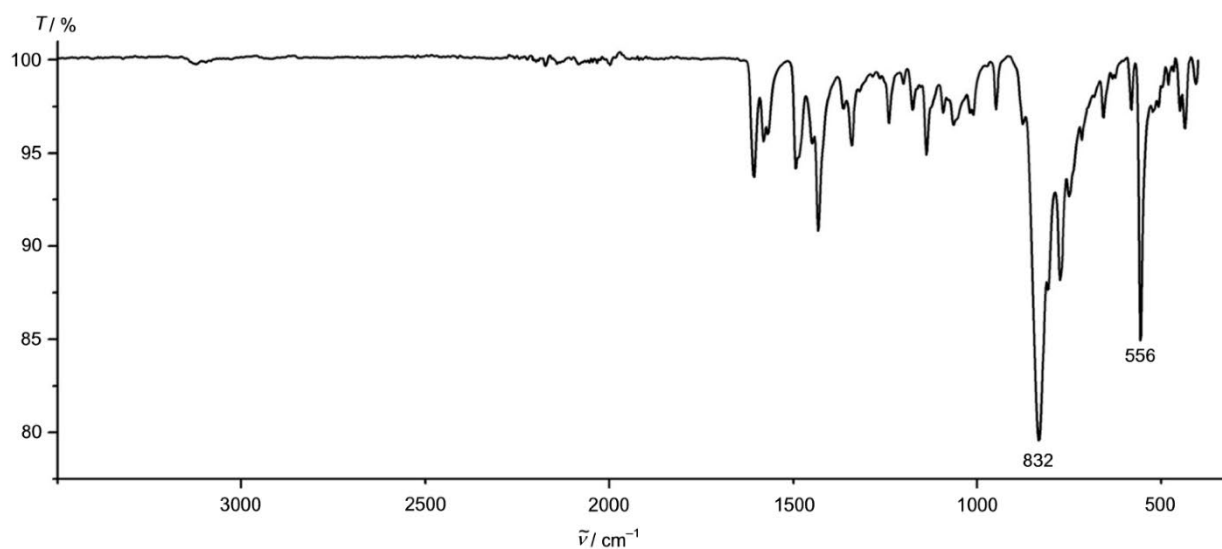


Figure S2. ATR IR spectrum of $\text{mer-}[V^{III}(\text{ddpd})_2][\text{PF}_6]_3$.

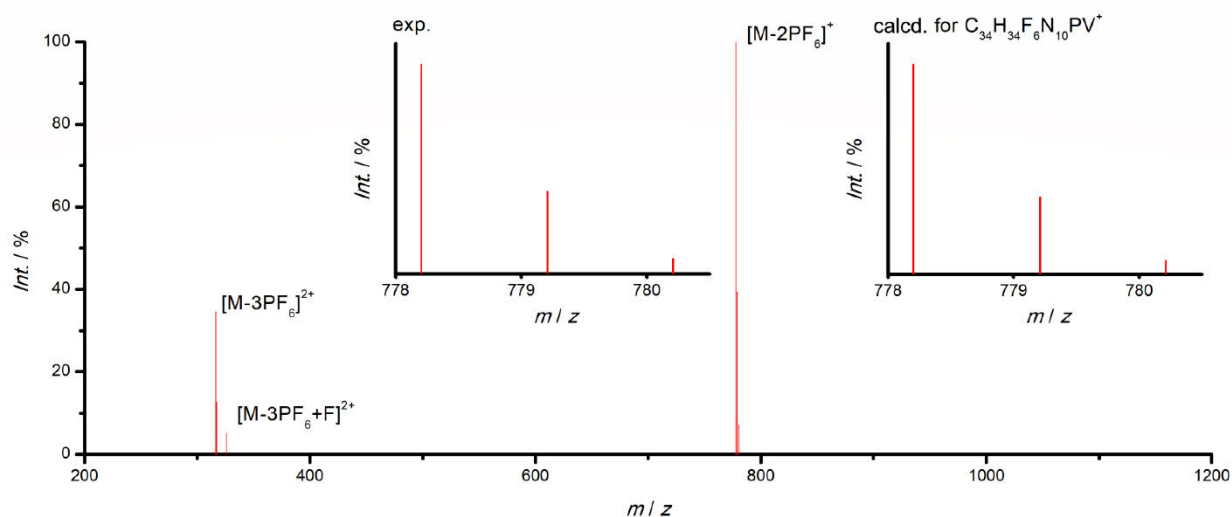


Figure S3. ESI⁺ mass spectrum of *mer*-[V^{III}(dddpd)₂][PF₆]₃ in CH₃CN. The insets show the experimental and calculated isotopic pattern of the largest peak.

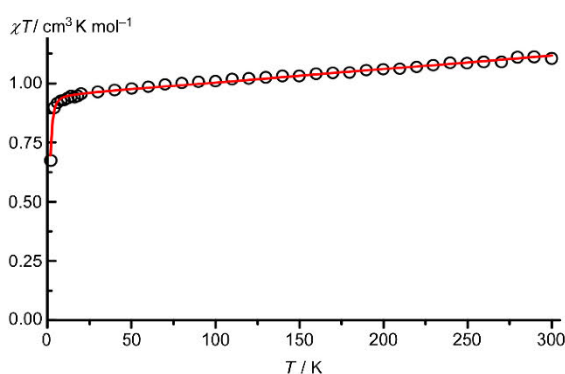


Figure S4. Temperature-dependence of χ_{MT} of *mer*-[V(dddpd)₂][PF₆]₃ (black circles) with fit (red line, $g = 1.946(2)$, $D = +2.87(11)$ cm⁻¹; TIP = 566×10^{-6} cm³ K mol⁻¹). Simulation with a negative D value gave a slightly poorer fit to the experimental data. As obtained by HF-EPR spectroscopy, reported vanadium(III) complexes exhibit positive D values.⁴³ Only two oxalates of vanadium(III) are reported to possess negative D values based on inelastic neutron scattering and single crystal high-resolution FT absorption spectroscopy.⁴⁴

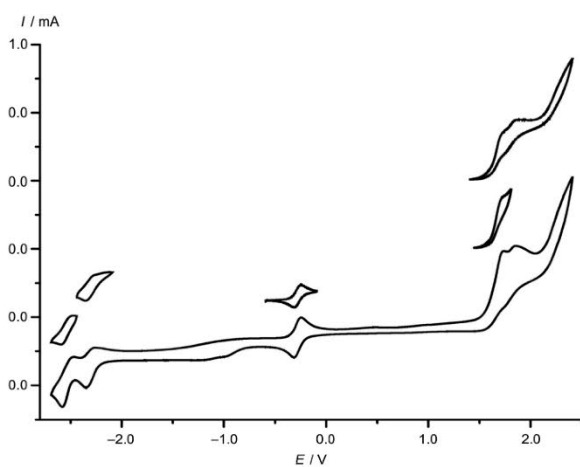
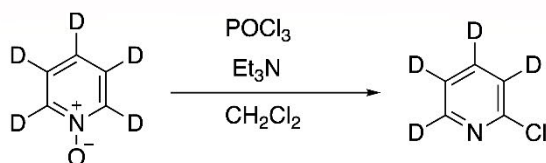
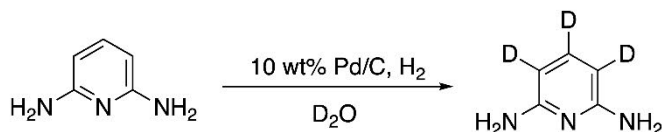


Figure S5. Cyclic voltammogram of *mer*-[V^{III}(dddpd)₂][PF₆]₃ in [ⁿBu₄N][PF₆] in CH₃CN; E vs. ferrocene.

Synthesis and characterization of [D₁₇]-ddpd[D₄]-2-Chloropyridine⁴⁵

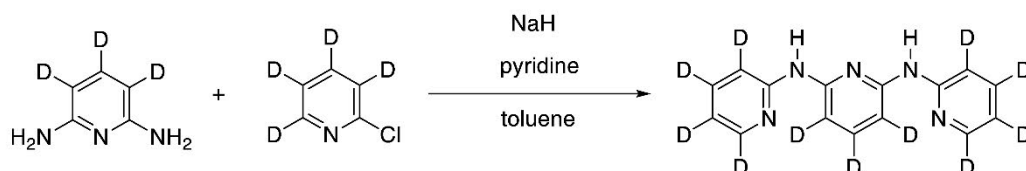
To a stirred solution of [D₅]-pyridine-N-oxide⁴⁶ (8.1 g, 81 mmol, 1.0 eq.) and triethylamine (13.4 ml, 9.8 g, 97 mmol, 1.2 eq.) in dichloromethane (80 ml) was slowly added a solution of POCl₃ (8.8 ml, 14.9 g, 97 mmol, 1.2 eq.) in dichloromethane (50 ml) at 10 °C. After stirring for 30 minutes at room temperature, the reaction mixture was refluxed for 1 h. The solution was cooled to room temperature and ice was slowly added until all excess phosphoroychloride was hydrolysed. After addition of water (30 ml), the solution pH was adjusted to 10 with aq. NaOH (2 M). The organic layer was separated and the aqueous layer was extracted with CH₂Cl₂ (5 × 30 ml). The combined organic layers were washed with a saturated NaCl solution, dried (MgSO₄) and concentrated at reduced pressure. The resulting red oil was subjected to column chromatography (SiO₂, CH₂Cl₂, preloading onto SiO₂, detection: UV). The product was obtained as a colorless oil (3.8 g, 40 %, >99.5 %D).

¹³C{¹H} NMR (101 MHz, CDCl₃): δ = 151.4 (s), 149.3 (t, *J* = 28.0 Hz), 138.3 (t, *J* = 25.0 Hz), 124.0 (t, *J* = 26.2 Hz), 121.7 (t, *J* = 25.6 Hz) ppm. MS (ESI⁺): *m/z* (%) = 118.04 (100, [M+H]⁺).

[D₃]-2,6-Diaminopyridine

In analogy to a published procedure,⁴⁷ a mixture of 2,6-diaminopyridine (500 mg, 4.6 mmol, 1.0 eq.) and 10 % Pd/C (10 wt-%, 50 mg) in D₂O (20 ml, NMR grade, 99.9 %D) in a steel autoclave was set under an atmosphere of H₂ (1 bar) and stirred at 180 °C (bath temperature) for 24 h. After cooling to room temperature, methanol (20 ml) was added and the dark green reaction mixture was filtered through celite. The filter cake was washed with additional methanol (3 × 10 ml) and the combined filtrate was concentrated under reduced pressure. The product was obtained as dark green solid (510 mg, 99 %, H^{3/5}: 87 %D, H⁴: 97 %D, overall: 90.5 %D).

¹H NMR (400 MHz, CD₃OD): δ = 7.18 (0.03 H, non-deuterated residual signal), 5.84 (0.25 H, non-deuterated residual signal), 4.84 (s, 4 H) ppm. MS (ESI⁺): *m/z* (%) = 113.1 (100, [M+H]⁺).

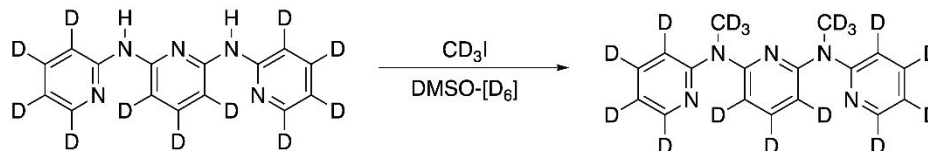
[D₁₁]-*N,N'*-Bis(2-pyridyl)-2,6-diaminopyridine

In analogy to a published procedure,⁴⁸ under an argon atmosphere a mixture of [D₃]-2,6-diaminopyridine (0.5 g, 4.4 mmol, 1 eq.) and NaH (60 wt% dispersion in mineral oil, 1.2 g, 29 mmol, 6.8 eq.) was stirred for 5 min

at room temperature. [D₄]-2-Chloropyridine (1.2 ml, 1.5 g, 13 mmol, 3 eq.) and pyridine (2.5 ml) were added, followed by stirring for 5 min at room temperature. The reaction mixture was immersed in a preheated oil bath at 150 °C resulting in immediate, strong gas evolution. A few minutes later, just before the red brown suspension became a solid mass, dry toluene (15 ml) was added. The mixture was stirred at 150°C (bath temperature) for 4 h. After cooling to room temperature, the solvent was removed under reduced pressure. Cautiously, ice-cold water (30 ml) was added dropwise. After stirring for 10 minutes, the brown precipitate was collected on a sintered-glass frit (porosity 3), washed extensively with water (3 × 20 ml) and *n*-hexane (3 × 10 ml). The light brown solid was dissolved in THF (60 ml) and filtered through a short plug of silica. The plug was washed with additional THF (3 × 10 ml) and the combined THF filtrates were concentrated under reduced pressure resulting in a brown solid. The crude product was transferred into a 25 ml round bottom flask and MeOH (3 ml), CH₂Cl₂ (3 ml) and Et₂O (3 ml) were added. After stirring for 3 h at room temperature, the mixture was cooled in an ice bath. The beige solid was collected on a filter, washed with Et₂O (3 × 5 ml) and dried under vacuum. The product was obtained as beige solid (0.36 g, 29 %, 90.3 %D).

¹H NMR (400 MHz, [D₆]-DMSO): δ = 9.36 (s, 2 H), 7.12 (0.9 H, non-deuterated residual signal) ppm.

[D₁₇]-ddpd⁴⁹



Under an argon atmosphere, powdered KOH (99 mg, 1.8 mmol, 4.0 eq.) was added to a yellow solution of [D₁₁]-*N,N'*-bis(2-pyridyl)-2,6-diaminopyridine (120 mg, 0.4 mmol, 1.0 eq.) in [D₆]-DMSO (10 ml, NMR grade, 99.8 %D). The mixture was stirred at room temperature for 30 min. CD₃I (60 μl, 140 mg, 0.97 mmol, 2.2 eq.) was added to the red reaction solution and stirring was continued overnight (16 h). Water (40 ml) was added and the yellow aqueous suspension was extracted with a 1:1 (v/v) mixture of Et₂O/THF (3 × 30 ml). The combined organic phases were washed with aqueous sat. Na₂CO₃ (25 ml), dried (MgSO₄) and concentrated under reduced pressure. The resulting yellow oil was subjected to column chromatography (SiO₂, *n*-hexane/EtOAc, 12:1) to obtain the product as a pale-yellow oil (75 mg, 55 %, >93.6 %D).

¹H NMR (400 MHz, CDCl₃): δ = 6.76 (non-deuterated residual signal) ppm (Fig. S6). MS (ESI⁺): *m/z* (%) = 308.3 (100, [M+H]⁺) (Fig. S7 – S8).

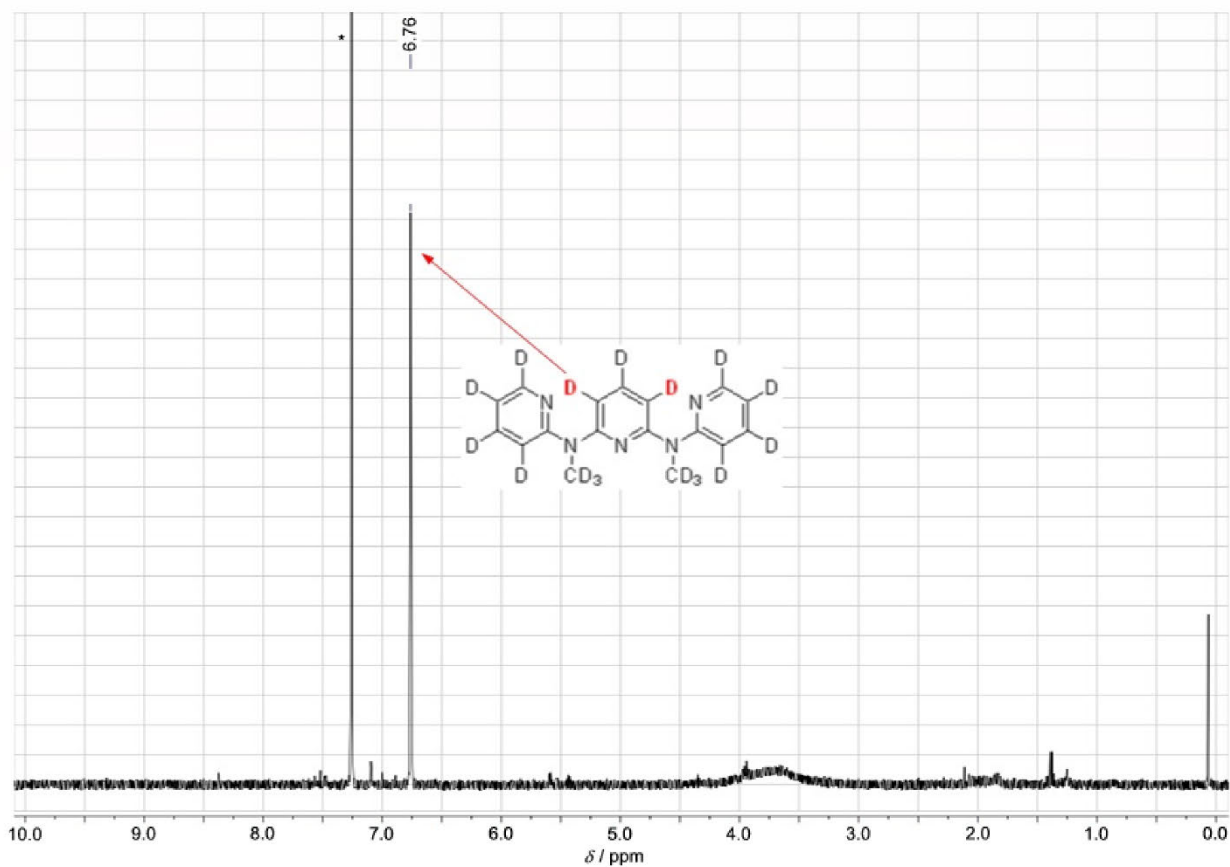


Figure S6. ^1H NMR spectrum (400 MHz) of $[\text{D}_{17}]$ -ddpd in CDCl_3 showing the only major residual proton resonance due to incomplete deuteration at the position indicated in bold red. The asterisk marks residual solvent resonance.

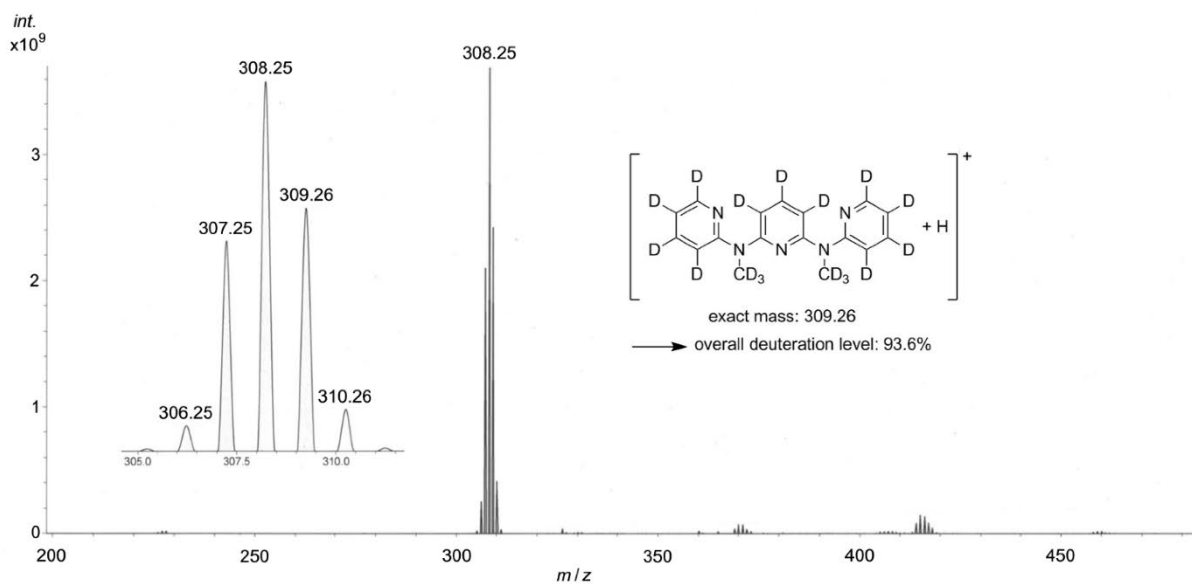


Figure S7. ESI^+ mass spectrum of $[\text{D}_{17}]$ -ddpd.

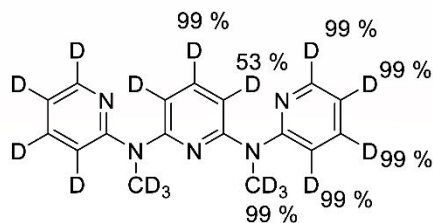


Figure S8. Detailed deuteration pattern of $[D_{17}]$ -ddpd from combined 1H NMR and mass spectrometry data.

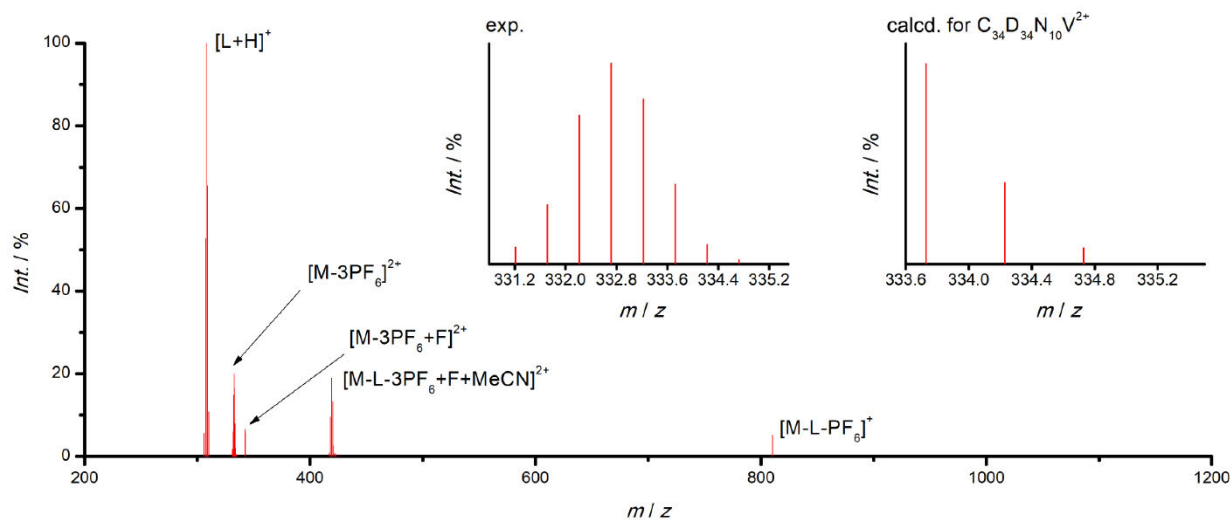


Figure S9. ESI⁺ mass spectrum of mer - $[V^{III}]([D_{17}]$ -ddpd)₂[PF₆]₃ in CH₃CN. The insets show the experimental and calculated isotopic pattern of the $[M-3PF_6]^{2+}$ peak.

Synthesis of [V(ddpd)₂][PF₆]₃: [V(NCMe)₆][BPh₄]₂ (42.0 mg, 0.05 mmol, 1.0 eq) was dissolved in acetonitrile (4 ml) and [ⁿBu₄N][PF₆] (52.2 mg, 0.14 mmol, 2.8 eq.), dissolved in acetonitrile (2 ml), was added under stirring. The ligand ddpd (27.7 mg, 0.09 mmol, 1.8 eq.), dissolved in acetonitrile (2 ml), was added. The turquoise solution was stirred for 18 h and turned dark red within the first several hours. Upon addition of ferrocenium hexafluorophosphate (15.0 mg, 0.05 mmol, 1.0 eq.), dissolved in acetonitrile (4 ml), the red solution turned green. The solvent was removed under reduced pressure and the dark green residue was washed with 2 ml aliquots of petroleum ether (40/60) until the washing solution remained colorless. After dissolving the green product in acetonitrile (4 ml), black crystals were obtained from slow diffusion of diethyl ether into the solution. Yield: 18.2 mg (0.02 mmol, 44 %). C₃₄H₃₄F₁₈N₁₀P₃V: calcd. C 38.22; H 3.21; N 13.11 %; found: C 38.22; H 3.43; N 13.56 %. IR (ATR): $\tilde{\nu}$ = 1607 (m), 1581 (w), 1568 (w), 1494 (m), 1449 (w), 1432 (m), 1364 (w), 1341 (w), 1319 (w), 1240 (w), 1201 (w), 1175 (w), 1138 (w), 1093 (w), 1065 (w), 1052 (w, sh), 1020 (w), 1011 (w), 949 (w), 876 (w), 832 (s), 807 (s), 775 (s), 750 (m), 716 (w), 656 (w), 633 (w), 582 (w), 556 (s), 523 (w), 507 (w), 480 (w), 467 (w), 449 (w), 436 (w) cm⁻¹. MS (ESI⁺, CH₃CN): *m/z* (%) = 316.6 (35) [M-3PF₆]³⁺, 326.1 (5) [M-3PF₆+F]⁺, 778.2 (100) [M-2PF₆]⁺. UV/VIS/NIR (CH₃CN): λ (ϵ / M⁻¹cm⁻¹) = 207 (25015), 241 (26040), 301 (23585), 422 (3775) 597 (1945) nm. CV ([ⁿBu₄N][PF₆]/CH₃CN, vs. ferrocene): *E*_{1/2} = -2.53 (qrev.), -2.31 (qrev.), -0.275 (rev.) V; *E*_p = 1.74 (irrev.), 1.86 (irrev.) V.

Synthesis of [V([D₁₇]-ddpd)₂][PF₆]₃: The deuterated complex was prepared analogously, starting from [D₁₇]-ddpd (27.7 mg, 0.09 mmol, 2.0 eq.). Yield: 8.6 mg (0.008 mmol, 13 %). The degree of deuteration was fully retained according to ESI⁺ mass spectrometry.

Table S1. Bond distances / Å and angles / ° of *mer*-[V^{III}(ddpd)₂][PF₆]₃·3CH₃CN (XRD) and *mer*-[V^{III}(ddpd)₂]³⁺ (DFT-UKS).

	ddpd(A)		ddpd(B)		shape parameter <i>S</i> (OC-6) ⁴⁷
	V-N1 / V-N2 / V-N3	N1-V-N2 / N1-V-N3 / N2-V-N3	V-N4 / V-N5 / V-N6	N4-V-N5 / N4-V-N6 / N5-V-N6	
XRD	2.079(2)/ 2.062(1)/ 2.068(2)	84.14(6)/ 168.23(6)/ 84.13(6)	2.074(2)/ 2.058(1)/ 2.081(2)	85.12(6)/ 169.73(6)/ 84.69(6)	0.63
DFT-UKS	2.095 2.078 2.097	84.24 168.56 84.32	2.092 2.077 2.096	84.16 168.40 84.25	0.68

Table S2. Cartesian Coordinates of the DFT-UKS calculated ground state geometry of *mer*-[V^{III}(ddpd)₂]³⁺.

23	-0.436272000	4.887622000	1.498586000
7	0.057762000	4.359394000	3.465344000
7	0.566002000	2.182490000	2.743718000
7	1.171885000	3.674479000	0.990576000
7	1.735378000	5.193304000	-0.753156000
7	-0.608309000	5.160298000	-0.568481000
7	-1.881315000	3.370031000	1.418202000
7	-2.967475000	4.322157000	3.270756000
7	-2.043433000	6.107196000	1.995698000
7	-1.078209000	7.861890000	0.710978000
7	0.685217000	6.647703000	1.684615000
6	-0.136059000	5.257662000	4.457962000
1	-0.259546000	6.284304000	4.150607000
6	-0.211793000	4.895243000	5.778999000
1	-0.382655000	5.644256000	6.536428000
6	-0.081057000	3.543448000	6.097041000
1	-0.146249000	3.212495000	7.123799000
6	0.163009000	2.623064000	5.098671000
1	0.313028000	1.585384000	5.342659000
6	0.261183000	3.065063000	3.774103000
6	0.413147000	0.745847000	3.014200000
1	-0.540605000	0.588956000	3.509025000
1	1.213525000	0.349688000	3.639044000
1	0.400412000	0.219756000	2.065843000
6	1.420814000	2.536984000	1.690707000
6	2.497005000	1.718823000	1.381436000
1	2.690014000	0.831463000	1.959805000
6	3.346353000	2.091812000	0.355262000
1	4.198093000	1.474345000	0.108427000
6	3.106104000	3.253067000	-0.356363000
1	3.743171000	3.535313000	-1.177084000
6	2.000162000	4.024811000	-0.028203000
6	2.891430000	5.883199000	-1.344184000
1	2.632379000	6.928522000	-1.483488000
1	3.191768000	5.454711000	-2.300306000
1	3.718554000	5.823470000	-0.645115000
6	0.483182000	5.466337000	-1.293928000
6	0.357628000	6.053399000	-2.558570000
1	1.231585000	6.307009000	-3.133546000
6	-0.902124000	6.260699000	-3.081259000
1	-1.006918000	6.701378000	-4.062468000
6	-2.027893000	5.874740000	-2.353587000
1	-3.027361000	6.005690000	-2.738081000
6	-1.836368000	5.328887000	-1.109826000
1	-2.670761000	5.035170000	-0.492501000
6	-1.729583000	2.362329000	0.528906000
1	-1.035394000	2.541877000	-0.277137000
6	-2.384217000	1.162843000	0.651400000
1	-2.220705000	0.380897000	-0.073714000
6	-3.239090000	0.990094000	1.739795000
1	-3.767402000	0.057720000	1.879655000
6	-3.435458000	2.025466000	2.630370000
1	-4.127804000	1.914655000	3.447243000
6	-2.758753000	3.234073000	2.429724000
6	-3.604148000	4.064075000	4.570470000
1	-3.131234000	3.195145000	5.018379000
1	-4.676344000	3.887573000	4.485973000
1	-3.427930000	4.921238000	5.211336000
6	-3.045409000	5.633621000	2.781636000
6	-4.137792000	6.421152000	3.112467000
1	-4.931914000	6.021879000	3.720181000
6	-4.214122000	7.705453000	2.603668000
1	-5.063960000	8.329648000	2.839898000

Appendix

6	-3.204065000	8.191998000	1.793981000
1	-3.239019000	9.200534000	1.418905000
6	-2.117001000	7.375772000	1.514158000
6	-1.433285000	8.883518000	-0.284577000
1	-0.691772000	8.861308000	-1.077409000
1	-1.478835000	9.886173000	0.140329000
1	-2.398162000	8.626338000	-0.708437000
6	0.257173000	7.779071000	1.094684000
6	1.137328000	8.843198000	0.867841000
1	0.793923000	9.744769000	0.390211000
6	1.954271000	6.577639000	-2.147616000
6	2.440965000	8.742728000	1.308045000
6	2.860348000	7.594130000	1.978984000
1	2.229881000	5.657694000	2.639060000
1	3.867457000	7.488226000	2.351171000
1	3.123251000	9.565649000	1.149268000

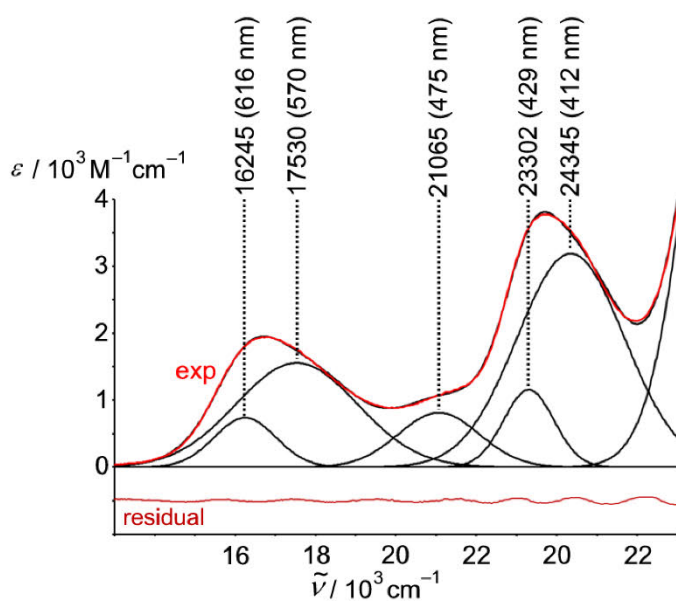


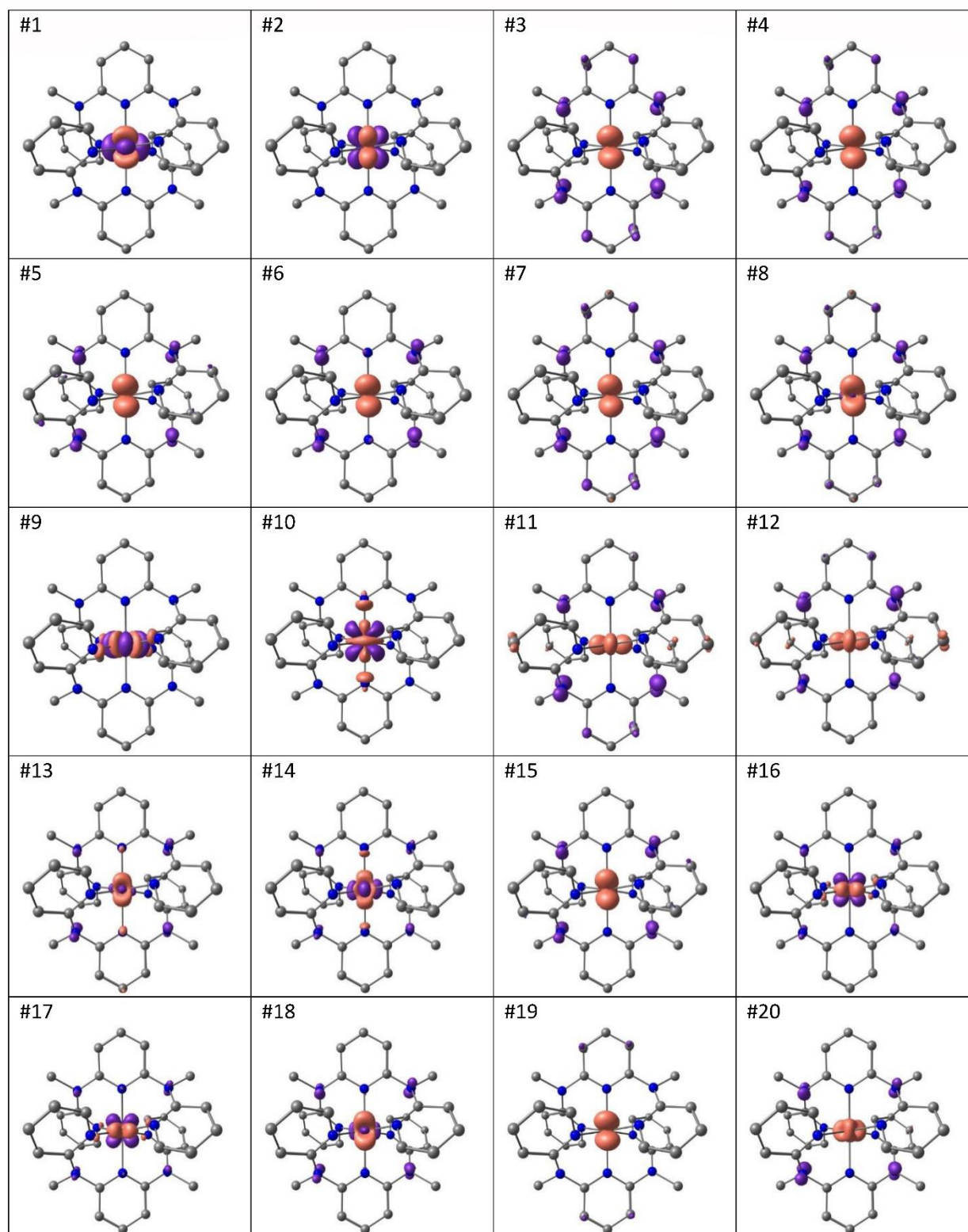
Figure S10. UV/Vis spectrum of *mer*-[V^{III}(ddd)₂][PF₆]₃ in CH₃CN (red) including Gaussian deconvolution (black).

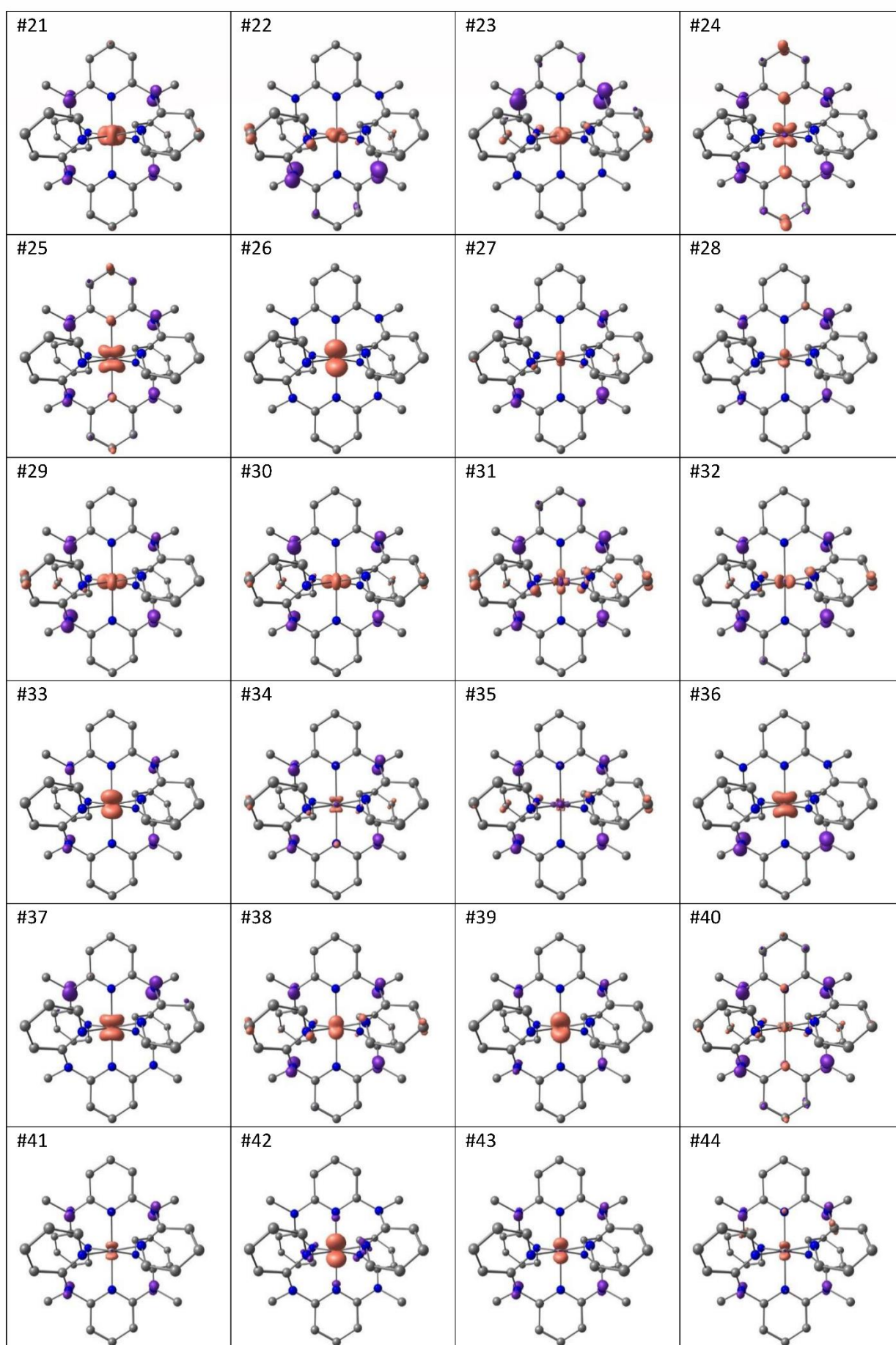
Table S3. TD-DFT calculated spin-allowed transitions (UKS) and triplet states (RKS). The assignment of the UKS states was accomplished by visual inspection of difference electron densities (Table S4). The assignment of the RKS states corresponds to the largest contribution to the charge transfer number (Fig. S21).

TD-DFT-UKS						TD-DFT-RKS				
state	$\tilde{\nu} / \text{cm}^{-1}$	λ / nm	E / eV	f_{osc}	assignment	$\tilde{\nu} / \text{cm}^{-1}$	λ / nm	E / eV	assignment	
1	3589	2786	0.445	7.71E-04	³ MC	2084	4800	0.258	³ MC	
2	5077	1970	0.629	7.41E-06	³ MC					
3	15858	631	1.966	1.31E-02	³ LMCT(NMe→V)					
4	16237	616	2.013	9.71E-04	³ LMCT(NMe→V)					
5	19875	503	2.464	3.64E-03	³ LMCT(NMe→V)					
6	20343	492	2.522	3.32E-06	³ LMCT(NMe→V)					
7	22097	453	2.740	2.93E-02	³ LMCT(NMe→V)					
8	22543	444	2.795	1.20E-03	³ LMCT(NMe→V)					
9	22675	441	2.811	2.66E-04	³ MC	22529	444	2.793	³ MC	
10	24203	413	3.001	2.42E-06	³ MC	24786	404	3.073	³ MC	
11	24582	407	3.048	1.62E-04	³ LMCT(NMe→V)	26901	372	3.335	³ LMCT	
12	24875	402	3.084	1.12E-02	³ LMCT(NMe→V)	27316	366	3.387	³ LMCT	
13	26190	382	3.247	7.63E-04	³ LMCT(NMe→V)/ ³ MC	27616	362	3.424	³ LMCT	
14	26214	382	3.250	3.31E-04	³ MC/LMCT(NMe→V)					
15	26329	380	3.264	1.01E-04	³ LMCT(NMe→V)					
16	26661	375	3.306	4.13E-04	³ MC/ ³ LMCT(NMe→V)	28058	356	3.479	³ LMCT	
17	26932	371	3.339	3.68E-04	³ MC/ ³ LMCT(NMe→V)	30461	328	3.777	³ LMCT	
18	27056	370	3.355	8.04E-07	³ MC/ ³ LMCT(NMe→V)	30586	327	3.792	³ LMCT	
19	27374	365	3.394	2.14E-03	³ MC	31428	318	3.897	³ LMCT	
20	27914	358	3.461	2.08E-04	³ LMCT(NMe→V)	31650	316	3.924	³ LMCT	
21	28340	353	3.514	3.22E-04	³ LMCT(NMe→V)					
22	28285	354	3.507	6.86E-03	³ LMCT(NMe→V)/ ³ ILCT					
23	28368	353	3.517	2.12E-03	³ LMCT(NMe→V)/ ³ ILCT					
24	29010	345	3.597	1.71E-02	³ LMCT(NMe→V)/ ³ ILCT					
25	29431	340	3.649	2.62E-02	³ LMCT(NMe→V)/ ³ ILCT					
26	30068	333	3.728	4.04E-03	³ MC					
27	30568	327	3.790	1.51E-04	³ LMCT(NMe→V)					
28	30709	326	3.807	9.10E-05	³ LMCT(NMe→V)/ ³ ILCT					
29	30659	326	3.801	3.28E-04	³ LMCT(NMe→V)/ ³ ILCT					
30	30835	324	3.823	1.10E-02	³ LMCT(NMe→V)/ ³ ILCT					
31	30814	325	3.820	2.33E-04	³ LMCT(NMe→V)/ ³ ILCT					
32	31164	321	3.864	3.39E-02	³ LMCT(NMe→V)/ ³ ILCT					
33	31585	317	3.916	1.27E-04	³ LMCT(NMe→V)					
34	31725	315	3.933	1.19E-04	³ LMCT(NMe→V)/ ³ ILCT					
35	31708	315	3.931	5.79E-03	³ LMCT(NMe→V)/ ³ ILCT					
36	31789	315	3.941	4.03E-03	³ LMCT(NMe→V)					
37	31794	315	3.942	2.68E-03	³ LMCT(NMe→V)					
38	31985	313	3.966	2.60E-02	³ LMCT(NMe→V)/ ³ ILCT					
39	32267	310	4.001	7.96E-04	³ LMCT(NMe→V)					
40	32293	310	4.004	5.48E-02	³ LMCT(NMe→V)/ ³ ILCT					
41	32487	308	4.028	1.44E-02	³ LMCT(NMe→V)					
42	32451	308	4.023	1.53E-03	³ LMCT(NMe→V)					
43	32912	304	4.081	3.15E-02	³ LMCT(NMe→V)					
44	32947	304	4.085	7.00E-03	³ LMCT(NMe→V)/ ³ ILCT					
45	32928	304	4.083	7.16E-02	³ LMCT(NMe→V)					
46	33231	301	4.120	3.10E-04	³ LMCT(NMe→V)					
47	33292	300	4.128	1.29E-02	³ LMCT(NMe→V)/ ³ ILCT					
48	33381	300	4.139	3.82E-05	³ LMCT(NMe→V)					
49	33701	297	4.178	2.04E-03	³ MC					
50	33750	296	4.185	1.87E-02	³ LMCT(NMe→V)/ ³ ILCT					

Appendix

Table S4. Difference electron densities of the 50 lowest-lying TD-DFT-UKS calculated states. (isosurface value at 0.007 a.u.; purple = electron depletion; orange = electron gain; hydrogen atoms omitted).





Appendix

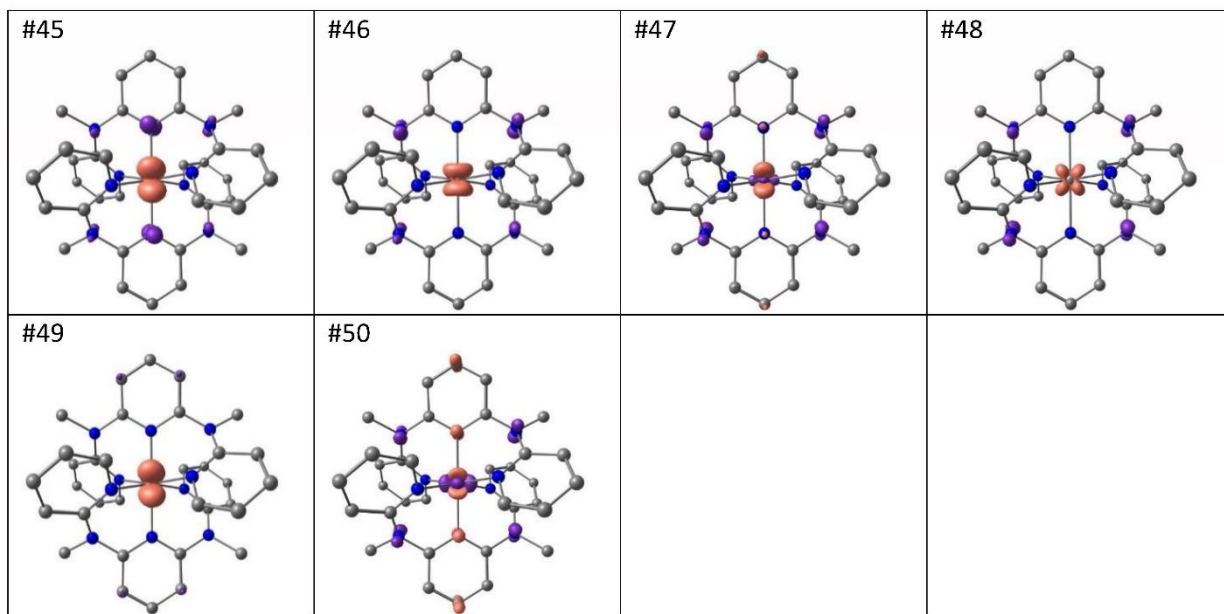
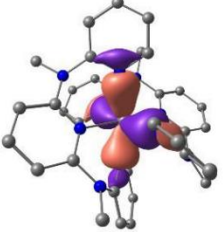
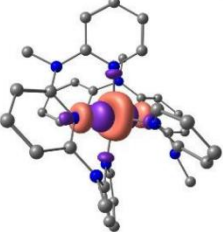
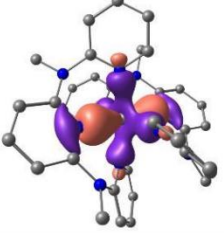
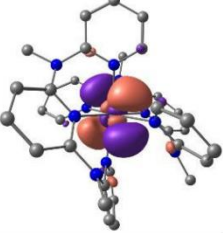
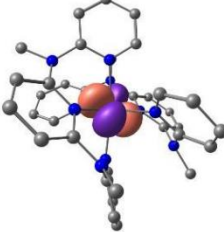
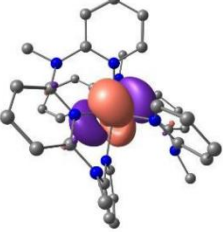
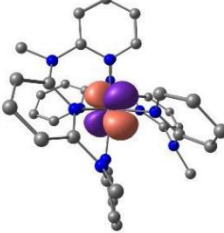
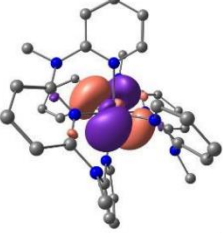
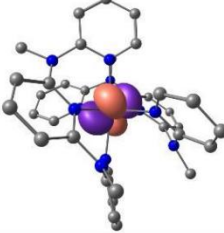
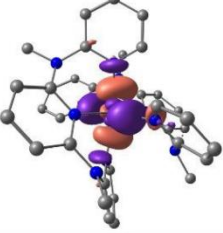
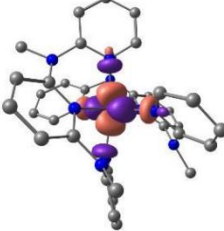
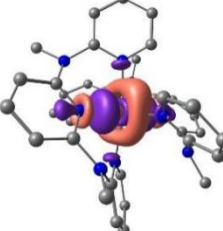


Table S5. Orbital energies/Hartree of the canonical orbitals used in the active space of the CASSCF(6,12)-FIC-NEVPT2 calculation, depicted at a contour value of 0.05 a.u. (hydrogen atoms omitted for clarity).

#	E/H	orbital	#	E/H	orbital
161	-0.59153		167	+0.12076	
162	-0.59466		168	+0.8329	
163	-0.00153		169	+0.85194	
164	+0.00038		170	+0.89659	
165	+0.00753		171	+1.31242	
166	+0.11194		172	+1.49528	

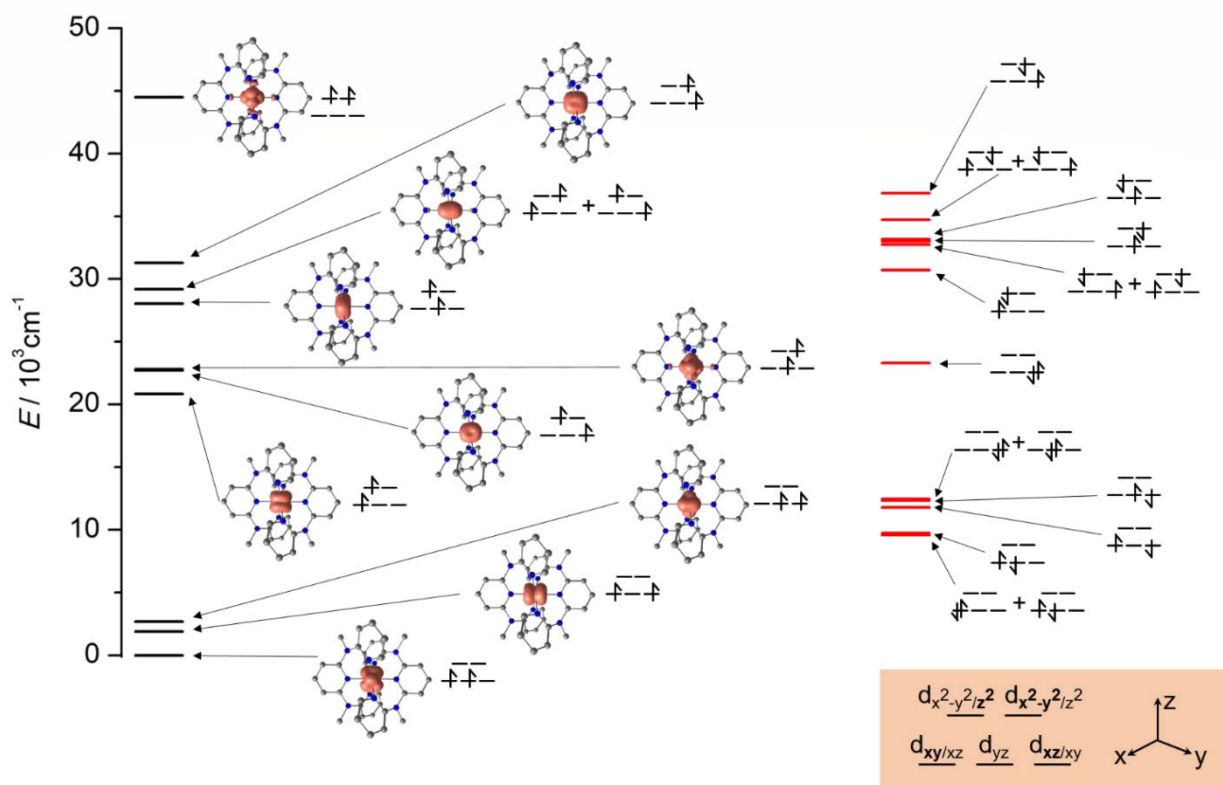


Figure S11. Energy diagram of the electronic states of $mer-[V^{III}(ddpd)_2]^{3+}$ constructed from CASSCF(6,12)-FIC-NEVPT2 energies with spin densities in orange (0.05 a.u. isosurface value, hydrogen atoms omitted for clarity, triplet states in black, singlet states in red; a coordinate system referring to the displayed structures and d orbital labels is shown in the orange box).

Table S6. CASSCF(6,12)-FIC-NEVPT2 state compositions (the configurations are the occupation numbers for the individual active orbitals in rising energy (in eV and cm^{-1}). The first two numbers of the configuration represent the ligand-metal σ -bonding orbitals, the next five the metal 3d orbitals and the last five the 4d orbitals (Table S6). Singlet states shown in red, triplet states shown in black.

state	root	mult	configuration	weight	$\Delta E/\text{eV}$	$\tilde{\nu} / \text{cm}^{-1}$	λ/nm
0	0	3	221100000000	0.94971	0		
1	1	3	221010000000	0.94790	0.232	1873	5344
2	2	3	220110000000	0.95301	0.333	2687	3723
3	0	1	222000000000	0.65408	1.192	9612	1040
4	1	1	221100000000	0.96124	1.207	9736	1027
5	2	1	221010000000	0.97424	1.459	11769	850
6	3	1	220110000000	0.95454	1.529	12333	811
7	4	1	220020000000	0.48695	1.541	12431	805
8	3	3	221001000000	0.83676	2.584	20844	480
9	4	3	220011000000	0.70074	2.815	22706	440
10	5	3	220100100000	0.42279	2.827	22803	439
11	5	1	220020000000	0.98358	2.887	23283	429
12	6	3	220101000000	0.94490	3.475	28026	357
13	7	3	221000100000	0.67288	3.618	29183	343
14	6	1	221001000000	0.91877	3.809	30720	326
15	8	3	220010100000	0.81832	3.878	31278	320
16	7	1	220011000000	0.57938	4.059	32735	305
17	8	1	220100100000	0.96151	4.095	33028	303
18	9	1	220101000000	0.97839	4.112	33163	302
19	10	1	221000100000	0.58977	4.303	34708	288
20	11	1	220010100000	0.93700	4.567	36835	271
21	9	3	220001100000	0.99098	5.518	44503	225

Table S7. Partial quantum yields Φ and luminescence lifetimes τ for $[\text{V}(\text{ddpd})_2][\text{PF}_6]_3$ and $[\text{V}([\text{D}_{17}]\text{-ddpd})_2][\text{PF}_6]_3$ in deoxygenated solutions.

compound	$\Phi_F / \%$ ^a	τ_F / ns (fraction) ^b	$\Phi_P / \%$ ^c	τ_P / ns	τ_F / ns
				(fraction) ^d	(fraction)
				in ${}^n\text{BuCN}$, 77 K	in ${}^n\text{PrCN}$, 77 K
		in CD_3CN , 298 K			
$[\text{V}(\text{ddpd})_2][\text{PF}_6]_3$	2.1	3.2 (56 %) 8.2 (44 %)	1.8×10^{-4}	790 (93 %) 8800 (7 %)	1.7 (51 %) 6.3 (49 %)
$[\text{V}([\text{D}_{17}]\text{-ddpd})_2][\text{PF}_6]_3$	1.2	3.3 (88 %) 7.2 (12 %)	1.6×10^{-4}	800 (91 %) 8300 (9 %)	–

^a $\lambda_{\text{exc}} = 308 \text{ nm}$, $\lambda_{\text{em}} \approx 340 - 580 \text{ nm}$, measured relative to the quantum yield standard quinine in 0.1 M aqueous H_2SO_4 , estimated uncertainties $\pm 40 \%$; ^b $\lambda_{\text{exc}} = 306 \text{ nm}$, $\lambda_{\text{em}} 390$, biexponential fitting, estimated uncertainties $\pm 10 \%$; ^c $\lambda_{\text{exc}} = 308 \text{ nm}$, $\lambda_{\text{em}} \approx 1050 - 1200 \text{ nm}$, measured relative to the quantum yield standard $[\text{Yb}(\text{tta})_3(\text{phen})]$ in toluene, estimated uncertainties $\pm 50 \%$; ^d $\lambda_{\text{exc}} = 300 \text{ nm}$, $\lambda_{\text{em}} 1110 \text{ nm}$, biexponential fitting, estimated uncertainties $\pm 20 \%$.

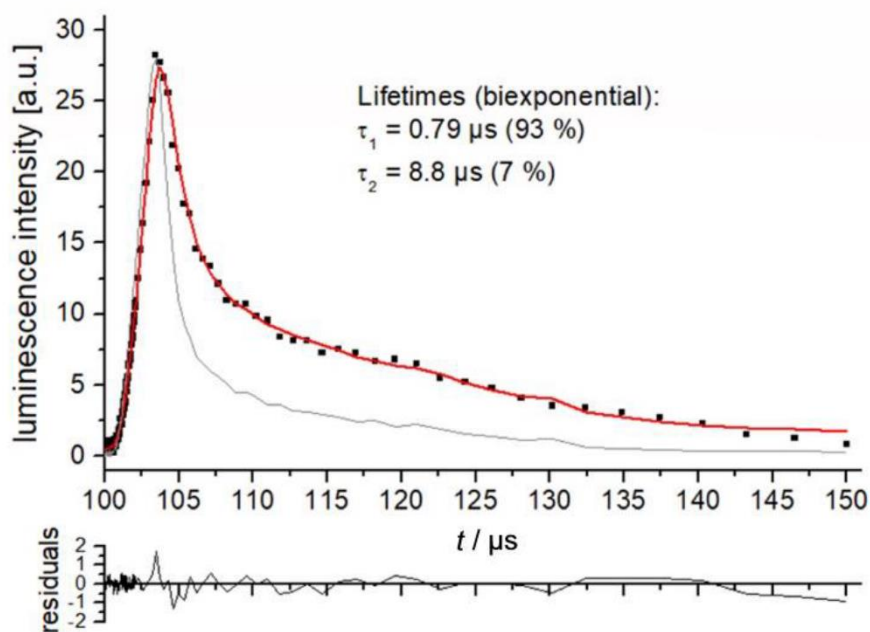


Figure S12. Luminescence decay (black scatter) for *mer*-[V(ddpd)₂][PF₆]₃ in deoxygenated ¹³BuCN at 77 K ($\lambda_{exc} = 300$ nm, $\lambda_{em} = 1110$ nm, emission path: long pass filter RG850) with biexponential fit function (red) and instrument response function (gray).

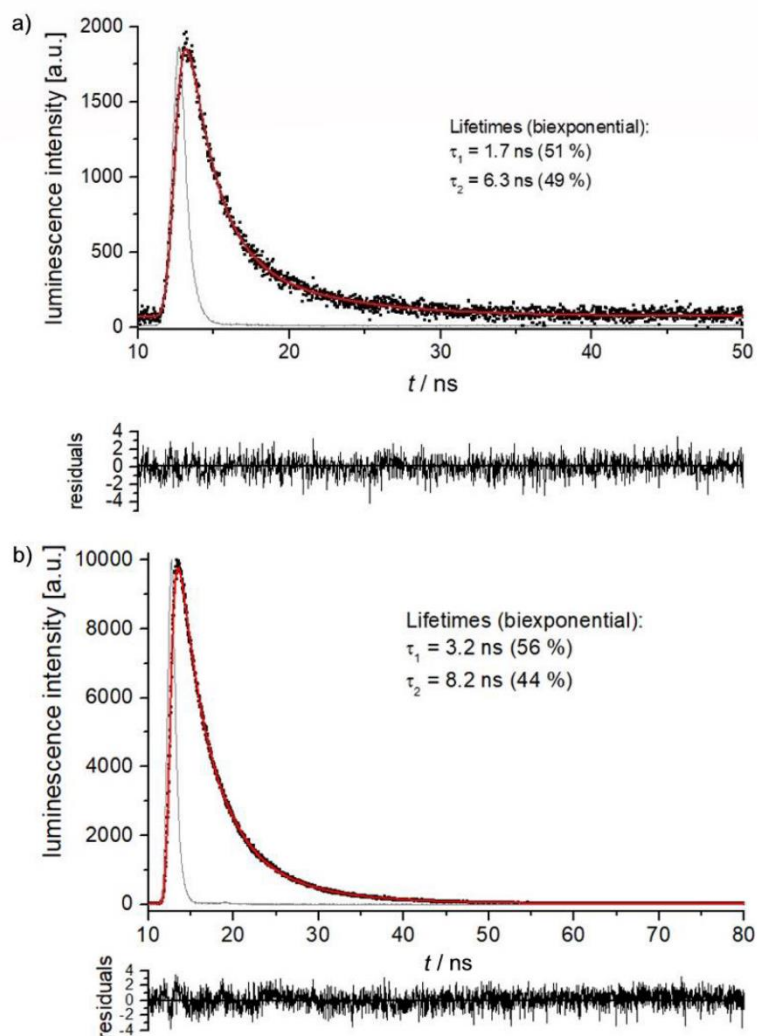


Figure S13. a) Luminescence decay (black scatter) for *mer*-[V(ddpd)₂][PF₆]₃ in deoxygenated ${}^9\text{PrCN}$ at 77 K ($\lambda_{\text{exc}} = 306 \text{ nm}$, $\lambda_{\text{em}} = 416 \text{ nm}$) with biexponential fit function (red) and instrument response function (gray) and b) luminescence decay (black scatter) for *mer*-[V(ddpd)₂][PF₆]₃ in deoxygenated CD_3CN at 298 K ($\lambda_{\text{exc}} = 306 \text{ nm}$, $\lambda_{\text{em}} = 390 \text{ nm}$) with biexponential fit function (red) and instrument response function (gray).

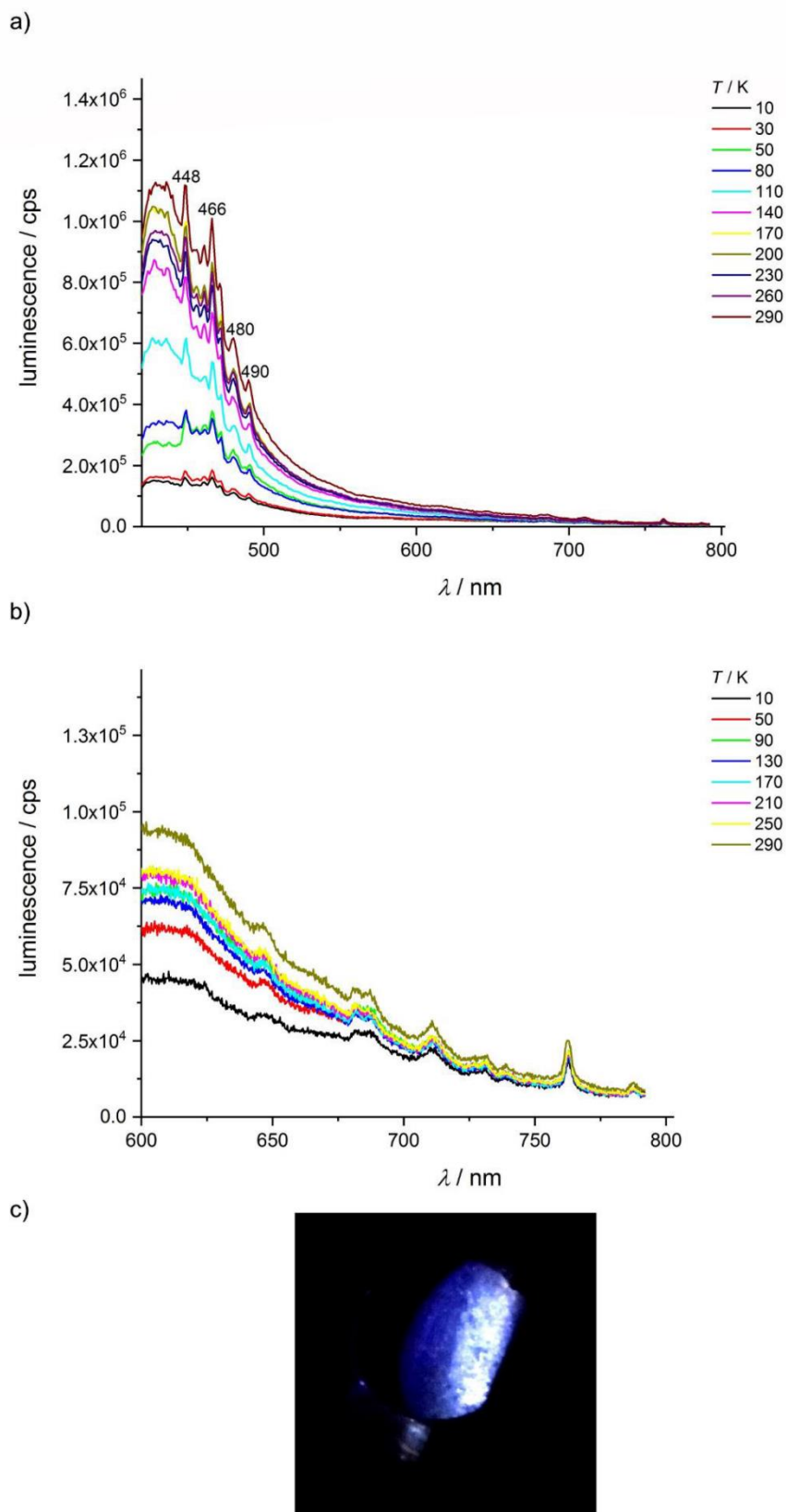


Figure S14. Emission spectra of *mer*-[V(ddpd)₂][PF₆]₃ in a KBr pellet at different temperatures using **a.** 420 and **b.** 600 nm longpass filters; $\lambda_{\text{exc}} = 400$ nm. The quite surprising decrease of the intensity of blue fluorescence upon cooling the sample may be explained by a more favorable ISC to the singlet manifold at low temperature, compared to other radiative and non-radiative processes. **c.** Photograph of *mer*-[V(ddpd)₂][PF₆]₃ in a KBr pellet under excitation with $\lambda_{\text{exc}} = 350$ nm (290 K).

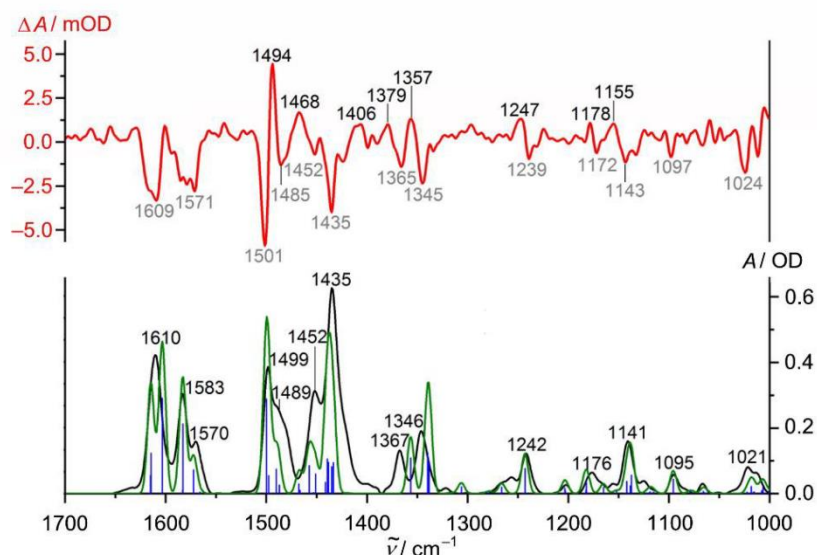


Figure S15. Step-scan FTIR spectrum of $[V(\text{ddpd})_2][\text{PF}_6]_3$ (KBr pellet, 20 K) 0 to 300 ns after laser excitation at $\lambda_{\text{exc}} = 355$ nm (red) and ground state FTIR spectrum (black) (KBr pellet, 20 K), DFT-UKS calculated IR absorption transitions (blue) (scaled by 0.98), and DFT-UKS calculated IR spectrum (green) of $[V(\text{ddpd})_2]^{3+}$ (scaled by 0.98, FWHM = 8 cm^{-1} , gaussian profile).

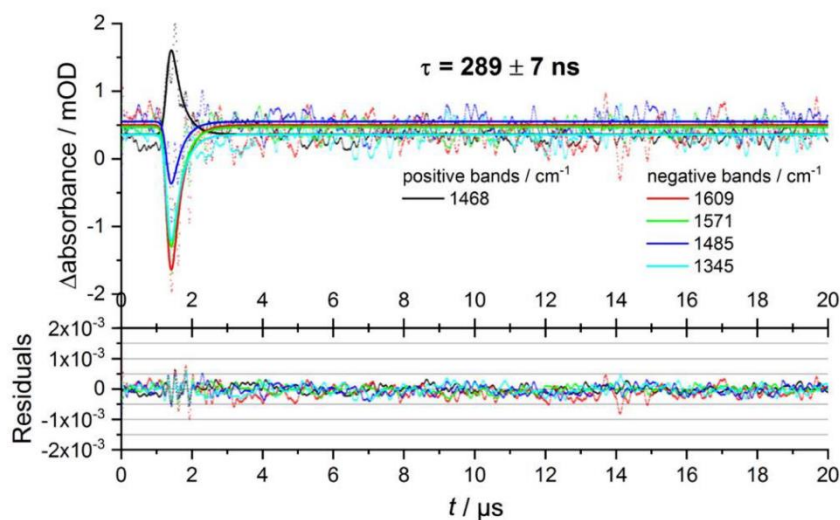


Figure S16. Global monoexponential fit and residuals performed for the most prominent positive and negative peaks in the step-scan spectrum of $[V(\text{ddpd})_2][\text{PF}_6]_3$ (KBr pellet, 20 K).

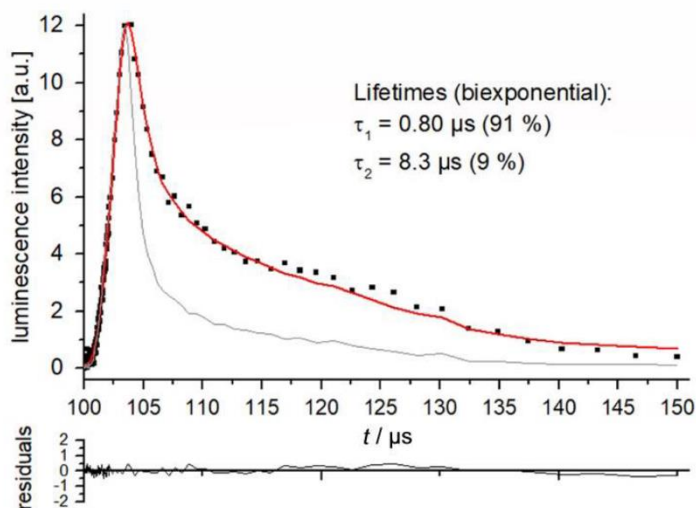


Figure S17. Luminescence decay (black scatter) for *mer*-[V([D₁₇]-ddpd)₂][PF₆]₃ in deoxygenated ⁿBuCN at 77 K ($\lambda_{\text{exc}} = 300 \text{ nm}$, $\lambda_{\text{em}} = 1110 \text{ nm}$, emission path: long pass filter RG850) with biexponential fit function (red) and instrument response function (gray).

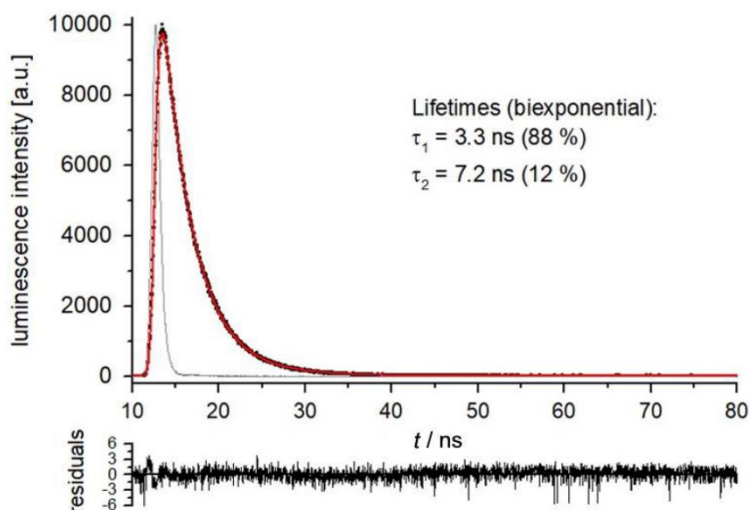


Figure S18. Luminescence decay (black scatter) for *mer*-[V([D₁₇]-ddpd)₂][PF₆]₃ in deoxygenated CD₃CN at 298 K ($\lambda_{\text{exc}} = 306 \text{ nm}$, $\lambda_{\text{em}} = 390 \text{ nm}$) with biexponential fit function (red) and instrument response function (gray).

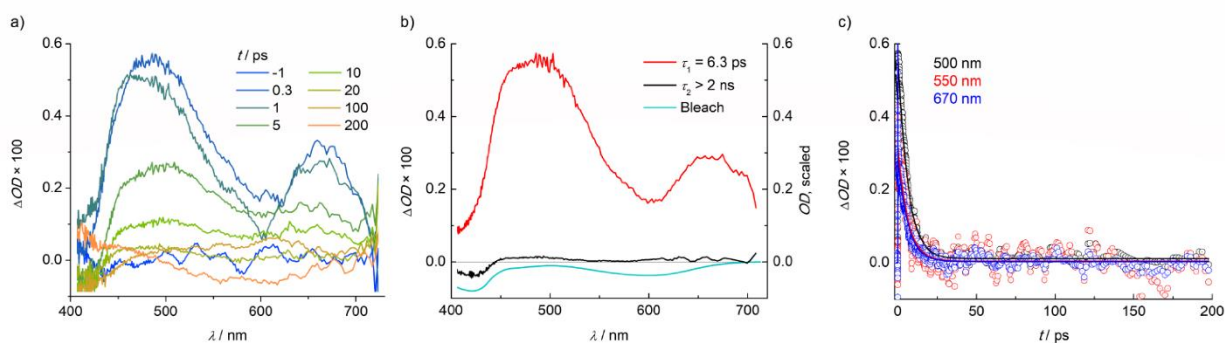


Figure S19. a. Transient absorption spectra of $[\text{V}^{\text{III}}(\text{ddpd})_2][\text{PF}_6]_3$ in CH_3CN excited with 620 nm laser pulses. **b.** Decay associated amplitude spectra labelled by the corresponding time constants and compared to the bleach. **c.** Transient signals as a function of the pump-probe delay time observed at 500 nm (black), 550 nm (red) and 670 nm (blue).

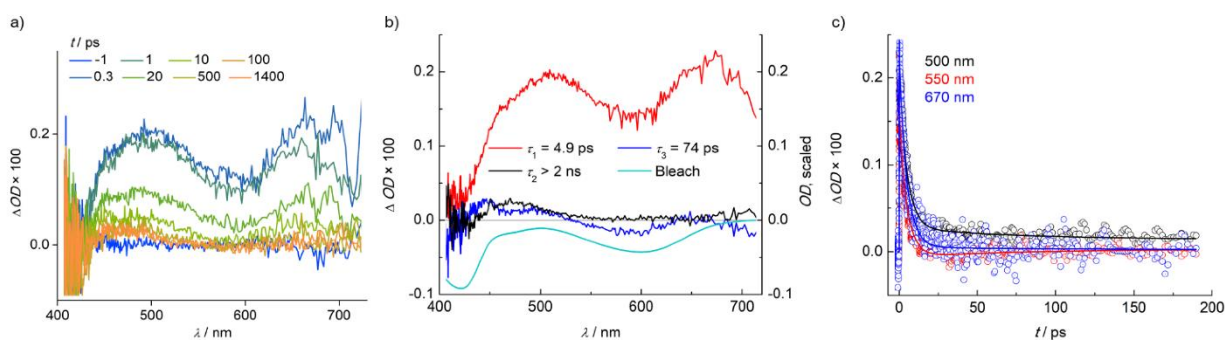


Figure S20. a. Transient absorption spectra of $[\text{V}^{\text{III}}(\text{ddpd})_2][\text{PF}_6]_3$ in CH_3CN excited with 400 nm laser pulses. **b.** Decay associated amplitude spectra labelled by the corresponding time constants and compared to the bleach. **c.** Transient signals as a function of the pump-probe delay time observed at 500 nm (black), 550 nm (red) and 670 nm (blue).

Appendix

Table S8. TD-DFT-RKS relative energies (eV) with respect to the triplet ground state ${}^3T_{1g}$ and corresponding assignment based on the largest contribution of the charge transfer numbers (Fig. S21) of the electronic states used to parameterize the potential energy surfaces employed in the SHARC-LVC simulations. Irreducible representations labels correspond to an idealized octahedral geometry (Fig. S1).

State	Triples	ΔE /eV	Singlets	ΔE /eV
1	1^3MC (${}^3T_{1g}$)	0	1^1MC (1E_g)	1.16
2	2^3MC (${}^3T_{1g}$)	0.26	2^1MC (${}^1T_{2g}$)	1.36
3	3^3MC (${}^3T_{2g}$)	2.79	3^1MC	1.47
4	4^3MC (${}^3T_{2g}$)	3.07	1^1LMCT	3.44
5	1^3LMCT	3.33	2^1LMCT	3.50
6	2^3LMCT	3.39	3^1LMCT	3.59
7	3^3LMCT	3.42	4^1LMCT	3.64
8	4^3LMCT	3.48	4^1MC	3.72
9	5^3LMCT	3.78	5^1MC	3.79
10	6^3LMCT	3.79	5^1LMCT	3.94
11	7^3LMCT	3.90	6^1LMCT	3.96
12	8^3LMCT	3.92	7^1LMCT	4.08

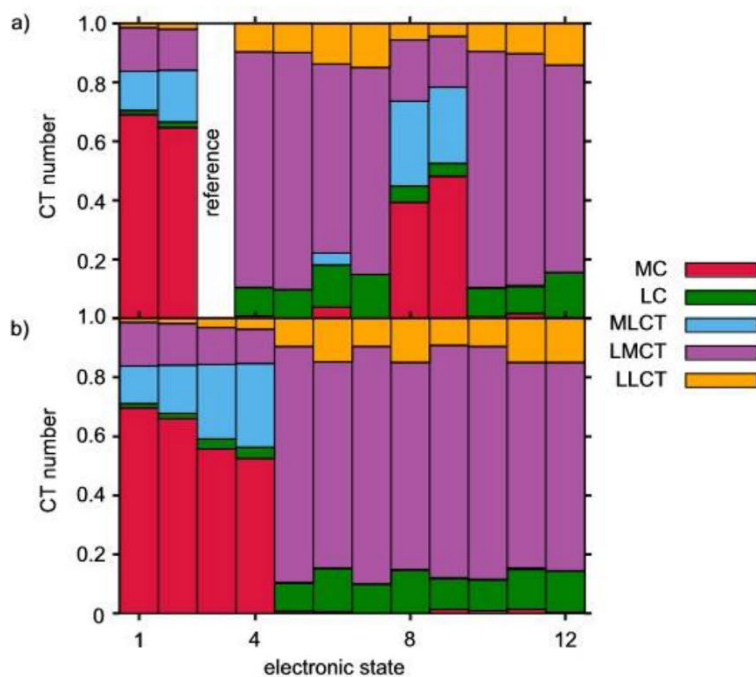


Figure S21. TD-DFT-RKS charge transfer (CT) numbers defined from 0 to 1 of the lowest-lying 12 singlets (a) and 12 triplets (b) states, calculated with respect to the closed-shell reference ${}^3{}^1A_{1g}$. The reference state is 100 % closed-shell and serves as a reference for the CT numbers calculated.

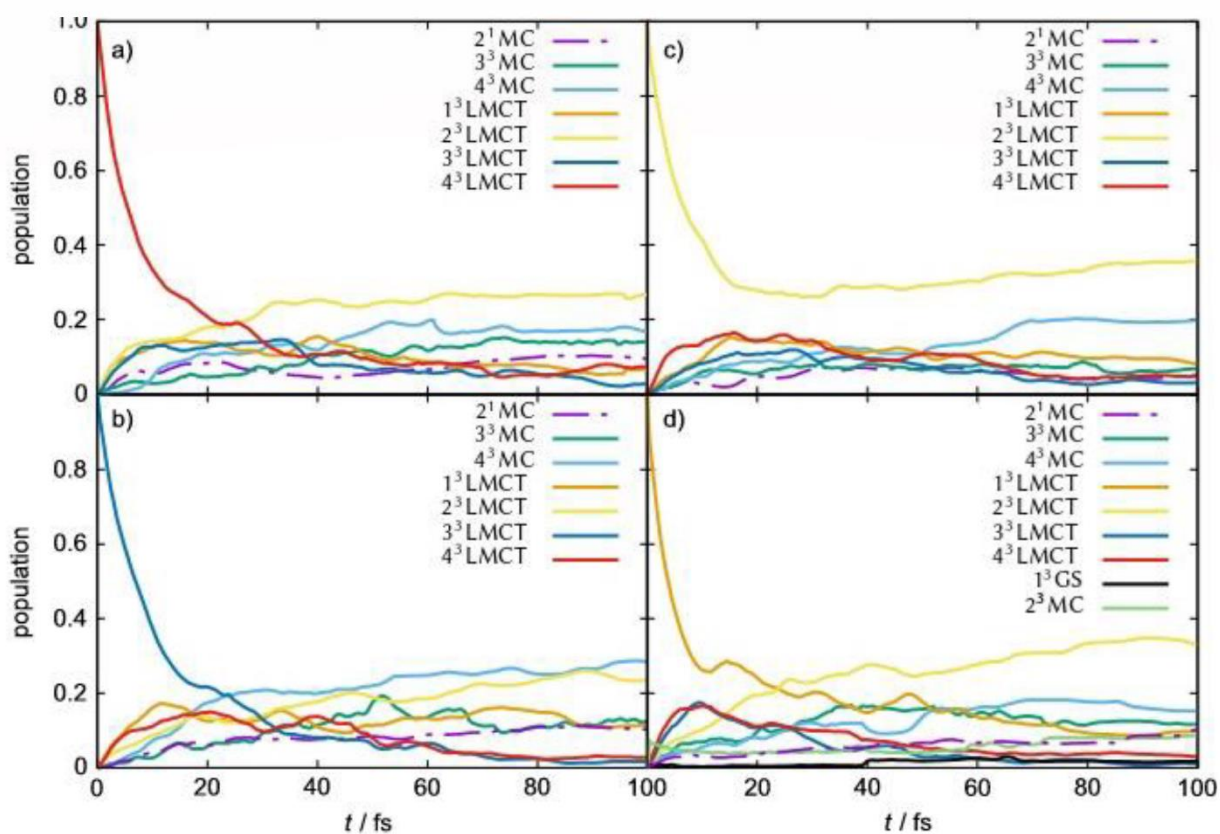


Figure S22. Time-evolution of the population on the excited states during the first 100 fs, after starting the dynamics on a) 4^3LMCT , b) 3^3LMCT , c) 2^3LMCT , d) 1^3LMCT triplet states. Population in any other singlet state other than 2^1MC is negligible and not plotted.

References.

1. Breivogel, A.; Förster, C.; Heinze, K. A Heteroleptic Bis(tridentate)ruthenium(II) Polypyridine Complex with Improved Photophysical Properties and Integrated Functionalizability. *Inorg. Chem.* **2010**, *49*, 7052–7056.
2. Anderson, S. J.; Wells, F. J.; Wilkinson, G.; Hussain, B.; Hursthouse, M. B. 1,2-Bis(dimethyl)phosphinoethane complexes of molybdenum and vanadium. X-ray crystal structure of trans-[MoCl(η^2 -NCMe)(dmpe)₂]BPh₄, trans-[(SPh)₂(dmpe)₂], trans-[V(NCMe)₂(dmpe)₂]BPh₄, trans-[V(CNBU^t)₂(dmpe)₂](PF₆)₂. *Polyhedron* **1988**, *7*, 2615–2626.
3. Fulmer, G. R.; Miller, A. J. M.; Sherden, N. H.; Gottlieb, H. E.; Nudelman, A.; Stoltz, B. M.; Bercaw, J. E.; Goldberg, K. I. NMR Chemical Shifts of Trace Impurities: Common Laboratory Solvents, Organics, and Gases in Deuterated Solvents Relevant to the Organometallic Chemist. *Organometallics* **2010**, *29*, 2176–2179.
4. Melhuish, W. H. Quantum efficiencies of fluorescence of organic substrates: effect of solvent and concentration of the fluorescent solute. *J. Phys. Chem.* **1961**, *65*, 229–235.
5. Meshkova, S. B.; Topilova, Z. M.; Bolshoy, Z. M.; Beltyukova, S. V.; Tsvirko, M. P.; Venchikov, V. Y. Quantum Efficiency of the Luminescence of Ytterbium(III) β -Diketonates. *Acta Phys. Pol. A* **1999**, *95*, 983–990.
6. a) Zimmer, M.; Rupp, F.; Singer, P.; Walz, F.; Breher, F.; Klopper, W.; Diller, R.; Gerhards, M. Time-resolved IR spectroscopy of a trinuclear palladium complex in solution. *Phys. Chem. Chem. Phys.* **2015**, *17*, 14138–14144; b) Bäßler, F.; Zimmer, M.; Dietrich, F.; Gruppe, M.; Wallesch, M.; Volz, D.; Bräse, S.; Gerhards, M.; Diller, R. Photophysical dynamics of a binuclear Cu(I)-emitter on the fs to μ s timescale, in solid phase and in solution. *Phys. Chem. Chem. Phys.* **2017**, *19*, 29438–29448; c) Zimmer, M.; Dietrich, F.; Volz, D.; Bräse, S.; Gerhards, M. Solid-State Step-Scan FTIR Spectroscopy of Binuclear Copper(I) Complexes. *ChemPhysChem* **2017**, *18*, 3023–3029.
7. STOE & Cie, X-Red, STOE & Cie, Darmstadt, Germany 2002.
8. Blessing, R. H. An empirical correction for absorption anisotropy. *Acta Crystallogr. Sect. A* **1995**, *51*, 33–38.
9. Spek, A. L. Structure validation in chemical crystallography. *Acta Crystallogr. Sect. D* **2009**, *65*, 148–55.
10. Sheldrick, G. M. SHELXL-2014/7, University of Göttingen, Göttingen, Germany, 2014.
11. Sheldrick, G. M. SHELXT – Integrated space-group and crystal-structure determination. *Acta Crystallogr. Sect. A* **2015**, *71*, 3–8.
12. Neese, F. The ORCA program system. *WIREs Comput. Mol. Sci.* **2012**, *2*, 73–78.
13. Becke, A. D. Density-functional thermochemistry. III. The role of exact exchange. *J. Chem. Phys.* **1993**, *98*, 5648–5652.
14. Weigend, F.; Ahlrichs, R. Balanced basis sets of split valence, triple zeta valence and quadruple zeta valence quality for H to Rn: Design and assessment of accuracy. *Phys. Chem. Chem. Phys.* **2005**, *7*, 3297–3305.
15. Weigend, F. Accurate Coulomb-fitting basis sets for H to Rn. *Phys. Chem. Chem. Phys.* **2006**, *8*, 1057–1065.
16. Neese, F.; Wennmohs, F.; Hansen, A.; Becker, U. Efficient, approximate and parallel Hartree–Fock and hybrid DFT calculations. A ‘chain-of-spheres’ algorithm for the Hartree–Fock exchange. *Chem. Phys.* **2009**, *356*, 98–109.
17. Izsák, R.; Neese, F. An overlap fitted chain of spheres exchange method. *J. Chem. Phys.* **2011**, *135*, 144105.
18. Pantazis, D. A.; Chen, X.-Y.; Landis, C. R.; Neese, F. All-Electron Scalar Relativistic Basis Sets for Third-Row Transition Metal Atoms. *J. Chem. Theory Comput.* **2008**, *4*, 908–919.
19. van Lenthe, E.; Baerends, E. J.; Snijders, J. G. Relativistic regular two-component Hamiltonians. *J. Chem. Phys.* **1993**, *99*, 4597–4610.
20. Grimme, S.; Antony, J.; Ehrlich, S.; Krieg, H. A consistent and accurate ab initio parametrization of density functional dispersion correction (DFT-D) for the 94 elements H–Pu. *J. Chem. Phys.* **2010**, *132*, 154104.

21. Grimme, S.; Ehrlich, S.; Goerigk, L. Effect of the damping function in dispersion corrected density functional theory. *J. Comput. Chem.* **2011**, *32*, 1456–1465.
22. Barone, V.; Cossi, M. Quantum Calculation of Molecular Energies and Energy Gradients in Solution by a Conductor Solvent Model. *J. Phys. Chem. A* **1998**, *102*, 1995–2001.
23. Roos, B. O.; Taylor, P. R.; Siegbahn, P. E. M. A Complete Active Space SCF Method (CAS-SCF) Using a Density-Matrix Formulated Super-CI Approach. *Chem. Phys.* **1980**, *48*, 157–173.
24. Siegbahn, P. E. M.; Almlöf, J.; Heiberg, A.; Roos, B. O. The Complete Active Space SCF (CAS-SCF) Method in a Newton-Raphson Formulation with Application to the HNO Molecule. *J. Chem. Phys.* **1981**, *74*, 2384–2396.
25. Angeli, C.; Cimiraglia, R.; Evangelisti, S.; Leininger, T.; Malrieu, J.-P. Introduction of n-electron valence states for multireference perturbation theory. *J. Chem. Phys.* **2001**, *114*, 10252–10264.
26. Angeli, C.; Cimiraglia, R. Multireference perturbation configuration interaction V. Third-order energy contributions in the Møller–Plesset and Epstein–Nesbet partitions. *Theor. Chem. Acc.* **2002**, *107*, 313–317.
27. Neese, F. Efficient and accurate approximations to the molecular spin-orbit coupling operator and their use in molecular g-tensor calculations. *J. Chem. Phys.* **2005**, *122*, 34107.
28. Hess, B. A.; Marian, C. M. In *Computational Molecular Spectroscopy*; Jensen, P. B., Ed.; Wiley: New York, 2000; p. 169ff.
29. Cahier, B.; Maurice, R.; Bolvin, H.; Mallah, T.; Guihéry, N. Tools for Predicting the Nature and Magnitude of Magnetic Anisotropy in Transition Metal Complexes: Application to Co(II) Complexes. *Magnetochemistry* **2016**, *2*, 31–45.
30. Roos, B. O.; Malmqvist, P.-Å. Relativistic quantum chemistry: the multiconfigurational approach. *Phys. Chem. Chem. Phys.* **2004**, *6*, 2919–2927.
31. Durand, P.; Malrieu, J.-P. In *Advances in Chemical Physics: Ab Initio Methods in Quantum Chemistry*; Lawley, K. P., Ed.; John Wiley & Sons Ltd.: Hoboken, NJ, 1987; Vol. 67, Part 1, pp 321–412.
32. Pierloot, K. Transition metals compounds: Outstanding challenges for multiconfigurational methods. *Int. J. Quantum Chem.* **2011**, *111*, 3291–3301.
33. Richter, M.; Marquetand, P.; González-Vázquez, J.; Sola, I.; González, L. SHARC: ab Initio Molecular Dynamics with Surface Hopping in the Adiabatic Representation Including Arbitrary Couplings. *J. Chem. Theory Comput.* **2011**, *7*, 1253–1258.
34. Mai, S.; Marquetand, P.; González, L. *WIREs Comput. Mol. Sci.* **2018**, e1370.
35. Mai, S.; Marquetand, P.; González, L. *Int. J. Quantum Chem.* **2015**, *115*, 1215–1231.
36. Mai, S.; Richter, M.; Heindl, M.; Menger, M. F. S. J.; Atkins, A.; Ruckebauer, M.; Plasser, F.; Oppel, M.; Marquetand, P.; González, L. *Sharc2.0: Surface Hopping Including Arbitrary Couplings – Program Package for Non-Adiabatic Dynamics* (2018), available from <http://sharc-md.org>.
37. Plasser, F.; Gómez, S.; Menger, M. F. S. J.; Mai, S.; González, L. Highly efficient surface hopping dynamics using a linear vibronic coupling model. *Phys. Chem. Chem. Phys.* **2019**, *21*, 57–69.
38. a) Mai, S.; Plasser, F.; Dorn, J.; Fumana, M.; Daniel, C.; González, L. Quantitative wave function analysis for excited states of transition metal complexes. *Coord. Chem. Rev.* **2018**, *361*, 74–97; b) <http://theodore-qc.sourceforge.net>.
39. Granucci, G.; Persico, M. Direct semiclassical simulation of photochemical processes with semiempirical wave functions. *J. Chem. Phys.* **2001**, *114*, 10608.
40. Granucci, G.; Persico, M. Critical appraisal of the fewest switches algorithm for surface hopping. *J. Chem. Phys.* **2007**, *126*, 134114.
41. Alemany, P.; Casanova, D.; Álvarez, S.; Dryzun, C.; Avnir, D. Continuous Symmetry Measures: A New Tool in Quantum Chemistry. In *Reviews in Computational Chemistry*. Parrill, A. L., Lipkowitz, K. B., Eds., John Wiley & Sons: Hoboken, NJ, USA, Volume 30, **2017**, pp. 289–352.
42. Tanabe, Y.; Sugano, S. On the Absorption Spectra of Complex Ions. II. *J. Phys. Soc. Jpn.* **1954**, *9*, 766–779.

43. Krzystek, J.; Ozarowski, A.; Telser, J.; Crans, D. C. High-frequency and -field electron paramagnetic resonance of vanadium(IV, III, and II) complexes. *Coord. Chem. Rev.* **2015**, *301–302*, 123–133.
44. Kittilstved, K. R.; Sorgho, L. A.; Amstutz, N.; Tregenna-Piggott, P. L. W.; Hauser, A. Ground-State Electronic Structure of Vanadium(III) Trisoxalate in Hydrated Compounds. *Inorg. Chem.* **2009**, *48*, 7750–7764.
45. Jung, J.; Jung, Y.; Park, O. Preparation of 2-chloropyridine. *Synth. Commun.* **2001**, *31*, 2507–2511.
46. Jha, A. K.; Jain, N. The microwave-assisted ortho-alkylation of azine N-oxides with N-tosylhydrazones catalyzed by copper(I) iodide. *Chem. Commun.* **2016**, *52*, 1831–1834.
47. Esaki, H.; Ito, N.; Sakai, S.; Maegawa, T.; Monguchia, Y.; Sajikia, H. General method of obtaining deuterium-labeled heterocyclic compounds using neutral D₂O with heterogeneous Pd/C. *Tetrahedron* **2006**, *62*, 10954–10961.
48. Dirvanauskas, A.; Galavotti, R.; Lunghi, A.; Nicolini, A.; Roncaglia, F.; Totti, F.; Cornia, A. Solution structure of a pentachromium(II) single molecule magnet from DFT calculations, isotopic labelling and multinuclear NMR spectroscopy. *Dalton Trans.* **2018**, *47*, 585–595.
49. Wang, C.; Otto, S.; Dorn, M.; Kreidt, E.; Lebon, J.; Sršan, L.; Di Martino-Fumo, P.; Gerhards, M.; Resch-Genger, U.; Seitz, M.; Heinze, K. Deuterated Molecular Ruby with Record Luminescence Quantum Yield. *Angew. Chem. Int. Ed.* **2018**, *57*, 1112–1116.

6.2. Supporting Information to Chapter 3.2. (“Ultrafast and long-time excited state kinetics of an NIR-emissive vanadium(III) complex I: Synthesis, spectroscopy and static quantum chemistry”)

Ultrafast and long-time excited state kinetics of an NIR-emissive vanadium(III) complex I: Synthesis, spectroscopy and static quantum chemistry†

Matthias Dorn^a, Jens Kalmbach^b, Pit Boden^c, Ayla Kruse^d, Chahinez Dab^e, Christian Reber^e, Gereon Niedner-Schatteburg^c, Stefan Lochbrunner^d, Markus Gerhards^c, Michael Seitz^{*b}, Katja Heinze^{*a}

a. Department of Chemistry, Johannes Gutenberg University of Mainz, Duesbergweg 10-14, 55128 Mainz, Germany.

b. Institute of Inorganic Chemistry, University of Tübingen, Auf der Morgenstelle 18, 72076 Tübingen, Germany.

c. Department of Chemistry and Research Center Optimas, Technical University Kaiserslautern, Erwin-Schrödinger-Straße, 67663 Kaiserslautern, Germany.

d. Institute for Physics and Department of Life, Light and Matter, University of Rostock, 18051 Rostock, Germany.

e. Département de chimie, Université de Montréal, Montréal, Québec, H3C 3J7, Canada.

Figure S1. Geometry of $VCl_3(\text{ddpd})$ calculated by DFT-UKS [CPCM(acetonitrile)-RIJCOSX-B3LYP-D3BJ-ZORA/def2-TZVPP].

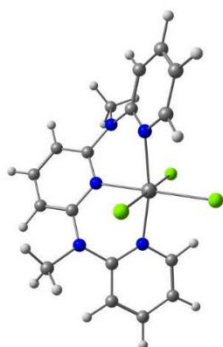


Figure S2. TD-DFT-UKS charge transfer (CT) numbers of $\text{VCl}_3(\text{ddpd})$ defined from 0 to 1 of the lowest-lying 50 triplet states.

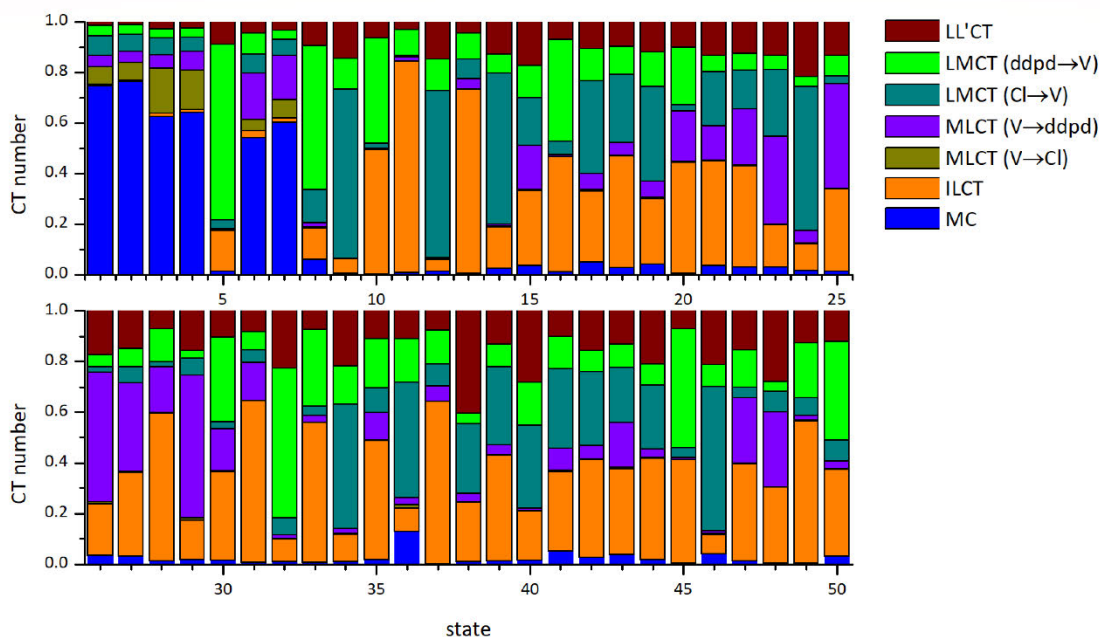


Table S1 Bond distances / Å and angles / ° of *mer*- $\text{VCl}_3(\text{ddpd})$ ^{S1} (XRD and DFT-UKS).

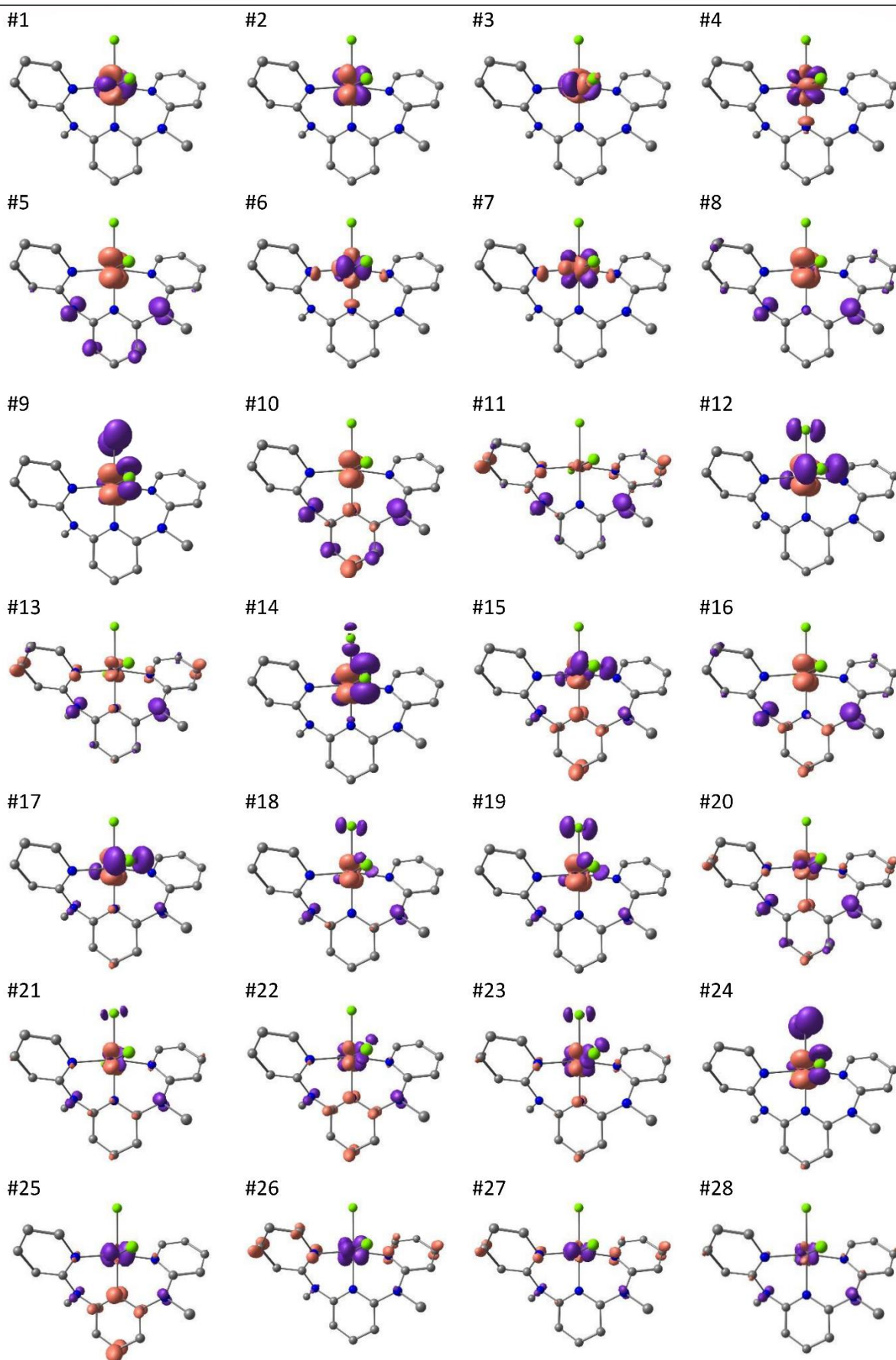
	V-N1/ V-N2/ V-N3	N1-V-N2/ N1-V-N3 N2-V-N3	V-Cl1 V-Cl2 V-Cl3	Cl1-V-Cl2 Cl1-V-Cl3 Cl2-V-Cl3	Shape parameter <i>S</i> (OC-6)
XRD	2.123(3) 2.119(3) 2.109(3)	84.68(12) 170.41(12) 85.85(12)	2.354(12) 2.325(13) 2.335(12)	90.42(4) 178.75(5) 90.72(4)	0.48
DFT-UKS	2.123 2.114 2.123	84.25 168.53 84.28	2.387 2.375 2.386	90.19 179.66 90.08	0.64

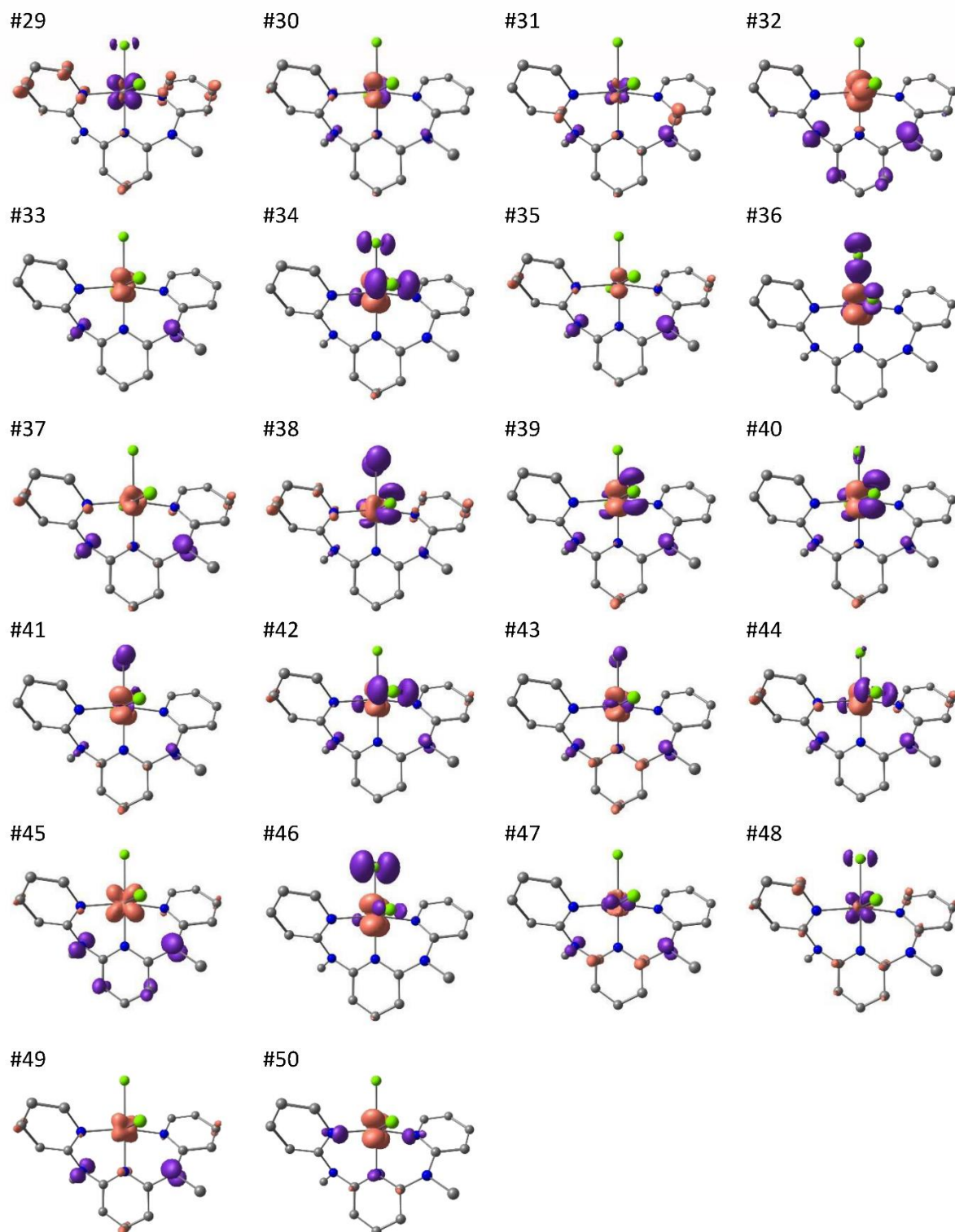
Table S3. TD-DFT calculated spin-allowed transitions (UKS, unshifted). The assignment of the UKS states corresponds to the largest contribution to the charge transfer number (Fig. S2).

state	$\tilde{\nu} / \text{cm}^{-1}$	λ / nm	E / eV	f_{osc}	assignment
1	2431	4114	0.301	7.24E-05	³ MC
2	3593	2783	0.445	4.10E-08	³ MC
3	17221	581	2.135	1.11E-05	³ MC
4	17358	576	2.152	6.54E-05	³ MC
5	18198	550	2.256	1.14E-02	³ LMCT(ddpd→V)
6	21692	461	2.689	1.35E-05	³ MC
7	22346	448	2.771	1.15E-04	³ MC
8	22681	441	2.812	2.01E-03	³ LMCT(ddpd→V)
9	24096	415	2.988	1.18E-03	³ LMCT(Cl→V)
10	24734	404	3.067	2.80E-02	³ LMCT(ddpd→V)
11	26178	382	3.246	2.11E-03	³ ILCT(ddpd)
12	26983	371	3.346	1.16E-03	³ LMCT(Cl→V)
13	27255	367	3.379	1.89E-03	³ ILCT(ddpd)
14	27465	364	3.405	1.03E-02	³ LMCT(Cl→V)
15	28474	351	3.530	1.54E-02	³ LMCT(Cl→V), ³ ILCT (ddpd)
16	28777	348	3.568	9.71E-04	³ LMCT(ddpd→V), ³ ILCT (ddpd)
17	29334	341	3.637	1.42E-02	³ LMCT(ddpd,Cl→V)
18	29878	335	3.704	7.47E-03	³ LMCT(ddpd,Cl→V), ³ ILCT(ddpd)
19	29940	334	3.712	3.17E-02	³ LMCT(ddpd,Cl→V)
20	30211	331	3.746	5.13E-03	³ LMCT(ddpd→V), ³ ILCT(ddpd)
21	30469	328	3.778	1.46E-02	³ ILCT(ddpd)
22	30562	327	3.789	6.74E-03	³ ILCT(ddpd)
23	30931	323	3.835	4.33E-04	³ LMCT(Cl→V)
24	30979	323	3.841	6.18E-05	³ LMCT(Cl→V)
25	31037	322	3.848	1.24E-02	³ MLCT(V→ddpd)
26	31397	319	3.893	1.42E-02	³ MLCT(V→ddpd)
27	31666	316	3.926	8.54E-03	³ MLCT(V→ddpd)
28	31726	315	3.934	3.99E-02	³ ILCT(ddpd)
29	32248	310	3.998	1.74E-04	³ MLCT(V→ddpd)
30	32468	308	4.025	2.51E-02	³ LMCT(ddpd→V)
31	32489	308	4.028	2.70E-03	³ ILCT(ddpd)
32	32765	305	4.062	3.27E-05	³ LMCT(ddpd→V)
33	32819	305	4.069	2.86E-03	³ LMCT(ddpd→V), ³ ILCT(ddpd)
34	33478	299	4.151	6.89E-06	³ LMCT(Cl→V)
35	33557	298	4.161	7.23E-02	³ ILCT(ddpd)
36	33795	296	4.190	8.51E-04	³ LMCT(Cl→V)
37	34118	293	4.230	7.47E-03	³ ILCT(ddpd)
38	34423	291	4.268	9.86E-03	³ LLCT(Cl→ddpd)
39	34530	290	4.281	1.32E-02	³ LMCT(ddpd,Cl→V), ³ ILCT(ddpd)
40	34674	288	4.299	2.53E-02	³ LMCT(ddpd,Cl→V)
41	34953	286	4.334	1.29E-03	³ LMCT(ddpd,Cl→V)
42	35026	286	4.343	4.10E-03	³ LMCT(ddpd,Cl→V), ³ ILCT(ddpd)
43	35063	285	4.347	7.91E-04	³ LMCT(ddpd,Cl→V), ³ ILCT(ddpd)
44	35162	284	4.360	1.23E-02	³ LMCT(ddpd,Cl→V), ³ ILCT(ddpd)
45	35386	283	4.387	2.20E-03	³ LMCT(ddpd→V)
46	35549	281	4.408	1.64E-03	³ LMCT(Cl→V)
47	35791	279	4.438	5.90E-02	³ ILCT(ddpd)
48	36062	277	4.471	9.19E-04	³ MLCT(V→ddpd)
49	36377	275	4.510	1.06E-05	³ ILCT(ddpd)
50	36670	273	4.547	4.40E-03	³ LMCT(ddpd→V)

Appendix

Table S4. Difference electron densities of the 50 lowest-lying TD-DFT-UKS calculated states (isosurface value at 0.007 a.u.; purple = electron depletion; orange = electron gain; hydrogen atoms omitted).





Appendix

Table S5. Orbital energies/Hartree of the canonical orbitals used in the active space of the CASSCF(6,12)-FICNEVPT2 calculation, depicted at a contour value of 0.05 a.u. (hydrogen atoms omitted for clarity).

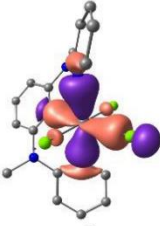
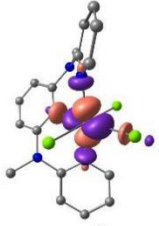
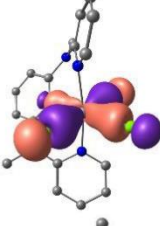
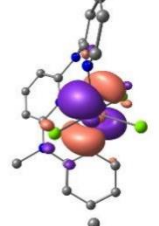
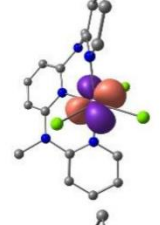
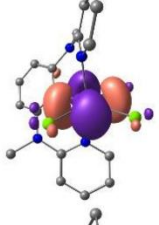
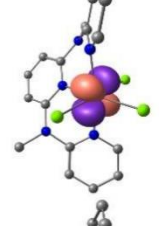
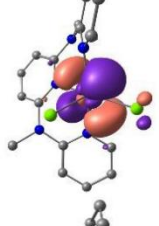
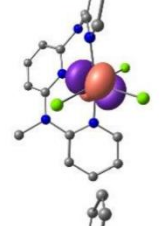
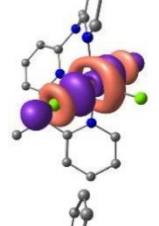
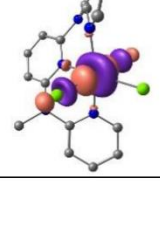
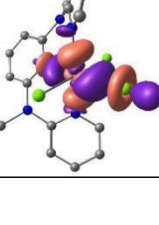
MO #	E / H	orbital	MO #	E / H	orbital
111	-0.53269		117	+0.15634	
112	-0.48346		118	+0.87582	
113	+0.02254		119	+0.90233	
114	+0.02553		120	+0.91763	
115	+0.02877		121	+1.13585	
116	+0.10787		122	+1.27999	

Figure S3. Energy diagram of the electronic states of $\text{VCl}_3(\text{ddpd})$ constructed from CASSCF(6,12)-FIC-NEVPT2 energies with spin densities in orange (0.007 a.u. isosurface value, hydrogen atoms omitted for clarity, triplet states in blue, singlet states in red; a coordinate system referring to the displayed structures and d orbital labels is shown in the grey box).

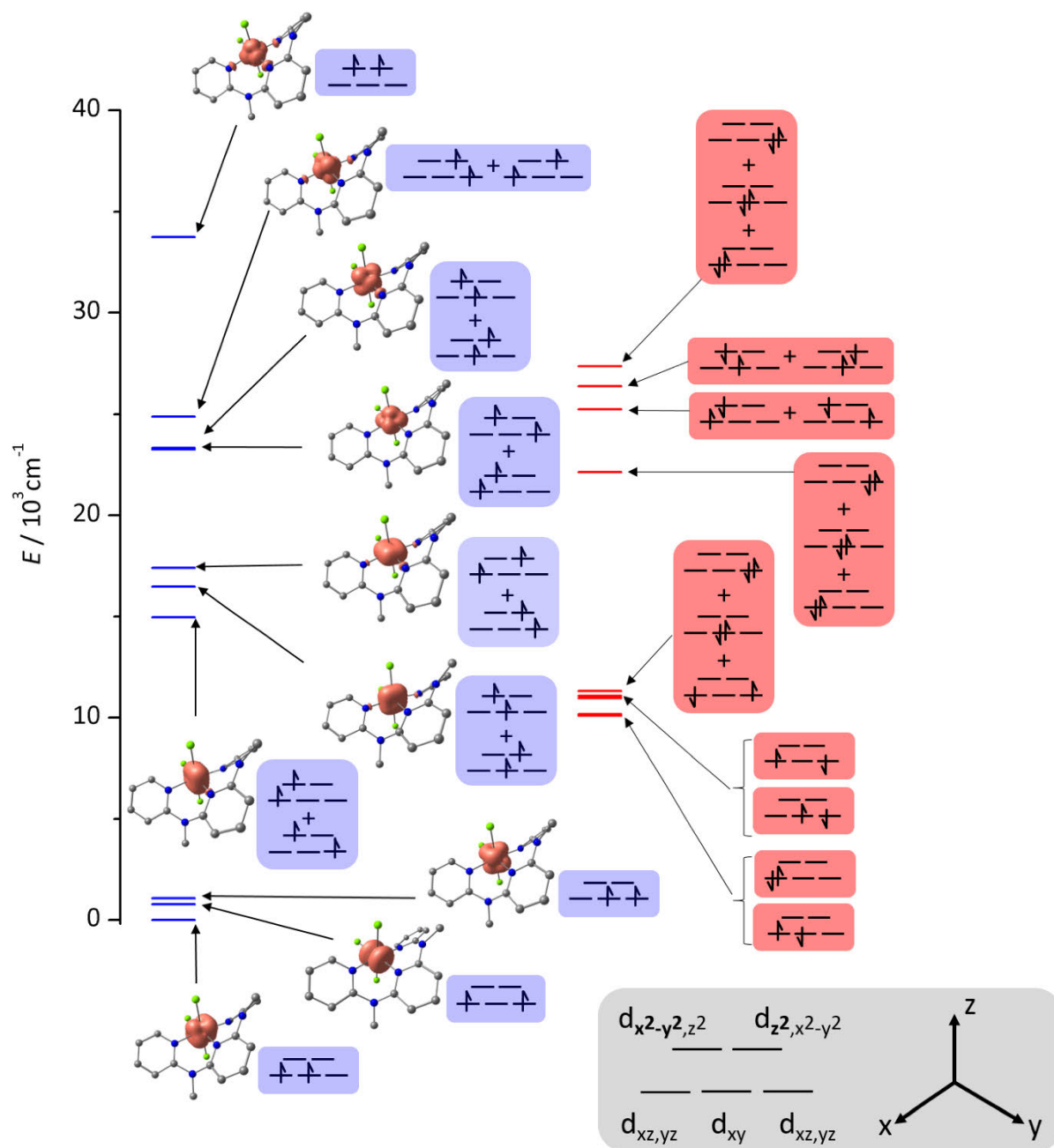


Table S6. Energies of triplet and singlet states/cm⁻¹ from the CASSCF(6,12) calculations without and with NEVPT2 (assignments according to the dominant contribution).

state	E / cm^{-1} without NEVPT2	E / cm^{-1} with NEVPT2	$\Delta E / \text{cm}^{-1}$
GS (³ T ₁)	574.7	755.4	180.7
GS (³ T ₁)	874.1	1076.3	202.2
¹ E	12658.8	10085.9	-2572.9
¹ T ₂	12804.9	10160.5	-2644.4
¹ E/ ¹ T ₂	13456.4	10949.1	-2507.3
¹ E/ ¹ T ₂	13580.0	11068.3	-2511.7
¹ E/ ¹ T ₂	13837.7	11309.1	-2528.6
³ T ₂	13857.6	14967.5	1109.9
³ T ₂	15252.7	16463.5	1210.8
³ T ₂	16114.6	17393.1	1278.5
¹ A ₁	26337.3	22141.7	-4195.6
³ T ₁ (P)	25522.4	23253.9	-2268.5
³ T ₁ (P)	25841.4	23318.7	-2522.7
³ T ₁ (P)	27384.5	24890.9	-2493.6
¹ T ₂ (G)	27538.6	25238.5	-2300.1
¹ T ₂ (G)	28592.3	26376.7	-2215.6
¹ T ₂ (G)	29508.1	27339.6	-2168.5

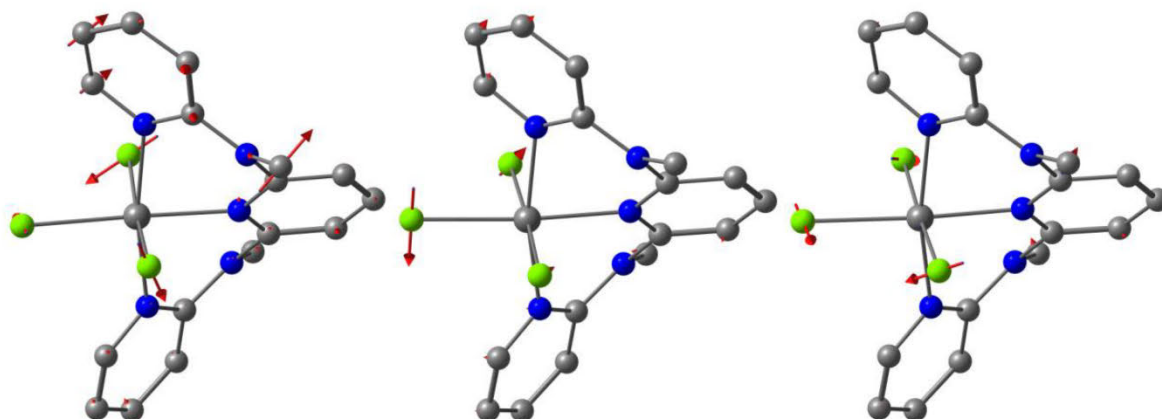
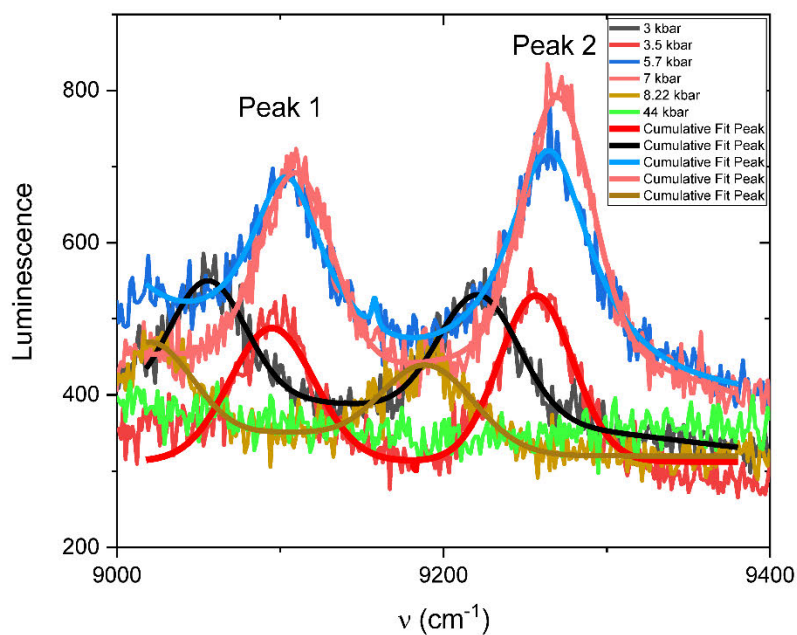
Figure S4. Displacement vectors of Cl–V–Cl deformation vibrations calculated by DFT at 125, 136, 159 cm⁻¹ (unscaled).

Figure S5. (a) NIR emission bands (peak 1 and 2) of solid $\text{VCl}_3(\text{D}_0\text{-ddpd})$ under hydrostatic pressure and (b) corresponding peak shift (peak 1 and 2) versus pressure plots.

(a)



(b)

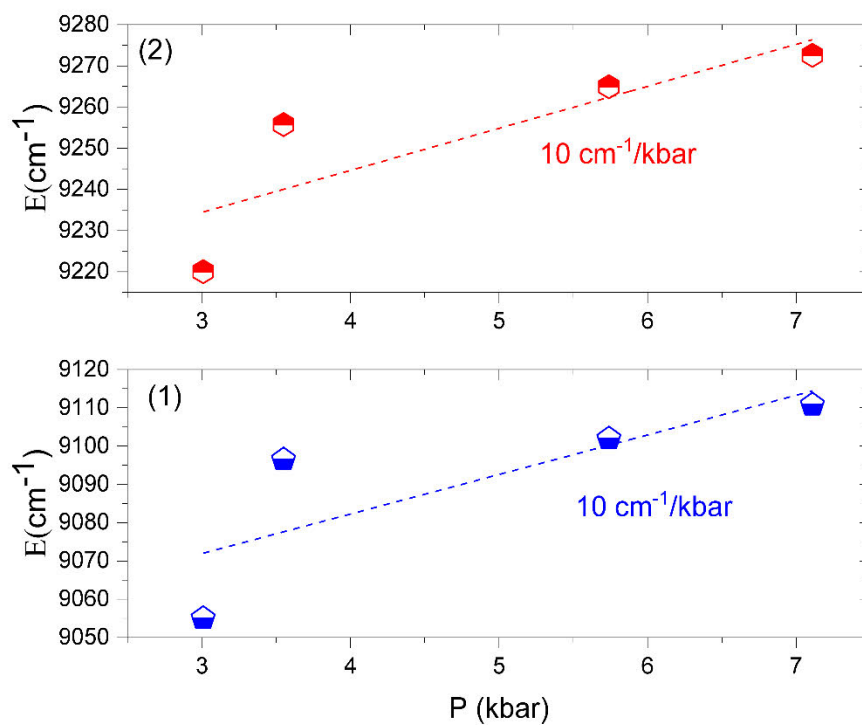
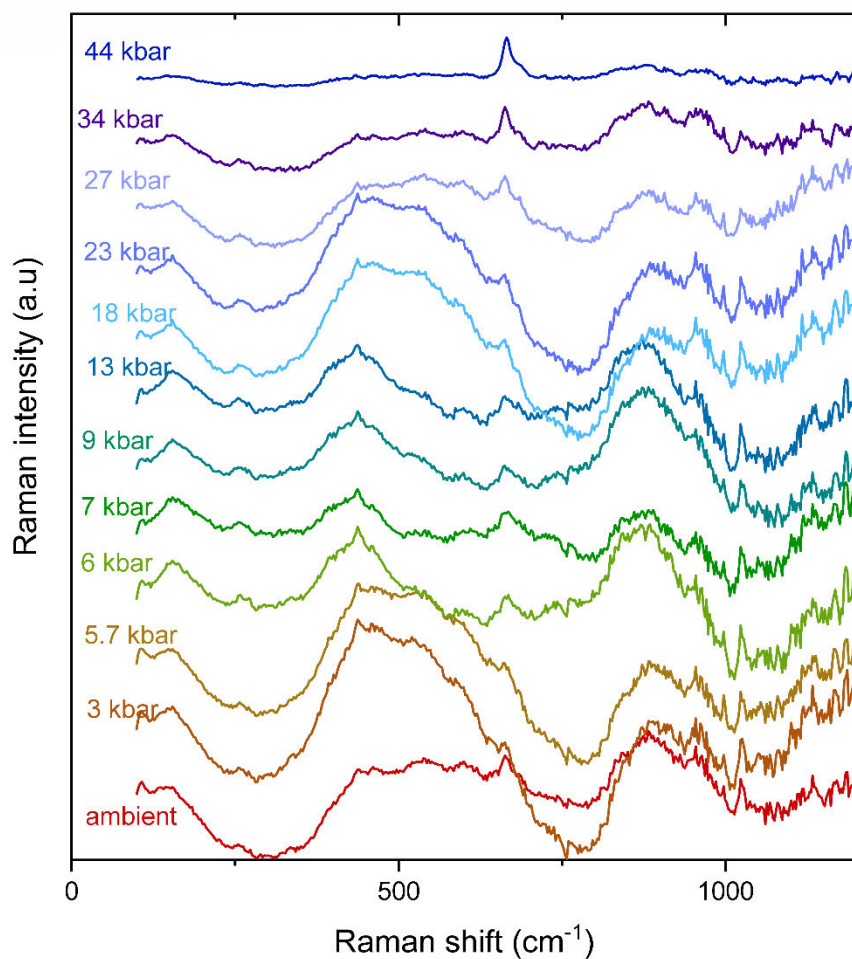


Figure S6. Raman spectra of solid $\text{VCl}_3(\text{D}_0\text{-ddpd})$ under hydrostatic pressure ($\lambda_{\text{exc}} = 785.0 \text{ nm}$).

At 44 kbar, the highest pressure achieved for this study, only the vibrational peaks at approximately 665 cm^{-1} are observed, documenting that the electronic Raman signals, dominant at lower pressure, are broadened out to the extreme so that they are no longer clearly identifiable.

Figure S7. Luminescence decay (black scatter) for **VCl₃(ddpd-[D₀])** in the solid state under a dry and deoxygenated argon atmosphere ($\lambda_{\text{exc}} = 350 \text{ nm}$, $\lambda_{\text{em}} = 1106 \text{ nm}$, excitation path: band pass filter UG11, emission path: long pass filter RG850) with monoexponential fit function (red) and instrument response function (grey).

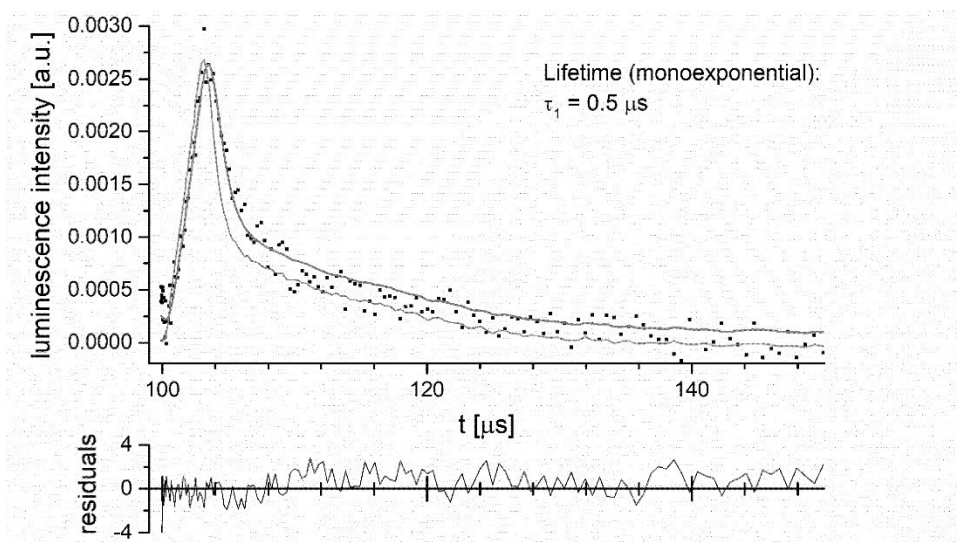


Figure S8. Luminescence decay (black scatter) for **VCl₃(ddpd-[D₁₇])** in the solid state under a dry and deoxygenated argon atmosphere ($\lambda_{\text{exc}} = 350 \text{ nm}$, $\lambda_{\text{em}} = 1106 \text{ nm}$, excitation path: band pass filter UG11, emission path: long pass filter RG850) with monoexponential fit function (red) and instrument response function (grey).

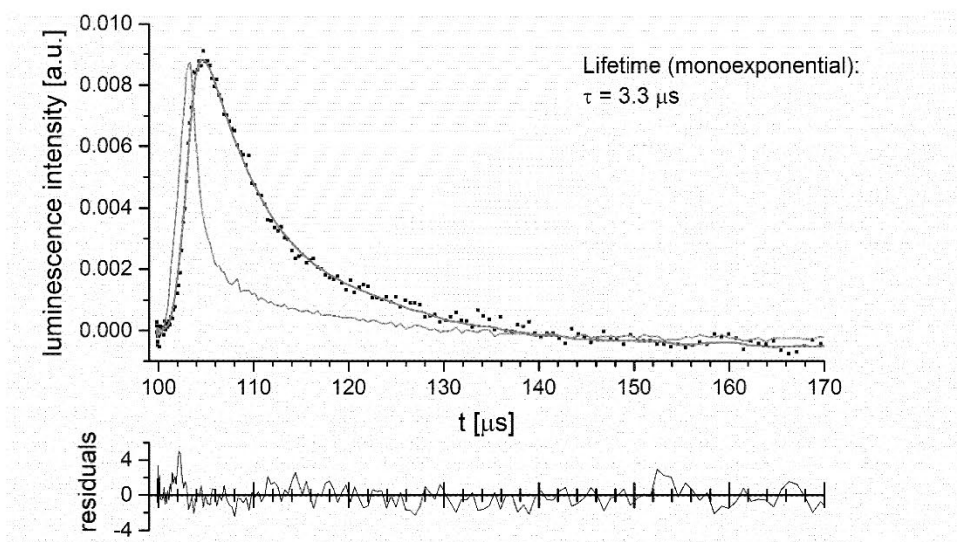
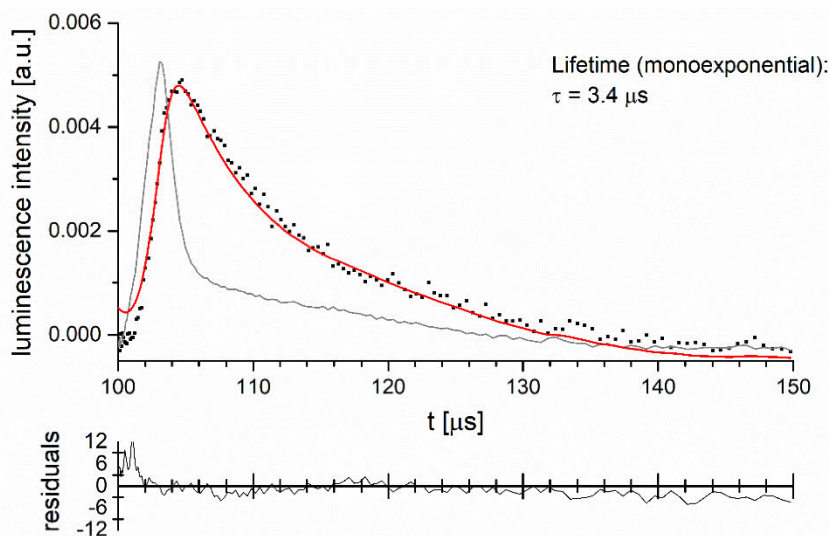


Figure S9. Luminescence decay (black scatter) for **VCl₃(ddpd-[D₁₇])** in the solid state under a dry and deoxygenated argon atmosphere ($\lambda_{exc} = 350$ nm, $\lambda_{em} = 1222$ nm, excitation path: band pass filter UG11, emission path: long pass filter RG850) with monoexponential fit function (red) and instrument response function (grey).



NIR Absorption Spectroscopy / Vibrational Overtone Analysis

Since the isotopologic vanadium(III) complexes were not available in sufficient quantities, the analysis of the position and intensity of the C–H and C–D vibrational overtones for the vanadium complexes was carried out on simpler pyridine-containing model compounds. The vibrational signatures of the protiated and deuterated methyl protons in ddpd were not investigated due to insufficient quantities and because deuteration did not show an effect on the non-radiative deactivation of the metal centered emission of $[\text{Cr}(\text{ddpd})_2]^{3+}$.⁵³ Previously, the vibrational overtone data of the isotopologues of 6,6'-dimethyl-2,2'-bipyridine ($\text{Me}_2\text{-bpy}$ and $[\text{D}_{12}]\text{-Me}_2\text{-bpy}$, Figure S11)⁵² proved to be a successful model system for the analysis of the vibrational overtone structure of ddpd.⁵³ For the present analysis, we used the previously obtained aromatic C–(H/D) overtone bands (Gaussians)⁵² of $\text{Me}_2\text{-bpy}$ and $[\text{D}_{12}]\text{-Me}_2\text{-bpy}$ for the calculations of the spectral overlap integral (SOI) between these oscillators and the vanadium emission.

Figure S10. Comparison of ddpd with the model compounds $\text{Me}_2\text{-bpy}$ and $[\text{D}_{12}]\text{-Me}_2\text{-bpy}$ used for the analysis of the vibrational C–H and C–D overtones.

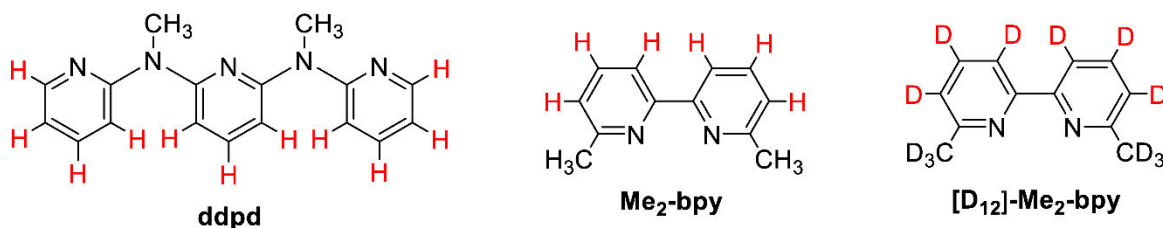


Figure S11. Reconstructed vibrational overtone absorption bands ($\nu = 2, 3,$ and 4) for the aromatic C–H oscillators of Me₂-bpy (black) with single Gaussian fits (dashed red).^{S3}

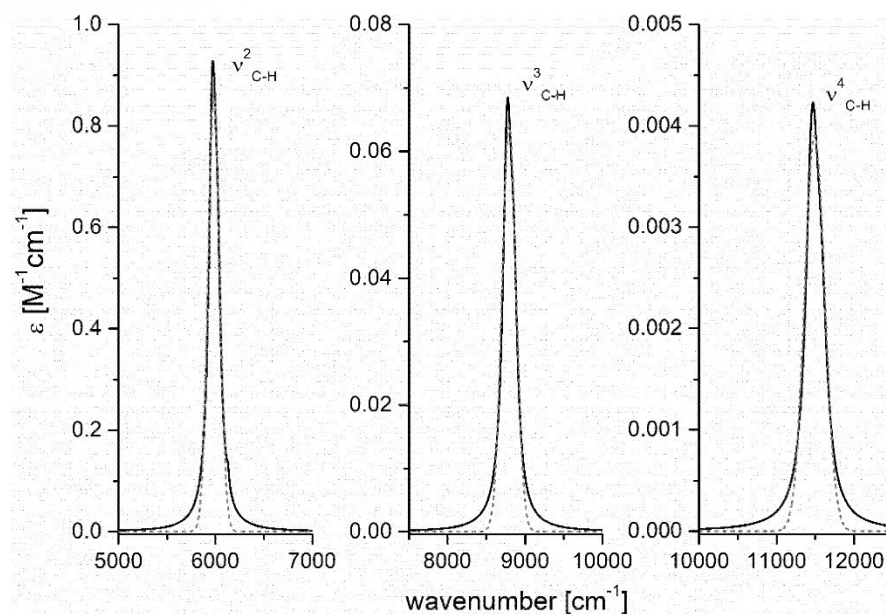
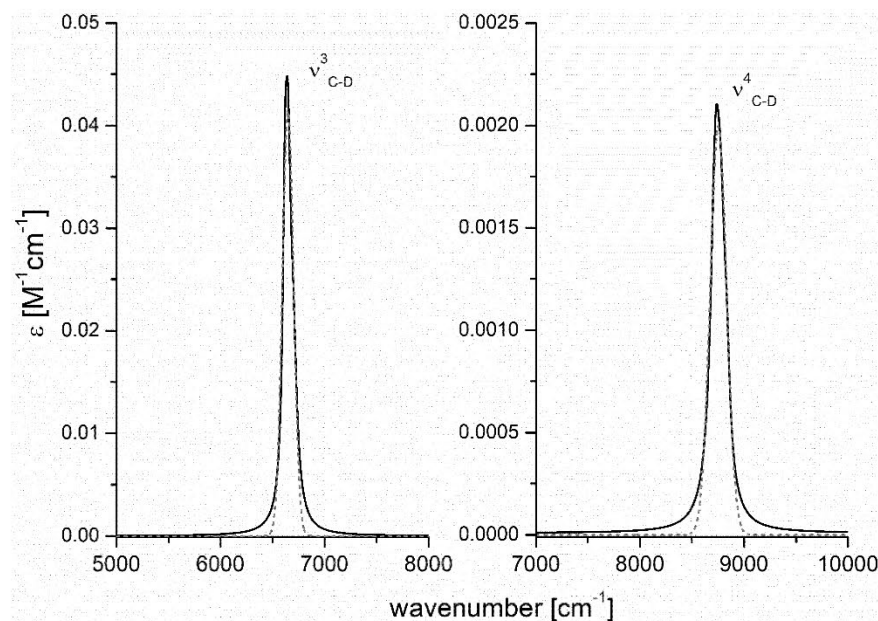


Figure S12. Reconstructed vibrational overtone absorption bands ($\nu = 3$ and 4) for the aromatic CD oscillators of Me₂-bpy (black) with single Gaussian fits (dashed red).^{S3}



The integrand functions for the SOIs between the vanadium emission and the relevant C–(H/D) overtones were constructed according to the mathematical definition of the SOIs:

$$\text{SOI} = \int I_{\text{norm}}(\tilde{\nu}) \cdot \varepsilon_{\text{vib}}(\tilde{\nu}) \cdot \tilde{\nu}^{-4} d\tilde{\nu}$$

with I_{norm} being the vanadium emission spectrum (normalized to unit area) and ε the molar vibrational extinction coefficient (extracted and extrapolated absorption spectra of the relevant overtones), both expressed in the wavenumber scale $\tilde{\nu}$. The integrand functions were generated with a set of data points with a step size of 1 cm⁻¹. Numerical integration gave the corresponding values for SOI.

Figure S13. Integrand function of the spectral overlap integral (SOI) for the vanadium emission band in $\text{VCl}_3(\text{ddpd})$ and the second aromatic C–H ($\nu = 3$) oscillators in $\text{Me}_2\text{-bpy}$.

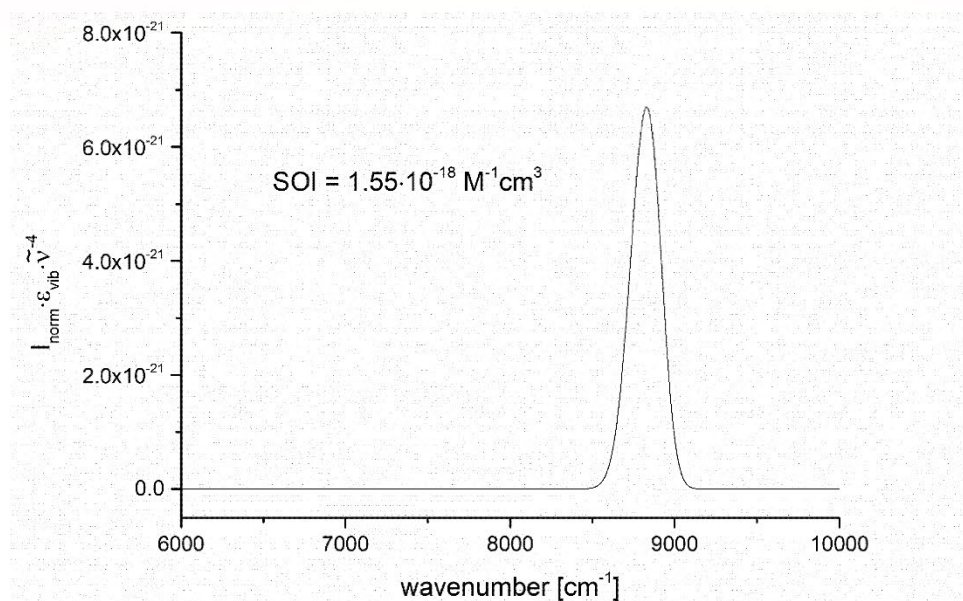
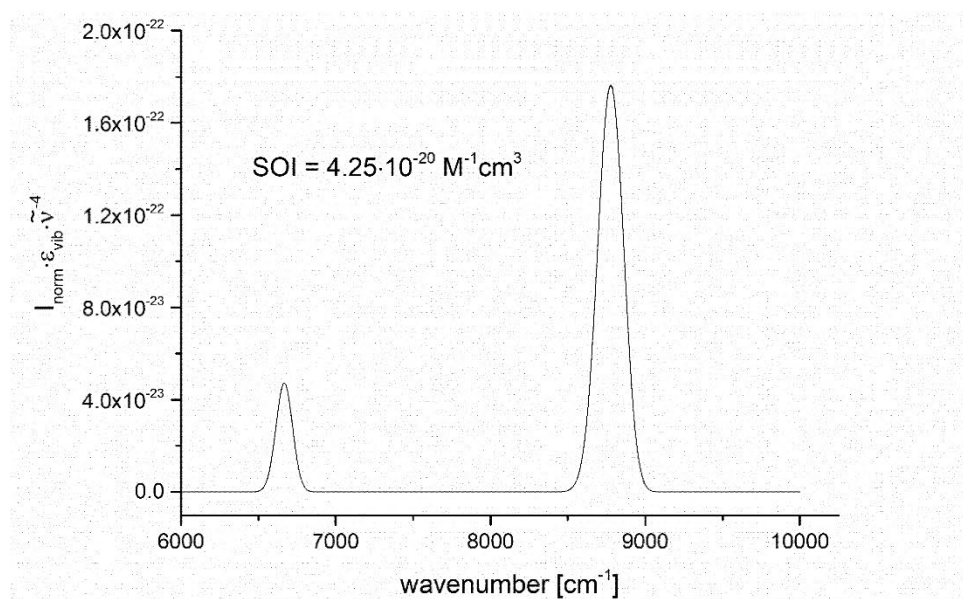


Figure S14. Integrand function of the spectral overlap integral (SOI) for the vanadium emission band in $\text{VCl}_3(\text{ddpd})$ and the second ($\nu = 3$) and third ($\nu = 4$) aromatic C–D oscillators in $[\text{D}_{12}]\text{-Me}_2\text{-bpy}$.



Based on the obtained SOIs, the ratio of the non-radiative deactivation rates of vanadium excited states from $\text{VCl}_3(\text{ddpd}-[\text{D}_0])$ and $\text{VCl}_3(\text{ddpd}-[\text{D}_{17}])$ is estimated as:

$$\frac{k_{\text{nr}}(\text{C-H})}{k_{\text{nr}}(\text{C-D})} = \frac{\text{SOI}(\text{C-H})}{\text{SOI}(\text{C-D})} = \frac{1.55 \cdot 10^{-18} \text{ M}^{-1} \text{ cm}^3}{4.25 \cdot 10^{-20} \text{ M}^{-1} \text{ cm}^3} = 3.63 \cdot 10^1$$

Figure S15. Normalized spectra for the vanadium ^1E emission of $\text{VCl}_3(\text{ddpd})$ (red) and the relevant vibrational aromatic C–H overtone absorption band (dashed black).

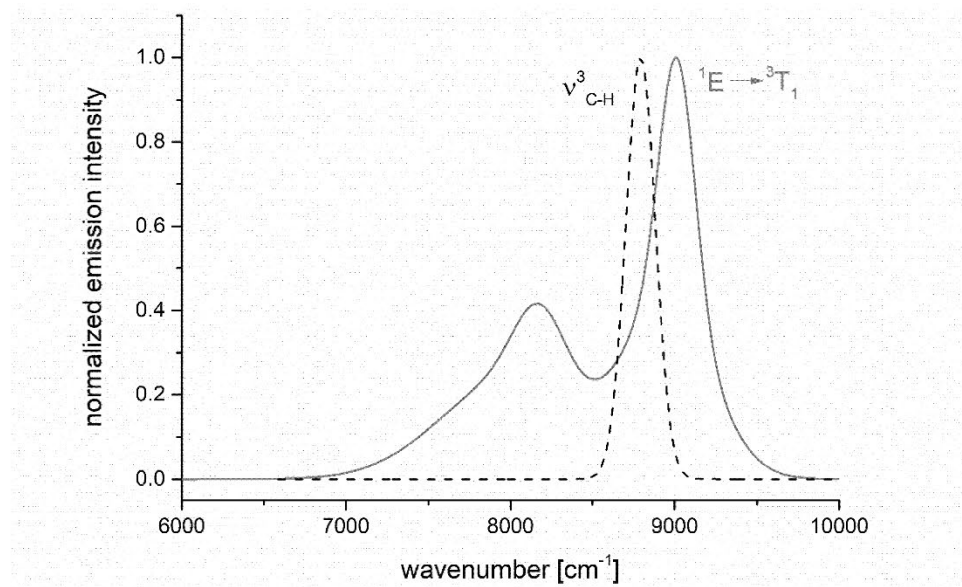


Figure S16. Spectra for the vanadium ^1E emission of $\text{VCl}_3(\text{ddpd})$ (red) and the relevant vibrational aromatic C–D overtone absorption bands (dashed black). The overtone intensities are shown with their actual intensity ratios.

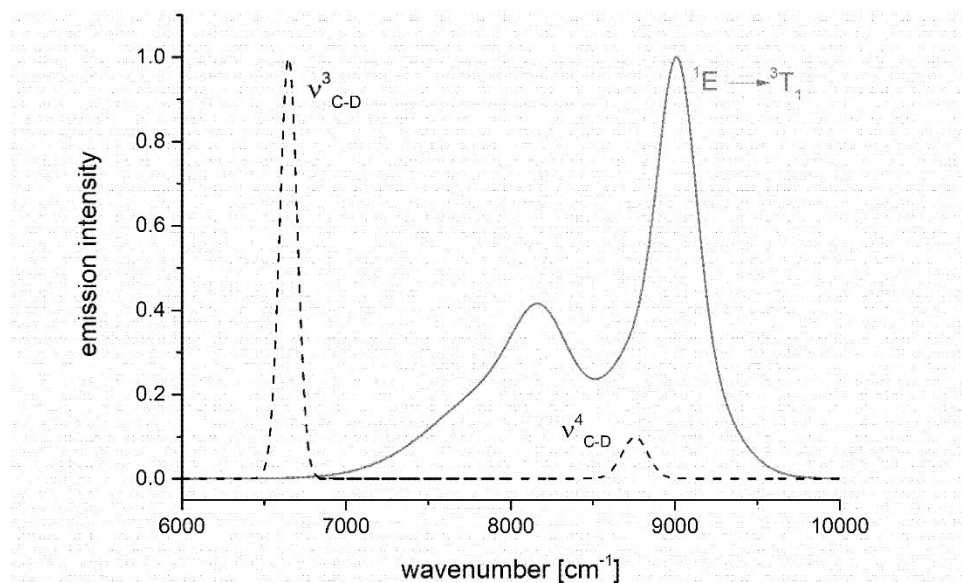


Figure S17. Luminescence spectra of $\text{VCl}_3(\text{ddpd-}[\text{D}_0])$ as neat powder at 5–290 K ($\lambda_{\text{exc}} = 350 \text{ nm}$).

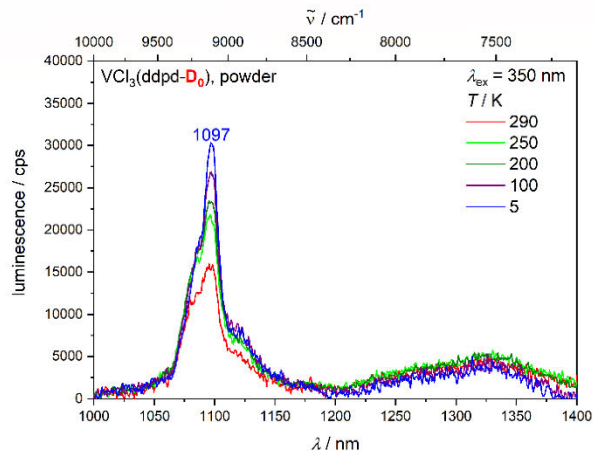


Figure S18. Luminescence spectra of $\text{VCl}_3(\text{ddd-}[\text{D}_0])$ as KBr pellet at 5–290 K ($\lambda_{\text{exc}} = 350 \text{ nm}$).

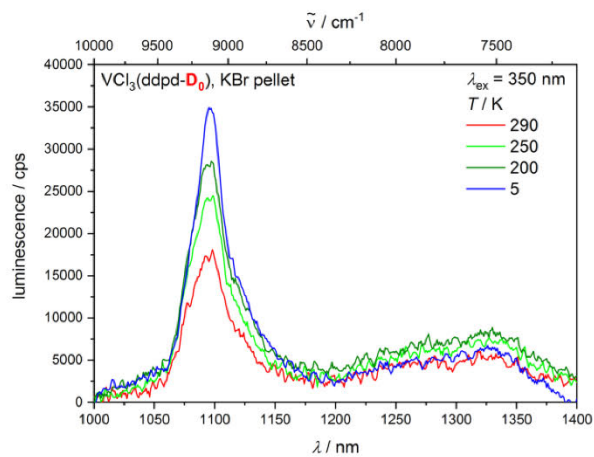


Figure S19. Plot of the integrated luminescence versus temperature for $\text{VCl}_3(\text{ddd-}[\text{D}_0])$ and $\text{VCl}_3(\text{ddd-}[\text{D}_{17}])$.

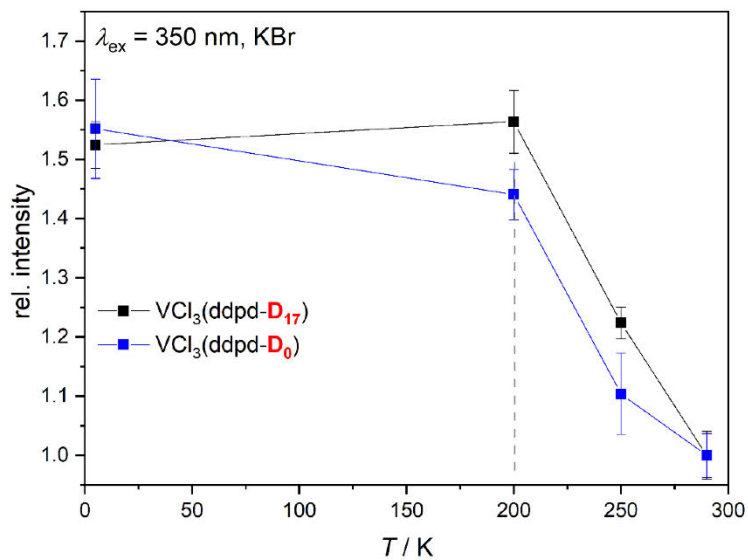


Figure S20. Ground state (black) and step-scan FTIR spectrum (red, $\lambda_{\text{exc}} = 355$ nm; 0–500 ns) of $\text{VCl}_3(\text{ddpd}-[\text{D}_0])$ in a KBr pellet at 20 K.

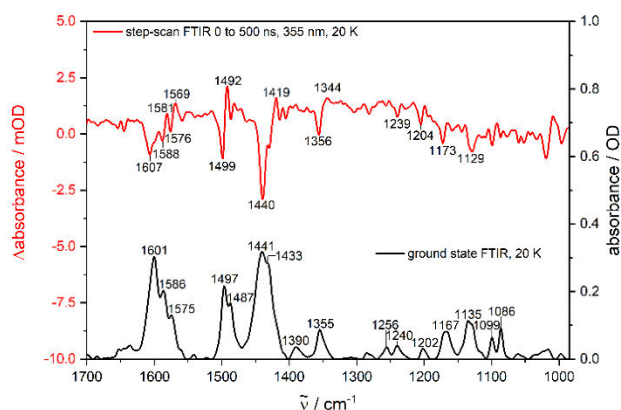


Figure S21. Experimental (black), DFT-calculated ground state (green) and step-scan FTIR spectrum (red, $\lambda_{\text{exc}} = 355$ nm; 0–500 ns) of $\text{VCl}_3(\text{ddpd}-[\text{D}_{17}])$ in a KBr pellet at 290 K (red).

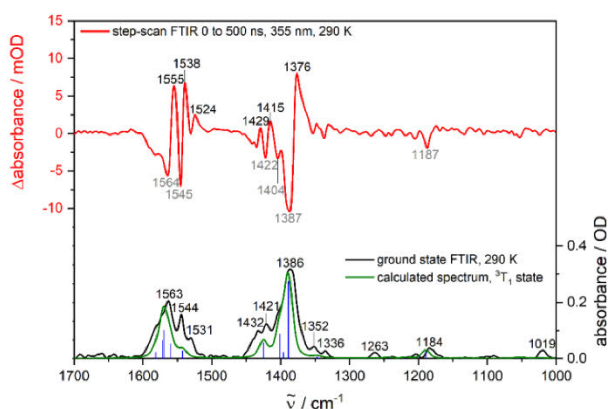
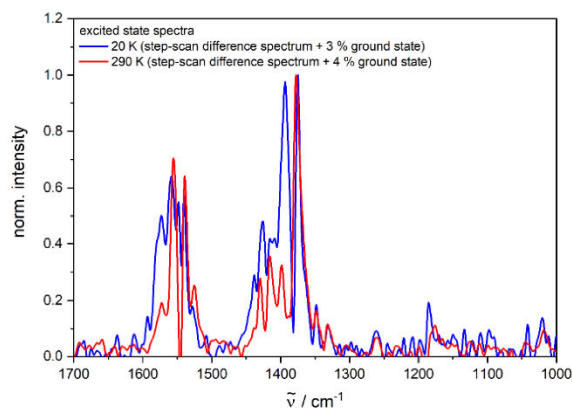


Figure S22. Excited state FTIR spectra of $\text{VCl}_3(\text{ddpd}-[\text{D}_{17}])$ in a KBr pellet obtained from step-scan FTIR spectra ($\lambda_{\text{exc}} = 355$ nm; 0–500 ns) (and small contributions of the respective ground state spectrum of 3 %) at 20 K (blue) and 290 K (red).



Appendix

Figure S23. Ground state (black) and step-scan FTIR spectrum (red, $\lambda_{\text{exc}} = 355 \text{ nm}$; 0–500 ns) of $\text{VCl}_3(\text{ddpd}-[\text{D}_{17}])$ in a KBr pellet at 20 K.

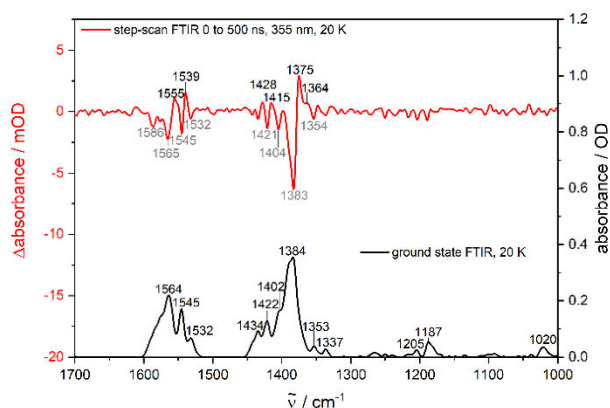


Figure S24. Global monoexponential fit and residuals performed for the most prominent positive and negative peaks in the step-scan spectrum of $\text{VCl}_3(\text{ddpd}-[\text{D}_0])$ in a KBr pellet at 290 K.

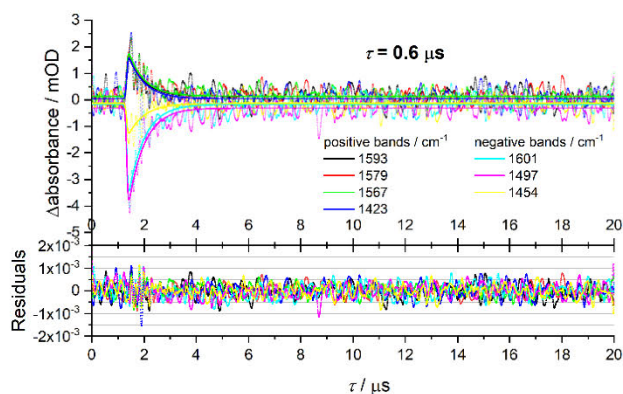


Figure S25. Global monoexponential fit and residuals performed for the most prominent positive and negative peaks in the step-scan spectrum of $\text{VCl}_3(\text{ddpd}-[\text{D}_0])$ in a KBr pellet at 20 K.

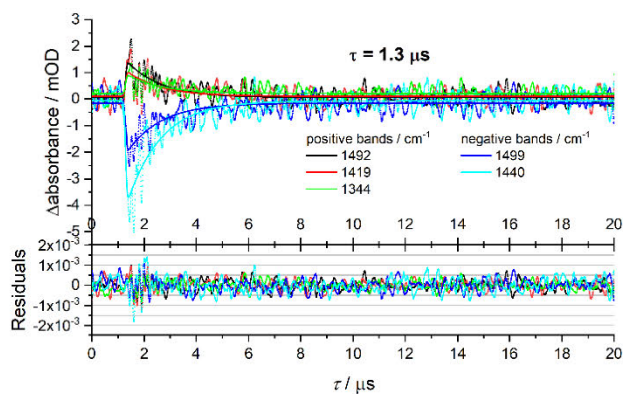


Figure S26. Global monoexponential fit and residuals performed for the most prominent positive and negative peaks in the step-scan spectrum of $\text{VCl}_3(\text{ddpd-}[D_{17}])$ in a KBr pellet at 290 K.

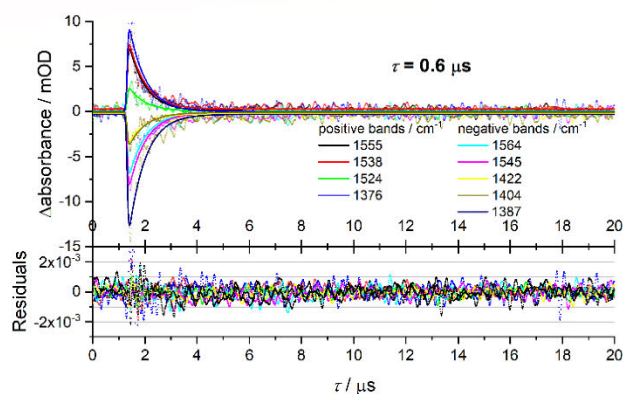


Figure S27. Global monoexponential fit and residuals performed for the most prominent positive and negative peaks in the step-scan spectrum of $\text{VCl}_3(\text{ddpd-}[D_{17}])$ in a KBr pellet at 20 K.

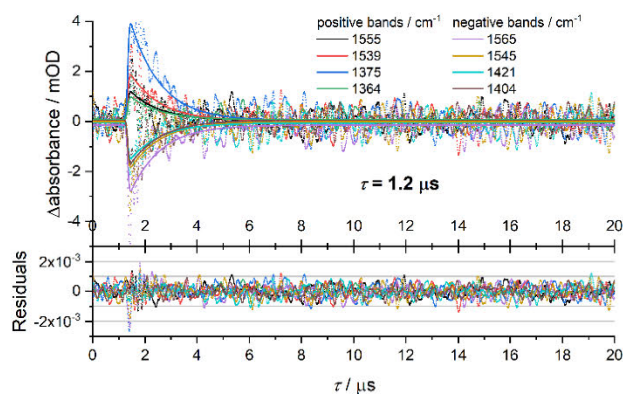


Figure S28. Changes of the UV/Vis absorption spectra of $\text{VCl}_3(\text{ddpd-}[\text{D}_0])$ in CH_3CN under irradiation with a Xe lamp at 350 ± 5 nm.

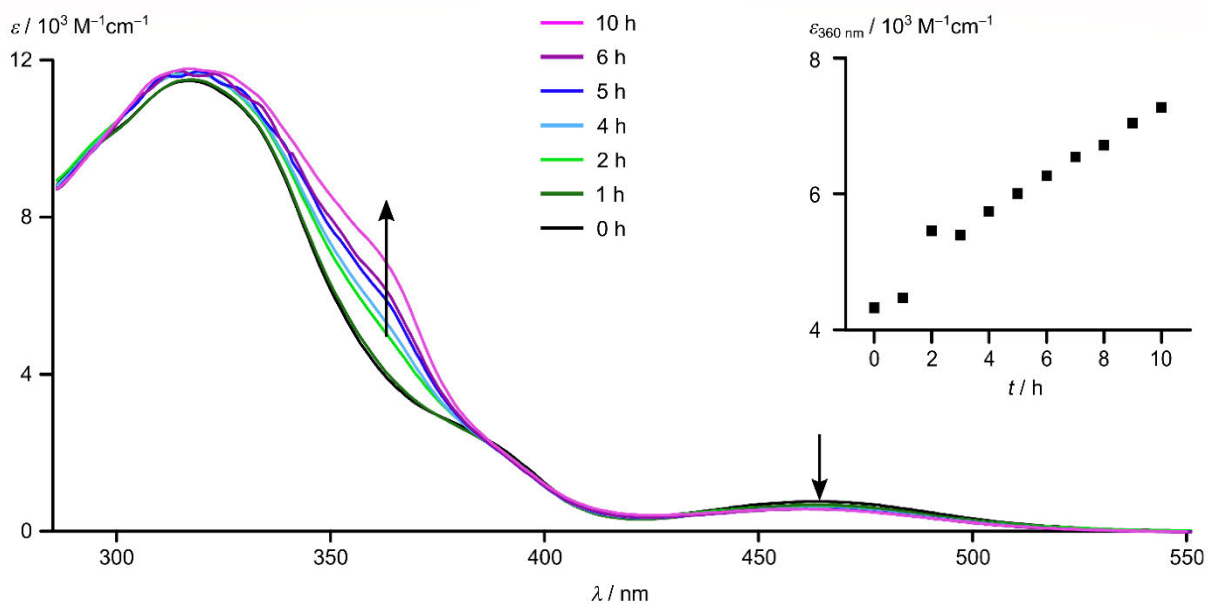


Figure S29. Changes of the emission spectra of $\text{VCl}_3(\text{ddpd-}[\text{D}_0])$ in CH_3CN under irradiation with a Xe lamp at 350 ± 5 nm.

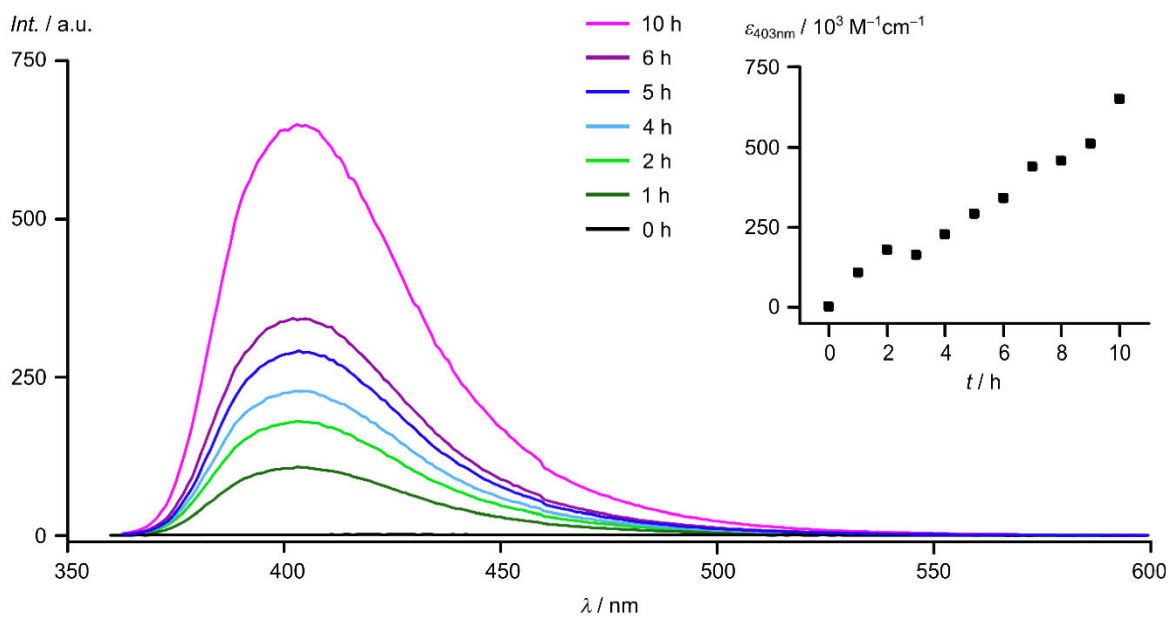


Figure S30. Changes of the UV/Vis absorption spectra of $\text{VCl}_3(\text{ddpd-}[\text{D}_0])$ in CH_3CN under irradiation with a Xe lamp at 400 ± 5 nm.

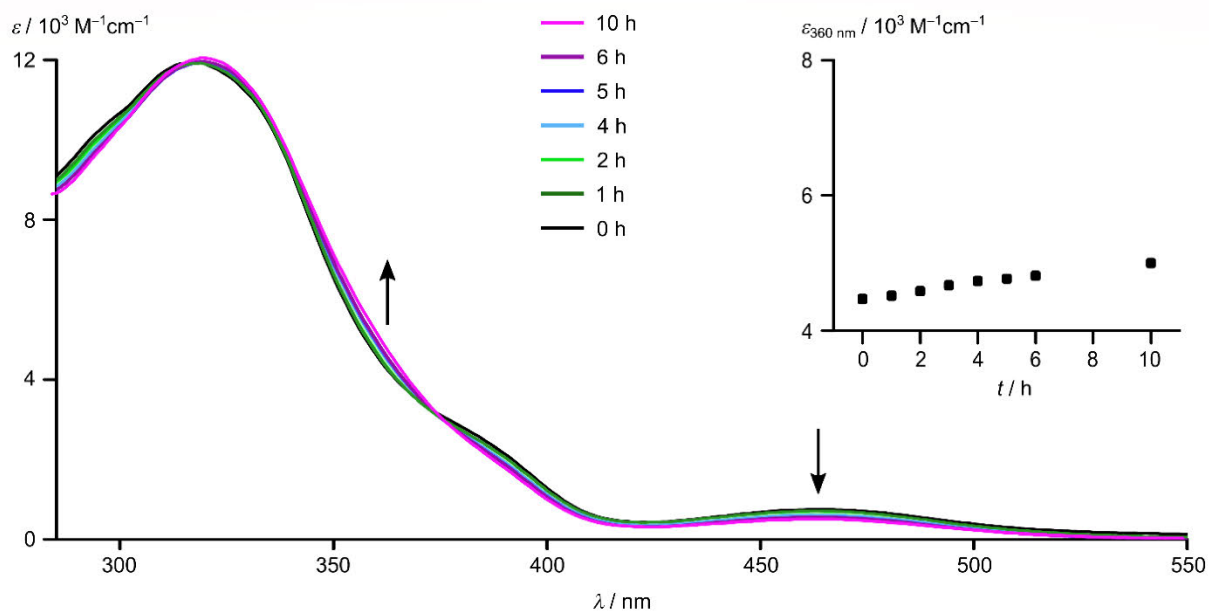


Figure S31. Changes of the emission spectra of $\text{VCl}_3(\text{ddpd-}[\text{D}_0])$ in CH_3CN under irradiation with a Xe lamp at 400 ± 5 nm.

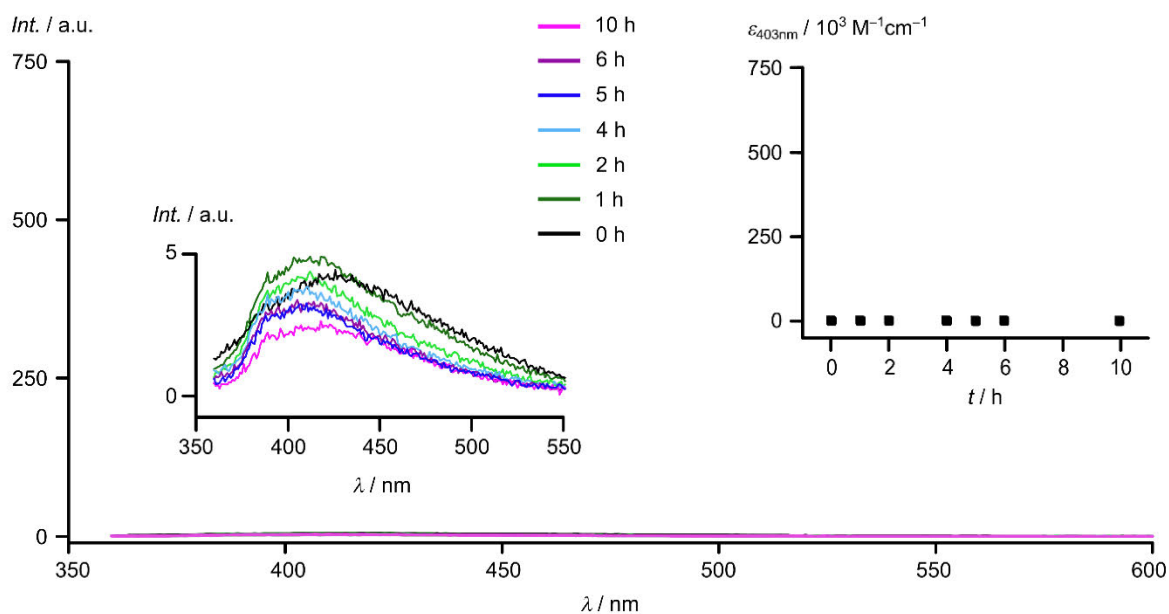


Figure S32. Spectral irradiance of the employed light source Asahi Spectra Max-303 Xenon Light Source (300 W).

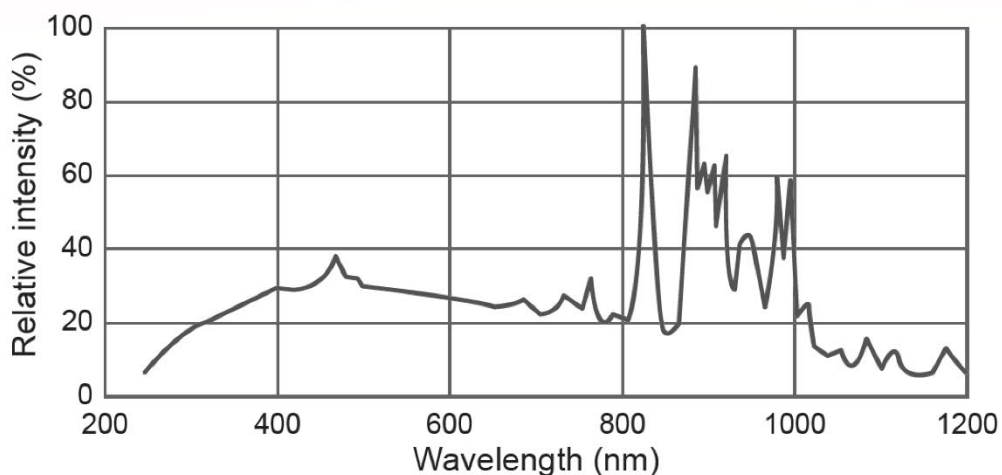
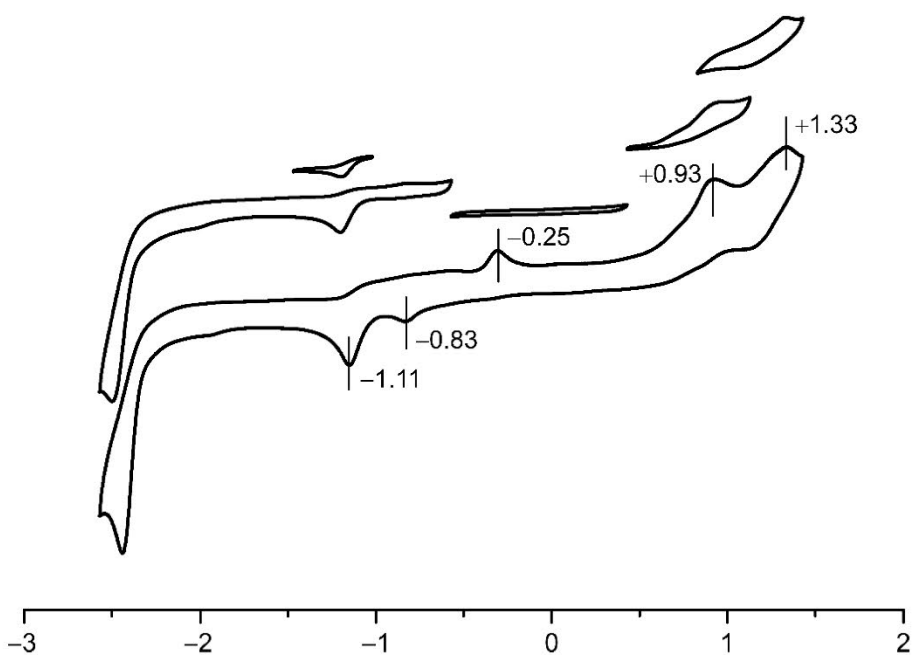


Figure S33 Cyclic voltammograms of $VCl_3(\text{ddpd})$ at 298 K in $[\text{tBu}_4\text{N}][\text{PF}_6]/\text{CH}_3\text{CN}$. Potentials given vs. ferrocene/ferrocenium.



References

- S1 C. Förster, M. Dorn, T. Reuter, S. Otto, G. Davarci, T. Reich, L. Carrella, E. Rentschler and K. Heinze, *Inorganics* 2018, **6**, 86.
- S2 C. Doffek, N. Alzakhem, C. Bischof, J. Wahsner, T. Güden-Silber, J. Lügger, C. Platas-Iglesias and M. Seitz, *J. Am. Chem. Soc.* **2012**, *134*, 16413–16423.
- S3 C. Wang, S. Otto, M. Dorn, E. Kreidt, J. Lebon, L. Sršan, P. Di Martino-Fumo, M. Gerhards, U. Resch-Genger, M. Seitz and K. Heinze, *Angew. Chem.* **2018**, *130*, 1125–1130.

6.3. Supporting Information to Chapter 3.3. (“Towards luminescent vanadium(II) complexes with slow magnetic relaxation”)

Towards Luminescent Vanadium(II) Complexes with Slow Magnetic Relaxation and Quantum Coherence

Matthias Dorn,^{[a]‡} David Hunger,^{[b]‡} Christoph Förster,^[a] Robert Naumann,^[a] Joris van Slageren,^{*[b]} and Katja Heinze^{*[a]}

[a] M. Dorn, Dr. C. Förster, Dr. R. Naumann, Prof. Dr. K. Heinze
Department of Chemistry, Johannes Gutenberg University, Duesbergweg 10-14, 55128 Mainz, Germany
E-mail: katja.heinze@uni-mainz.de. www.ak-heinze.chemie.uni-mainz.de

[b] D. Hunger, Prof. Dr. J. van Slageren
Institute of Physical Chemistry and Center for Integrated Quantum Science and Technology, University of Stuttgart, Pfaffenwaldring 55, 70569 Stuttgart, Germany. E-mail: slageren@ipc.uni-stuttgart.de. www.ipc.uni-stuttgart.de/slageren
‡These authors contributed equally.

Supporting Information

General Procedures. Glassware used for storage of dry solvents and in the synthesis of vanadium(II) precursors and title complexes was treated according to standard Schlenk procedures prior to use. Syntheses involving vanadium complexes were generally carried out in dry solvents. Diethyl ether and acetonitrile were distilled under an argon atmosphere over sodium and calcium hydride, respectively. Sodium tetrphenylborate (99.5 %; abcr) was dried under reduced pressure at 180°C for 18 h prior to use. Vanadium(III) chloride (anhydrous, 95 %; abcr) for the preparation of hexa(acetonitrile)vanadium(II) tetrphenylborate^[1] was used as received. The ligand ddpd^[2] and hexa(acetonitrile)vanadium(II) tetrphenylborate^[1] were prepared according to reported procedures. NMR spectroscopic and mass spectrometric data matched the literature values. A glovebox (UniLab/MBraun, Ar 4.8, O₂ < 1 ppm, H₂O < 0.1 ppm) was used for storage and weighing of sensitive compounds and degassed solvents.

IR spectra were recorded with a *Bruker Alpha II FT-IR* spectrometer with a Platinum Di-ATR module inside an Ar filled glove box.

ESI⁺ mass spectra were recorded on a *Micromass Q-TOF-Ultima* spectrometer by the central analytical facility of the Department of Chemistry of the University of Mainz.

Electrochemical experiments were carried out on a *BioLogic SP-200* voltammetric analyzer using platinum wires as counter and working electrodes and a 0.01 M Ag/Ag[NO₃] electrode as reference electrode. Cyclic voltammetry measurements were carried out at scan rates of 50–200 mV s⁻¹ using 0.1 M [ⁿBu₄N][PF₆] in CH₃CN as supporting electrolyte. Potentials are referenced against the ferrocene/ferrocenium couple.

UV/Vis/NIR spectra were recorded on a *JASCO V-770* spectrophotometer using 1.0 cm inert gas cells.

Luminescence experiments were carried out on an *Edinburgh FLS 1000* photoluminescence spectrometer. Photomultiplier detectors PMT-980 and N-GO9 PMT-1700 were used for luminescence measurements in the visible and NIR spectral region. A xenon arc lamp Xe2 (450 W) was used for excitation in steady-state measurements. Measurements at low temperature were conducted using a liquid nitrogen cooled cryostat *Optistat DN 0.8* from Edinburgh Instruments. For luminescence measurements in deoxygenated solvents, the respective solvent was degassed by freezing it with liquid nitrogen, evacuating the vessel for 30 minutes and warming to room temperature. The procedure was repeated until no more gas evolution occurred upon thawing, but at least three times.

High-frequency electron paramagnetic resonance (HF-EPR) spectra were recorded on pressed powder pellets by means of a home-built spectrometer that has been described in the literature.^[3] Simulations were carried out by using the Easyspin tool.^[4]

Magnetic circular dichroism (MCD) spectra were recorded on frozen solution samples by means of a home-built spectrometer based on an *Aviv 41CD* spectrometer and an Oxford Instruments 10T Spectromag optical cryomagnet.^[5]

Pulsed Q-band EPR measurements were performed on a home-built spectrometer that has been described in the literature.^[6,7] Samples were freeze-pump-thaw degassed three times prior to measurement. The echo-detected spectra, as well as T_M decay curves were recorded by a Hahn echo sequence $\pi/2-\tau-\pi-\tau$ -echo with constant $\tau = \tau_{\text{fix}}$ for the former and variable τ for the latter. The spin-lattice relaxation time T_1 was determined by means of the inversion recovery sequence $\pi-\tau-\pi/2-\tau_{\text{fix}}-\pi-\tau_{\text{fix}}$ -echo. Simulations were carried out by using the Easyspin tool.^[4]

DC and AC magnetic studies were carried out on a Quantum Design MPMS3 SQUID magnetometer. Measurements were carried out at a constant magnetic field of 1000 Oe in a temperature range from

1.8 K to 50 K and at 10 000 Oe in a temperature range from 40 K to 300 K. The measured data in the intersection of the temperature ranges served to compensate for possible ferromagnetic impurities. Samples were pressed into a pellet with a diameter of 5 mm and fixed in a plastic tube. Data were corrected for the diamagnetic contribution to the susceptibility by means of Pascal's constants. All sample handling was done under a nitrogen atmosphere due to the air sensitivity of the samples.

Elemental analyses were carried out by the *Mikroanalytisches Labor Kolbe*, Oberhausen, Germany.

Crystal structure determination. Intensity data were collected with a *STOE IPDS-2T* diffractometer and an Oxford cooling system and corrected for absorption and other effects using Mo-K α radiation ($\lambda = 0.71073 \text{ \AA}$). The diffraction frames were integrated using the *STOE X-Area* software package^[8], and most were corrected for absorption with *MULABS*^[9] of the *PLATON* package^[10]. The structure was solved by direct methods and refined by the full-matrix method based on F^2 using the *SHELXTL* software package.^[11,12] All non-hydrogen atoms were refined anisotropically, while the positions of all hydrogen atoms were generated with appropriate geometric constraints and allowed to ride on their respective parent carbon atoms with fixed isotropic thermal parameters. CCDC 2177572 (*mer*-[V(ddpd)₂][BPh₄]₂) and 2177573 (*cis-fac*-[V(ddpd)₂][PF₆]₂) contain the supplementary crystallographic data for this paper. These data are provided free of charge by The Cambridge Crystallographic Data Centre.

Computational Details

Static unrestricted Kohn-Sham orbitals DFT (UKS): All calculations were performed with the quantum computing suite ORCA 5.0.1.^[13] Unrestricted Kohn-Sham orbitals DFT (UKS) and the B3LYP functional^[14] in combination with Ahlrichs' split-valence triple- ζ basis set def2-TZVPP for all atoms were employed in the geometry optimizations (Tables S3, S4, S11, S12).^[15] Tight convergence criteria were chosen for geometry and frequency calculations (keywords tightscf and tightopt). All DFT-UKS calculations make use of the resolution of identity (Split-RI-J) approach for the Coulomb term in combination with the chain-of-spheres approximation for the exchange term (COSX).^[16] The zero order relativistic approximation was used to describe relativistic effects in all calculations (keyword ZORA).^[17,18] Grimme's empirical dispersion correction D3(BJ) was employed (keyword D3BJ).^[19,20] A conductor-like screening model (keyword CPCM) modeling acetonitrile was used in all calculations to incorporate solvent effects.^[21] Explicit solvent molecules and/or counter ions were neglected. TD-DFT calculations were conducted at the same level of theory using unrestricted Kohn-Sham orbitals (UKS). Seventy vertical spin-allowed transitions were calculated. The charge transfer number analyses of the time-dependent DFT (TD-DFT) calculated transitions were done using TheoDRE 2.2.^[22,23]

CASSCF(12,7)-SC-NEVPT2: Calculations of ground- and excited-state properties of pure metal-centered (MC) states were performed using the complete-active-space self-consistent field method including spin-orbit coupling (SOC-CASSCF)^[24,25] in conjunction with the strongly contracted N-electron valence perturbation theory to second order (SC-NEVPT2)^[26,27] to recover missing dynamic electron correlation. SOC was treated through the mean-field (SOMF) approximation^[28,29] and the effective Hamiltonian approach^[30-32] was used to compute the spin-Hamiltonian parameters. An active space of (7,12) along with 10 quartet roots and 10 doublet roots was chosen (Tables S5 and S6). In addition to the minimal active space of (3,5), two occupied V–N σ bonding orbitals and a second d shell were included.

MCD Spectrum: The MCD spectrum of *mer*-[V(ddpd)₂][BPh₄]₂ was modelled using CASSCF methods with NEVPT2. As an active space a CAS(7,7) was chosen, after identifying orbitals with significant d orbital character. 10 quartet and 9 doublet roots were calculated. The best overlap with the experiment was obtained with the smallest basis set (def2-SVP). Additional larger basis sets (def2-TZVP and def2-TZVPP) resulted in a red shift of the calculated spectra.

ZFS splitting: From the CASSCF(12,7) (TZVPP basis) calculation of *cis-fac*-[V(ddpd)₂]²⁺, the second-order spin-orbit coupling contribution and the effective Hamiltonian spin-orbital coupling as implemented in ORCA 5.0.1 yield $D = -0.31 \text{ cm}^{-1}$, $E = 0.10 \text{ cm}^{-1}$ and $D = -0.32 \text{ cm}^{-1}$, $E = -0.10 \text{ cm}^{-1}$, respectively. These values change negligibly to $D = -0.32 \text{ cm}^{-1}$, $E = 0.10 \text{ cm}^{-1}$ and $D = -0.33 \text{ cm}^{-1}$, $E = 0.11 \text{ cm}^{-1}$, respectively, after the NEVPT2 treatment. The corresponding calculated values for *mer*-[V(ddpd)₂]²⁺ are $D = -0.28 \text{ cm}^{-1}$, $E = -0.04 \text{ cm}^{-1}$, $D = -0.27 \text{ cm}^{-1}$, $E = -0.04 \text{ cm}^{-1}$ and $D = -0.27 \text{ cm}^{-1}$, $E = -0.04 \text{ cm}^{-1}$, $D = -0.29 \text{ cm}^{-1}$, $E = -0.05 \text{ cm}^{-1}$ after NEVPT2. Irrespective of the method employed and inclusion of the NEVPT2 treatment, the sign of D differs from the experimental values. This discrepancy might be a signature of the missing π accepting ligand orbitals and hence missing charge transfer contributions in the CASSCF calculations of the vanadium(II) complexes.

With a smaller basis set (def2-SVP) and a smaller active space CAS(7,7), as used for the MCD spectrum of *mer*-[V(ddpd)₂][BPh₄]₂, a positive value $D = 0.076 \text{ cm}^{-1}$ is obtained.

Experimental details

Synthesis of *cis-fac*-[V(ddpd)₂][BPh₄]₂: [V(NCCH₃)₆][BPh₄]₂ (170 mg, 0.17 mmol, 1.0 eq) was suspended in acetonitrile (15 mL) under an argon atmosphere under vigorous stirring to yield a turquoise suspension. A pale yellow solution of ddpd (101.4 mg, 0.35 mmol, 2.0 eq.) in acetonitrile (2 mL) was added. Within two hours, a dark red solution formed, which was stirred for another 15 h. The solvent was removed under reduced pressure. A reddish-brown powder (143.5 mg) was isolated and washed with diethyl ether (2x15 mL). The product was recrystallized from an acetonitrile solution (3.5 mg mL⁻¹ CH₃CN) via diethyl ether diffusion to yield small, dark red crystals in the course of several days. Yield: 143.5 mg (0.11 mmol, 66 %). C₈₂H₇₄B₂N₁₀V: Calcd. C 77.42; H 5.86; N 11.01 %; found: C 77.20; H 5.91; N 10.98 %. IR (ATR): $\tilde{\nu}$ = 3052 (w), 3034 (w), 3006 (w), 2997 (w), 2980 (w), 2915 (w), 1592 (m), 1579 (m), 1332 (m), 1332 (m), 1484 (s), 1445 (s), 1432 (s), 1274 (w), 1193 (w), 1163 (m), 1133 (m), 1120 (m), 1084 (w), 1098 (w), 1012 (w), 946 (w), 864 (w), 844 (w), 794 (m), 779 (m), 774 (m), 732 (s), 704 (s), 675 (w), 623 (w), 612 (s), 584 (w), 560 (w), 495 (w), 467 (w), 438 (w), 421 (w), 412 (w) cm⁻¹. MS (ESI⁺, CH₃CN): *m/z* (%) = 292.1 (25) [ddpd+H]⁺, 316.6 (100) [M-2BPh₄]²⁺, 952.4 (80) [M-BPh₄]⁺. UV/Vis/NIR (CH₃CN): λ (ϵ) = 303 (26400), 486 (4400 M⁻¹cm⁻¹) nm. CV ([ⁿBu₄N][PF₆]/CH₃CN, vs. ferrocene): *E*_{1/2} = -0.20 (qrev.), -2.30 (qrev.) V.

Synthesis of *cis-fac*-[V(ddpd)₂][PF₆]₂ for XRD analysis: *cis-fac*-[V(ddpd)₂][BPh₄]₂ (20 mg, 0.016 mmol, 1.0 eq) was dissolved in acetonitrile (8 mL) under an argon atmosphere at room temperature while stirring to yield a dark red solution. [ⁿBu₄N][PF₆] (31 mg, 0.03 mmol, 5.0 eq.) was added to the solution. The solution was stirred for a few minutes before filtering through a syringe filter (0.3 μ m pore size). Slow diffusion of diethyl ether into the solution yielded small, dark crystal platelets after one week. The crystals were re-dissolved in acetonitrile (6 mL) and the process was repeated with another batch of [ⁿBu₄N][PF₆] (30 mg, 0.03 mmol, 5. eq.), stirring, filtration and crystallization by ether diffusion. Crystals of *cis-fac*-[V(ddpd)₂][PF₆]₂ were obtained suitable for XRD analysis.

Synthesis of *mer*-[V(ddpd)₂][BPh₄]₂: [V(NCCH₃)₆][BPh₄]₂ (380 mg, 0.41 mmol, 1.0 eq) was suspended in acetonitrile (30 mL) under an argon atmosphere while stirring to yield a turquoise suspension. A pale yellow solution of ddpd (243 mg, 0.83 mmol, 2.0 eq.) in acetonitrile (10 mL) was added after a few minutes. The reaction mixture was heated to reflux for 17 h before cooling to ambient temperature. The solvent volume was reduced to approximately 10 mL under reduced pressure. Diethyl ether (50 mL) was added and a dark solid precipitated. The solid was collected on a glass frit under an argon atmosphere and washed with diethyl ether (2x15 mL). Yield: 330 mg (0.26 mmol, 63 %). The product was recrystallized as dark red crystals from acetonitrile via diethyl ether diffusion. C₈₂H₇₄B₂N₁₀V: Calcd. C 77.42; H 5.86; N 11.01 %; found: C 77.06; H 5.83; N 10.95 %. IR (ATR): $\tilde{\nu}$ = 3052 (w), 3034 (w), 3006 (w) 2998 (w), 2981 (w), 2902 (w), 1599 (m), 1589 (m), 1577 (m), 1564 (m), 1480 (m), 1445 (m), 1428 (s), 1360 (m), 1331 (m), 1308 (w), 1266 (w), 1251 (w), 1231 (m), 1190 (vw), 1167 (m), 1129 (m), 1094 (m), 1082 (w), 1061 (w), 1033 (w), 1013 (w), 944 (w), 859 (w), 845 (w), 801 (m), 775 (m), 745 (m), 732 (s), 704 (s), 645 (w), 623 (w), 611 (s), 581 (m), 522 (vw), 509 (w), 468 (w), 457 (w), 432 (w), 427 (w) cm⁻¹. MS (ESI⁺, CH₃CN): *m/z* (%) = 316.6 (100) [M-2BPh₄]²⁺, 952.4 (16) [M-BPh₄]⁺. UV/Vis/NIR (CH₃CN): λ (ϵ) = 308 (27200), 490 (4400 M⁻¹cm⁻¹) nm. CV ([ⁿBu₄N][PF₆]/CH₃CN, vs. ferrocene): *E*_{1/2} = -0.28 (qrev.), -2.31 (qrev.) V.

Chemical oxidation and back-reduction of *cis-fac*-[V(ddpd)₂][BPh₄]₂: A solution of *cis-fac*-[V(ddpd)₂][BPh₄]₂ (4.3 mg, 3.4 μ mol, 2 eq.) in acetonitrile (2 mL) was prepared under an argon atmosphere (0.0017 M). The solution was split in two parts A and B of 1 mL volume each. A sample

of A (100 μL) was diluted with acetonitrile (2.9 mL), filled into an inert gas cell and an absorption spectrum was recorded. To oxidize the complex, a silver tetrafluoroborate solution in acetonitrile (30 μL , 0.17 M, 3 eq.) was added to solution B while stirring. The color changed immediately from dark red to green and a solid precipitated. The mixture was stirred for 20 min. A sample of B/Ag[BF₄] (100 μL) was diluted with acetonitrile (2.9 mL), filtered through a syringe filter (0.3 μm pore size) into an inert gas cell and an absorption spectrum was recorded. A cobaltocene solution in acetonitrile (43 μL , 0.11 M, 3.1 eq.) was added to B/Ag[BF₄]. The solution assumed a brownish red color. A sample of this solution B (100 μL) was diluted with acetonitrile (2.9 mL), filtered through a syringe filter (0.3 μm pore size) into an inert gas cell and an absorption spectrum was recorded. An analogous oxidation procedure with Ag[BF₄] was performed in butyronitrile to record an emission spectrum at 78 K.

Chemical oxidation and back-reduction of *mer*-[V(ddpd)₂][BPh₄]₂: A solution of *mer*-[V(ddpd)₂][BPh₄]₂ (4.1 mg, 3.1 mmol, 2 eq.) in acetonitrile (2 mL) was prepared under an argon atmosphere (0.0016 M). The solution was split in two parts A and B of 1 mL volume each. A sample of A (100 μL) was diluted with acetonitrile (2.9 mL), filled into an inert gas cell and an absorption spectrum was recorded. To oxidize the complex, a silver tetrafluoroborate solution in acetonitrile (28 μL , 0.17 M, 3 eq.) was added to solution B while stirring. The color changed immediately from dark red to bluish green and a solid precipitated. The mixture was stirred for 20 min. A sample of B/Ag[BF₄] (100 μL) was diluted with acetonitrile (2.9 mL), filtered through a syringe filter (0.3 μm pore size) into an inert gas cell and an absorption spectrum was recorded. A cobaltocene solution in acetonitrile (41 μL , 0.11 M, 3.1 eq.) was added to B/Ag[BF₄]. The solution assumed a dark red color. The mixture was stirred for 20 min. A sample of this solution B (100 μL) was diluted with acetonitrile (2.9 mL), filtered through a syringe filter (0.3 μm pore size) into an inert gas cell and an absorption spectrum was recorded. An analogous oxidation procedure with Ag[BF₄] was performed in butyronitrile to record an emission spectrum at 78 K.

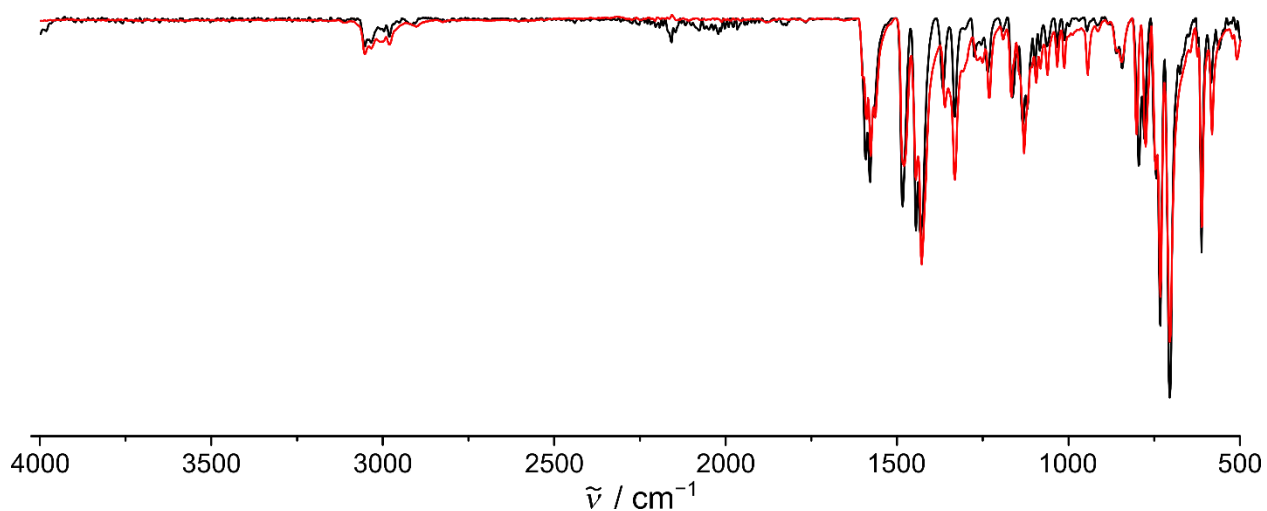


Figure S1. ATR-IR spectra of *cis-fac*-[V(ddpd)₂][BPh₄]₂ (black) and *mer*-[V(ddpd)₂][BPh₄]₂ (red).

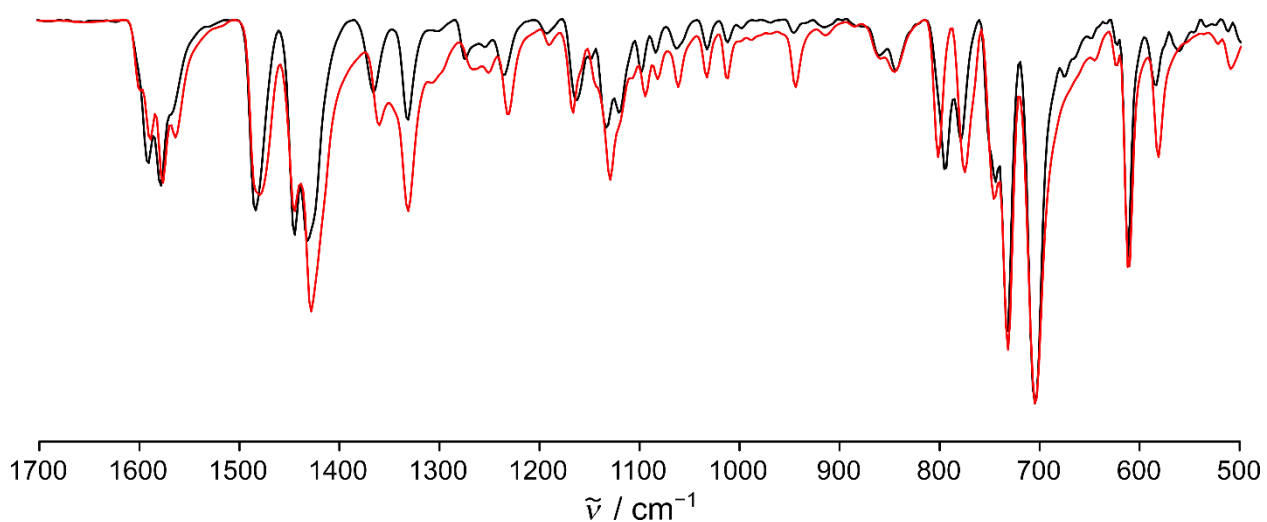


Figure S2. ATR-IR spectra of *cis-fac*-[V(ddpd)₂][BPh₄]₂ (black) and *mer*-[V(ddpd)₂][BPh₄]₂ (red) between 1700 and 500 cm^{-1} .

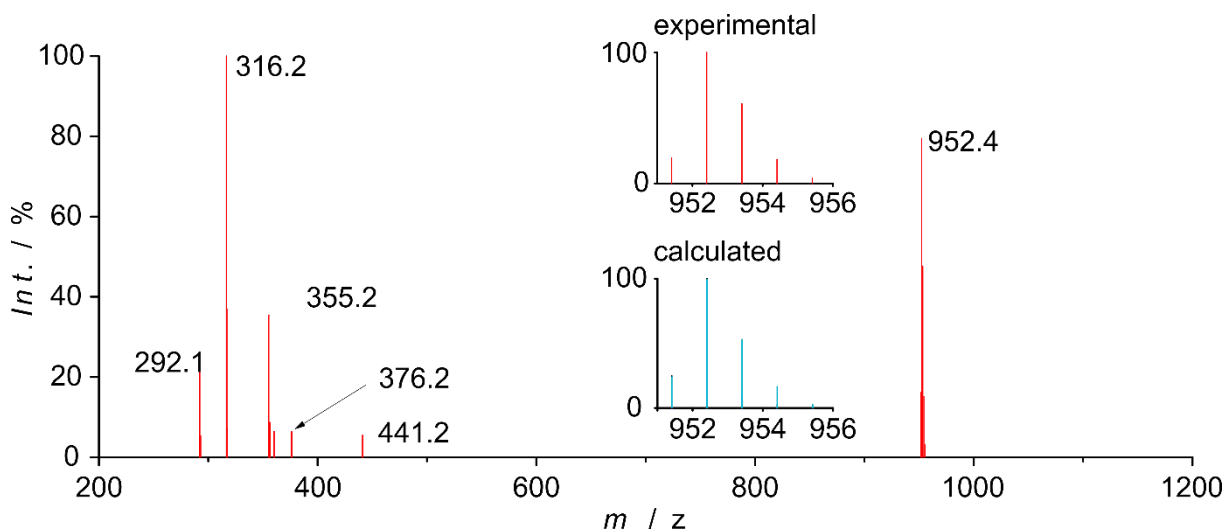


Figure S3. ESI⁺ mass spectrum of *cis-fac*-[V(ddpd)₂][BPh₄]₂ in acetonitrile.

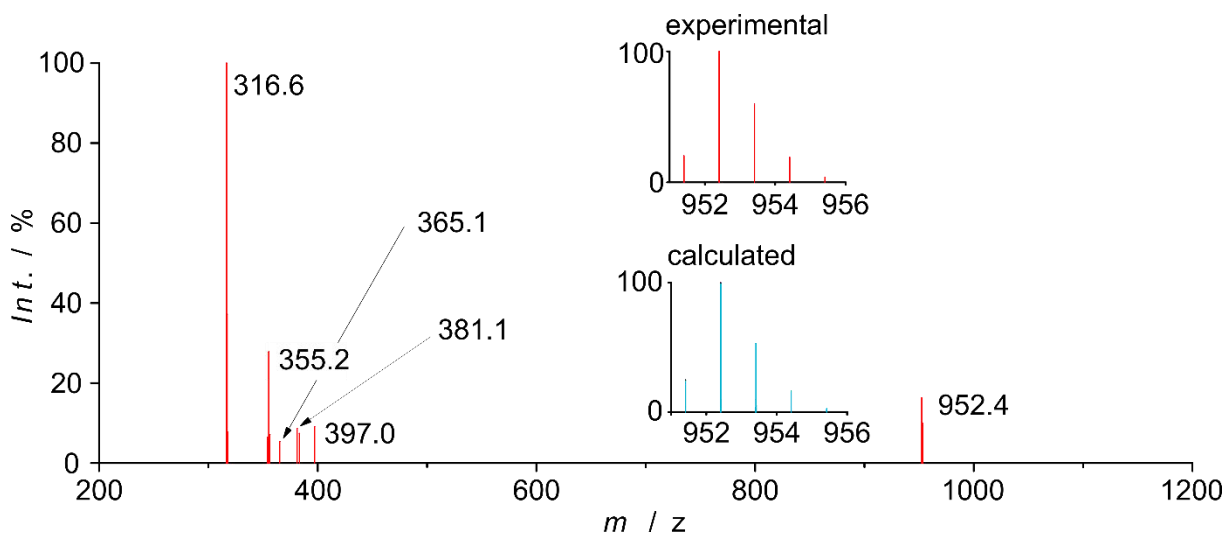


Figure S4. ESI⁺ mass spectrum of *mer*-[V(ddpd)₂][BPh₄]₂ in acetonitrile.

Table S1. Selected bond distances / Å and bond angles / ° of *cis-fac*-[V(ddpd)₂]²⁺ (XRD analysis of *cis-fac*-[V(ddpd)₂][PF₆]₂ and DFT-UKS calculation of *cis-fac*-[V(ddpd)₂]²⁺).

	V-N1/ V-N2/ V-N3	N1-V-N3/ N1-V-N8/ N3-V-N5	V-N4/ V-N5/ V-N6	N6-V-N8/ N6-V-N5/ N8-V-N10/	Shape parameter S(OC-6) of the [VN ₆] polyhedron ^[33]
	2.165(3)	81.67(9)	2.172(3)	79.88(9)	
XRD	2.126(2)	176.15(9)	2.141(3)	165.63(9)	0.88
	2.154(2)	81.63(9)	2.139(2)	83.13(9)	
	2.159	81.65	2.160	81.49	
DFT-UKS	2.151	174.11	2.155	169.65	0.79
	2.160	81.32	2.158	81.44	

Table S2. Selected bond distances / Å and angles / ° of *mer*-[V(ddpd)₂]²⁺ (XRD analysis of *mer*-[V(ddpd)₂][BPh₄]₂ and DFT-UKS calculation of *mer*-[V(ddpd)₂]²⁺).

	V-N1/ V-N3/ V-N5	N1-V-N3/ N1-V-N5/ N3-V-N5	V-N6/ V-N8/ V-N10	N6-V-N8/ N6-V-N10/ N8-V-N10/	Shape parameter S(OC-6) of the [VN ₆] polyhedron ^[33]
	2.120(2)	86.24(7)	2.120(2)	85.52(7)	
XRD	2.094(2)	171.47(7)	2.084(2)	171.08(7)	0.40
	2.117(2)	85.35(7)	2.120(2)	85.62(7)	
	2.137	84.80	2.146	84.56	
DFT-UKS	2.124	169.22	2.117	168.90	0.61
	2.145	84.46	2.147	84.34	

Table S3. Cartesian Coordinates of the DFT-UKS calculated ground state geometry of *cis-fac*-[V(ddpd)₂]²⁺.

Atomic number	x	y	z
23	3.82062	9.31453	15.05076
7	4.7576	7.41266	15.46071
7	6.64681	8.12095	14.21054
7	4.7476	9.00359	13.13523
7	2.74792	9.68181	12.08862
7	2.14037	8.43761	14.01402
7	5.52624	10.42397	15.77568
7	5.22269	11.95039	13.98412
7	3.07569	11.30685	14.70494
7	1.00366	10.68695	15.6385
7	2.68667	9.55399	16.87123
6	4.15858	6.47512	16.22098
1	3.16472	6.70717	16.56771
6	4.75706	5.28941	16.58628
1	4.22657	4.58748	17.21163
6	6.04753	5.03998	16.13076
1	6.55737	4.12066	16.38247
6	6.66938	5.97856	15.32995
1	7.65666	5.79268	14.93941
6	5.99875	7.16056	15.00245
6	8.10552	8.19891	14.32459
1	8.62432	7.48923	13.67802
1	8.3809	8.00619	15.35659
1	8.42014	9.20715	14.06821
6	6.05745	8.6902	13.08241
6	6.82616	8.95865	11.95014
1	7.87443	8.71777	11.91846
6	6.19637	9.50496	10.8462
1	6.76612	9.71037	9.95068
6	4.83263	9.74088	10.86125
1	4.3337	10.10858	9.98183
6	4.12503	9.45574	12.02834
6	2.16714	10.55891	11.06824
1	2.80604	11.42914	10.95391
1	1.195	10.8945	11.41503
1	2.0535	10.06944	10.0994
6	1.86235	8.81933	12.75548
6	0.68557	8.4115	12.11735
1	0.48535	8.71471	11.10307
6	-0.20584	7.59633	12.7879
1	-1.11555	7.27559	12.30006
6	0.09223	7.18787	14.08375
1	-0.57307	6.55384	14.6499
6	1.27081	7.62731	14.64485
1	1.52314	7.3577	15.65756
6	6.25526	9.9962	16.82308
1	5.89342	9.11348	17.32529
6	7.4269	10.59398	17.23241

1	7.97496	10.19109	18.07059
6	7.87139	11.70967	16.5307
1	8.77998	12.22044	16.81703
6	7.12733	12.1716	15.46218
1	7.44046	13.04969	14.92191
6	5.95062	11.50691	15.10194
6	5.98692	12.62267	12.92971
1	5.45043	12.52013	11.99133
1	6.94569	12.12422	12.82894
1	6.15305	13.68229	13.13191
6	3.84605	12.17739	14.0219
6	3.2909	13.25236	13.3287
1	3.90728	13.93991	12.77651
6	1.92115	13.43828	13.39601
1	1.46662	14.26903	12.87435
6	1.1359	12.60032	14.16737
1	0.08028	12.78215	14.26847
6	1.75619	11.54662	14.83918
6	-0.44709	10.66722	15.43165
1	-0.64544	10.64883	14.36339
1	-0.9535	11.52678	15.874
1	-0.845	9.7568	15.8682
6	1.47918	10.15029	16.8444
6	0.67244	10.2095	17.98498
1	-0.28391	10.70496	17.94449
6	1.12181	9.6558	19.16846
1	0.50457	9.70041	20.05476
6	2.38014	9.06348	19.20341
1	2.77928	8.62231	20.10418
6	3.12006	9.04627	18.04168
1	4.09349	8.58357	18.02706

Table S4. Cartesian Coordinates of the DFT-UKS calculated ground state geometry of *mer*-[V(ddpd)₂]²⁺.

Atomic number	x	y	z
23	-0.456657	4.889414	1.501596
7	0.002849	4.363064	3.520798
7	0.579771	2.20372	2.770289
7	1.205219	3.662114	1.007041
7	1.774298	5.179912	-0.727343
7	-0.580795	5.215553	-0.614454
7	-1.914519	3.3183	1.393928
7	-3.03067	4.29052	3.231535
7	-2.106649	6.111055	2.017284
7	-1.128961	7.889116	0.781278
7	0.677804	6.700074	1.711039
6	-0.18162	5.248191	4.518065
1	-0.419586	6.25608	4.212581
6	-0.108396	4.903625	5.849081
1	-0.280011	5.647244	6.612408
6	0.181414	3.579764	6.167635
1	0.250665	3.262032	7.198754
6	0.407998	2.669189	5.15302
1	0.67458	1.651648	5.386263
6	0.332973	3.09674	3.822299
6	0.389044	0.778073	3.046087
1	-0.531625	0.656157	3.610789
1	1.211872	0.332657	3.607898
1	0.282329	0.257062	2.099107
6	1.442841	2.531668	1.707084
6	2.500786	1.685662	1.390125
1	2.682826	0.795538	1.968956
6	3.341279	2.032926	0.345779
1	4.173144	1.394093	0.084095
6	3.113965	3.200514	-0.362986
1	3.745404	3.473547	-1.192414
6	2.026788	3.993653	-0.011811
6	2.938799	5.878704	-1.279513
1	2.671387	6.920044	-1.437124
1	3.292525	5.456417	-2.221666
1	3.740441	5.835385	-0.548526
6	0.536529	5.429059	-1.33003
6	0.471854	5.912003	-2.642369
1	1.373187	6.085345	-3.20664
6	-0.763325	6.135065	-3.219733
1	-0.821574	6.498724	-4.236047
6	-1.91929	5.873206	-2.489019
1	-2.902283	6.031024	-2.906123
6	-1.777402	5.413811	-1.198759
1	-2.638793	5.214646	-0.578779
6	-1.771112	2.308952	0.514674
1	-1.029992	2.461715	-0.256462
6	-2.479641	1.131217	0.598473

1	-2.310135	0.343619	-0.12029
6	-3.391145	0.9904	1.642219
1	-3.960784	0.079147	1.759916
6	-3.580004	2.034638	2.526336
1	-4.307656	1.951042	3.31643
6	-2.839566	3.212283	2.363309
6	-3.63378	4.007764	4.538652
1	-3.163692	3.118763	4.950739
1	-4.713282	3.851889	4.49463
1	-3.424752	4.844854	5.197094
6	-3.104771	5.622353	2.783754
6	-4.187905	6.409405	3.162476
1	-4.988368	5.99186	3.750045
6	-4.230034	7.729316	2.749197
1	-5.058316	8.36156	3.036328
6	-3.205925	8.236539	1.967697
1	-3.2115	9.267466	1.654612
6	-2.157084	7.397038	1.609928
6	-1.520622	8.890705	-0.213993
1	-0.802523	8.868329	-1.02998
1	-1.565623	9.902435	0.193293
1	-2.495357	8.620758	-0.608911
6	0.220145	7.824241	1.134393
6	1.083431	8.894836	0.866941
1	0.718821	9.787759	0.387671
6	1.957327	6.647974	2.122946
6	2.406925	8.808105	1.254718
6	2.857105	7.668741	1.917629
1	2.257271	5.728128	2.602878
1	3.877891	7.569736	2.254018
1	3.07735	9.6324	1.054878

Table S5. Active orbitals of the CASSCF(7,12)-SC-NEVPT2 calculation on *cis-fac*-[V(ddpd)₂]²⁺, depicted at a contour value of 0.05 a.u. (hydrogen atoms omitted for clarity).

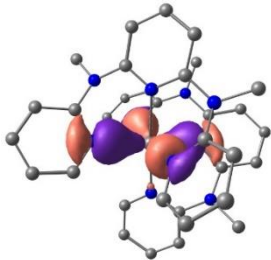
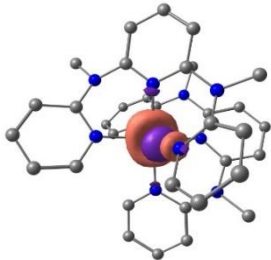
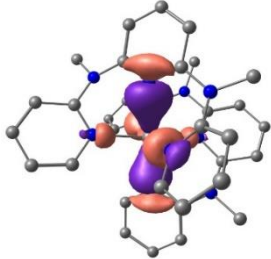
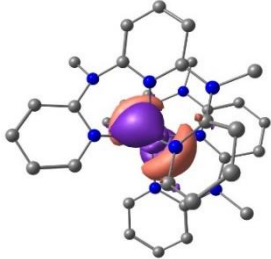
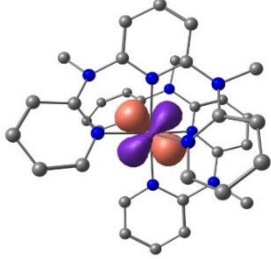
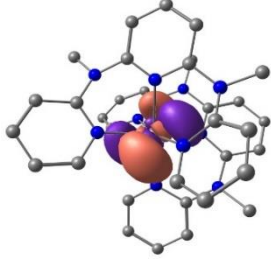
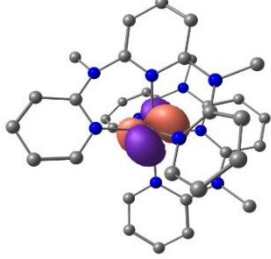
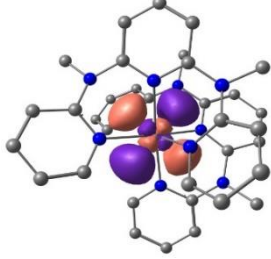
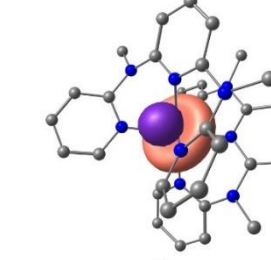
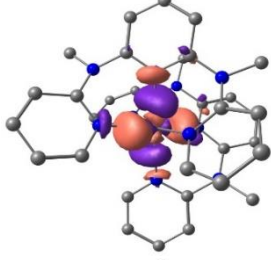
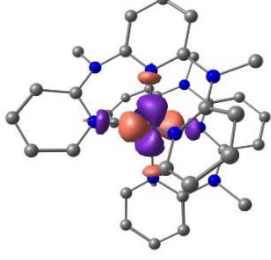
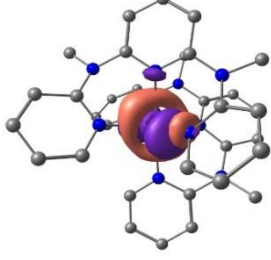
#	<i>E</i> / Ha	orbital	#	<i>E</i> / Ha	orbital
161	-0.53303		167	0.26023	
162	-0.53288		168	0.72996	
163	0.05837		169	0.87278	
164	0.05975		170	0.91617	
165	0.08981		171	1.33304	
166	0.25441		172	1.44659	

Table S6. Active orbitals of the CASSCF(7,12)-SC-NEVPT2 calculation on *mer*-[V(ddpd)₂]²⁺, depicted at a contour value of 0.05 a.u. (hydrogen atoms omitted for clarity).

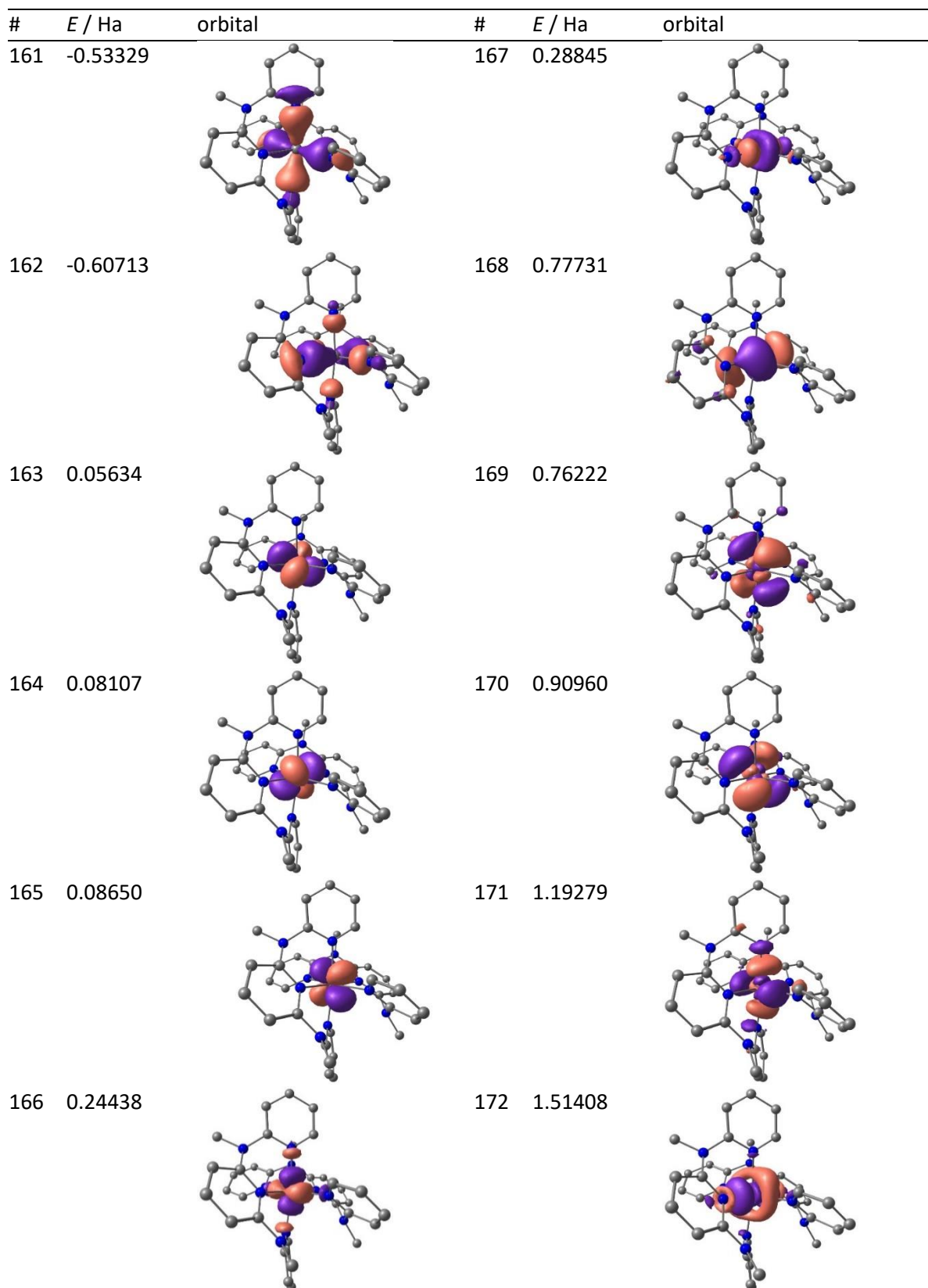


Figure S5: Energy diagram of the electronic states of *cis-fac*-[V(ddpd)₂]²⁺ constructed from CASSCF(7,12)-SC-NEVPT2 energies with spin densities in orange (0.01 a.u. isosurface value, hydrogen atoms omitted for clarity, quartet states in blue, doublet states in red; a coordinate system referring to the displayed structures and d orbital labels are shown in the bottom right corner).

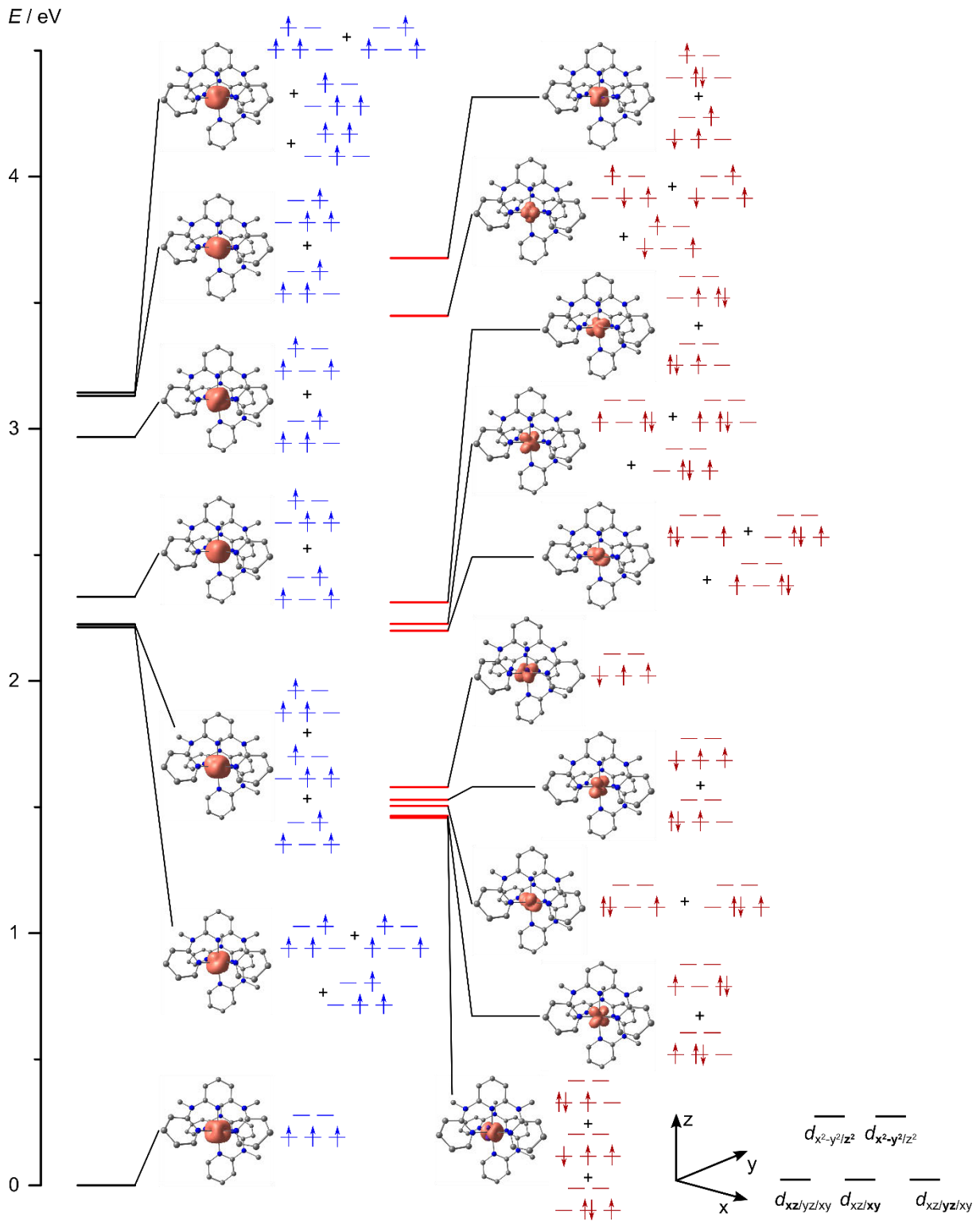


Figure S6: Energy diagram of the electronic states of $mer-[V(ddpd)_2]^{2+}$ constructed from CASSCF(7,12)-SC-NEVPT2 energies with spin densities in orange (0.01 a.u. isosurface value, hydrogen atoms omitted for clarity, quartet states in blue, doublet states in red; a coordinate system referring to the displayed structures and d orbital labels are shown in the bottom right corner).

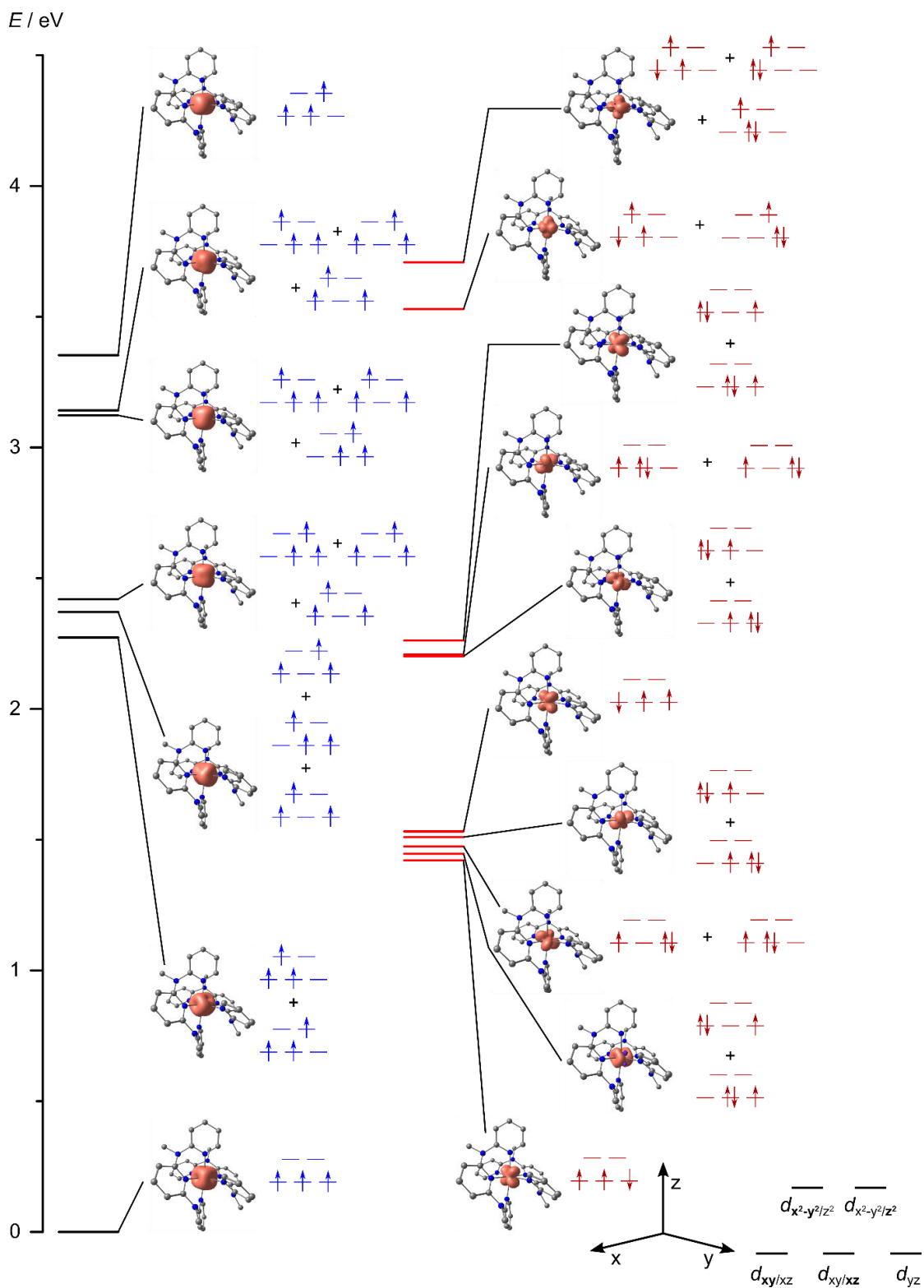


Figure S7. Proposed energy level diagram of *cis-fac*-[V(ddpd)₂]²⁺ with the pure metal centred states (black and red) obtained from the CASSCF-NEVPT2 calculation, the ⁴MLCT states (blue) estimated from the experimental absorption spectrum and the TD-DFT calculation and the ²MLCT states (pale blue) set to the ⁴MLCT energies. The mixing between ²E and ²MLCT states (purple) is set to an arbitrary value. (i) Spin density of the ⁴A₂ ground state from the CASSCF-NEVPT2 calculation. (ii) Difference electron density of the lowest ⁴MLCT state obtained from the TD-DFT calculation (isosurface value of 0.003 a.u.; purple = electron depletion; orange = electron density gain). (iii) Spin density of the lowest ⁴T₂ derived state from the CASSCF-NEVPT2 calculation. (iv) Spin density of the lowest ²E derived state from the CASSCF-NEVPT2 calculation. (v) Spin density of the optimized lowest doublet state (²MC/²MLCT) from a DFT geometry optimization calculation with the ligand contributions highlighted by arrows. All spin densities at an isosurface value of 0.006 a.u., except (iv) at an isosurface value of 0.0035 a.u.

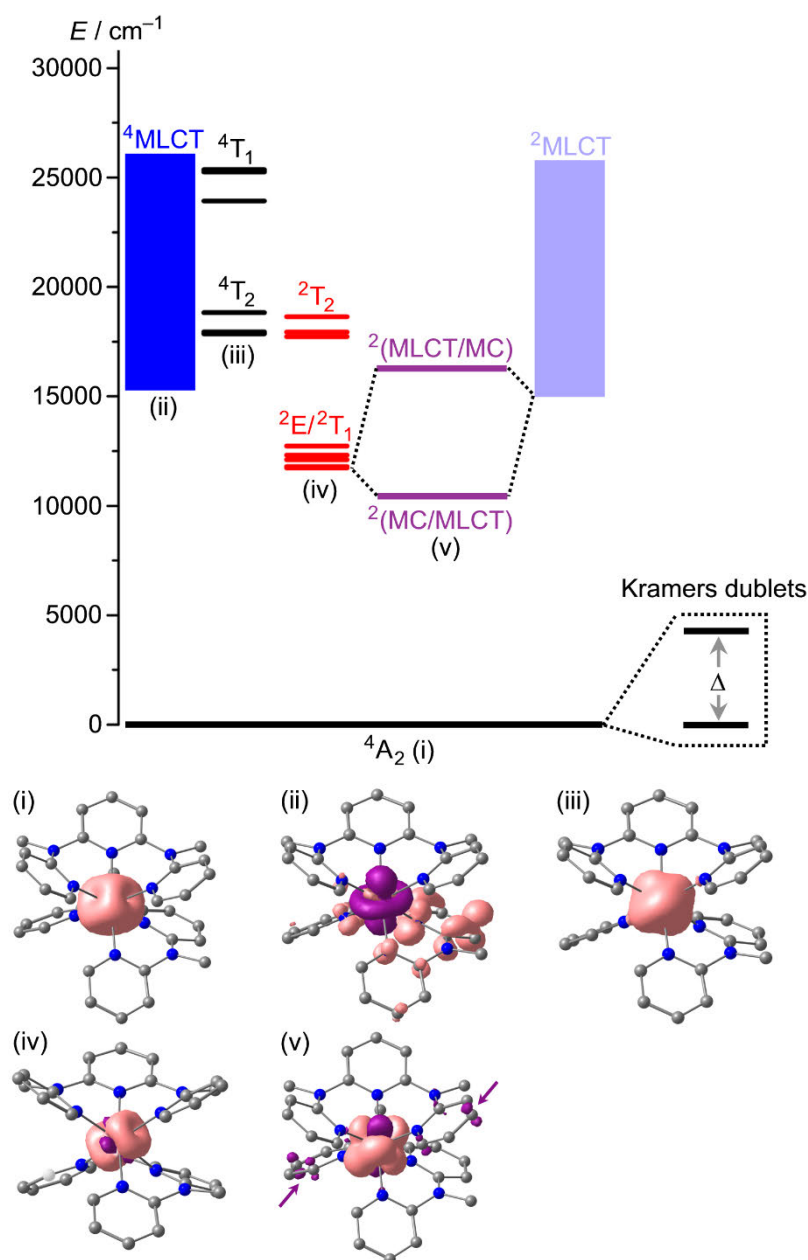


Figure S8. Emission spectra of a) *cis-fac*-[V(ddpd)₂][BPh₄]₂ and b) *mer*-[V(ddpd)₂][BPh₄]₂ in acetonitrile at room temperature during irradiation with a xenon lamp at 300±5 nm excitation wavelength for 300 min. The insets show the emission intensity at the maximum wavelength (395 nm).

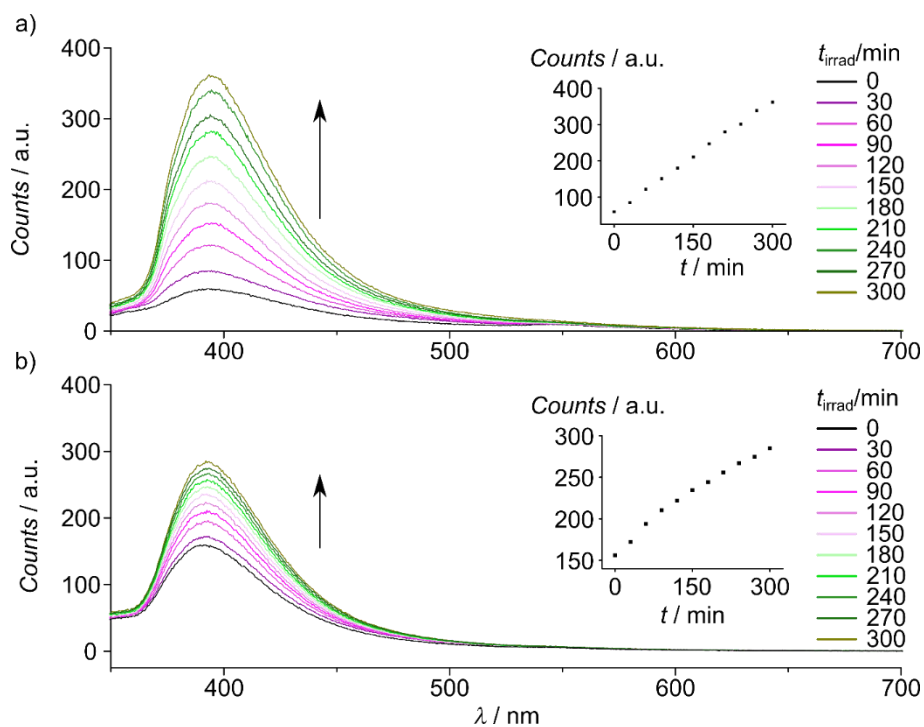


Figure S9. Excitation and emission spectra (solid and dotted lines) of *cis-fac*-[V(ddpd)₂][BPh₄]₂ (red) and *mer*-[V(ddpd)₂][BPh₄]₂ (blue) and excitation spectrum of ddpd (green) in acetonitrile at room temperature with 300 nm excitation.

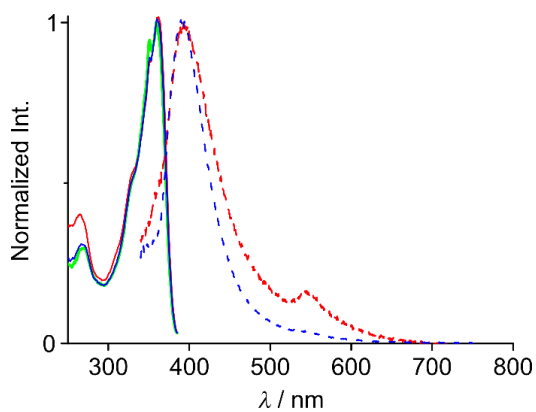


Figure S10. Absorption spectra of a) *cis-fac*-[V(ddpd)₂][BPh₄]₂ and b) *mer*-[V(ddpd)₂][BPh₄]₂ in acetonitrile at room temperature before and after irradiating for 300 min with a xenon lamp at 300±5 nm excitation wavelength.

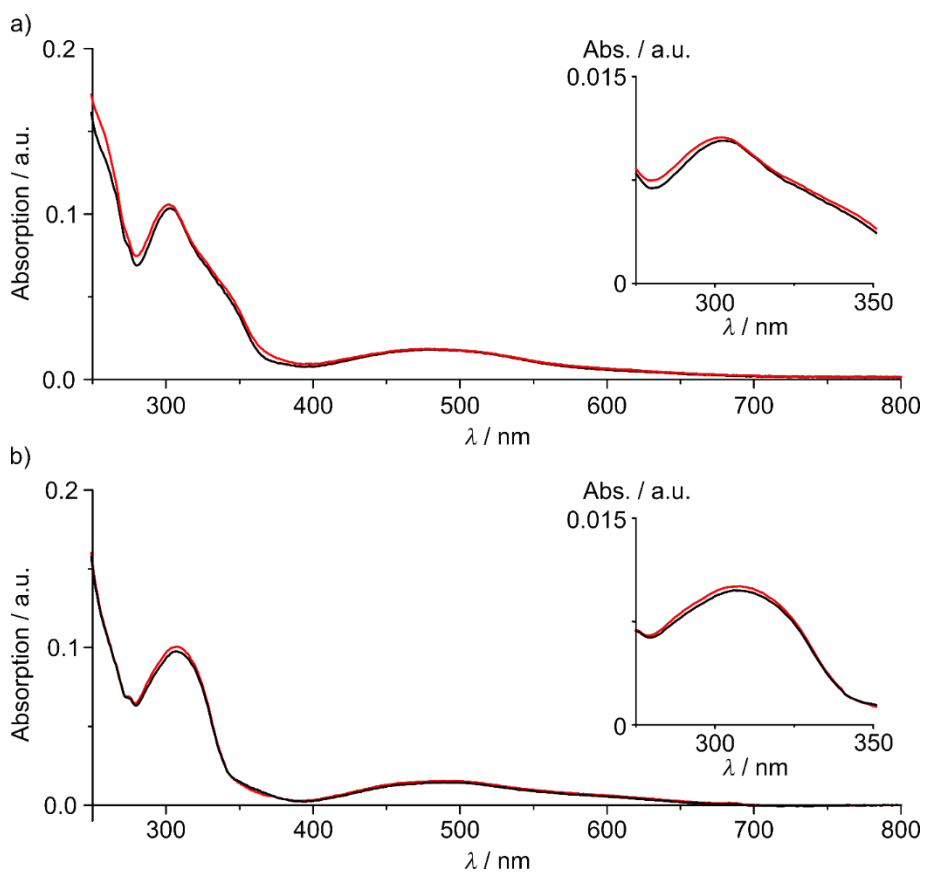


Table S7. TD-DFT calculated spin-allowed quartet-quartet transitions of *cis-fac*-[V(ddpd)₂]²⁺. The assignment was accomplished by evaluation of the transition difference densities with the TheoDRE software package (v2.4).^[22,23]

State	E / cm^{-1}	λ / nm	E / eV	$f_{\text{osc.}}$	Assignment
1	16119	620	1.998	1.00E-2	⁴ MLCT
2	16215	617	2.010	1.15E-2	⁴ MLCT
3	17743	564	2.200	2.73E-2	⁴ MLCT
4	18228	549	2.260	8.47E-4	⁴ MLCT
5	18440	542	2.286	6.16E-3	⁴ MLCT
6	18636	537	2.311	1.21E-2	⁴ MLCT
7	18737	534	2.323	5.27E-2	⁴ MLCT
8	19157	522	2.375	5.80E-3	⁴ MLCT
9	19425	515	2.408	2.52E-3	⁴ MLCT
10	19489	513	2.416	7.54E-4	⁴ MLCT
11	19566	511	2.426	1.94E-4	⁴ MLCT
12	19869	503	2.463	3.21E-3	⁴ MLCT
13	20479	488	2.539	3.16E-3	⁴ MLCT
14	20678	484	2.564	1.36E-2	⁴ MLCT
15	20725	483	2.570	4.81E-3	⁴ MLCT
16	21000	476	2.604	7.71E-3	⁴ MLCT
17	21259	470	2.636	6.54E-3	⁴ MLCT
18	21863	457	2.711	1.90E-3	⁴ MLCT
19	21901	457	2.715	1.38E-4	⁴ MLCT
20	21954	456	2.722	3.69E-3	⁴ MLCT
21	22978	435	2.849	1.96E-3	⁴ MLCT
22	23277	430	2.886	4.75E-3	⁴ MLCT
23	24284	412	3.011	8.81E-3	⁴ MLCT
24	24426	409	3.028	2.25E-4	⁴ MLCT
25	25025	400	3.103	4.46E-4	⁴ MLCT
26	25259	396	3.132	9.68E-4	⁴ MLCT
27	25329	395	3.140	5.12E-3	⁴ MLCT
28	25439	393	3.154	3.49E-4	⁴ MLCT
29	25853	387	3.205	3.48E-5	⁴ MLCT
30	26420	379	3.276	2.14E-3	⁴ LC
31	26610	376	3.299	8.98E-4	⁴ LC
32	26631	376	3.302	8.90E-4	⁴ MLCT
33	27027	370	3.351	3.61E-3	⁴ MLCT
34	27579	363	3.419	6.41E-5	⁴ LC
35	27724	361	3.437	4.35E-5	⁴ LC
36	27840	359	3.452	4.17E-3	⁴ MLCT
37	27886	359	3.457	2.55E-4	⁴ MLCT
38	27925	358	3.462	9.53E-5	⁴ MLCT
39	28305	353	3.509	1.90E-4	⁴ MLCT
40	28361	353	3.516	8.42E-4	⁴ LC
41	28466	351	3.529	8.85E-4	⁴ LC
42	28744	348	3.564	3.62E-4	⁴ MLCT
43	28802	347	3.571	2.37E-4	⁴ MLCT
44	28843	347	3.576	1.96E-3	⁴ MLCT

Appendix

45	30157	332	3.739	3.35E-3	⁴ LC
46	30257	331	3.751	1.29E-3	⁴ LC
47	30266	330	3.753	1.07E-4	⁴ MLCT
48	30395	329	3.769	2.36E-4	⁴ MLCT
49	30479	328	3.779	8.11E-3	⁴ LC
50	30684	326	3.804	1.52E-2	⁴ LC
51	30694	326	3.806	3.54E-4	⁴ MLCT
52	30722	326	3.809	1.55E-3	⁴ LC
53	30902	324	3.831	5.82E-2	⁴ LC
54	31368	319	3.889	7.06E-3	⁴ MLCT
55	31447	318	3.899	6.30E-3	⁴ MLCT
56	31626	316	3.921	1.32E-3	⁴ LC
57	31756	315	3.937	6.46E-2	⁴ LC
58	31776	315	3.940	1.99E-3	⁴ LC
59	31786	315	3.941	4.50E-2	⁴ LLCT
60	31837	314	3.947	6.20E-4	⁴ LLCT
61	32144	311	3.985	5.00E-2	⁴ LLCT
62	32227	310	3.996	1.42E-2	⁴ LC
63	32279	310	4.002	3.99E-2	⁴ LLCT
64	32446	308	4.023	4.09E-2	⁴ LC
65	32595	307	4.041	2.16E-2	⁴ LC
66	32723	306	4.057	5.44E-3	⁴ LLCT
67	32744	305	4.060	2.25E-2	⁴ LC
68	33212	301	4.118	4.52E-3	⁴ LC
69	33223	301	4.119	5.40E-2	⁴ LC
70	33333	300	4.133	4.71E-2	⁴ LC

Table S8. TD-DFT calculated spin-allowed quartet-quartet transitions of *mer*-[V(ddpd)₂]²⁺. The assignment was accomplished by evaluation of the transition difference densities with the TheoDRE software package (v2.4).^[22,23]

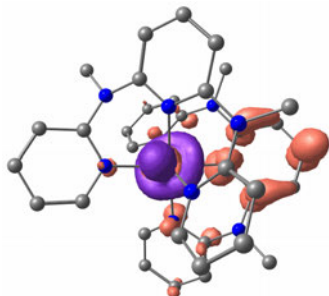
State	E / cm^{-1}	λ / nm	E / eV	$f_{\text{osc.}}$	Assignment
1	16083	622	1.994	7.41E-3	⁴ MLCT
2	16591	603	2.057	1.16E-2	⁴ MLCT
3	16986	589	2.106	2.29E-2	⁴ MLCT
4	17478	572	2.167	1.13E-2	⁴ MLCT
5	17769	563	2.203	1.02E-2	⁴ MLCT
6	18131	552	2.248	4.28E-4	⁴ MLCT
7	18252	548	2.263	7.30E-4	⁴ MLCT
8	18527	540	2.297	9.64E-3	⁴ MLCT
9	18648	536	2.312	6.66E-3	⁴ MLCT
10	19454	514	2.412	3.76E-2	⁴ MLCT
11	19632	509	2.434	1.22E-2	⁴ MLCT
12	19648	509	2.436	7.13E-4	⁴ MLCT
13	19817	505	2.457	5.90E-3	⁴ MLCT
14	19841	504	2.460	3.94E-3	⁴ MLCT
15	20414	490	2.531	4.40E-2	⁴ MLCT
16	21003	476	2.604	9.03E-4	⁴ MLCT
17	21019	476	2.606	9.49E-3	⁴ MLCT
18	21325	469	2.644	3.02E-4	⁴ MLCT
19	22205	450	2.753	1.22E-3	⁴ MC
20	22584	443	2.800	8.78E-4	⁴ MC
21	22745	440	2.820	3.68E-3	⁴ MLCT
22	22818	438	2.829	2.29E-3	⁴ MLCT
23	23592	424	2.925	8.36E-5	⁴ MLCT
24	23995	417	2.975	4.38E-4	⁴ MLCT
25	24511	408	3.039	1.14E-3	⁴ MLCT
26	24810	403	3.076	2.96E-3	⁴ MLCT
27	25358	394	3.144	1.03E-2	⁴ MLCT
28	25632	390	3.178	1.48E-3	⁴ MLCT
29	25947	385	3.217	9.93E-4	⁴ MLCT
30	26092	383	3.235	4.04E-3	⁴ MLCT
31	26100	383	3.236	8.03E-4	⁴ MLCT
32	26439	378	3.278	2.85E-5	⁴ MLCT
33	26850	372	3.329	2.17E-5	⁴ MLCT
34	27020	370	3.350	9.21E-5	⁴ MLCT
35	27108	369	3.361	8.14E-5	⁴ MLCT
36	27641	362	3.427	2.20E-4	⁴ MLCT
37	27810	360	3.448	1.07E-2	⁴ LC
38	27818	359	3.449	4.52E-5	⁴ MC
39	27915	358	3.461	4.14E-4	⁴ MLCT
40	27988	357	3.470	2.38E-3	⁴ LC
41	28044	357	3.477	2.96E-3	⁴ LC
42	28165	355	3.492	1.72E-3	⁴ LC
43	28584	350	3.544	2.53E-4	⁴ MLCT
44	28722	348	3.561	4.21E-4	⁴ LC

Appendix

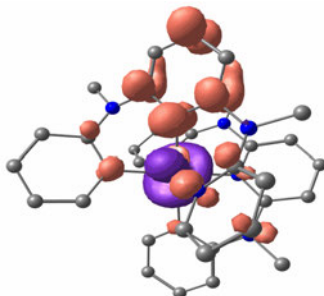
45	28738	348	3.563	2.51E-4	⁴ MLCT
46	28802	347	3.571	1.78E-3	⁴ MLCT
47	28891	346	3.582	4.07E-4	⁴ LC
48	30238	331	3.749	2.70E-4	⁴ MLCT
49	30367	329	3.765	3.55E-3	⁴ LC
50	30665	326	3.802	4.14E-4	⁴ LC
51	31093	322	3.855	4.82E-5	⁴ LC
52	31569	317	3.914	1.94E-2	⁴ LC
53	31843	314	3.948	2.68E-2	⁴ LC
54	31924	313	3.958	5.41E-2	⁴ LC
55	32287	310	4.003	4.43E-4	⁴ LC
56	32633	306	4.046	6.00E-4	⁴ LC
57	32650	306	4.048	6.44E-2	⁴ LLCT
58	32746	305	4.060	1.29E-2	⁴ LC
59	32762	305	4.062	1.63E-1	⁴ LC
60	32779	305	4.064	1.39E-2	⁴ LC
61	32827	305	4.070	4.91E-3	⁴ LC
62	32964	303	4.087	1.65E-2	⁴ LLCT
63	33101	302	4.104	4.34E-3	⁴ LC
64	33133	302	4.108	8.96E-3	⁴ LLCT
65	33351	300	4.135	2.04E-2	⁴ LLCT
66	33408	299	4.142	3.71E-3	⁴ LC
67	33521	298	4.156	2.81E-3	⁴ LC
68	33577	298	4.163	1.67E-2	⁴ LLCT
69	33593	298	4.165	1.79E-2	⁴ LLCT
70	33593	298	4.165	3.72E-2	⁴ LLCT

Table S9: Difference electron densities of the 70 lowest-lying TD-DFT-UKS calculated quartet states of *cis-fac*-[V(ddpd)₂]²⁺ (isosurface value at 0.003 a.u.; purple = electron depletion; orange = electron density gain; hydrogen atoms omitted).

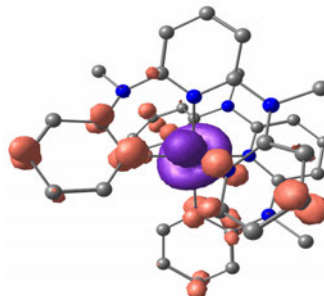
1 (620 nm)



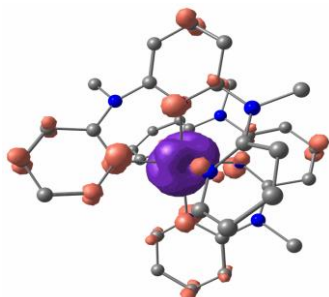
2 (617 nm)



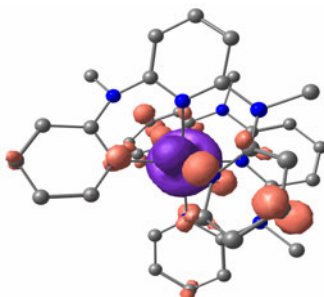
3 (564 nm)



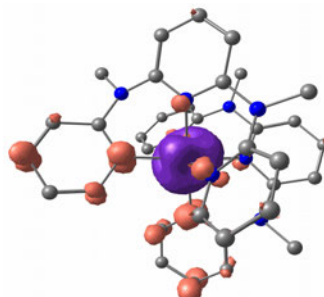
4 (549 nm)



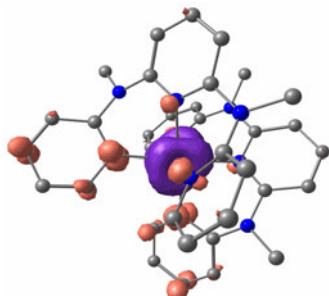
5 (542 nm)



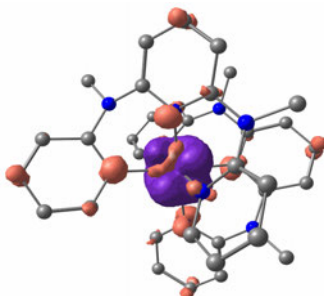
6 (537 nm)



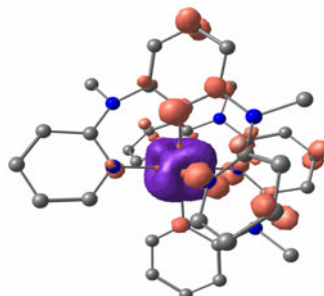
7 (534 nm)



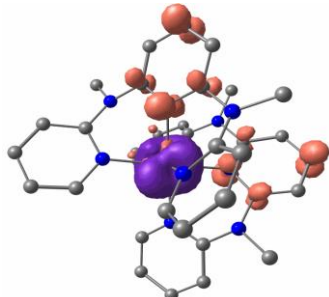
8 (522 nm)



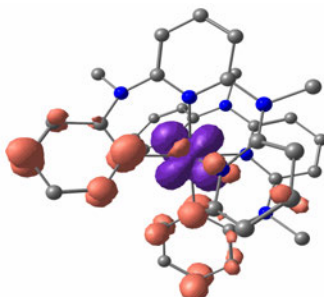
9 (515 nm)



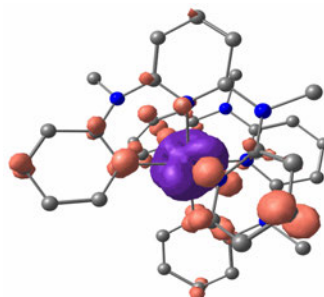
10 (513 nm)



11 (511 nm)



12 (503 nm)



13 (488 nm)

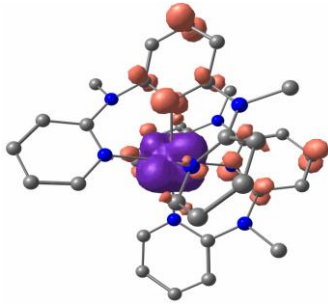


14 (484 nm)

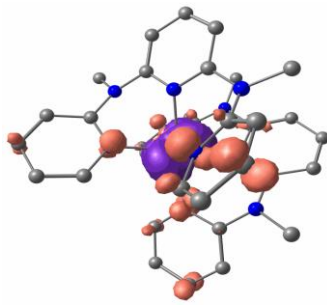


15 (483 nm)

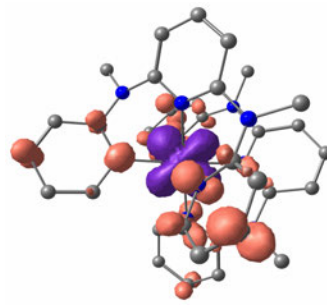




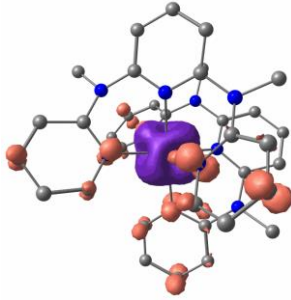
16 (476 nm)



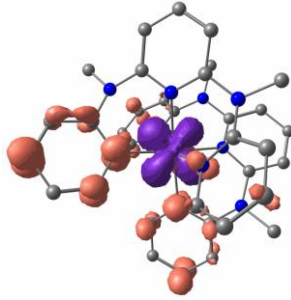
17 (470 nm)



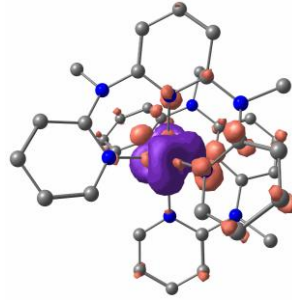
18 (457 nm)



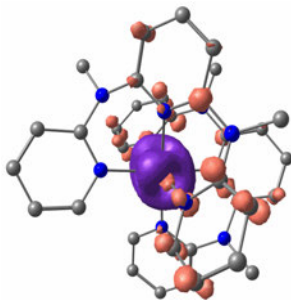
19 (457 nm)



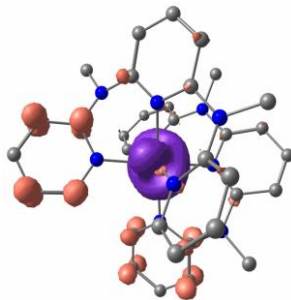
20 (456 nm)



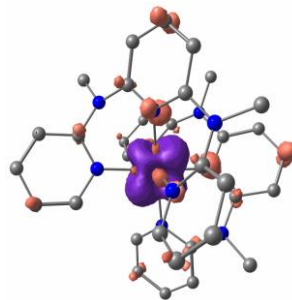
21 (435 nm)



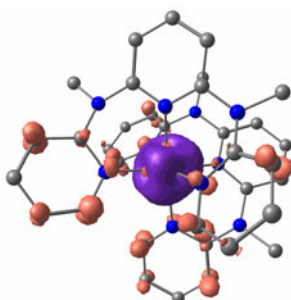
22 (430 nm)



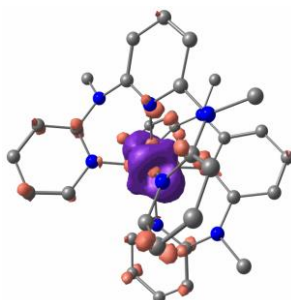
23 (412 nm)



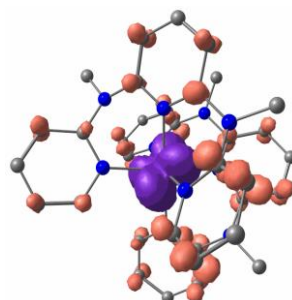
24 (409 nm)



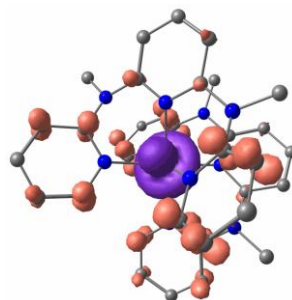
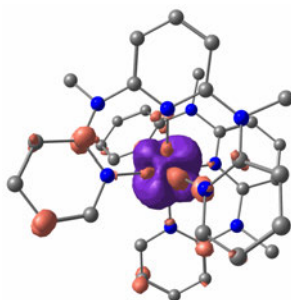
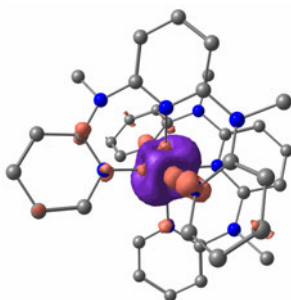
25 (400 nm)



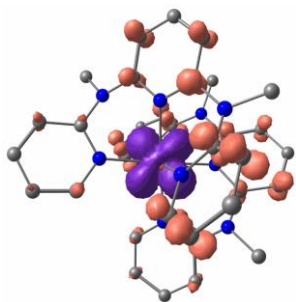
26 (396 nm)



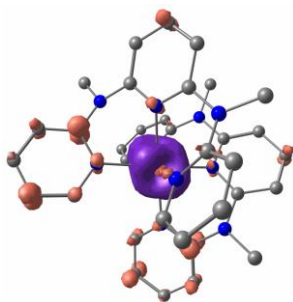
27 (395 nm)



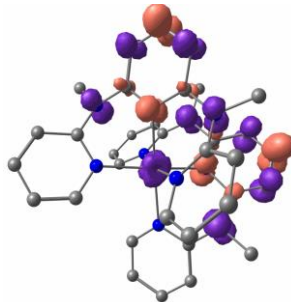
28 (393 nm)



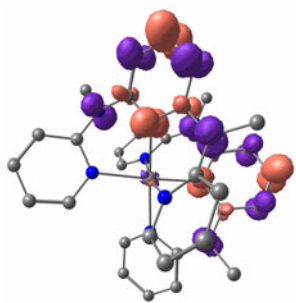
29 (387 nm)



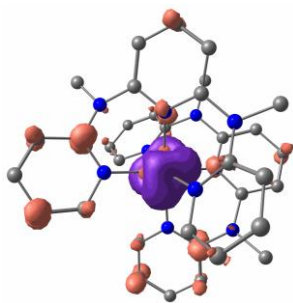
30 (379 nm)



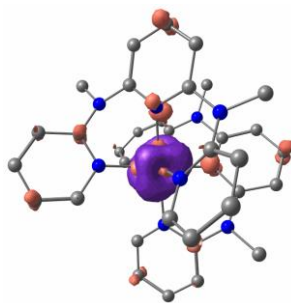
31 (376 nm)



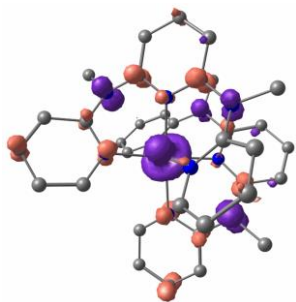
32 (376 nm)



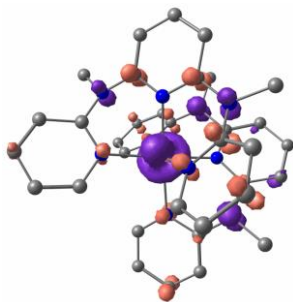
33 (370 nm)



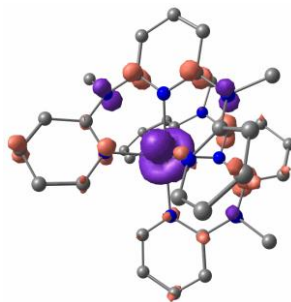
34 (363 nm)



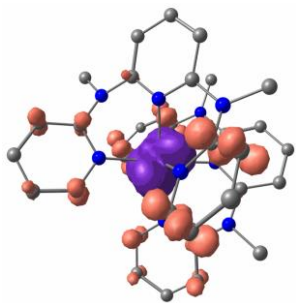
35 (361 nm)



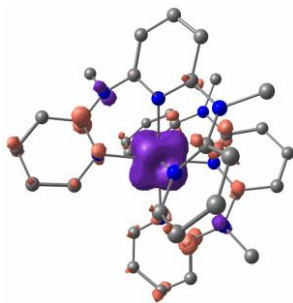
36 (359 nm)



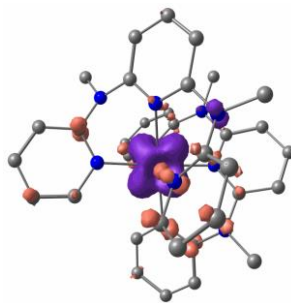
37 (359 nm)



38 (358 nm)



39 (353 nm)



40 (353 nm)



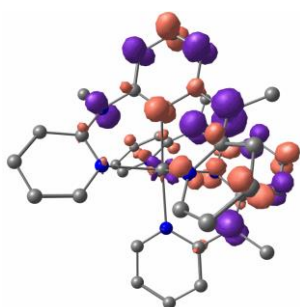
41 (351 nm)



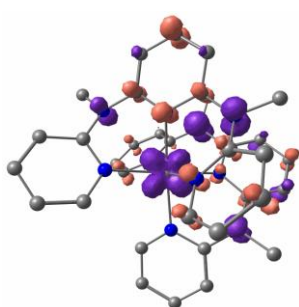
42 (348 nm)



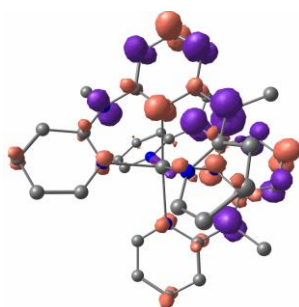
55 (318 nm)



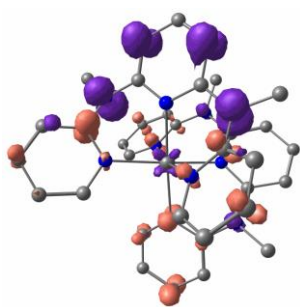
56 (316 nm)



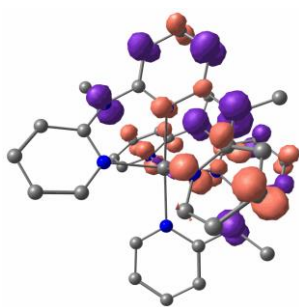
57 (315 nm)



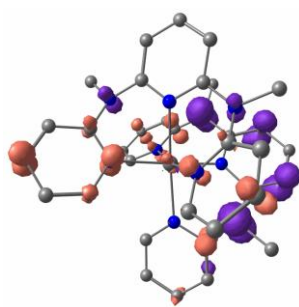
58 (315 nm)



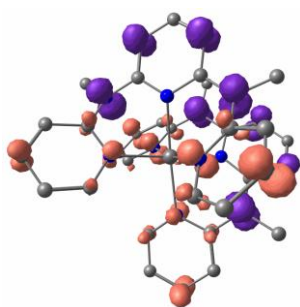
59 (315 nm)



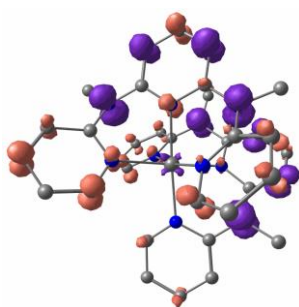
60 (314 nm)



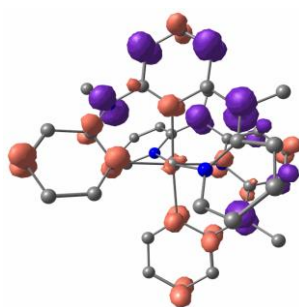
61 (311 nm)



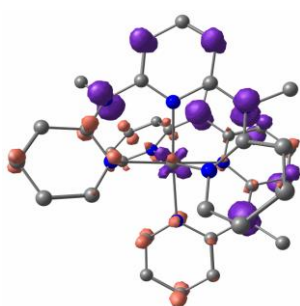
62 (310 nm)



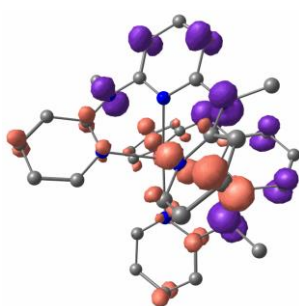
63 (310 nm)



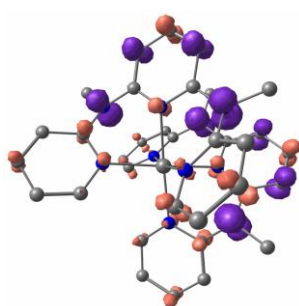
64 (308 nm)



65 (307 nm)



66 (306 nm)



67 (305 nm)

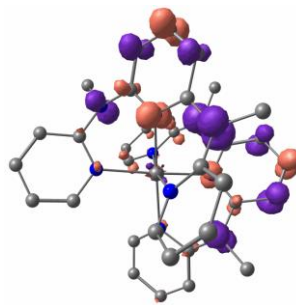
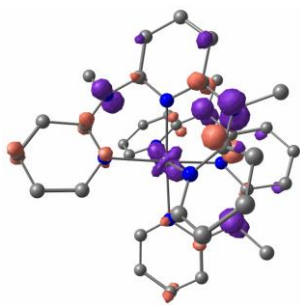
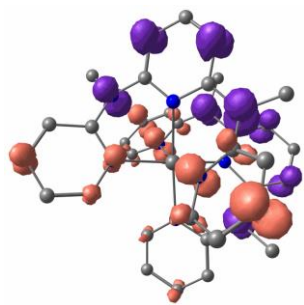


68 (301 nm)



69 (301 nm)





70 (300 nm)

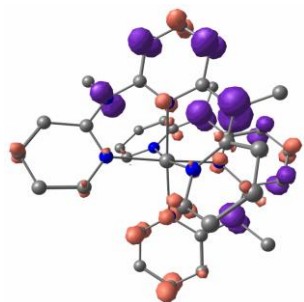
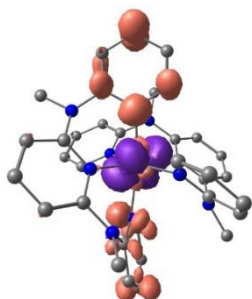
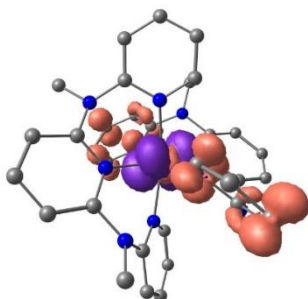


Table S10: Difference electron densities of the 70 lowest-lying TD-DFT-UKS calculated quartet states of *mer*-[V(ddpd)₂]²⁺ (isosurface value at 0.007 a.u.; purple = electron depletion; orange = electron density gain; hydrogen atoms omitted).

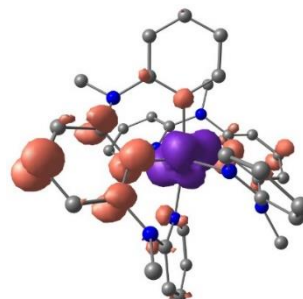
1 (622 nm)



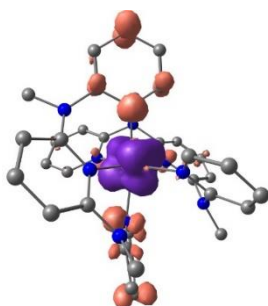
2 (603 nm)



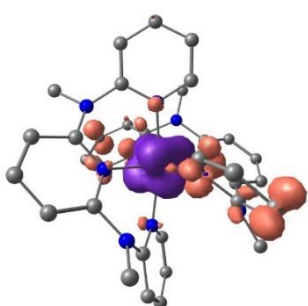
3 (589 nm)



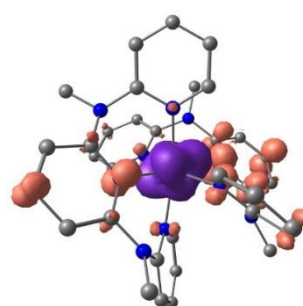
4 (572 nm)



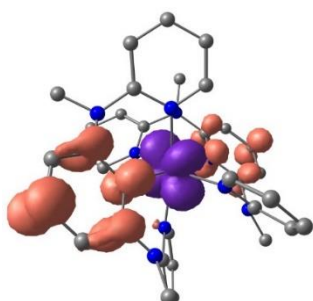
5 (563 nm)



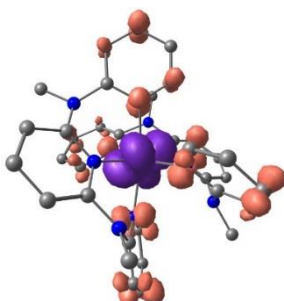
6 (552 nm)



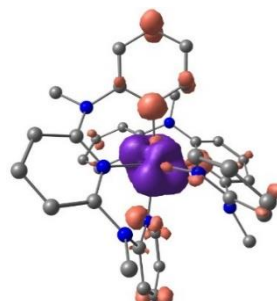
7 (548 nm)



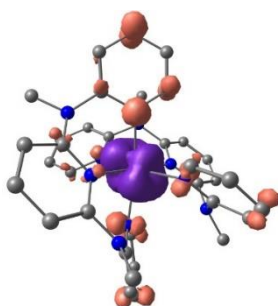
8 (540 nm)



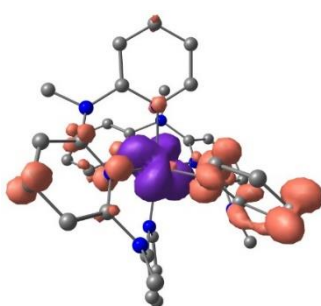
9 (536 nm)



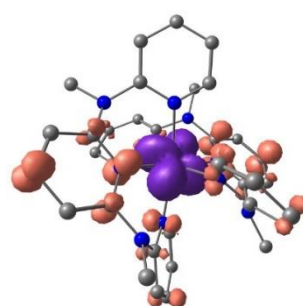
10 (514 nm)



11 (509 nm)



12 (509 nm)



13 (505 nm)

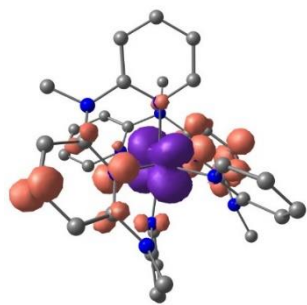


14 (504 nm)

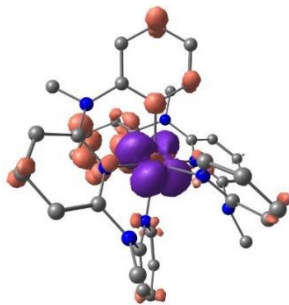


15 (490 nm)

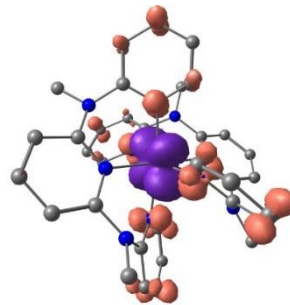




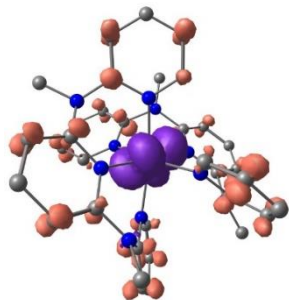
16 (476 nm)



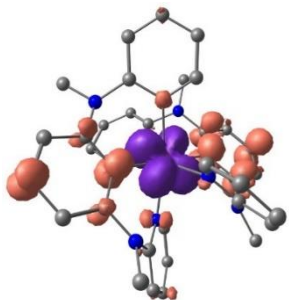
17 (476 nm)



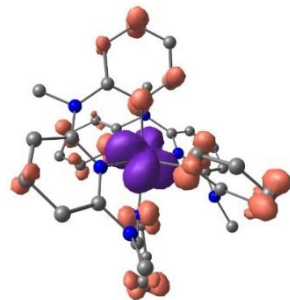
18 (469 nm)



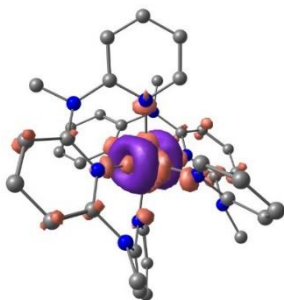
19 (450 nm)



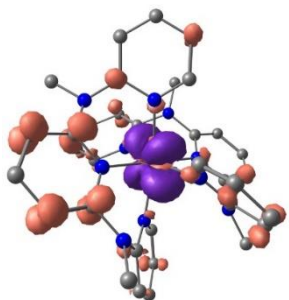
20 (443 nm)



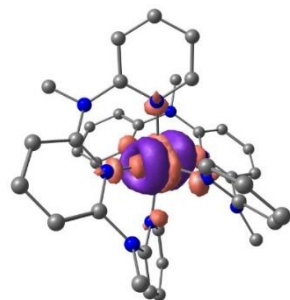
21 (440 nm)



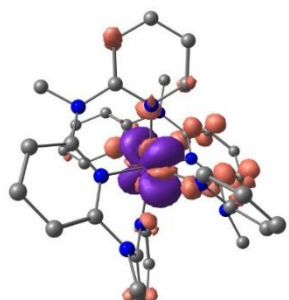
22 (438 nm)



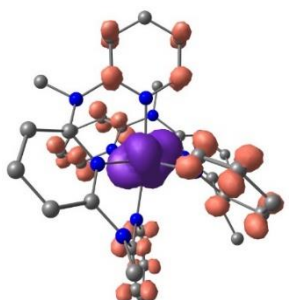
23 (424 nm)



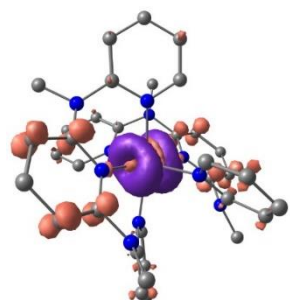
24 (417 nm)



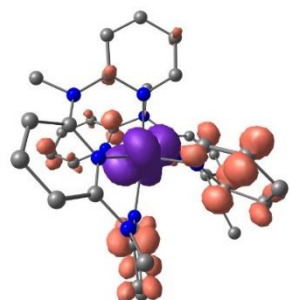
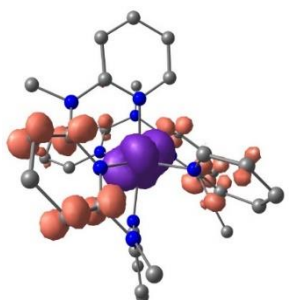
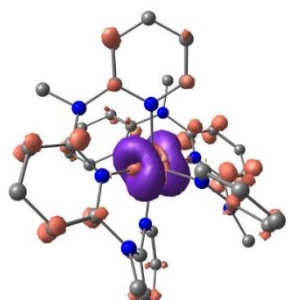
25 (408 nm)



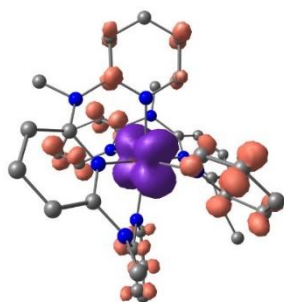
26 (403 nm)



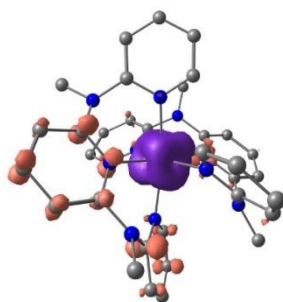
27 (394 nm)



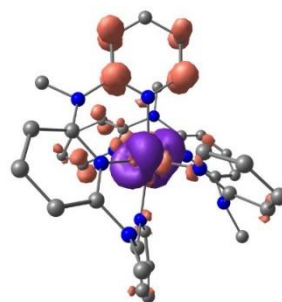
28 (390 nm)



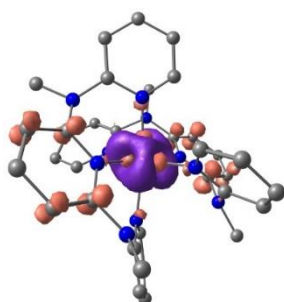
29 (385 nm)



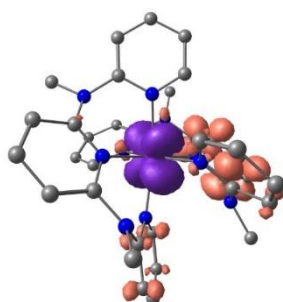
30 (383 nm)



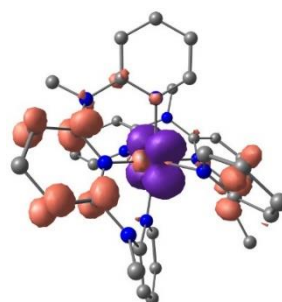
31 (383 nm)



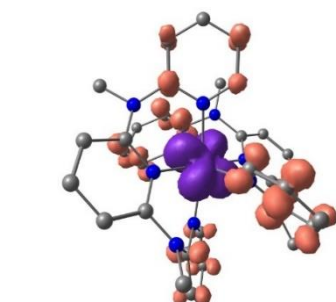
32 (378 nm)



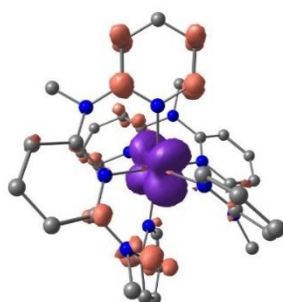
33 (372 nm)



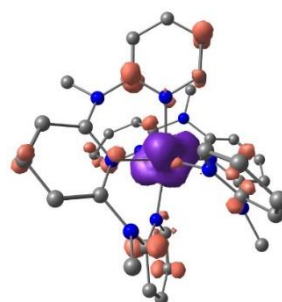
34 (370 nm)



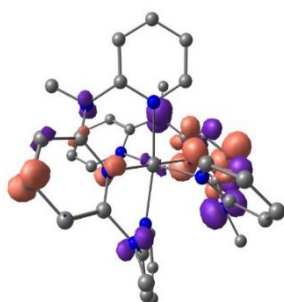
35 (369 nm)



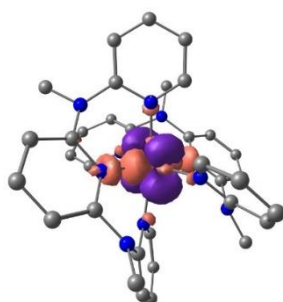
36 (362 nm)



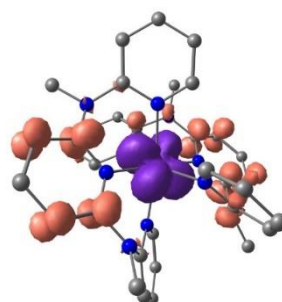
37 (360 nm)



38 (359 nm)



39 (358 nm)



40 (357 nm)

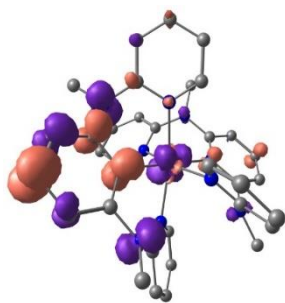


41 (357 nm)

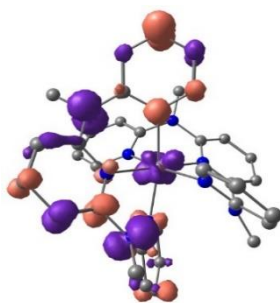


42 (355 nm)

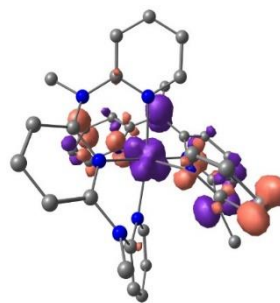




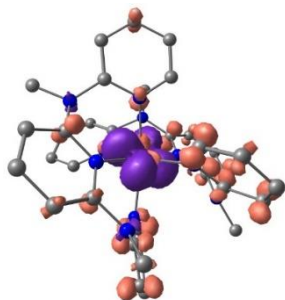
43 (350 nm)



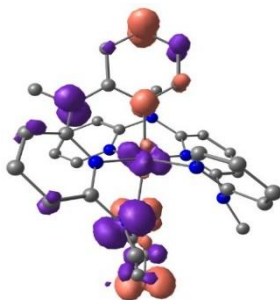
44 (348 nm)



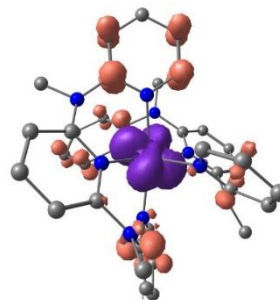
45 (348 nm)



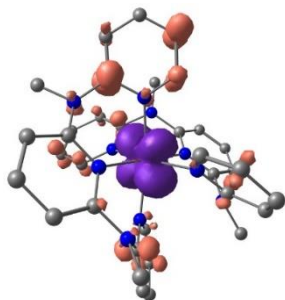
46 (347 nm)



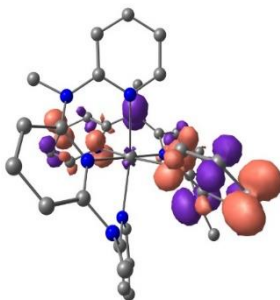
47 (346 nm)



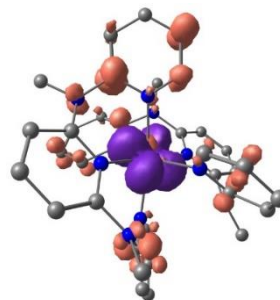
48 (331 nm)



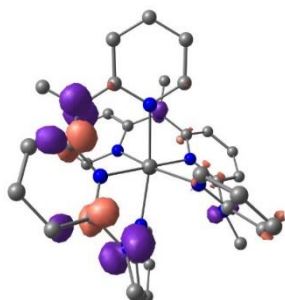
49 (329 nm)



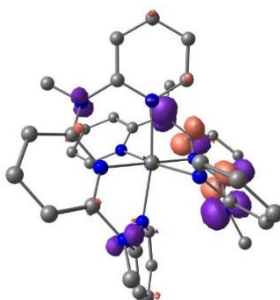
50 (326 nm)



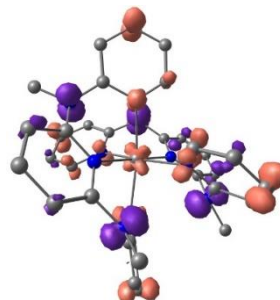
51 (322 nm)



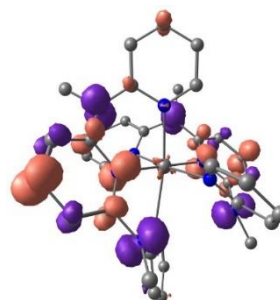
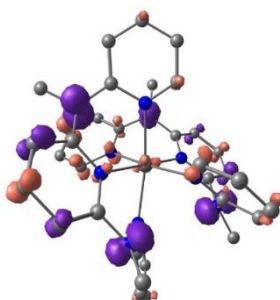
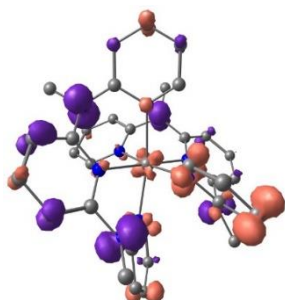
52 (317 nm)

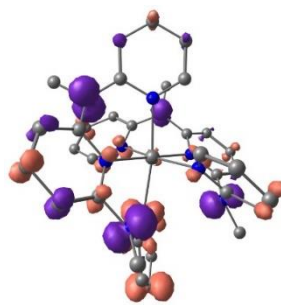
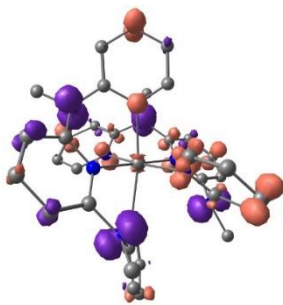
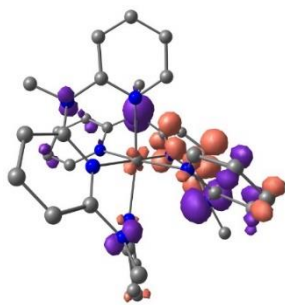


53 (314 nm)



54 (313 nm)





70 (298 nm)

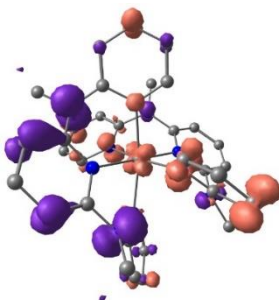


Figure S11. TD-DFT-UKS charge transfer (CT) numbers of the lowest-lying 70 quartet states of *cis-fac*-[V(ddpd)₂]²⁺ defined from 0 to 1.

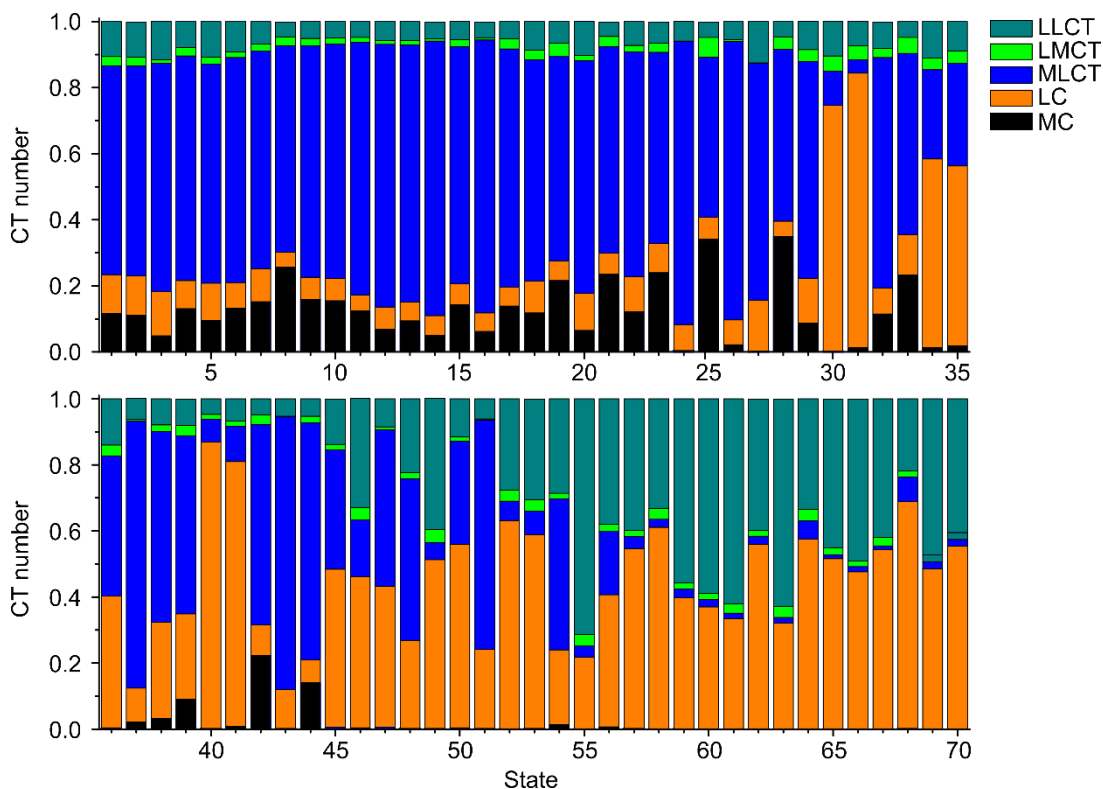


Figure S12. TD-DFT-UKS charge transfer (CT) numbers of the lowest-lying 70 quartet states of *mer*-[V(ddpd)₂]²⁺ defined from 0 to 1.

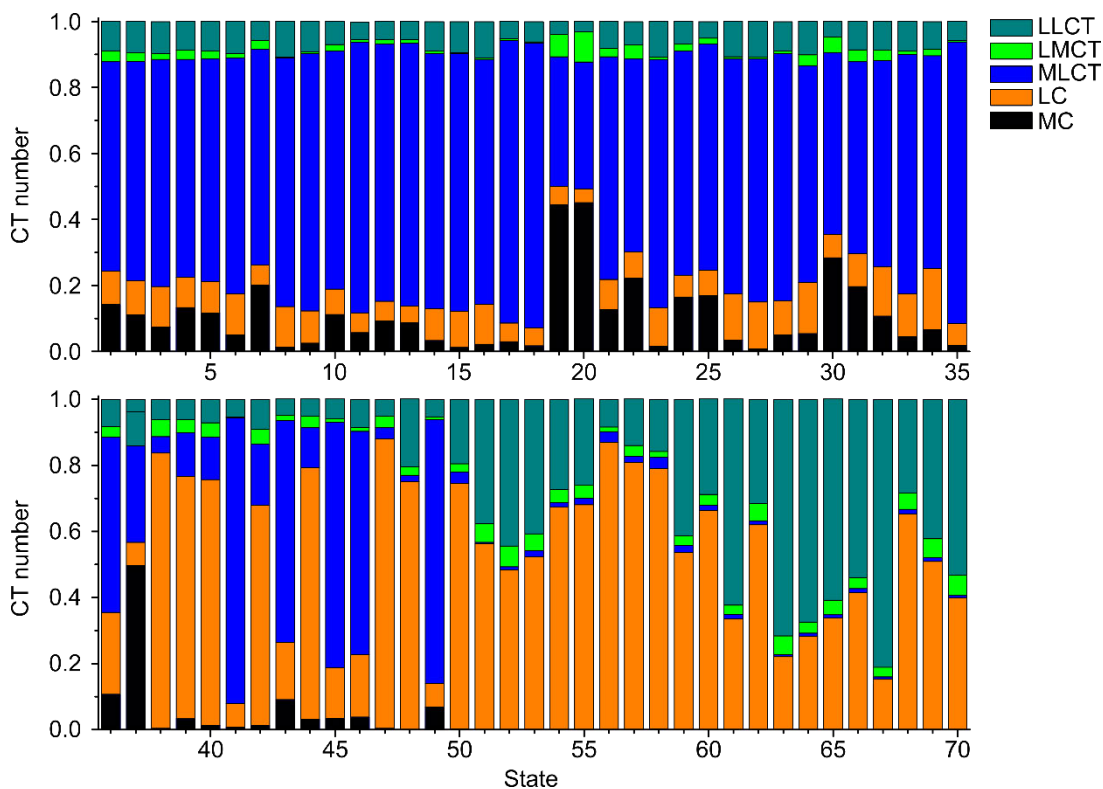


Figure S13. Cyclic voltammograms of a) *cis-fac*-[V(ddpd)₂][BPh₄]₂ and b) *mer*-[V(ddpd)₂][BPh₄]₂ with [nBu₄N][PF₆] as supporting electrolyte in CH₃CN; E vs. ferrocene.

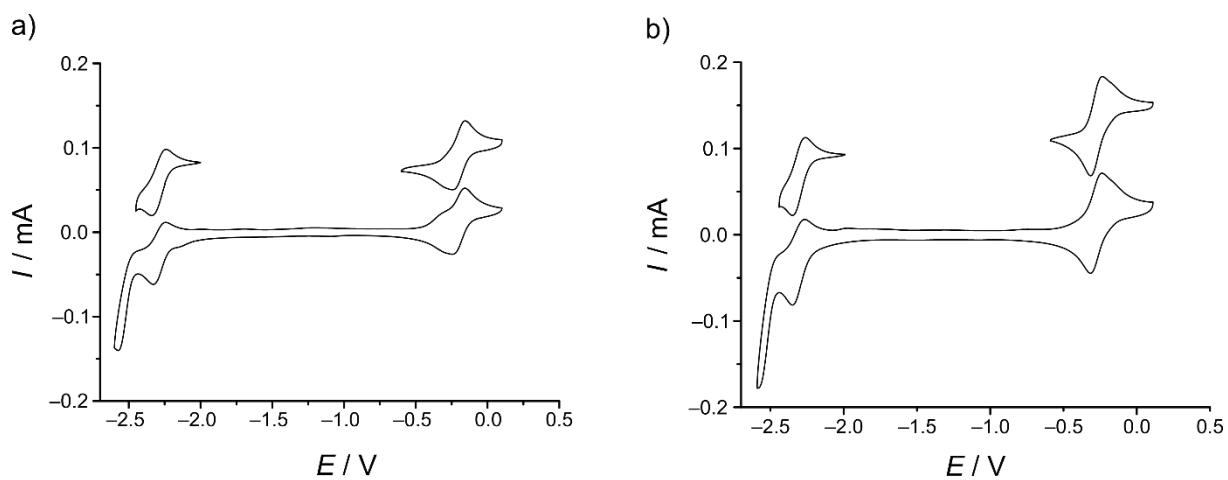


Figure S14. Absorption spectra of a solution of *cis-fac*-[V(ddpd)₂][BPh₄]₂ in acetonitrile ($c = 5 \times 10^{-5}$ M) (black) after oxidation with 3 eq. of Ag[BF₄] (red) and subsequent back-reduction with 3.1 eq. of CoCp₂ (blue). Absorption spectra of CoCp₂ (green) and [CoCp₂][PF₆] (pink) are given for comparison. Photographs depict the cuvettes before and after the oxidation.

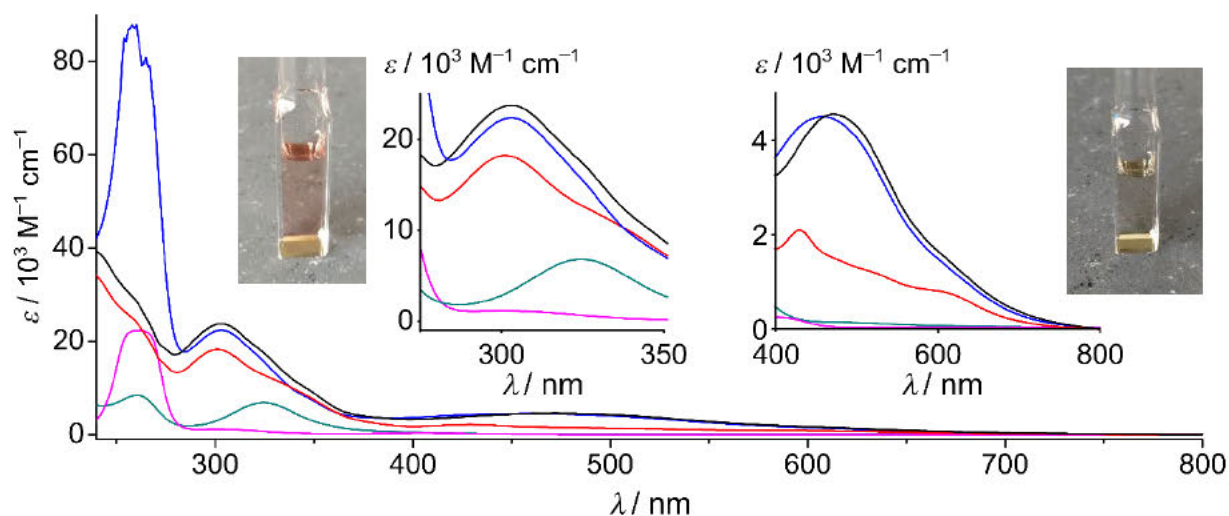


Figure S15. Absorption spectra of a solution of *mer*-[V(ddpd)₂][BPh₄]₂ in acetonitrile ($c = 5 \times 10^{-5}$ M) (black) after oxidation with 3 eq. of Ag[BF₄] (red) and subsequent back-reduction with 3.1 eq. of CoCp₂ (blue). Absorption spectra of CoCp₂ (green) and [CoCp₂][PF₆] (pink) are given for comparison. Photographs depict the cuvettes before and after the oxidation.

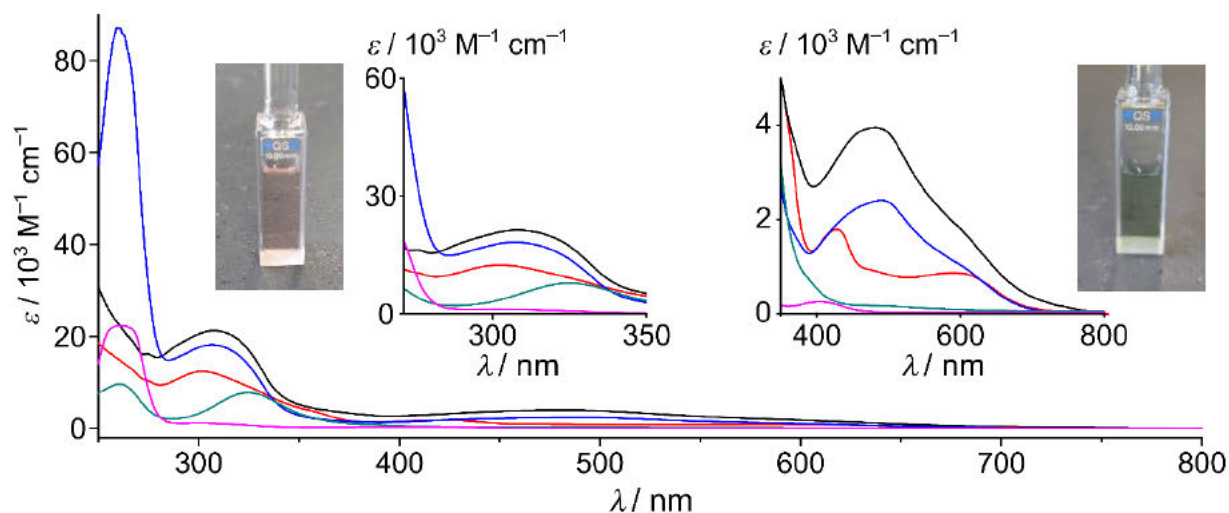


Figure S16. NIR emission spectra of *mer*-[V(ddpd)₂][BPh₄]₂ (black) and *cis-fac*-[V(ddpd)₂][BPh₄]₂ in butyronitrile glass at 78 K after oxidation with 3 eq. of Ag[BF₄] to the respective vanadium(III) complexes.

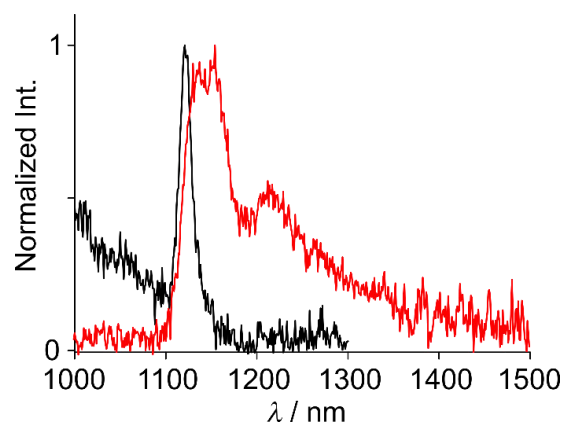


Figure S17. MCD spectra recorded for *cis-fac*-[V(ddpd)₂][BPh₄]₂ in 1 mM frozen solution at the indicated temperatures and magnetic fields (top). Bottom: Spectral components of the 7 T/10 K measurement obtained after deconvolution (black) and their sum (red).

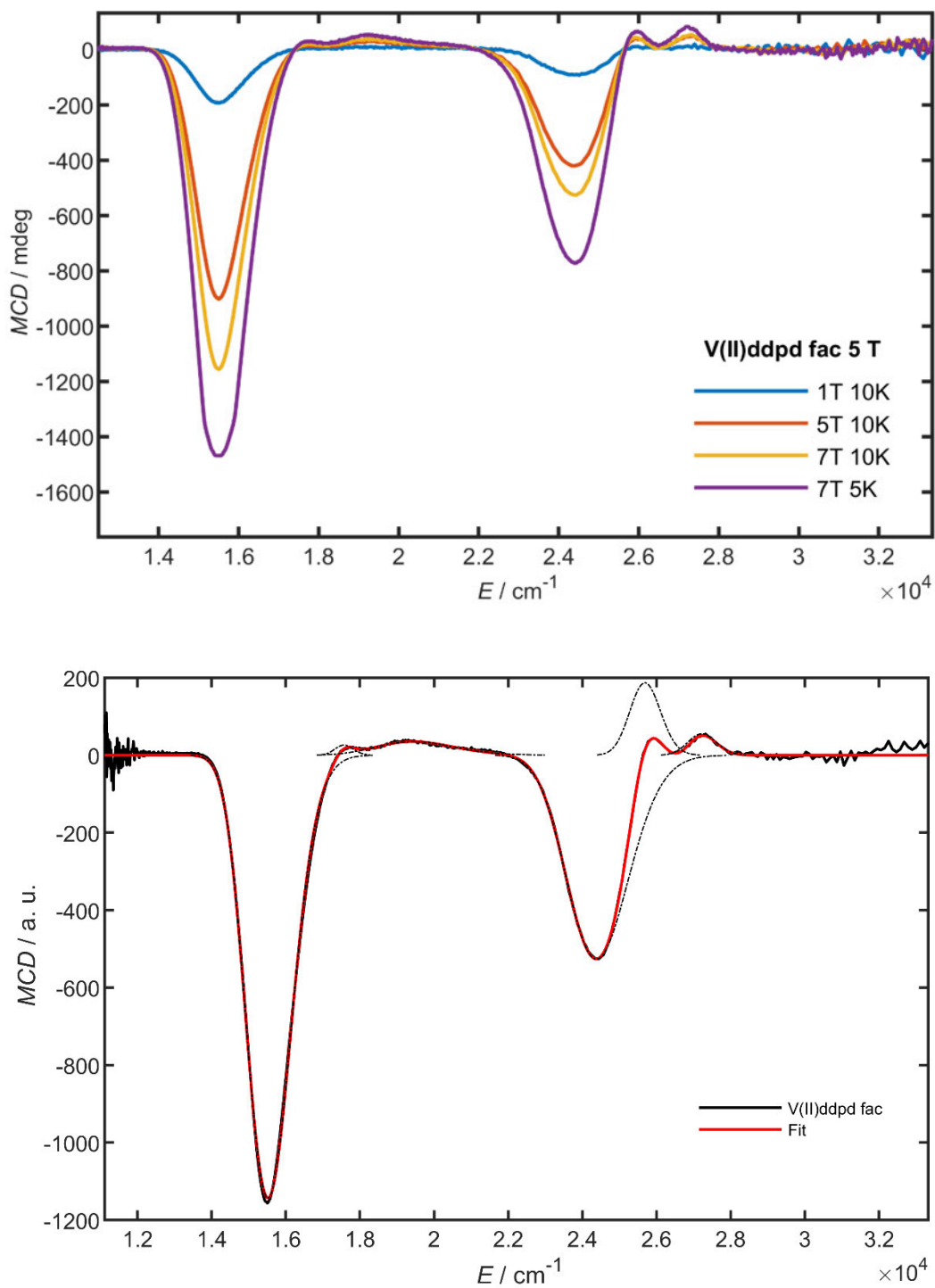
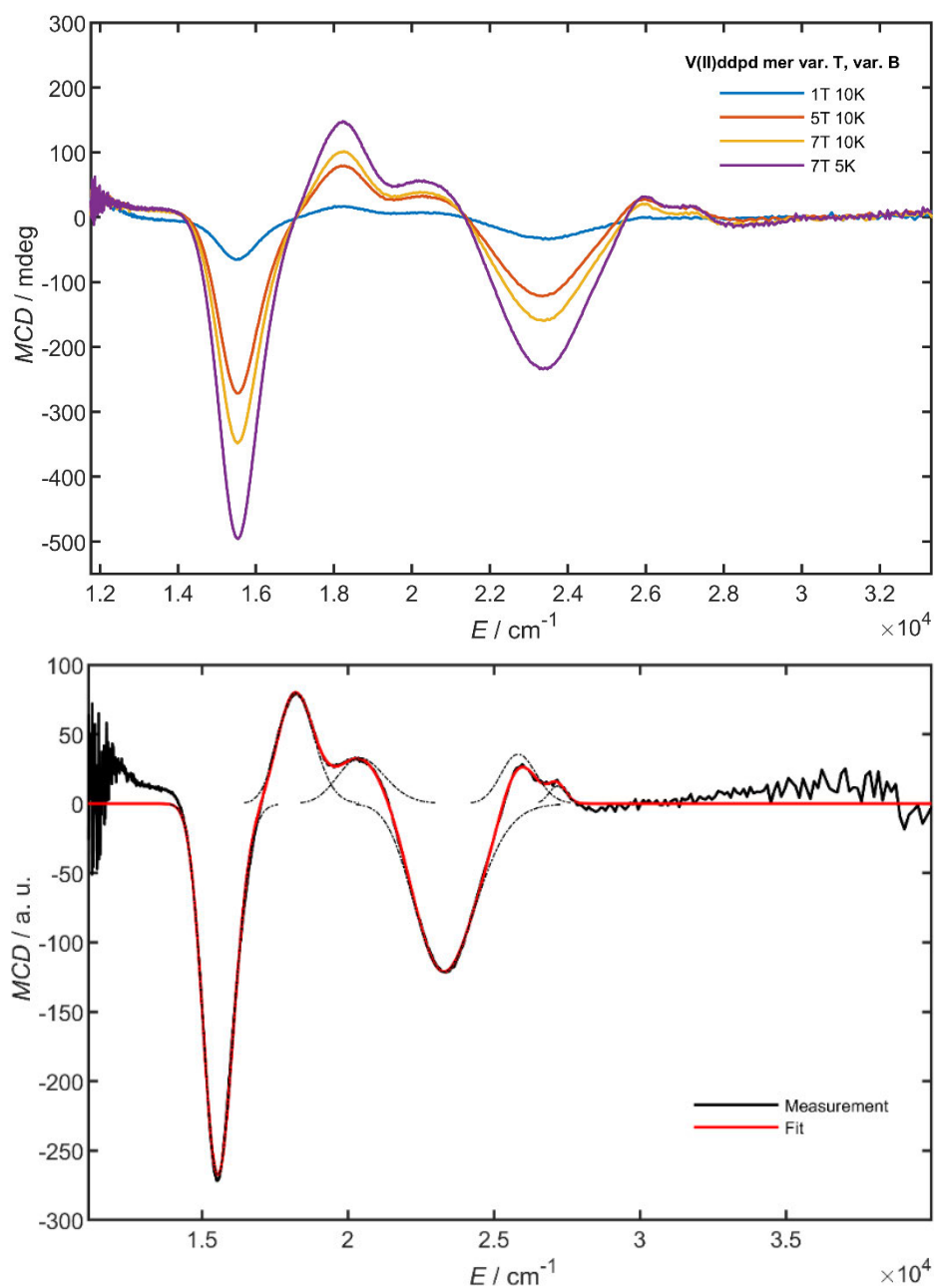


Figure S18. MCD spectra recorded for *mer*-[V(ddpd)₂][BPh₄]₂ in 1mM frozen solution at the indicated temperatures and magnetic fields (top). Middle: Spectral components of the 7 T/5 K measurement obtained after deconvolution (black) and their sum (red). Bottom: Calculated MCD spectra for *mer*-[V(ddpd)₂]²⁺ using larger basis sets than def2-SVP.



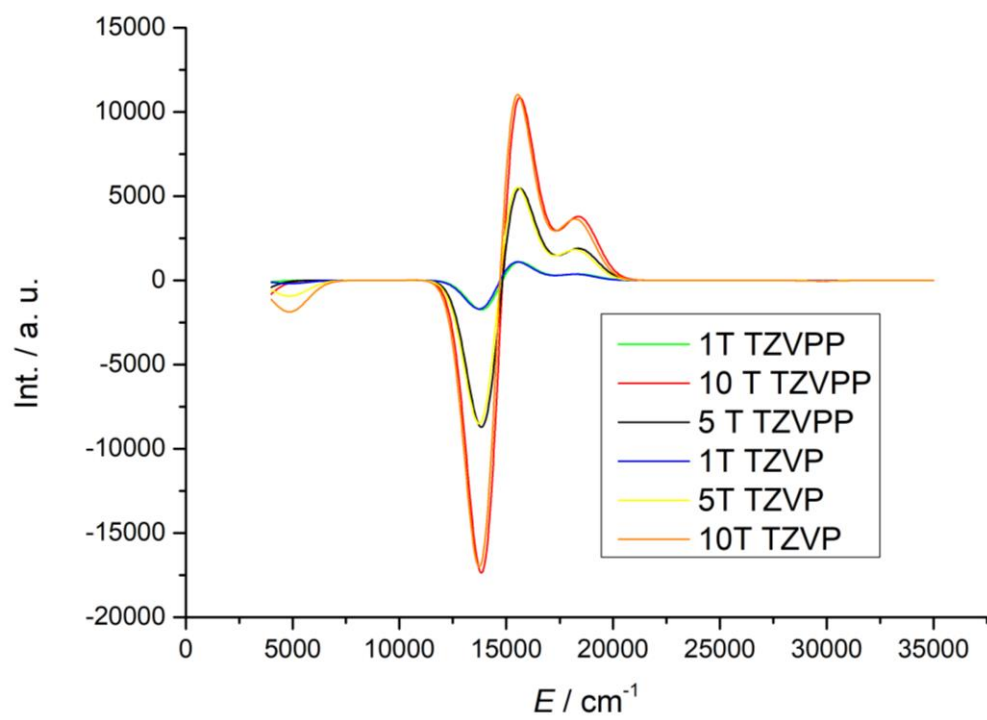


Table S11. Cartesian Coordinates of the DFT-UKS calculated lowest doublet state geometry of *cis-fac*-[V(ddpd)₂]²⁺.

Atomic number	x	y	z
23	3.820683000	9.306950000	15.023187000
7	4.750891000	7.419021000	15.437260000
7	6.648605000	8.138243000	14.206751000
7	4.749678000	9.008549000	13.123297000
7	2.750154000	9.673272000	12.074898000
7	2.139892000	8.446432000	14.012237000
7	5.518456000	10.398363000	15.742930000
7	5.232674000	11.908665000	13.934704000
7	3.084882000	11.282143000	14.658261000
7	1.018334000	10.684908000	15.609728000
7	2.703317000	9.544262000	16.836491000
6	4.153433000	6.475015000	16.194590000
1	3.149029000	6.688523000	16.519759000
6	4.767046000	5.305128000	16.584356000
1	4.235556000	4.600411000	17.206149000
6	6.071706000	5.074755000	16.161236000
1	6.594237000	4.169270000	16.436889000
6	6.690433000	6.014935000	15.359154000
1	7.688215000	5.842965000	14.989060000
6	6.006055000	7.180092000	15.003332000
6	8.104520000	8.241078000	14.330045000
1	8.639162000	7.521570000	13.706997000
1	8.372814000	8.081392000	15.369866000
1	8.403182000	9.247491000	14.048785000
6	6.057965000	8.684357000	13.068366000
6	6.820738000	8.922948000	11.926432000
1	7.868140000	8.676602000	11.896244000
6	6.189630000	9.449239000	10.813572000
1	6.756453000	9.633265000	9.911319000
6	4.827132000	9.692535000	10.831253000
1	4.324735000	10.045628000	9.947485000
6	4.124144000	9.438665000	12.007193000
6	2.165111000	10.544660000	11.052569000
1	2.806898000	11.412309000	10.932380000
1	1.195066000	10.882183000	11.403890000
1	2.045870000	10.050046000	10.086388000
6	1.872247000	8.799596000	12.739995000
6	0.720470000	8.353045000	12.087218000
1	0.536113000	8.636742000	11.063925000
6	-0.167041000	7.527723000	12.752298000
1	-1.058429000	7.175457000	12.252172000
6	0.114042000	7.154695000	14.062147000
1	-0.549448000	6.519256000	14.629362000
6	1.269105000	7.630906000	14.641167000
1	1.495553000	7.393403000	15.667341000
6	6.235068000	9.991639000	16.810581000
1	5.879878000	9.107728000	17.313662000
6	7.391301000	10.608468000	17.234544000
1	7.926529000	10.218753000	18.087507000
6	7.840160000	11.720471000	16.530329000
1	8.738797000	12.242544000	16.828037000
6	7.110301000	12.160983000	15.441783000

1	7.424044000	13.035308000	14.895033000
6	5.948534000	11.481938000	15.067543000
6	6.003032000	12.560847000	12.872962000
1	5.460756000	12.453869000	11.938098000
1	6.955116000	12.048161000	12.777438000
1	6.181856000	13.620945000	13.063545000
6	3.859955000	12.150426000	13.974730000
6	3.311066000	13.231195000	13.287728000
1	3.933440000	13.911383000	12.732679000
6	1.942976000	13.428594000	13.359829000
1	1.492565000	14.262305000	12.838913000
6	1.155127000	12.597366000	14.135941000
1	0.100973000	12.785899000	14.242385000
6	1.768455000	11.537593000	14.803246000
6	-0.433446000	10.668666000	15.413642000
1	-0.637493000	10.641283000	14.346424000
1	-0.933408000	11.534627000	15.851861000
1	-0.829968000	9.762792000	15.861222000
6	1.502492000	10.159472000	16.817097000
6	0.712624000	10.249620000	17.965990000
1	-0.235693000	10.760981000	17.928436000
6	1.164789000	9.706015000	19.153547000
1	0.560233000	9.777717000	20.046982000
6	2.409628000	9.086755000	19.179579000
1	2.810140000	8.646807000	20.080608000
6	3.136220000	9.038187000	18.010471000
1	4.095553000	8.548169000	17.993893000

Table S12. Cartesian Coordinates of the DFT-UKS calculated lowest doublet state geometry of *mer*-[V(ddpd)₂]²⁺.

Atomic number	x	y	z
23	-0.437484	4.882287	1.502872
7	0.022931	4.404842	3.509542
7	0.598281	2.226374	2.814841
7	1.19658	3.644682	1.008239
7	1.750465	5.115875	-0.775931
7	-0.597527	5.190984	-0.596835
7	-1.852263	3.317272	1.384583
7	-2.999456	4.268395	3.21187
7	-2.080129	6.102229	2.017521
7	-1.113092	7.891141	0.787559
7	0.705053	6.674097	1.661188
6	-0.172477	5.306839	4.494232
1	-0.391923	6.313274	4.170702
6	-0.142761	4.979465	5.830719
1	-0.330451	5.736712	6.577236
6	0.121991	3.656989	6.178064
1	0.151264	3.351963	7.214968
6	0.376619	2.733283	5.180823
1	0.624734	1.715801	5.434026
6	0.338093	3.139502	3.843231
6	0.411899	0.805679	3.120335
1	-0.521019	0.693358	3.666431
1	1.225022	0.380865	3.712417
1	0.331148	0.261659	2.184016
6	1.445147	2.532884	1.73561
6	2.502695	1.682521	1.430424
1	2.698121	0.814962	2.038648
6	3.317672	1.991781	0.355332
1	4.145487	1.345094	0.099283
6	3.070559	3.131261	-0.389761
1	3.681539	3.372107	-1.243981
6	1.997151	3.943697	-0.038389
6	2.919634	5.784661	-1.354829
1	2.676631	6.833305	-1.503605
1	3.234538	5.351584	-2.306208
1	3.737661	5.718885	-0.644316
6	0.504707	5.410069	-1.334021
6	0.411171	5.94381	-2.625823
1	1.298985	6.125378	-3.208286
6	-0.835392	6.202208	-3.162194
1	-0.916017	6.607137	-4.161571
6	-1.976318	5.9109	2.418057
1	-2.968842	6.082126	-2.806951
6	-1.807914	5.403429	-1.149975
1	-2.655513	5.178713	-0.519619
6	-1.694286	2.317105	0.49254
1	-0.934023	2.474881	-0.257698
6	-2.412501	1.144153	0.543029

1	-2.227495	0.365269	-0.181592
6	-3.36089	0.997124	1.552512
1	-3.94657	0.092002	1.634516
6	-3.569871	2.035632	2.441562
1	-4.327878	1.95337	3.202904
6	-2.807282	3.202281	2.326132
6	-3.608533	3.960185	4.508248
1	-3.144655	3.058235	4.899115
1	-4.688821	3.811347	4.45342
1	-3.39533	4.779192	5.188562
6	-3.07836	5.603432	2.77985
6	-4.165466	6.384313	3.159313
1	-4.963701	5.961629	3.746909
6	-4.219879	7.701686	2.738569
1	-5.054612	8.327493	3.022487
6	-3.203552	8.215141	1.952147
1	-3.218618	9.245048	1.635658
6	-2.141091	7.387148	1.604934
6	-1.496298	8.906854	-0.197567
1	-0.769152	8.892801	-1.005115
1	-1.547738	9.914324	0.220384
1	-2.466911	8.639669	-0.603765
6	0.235204	7.823157	1.146071
6	1.079741	8.923365	0.951293
1	0.696213	9.838866	0.532581
6	1.987645	6.617033	2.070699
6	2.403879	8.83536	1.335112
6	2.870967	7.661988	1.922779
1	2.300138	5.677653	2.502237
1	3.894815	7.557505	2.249085
1	3.060824	9.682985	1.196447

Figure S19. Temperature dependence of the magnetic susceptibility in $\chi_M T$ vs. T for *cis-fac*-[V(ddpd)₂][BPh₄]₂. The red line corresponds to the fit obtained with $S = 3/2$; $g_{1,2,3} = 1.99, 1.99, 2.0$; $D = 0.40(2) \text{ cm}^{-1}$ and $E = 0.3D$.

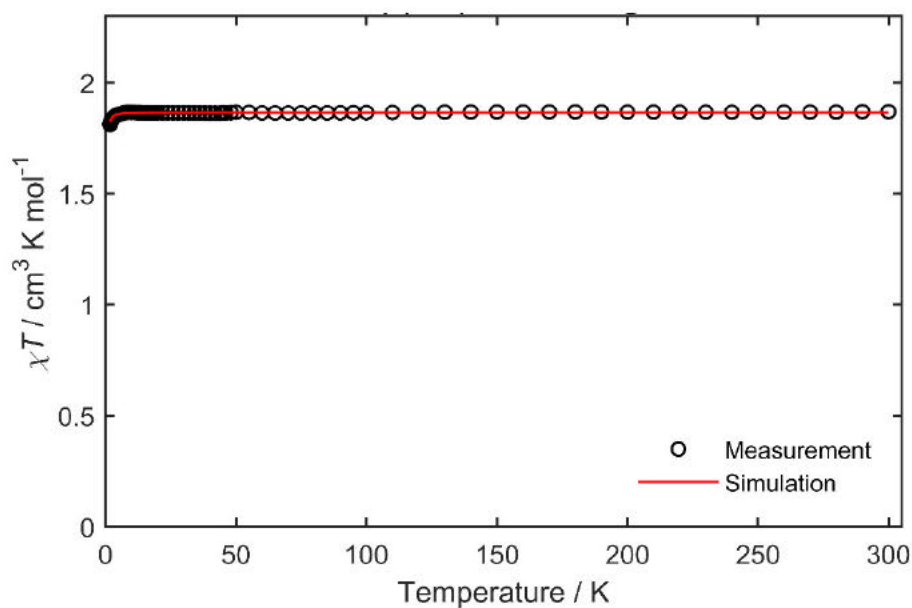


Figure S20. Field dependence of the magnetization of *cis-fac*-[V(ddpd)₂][BPh₄]₂ at different temperatures. Best fit with $S = 3/2$; $g_{1,2,3} = 1.99, 1.99, 2.0$; $D = 0.40(2) \text{ cm}^{-1}$ and $E = 0.3D$.

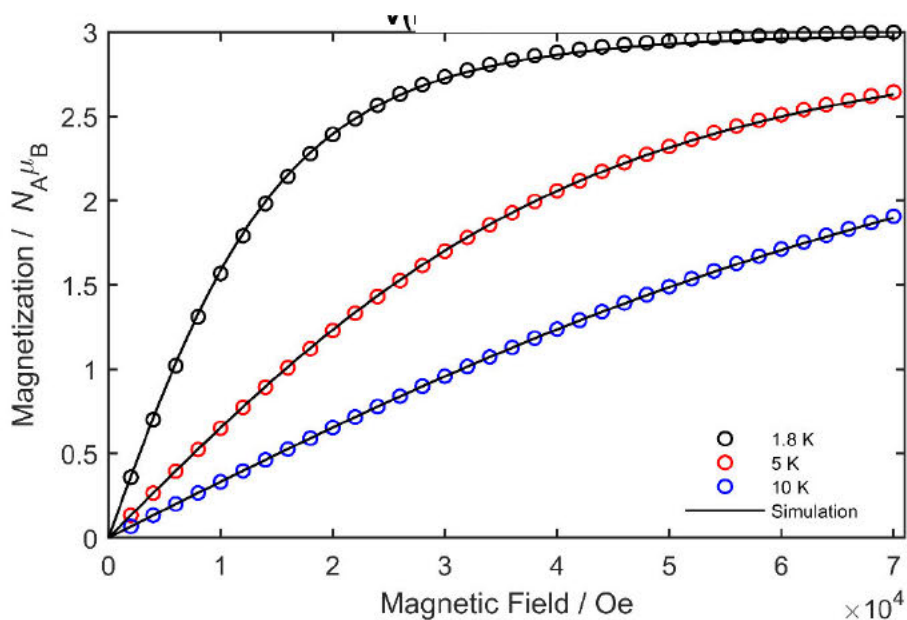


Figure S21. Temperature dependence of the magnetic susceptibility in $\chi_M T$ vs. T for *mer*-[V(ddpd)₂][BPh₄]₂. The red line corresponds to the fit obtained with $S = 3/2$; $g = 1.99(1)$; $D = 0.2(1)$ cm⁻¹ and $E = 0$ cm⁻¹.

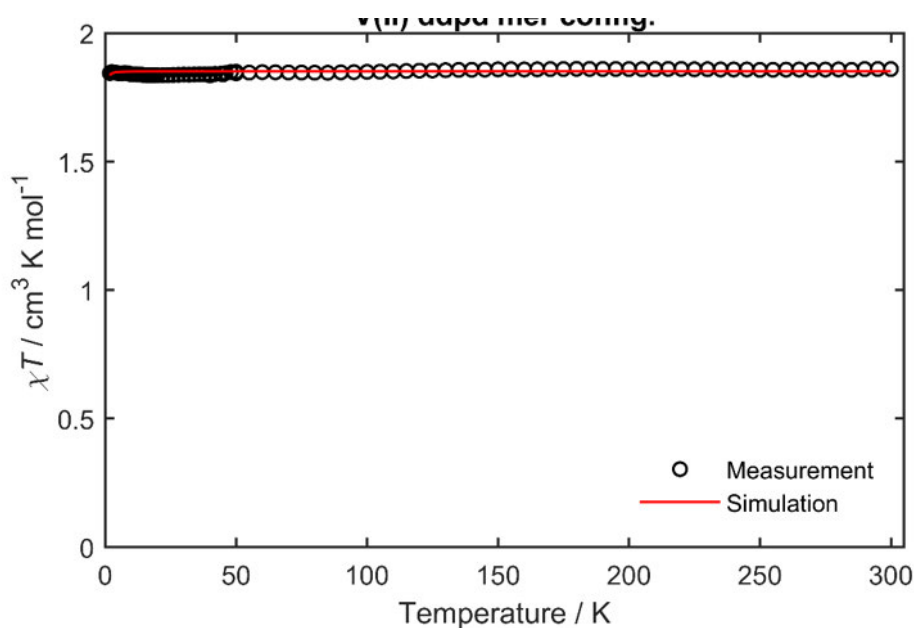


Figure S22. Field dependence of the magnetization of *mer*-[V(ddpd)₂][BPh₄]₂ at different temperatures. Best fit with $S = 3/2$; $g = 1.99(1)$; $D = 0.2(1)$ cm⁻¹ and $E = 0$ cm⁻¹.

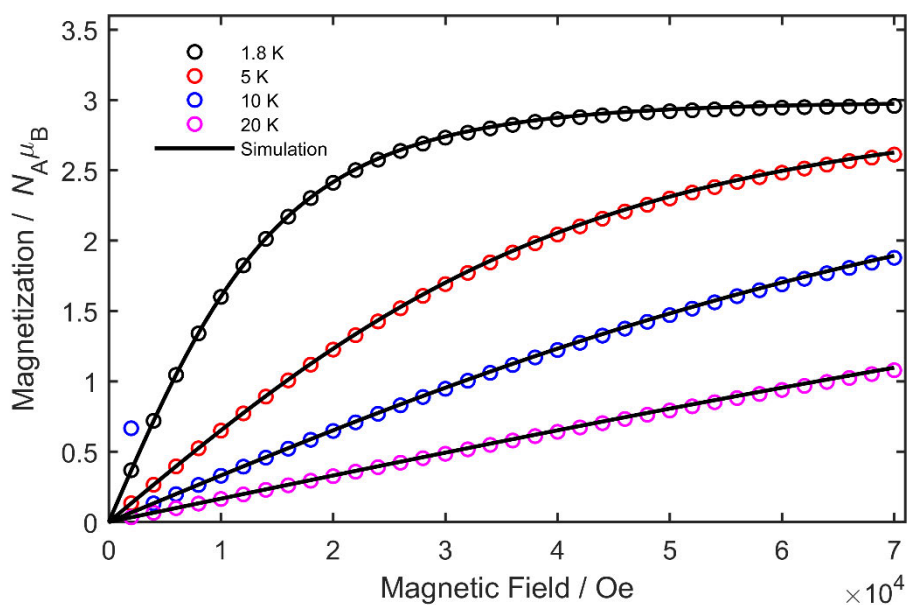


Figure S23. HFEPR spectra of *cis-fac*-[V(ddpd)₂][BPh₄]₂ at 5 K and different frequencies as indicated (top) together with simulations (bottom) based on the spin Hamiltonian parameters of $S = 3/2$; $g_{1,2,3} = 1.99, 1.99, 2.0$; $D = 0.47(2) \text{ cm}^{-1}$ and $E = 0.19 D$. The vertical axis corresponds to the microwave frequency.

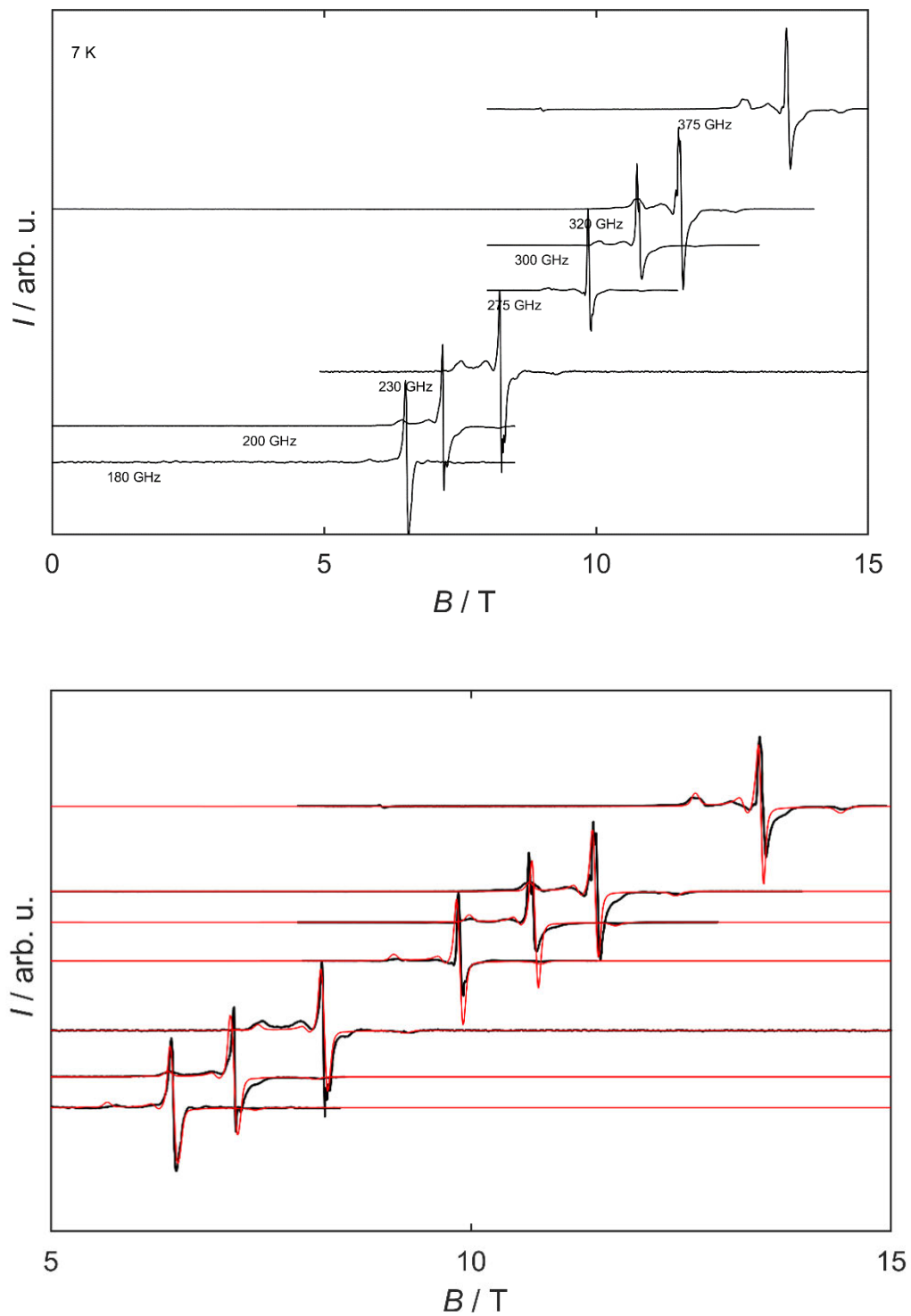


Figure S24. Measured and simulated HFEPR spectra of *cis-fac*-[V(ddpd)₂][BPh₄]₂ at 375 GHz and different temperatures as indicated. The simulations are based on the spin Hamiltonian parameters of $S = 3/2$; $g_{1,2,3} = 1.99, 1.99, 2.0$; $D = 0.47(2) \text{ cm}^{-1}$ and $E = 0.19 D$.

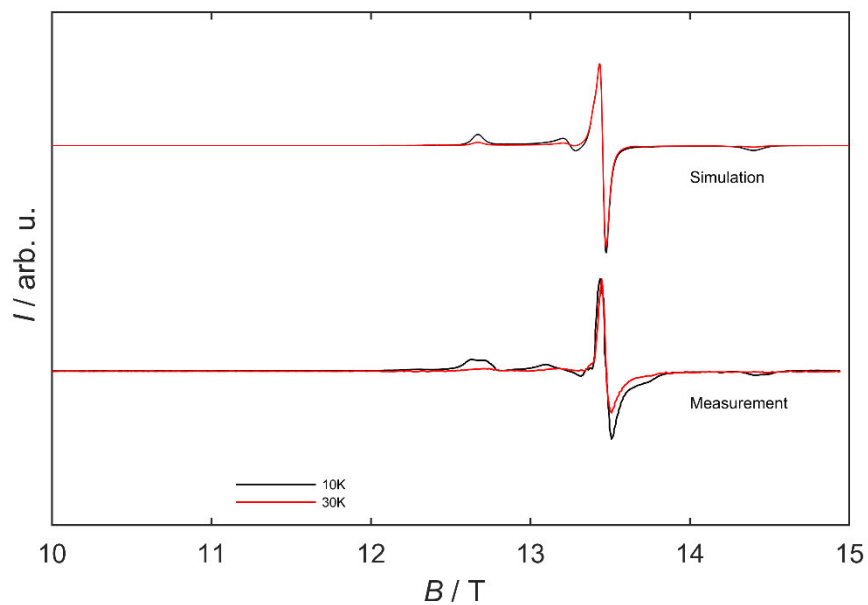


Figure S25. HFEPR spectra of *mer*-[V(ddpd)₂][BPh₄]₂ at 5 K and different frequencies as indicated (top) together with simulations (bottom) based on the spin Hamiltonian parameters of $S = 3/2$; $g_{1,2,3} = 1.985(5), 1.993(5), 1.996(4)$; $D = 0.2(1) \text{ cm}^{-1}$ and $E = 0.08 D$. The vertical axis corresponds to the microwave frequency.

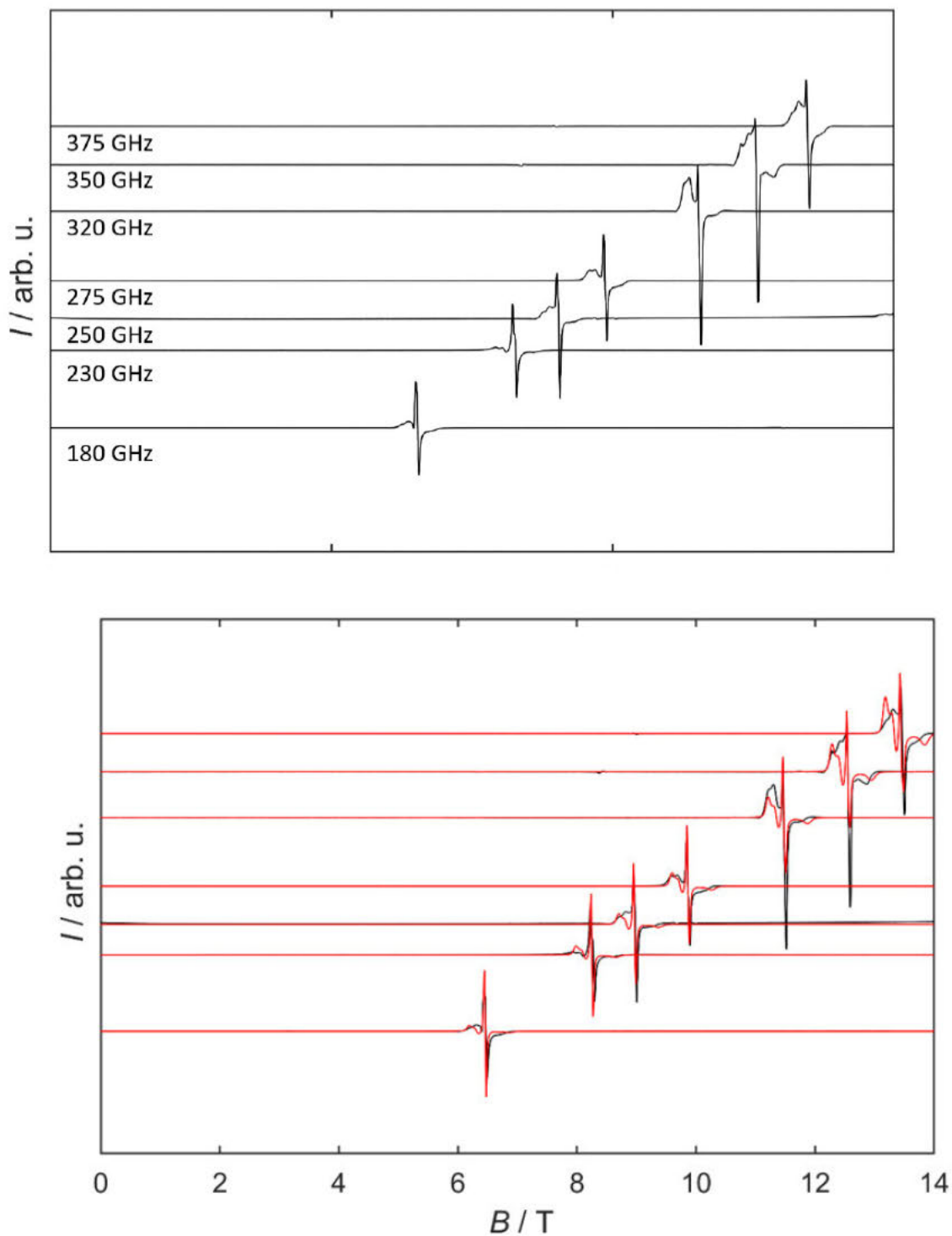


Figure S26. Measured and simulated HFEPR spectra of *mer*-[V(ddpd)₂][BPh₄]₂ at 275 GHz and different temperatures as indicated. Top: Simulations based on a positive value for D with the spin Hamiltonian parameters of $S = 3/2$; $g_{1,2,3} = 1.985(5), 1.993(5), 1.996(4)$; $D = 0.2(1) \text{ cm}^{-1}$ and $E = 0.08 D$. Bottom: Measurements and best simulation based on a ZFS parameter with a negative sign ($g_{1,2,3} = 1.94(2), 1.966(4), 1.966(4)$; $D = -0.08(1) \text{ cm}^{-1}$ and $E = 0.29 D$).

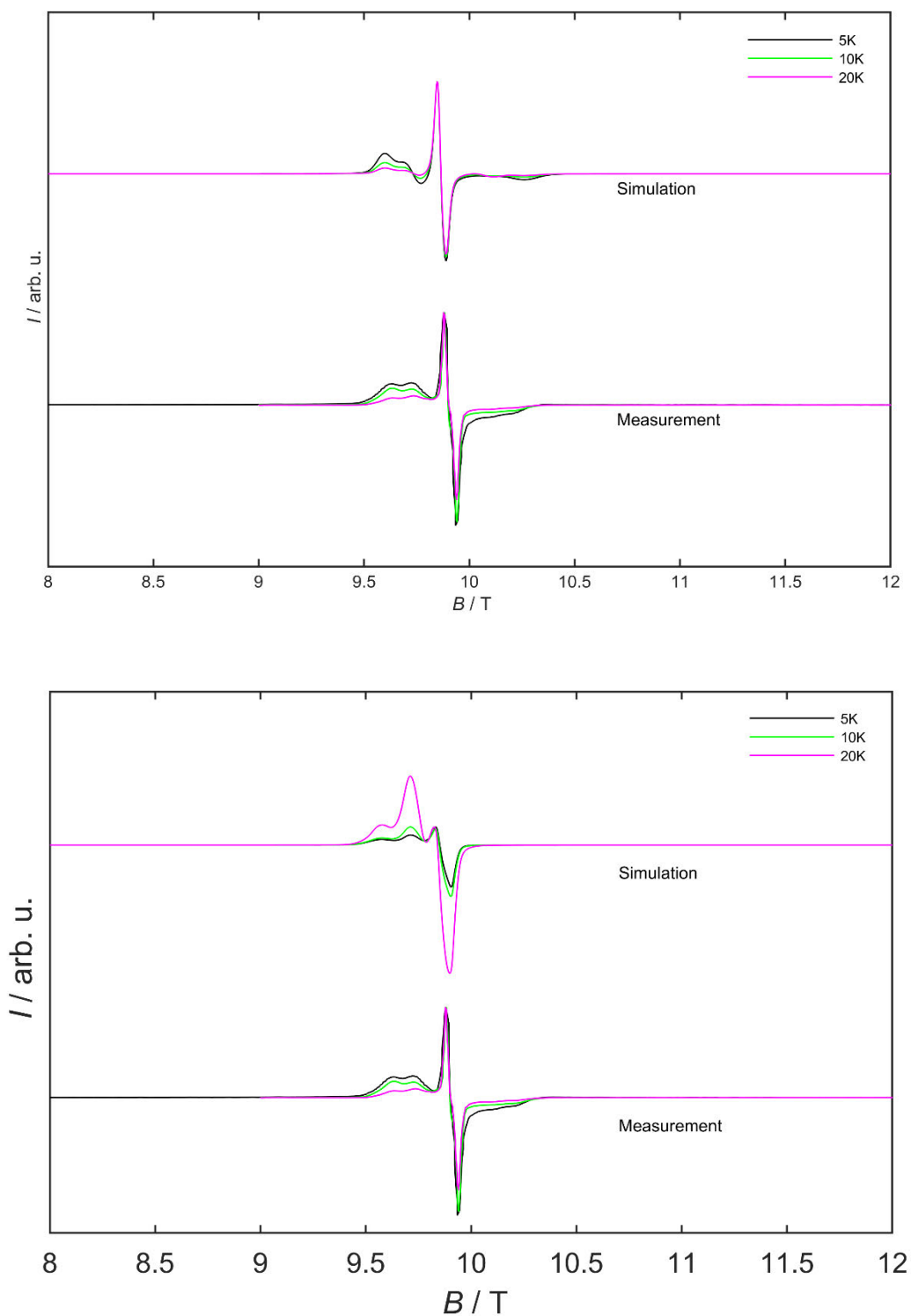


Figure S27. Measured and simulated X-Band EPR spectra of *cis-fac*-[V(ddpd)₂][BPh₄]₂ (top) and *mer*-[V(ddpd)₂][BPh₄]₂ (bottom) at 7 K in a 3 mM butyronitrile/propionitrile (1:1) solution. Simulations are based on the following parameters: *cis-fac*-[V(ddpd)₂][BPh₄]₂: $S = 3/2$; $g = 1.94(1)$; $D = 0.30(2)$ cm⁻¹ and $E = 0.3 D$; $A = 200(20)$ MHz and for *mer*-[V(ddpd)₂][BPh₄]₂: $S = 3/2$; $g = 1.989(5)$; $D = 0.12(2)$ cm⁻¹ and $E = 0.08 D$; $A = 200(20)$ MHz.

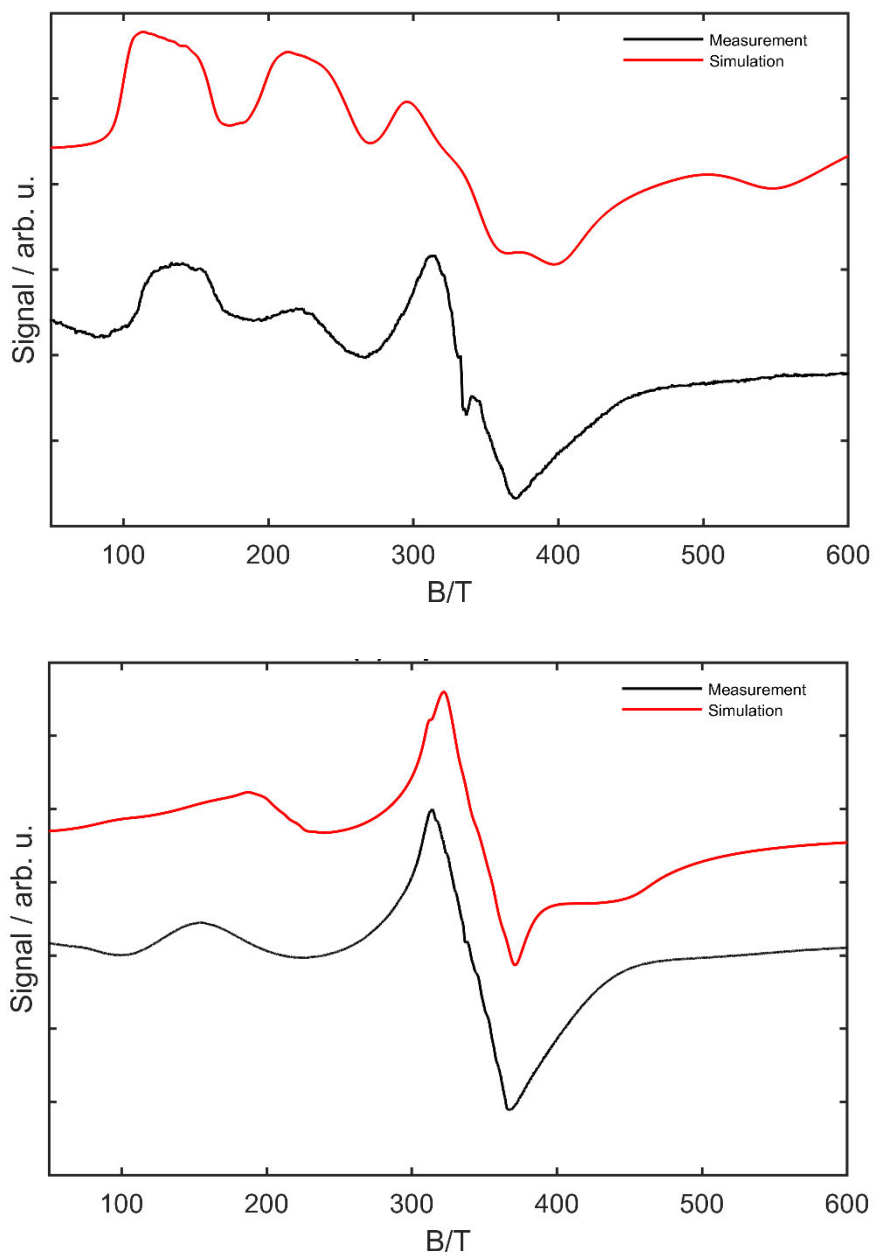


Figure S28. Measured inversion recovery curves of *cis-fac*-[V(ddpd)₂][BPh₄]₂ in a 3 mM solution (butyronitrile/propionitrile (1:1)) at the indicated fields and temperatures. The fits are based on an exponential of the form $I(\tau) = -A \exp\left(-\frac{\tau}{T_1}\right) + y$.

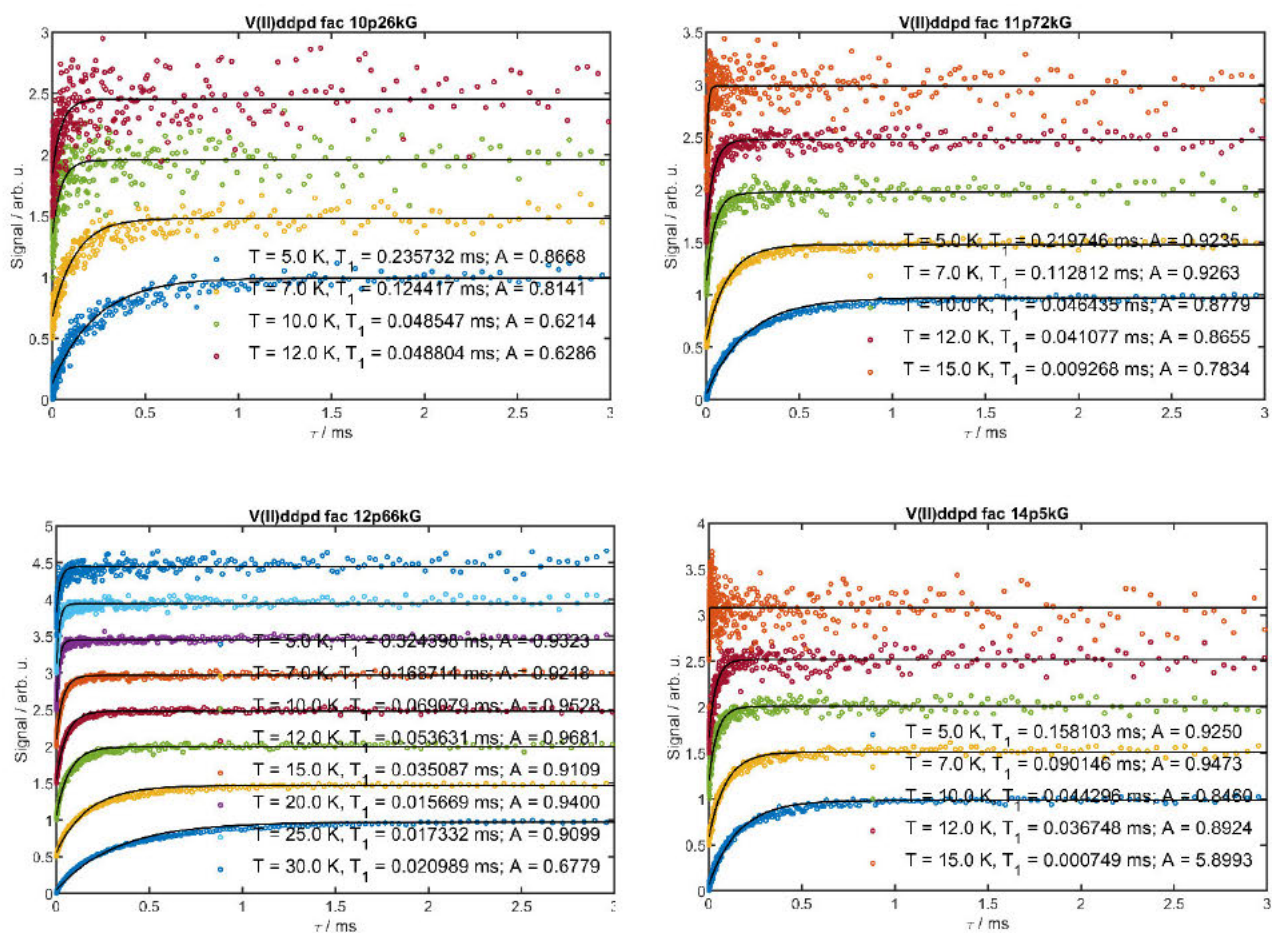


Figure S29. Measured Hahn-Echo decay curves of *cis-fac*-[V(ddpd)₂][BPh₄]₂ in a 3 mM solution (butyronitrile/propionitrile (1:1)) at the indicated fields and temperatures. The fits are based on an exponential of the form $I(\tau) = I(0)\exp(-\tau/T_M)^k$.

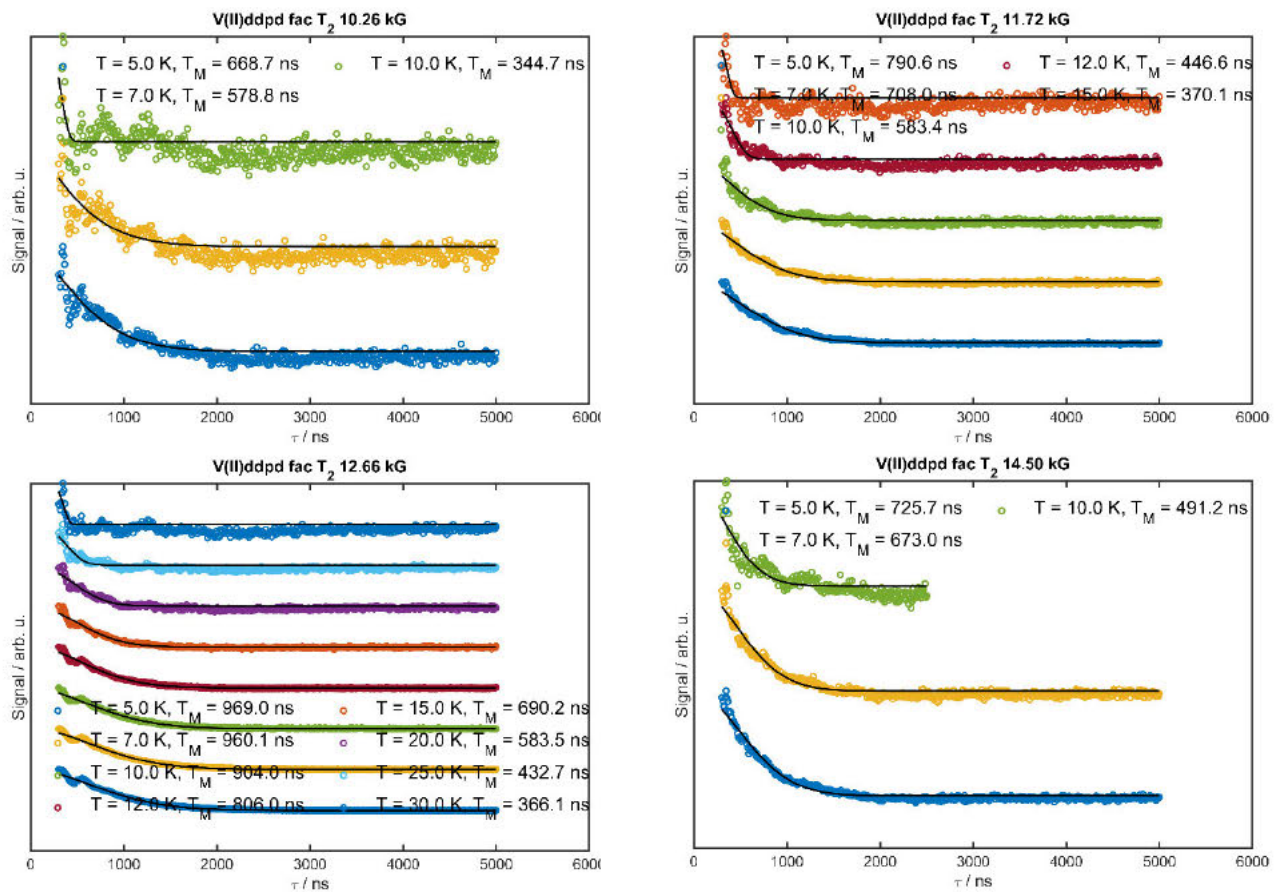


Figure S30. Measured inversion recovery curves of *mer*-[V(ddpd)₂][BPh₄]₂ in a 3 mM solution (butyronitrile/propionitrile (1:1)) at the indicated temperatures at 1100 mT (left) and at 1275 mT (right). The fits are based on an exponential of the form $I(\tau) = -A \exp\left(-\frac{\tau}{T_1}\right) + y$.

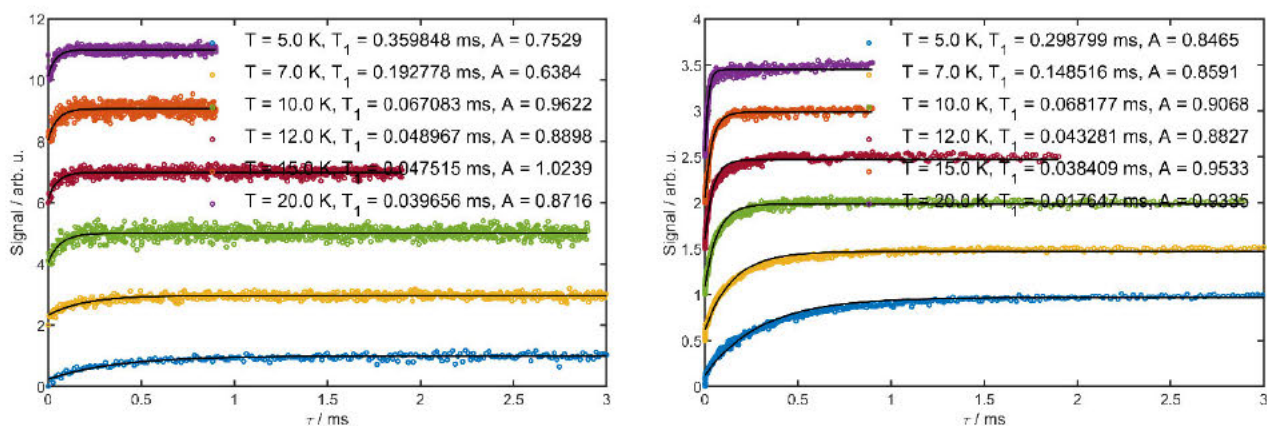


Figure S31. Measured Hahn-Echo decay curves of *mer*-[V(ddpd)₂][BPh₄]₂ in a 3 mM solution (butyronitrile/propionitrile (1:1)) at the indicated temperatures at 1100 mT (left) and 1275 mT (right). The fits are based on an exponential of the form $I(\tau) = I(0)\exp(-\tau/T_M)^k$.

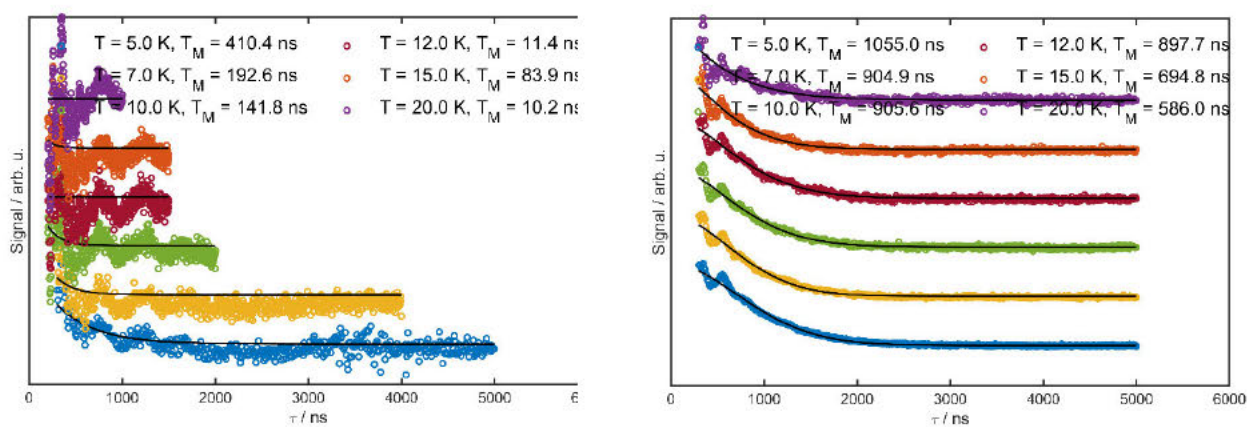


Figure S32. Fourier transform of the subtraction of the experiment and the exponential decay of the Hahn-Echo decay curves of *cis-fac*-[V(ddpd)₂][BPh₄]₂ (experiments see Figure S29).

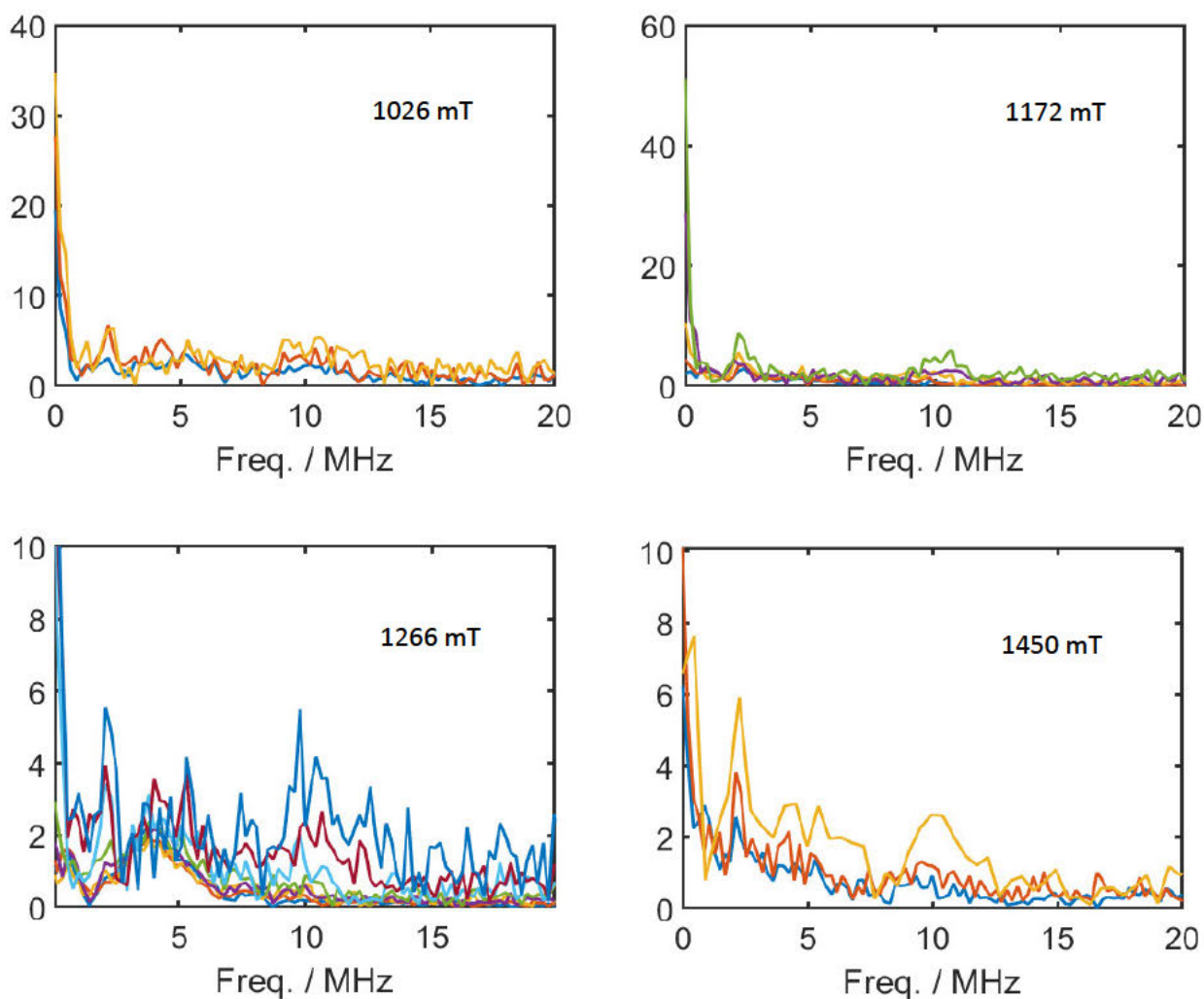


Figure S33. Fourier transform of the subtraction of the experiment and the exponential decay of the Hahn-Echo decay curves of *mer*-[V(ddpd)₂][BPh₄]₂ (experiments see Figure S31).

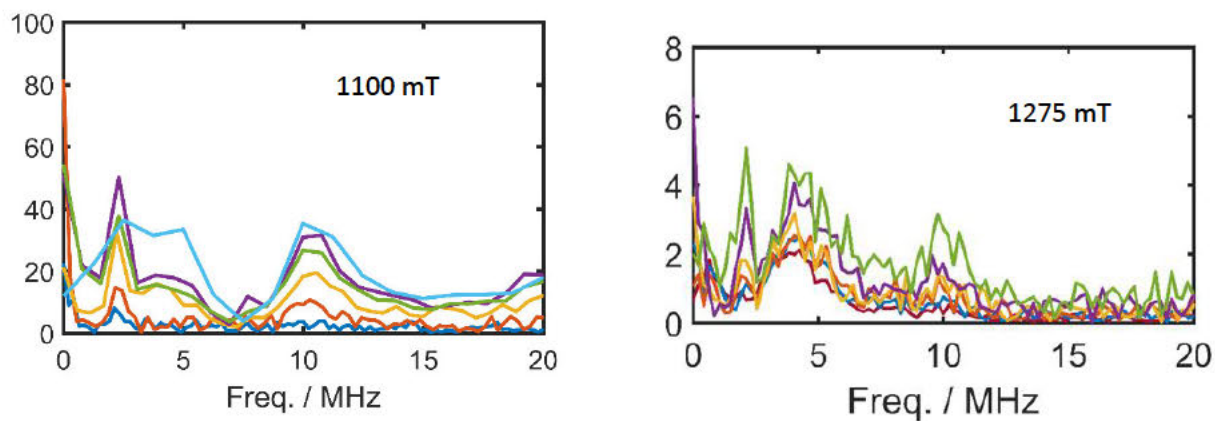
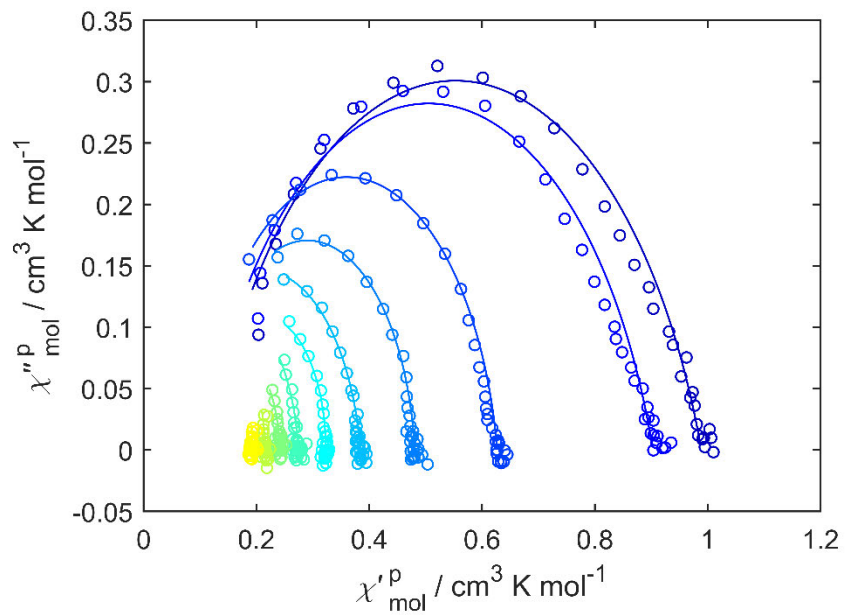


Figure S34. Cole-Cole plot of the AC susceptometry measurements on a pressed pellet of *mer*-[V(ddpd)₂][BPh₄]₂. Measured values are shown as open circles, while fits to the standard modified Debye function are shown as solid lines



Derivation of the Λ Tensor

The lambda tensor is given as^[34]

$$\Lambda_{ab} = \sum_{k \neq 0} \frac{\langle 0 | \hat{L}_a | k \rangle \langle k | \hat{L}_b | 0 \rangle}{E_k - E_0} \quad (1)$$

where $a, b \in \{x, y, z\}$. Here $|0\rangle$ is the electronic ground state, $|k\rangle$ are the excited states, and $E_{k/0}$ their respective energies.

The ZFS parameters D and E can be obtained from the lambda tensor via

$$D = \frac{1}{2} \lambda^2 (2 \Lambda_{zz} - \Lambda_{xx} - \Lambda_{yy}); E = \frac{1}{2} \lambda^2 (\Lambda_{xx} - \Lambda_{yy}) \quad (2)$$

A matrix element is non-vanishing only when the direct product of the symmetries of the three terms of the integrand spans the totally symmetric irrep. This symmetry requirement allows the determination of the relevant excited states from the symmetries spanned by the ground state and the orbital angular momentum. The relevant symmetry point group for the present complex *cis-fac*-[V(ddpd)₂]²⁺ is C_2 . The excited states transform either as E , T_1 or T_2 , while the orbital angular momentum operator transforms as T_1 . The ground state transforms as A_2 . Hence, non-vanishing matrix elements are only obtained for the T_2 excited state. Additionally, only the diagonal elements of the lambda tensor are non-zero.

Evaluation of the matrix elements^[35]

Making use of the Wigner-Eckhart theorem and considering the effects of symmetry lowering (from O to C_2) according Butler's chain of groups, each matrix element can be written as products of 2jm symbols, 3jm symbols and a reduced matrix element (RME) as:

$$\begin{aligned} \langle \Gamma_{GS} | \Gamma_{\hat{L}} | \Gamma_{ES} \rangle^{O \supset D_4 \supset D_2 \supset C_2} &= \left(\Gamma_{GS}(O) \right)_O^0 \cdot \left(\Gamma_{GS}(O) \quad \Gamma_{\hat{L}}(O) \quad \Gamma_{ES}(O) \right)_O^0 \cdot \left(\Gamma_{GS}(O) \right)_{D_4}^0 \\ &\cdot \left(\Gamma_{GS}(D_4) \quad \Gamma_{\hat{L}}(D_4) \quad \Gamma_{ES}(D_4) \right)_{D_4}^{D_4} \cdot \left(\Gamma_{GS}(D_4) \quad \Gamma_{\hat{L}}(D_4) \quad \Gamma_{ES}(D_4) \right)_{D_2}^{D_4} \cdot \left(\Gamma_{GS}(D_2) \right)_{C_2}^{D_2} \\ &\cdot \left(\Gamma_{GS}(D_2) \quad \Gamma_{\hat{L}}(D_2) \quad \Gamma_{ES}(D_2) \right)_{D_2}^{D_2} \cdot \left(\Gamma_{GS}(D_2) \quad \Gamma_{\hat{L}}(D_2) \quad \Gamma_{ES}(D_2) \right)_{C_2}^{D_2} \cdot \left(\Gamma_{GS}(C_2) \right)_{C_2}^{D_2} \\ &\cdot \langle \Gamma_{GS} || \Gamma_{\hat{L}} || \Gamma_{ES} \rangle^O \end{aligned} \quad (3)$$

Here, the first 2jm and the first 3jm symbol are due to the decomposition of the integral due to the Wigner-Eckhart theorem. The following 2jm and 3jm symbols take into account the symmetry lowering. GS and ES (ζ, ξ , or η for T_2) are the components of the ground state and excited state irreps, respectively. Since the ground state is non degenerate, GS is in all cases a_2 . k is the component of the irrep of the orbital angular momentum operator (x, y , or z for T_1).^[37]

Only a few combinations of components will deliver non-zero results, and Table C12.1 in Piepho and Schatz can be used to find non-zero contributions.^[36] All 2jm- and 3jm-symbols are tabulated in Butler.^[35] Finally, the reduced matrix element is evaluated under the assumption that the transition from ground to excited state can be assigned to a transition of one electron from an orbital to another orbital. In our case, the transition from ground to excited state is always assumed to correspond to excitation of one electron ($l=2$) from an $e-$ to a t_2 -orbital in O symmetry. The symmetries of the states are then replaced by those of the orbitals and that of the total orbital angular momentum operator to that of the one-electron orbital angular momentum operator. The effect of symmetry reduction

from the pure rotational symmetry SO_3 of the angular momentum to the O point group is considered as:

$$\begin{aligned} \langle \Gamma_{GS} || \Gamma_{\tilde{L}} || \Gamma_{ES} \rangle^O &= \langle e || \Gamma_{\tilde{L}} || t_2 \rangle^O = \langle t_2 || \Gamma_{\tilde{L}} || e \rangle^O = \begin{pmatrix} 2 \\ e \end{pmatrix}_O^{SO_3} \cdot \begin{pmatrix} 2 & 1 & 2 \\ e & t_1 & t_2 \end{pmatrix}_O^{SO_3} \sqrt{l(l+1)(2l+1)} \\ &= 1 \cdot \left(-\frac{\sqrt{2}}{\sqrt{5}} \right) \cdot \sqrt{30} \\ &= -2\sqrt{3} \end{aligned}$$

Derivation of the relevant integrals

With the above, the only non-zero integrals are:

$$\begin{aligned} \langle A_2 | T_{1x} | T_{2\xi} \rangle^{O \supset D_4 \supset D_2 \supset C_2} \\ \langle A_2 | T_{1y} | T_{2\eta} \rangle^{O \supset D_4 \supset D_2 \supset C_2} \\ \langle A_2 | T_{1z} | T_{2\zeta} \rangle^{O \supset D_4 \supset D_2 \supset C_2} \\ \langle T_{2\xi} | T_{1x} | A_2 \rangle^{O \supset D_4 \supset D_2 \supset C_2} \\ \langle T_{2\eta} | T_{1y} | A_2 \rangle^{O \supset D_4 \supset D_2 \supset C_2} \\ \langle T_{2\zeta} | T_{1z} | A_2 \rangle^{O \supset D_4 \supset D_2 \supset C_2} \end{aligned}$$

These integrals can be solved by using the Wigner-Eckhart theorem as stated above. For the first integral this is:

$$\begin{aligned} \langle A_2 | T_{1x} | T_{2\xi} \rangle^{O \supset D_4 \supset D_2 \supset C_2} &= \begin{pmatrix} A_2 \\ a_2 \end{pmatrix}_O \cdot \begin{pmatrix} A_2 & T_{1x} & T_{2\xi} \\ a_2 & x & \xi \end{pmatrix}_O \cdot \begin{pmatrix} A_2 \\ B_1 \end{pmatrix}_{D_4}^O \cdot \begin{pmatrix} A_2 & T_{1x} & T_{2\xi} \\ B_1 & E & E \end{pmatrix}_{D_4}^O \cdot \begin{pmatrix} B_1 \\ A_1 \end{pmatrix}_{D_2}^{D_4} \cdot \begin{pmatrix} B_1 & E & E \\ A_1 & B_1 & B_1 \end{pmatrix}_{D_2}^{D_4} \cdot \begin{pmatrix} A_1 \\ A_1 \end{pmatrix}_{C_2}^{D_2} \cdot \\ &\begin{pmatrix} A_1 & B_1 & B_1 \\ A_1 & B_1 & B_1 \end{pmatrix}_{C_2}^{D_2} \cdot RME \end{aligned}$$

The 2jm and 3jm signals are tabulated in Butler. For this, one has to move to the corresponding Butler notation. For the above integral this is:

$$\langle A_2 | T_{1x} | T_{2\xi} \rangle^{O \supset D_4 \supset D_2 \supset C_2} = \begin{pmatrix} A_2 \\ a_2 \end{pmatrix}_O \begin{pmatrix} A_2 & T_{1x} & T_{2\xi} \\ a_2 & x & \xi \end{pmatrix}_O \cdot \begin{pmatrix} \tilde{0} \\ 2 \end{pmatrix}_{D_4}^O \cdot \begin{pmatrix} \tilde{0} & 1 & \tilde{1} \\ 2 & 1 & 1 \end{pmatrix}_{D_4}^O \cdot \begin{pmatrix} 2 \\ 0 \end{pmatrix}_{D_2}^{D_4} \cdot \begin{pmatrix} 2 & 1 & 1 \\ 0 & \tilde{1} & \tilde{1} \end{pmatrix}_{D_2}^{D_4} \cdot \begin{pmatrix} 0 \\ 0 \end{pmatrix}_{C_2}^{D_2} \cdot \begin{pmatrix} 0 & \tilde{1} & \tilde{1} \\ 0 & 1 & 1 \end{pmatrix}_{C_2}^{D_2} \cdot RME$$

With the 2jm and 3jm symbols evaluated:

$$\begin{aligned} \langle A_2 | T_{1x} | T_{2\xi} \rangle^{O \supset D_4 \supset D_2 \supset C_2} &= 1 \cdot \frac{1}{\sqrt{3}} \cdot 1 \cdot -\frac{\sqrt{2}}{\sqrt{3}} \cdot 1 \cdot -\frac{1}{\sqrt{2}} \cdot 1 \cdot -1 \cdot RME = 1 \cdot \frac{1}{\sqrt{3}} \cdot 1 \cdot -\frac{\sqrt{2}}{\sqrt{3}} \cdot 1 \cdot -\frac{1}{\sqrt{2}} \cdot 1 \cdot -1 \cdot -2\sqrt{3} \\ &= \frac{1}{\sqrt{3}} \cdot -\frac{\sqrt{2}}{\sqrt{3}} \cdot -\frac{1}{\sqrt{2}} \cdot 2\sqrt{3} = \frac{2\sqrt{3}}{3} \end{aligned}$$

For the other matrix elements, the procedure is equivalent and will lead to the elements of the lambda tensor:

Appendix

$\Lambda_{zz} = \frac{4}{3E_1}$, $\Lambda_{yy} = \frac{4}{3E_2}$ and $\Lambda_{xx} = \frac{4}{3E_3}$. With that the ZFS parameters are the following:

$$D = \frac{1}{2}\lambda^2\left(2\frac{4}{3E_1} - \frac{4}{3E_3} - \frac{4}{3E_2}\right) \text{ and } E = \frac{1}{2}\lambda^2\left(\frac{4}{3E_3} - \frac{4}{3E_2}\right)$$

References

- [1] S. J. Anderson, F. J. Wells, G. Wilkinson, B. Hussain, M. B. Hursthouse, *Polyhedron* **1988**, *7*, 2615–2626.
- [2] a) A. Breivogel, C. Förster, K. Heinze, *Inorg. Chem.* **2010**, *49*, 7052–7056. b) C. Wang, W. R. Kitzmann, F. Weigert, C. Förster, X. Wang, K. Heinze, U. Resch-Genger, *ChemPhotoChem* **2022**, *6*, e202100296.
- [3] P. Neugebauer, D. Bloos, R. Marx, P. Lutz, M. Kern, D. Aguila, J. Vaverka, O. Laguta, C. Dietrich, R. Clerac, J. van Slageren, *Phys. Chem. Chem. Phys.* **2018**, *20*, 15528–15534.
- [4] S. Stoll, A. Schweiger, *J. Magn. Reson.* **2006**, *178*, 42–55.
- [5] Y. Rechkemmer, PhD Thesis, University of Stuttgart, **2016**.
- [6] I. Tkach, A. Baldansuren, E. Kalabukhova, S. Lukin, A. Sitnikov, A. Tsvir, M. Ischenko, Y. Rosentzweig, E. Roduner, *Appl. Magn. Reson.* **2008**, *35*, 95–112.
- [7] D. Dengler, PhD Thesis, University of Stuttgart, **2016**.
- [8] STOE & Cie. X-Red, Darmstadt, Germany, **2002**.
- [9] R. H. Blessing, *Acta Crystallogr., Sect. A* **1995**, *51*, 33–38.
- [10] A. L. Spek, *Acta Crystallogr., Sect. D* **2009**, *65*, 148–155.
- [11] G. M. Sheldrick. SHELXL-2014/7, Göttingen, Germany, **2014**.
- [12] G. M. Sheldrick, *Acta Crystallogr., Sect. A* **2015**, *71*, 3–8.
- [13] F. Neese, *WIREs Comput. Mol. Sci.* **2012**, *2*, 73–78.
- [14] A. D. Becke, *J. Chem. Phys.* **1993**, *98*, 5648–5652.
- [15] F. Weigend, R. Ahlrichs, *Phys. Chem. Chem. Phys.* **2005**, *7*, 3297–3305.
- [16] F. Weigend, *Phys. Chem. Chem. Phys.* **2006**, *8*, 1057–1065.
- [17] D. A. Pantazis, X.-Y. Chen, C. R. Landis, F. Neese, *J. Chem. Theory Comput.* **2008**, *4*, 908–919.
- [18] E. van Lenthe, E. J. Baerends, J. G. Snijders, *J. Chem. Phys.* **1993**, *99*, 4597–4610.
- [19] S. Grimme, J. Antony, S. Ehrlich, H. Krieg, *J. Chem. Phys.* **2010**, *132*, 154104.
- [20] S. Grimme, S. Ehrlich, L. Goerigk, *J. Comput. Chem.* **2011**, *32*, 1456–1465.
- [21] V. Barone, M. Cossi, *J. Phys. Chem. A* **1998**, *102*, 1995–2001.
- [22] F. Plasser, TheoDORE: at <http://theodore-qc.sourceforge.net>.
- [23] F. Plasser, *J. Chem. Phys.* **2020**, *152*, 84108.
- [24] B. O. Roos, P. R. Taylor, P. E. Sigbahn, *Chem. Phys.* **1980**, *48*, 157–173.
- [25] P. E. M. Siegbahn, J. Almlöf, A. Heiberg, B. O. Roos, *J. Chem. Phys.* **1981**, *74*, 2384–2396.
- [26] C. Angeli, R. Cimraglia, S. Evangelisti, T. Leininger, J.-P. Malrieu, *J. Chem. Phys.* **2001**, *114*, 10252–10264.

- [27] C. Angeli, R. Cimiraglia, *Theoret. Chim. Acta* **2002**, *107*, 313–317.
- [28] F. Neese, *J. Chem. Phys.* **2005**, *122*, 034107.
- [29] B. A. Hess, C. M. Marian, In *Computational Molecular Spectroscopy*, P. B. Jensen, Ed. Wiley: New York, **2000**, pp. 169.
- [30] B. Cahier, R. Maurice, H. Bolvin, T. Mallah, N. Guihéry, *Magnetochemistry* **2016**, *2*, 31.
- [31] B. O. Roos, P. A. Malmqvist, *Phys. Chem. Chem. Phys.* **2004**, *6*, 2919–2927.
- [32] P. Durand, J.-P. Malrieu, In *Advances in Chemical Physics: Ab Initio Methods in Quantum Chemistry*, K. P. Lawley, Ed., John Wiley & Sons Ltd.: Hoboken, NJ, **1987**, Vol. 67, Part 1, pp. 321–412.
- [33] P. Alemany, D. Casanova, S. Alvarez, C. Dryzun, D. Avnir, *Continuous Symmetry Measures: A New Tool in Quantum Chemistry* in *Reviews in Computational Chemistry* (Eds.: A. L. Parrill , K. B. Lipkowitz), Vol. 30, John Wiley & Sons, Hoboken, NJ, USA, **2017**, pp. 289–352.
- [34] R. Boça, *Coord. Chem. Rev.* **2004**, *248*, 757–815.
- [35] P. H. Butler, *Point Group Symmetry Applications: Methods and Tables*, Plenum Press, New York, **1981**.
- [36] S. B. Piepho and P. N. Schatz, *Group Theory in Spectroscopy with Applications to Magnetic Circular Dichroism*, John Wiley & Sons, New York, **1983**.
- [37] J. Bradley, A. Thomson, E. McInnes, R. Winpenny, G. Timco, *Dalton Trans.* **2008**, 3311–3319.

6.4 Supporting Information to Chapter 3.4 („Structure and Electronic Properties of an Expanded Terpyridine Complex of Nickel(II) [Ni(ddpd)₂](BF₄)₂)”)

Z. Anorg. Allg. Chem. **2018** · ISSN 0044–2313

SUPPORTING INFORMATION

Title: Structure and Electronic Properties of an Expanded Terpyridine Complex of Nickel(II) [Ni(ddpd)₂](BF₄)₂

Author(s): M. Dorn, K. Mack, L. M. Carrella, E. Rentschler, C. Förster,* K. Heinze*

Ref. No.: z201800101

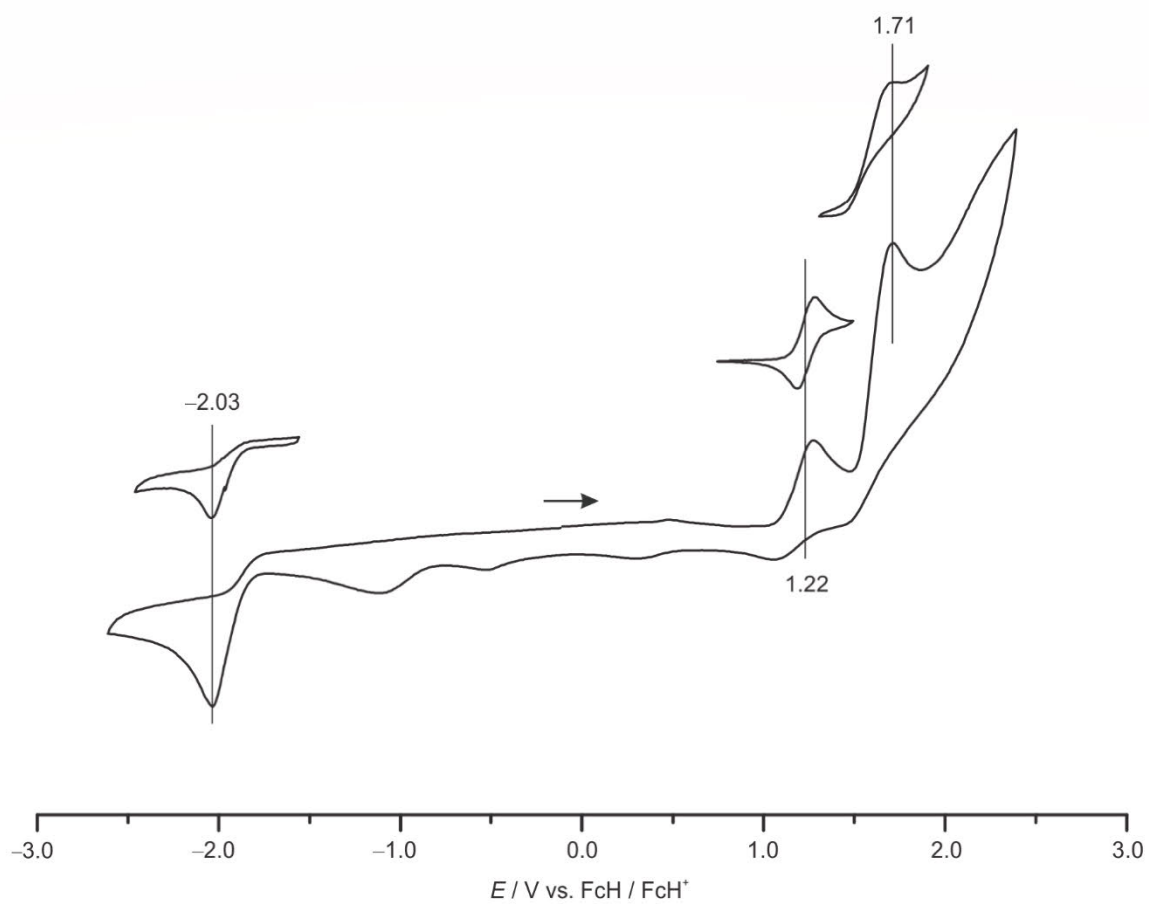


Figure S1. Cyclic voltammogram of $1(\text{BF}_4)_2$ in acetonitrile / $[\text{nBu}_4\text{N}][\text{PF}_6]$ Insets show single redox waves.

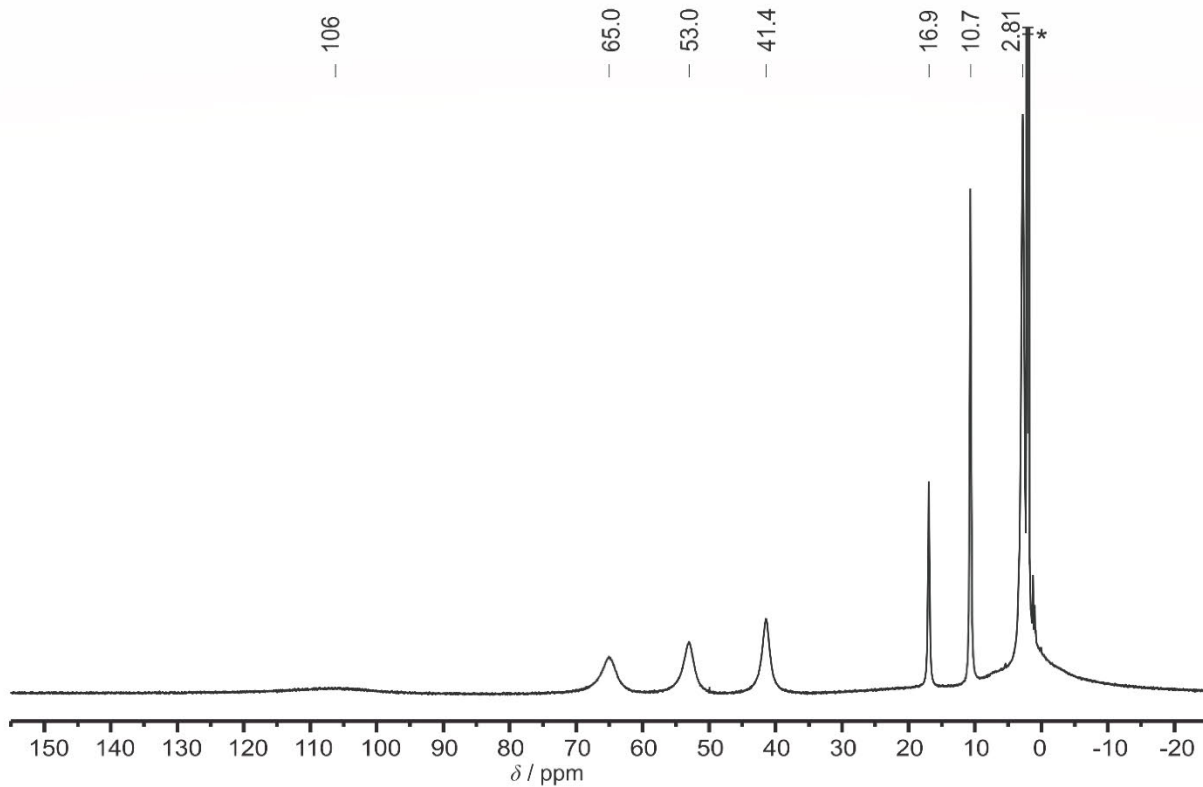


Figure S2. ^1H NMR spectrum of $\mathbf{1}(\text{BF}_4)_2$ in CD_3CN . * indicates solvent and water signal.

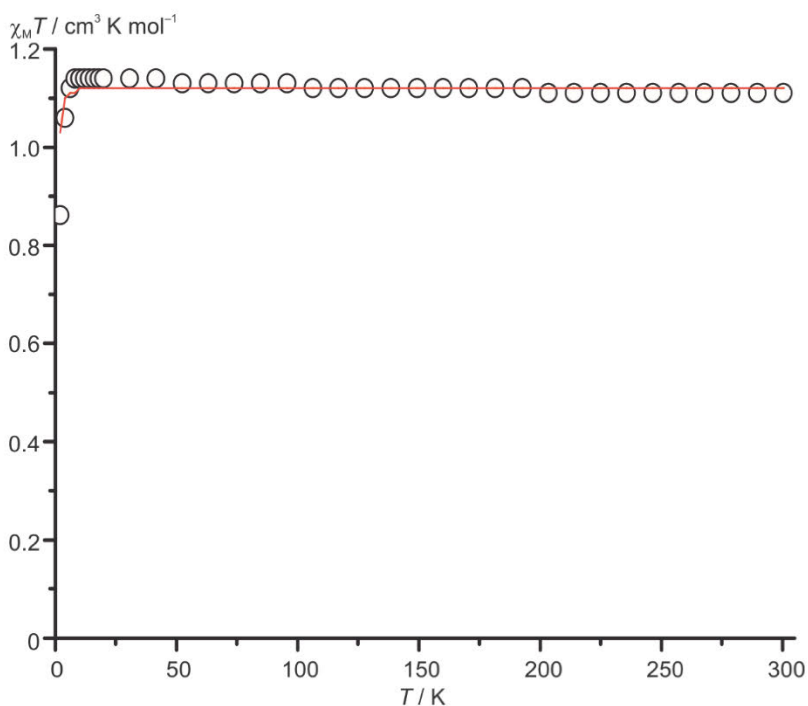


Figure S3. Temperature-dependence of $\chi_M T$ of $\mathbf{1}(\text{BF}_4)_2$ (circles) with fit (solid line, $g = 2.12$).

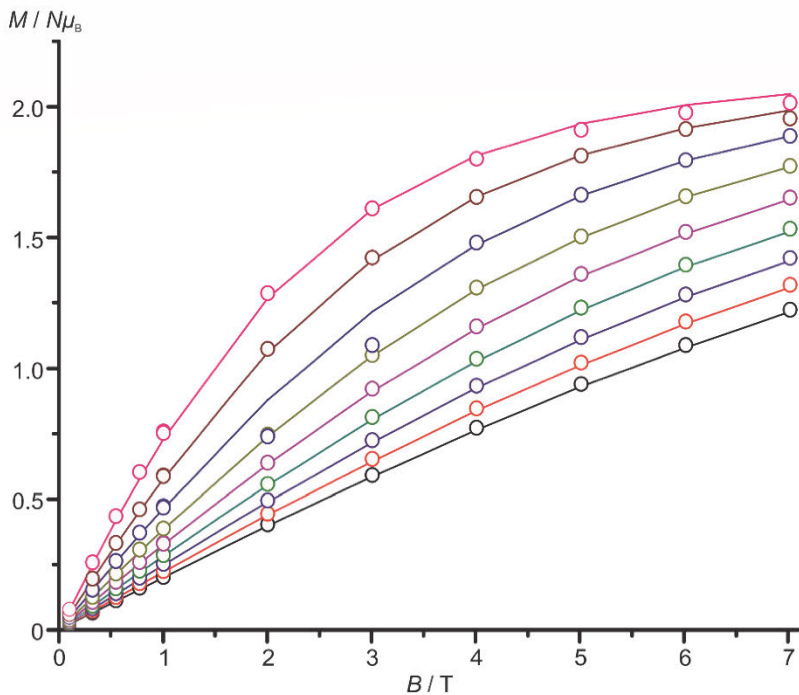


Figure S4. Magnetization measurements of $1(\text{BF}_4)_2$ at 10, 9, 8, 7, 6, 5, 4, 3 and 2 K (circles) and simulation (solid lines) with $g = 2.13(1)$ and ZFS $D = +2.98(11) \text{ cm}^{-1}$.

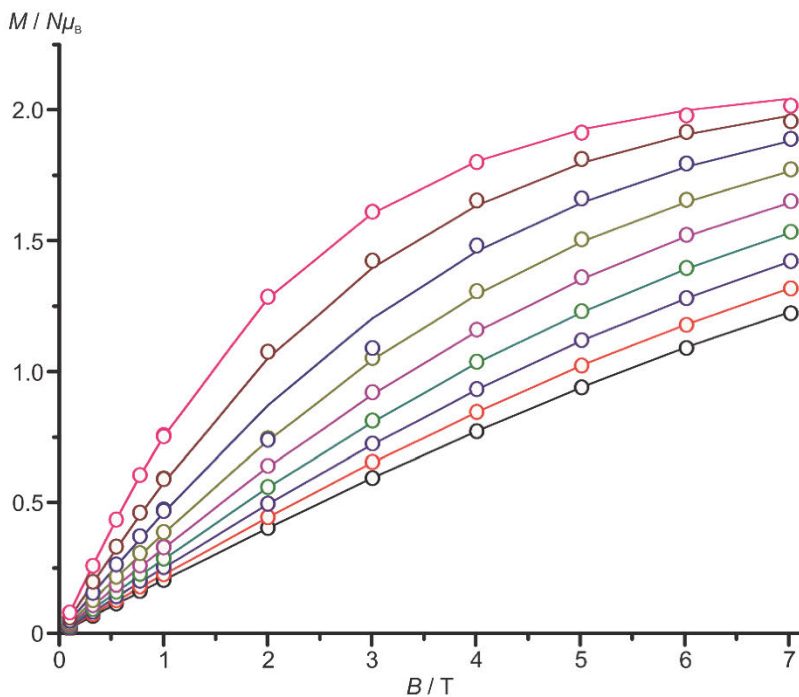


Figure S5. Magnetization measurements of $1(\text{BF}_4)_2$ at 10, 9, 8, 7, 6, 5, 4, 3 and 2 K (circles) and simulation (solid lines) with $g = 2.15(1)$ and ZFS $D = -4.62(18) \text{ cm}^{-1}$.

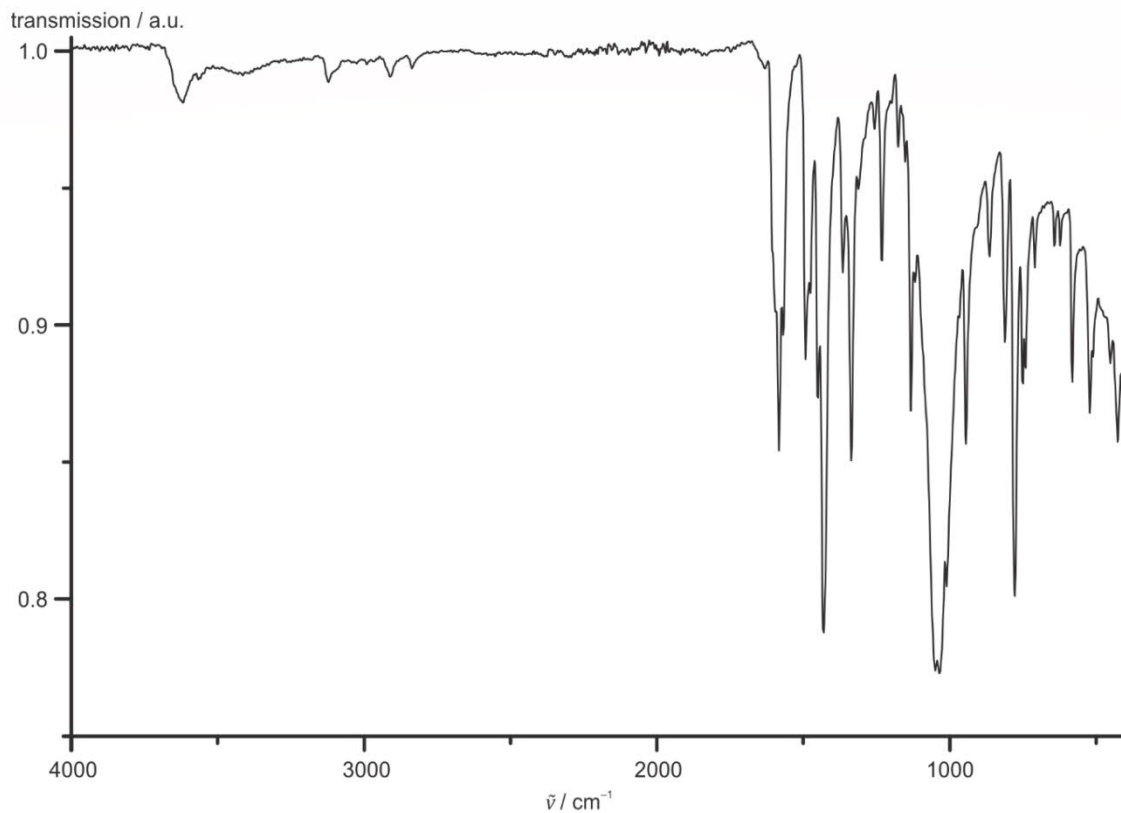


Figure S6. ATR IR spectrum of $1(\text{BF}_4)_2$.

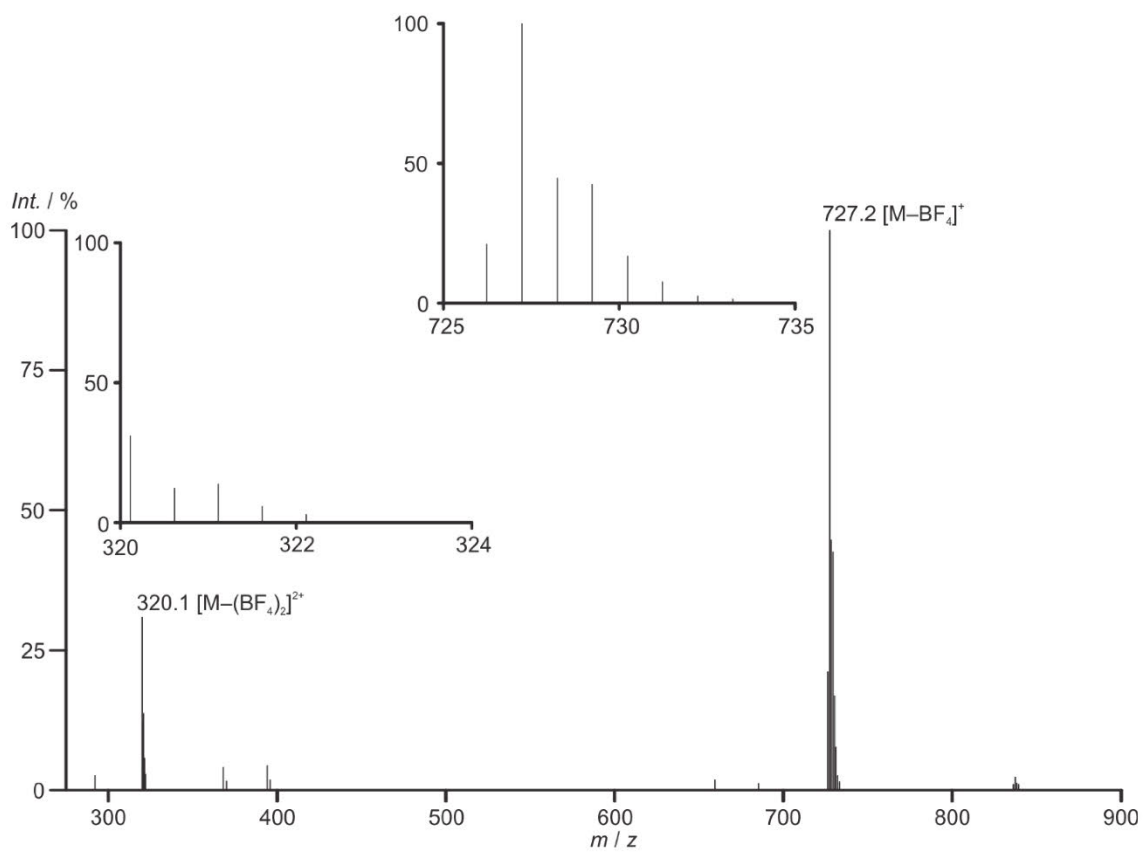


Figure S7. ESI⁺ mass spectrum of $1(\text{BF}_4)_2$.

7. Acknowledgements

[Redacted text block]

8. Curriculum Vitae

Matthias Dorn

Anschrift: Am Sportfeld 3 b, 55124 Mainz

Geboren am 24.10.1990

Geburtsort: Weilburg a. d. Lahn

Mobil: +49 152 0210 0329



Berufserfahrung

[Redacted]

[Redacted]

- [Redacted]
- [Redacted]
- [Redacted]

Bildungsweg

[Redacted]

- [Redacted]

[Redacted]

- [Redacted]

[Redacted]

[Redacted]

Kenntnisse

